Transactions of the ASME

Journal of Heat Transfer (ISSN 0022-1481) is edited and published quarterly at the offices of The American Society of Mechanical Engineers, United Engineering Center, 345 E. 47th St., New York, N. Y. 10017. ASME-TWX No. 710-581-5267, New York. Second-class postage paid at New York, N. Y., and at additional mailing offices.

CHANGES OF ADDRESS must be received at Society headquarters seven weeks before they are to be effective. Please send old label and new address.

PRICES: To members, $30.00, annually; to nonmembers, $60.00. Single copies, $20.00 each. Add $5.00 for postage to countries outside the United States and Canada.

INDEXED by the Engineering Index, Inc.

Journal of Heat Transfer

Published Quarterly by The American Society of Mechanical Engineers
VOLUME 103 • NUMBER 4 • NOVEMBER 1981

ANNOUNCEMENTS

622 Mandatory excess-page charges

678 Change of address form for subscribers

796 Call for papers: International Symposium on Applications of Laser-Doppler Anemometry to Fluid Mechanics

826 Call for papers: 1982 ASME Winter Annual Meeting, Heat Transfer Sessions

Inside back cover Information for Authors

TECHNICAL PAPERS

609 The Influences of Property Variations on Natural Convection from Vertical Surfaces
A. M. Clausing and S. N. Kempka

613 Reference Temperatures for Supercritical Laminar Free Convection on a Vertical Flat Plate
A. J. Ghajar and J. D. Parker

617 Heat Transfer in Air Enclosures of Aspect Ratio Less than One
V. Sernas and E. I. Lee

623 Natural Convection in Undivided and Partially Divided Rectangular Enclosures
M. W. Nansteel and R. Greif

630 Natural Convection Heat Transfer Coefficients for a Short Horizontal Cylinder Attached to a Vertical Plate
E. M. Sparrow and G. M. Chrysler

638 Effect of Vertical Separation Distance and Cylinder-to-Cylinder Temperature Imbalance on Natural Convection for a Pair of Horizontal Cylinders
E. M. Sparrow and J. E. Niethammer

645 Experimental and Analytical Investigation of a Natural Circulation System with Parallel Loops
Y. Zvirin, P. R. Jeuck III, C. W. Sullivan, and R. B. Duffey

653 Refilling and Rewetting of a Hot Horizontal Tube
A. M. C. Chan and S. Banerjee

660 Critical Heat Flux in Helically Coiled Tubes
M. K. Jensen and A. E. Bergles

667 A Nondimensional Analysis of Boiling Dry a Vertical Channel with a Uniform Heat Flux (81-WA/HT-60)
K. H. Sun, R. B. Duffey and C. Lin

673 An Analytical and Experimental Investigation of Bubble Waiting Time in Nucleate Boiling
Ameer Ali and R. L. Judd

679 Convective Heat Transfer to Turbulent Droplet Flow in Circular Tubes
A. G. Rane and Shi-Chune Yao

685 Steam Condensation on Various Gold Surfaces (81-HT-15)
D. W. Woodruff and J.W. Westwater

693 Heat-Exchanger Effectiveness in Thermoelectric Power Generation
M. S. Bohn

699 A General Extended Surface Analysis Method
A. D. Snider and A. D. Kraus

705 Prediction of Heat Transfer Coefficients in Gas Flow Normal to Finned and Smooth Tube Banks
J. C. Biery

715 Modeling of a Rotary Dry Cooling Tower (80-HT-95)
J. A. Valenzuela and L. R. Glickman

720 Heat Transfer and Interface Motion During Melting and Solidification around a Finned Heat Source/Sink (80-HT-10)
A. G. Bathelt and R. Viskanta

727 On the Prediction of Fusion Rate of Ice by Finite Element Analysis
T. R. Hsu and G. Pizey

(Contents continued on page 629)

733 An Experimental Investigation of Ice Formation around an Isothermally Cooled Cylinder in Crossflow
K. C. Cheng, Hideo Inaba, and R. R. Gilpin

739 Quasi-Steady-State Temperature Distribution in Periodically Contacting Finite Regions
B. Vick and M. N. Ozisik

745 Thermally Symmetric Nonlinear Heat Transfer in Solids
M. Imber

753 Numerical Solution to a Two-Dimensional Conduction Problem Using Rectangular and Cylindrical Body-Fitted Coordinate Systems
A. Goldman and Y. C. Kao

759 Unsteady Surface Element Method
N. R. Keltner and J. V. Beck

765 Heat Transfer in Cooled Porous Region with Curved Boundary
R. Siegel and A. Snyder

772 An Integral Analysis for Heat Transfer in Turbulent Incompressible Boundary Layer Flow
L. C. Thomas and M. M. Al-Sharif

778 Measured Heat Transfer Coefficients at and Adjacent to the Tip of a Wall-Attached Cylinder in Crossflow—Application to Fins
E. M. Sparrow and F. Samie

785 Steady Laminar Flow through Twisted Pipes: Fluid Flow in Square Tubes
J. H. Masliyah and K. Nandakumar

791 Steady Laminar Flow through Twisted Pipes: Heat Transfer in Square Tubes
J. H. Masliyah and K. Nandakumar

797 A Numerical Study of Natural Convection in a Horizontal Porous Layer Subjected to an End-to-End Temperature Difference
C. E. Hickox and D. K. Gartling

803 Natural Convective Boundary-Layer on Two-Dimensional and Axisymmetric Surfaces in High-Pr Fluids or in Fluid-Saturated Porous Media
R. H. Nilson

808 A Simplified Approach to the Evaluation of the Geometric-Mean Transmittance and Absorptance for Gas Enclosures
W. W. Yuen

TECHNICAL NOTES

814 Optimum Cylindrical Pin Fin
A. Sonn and A. Bar-Cohen

815 Heat Transfer from a Cone Spinning in a Corotating Fluid
N. R. Vira and Dah-Nien Fan

817 Experimental Free Convection from an Inclined Cylinder
W. E. Stewart

819 Laminar Free Convection Boundary Layer Heat Transfer over Non-Isothermal Surface
F. N. Lin and S. Y. Chern

821 Conduction Shape Factors for Certain Multi-Hole Prismatic Bars
A. K. Naghdi

DISCUSSION

824 Discussion of previously published papers by
E. M. Sparrow and K. K. Tien, K. K. Tien and E. M. Sparrow, and E. M. Sparrow, J. W. Ramsey, and E. A. Mass

825 Discussion of previously published paper by
E. M. Sparrow, J. W. Ramsey, and J. S. Harris

The Influences of Property Variations on Natural Convection from Vertical Surfaces

A. M. Clausing
Associate Professor.
Mem. ASME

S. N. Kempka
Graduate Research Assistant.

Department of Mechanical and Industrial Engineering,
University of Illinois at Urbana-Champaign,
Urbana, Ill. 61801

The objective of this paper is to show the influences of property variations in natural convection. Heat transfer from a vertical isothermal, heated surface to gaseous nitrogen is experimentally investigated. The ambient temperature, T_∞, is varied in order to cover a large range of the Rayleigh number and also to enable the generation of large values of this parameter. The range 80 K $< T_\infty <$ 320 K results in Rayleigh numbers between 10^7 and 2×10^{10} for the 0.28 m model. By using a cryogenic environment, large ratios of the absolute temperature of the wall to the ambient temperature, T_w/T_∞, are generated without the results being masked by radiative heat transfer. The range $1 < T_w/T_\infty < 2.6$ is investigated. Variable properties cause dramatic increases in heat transfer rates in the turbulent regime, and virtually no influence is seen in the laminar regime. The results obtained correlate extremely well with the addition of a single parameter T_w/T_∞.

Introduction

Free-convective flow results from the presence of a buoyancy force. The buoyancy arises from density differences which, in the absence of mass transfer, are a consequence of temperature gradients in the fluid. A common practice in the many experimental and analytical studies during the past decades is to neglect all property variations other than the essential density difference just noted. This greatly simplifies analytical and experimental studies since the number of variables which must be considered is vastly reduced.

This approach, which will be referred to as the constant property case or the constant property assumption, is valid as long as the ratio of the absolute temperature of the wall to the absolute ambient temperature, T_w/T_∞, is near unity. Many applications exist, however, where T_w/T_∞ is appreciably different than unity. For example, in the determination of the convective heat loss from solar receivers, the regime of interest is $1 < T_w/T_\infty < 4$. Likewise, experimentalists often use ratios of T_w/T_∞ which are noticeably different than unity. The reference temperature can strongly influence the values of the governing dimensionless parameters and the agreement which is obtained with other investigators.

If the influence of variable properties is not important, liquids can be substituted for gases in natural convection studies as is sometimes done in order to generate larger Rayleigh numbers. However, the properties of liquids behave quite differently with temperature changes. For example, the thermal conductivity and viscosity of air at moderate temperatures are proportional to the absolute temperature to the 0.8 power. The thermal conductivity of most liquids, on the other hand, is relatively independent of temperature, and the viscosity *decreases* markedly with *increasing* temperature. Thus, such substitutions are clearly valid only if the influences of variable properties are known to be small. For the same reason, utilization of the analogy between heat and mass transfer also has its limitations. Natural convection heat transfer in gases is of interest in this study.

Although few systematic studies of the influences of variable properties have been made, some investigators have attempted to account for such influences by one of two commonly used schemes: the *reference temperature method* and the *property ratio method*. A temperature is chosen in the reference temperature method at which the properties are evaluated such that empirically or analytically derived constant-property results approximate the variable property behavior. In the property ratio method, all properties are typically evaluated at the free-stream temperature or the film temperature, $T_f = (T_w + T_\infty)/2$. Variable property influences are then accounted for with multiplication by a function of the ratio of some pertinent property evaluated at the surface temperature to that property evaluated at the free-stream or film temperature.

Some early studies indicate that variable property influences can be adequately accounted for using the reference temperature method with the reference temperature, T_r, simply set equal to the film temperature, $T_f = (T_w + T_\infty)/2$. Data reviewed by Morgan [1] for natural convection from horizontal cylinders showed no systematic effect of T_w/T_∞ on Nu_f for $10^4 < \mathrm{Ra}_f < 10^8$ for the range $1.02 < T_w/T_\infty < 5.78$. Data for vertical plates are not available, but the analytical study by Sparrow and Gregg [2] for laminar free convection on an isothermal vertical flat plate showed little or no effect. Specifically, the constant-property problem is identical to that for a perfect gas having the property variations: $\rho\mu$ = constant and ρk = constant. Results presented for a more realistic gas model showed an error of less than 2 percent if β is based on T_∞ and all other properties are based on T_f for the range $0.3 < T_w/T_\infty < 4$. These results need to be experimentally verified.

On the other hand, a recent numerical solution by Siebers [3] of turbulent, two-dimensional, natural convection heat transfer for a high temperature, vertical surface showed a strong influence due to variable properties. He investigated the natural convection heat transfer from an external solar receiver—the same problem being experimentally studied by the authors. Siebers concluded that "the model, which is based on realistic physical assumptions, estimates heat transfer rates 50 to 100 percent higher[1] for temperature and Grashof numbers in the range of interest to receivers." Again no experimental evidence is available to support this conclusion.

One of the problems associated with studying the influence of variable properties experimentally is the difficulty of accurately measuring the convective heat exchange. An investigation of the turbulent regime necessitates the use of large characteristic lengths, and large values of the ratio T_w/T_∞ usually result in radiative heat transfer rates which mask the convective heat flow. Clausing [4] showed the advantage of using a cryogenic environment in the experimental study of natural, forced, and combined convective heat transfer. The advantage of this environment for an investigation of the influences of variable properties was also indicated.

The objective of this investigation is to show the influences of variable properties in natural convection. Laminar, transitional and turbulent flow regimes are considered. A single cylindrical model with

Contributed by the Heat Transfer Division and presented in a symposium volume of the Winter Annual Meeting, November 15–20, 1981, Washington, D. C., of THE AMERICAN SOCIETY OF MECHANICAL ENGINEERS. Manuscript received by the Heat Transfer Division February 16, 1981.

[1] Higher than estimates obtained with the same numerical model with T_w/T_∞ near unity.

an aspect ratio of two, a model of the Barstow solar receiver, is used in order to enable the simultaneous investigations of the combined and forced convection regimes. This paper is limited to pure natural convection from a vertical surface.

Description of Experimental Apparatus and Procedure

The Cryogenic Heat Transfer Facility (CHTF) constructed at the University of Illinois at Urbana-Champaign is being used in this investigation. It has an 0.6 m wide by 1.2 m high test section and is capable of operation at any ambient temperature in the range 80 K < T_∞ < 350 K. The facility was constructed for the study of forced and combined convection as well as pure natural convection. It is a recirculating, liquid-nitrogen cooled design which uses gaseous nitrogen as the working fluid. An 11.5 kW d-c motor drives two 0.5 m dia cast aluminum fans to provide test section velocities from 0 to 8 m/s. A 0.4 m thick wall of closed-cell polyurethane foam is sandwiched around a vapor barrier to reduce heat gain and air infiltration. The tunnel ambient temperature is reduced by the vaporization of liquid nitrogen in wall mounted heat exchanger panels. A more detailed description of the facility including velocity and turbulence intensity distributions in the test section is given in reference [5]. Drag coefficient, base pressure coefficient, and heat transfer data for forced convection over a full span cylinder are also provided in reference [5].

In natural convection tests, the flow of liquid nitrogen is stopped, and the liquid nitrogen is purged from the heat exchanger panels. The gaseous nitrogen in the tunnel is circulated until all of the tunnel hardware reaches thermal equilibrium. The variation of the ambient temperature and the thermal stratification in the test section, which occur during any given natural convection test, are both reduced to negligible quantities in this manner. A natural convection test is not begun until at least four minutes after the fans are shut off in order to insure a quiescent environment.

A truncated cylinder with a diameter, D, of 0.14 m and a length, L, of 0.28 m is being used. The 6.60 mm thick, aluminum walls of the model serve as a transient calorimeter. Hence, the average heat transfer coefficient is determined from

$$h = \frac{-mc_p/A\ (dT_w/dt) - \epsilon\sigma(T_w{}^4 - T_\infty{}^4)}{(T_w - T_\infty)} \quad (1)$$

where m is the mass of the aluminum cylinder; c_p is its specific heat; A ($=\pi DL$) is the heat transfer area; ϵ is the emittance which for the polished aluminum cylinder is assumed to be 0.11; and σ is the Stefan-Boltzmann constant. The heat transfer surface is assumed to be gray, and the surroundings are assumed to be isothermal and black. The model is heated to a desired temperature level while located in an insulating shroud. The average heat transfer coefficient is determined from the rate at which the model cools, dT_w/dt. Equation (1) is valid since the gradients within the model are negligible (note: the Biot modulus is less than 10^{-3}), and the thermal capacitance of the components which are in thermal contact with the model are negligible.

The design of the model is depicted in Fig. 1. The model is heated with 6.4 mm wide ribbons of nichrome foil which are mounted on a 3.2 mm thick, NTF foam cylinder that fits concentrically within the aluminum model. The NTF foam is a proprietary, low density, low conductivity, cryogenic insulation which was developed for the National Transonic Facility. The interior of this cylinder is filled with fiberglass insulation to eliminate convection inside the model. NTF

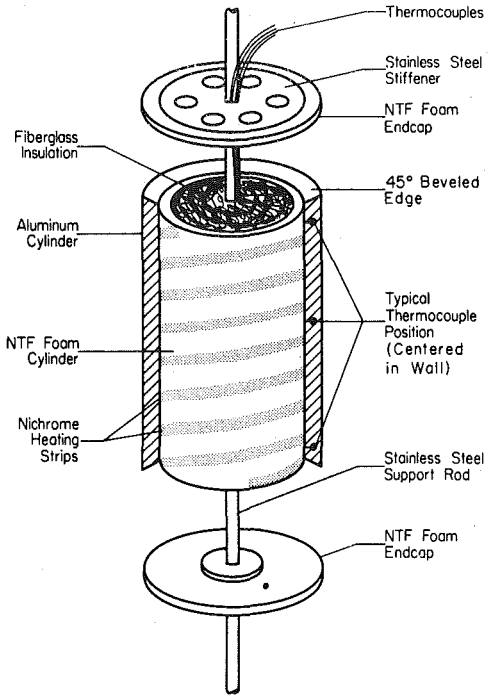

Fig. 1 Model assembly

foam endcaps serve to locate the model on the stainless steel support rod and seal the interior of the model from the external flow. The endcaps have 45 deg beveled edges and are glued to the top and bottom of the aluminum cylinder which also has 45 deg beveled edges (see Fig. 1). The endcaps are externally reinforced with perforated, 0.39 mm thick, stainless steel disks. The thermal capacitance of the nichrome heater and the NTF foam cylinder on which the nichrome ribbon is mounted is 1.3 percent of the thermal capacitance of the aluminum calorimeter.

The temperature of the gas in the test section is measured with a grid of eight 30-gauge copper-constantan special accuracy thermocouples. Wire from the same spool was used for the 12 thermocouples strategically located in the model which are used to determine dT_w/dt and to detect axial and circumferential temperature gradients. These thermocouples are inserted into 1.2 mm dia by 3.2 mm deep holes which are radially drilled from the inside of the cylinder. Lead foil is compacted around the thermocouples to hold them in place and insure good thermal contact with the model. A thermoelectric refrigerator system is used to establish O C reference junctions for all thermocouples.

All thermocouples outputs are scanned at 5 s intervals with a data logger, recorded on magnetic tape, and computer processed. The derivative, dT_w/dt, is calculated numerically. The total error in h resulting from errors in $(T_w - T_\infty)$ and dT_w/dt is estimated to be less than 3 percent. A typical test lasts 500 s during which time the change in T_w is several degrees Kelvin. Hence, each test run results in es-

Nomenclature

A = heat transfer area, m^2
c_p = specific heat, kJ/kg-K
g = gravitational constant, m/s^2
h = convective heat transfer coefficient, W/m^2-K
k = thermal conductivity, W/m-K
L = characteristic vertical length, m
m = mass of model, kg
T = temperature, K
t = time, s
β = coefficient of thermal expansion, 1/K
$\Delta T = T_w - T_\infty$, K
ϵ = emissivity
μ = dynamic viscosity, kg/m-s
ρ = density, kg/m^3
σ = Stefan-Boltzmann constant, W/m^2-K^4
Gr = Grashoff number, $\rho^2 g\beta\Delta TL^3/\mu^2$
Nu = Nusselt number, hL/k
Pr = Prandtl number, $\mu c_p/k$
Ra = Rayleigh number, GrPr

Subscripts

f = properties based on film temperature, $T_f = \frac{1}{2}(T_w + T_\infty)$
r = reference value
w = wall
∞ = ambient fluid

sentially a single data point. Additional details on the experimental apparatus, the procedure, and the accuracy of the results are provided in reference [6].

Similitude Considerations

Although a cylindrical geometry is being used, the effect of the transverse curvature is negligible for the conditions of this investigation (see references and results provided in [6]). Thus, a single characteristic length L, the height of the cylinder, is of importance. The set of dimensionless groups which influence the natural convection heat transfer is deduced by an examination of the governing equations. The simplifying assumptions are: (*i*) a laminar flow of a Newtonian fluid, (*ii*) a perfect gas, (*iii*) negligible viscous dissipation and work done by compression, (*iv*) the dependent variables c_p/c_{pr}, μ/μ_r, and k/k_r are general functions of the dimensionless temperature, T/T_r, (*v*) an isothermal surface at T_w, and (*vi*) an isothermal ambient at T_∞ which is quiescent. The Boussinesq approximation is not used.

The dimensional analysis with these assumptions shows that the average Nusselt number is dependent on

$$\mathrm{Nu}_f = f(\mathrm{Gr}_f, \mathrm{Pr}_f, T_w/T_\infty) \tag{2}$$

where Gr and Pr are the Grashof and Prandtl numbers, respectively. Thus, variable properties result in the addition of a single additional dimensionless group, T_w/T_∞.

The Prandtl number in this investigation is essentially a constant, 0.7, and its influence is not resolved. Experience has shown that for T_w/T_∞ near unity, the form of equation (2) is valid for both laminar and turbulent flow, and Gr and Pr can be replaced by a single variable, the Rayleigh number, Ra = GrPr. The specific form of the correlation used in this investigation is

$$\mathrm{Nu}_f = g(\mathrm{Ra}_f) f(T_w/T_\infty) \tag{3}$$

Furthermore, the function $g(\mathrm{Ra})$ is defined to be the constant property correlation; i.e., $f(2)$ is unity. Dimensional analysis does not enable one to reduce equation (2) to equation (3). Equation (3) is experimentally verified.

The proposed method of accounting for variable properties, equation (3), is seen to be different than both commonly used procedures, the reference temperature method and the property ratio method. It is similar to the property ratio method. Yet, the stringent constraint of having to account for variable property influences with a function of a single property ratio is alleviated.

Results

Results from experiments with $T_w/T_\infty < 1.15$ and ambient temperatures from 300 to 80 K are shown in Fig. 2. The parameter, T_∞, is given for each data point. It is seen that a range of approximately three orders of magnitude in the Rayleigh number is covered by changing T_∞—a big advantage of the cryogenic facility. The laminar data, $\mathrm{Ra}_f < 3.8 \times 10^8$, all lie within 2 percent of the Schmidt and Beckmann correlation [7], $\mathrm{Nu}_f = 0.52\,\mathrm{Ra}_f^{1/4}$. In the turbulent regime, $\mathrm{Ra}_f > 1.6 \times 10^9$, the data agree best with the Bayley correlation [8], $\mathrm{Nu}_f = 0.10\,\mathrm{Ra}_f^{1/3}$. The maximum deviation from this correlation is less than 8 percent.

All of the data from this investigation are given in Fig. 3. This figure is identical to Fig. 2 except the data are not limited to $T_w/T_\infty < 1.15$ but cover the range $1 < T_w/T_\infty < 2.6$. In the laminar regime, no influence of the parameter T_w/T_∞ is seen; all data still lie within 3 percent of the Schmidt and Beckmann correlation. On the other hand, large deviations from the Bayley correlation are now present in the turbulent regime which are even more evident in the enlarged view of this regime provided in Fig. 4. The parameter, T_w/T_∞, which is provided for the one set of data in Fig. 4, reveals the dependence of the deviation on T_w/T_∞.

Consider next the application of the variable property correlation, equation (3). If the correlation for the constant property Nusselt number, $g(\mathrm{Ra}_f)$, is assumed to be the Bayley correlation, then the function $f(T_w/T_\infty)$ follows from equation (3) as $\mathrm{Nu}_f/(0.10\,\mathrm{Ra}^{1/3})$. The experimental measurements of $f(T_w/T_\infty)$ are given in Fig. 5. A second degree, least squares fit of all data with $1.3 < T_w/T_\infty < 2.6$ gives the function $f(T_w/T_\infty)$—the solid line provided in Fig. 5.

$$f(T_w/T_\infty) = -0.303 + 1.604(T_w/T_\infty) - 0.330(T_w/T_\infty)^2 \qquad 1.3 < T_w/T_\infty < 2.6 \tag{4}$$

The success of this correlation is clearly evident in Fig. 6 which is a plot of $\mathrm{Nu}_f/f(T_w/T_\infty)$. The average deviation between the Bayley correlation $g(\mathrm{Ra}_f)$ and the experimentally derived values of $\mathrm{Nu}_f/f(T_w/T_\infty)$ is only 0.9 percent. The maximum deviation is 3 percent.

The limiting case of $T_w/T_\infty = 1$, the constant property problem, can only be approached experimentally. Equation (4) is valid for the

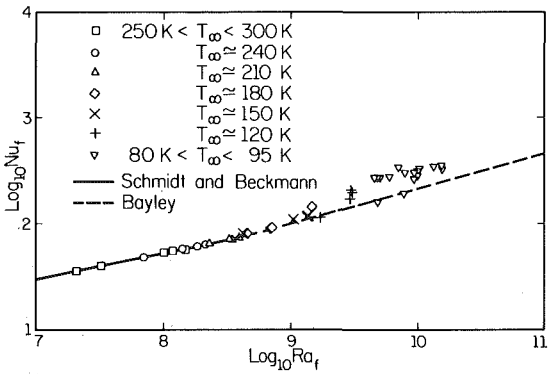

Fig. 3 All data from investigation, $1 < T_w/T_\infty < 2.6$

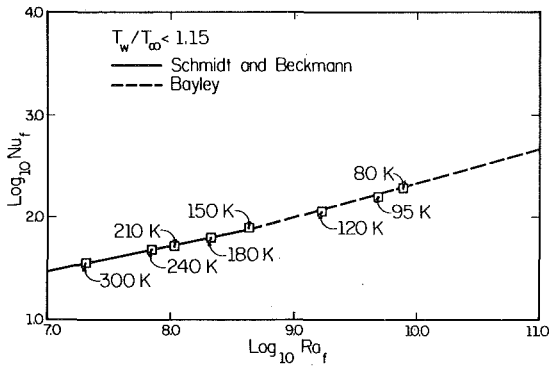

Fig. 2 Comparisons of experimental data with Schmidt/Beckmann and Bayley correlations, $T_w/T_\infty < 1.15$

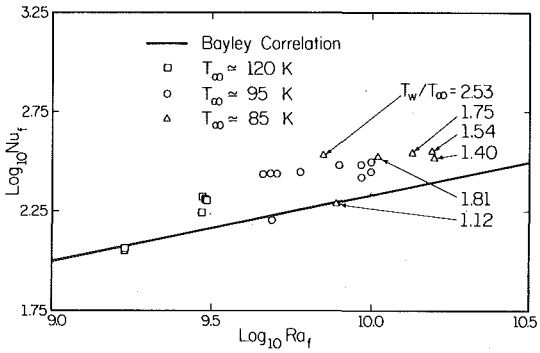

Fig. 4 Turbulent free convection data, $1 < T_w/T_\infty < 2.6$

regime $1.3 < T_w/T_\infty < 2.6$. The simpler correlation

$$\mathrm{Nu}_f = g(\mathrm{Ra}_f)(T_w/T_\infty)^{0.68} \tag{5}$$

can be used in place of equation (3) in the regime $1 < T_w/T_\infty < 2.1$. It has the advantages of simplicity and applicability near $T_w/T_\infty = 1$. The function $(T_w/T_\infty)^{0.68}$ lies within 3 percent of equation (4) over the range $1.1 < T_w/T_\infty < 2.1$. Although the Bayley correlation was assumed for the function $g(\mathrm{Ra}_f)$, the data indicate a $g(\mathrm{Ra}_f)$ which is approximately ten percent smaller.

The transition region was determined from the data to be $3.8 \times 10^8 < \mathrm{Ra}_f < 1.6 \times 10^9$. Specifically, the influence of T_w/T_∞ was negligible for $\mathrm{Ra}_f < 3.8 \times 10^8$ and could be correlated with equation (4) if $\mathrm{Ra}_f > 1.6 \times 10^9$. In the transition region, the data lie between 4 and 9 percent above the predictions of Schmidt and Beckmann ($\mathrm{Ra}_f < 10^9$) and Bayley ($\mathrm{Ra}_f > 10^9$); see Fig. 6.

The advantages of basing all properties in the dimensionless groups on the film temperature as was done in this investigation are: it is a more universal datum; and the influence of T_w/T_∞ is negligible in the laminar regime. On the other hand, the dependency on T_w/T_∞ would be reduced in the turbulent regime if T_∞ were used as the reference temperature.

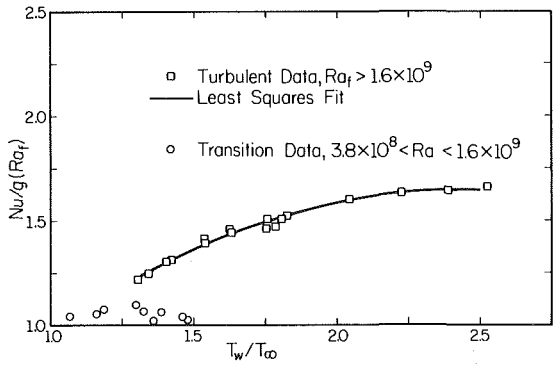

Fig. 5 Variable property data with correlation, $f(T_w/T_\infty)$

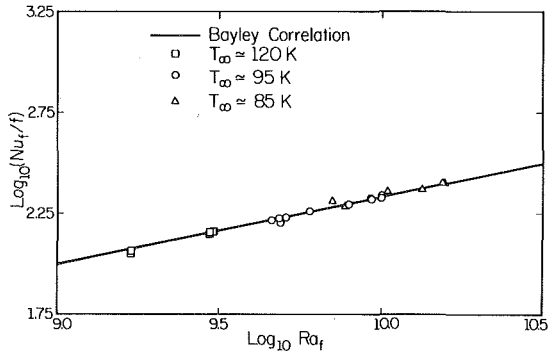

Fig. 6 Comparison of Bayley correlation and experimental data after division by $f(T_w/T_\infty)$ (See equation (3))

Conclusions

The following conclusions are drawn from the results of this investigation of natural convection of a gas over an isothermal vertical surface.

1 The ambient temperature, T_∞, has no explicit, independent influence on the Nusselt number. On the other hand, the Rayleigh number is a strong function of T_∞ as was shown in [4] and is clearly evidenced by the results given in Fig. 2.

2 The results in the laminar regime lie within three percent of the Schmidt and Beckmann correlation, $\mathrm{Nu}_f = 0.52\,\mathrm{Ra}_f^{1/4}$, and the parameter T_w/T_∞ has no detectable influence in this regime provided all properties in the Nusselt and Rayleigh numbers are based on the film temperature.

3 The Nusselt number in the turbulent regime is strongly affected by property variations. Correlations proposed in the literature such as the Bayley correlation, $\mathrm{Nu}_f = 0.10\,\mathrm{Ra}_f^{1/3}$, are only acceptable if T_w/T_∞ is near unity. For example, the Nusselt number at $T_w/T_\infty = 1.8$ is 50 percent greater than the value predicted by the Bayley correlation.

4 In the turbulent regime, the influences of variable properties can be accounted for with a single additional parameter, T_w/T_∞. The form of equation (2), $\mathrm{Nu}_f = g(\mathrm{Ra}_f)\,f(T_w/T_\infty)$, is acceptable. If the Bayley correlation is used for $g(\mathrm{Ra}_f)$, a least squares fit of the data for the range $1.3 < T_w/T_\infty < 2.6$ gives a correlation which lies within 2.7 percent of all data. The average absolute deviation is only 0.9 percent.

Acknowledgment

The authors gratefully acknowledge the financial support of Sandia National Laboratories, Livermore, California, Research Grant No. 87-9180, DOE Subcontract, and the Department of Mechanical Engineering, University of Illinois at Urbana-Champaign.

References

1 Morgan, V. T., "The Overall Convective Heat Transfer from Smooth Circular Cylinders," *Advances in Heat Transfer*, Vol. 11, Academic Press, New York, 1975, pp. 199–264.

2 Sparrow, E. M., and Gregg, J. L., "The Variable Fluid-Property Problem in Free Convection," *Trans. ASME*, Vol. 80, May 1958, pp. 879–886.

3 Siebers, D., "Natural Convection Heat Transfer from an External Receiver," Sandia Laboratories Report SAND 78-8276, Livermore, Calif., Dec. 1979.

4 Clausing, A. M., "Experimental Studies of Forced, Natural, and Combined Convection Heat Transfer at Cryogenic Temperatures," *Proceedings, 1st International Symposium on Cryogenic Wind Tunnels*, Southampton, England, Apr. 1979, pp. 24.1–24.8.

5 Mueller, M. H., et al., "Description of UIUC Cryogenic Wind Tunnel Including Pressure Distributions, Turbulence Measurements and Heat Transfer Data," Univ. of Illinois Tech. Report ME-TN-79-9180-1, Dec. 1979.

6 Kempka, S. N., and Clausing, A. M., "The Influences of Variable Properties on Natural Convection from Vertical Surfaces," Univ. of Illinois Tech. Report ME-TN-81-91802, Jan. 1981.

7 McAdams, W. H., *Heat Transmission*, 3rd ed., McGraw-Hill, New York, 1954, p. 171.

8 Bayley, F. J., "An Analysis of Turbulent Free Convection Heat Transfer," *Proceedings, Institute of Mechanical Engineers*, Vol. 169, No. 20, 1955, pp. 361–370.

Reference Temperatures for Supercritical Laminar Free Convection on a Vertical Flat Plate

A. J. Ghajar
Assistant Professor.
Assoc. Mem. ASME

J. D. Parker
Professor.
Mem. ASME

School of Mechanical and Aerospace Engineering,
Oklahoma State University,
Stillwater, Okla.

A reference temperature method was developed by which heat transfer to fluids in the supercritical region under variable property conditions in laminar free convection on a vertical flat plate can be readily evaluated. Based on this method three generalized plots for Refrigerant-114, water, and carbon dioxide were developed. The results obtained with the reference temperature scheme showed good agreement with the existing experimental data and theoretical results for these three variable property fluids.

An excellent survey of heat transfer to near critical fluids is given by Hendricks, et al. [1]. It has been common to use the reference temperature expression, given by

$$T_{\text{ref}} = T_w - r\,(T_w - T_\infty) \tag{1}$$

In development of the reference temperature method of this study, five different steps had to be accomplished:

1 Calculation of heat transfer coefficients. With the use of the conservation equations and the numerical methods of [2] and [3] variable property Nusselt numbers were calculated for several cases.

2 Development of a correlation for the calculated dimensionless heat transfer data, using results obtained from step 1.

The following basic form was employed to correlate the heat transfer data for the variable property conditions:

$$\text{Nu}_{x,w} = a(\text{Gr}_{x,w})^b\,(\text{Pr}_\infty)^c\left(\frac{T_\infty}{T_w - T_\infty}\right)^d \tag{2}$$

where the constants a, b, c, and d of equation (2) were obtained using a non-linear least squares code [4].

3 Development of a correlation for constant property results. The slope of the temperature profile at the wall, $\theta'(0)$, used in these analyses was obtained from the solutions of the following constant property momentum and energy equations, and their boundary conditions:

$$F''' + 3FF'' - 2(F')^2 + \theta = 0 \tag{3}$$

$$\theta'' + 3\text{Pr}F\theta' = 0 \tag{4}$$

$$\left.\begin{aligned} F &= 0 \\ F' &= 0 \\ \theta &= 1 \end{aligned}\right\}\ \eta = 0 \qquad \left.\begin{aligned} F' &= 0 \\ \theta &= 0 \end{aligned}\right\}\ \eta = \infty \tag{5}$$

In equations (3) and (4), Prandtl number is the single parameter of these equations. However F is a stretched coordinate and this needs to be properly considered. For the pressures and temperatures in this study, Prandtl number covered a range from 0 to 40. For this range of Prandtl numbers the following correlation was obtained for $\theta'(0)$ as a function of Prandtl number:

$$[-\theta'(0)]_{c.p.} = a_1 + b_1(\text{Pr})^{c_1} \tag{6}$$

where $a_1 = 0.10$; $b_1 = 0.486$; and $c_1 = 0.331$.

These constants were obtained using the MARQ program [4]. Equation (6) with the constants given above predicts the slope of the temperature profile at the wall for the constant property cases within an average absolute error of 1.3 percent.

Based on the equations presented in [2] and [3], the slope of the temperature profile at wall, $\theta'(0)$, can be expressed in terms of the dimensionless groups Nusselt number and Grashof number as follows:

$$[-\theta'(0)]_{c.p.} = \frac{\text{Nu}_{x,w}}{(\text{Gr}_{x,w}/4)^{1/4}} \tag{7}$$

4 Development of an optimization procedure to predict reference temperature. For this purpose equation (2) was represented as

$$(\text{Nu}_{x,w})_T = a(\text{Gr}_{x,w})^b{}_T\,(\text{Pr})^c{}_T\left(\frac{T_\infty}{T_w - T_\infty}\right)^d \tag{8}$$

where the properties in the Nusselt number, Grashof number, and Prandtl number were evaluated at a characteristic temperature T, which is a complicated function of wall, free stream, and transposed critical temperatures. The value of T was then optimized between the free stream and wall temperatures until the best agreement between the correlated values, $(\text{Nu}_{x,w})_T$ and $[\text{Nu}_{x,w}/(\text{Gr}_{x,w}/4)^{1/4}]_T$, obtained from equation (8) at temperature T, and the calculated values of $(\text{Nu}_{x,w})$ and $[-\theta'(0)_{c.p.} = \text{Nu}_{x,w}/(\text{Gr}_{x,w}/4)^{1/4}]$ at fixed a, b, c, and d values were reached. This optimum temperature is the reference temperature for that case. In this comparison the calculated Nusselt numbers $(\text{Nu}_{x,w})$ were obtained from the variable property analysis for the cases considered (i.e., step 1), and the values of $\theta'(0)_{c.p.}$ were calculated from equation (6).

5 Development of a general plot for reference temperature. The reference temperature for fluids in the supercritical region is a complicated function of wall, free stream, and transposed critical temperatures. Therefore, it was not possible to express this temperature with a single equation that would represent the fluids in the supercritical region under the physical conditions considered.

The parameter r was plotted with the parameter $(T_M - T_\infty)/(T_w - T_\infty)$ in Fig. 1. This plot was generated for Refrigerant 114 at a constant pressure of 3.7×10^3 kPa (540 psia), and ten different wall temperatures. T_M is that temperature at which specific heat assumes its maximum value. With this type of presentation, the influence of wall temperature T_w has been eliminated since all the points for different T_w values align quite well along a single curve.

The next step was to generalize the single curve in Fig. 1 to cover a wide range of supercritical temperatures and pressures for several fluids. For this purpose Refrigerant-114, water, and carbon dioxide were chosen. The ranges of supercritical temperatures and pressures used to develop the reference temperature plots for the three fluids were:

1 Refrigerant-114 ($P_c = 3.3 \times 10^3$ kPa, $T_c = 145.7$ °C)
   (*a*) Pressure range, $P = 3.4 \times 10^3$, 3.7×10^3, 4.1×10^3 kPa (500, 540, 600 psia)
   (*b*) Temperature range, $T = 149$ to 177°C (300 to 350°F)
2 Water ($P_c = 2.2 \times 10^4$ kPa, $T_c = 374.13$ °C)
   (*a*) Pressure range, $P = 2.3 \times 10^4$, 2.5×10^4, 2.6×10^4 kPa (3400, 3600, 3800 psia)
   (*b*) Temperature range, $T = 379$ to 399°C (715 to 750°F)

Contributed by the Heat Transfer Division for publication in The JOURNAL OF HEAT TRANSFER. Manuscript received by The Heat Transfer Division October 17, 1980.

3 Carbon Dioxide ($P_c = 7.4 \times 10^3$ kPa, $T_c = 31°C$)
   (*a*) Pressure range, $P = 8.3 \times 10^3$, 9.7×10^3, 1.1×10^4 kPa (1200, 1400, 1600 psia)
   (*b*) Temperature range, $T = 32$ to 60°C (90 to 140°F)

The ranges chosen for the above fluids cover the experimental pressure and temperature ranges reported in the literature (see Ghajar [3]).

The first step in the generalization of Fig. 1 was to obtain the dimensionless heat transfer coefficients. For each of the pressures assumed for the three fluids, ten different wall temperatures were chosen. These temperatures were selected to cover the range of temperatures given above. For each case the wall temperature was kept constant and the free stream temperature was varied to within one degree of the specified wall temperature. The dimensionless heat transfer coefficients were then calculated based on the equations, procedures, and computer programs introduced in [2] and [3]. The variable property heat transfer results for each fluid were then correlated with the same type of correlation given by equation (2). The three sets of constants a, b, c, and d are tabulated in Table 1.

Reference Temperature Results

The results for R-114, water, and carbon dioxide are presented in Figs. 2–4. Before discussing the results of these figures, it would be important to first consider the single curve in Fig. 1 (i.e., Refrigerant-114 at a constant pressure of 3.7×10^3 kPa). There are several interesting points to be noted. The curve behaves very nicely and smoothly up to certain values of $(T_M - T_\infty)/(T_w - T_\infty)$ and then there is a sudden abrupt change in the direction and behavior. This abrupt change in the direction of the curve appears to be primarily due to the large influence of closeness of T_w or T_∞ to T_M, the temperature at which specific heat assumes its maximum. This change occurs for the values of $(T_M - T_\infty)/(T_w - T_\infty)$ in the range of −0.25 to 2.00. These values occur where the wall temperature T_w or the free stream temperature T_∞ are within about 2.8°C (5°F) of T_M on both sides of the specific heat peak.

For the cases where both T_w and T_∞ are away from the T_M (on the right side of the specific heat maximum) the direct and strong influence of T_M on the reference temperature vanishes and the variation of r can be represented by a simple curve. In Fig. 1, this simple curve covers the values of $(T_M - T_\infty)/(T_w - T_\infty)$ in the range of −43.0 to 2.0.

The variation of r for Refrigerant-114, water, and carbon dioxide at different supercritical pressures and over a range of temperatures show results similar to the ones presented in Fig. 1. Therefore, the observations and conclusions made about Fig. 1, for a specific fluid at a single pressure, can be employed for Figs. 2–4, for several fluids at several different pressures and temperatures.

Figures 2–4 indicate that it is possible to obtain a single curve for different pressures up to where the influence of closeness to T_M is not significant, that is, when the wall and free stream temperatures were more than about 2.8°C (5°F) to the right of the specific heat peak. For

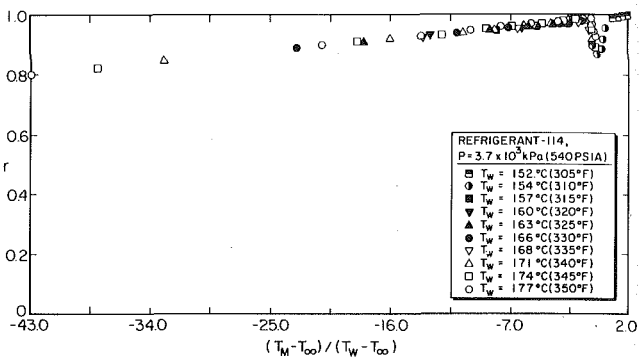

Fig. 1 Variation of r at various temperatures and a single pressure

Table 1 Constants for heat transfer correlation

Fluid	Constants a	b	c	d	Percent Deviation	Range of Application T/T_c	P/P_c
Refrigerant-114	0.3999	0.25	0.3085	0.004972	1.5	1.0076 to 1.0740	1.0638 to 1.2766
Water	0.3153	0.25	0.3921	−0.02230	2.5	1.0080 to 1.0380	1.0598 to 1.1845
Carbon Dioxide	0.3265	0.25	0.4054	−0.02750	2.4	1.0038 to 1.0950	1.1194 to 1.4925

Nomenclature

a,b,c,d = constants used in equations (2) and (8)
a_1,b_1,c_1 = constants used in equation (6)
c_p = specific heat at constant pressure
C = constant, $C = \left[\frac{g}{4\nu^2}\left(\frac{\rho_\infty - \rho_w}{\rho_w}\right)\right]^{1/4}$
$F(\eta)$ = similarity variable, $F(\eta) = \left(\frac{1}{4\nu_w C_w}\right)\left(\frac{\psi}{x^{3/4}}\right)$
Gr = Grashof number, $\mathrm{Gr} = \frac{gL^3}{\nu^2}\left(\frac{\rho_\infty - \rho_w}{\rho_w}\right)$
g = acceleration due to gravity
h = heat transfer coefficient
k = thermal conductivity
L = overall length of plate
Nu = Nusselt number, Nu = hL/k
p = pressure
Pr = Prandtl number
$\dot{q}''$ = heat flux
r = parameter in the reference temperature equation
T = temperature
T_{ref} = reference temperature
T_M = pseudocritical or transposed critical temperature
u = velocity component along the plate
v = velocity component perpendicular to the plate
x = coordinate along the plate
y = coordinate perpendicular to the plate
η = similarity coordinate, $\eta = C_w x^{-1/4} \int_0^y \frac{\rho}{\rho_w} dy$
μ = absolute viscosity
ν = kinematic viscosity, $\nu = \mu/\rho$
ρ = density
ψ = stream function, $u = \frac{\rho_w}{\rho}\left(\frac{\partial \psi}{\partial y}\right)$ and $v = -\frac{\rho_w}{\rho}\left(\frac{\partial \psi}{\partial x}\right)$
$\theta(\eta)$ = dimensionless temperature, $\theta(\eta) = \frac{T - T_\infty}{T_w - T_\infty}$

Subscripts

c = refers to critical property
$c.p.$ = refers to constant property solution
ref = evaluated at the reference temperature
T = evaluated at a characteristic temperature
$v.p.$ = refers to variable property solution
w = evaluated at the wall temperature
x = evaluated at a particular point along a surface, a local parameter as opposed to a mean parameter
∞ = evaluated at the free stream temperature

the cases where T_w or T_∞ are in the vicinity of T_M, a single curve was not obtainable. This was primarily due to the fact that for each pressure the specific heat assumes a different maximum value, since in these cases being close to T_M has a direct and signficant influence on the prediction of the reference temperature.

However, it is interesting to note that for the cases where T_w and T_∞ were close to T_M, the curves for all three pressures for each fluid branched off from the same line. The amount of departure of these curves from the single curve increases as the pressure is increased, since in this range the higher the pressure the further is the maximum peak of specific heat removed from the critical point. For the cases where the free stream temperature was on the left of the specific heat peak, where $(T_M - T_\infty)/(T_w - T_\infty)$ was positive, as soon as the influence of closeness to specific heat maximum was diminished, the curves behaved smoothly again. This phenomenon can best be observed by considering those curves presented obtained for the highest pressure utilized.

The solid lines drawn through the data points present the best fit obtained for the data generated for the fluids under study. Plots similar to the one given in Fig. 1 were generated for the three fluids at every one of the pressures considered. Then, the best fit through the data points in these plots was demonstrated by a solid curve which expresses the variation of r in Figs. 2–4.

Heat Transfer Results

The validity and universality of this method was accomplished by comparing the results calculated with the predicted reference temperatures with the experimental and theoretical variable property results of Fritsch and Grosh [5] for water, Nishikawa, et al. [6] for carbon dioxide, and Parker and Mullin [7] for Refrigerant-114. In addition, some of the variable property heat transfer results obtained with the use of the equations, procedures, and computer programs introduced in [2] and [3] were compared with the constant property heat transfer results obtained with the predicted reference temperatures.

In order to calculate the constant property results, for the free convective problems considered, the dimensionless reference temperatures were obtained from Figs. 2–4 for different values of $(T_M - T_\infty)/(T_w - T_\infty)$ for the fluids of interest. The reference temperatures were then calculated. These reference temperatures were used to evaluate the value of Prandtl number in the constant property equations. The following constant property equations for momentum and energy were used:

$$F''' = -3FF'' + 2(F')^2 - \theta \tag{9}$$

$$\theta'' = -3\mathrm{Pr}_{\mathrm{ref}} F\theta' \tag{10}$$

where $\mathrm{Pr}_{\mathrm{ref}}$ is Prandtl number evaluated at a reference temperature. The boundary conditions for equations (9) and (10) are identical to those given by equation (5).

Equations (9) and (10) were solved using a Lentini-Pereyra Program [8] (see also [2, 3]). The slope of the dimensionless temperature profile at the wall, $\theta'(0)$, obtained from the solution of the conservation equations was used in the following equations to obtain the local Nusselt number for the constant property problem:

$$(\mathrm{Nu}_{w,x})_{c.p.} = \mathrm{Gr}_{x,\mathrm{ref}}^{1/4} [-\theta'(0)]_{\mathrm{ref}} \tag{11}$$

where, from equation (6)

$$-\theta'(0)_{\mathrm{ref}} = \sqrt{2}\,(a_1 + b_1 \mathrm{Pr}_{\mathrm{ref}}^{c_1}) = \sqrt{2}\,(0.1 + 0.486\,\mathrm{Pr}_{\mathrm{ref}}^{0.331}) \tag{12}$$

The constant property heat flux results were compared with experimental and theoretical results of the three fluids under study, Fig. 5. It can be seen that the constant property heat flux results are within

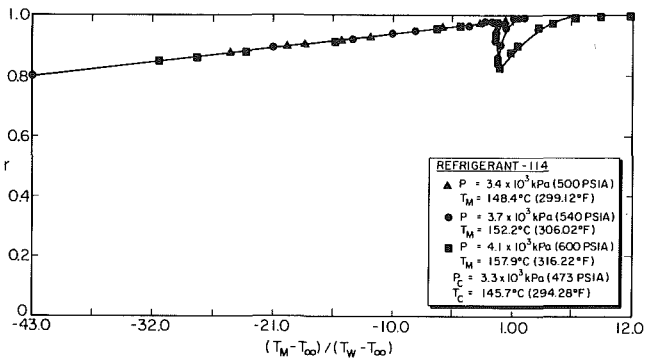

Fig. 2 Variation of r at various temperatures and pressures

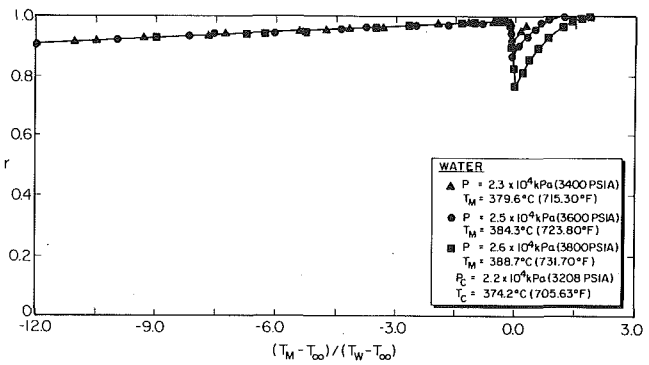

Fig. 3 Variation of r at various temperatures and pressures

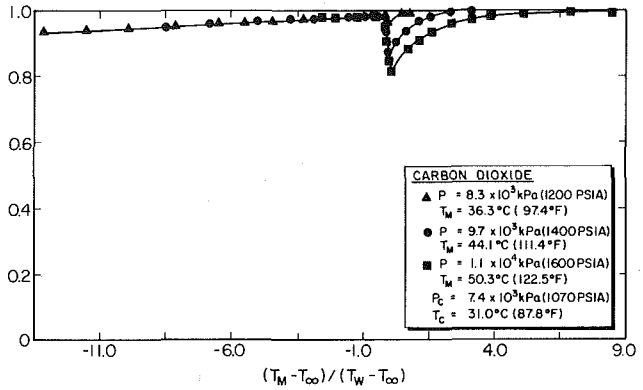

Fig. 4 Variation of r at various temperatures and pressures

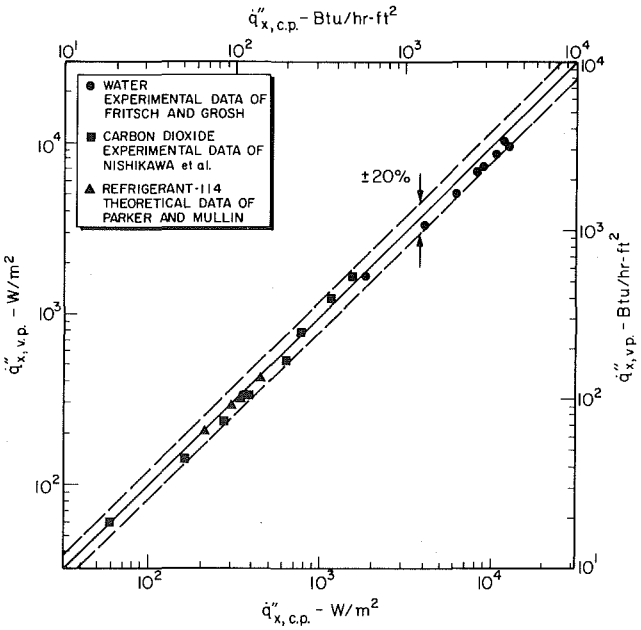

Fig. 5 Comparison of predicted constant property local heat flux with variable property local heat flux

± 20 percent of the variable property experimental and theoretical results.

The variable property results for Refrigerant-114 at 3.7×10^3 kPa (540 psia), based on [2] and [3] were compared with the constant property heat transfer results obtained with the predicted reference temperatures. This was achieved by choosing 37 points on the 3.7×10^3 kPa (540 psia) curve in Fig. 2 for Refrigerant-114 that would best reproduce the curve. Most of the data points were chosen for the wall and free stream temperatures that best represented the abrupt change in the curve. The heat transfer results obtained for these data points cover a temperature range of 149 to 177°C (300 to 350°F). The comparison between the constant property Nusselt numbers obtained from equation (11) and variable property results obtained from [2] and [3] are presented in Fig. 6. The constant property Nusselt numbers predicted by the reference temperature method are within ± 10 percent of the variable property results.

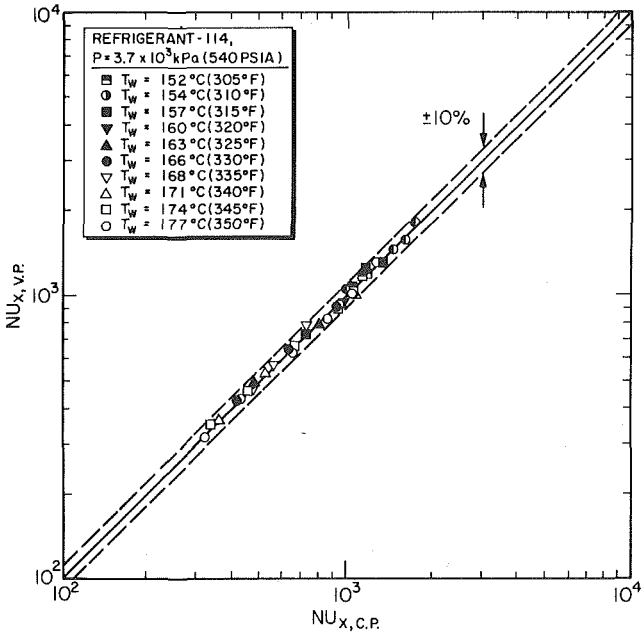

Fig. 6 Comparison of predicted constant property Nusselt numbers with variable property Nusselt numbers

Discussion

One single curve for prediction of reference temperature can be established where T_w, the wall temperature, or T_∞, the free stream temperature were not close to T_M, the temperature at which specific heat assumes its maximum value. The heat transfer results obtained using the predicted reference temperatures with the constant property equations compared well with the experimental and theoretical variable property results for Refrigerant-114, water, and carbon dioxide. For the regions where closeness to T_M was significant, it was still possible to predict reference temperature and heat transfer coefficients with good accuracy, but the curve used for these predictions were pressure dependent.

For a specified problem the free convective heat transfer coefficients to fluids in the supercritical region can be directly calculated from equation (2). The constants a, b, c, and d of equation (2) for Refrigerant-114, water, and carbon dioxide along with its range of application are tabulated in Table 1. Equation (2) required information on physical properties, which can be obtained from the equations and computer programs developed in [3] and [9].

The utility of the reference temperature lies in the fact that it allows the more easily obtained constant property solutions to be used to compute solutions where variable properties occur.

References

1 Hendricks, R. C., Simoneau, R. J., and Smith, R. V., "Survey of Heat Transfer to Near-Critical Fluids," NASA Technical Note D-5886, 1970.

2 Ghajar, A. J., and Parker, J. D., "Laminar Free Convection in the Supercritical Region with Variable Properties," *Proceedings of the 1980 Heat Transfer and Fluid Mechanics Institute*, M. Gerstein and P. R. Choudhury, eds., Stanford University Press, 1980, pp. 196–208.

3 Ghajar, A. J., "Laminar Free Convective Heat Transfer in the Supercritical Region with Variable Fluid Properties," Ph.D. thesis, Oklahoma State University, 1979.

4 Chandler, J. P., MARQ Code, personal communication, Department of Computing and Information Sciences, Oklahoma State University, Stillwater, Okla.

5 Fritsch, C. A., and Grosh, R. J., "Free Convection Heat Transfer to Supercritical Water Experimental Measurements," ASME JOURNAL OF HEAT TRANSFER, Vol. 85, No. 4, Nov. 1963, pp. 289–294.

6 Nishikawa, K., et al., *Technical Report Kyushu University*, Vol. 40, 1967, p. 986.

7 Parker, J. D., and Mullin, T. E., "Natural Convection in the Supercritical Region," Presented at the Institution of Mechanical Engineers Symposium on Heat Transfer and Fluid Dynamics of Near Critical Fluids, Paper 1, Mar. 27–29, Bristol, England, 1968.

8 Lentini, M., and Pereyra, V., "A Variable Order Finite Difference Method for Nonlinear Multipoint Boundary Value Problems," *Mathematics of Computation*, Vol. 28, No. 128, Oct. 1974, pp. 981–1003.

9 Ghajar, A. J., and Parker, J. D., "Physical Property Expressions for Some Fluids in the Supercritical Region," AIAA-80-1533, AIAA 15th Thermophysics Conference, July 14–16, Snowmass, Colo. 1980.

Heat Transfer in Air Enclosures of Aspect Ratio Less than One

V. Sernas
Professor,
Department of Mechanical and Aerospace Engineering,
Rutgers University,
New Brunswick, N. J. 08903

E. I. Lee
M.I.T. Lincoln Laboratories,
Lexington, Mass.

The heat transfer rates inside rectangular air enclosures of aspect ratios between 0.1 and 1.0 were investigated interferometrically for a Grashof number range between 2.64×10^6 and 5.45×10^6. The enclosures were composed of dissimilar temperature vertical walls and two types of ceilings and floors. One type was made from constant temperature plates kept at the vertical wall temperatures, and the other type was made of low thermal conductivity polyurethane foam rubber. The heat transfer characteristics and flow patterns within these two types of enclosures were found to be significantly different. For aspect ratios between 0.4 and 1.0 the isothermal ceiling and floor approximate an adiabatic boundary condition much better than foam because much less heat was interchanged between the floor (or ceiling) and the air in the enclosure.

Introduction

Rectangular enclosures containing air are commonly used to provide thermal insulation. Double pane windows and empty walls in frame construction houses are examples of rectangular enclosures of large aspect ratio (large height to width ratio). In the enclosures, one vertical wall is usually considered to be at a high temperature and the other vertical wall at a lower temperature. The horizontal surfaces of the enclosure are normally treated as adiabatic surfaces. Heat is transferred between the two vertical walls by conduction and/or convection. A vast majority of research in enclosures has been aimed at high aspect ratio (Ar) enclosures perhaps because there are many applications of large aspect ratio enclosures. However, very few studies have been reported for enclosures of aspect ratio less than one, i.e., enclosures that are wider than they are high. The only experimental studies of $Ar < 1$ were reported by Sernas, et al. [1] and Imberger [2], while analytical and numerical studies were reported by Boyack and Kearney [3], Cormack, Leal, and Imberger [4], Cormack, Leal, and Seinfeld [5], Cormack, Stone, and Leal [6] and Bejan and Tien [7].

A considerable amount of work has been done for enclosures of aspect ratio equal to one. Experimental data for $Ar = 1$ have been reported by Arnold, et al. [8], and theoretical (numerical) results have been reported by Wilkes and Churchill [9], de Vahl Davis [10], MacGregor and Emery [11], Newell and Schmidt [12], and Briggs [13]. The numerical studies, except for Briggs [13] were limited by numerical stability to Grashof numbers (Gr) below 3×10^5. Thus most of the available data for $Ar = 1$ are in the low Grashof number range.

When the aspect ratio of an enclosure gets below one, the area of the ceiling and floor begins to account for the majority of the enclosure surface area. It then becomes increasingly important to choose the ceiling and floor materials in an experiment in order to approach adiabatic conditions at the ceiling and floor. This paper presents a comparison of the heat transfer rates between the vertical walls resulting from two types of horizontal boundary conditions in air enclosures of aspect ratio between 0.1 and 1. The first horizontal boundary condition was produced by constant temperature plates that simulated an isothermal ceiling and floor. The second type of ceiling and floor was made from low thermal conductivity polyurethane foam rubber which was supposed to have simulated an adiabatic ceiling and floor. A Wollaston prism schlieren interferometer was used to measure the heat flux on the walls of the enclosure including the ceiling and the floor. Thus it was possible to evaluate how much heat was actually exchanged between the horizontal surfaces and the enclosure air. It was found that in many cases the isothermal ceiling and floor transferred less heat to the enclosure than the polyurethane foam.

Contributed by the Heat Transfer Division for publication in the JOURNAL OF HEAT TRANSFER. Manuscript received by the Heat Transfer Division, October 25, 1979.

Apparatus

Isothermal Boundary Conditions. The enclosure was made from two identical vertical constant temperature walls and two horizontal constant temperature walls with glass end walls as shown in Fig. 1. The vertical walls were constructed from 1.58 cm thick aluminum plates, 30.5 cm high and 18.1 cm wide. A continuous snake-like groove, 1.3 cm wide and 1 cm deep, was milled into the backside of each vertical wall. Then the backside was covered with a neoprene gasket and a thin aluminum plate to form a circulating water passage from the milled groove. Water from two constant temperature baths was circulated through these vertical plates. One plate was kept at a high temperature while the other vertical plate, referred to as the cold wall, was kept at 21.1°C (70°F). The room temperature was about 21°C.

The two vertical walls were separated by two horizontal plates which formed the ceiling and the floor of the enclosure. These plates were made from 1.27 cm thick aluminum and contained water channels similar to the ones on the vertical plates. The ceiling plate was made slightly wider than the floor plate by gluing on Bakelite strips on the edges. This was done to permit the ceiling plate to fit loosely into a milled horizontal groove on the inside surface of the vertical plate. The position of the ceiling plate was thus fixed and the aspect ratio of the enclosure was changed by lowering or raising the floor only. The floor plate had thin rubber gaskets on its edges and was held in place by the vertical plates. The distance between the vertical plates was maintained at 10.0 cm by four spacer rods which held the vertical plates together and allowed the ceiling plate to expand when heated into the horizontal grooves on the vertical plates.

The temperature of the ceiling plate was maintained at the same temperature as the hot wall by introducing the outgoing hot water from the hot wall to the ceiling plate. The temperature of the bottom (floor) plate was maintained at the same temperature as the cold wall (i.e., 21.1°C) in a like manner. Fourteen thermocouples were imbedded in the four walls to monitor the actual temperature of the plates. It was found that the hot and cold walls could be maintained indefinitely to within 0.1°C of the set temperature.

The enclosure was completed with two 0.64 cm thick glass plates whose weight was supported by the bottom edges. The glass was clamped lightly to the outside edges of the vertical walls by two holding bars. A soft rubber gasket separated the glass from the edges of the aluminum plates. The inside distance between the glass plates was maintained at 18.7 cm. The thermal expansion of the walls was absorbed by the soft rubber gaskets so that the glass windows were free of bending stresses.

Movement of the hot vertical wall due to thermal expansion was partially compensated by lowering the hot wall on its adjustable leveling screw (see Fig. 1). The thermal expansion of the hot wall was monitored by a properly placed dial indicator. The height adjustments were such that the top corner of the hot wall was always in the same point in space relative to the laboratory floor and the interferometer light beam.

Polyurethane Foam Ceiling and Floor Enclosure. To achieve

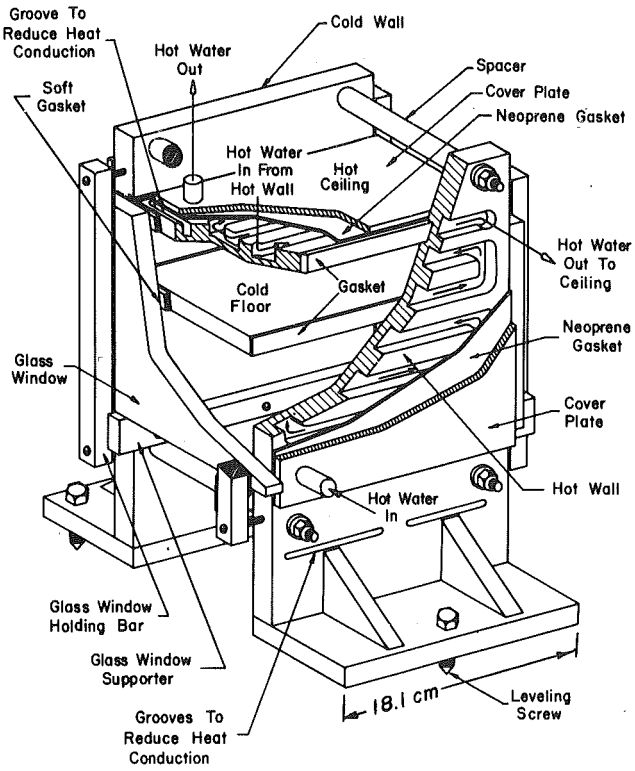

Fig. 1 Cut-away view of enclosure test section with isothermal ceiling and floor installed

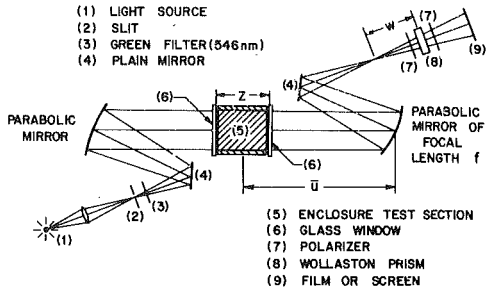

Fig. 2 Schematic diagram of the Wollaston prism schlieren interferometer with the enclosure test section

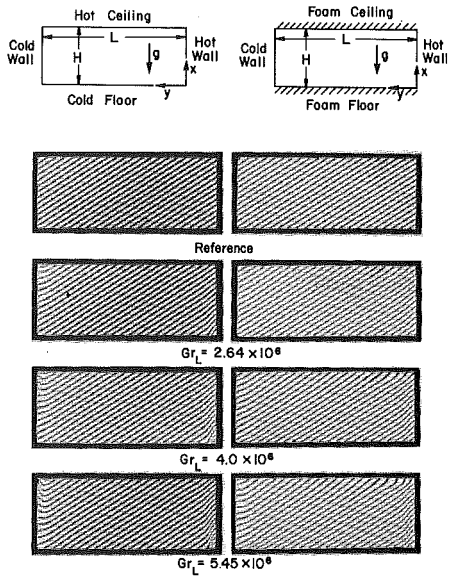

Fig. 3 Representative interferograms for the $Ar = 0.4$ enclosure. The isothermal enclosure interferograms are on the left, and the foam enclosure interferograms are on the right.

an adiabatic condition at the ceiling and floor, two pieces of polyurethane foam rubber 2.5 cm thick were used as the ceiling and floor plates instead of the grooved aluminum plates. The polyurethane foam rubber had an estimated thermal conductivity of 0.04 W/m-C (about 1.5 times that of air) and a density of 27 kg/m^3. Eight thermocouples were imbedded under the foam surface (on the enclosure side) to monitor the temperature of the ceiling and the floor. All other constructional details were the same as in the all isothermal boundary condition enclosures.

For the sake of brevity the enclosures made with an isothermal ceiling and floor will be referred to as "isothermal enclosures," and the enclosures constructed with polyurethane foam rubber ceilings and floors will be referred to as "foam enclosures."

Optical System. The assembled enclosures were placed in a Wollaston prism schlieren interferometer in order to measure interferometrically the local heat fluxes at the vertical walls and at the ceiling and floor. The arrangement of the interferometer is shown in Fig. 2. This interferometer is a "shearing interferometer" that is sensitive to the gradient of temperature (or gradient of index of refraction) within the test section. Since the operation of the interferometer has been described in the literature [14–17] it is not necessary to repeat it here.

Experimental Procedure

When the test section was at ambient temperature throughout, a reference interferogram of the enclosure was made. Then the temperature controller for the hot wall was raised consecutively to 43.3, 57.2, and 79.4°C while the cold wall temperature was always maintained at 21.1°C. The enclosure was allowed to operate at each of these temperatures for an hour before an interferogram was made at the hot wall temperature. These hot wall temperatures corresponded to Grashof numbers of 2.64×10^6, 4.0×10^6, and 5.45×10^6 where the Grashof number, based on enclosure width, was defined as:

$$\mathrm{Gr}_L = \frac{gL^3(T_h - T_c)}{T_m \nu_m{}^2}$$

Examples of the interferograms produced in this way are shown in Fig. 3.

The film on which the interferograms were taken was developed and mounted between glass plates in an optical comparitor. The upper hot wall corner was selected as a reference point for the hot wall and ceiling and the lower cold wall corner was selected as the reference point for the cold wall and floor. Then the locations (in optical comparitor micrometer units) of the fringes on all four walls were measured both for the reference interferograms and the heated test section interferogram. The difference between the fringe location on the reference interferogram and the fringe location on the heated test section interferogram was proportional to the local heat flux from the wall. In this manner the local heat flux at every fringe on all four walls was calculated using the interpretation formula derived in references [14, 15] and [17]. The heat flux at the enclosure corners, for example at $x/H = 0.0$ and 1.0 for the vertical heated wall, was found by ex-

Nomenclature

Ar = aspect ratio, H/L
g = acceleration due to gravity
Gr_L = Grashof number based on width
H = height of enclosure
k_m = thermal conductivity of air at T_m
L = width of enclosure
$\bar{q}_{av}$ = average heat flux
$\bar{q}$ = local heat flux
T_c = cold wall temperature
T_h = hot wall temperature
T_m = mean enclosure temperature, $(T_h + T_c)/2$
x = vertical coordinate
y = horizontal coordinate
ν_m = kinematic viscosity of air at T_m

trapolation from the two adjacent inner points. The average heat flux over a surface was determined by numerical integration of the local heat flux distribution curve. The accuracy of the local heat flux measurements using this interferometric technique was estimated to be 6 percent.

The spacing of the reference fringes was chosen to provide as many fringes as possible at the heated vertical wall. Two different fringe spacings were used in this study, one for smaller aspect ratios and one for larger aspect ratio enclosures. Three reference fringes intersected the hot wall in the 0.1 aspect ratio enclosure, while 25 fringes terminated at the hot wall for the 1.0 aspect ratio enclosure.

Results and Discussion

The experiments were carried out over a Gr_L range of 2.64×10^6 to 5.45×10^6. The other controllable variable in the experiments was the aspect ratio which was varied from 0.1 to 1.0. This range of the variables produced convective flows that fall within all three flow regimes proposed by Bejan and Tien [7]. Figure 4 shows our experimental conditions on Bejan and Tien's regime map that is a plot of Ar versus Rayleigh number based on height. It is quite clear from Fig. 4 that the tests in the Ar range of 0.6 to 1.0 were operating in the boundary layer regime, while the tests at $Ar = 0.1$ must have been in the Rayleigh number approaching zero regime. The tests at the intermediate Ar must have been operating in the intermediate regime.

The local heat flux distribution along the floor of the enclosure is shown in Fig. 5 for the $Ar = 0.4$ enclosures. These are the same tests for which the interferograms are shown in Fig. 3. It can be seen that the amount of heat added to the air from the foam floor is much larger than the heat which is taken up by the isothermal floor from the enclosure air. This implies that for this Ar the isothermal floor acts more like an adiabatic floor than the foam floor. The high heat flux from the floor near the hot wall corner is the result of a higher temperature of the floor due to heat conduction through the gasket. A groove on the backside of the floor (shown to scale in Fig. 5) was made to reduce this heat conduction and to confine the higher temperature region to the corner.

The magnitude of the average heat flux at the floor as a function of Gr_L and Ar is shown in Fig. 6. It can be seen from this figure that the isothermal floor approximates the adiabatic boundary condition much better than the foam floor in the aspect ratio range of 0.4 to 1.0 because much less heat is interchanged between the floor and the air in the enclosure. At aspect ratios less than 0.2 the foam seems to produce a better adiabatic condition. This is due to the fact that as the isothermal hot ceiling and isothermal cold floor get close together direct conduction between the hot ceiling and the cold floor increases significantly.

The measured temperature distribution along the floor surface is shown in Fig. 7 for $Ar = 0.4$. The surface temperature of the foam floor changes gradually from the cold wall temperature to the hot wall temperature. The temperature of the isothermal floor was kept the same as the cold wall temperature (21.1°C) except for the corner close to the hot wall where rapid changes of temperature occurred due to heat conduction through the rubber gasket. This rapid increase in the floor temperature at the hot wall corner is not unlike the floor temperature distribution in the corner obtained by Briggs [13] and Lee [18] in ideally adiabatic enclosures at high Grashof numbers.

Figure 8 shows a dimensionless comparison of the floor temperature distribution for four different floor boundary conditions. The linear temperature distribution would be obtained in an enclosure whose floor was made of a very high thermal conductivity material (i.e. $(k_w/k_{air}) \to \infty$) and whose floor was in good thermal contact with the vertical isothermal walls. The adiabatic temperature distribution was obtained from Lee's [18] finite difference simulation of the flow inside an ideally insulated enclosure. One would expect an experimental floor

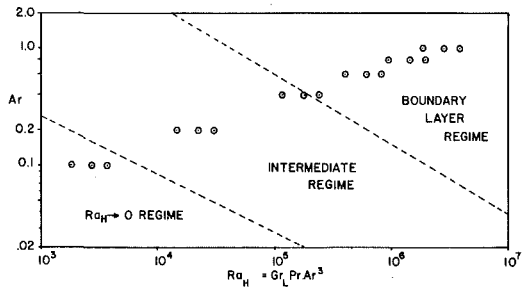

Fig. 4 Experimental test conditions on regime map proposed by Bejan and Tien [7]

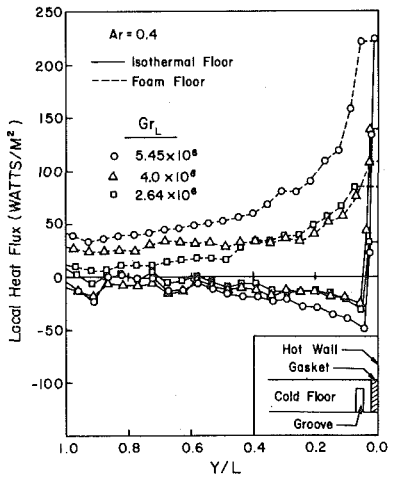

Fig. 5 Heat flux distribution along the floor for the interferograms shown in Fig. 3

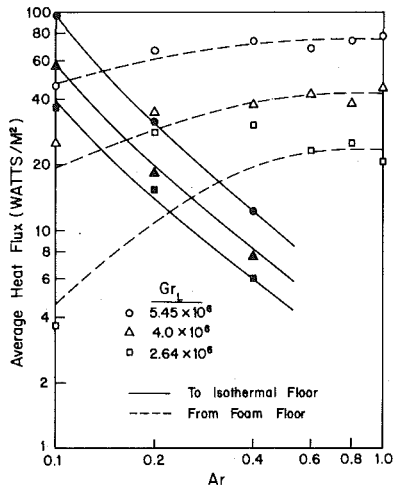

Fig. 6 Average heat flux to isothermal floor and from the polyurethane foam floor. The direction of the average heat flux from the isothermal floor is opposite to that of the foam floor

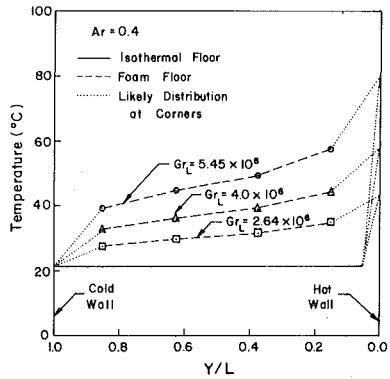

Fig. 7 Temperature distribution along the floor for the interferograms shown in Fig. 3

to approach this temperature distribution if the floor's thermal conductivity were many times smaller than that of air (i.e. $(k_w/k_{air}) \rightarrow 0$). It can be seen from this figure that the foam floor, which had a thermal conductivity of 1.5 times that of air, produced a floor temperature distribution that is between the linear and the adiabatic temperature profile limits. Thus it appears that polyurethane foam does not produce a fundamental boundary condition for air enclosures. Apparently the thermal conductivity of the wall material must be considerably less than that of air to approach the adiabatic boundary condition.

The hot wall heat flux distribution for all the isothermal enclosure tests is shown in Fig. 9. It can be seen that the curves are grouped into three distinct groups according to their Grashof numbers. For each group (i.e., Gr_L) the average heat rate (represented by the area under each curve) is approximately constant. It can also be seen from Fig. 9 that the isothermal enclosure produces a very high heat flux at the lower corner which seems to act as the "leading edge" of the thermal boundary layer on the hot wall.

The local heat flux on the hot wall for the foam enclosures is shown in Fig. 10. It can be seen that the maximum heat flux does not occur at the bottom corner but rather some distance up from the lower corner. It seems that the higher the aspect ratio, the closer the maximum is to the lower corner. The curves are grouped together according to the Gr_L only for $Ar \geq 0.4$. Below an aspect ratio of 0.4 there is a significant drop in the heat flux from the hot wall.

A comparison of the average heat flux from the hot wall for all the isothermal and foam enclosures is shown in Fig. 11. The comparison is made on a Nusselt number basis where:

$$\mathrm{Nu} = \frac{\ddot{q}_{av} L}{(T_h - T_c) k_m}.$$

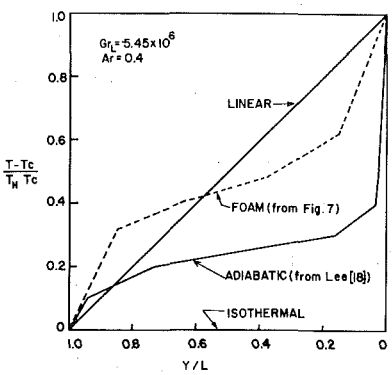

Fig. 8 Temperature distribution along the floor for four different boundary conditions imposed upon the floor

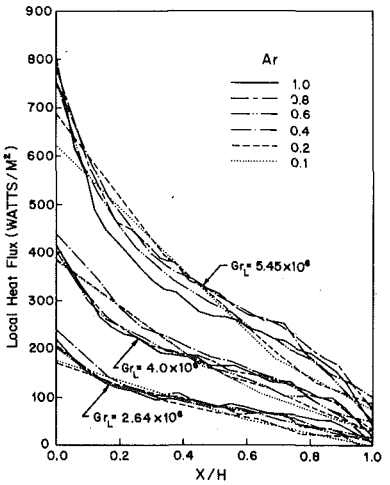

Fig. 9 Interferometrically measured heat flux distribution along the hot wall for isothermal enclosures

Since for a fixed Gr_L test the values for L, T_h, T_c, and k_m were fixed, the Nu becomes a direct indication of the average heat flux on the hot wall. Figure 11 confirms what has already been deduced from Figs. 9 and 10, namely that for the isothermal enclosures the heat flux from the hot wall is constant over the aspect ratio range of 0.1 to 1.0, and that for the foam enclosures the average heat flux from the hot wall falls off as the aspect ratio decreases below 0.4. Figure 11 also shows that there is no significant difference in the Nu for the two types of enclosures in the aspect ratio range of 0.6 to 1.0. However, there is a significant difference in the heat transfer between the air in the enclosure and the floor or ceiling, as can be seen in Fig. 6. The Nu values shown in Fig. 11 for the foam enclosure have been shown by Wirtz and Tseng [20] to be consistent with those of Imberger [2] and those of Cormack, et al. [5].

Heat balances on the four visible walls of the enclosure indicated that a significant amount of heat added to the enclosure by the hot wall was lost through the glass windows that made up the remaining two walls of the enclosure. The table below gives the measured heat losses through the windows in Watts for the isothermal enclosure at $Gr_L = 4 \times 10^6$. In the last column the table shows the heat loss as a percentage of the heat added to the enclosure by the hot wall. This means that if the Nusselt number were based on the cold wall average heat flux, it would be less than the value given in Fig. 11 by the percentage shown in Table 1.

These heat losses through the windows might at first glance appear to be excessive. However, an estimate of the heat loss given in the Appendix of reference [19] shows that the measured heat losses were of the right order of magnitude. It is quite clear that the enclosures must contain considerable three-dimensional effects in order to

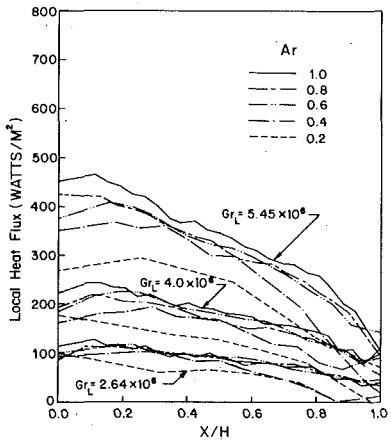

Fig. 10 Interferometrically measured heat flux distribution along the hot wall for foam enclosures

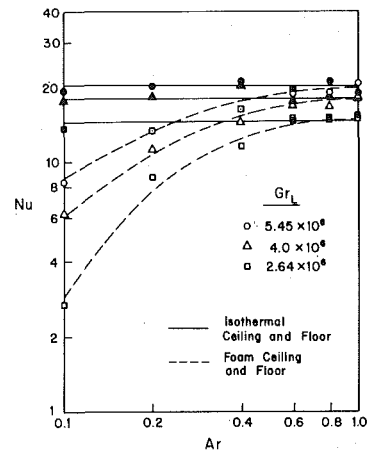

Fig. 11 Comparison of Nusselt numbers (based on hot wall average heat flux) in isothermal, and foam enclosures

Table 1

Ar	Measured Heat Loss in Watts	Percent of Hot Wall Heat Addition
1.0	1.03	31
0.8	1.02	38
0.6	0.65	34
0.4	0.59	40
0.2	0.18	27
0.1	0.06	18

generate window losses of 30–40 percent. The loss percentage could be reduced by increasing the length of the enclosure from 18.7 cm, but that would also increase the light refraction effects which were already becoming noticeable in the interferograms made at the highest wall temperature. Windows made from layers of thin polyethylene film make good insulators but are not optically smooth enough to use in an interferometer.

Flow Visualization

To visualize the flow pattern and three-dimensional effects within the enclosure, ordinary cigarette smoke was injected into the enclosure while the enclosure was illuminated by a 5mW He-Ne laser beam. It was found that the injected cigarette smoke circulated in the enclosure for about 10 min before it showed any signs of settling out on the walls. This confirmed the belief that cigarette smoke acts like it were neutrally buoyant in air. The injection temperature did not necessarily match the local temperature within the enclosure. However, by the time a photograph was made, the smoke had travelled around the enclosure a few times and should have come to equilibrium with the enclosed air.

The flow pattern at the center plane of the 0.4 aspect ratio enclosure is shown in Fig. 12(a) and 12(b) for the isothermal and foam enclosures respectively. These two photographs show that the flow pattern in these two enclosures is not the same. Figure 12(a) shows that the air close to the isothermal ceiling and floor keeps approximately the same distance from the horizontal surfaces (or even gets closer to them near the corners). Figure 12(b) shows that the air close to the foam floor is heated by the floor, becomes more buoyant and rises as it approaches the hot wall. This rise in the flow may explain why the maximum heat flux on the hot wall in the foam enclosure in Fig. 10 occurs about one third of the way up the hot wall and not at the lower hot corner. The rise in the flow in the foam enclosure was also seen by Lee [18] in a finite difference study that calculated the isotherms and streamlines in a two-dimensional foam enclosure whose ceiling and floor boundary condition was specified as a known temperature distribution that was identical to the measured temperature distribution shown in Fig. 7. The results of that numerical study are shown in Fig. 13 for the same aspect ratio and Grashof number as was used in the smoke visualization tests. It can be seen from Fig. 13 that the calculated streamlines appear quite similar to the smoke pattern of Fig. 12(b). The isotherms of Fig. 13(a) clearly indicate the local heating of the flow by the floor, and the cooling of the flow by the ceiling. The isotherms also indicate that the flow in that foam enclosure was partially driven by a horizontal temperature gradient. The flow in the isothermal enclosure of Fig. 12(a) was most likely driven only by the end boundary layers because the core of the enclosure was highly stratified.

Figures 12(a) and 12(b) show that the flow pattern at the central plane of the enclosure is made up of the "main cell" of relatively high velocity air that circulates counterclockwise around the entire enclosure. Also visible in the isothermal enclosure are two counterclockwise rotating small cells, one on the left near the cold wall named the "cold cell," and one on the right named the "hot cell." The smoke in Fig. 12(b) does not show up the small cells in the foam enclosure, but they have been made visible in other photographs. These small cells are comprised of very slow moving air and they do not seem to interchange mass with the main cell. In Fig. 12(a), these cells are located at the mid-height of the enclosure and are just outside of the vertical boundary layer, next to the almost stagnant core. For the

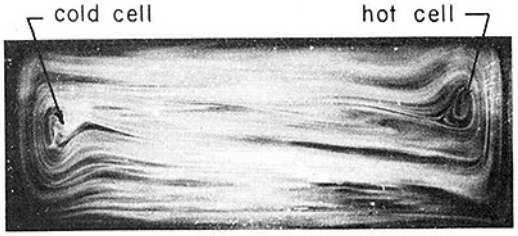

Fig. 12(a) Isothermal enclosure

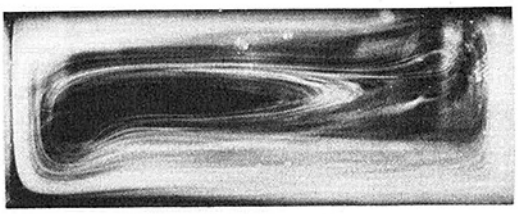

Fig. 12(b) Foam enclosure

Fig. 12 Smoke patterns in central plane of 0.4 aspect ratio enclosure at Gr = 5.45 × 10^6

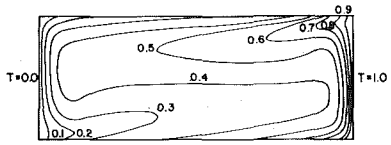

Fig. 13(a) Isotherms

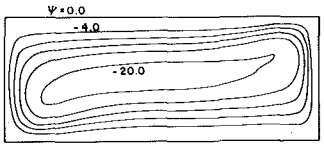

Fig. 13(b) Streamlines

Fig. 13 Isotherms and streamlines from numerical study by Lee [18] for foam enclosure of Ar = 0.4 and Gr = 5.45 × 10^6

larger Ar enclosures, the cold cell is located near the lower cold wall corner and the hot cell is located near the upper hot wall corner. More detailed observations on the cold and hot cell have been reported in references [18] and [19].

The smoke that is injected into the main cell at the center plane spiraled slowly outward toward the windows. The isothermal enclosures seemed to exhibit a larger spiraling velocity component than the foam enclosures. Once the smoke reached the windows it was usually drawn into complicated secondary flow cells that existed near the windows.

Acknowledgment

The authors gratefully acknowledge the financial support given this study by the National Science Foundation under Grant ENG 76-21920.

References

1 Sernas, V., Fletcher, L. S., and Rago, C., "An Interferometric Study of Natural Convection in Rectangular Enclosures of Aspect Ratios Less Than One," ASME Paper 75-HT-63, presented at the AIChE-ASME Heat Transfer Conference, San Francisco, CA, Aug. 1975.

2 Imberger, J., "Natural Convection in a Shallow Cavity with Differentially Heated End Walls. Part 3. Experimental Results," *Journal of Fluid Mechanics*, Vol. 65, 1974, pp. 247–260.

3 Boyack, B. E., and Kearney, D. W., "Heat Transfer by Laminar Natural Convection in Low Aspect Ratio Cavities," ASME Paper 72-HT-52, presented at the AIChE-ASME Heat Transfer Conference, Denver, CO, Aug. 1972.

4 Cormack, D. E., Leal, L. G., and Imberger, J., "Natural Convection in a Shallow Cavity with Differentially Heated End Walls. Part 1. Asymptotic Theory," *Journal of Fluid Mechanics*, Vol. 65, 1974, pp. 209–229.

5 Cormack, D. E., Leal, L. G., and Seinfeld, J. H., "Natural Convection in a Shallow Cavity with Differentially Heated End Walls. Part 2. Numerical

Solutions," *Journal of Fluid Mechanics*, Vol. 65, 1974, pp. 231–246.

6 Cormack, D. E., Stone, G. P., and Leal, L. G., "The Effect of Upper Surface Conditions on Convection in a Shallow Cavity with Differentially Heated End Walls," *International Journal of Heat and Mass Transfer*, Vol. 18, 1975, pp. 635–648.

7 Bejan, A., and Tien, C. L., "Laminar Natural Convection Heat Transfer in a Horizontal Cavity with Different End Temperatures," ASME JOURNAL OF HEAT TRANSFER, Vol. 100, 1978, pp. 641–647.

8 Arnold, J. N., Catton, I., and Edwards, D. K., "Experimental Investigation of Natural Convection in Inclined Rectangular Regions of Differing Aspect Ratios," ASME JOURNAL OF HEAT TRANSFER, Vol. 98, No. 1, 1976, pp. 67–71.

9 Wilkes, J. O., and Churchill, S. W., "The Finite-Difference Computation of Natural Convection in a Rectangular Enclosure," *AIChE Journal*, Vol. 12, No. 1, 1966, p. 161.

10 de Vahl Davis, G., "Laminar Natural Convection in an Enclosed Rectangular Cavity," *International Journal of Heat and Mass Transfer*, Vol. 11, 1968, pp. 1675–1693.

11 MacGregor, R. K., and Emery, A. F., "Free Convection Through Vertical Plane Layers—Moderate and High Prandtl Number Fluids," ASME JOURNAL OF HEAT TRANSFER, Vol. 91, No. 3, 1969, pp. 391–403.

12 Newell, M. E., and Schmidt, F. W., "Heat Transfer by Laminar Natural Convection within Rectangular Enclosures," ASME JOURNAL OF HEAT TRANSFER, Vol. 92, No. 1, 1970, pp. 159–168.

13 Briggs, D. G., "Numerical Solutions of High Rayleigh Number Two-Dimensional Free Convection in Enclosures With an Aspect Ratio of One," *Proceedings of AICA International Symposium on Computer Methods for Partial Differential Equations*, Lehigh University, Bethlehem, PA, June 1975.

14 Sernas, V., Fletcher, L. S., and Aurg, W., "Heat Transfer Measurements with a Wollaston Prism Schlieren Interferometer," ASME Paper 72-HT-9, presented at the AIChE-ASME Heat Transfer Conference, Denver, CO, Aug. 1972.

15 Sernas, V., Fletcher, L. S., and Jones, J. A., "An Interferometric Heat Flux Measuring Device," *ISA Transactions*, Vol. 11, No. 4, 1972, pp. 346–357.

16 Small, R. D., Sernas, V. A., and Page, R. H., "Single Beam Schlieren Interferometer Using a Wollaston Prism," *Applied Optics*, Vol. 11, No. 4, 1972, pp. 858–862.

17 Sernas, V., "The Wollaston Prism Schlieren Interferometer," in von Karman Institute for Fluid Dynamics Lecture Series 96, Advanced Measurement Techniques in Fluid Dynamics, Mar. 1977.

18 Lee, E. I., "Natural Convection in Rectangular Air Enclosures of Aspect Ratio Less than One," Ph.D. Thesis, Department of Mechanical, Industrial and Aerospace Engineering, Rutgers University, New Brunswick, N. J., Oct. 1979.

19 Sernas, V., and Lee, E. I., "Heat Transfer in an Enclosure of Aspect Ratio Less Than One," ASME Paper 78-WA/HT-7, presented at the ASME Winter Annual Meeting, San Francisco, CA, Dec. 1978.

20 Wirtz, R. A., and Tseng, W.-F., "Natural Convection across Tilted, Rectangular Enclosures of Small Aspect Ratio," in Symposium on Natural Convection in Enclosures held at the 19th AIChE/ASME National Heat Transfer Conference, Orlando, Fla, July 1980.

Natural Convection in Undivided and Partially Divided Rectangular Enclosures

M. W. Nansteel

R. Greif
Mem. ASME

Passive Solar Analysis and Design Group, Lawrence Berkeley Laboratory and Department of Mechanical Engineering, University of California, Berkeley, Calif. 94720

Heat transfer by natural convection in a two-dimensional rectangular enclosure fitted with partial vertical divisions is investigated experimentally. The horizontal walls of the enclosure are adiabatic while the vertical walls are maintained at different temperatures. The experiments are carried out with water, $Pr \simeq 3.5$, for Rayleigh numbers in the range, $2.3 \times 10^{10} \leqslant Ra_L \leqslant 1.1 \times 10^{11}$, and an aspect ratio, $A = H/L = \frac{1}{2}$. The effect of the partial vertical divisions on the fluid flow and temperature fields is investigated by dye-injection flow visualization and by thermocouple probes, respectively. The effect of the partitions on the heat transfer across the enclosure is also studied and correlations for the Nusselt number as a function of Ra_L and partition length are generated for both conducting and non-conducting partition materials. Partial divisions are found to have a significant effect on the heat transfer; especially when the divisions are adiabatic. The results also indicate that the partial divisions may have a stabilizing effect on the laminar-transitional flow on the heated vertical walls of the enclosure.

Introduction

Natural convection heat transfer in rectangular enclosures is of great importance in determining the energy transfer within buildings, especially those incorporating passive solar design features. This configuration has been studied extensively, e.g., [1–19, 25], but only for limited ranges of the Rayleigh number. The effect of a partial obstruction extending downward from the enclosure ceiling is also of importance but has received little attention [cf. 17, 20–24]. This geometry corresponds roughly, for example, to a ceiling beam or soffit. The experimental investigation of Duxbury [20] was carried out in rectangular enclosures of aspect ratios (see Fig. 1), $\frac{5}{8} \leqslant A = H/L \leqslant 5$, partially divided by vertical, heat conducting partitions using air as the working fluid, for Rayleigh numbers approaching 10^6. The driving force in Duxbury's experiment was the imposed temperature difference between the two vertical sidewalls of the enclosure. The experiments and numerical calculations of Lloyd, et al. [21, 22] were motivated by fire studies and there the flow was driven by methane combustion and by surface or volumetric heat sources. The experimental and numerical study of Bauman, et al. [17] was motivated by studies of heat transfer within buildings and focused on the undivided enclosure although some results are also presented for a partially divided enclosure. This study [17] was carried out in water in a partially divided rectangular enclosure of aspect ratio, $A = \frac{1}{2}$ and $Ra_L \sim 10^{10}$. Janikowski, et al. [23] experimentally investigated the temperature and flow fields inside a rectangular enclosure partially divided by solid and porous vertical divisions extending upward from the floor and downward from the ceiling simultaneously. Emery [24], on the other hand, studied the heat transfer and temperature field in a rectangular enclosure fitted with a vertical partial division extending from the center of the enclosure downward toward the floor and upward toward the ceiling. It appears, however, that there has not been any thorough investigation of the role played by partial vertical divisions at the high values of the Rayleigh number ($Ra_L \sim 10^{10} - 10^{12}$) that are commonly encountered.

The primary goal of this study is to develop, through careful experiments, an understanding of the convective heat transfer processes and fluid flow occurring in the two-dimensional, partially divided enclosure (see Fig. 1) at Rayleigh numbers representative of large scale applications. An immediate application is in convection analyses in passive solar heated buildings. The experiment is carried out in a rectangular enclosure of aspect ratio, $A = H/L = \frac{1}{2}$, with isothermal vertical sidewalls and insulated horizontal floor and ceiling. The enclosure is fitted with either thermally conducting or non-conducting vertical partitions of various lengths (aperture ratios, $A_p = h/H = 1$ (no partition), $\frac{3}{4}$, $\frac{1}{2}$ and $\frac{1}{4}$ are investigated). Experiments are carried out with water ($3 \leqslant Pr \leqslant 4.3$) as the working fluid at Rayleigh numbers over the range $2.3 \times 10^{10} \leqslant Ra_L \leqslant 1.1 \times 10^{11}$.

It is emphasized that over this Rayleigh number range the results without the partition are also new. Power law correlations are obtained giving the dependence of the Nusselt number on aperture ratio, Rayleigh number, and partition conductance. Temperature profiles are also obtained within the enclosure with thermocouple probes, and the basic flow structure is noted by using dye-injection flow visualization. Distinct differences are found between the flow pattern observed in these experiments and those observed in the lower Ra_L and lower Pr experiments of Duxbury. Also, the presence of laminar-transitional flow for $A_p = 1$ (no partition) and the suppression of transition for $A_p < 1$ are discussed.

Experimental Apparatus and Procedure

The experimental apparatus consisted basically of a rectangular enclosure of height, $H = 15.2$ cm, width, $L = 30.5$ cm (aspect ratio, $A = H/L = \frac{1}{2}$) and breadth, $B = 83.8$ cm. This system is similar to the one used by Bauman, et al. [17]. The heated and cooled vertical walls

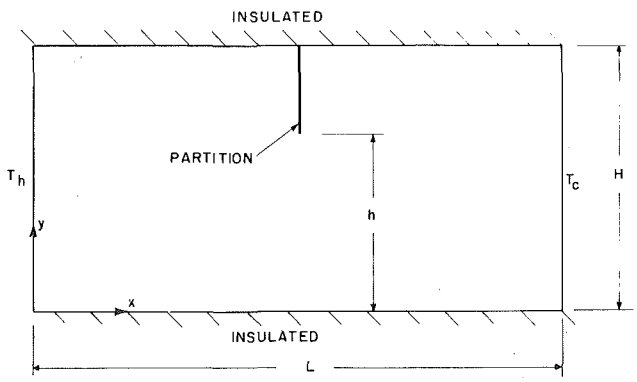

Fig. 1 Rectangular enclosure with partial vertical division

Contributed by the Heat Transfer Division for publication in the JOURNAL OF HEAT TRANSFER. Manuscript received by the Heat Transfer Division July 27, 1981.

were made from plates of copper, 4.8 mm thick, and aluminum, 15.9 mm thick, respectively, while the floor, ceiling, and endwalls of the enclosure were fabricated from clear, 1.27 cm thick plexiglas. The copper hot wall was heated electrically with 18 Minco "Thermofoil" resistance heaters. These were arranged in three vertical columns of six heaters each, see Fig. 2. In order to limit temperature variations along the hot wall, in the vertical direction, each pair of heaters in a given column was supplied by a separate 120V/240V a–c power supply. In this way, hot wall temperature deviations from the average hot wall temperature were kept to within about 10 percent of the overall temperature difference across the enclosure ($T_h - T_c$). The aluminum cold wall was cooled by passing tap water through two rectangular channels which were machined into the aluminum cold plate, traversing the full breadth of the enclosure seven times. It was found that temperature variations along the cold wall could be kept below about 10 percent of the temperature difference ($T_h - T_c$) by using a sufficiently high cooling water flow rate. Two streams entered the aluminum manifold near the top of the cold wall and were extracted near the bottom, see Fig. 2.

Joints between the copper and aluminum vertical walls and plexiglas floor were sealed with a 1.6 mm thick cork gasket to minimize conduction between the vertical surfaces and the floor. The ceiling was removable and was thermally isolated from the hot and cold walls by a small air gap, as in Fig. 2.

Partial vertical divisions of lengths 0, 3.8, 7.6 and 11.4 cm, extended downward from the center of the enclosure ceiling. The corresponding aperture ratios are $A_p = h/H = 1, \frac{3}{4}, \frac{1}{2}$, and $\frac{1}{4}$, respectively. All the partitions were 9.5 mm thick and traversed the full breadth of the enclosure in order to achieve, as nearly as possible, a two-dimensional system. Partitions which are effectively perfectly conducting are characterized by small temperature differences across the partition in comparison with the temperature difference ($T_h - T_c$), while effectively adiabatic partitions are characterized by negligible conduction heat transfer through the partition in comparison with the total energy transfer across the enclosure. A nondimensional partition conductance is defined by $k_p^* = (k_p/k)\,(L/\Delta x)/\mathrm{Nu}_L$, where Δx is the partition thickness. The criterion for a perfectly conducting partition is $k_p^* \gg 1$; for an adiabatic partition $k_p^* \ll 1$. In this experiment, the highly conducting partitions were fabricated from slabs of aluminum with $k_p^* \gtrsim 50$. The adiabatic partitions were made from polystyrene foam clad with 0.1 mm stainless steel sheets with $k_p^* \lesssim 0.02$.

To reduce energy losses to the surroundings, the entire apparatus was enclosed in a shell of polyurethane foam insulation, whose outer surface was covered with aluminum foil to reduce radiative losses.

The local surface temperatures of the hot and cold walls were determined with 30 gauge, copper-constantan thermocouples inserted in small holes which had been drilled horizontally into the hot and cold walls to a distance less than 1 mm from the inside (wet) surfaces of the hot and cold plates. Seventeen of these thermocouples were spread uniformly over each of the hot and cold walls.

The temperatures of the unheated surfaces (plexiglas floor and ceiling) were obtained with 50 gauge (0.025 mm dia), unsheathed, chromel-constantan thermocouples which were cemented to the plexiglas surface with a fine coating of polyurethane lacquer. The fine thermocouple wires ran perpendicular to the plane of Fig. 2 along the floor and ceiling. The thermocouple beads were located halfway between the two plexiglas endwalls at the positions $x/L = \frac{1}{4}, \frac{1}{2}$ and $\frac{3}{4}$. The very small diameter and the placement of the wires perpendicular to the plane of two-dimensionality minimized disturbance to the flow and axial conduction effects. The temperature at the lower edge of the partition, $y = h$, was measured with a fine, stainless-steel sheathed, chromel-constantan thermocouple probe with an overall dia of 0.25 mm. This sheathed thermocouple was also run perpendicular to the plane of Fig. 2, along the lower edge of the partition.

Local fluid temperatures within the enclosure were measured with thermocouple probe assemblies. Two fine, grounded junction, stainless-sheathed thermocouple probes (0.25 mm dia) were passed down through and out of a 1.6 mm dia stainless steel support tube, which was inserted vertically into the enclosure from the enclosure ceiling. The probe junctions were located about 6.5 cm from the larger support tube to minimize measurement errors due to the presence of the larger tube. Again, these fine probes were directed perpendicular to the plane of Fig. 2 to minimize heat conduction along the probe shafts. Three of these assemblies were used for measuring fluid temperature at the positions $x/L = \frac{1}{4}, \frac{1}{2}$ and $\frac{3}{4}$. Observations made during experiments both with and without the probes in place, revealed no detectable changes in either the flow or the overall heat transfer rate. Comparison of some of the thermocouples (both copper-constantan and chromel-constantan) with a precision mercury-in-glass thermometer showed that the standard calibration was adequate, with a maximum error of about ±1°C.

Energy input at the hot wall was measured with three single-element, electro dynamometer-type wattmeters, one for each power circuit, with accuracies of ± one percent. As a check on energy loss to the ambient, the heat transfer rate at the cold wall was measured and compared to the power input at the hot wall. Cooling water temperature entering and leaving the cold wall cooling manifold was mea-

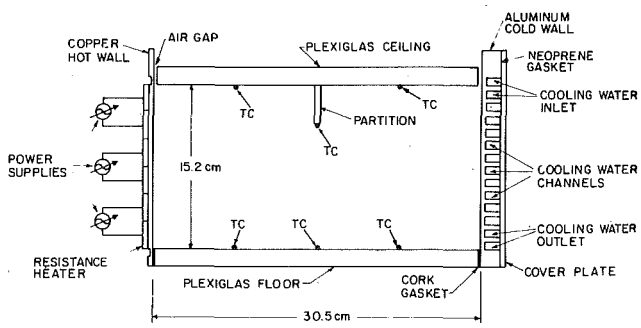

Fig. 2 Sketch of experimental apparatus

Nomenclature

$A = H/L$, aspect ratio
$A_p = h/H$, aperture ratio
B = enclosure breadth
c_p = constant pressure specific heat
g = acceleration due to gravity
H = enclosure height
h = distance from enclosure floor to partition
k = thermal conductivity
k_p = thermal conductivity of partition
k_p^* = nondimensional partition conductance
L = enclosure width
$\mathrm{Nu}_L = qL/(T_h - T_c)k$, Nusselt number
n = core temperature parameter
$\mathrm{Pr} = \frac{\nu}{\alpha}$, Prandtl number
$Q = (Q_h + Q_c)/2$, heat transfer across enclosure
Q_1 = heat transfer rate over lower third of hot wall
Q_2 = heat transfer rate over middle third of hot wall
Q_3 = heat transfer rate over upper third of hot wall
$q = \mathrm{Q}/(\mathrm{B} \cdot \mathrm{H})$, average heat flux
$\mathrm{Ra}_L = g\beta L^3(T_h - T_c)/\nu\alpha$, Rayleigh number
T = temperature
$T_r = (T_h + T_c)/2$, reference temperature
x = horizontal position coordinate
Δx = thickness of partial division
y = vertical position coordinate
α = thermal diffusivity
β = thermal coefficient of expansion
$\Lambda = \frac{k}{c_p}\left(\frac{\rho^2\beta}{\mu}\right)^{1/3}$ property group
μ = dynamic viscosity
ν = kinematic viscosity
ρ = density

Subscripts

c = cold wall
h = hot wall

sured with glass bead thermistors with a calibrated accuracy of ±0.05°C.

The procedure used in all of the experimental runs is as follows. The three heater circuits were used to heat the water to near-boiling temperature with the enclosure open to the atmosphere. Two to three hours at this temperature resulted in much of the dissolved gases being driven off. After the enclosure ceiling was inserted, the hot wall resistance heater power inputs were set and cooling water flow commenced. For the next four to five hours, adjustments were made in the relative power input to the three heater circuits to secure a reasonably isothermal condition on the hot wall. The cooling water flow rate was adjusted to limit temperature variations on the cold wall while still providing a moderate cooling water temperature increase (approximately 10°C). The wall temperatures T_h and T_c were taken as the average of the 17 temperatures measured on each of the hot and cold walls. Temperature variations from the mean wall temperature on the hot and cold walls seldom exceeded 10 percent of the overall temperature difference across the enclosure while the average deviation from the mean wall temperature was roughly three percent of $(T_h - T_c)$. There appeared to be no preferred direction for the wall temperature variation and observed local wall temperatures were very steady. The system was then allowed to equilibrate for an additional six hours. This extended beyond normal working hours in the laboratory so that perturbations in line voltage and cooling water flow rate and temperature were minimized.

The establishment of steady state conditions within the enclosure was a primary concern in the experimental procedure. Before any data were recorded, both cooling water inlet and exit temperature were carefully checked to insure that steady state conditions had been attained. This procedure was also repeated after the wall temperatures and fluid temperatures had been recorded. A sensitive check on the existence of steady state was provided by comparing the energy entering the enclosure at the hot wall, Q_h, to that leaving at the cold wall, Q_c. For all the experimental runs included in this study, these two rates of energy transfer differed by less than eight percent and in the great majority of cases the difference was less than five percent. These small fractional heat losses are a consequence of the large energy transfer rates occurring across the enclosure when water is the working fluid. For the total heat transfer across the enclosure, Q, required in determining the Nusselt number, the average of the heat transfer rates measured at the hot and cold walls was used, i.e., $Q = (Q_h + Q_c)/2$. Transport and thermodynamic properties for water were taken to be those at the reference temperature, $T_r = (T_h + T_c)/2$.

During many of the tests, an indication of the flow pattern within the enclosure was obtained by injecting dye into the flow. Roughly 0.5 cc of a dark blue dye was injected with a hypodermic syringe at the upper right-hand corner of the enclosure, midway between the two plexiglas endwalls. Observation of the subsequent dye motion was made through one of the endwalls and was enhanced by a white backdrop at the opposite endwall. The enclosure interior was illuminated by a photographic lamp mounted between the observer and the endwall observation window. The dye was injected and the dye front was allowed to progress a large distance from the point of injection before observations were made.

Results and Discussion

The laminar flow pattern observed in experiments for $A_p < 1$ is shown in Fig. 3. In general, for aperture ratios less than unity (i.e., when a partition was present), the flow was comprised of three relatively distinct regions. There was a peripheral, laminar boundary layer-type flow, a low velocity, relatively inactive core region, and a region of weak, clockwise recirculation in the upper left-hand quadrant of the enclosure. The peripheral flow was composed of thin, high-velocity boundary layers on the vertical surfaces with lower velocity, thicker layers (about 1 cm thickness) on the unheated horizontal surfaces. The boundary layer on the hot wall did not extend over the entire surface because most of the flow separated from the hot wall at approximately $y = h$ and then proceeded across the enclosure horizontally, in a thin, high-velocity layer until reaching the lower edge of the partition. The flow then, apparently without separating from the partition, turned upward along the cool side of the partition finally separating at a distance of one or two centimeters from the ceiling. In this region, the flow was observed to be somewhat unsteady, but the unsteadiness gradually disappeared as the fluid proceeded toward the top of the cold wall. The small amount of dye which entered the upper left quadrant of the enclosure allowed observation of the slowly recirculating flow there. The fraction of the flow entering this region was larger for conducting than for nonconducting partitions. The strength of the recirculating flow was also strongly dependent on the thermal boundary condition at the partition. Conducting partitions resulted in weak recirculation, while adiabatic partitions yielded either very weak or virtually no recirculation in that region. It is noted that in experiments with no partition (aperture ratio of unity) the recirculating region vanished, leaving only a large inactive central core and a peripheral boundary layer flow. It is very possible that interaction of the observed clockwise recirculating flow in the upper left hand quadrant and the high velocity layer at $y = h$ could have resulted in a multi-layer velocity profile in this region as in [21] via two counter-rotating vortices arranged vertically. However, in the vicinity of $y = h$, there was rather severe optical distortion due to the gradient in refractive index and the presumed lower, counterclockwise rotating vortex was not observed.

The flow pattern observed in the present high Ra_L experiments

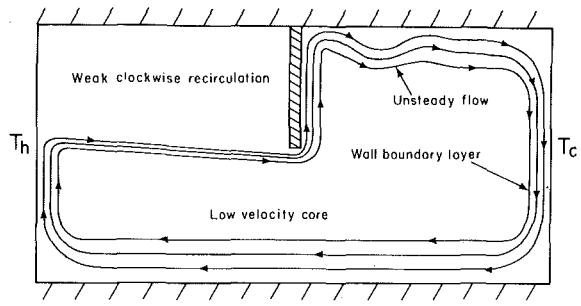

Fig. 3 Flow pattern observed in the cases of adiabatic and perfectly conducting partitions for $A_p < 1$ and $10^{10} \leq Ra_L \leq 10^{11}$

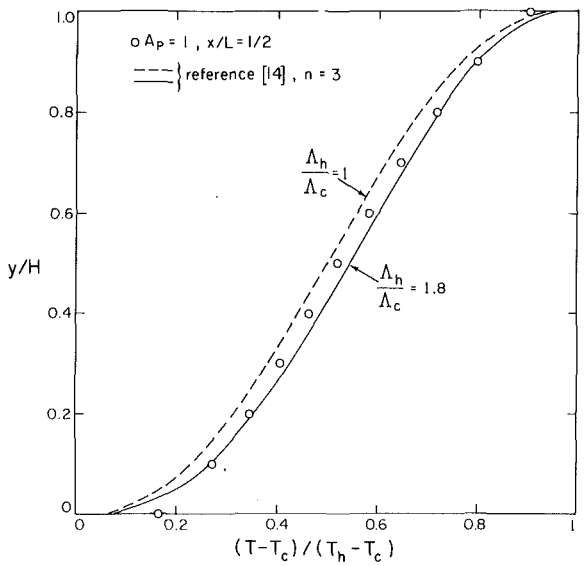

Fig. 4 Midslot vertical temperature profile in the undivided enclosure: $A = \frac{1}{2}$, $Ra_L = 6.41 \times 10^{10}$, Pr = 3.7, $T_h = 72°C$, $T_c = 25°C$

differed substantially from the flow pattern reported by Duxbury [20] in his partially divided enclosure with Ra_L approaching 10^6 and air (Pr = 0.7) as the working fluid. The flow visualization experiments of Duxbury show no distinct recirculating region and also little or no flow separation from the hot wall: two very prominent features of the high Ra_L experiments carried out in this study. Duxbury's experiments indicate some flow separation at the lower edge of the partition on the cool side. This may be due to the fact that in Duxbury's (lower Ra_L) experiments, the flow attempts to make a 180 deg turn as it passes the lower edge of the partition. Recall that in the high Ra_L experiments of this study, the flow only turns through an angle of about 90 deg because the main flow does not penetrate into the upper left quadrant of the enclosure. In general, the results of Duxbury indicate a much smaller inactive core region with thicker boundary layers.

From the flow visualization experiments, it was concluded that fully developed turbulent flow did not exist anywhere within the enclosure, even for Rayleigh numbers as high as 10^{11}. However, traveling wave-like motions, referred to by Elder [4] as "wall waves" were very prominent on both the heated and cooled vertical surfaces with no partition ($A_p = 1$). These waves, the first hint of transitional flow, developed at $y/H \simeq \frac{1}{3}$, and $y/H \simeq \frac{2}{3}$ on the hot and cold walls, respectively, and traveled in the same direction as the mean boundary layer flow. The waves, originally two-dimensional, traveled in a regular pattern up the hot wall and down the cold wall. Gradually, they developed three-dimensional characteristics and finally broke-up very near the upper left- and lower right-hand corners of the enclosure, so that a wave pattern could no longer be distinguished. In the experiments of Elder, with water in enclosures of aspect ratio, $10 \leqslant A \leqslant 30$ ($A = H/L$), the breaking up of the wall waves was accompanied by an intense wall layer-central core interaction. In the present experiments with $A = \frac{1}{2}$, very little, if any, interaction was observed. Perhaps the absence of this phenomena was due to the greater suppression of the interior flow by the horizontal walls for $A = \frac{1}{2}$. In the experiments with aperture ratio (A_p) less than unity (partial division present), the wall waves were indeed found to be significantly suppressed on both the hot and cold walls and completely absent on the hot wall for $y > h$.

A plot of the measured vertical temperature profile at $x/L = \frac{1}{2}$ for the case $A_p = 1$, i.e., no partition, is shown in Fig. 4. This profile exhibits the substantially linear, stable stratification in the enclosure core region which is a well-known characteristic of the boundary layer regime; see [2 and 16]. There is some asymmetry about the position $y/H = \frac{1}{2}$, which is probably due to the temperature dependence of the thermodynamic and transport properties of water. The dashed curve in Fig. 4 is the result of an approximate calculation of the core tem-

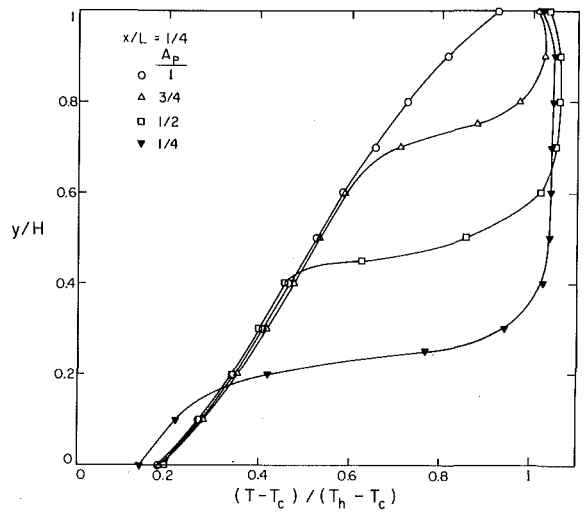

Fig. 5 Vertical temperature profiles at x/L = $\frac{1}{4}$, adiabatic partial divisions: $3.79 \times 10^{10} \leqslant Ra_L \leqslant 6.41 \times 10^{10}$, $3.7 \leqslant Pr \leqslant 4.2$

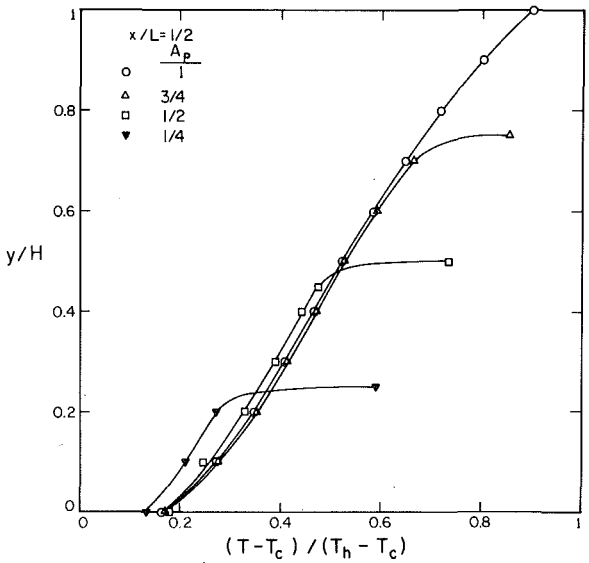

Fig. 6 Vertical temperature profiles at x/L = $\frac{1}{2}$ (in the aperture), adiabatic partial divisions: $3.79 \times 10^{10} \leqslant Ra_L \leqslant 6.41 \times 10^{10}$, $3.7 \leqslant Pr \leqslant 4.2$

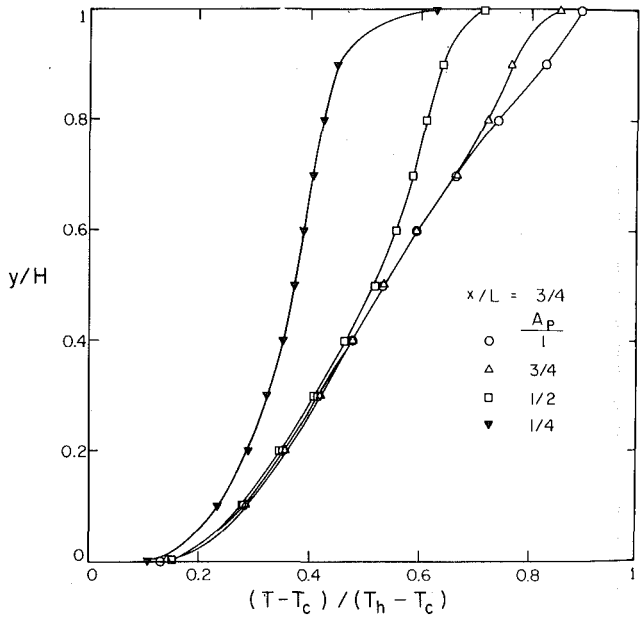

Fig. 7 Vertical temperature profiles at x/L = $\frac{3}{4}$, adiabatic partial divisions: $3.79 \times 10^{10} \leqslant Ra_L \leqslant 6.41 \times 10^{10}$, $3.7 \leqslant Pr \leqslant 4.2$

Table 1 Local heat transfer rates corresponding to Figs. 4–7

A_p	$Q_1(W)$ (Q_1/Q_h)	$Q_2(W)$ (Q_2/Q_h)	$Q_3(W)$ (Q_3/Q_h)	$Q_h(W)$
$\frac{1}{4}$	880 (0.965)	32 (0.035)	0 (0.0)	912
$\frac{1}{2}$	1020 (0.761)	288 (0.215)	32 (0.024)	1340
$\frac{3}{4}$	897 (0.627)	418 (0.292)	115 (0.080)	1430
1	1430 (0.559)	756 (0.295)	373 (0.146)	2559

perature distribution due to Raithby, et al. [14] for enclosures of aspect ratio, $A \gtrsim 5$, filled with a constant property fluid; that is $\Lambda_h = \Lambda_c$, where the property group,

$$\Lambda = \frac{k}{c_p}(\rho^2 \beta/\mu)^{1/3}. \quad (1)$$

Because the mid-cavity temperature gradient, $\partial[(T - T_c)/(T_h - T_c)]/\partial(y/H)$, at $x = L/2$, $y = H/2$, was measured to be 0.59, the Prandtl number-dependent parameter, n, of reference [14] was given a numerical value of 3.0 in generating the curves of Fig. 4 as suggested by Raithby, et al. [14]. The solid curve in Fig. 4 represents the result for the core temperature from [14] for $\Lambda_h/\Lambda_c = 1.8$ which corresponds to the actual wall temperatures ($T_h = 72°C$, $T_c = 25°C$) for the plotted data. Both core temperature predictions yield reasonably good estimates of the measured core temperature; the variable property calculation giving slightly better agreement. Apparently, the calculation technique of Raithby, et al. may be applied with some confidence even somewhat beyond its supposed range of validity ($A \gtrsim 5$).

Vertical temperature profiles at the positions $x/L = \frac{1}{4}, \frac{1}{2}$, and $\frac{3}{4}$ are plotted in Figs. 5, 6, and 7, respectively for the case of $k_p^* \ll 1$ (adiabatic partitions). All the data in these figures were taken in the Ra_L range, $10^{10} \leqslant Ra_L \leqslant 10^{11}$. Over this range it was found that for fixed A_p the non-dimensional temperature profiles are virtually independent of the Rayleigh number. It should be pointed out that no attempt was made to measure the temperature distribution in the thin boundary layers adjacent to the enclosure floor and ceiling. Detailed numerical computations for the case, $A_p = 1$, have shown that for large Ra_L the temperature gradient at the adiabatic surfaces approaches zero only in a very small region near the surface [9]. Measurements were not made in this region and therefore the data often exhibit an apparent non-zero gradient at $y/H = 0$ and 1. Note also that for aperture ratios of $\frac{3}{4}$ and $\frac{1}{2}$ the temperature profiles at each x position are very close to the profiles measured with no partial division ($A_p = 1$) for values of $y/H \lesssim A_p$. This indicates that for aperture ratios at least as small as $\frac{1}{2}$ the temperature field in the lower two quadrants of the partially divided enclosure is substantially unaffected by the partial division. However, for $A_p = \frac{1}{4}$ the partial division apparently has the effect of causing a small temperature decrease for $y/H \lesssim A_p$.

The profiles measured at $x/L = \frac{1}{4}$ (see Fig. (5)) exhibit a small region near $y/H = A_p$, where the temperature increases rapidly to the average hot wall temperature, T_h. The temperature then remains very nearly constant for elevations greater than $y \simeq h$. It was in this region of large temperature gradient that small temperature fluctuations, of the order of $\frac{1}{4}°C$, were detected during the experiments. The time scale, however, of the fluctuations could not be properly investigated due to the long response time of the measurement system. The finite temperature gradient at $y = H$ in Fig. 5 is probably indicative of a small conduction heat loss through the enclosure ceiling since very little or no convection occurs in this region. Also, note in Fig. 5 that the temperature in the upper left quadrant slightly exceeds the average hot wall temperature, T_h. The profiles measured at $x/L = \frac{1}{2}$ (in the aperture plane), Fig. 6, show a very rapid temperature increase in the region close to $y/H = A_p$. It is again emphasized (referring to Fig. 6) that the partial division seems to have little effect on the temperature below $y \simeq h$ except for aperture ratios approaching $\frac{1}{4}$.

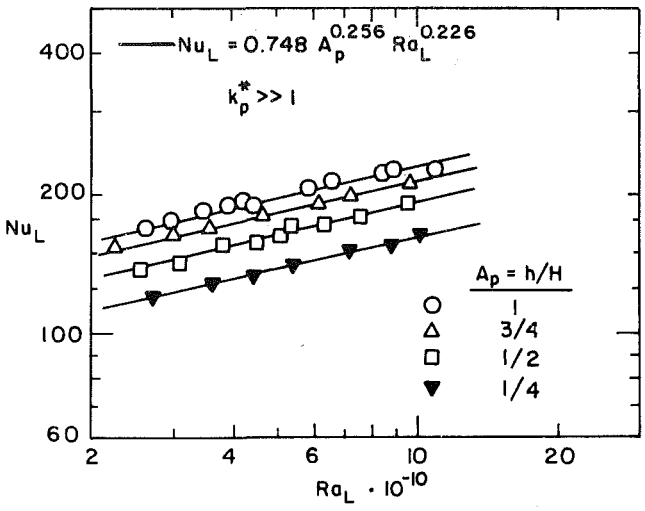

Fig. 8 Heat transfer results and correlation for conducting partial divisions: $3.0 \leqslant Pr \leqslant 4.3$

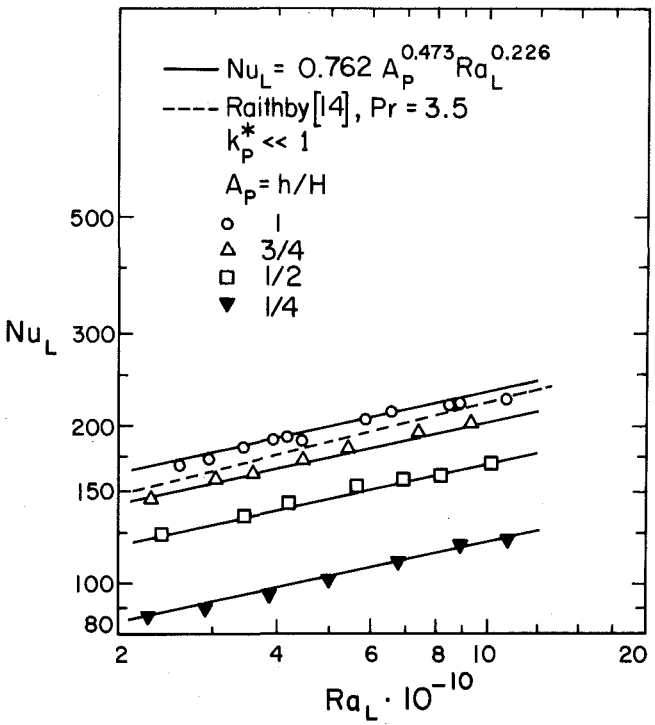

Fig. 9 Heat transfer results and correlation for adiabatic partial divisions: $3.0 \leqslant Pr \leqslant 4.3$, Raithby correlation with Pr = 3.5, $A = \frac{1}{2}$, $Nu_L = 0.392\ Ra_L^{1/4}$

Table 2 Data for the case $A_p = \frac{1}{2}$, adiabatic partial division

Run	$Ra_L \cdot 10^{-10}$	Pr	Nu_L	Q_h (W)	Q_c (W)	$\frac{Q_h - Q_c}{Q_h}$ (%)	T_h (°C)	T_c (°C)	$T_h - T_c$ (°C)
1	4.21	3.8	142	1290	1260	2.3	63.0	29.6	33.4
2	5.65	3.6	153	1680	1640	2.4	69.8	29.7	40.1
3	3.46	3.9	135	1050	1020	2.9	59.4	30.8	28.6
4	2.41	4.4	125	820	780	4.9	51.4	27.1	24.3
5	6.94	3.4	157	1940	1930	0.5	75.2	29.6	45.6
6	8.19	3.3	161	2220	2210	0.5	79.8	29.2	50.6
7	10.2	3.1	170	2640	2580	2.3	86.5	30.3	56.2

The effect of the partial divisions at $x/L = \frac{3}{4}$ (Fig. 7) is to decrease the temperature for $y/H \gtrsim A_p$, the effect becoming stronger with decreasing aperture ratio. This behavior seems reasonable because for a non-conducting partition as aperture ratio approaches zero: i.e., the completely divided enclosure, $T \to T_h$ for $x < L/2$ and $T \to T_c$ for $x > L/2$.

In general, the measured temperature profiles seem to verify the statements made concerning the basic nature of the flow in the partially divided enclosure: i.e., the existence of an inactive core region, a region of very weak recirculation and a peripheral boundary-layer flow.

Local hot wall heat transfer rates for experiments with and without adiabatic partial divisions are shown in table 1. (In this table, Q_1 represents the heat transfer rate over the lower one-third of the hot wall, while Q_2 and Q_3 are the rates for the middle and upper one-third, respectively.) The results of the seven heat transfer experiments for $A_p = \frac{1}{2}$ and $k_p^* \ll 1$ are listed in table 2. In all of the experiments the wall temperature difference was greater than 22°C but never exceeded 61°C. The heat transfer data for conducting and non-conducting partitions are presented graphically in Figs. 8 and 9. Note that in Fig. 9 the approximate Nusselt number prediction of Raithby, et al. [14] for undivided enclosures ($A_p = 1$) in the laminar boundary layer regime again gives a reasonably good estimate of the heat transfer in the enclosure of aspect ratio $A = \frac{1}{2}$, even though this prediction was generated on the basis of rather tall, narrow enclosures: i.e., vertical layers with $A \gtrsim 5$. From the data in Figs. 8 and 9 the following correlations were generated for the cases of conducting and non-conducting partial divisions:

$$\mathrm{Nu}_L = 0.748\, A_p^{0.256}\, \mathrm{Ra}_L^{0.226} \quad \text{(conducting partitions)} \tag{2}$$

$$\mathrm{Nu}_L = 0.762\, A_p^{0.473}\, \mathrm{Ra}_L^{0.226} \quad \text{(non-conducting partitions)} \tag{3}$$

where the root-mean-square deviation of the data from the correlations are 2.5 and 3.8 for conducting and non-conducting partitions, respectively. Note from Figs. 8 and 9 that there is virtually no difference in the Rayleigh number dependence of the Nusselt number as A_p is varied, that is, all curves have roughly the same slope regardless of the aperture ratio. This behavior was also found at a lower Ra_L, with air [20]. Also note that the heat transfer dependence on A_p increases substantially (the exponent of A_p in equations (2) and (3) changes approximately from $\frac{1}{4}$ to $\frac{1}{2}$) when the enclosure is partially divided by a non-conducting rather than by a conducting partition. This increased dependence on A_p supports the earlier observation that the flow recirculation in the upper left-hand quadrant of the partially divided enclosure is severely limited by non-conducting partition materials. Thus, adiabatic partitions represent an increased resistance to the heat transfer across the enclosure with a greater resulting sensitivity to the aperture ratio.

It is noted that the above cited results for the dependence of the heat transfer on A_p do not agree with the results of the low Rayleigh number experiments with air [20]. Duxbury's data for enclosures of aspect ratio, $A = \frac{5}{8}$, with conducting partitions, are found to be reasonably well correlated by a relation of the form given by equation (2) with an aperture ratio dependence of $A_p^{0.41}$ rather than $A_p^{0.256}$ as was found in this study. However, this discrepancy is not too surprising since the two experiments were carried out at different values of Pr (0.7 in [20] versus 3.5 for this study) and at widely different values of Ra_L (10^6 versus 10^{10}). In addition, it is believed that the substantial heat losses (15–40 percent) from the experimental cells of Duxbury may have adversely effected the accuracy of his results.

Conclusions

Experiments with water in a partially divided rectangular enclosure have revealed the existence of three relatively distinct regions at Rayleigh numbers approaching 10^{11}: i.e. the existence of an inactive core region, a region of very weak recirculation and a peripheral boundary-layer flow. The partial divisions were also shown to significantly decrease the overall heat transfer, especially when the partitions were non-conducting. Also, laminar-transitional flow on the enclosure vertical surfaces was found to be suppressed markedly by the presence of the divisions. These results could be significant with respect to design considerations in solar heating applications.

It is recommended that further study be directed toward the determination of the separate effects of Prandtl number and aspect ratio on the heat transfer. It is not clear, for example, how much of the discrepancy found between Duxbury's results and the present results is due to differences in Ra_L (10^6 versus 10^{10}) or due to differences in Pr (0.7 versus 3.5). Extending the range of Ra_L to larger values should also serve to expose the role of partial divisions in retarding the transition to turbulent flow, a subject which has only been alluded to in the present work. Finally, a more detailed accounting of the local fluid velocities within the enclosure would be instrumental in gaining an understanding of the rather complex flow observed in these experiments.

Acknowledgement

This work has been supported in part by the Research and Development Branch, Passive and Hybrid Division, of the Office of Solar Applications for Buildings, U.S. Department of Energy, under Contract No. W-7405-ENG-48. The authors also wish to acknowledge Fred Bauman of the Lawrence Berkeley Laboratory for his assistance during the early stages of this research.

References

1 Batchelor, G. K., "Heat Transfer by Free Convection Across a Closed Cavity Between Vertical Boundaries at Different Temperatures," *Quart. of Applied Mathematics*, Vol. XII, 1954, pp. 209–233.

2 Eckert, E. R. G. and Carlson, W. D., "Natural Convection in an Air Layer Enclosed Between Two Vertical Plates with Different Temperatures," *International Journal of Heat Mass Transfer*, Vol. 2, 1961, pp. 106–120.

3 Dropkin, D. and Somerscales, E., "Heat Transfer by Natural Convection in Liquids Confined by Two Parallel Plates Which are Inclined at Various Angles with Respect to the Horizontal," JOURNAL OF HEAT TRANSFER, Vol. 87, 1965, pp. 77–84.

4 Elder, J. W., "Turbulent Free Convection in a Vertical Slot," *Journal of Fluid Mechanics*, Vol. 23, 1965, pp. 99–111.

5 Emery, A. and Chu, N. C., "Heat Transfer Across Vertical Layers," JOURNAL OF HEAT TRANSFER, Vol. 87, 1965, pp. 110–116.

6 de Vahl Davis, G., "Laminar Natural Convection in an Enclosed Rectangular Cavity," *International Journal of Heat and Mass Transfer*, Vol. 11, 1968, pp 1675–1693.

7 Torrance, K. E., "Comparison of Finite-Difference Computations of Natural Convection," *Journal of Research of the National Bureau of Standards, B. Mathematical Sciences*, Vol. 72B, 1968, pp. 281–301.

8 Mac Gregor, R. K. and Emery, A. F., "Free Convection through Vertical Plane Layers, Moderate and High Prandtl Number Fluids," JOURNAL OF HEAT TRANSFER, Vol. 91, 1969, pp. 391–403.

9 Rubel, R. and Landis, F., "Numerical Study of Natural Convection in a Vertical Rectangular Enclosure," *Physics of Fluids Supplement II*, Vol. 12, 1969, pp. 203–213.

10 Newell, M. E. and Schmidt, F. W., "Heat Transfer by Laminar Natural Convection within Rectangular Enclosures," JOURNAL OF HEAT TRANSFER, Vol. 92, 1970, pp. 159–165.

11 Ostrach, S., "Natural Convection in Enclosures," *Advances in Heat Transfer*, Academic Press, Vol. 8, 1972, pp. 161–227.

12 Raithby, G. D. and Hollands, K. G. T., "A General Method of Obtaining Approximate Solutions to Laminar and Turbulent Free Convection Problems," *Advances in Heat Transfer*, Academic Press, Vol. 11, 1975, pp. 265–315.

13 Arnold, J. N., Catton, I. and Edwards, D. K., "Experimental Investigation of Natural Convection in Inclined Rectangular Regions of Differing Aspect Ratios," JOURNAL OF HEAT TRANSFER, Vol. 98, 1976, pp. 67–71.

14 Raithby, G. D., Hollands, K. G. T. and Unny, T. E., "Analysis of Heat Transfer by Natural Convection Across Vertical Fluid Layers," JOURNAL OF HEAT TRANSFER, Vol. 99, 1977, pp. 287–293.

15 Sernas, V. and Lee, E. I., "Heat Transfer in Air Enclosures of Aspect Ratio Less than One," ASME 78-WA/HT-7, 1978.

16 Lee, E. I. and Sernas, V., "Numerical Study of Heat Transfer in Rectangular Air Enclosures of Aspect Ratio Less Than One," ASME 80-WA/HT-45, 1980.

17 Bauman, F., Gadgil, A., Kammerud, R. and Greif, R. "Buoyancy Driven Convection in Rectangular Enclosures: Experimental Results and Numerical Calculations," ASME 80-HT-66, 1980.

18 ElSherbiny, S. M., Raithby, G. D., and Hollands, K. G. T., "Heat Transfer by Natural Convection Across Vertical and Inclined Air Layers," ASME 80-HT-67, 1980.

19 LeQuere, P., Humphrey, J. A. C. and Sherman, F. S., "Numerical Calculation of Thermally Driven Two-Dimensional Unsteady Laminar Flow in Cavities of Rectangular Cross-Section," University of California, Berkeley,

Report No. FM 80/1, 1980.

20 Duxbury, D., "An Interferometric Study of Natural Convection in Enclosed Plane Air Layers with Complete and Partial Central Vertical Divisions," Ph.D. thesis, University of Salford, 1979.

21 Lynch, N. P., and Lloyd, J. R., "An Experimental Investigation of the Transient Build-Up of Fire in a Room Corridor Geometry," *18th International Symposium on Combustion*, The Combustion Institute, Pittsburgh, Pa., 1980.

22 Ku, A. C., Doria, M. L. and Lloyd, J. R., "Numerical Modeling of Unsteady Buoyant Flows Generated by Fire in a Corridor," *16th International Symposium on Combustion*, The Combustion Institute, Pittsburgh, Pa., 1976, pp. 1373–1384.

23 Janikowski, H. E., Ward, J. and Probert, S. D., "Free Convection in Vertical Air-Filled Rectangular Cavities Fitted with Baffles," *6th International Heat Transfer Conference*, Toronto, Vol. 2, pp. 257–262.

24 Emery, A. F., "Exploratory Studies of Free Convection Heat Transfer Through an Enclosed Vertical Liquid Layer with a Vertical Baffle," JOURNAL OF HEAT TRANSFER, Vol. 91, 1969, pp. 163–165.

25 Bejan, A., and Tien, C. L., "Laminar Natural Convection Heat Transfer in a Horizontal Cavity with Different End Temperatures," JOURNAL OF HEAT TRANSFER, Vol. 100, 1978, pp. 641–647.

Natural Convection Heat Transfer Coefficients for a Short Horizontal Cylinder Attached to a Vertical Plate

E. M. Sparrow
Fellow ASME

G. M. Chrysler
Department of Mechanical Engineering,
University of Minnesota,
Minneapolis, Minn. 55455

Experiments were performed to investigate the natural convection heat transfer characteristics of a short isothermal horizontal cylinder attached to an equi-temperature vertical plate. The apparatus was designed so that the cylinder could be attached to the plate at any one of three positions along the height of the plate. Two cylinders were employed (one at a time) during the course of the experiments, one of which had a length equal to its diameter while the other had a length that was half the diameter. At each attachment position and for each cylinder, the Rayleigh number (based on the cylinder diameter) ranged from 1.4×10^4 to 1.4×10^5. It was found that the interaction of the flat plate boundary layer with the cylinder brought about a reduction of the cylinder Nusselt number relative to that for the classical case of the long isolated horizontal cylinder without end effects. The respective deviations of the Nusselt numbers for the shorter and longer of the participating cylinders from the literature correlation for the isolated cylinder were twenty percent and ten percent. At a given Rayleigh number, the cylinder Nusselt number was quite insensitive to the position of the cylinder along the plate, with the typical data spread due to height being in the 5–7 percent range. The Nusselt number was also rather insensitive to cylinder length, showing a ten percent increase as the length-diameter ratio was increased from one-half to one.

Introduction

Natural convection heat exchange devices, such as those employed in the cooling of electronic equipment, may involve the interaction of buoyant streams individually induced by heating (or cooling) at the various surfaces which comprise the device. Such an interaction occurs when a heated horizontal cylinder is attached at one of its ends to a heated vertical plate. The upward-moving natural convection boundary layer flow induced by the plate impinges on the cylinder which, in its own right, induces a buoyant upflow. This physical situation, which is the subject of the present experiments, not only constitutes a prototype study of natural convection interactions, but it also models the use of cylindrical fins to enhance the natural convection heat transfer from a vertical surface. Aside from fins, there may be cylinder-like protuberances on natural-convection cooled vertical surfaces, and the present research also applies to that situation.

The experiments were performed with a highly polished, isothermal vertical plate serving as the host surface fo the equi-temperature horizontal cylinder, which was also polished to a mirror-like finish. The plate was designed so that the cylinder could be attached to it at any one of three positions along its height, respectively ajdacent to the lower edge of the plate, at mid-height, and adjacent to the upper edge of the plate. This design feature was provided so that the cylinder might encounter flat plate boundary layers of different thickness.

Three parameters were varied during the course of the experiments. As already mentioned, one of these is the position of the cylinder at various distances from the leading edge of the plate. At each fixed position, the temperature difference between the equi-temperature surfaces and the ambient was varied systematically, so that the cylinder Rayleigh number ranged from about 10^4 to 10^5. Cylinders of two different length-diameter ratios were employed during the course of the experiments. One cylinder had a length equal to its diameter, while the length of the second was half that of the first. The selection of the latter cylinder was made with a view to increasing the portion of the cylindrical surface that is washed by the boundary layer of the plate. The experiments were performed in air.

Contributed by the Heat Transfer Division for publication in the JOURNAL OF HEAT TRANSFER. Manuscript received by the Heat Transfer Division January 19, 1981.

The main focus of the work is the determination of the heat transfer characteristics of the cylinder and the identification of the effects of the plate-cylinder interaction. Cylinder Nusselt numbers are reported as a function of the Rayleigh number, with special attention being given to how the Nusselt number is affected by the elevation at which the cylinder is attached to the plate and by the length-diameter ratio of the cylinder. Comparisons are also made between the present results and literature information for the classical single isolated cylinder. Furthermore, to provide perspective for certain remarkable features of the results, representative velocity and temperature profiles for the flat plate boundary layer are presented.

In recognition of the relatively low values of the natural convection heat transfer coefficient for surfaces situated in air, special precautions are employed to defend against extraneous heat losses due to conduction and to radiation. The special features of the apparatus and the procedures used to ensure results of high accuracy will be described in detail.

The spatial uniformity of the cylinder temperature and the equality of the cylinder and plate temperatures imply, relative to a fin, an efficiency of unity. Fin efficiencies in the neighborhood of unity are quite realistic for metallic fins which transfer heat to air via natural convection.

A search of the literature failed to reveal any published work related to the subject of the present research. A few papers were found which dealt with the interactions between clusters of horizontal cylinders [1–3]; in these cases, the cylinders were very long relative to their diameters and there were no wall attachments. Some work was encountered on interactions between surfaces in internal natural convection (i.e., within enclosures), but those configurations are quite remote from the present physical situation.

Experimental Apparatus and Procedure

Apparatus. A pictorial view of the experimental apparatus is presented in Fig. 1. As seen there, a vertical aluminum plate is framed by styrofoam block and sheet insulation. A horizontal cylinder is shown implanted in the plate surface at a point midway along the height of the plate. The mid-height position is one of three at which the cylinder can be attached to the plate. The other two positions are indicated by dashed circles on the plate surface. All three cylinder

positions are situated along the spanwise centerline of the plate. Also shown in the figure are styrofoam side baffles whose function was to prevent transverse fluid flows along the laterial edges of the plate. The suspension of the plate was accomplished by a pair of monofilament nylon lines attached to the upper edge of the plate by eyebolts, this suspension arrangement having been chosen to avoid extraneous heat conduction. The lines terminated in a wooden frame situated above the apparatus.

The plate is a rectangle, 45.72 cm high by 30.48 cm wide (18.00 by 12.00 in.), with a wall thickness of 1.250 cm (0.492 in.). Its edges were carefully machined to ensure parallelism, while the exposed face was subjected to a painstaking polishing procedure [4] which produced a surface finish which can be characterized as "highly polished" from the standpoint of thermal radiation properties. The plate was heated by electrical resistance wire affixed to its rear surface. The wire was deployed to give a heat flux distribution that varied approximately as the inverse one-quarter power of the distance from the leading edge, in accordance with the natural convection boundary layer solution for uniform wall temperature. In no case did measured nonuniformities of temperature at the exposed surface of the plate exceed $1\frac{1}{2}$ percent of the surface-to-ambient temperature difference (the plate thermocouples and their deployment will be discussed later).

To accommodate the horizontal cylinder, three holes were machined through the thickness of the plate at the positions shown in Fig. 1, respectively with centers situated 5.08, 22.86, and 40.64 cm (2, 9, and 16 in.) above the leading edge. Since only one cylinder was employed during a given data run, the other two holes were closed by specially machined plugs which, when in place, provided a hydrodynamically smooth surface for the airflow. The hole diameter was made to accommodate either a 1.905 cm (0.750 in.) dia plug for the closed holes or a Delrin plastic bushing of the same diameter which served as a liner for the hole in which the cylinder was to be implanted.

Each of the plugs consisted of an aluminum face pressed into a threaded brass body (brass was used to avoid galling). The underside of the face was contoured to precisely match the countersunk hole in which it fit. To promote heat conduction from the plate proper into the plug, a significant area of contact was provided along the beveled surfaces of the hole and plug. As a result, the temperature of a plug never differed by more than 1 μV from that of the surrounding plate.

As was noted earlier, the rear face and the edges of the plate were thermally isolated from the surroundings by styrofoam sheet and/or block insulation, which was employed in a thickness of 13 cm (5 in.). A thin layer of fiberglass was positioned immediately adjacent to the rear face of the plate (i.e., between the plate and the styrofoam) in order to provide a yielding bearing surface for the wires that were led out of the plate and cylinder. Fiberglass was also placed in the channels that had been recessed into the styrofoam to allow passage for the monofilament nylon support lines. Counterweights in conjunction with leveling screws in the support structure facilitated vertical alignment of the plate surface and horizontal alignment of the plate leading edge, with both alignments being viewed with a hairline-equipped cathetometer.

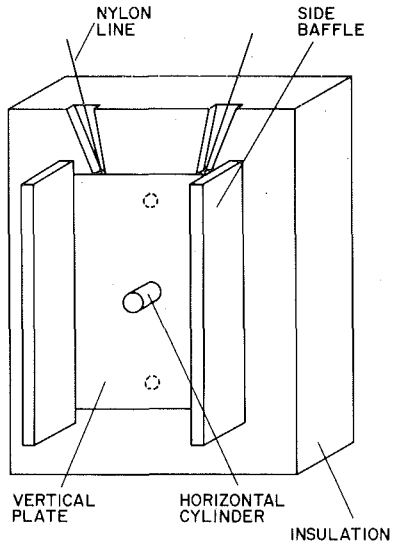

Fig. 1 Pictorial view of the experimental apparatus

Attention will now be turned to the test cylinders. Two cylinders were fabricated, each from a solid piece of aluminum. Each cylinder consisted of a convection section (i.e., the portion exposed to the airflow) and a threaded integral shank which mated with the Delrin liner of the host aperture of the plate. For both cylinders, the diameter of the convection section (hereafter called the cylinder diameter), was 4.000 cm (1.575 in.). The respective lengths of the convection portion of the cylinders (hereafter called the cylinder length) were 4.000 and 2.000 cm (1.575 and 0.787 in.). The shank was 1.27 cm (0.50 in.) in diameter and 1 cm ($\frac{3}{8}$ in.) long.

Each cylinder was bored axially from the shank end to create a 0.953-cm (0.375-in.) dia cavity to accommodate a specially wound heating element. The cavities for the two cylinders respectively terminated 0.762 and 0.381 cm (0.300 and 0.150 in.) from the circular end face of the convection portion of the cylinder. Each heating element consisted of a hollow Delrin cylinder wound with electrical resistance wire. The outer surface of the Delrin was slotted axially, with the slots being spaced at 30 deg intervals around the circumference. Heating wire, 0.008-cm (0.003-in.) dia teflon-coated chromel thermocouple wire, was laid in the slots in a back and forth arrangement. The heater, when completely assembled, was press fit into the cavity.

The heater design and the choice of heating wire were made to attain the highest possible resistance and, thereby, to keep the electric current flow as small as possible. Small currents enabled the use of small diameter copper lead wires (0.0254 cm, 0.010 in.) to deliver the power to the heater, thereby minimizing the possibility of extraneous heat losses by conduction. For this same reason, voltage tap wires, used for measuring the voltage drop across the heating element, were of 0.008-cm (0.003-in.) dia constantan.

Nomenclature

A = surface area
C = constant in equation (15)
C_1 = constant in equation (16)
c_p = specific heat
D = cylinder diameter
E = voltage across cylinder heater
F = angle factor
g = acceleration of gravity
h = cylinder heat transfer coefficient
I = current through cylinder heater
k = thermal conductivity
L = cylinder length
Nu = cylinder Nusselt number, hD/k
Q = natural convection heat transfer from cylinder
Q_r = radiation heat transfer from cylinder
Q_{rd} = direct component of Q_r
Q_{rr} = reflected component of Q_r
Ra = cylinder Rayleigh number, equation (13)
T_w = temperature of cylinder and plate
T_r = reference temperature, equation (14)
T_∞ = ambient air temperature and room wall temperature
x_c = distance between plate leading edge and lower stagnation point of cylinder
α = absorptivity of cylinder
β = thermal expansion coefficient
ϵ = emissivity of cylinder and plate
θ_∞^4 = shifted radiation temperature, $(T_w^4 - T_\infty^4)$
μ = viscosity
ρ = density
ρ_p = reflectivity of plate
σ = Stefan-Boltzmann constant

Subscripts

cc = cylindrical surface of cylinder
ct = tip of cylinder
p = plate
s = fictive black surface

As will be elaborated shortly, a main objective of the experimental procedure is the total elimination of heat transfer between the test cylinder and the host plate. Although the main factor in the defense against conduction is the attainment of temperature equality of the cylinder and plate, steps were also taken to minimize direct contact. In particular, contact between the plate-adjacent face of the cylinder and the plate surface was avoided by the presence of an O-ring seated in a circular groove in the face, adjacent to the outer rim. With the cylinder installed in the plate, the O-ring was compressed so as to leave a gap of 0.013 cm (0.005 in.) between the cylinder face and the plate.

Another factor in the defense against conduction between the plate and the cylinder was the Delrin liner which separated the shank of the cylinder from the plate. The liner, a relatively poor heat conductor, served as a thermal resistance which amplified the plate-to-cylinder temperature difference in the presence of a heat flow. This heightened sensitivity facilitated the nulling-out of the heat transfer.

Instrumentation and Experimental Procedure. The installation and function of the thermocouples in the plate and the cylinder will now be described. The characteristics of the thermocouple wire (i.e., small diameter, low thermal conductivity, high sensitivity) were selected with a view toward minimizing conduction-related measurement errors and maximizing resolution of small temperature differences. This objective was fulfilled by 0.008 cm (0.003 in.) dia teflon-coated chromel and constantan wire that was especially calibrated for these experiments.

There was a total of 12 thermocouples embedded in the wall of the flat plate, with the junctions positioned 0.076 cm (0.030 in.) from the surface exposed to the airflow. Each of the three cylinder-installation apertures was surrounded by three thermocouples, while the remaining three thermocouples were positioned adjacent to the lateral edges of the plate. The three aperture-adjacent thermocouples were located 120 deg apart on a 2.223-cm (0.875-in.) dia circle concentric with the aperture. These thermocouples were used to attain a precise match-up of temperatures with a corresponding trio of thermocouples situated in the shank of the test cylinder.

Each of the test cylinders was equipped with six thermocouples. Three of these were positioned in the convection portion of the cylinder, with the respective junctions situated 0.076 cm (0.030 in.) from the nearest exposed surface. The other three thermocouples were located in the shank of the cylinder, positioned in especially machined axial slots spaced at 120 deg intervals around the circumference of the shank. These thermocouples were so installed (and fixed with copper oxide cement) that when the cylinder was in place in any one of the plate apertures, there was precise angular and axial alignment of the three shank thermocouples and three plate thermocouples.

All lead wires from the cylinder emerged through the rear end of the shank. To avoid extraneous heat conduction effects, these wires, as well as those from the plate, were held against the rear face of the plate (an isothermal surface) by tape as they were led off to the side and out of the apparatus.

In addition to the plate and cylinder temperature measurements, the temperature of the ambient air was sensed (and possible stratification detected) by a vertical array of three thermocouples, with the respective heights corresponding to those of the apertures in the plate. These thermocouples were mounted just to the side of the insulation which framed the plate and, because of their positioning, were completely shielded with regard to radiation from the plate or the cylinder.

All thermocouple interfaces (i.e., connectors and terminals) were maintained spatially isothermal by means of an enveloping aluminum block and/or insulation. The thermocouple emfs were read to 1 μV by the very same digital voltmeter that had been used in the thermocouple calibration.

Power for the fully independent plate and cylinder heating circuits was provided by a regulated a-c supply having unusual stability (e.g., 0.03 percent over a three-day period). The power circuitry involved autotransformers for voltage control and a step-down transformer to increase the sensitivity of the control, thereby facilitating the precise balancing of the plate and cylinder temperatures that is the key factor in the attainment of accurate results. All heater-related voltages (current was measured as a voltage drop across a calibrated shunt) were read with a digital voltmeter having a rated accuracy of ± 0.15 percent of the reading.

The experimental apparatus was situated in a laboratory room of dimensions 4.3 × 7.6 × 3 m (14 × 25 × 10 ft), which possessed remarkable thermal isolation and stability characteristics. The laboratory is, in fact, a room within a room. Its walls, ceiling, and floor are each backed by a 46 cm ($1\frac{1}{2}$ ft) thickness of cork, which provides excellent thermal isolation. There are no ducts, grilles, vents, or heating pipes in the laboratory. The temperature of the air in the laboratory, as measured by fine thermocouple wires, is altogether devoid of fluctuations and is also very steady over long periods of time. Thermal stratification, even after long data runs, was negligible. To insure the absence of disturbances in the laboratory, all instrumentation and power supplies were situated in a room adjacent to the laboratory, the laboratory being sealed throughout the entire duration of each data run.

Each data run was initiated by setting the plate and cylinder power inputs at levels which, based on experience with prior runs, would yield the desired surface-to-ambient temperature difference and a near balance between the emfs of the thermocouples in the cylinder shank and in the adjacent portion of the plate. Then, an equilibration period of at least eight hours was allowed before any readings were made and, at that time, note was taken of the degree of emf imbalance between the shank and plate thermocouples. The power to the cylinder was raised or lowered in order to reduce the imbalance to zero, and one to two hours were allowed for the reinstatement of steady state conditions before the effects of the power change were recorded. If an imbalance remained, a further change was made in the cylinder power, and this procedure was continued until the shank and adjacent plate thermocouples read the same emf.

A high degree of temperature uniformity existed within each group of thermocouples. The three thermocouples embedded in the convection portion of the cylinder read identical values to within the 1 μV resolving power of the instrumentation. Among the three shank thermocouples, deviations of 1 μV were typical, and deviations in the 0 to 1 μV range were encountered among the three thermocouples in the adjacent portion of the plate. To place these findings in perspective, it may be noted that 1°C corresponds to 60 μV for the thermocouples employed and that the surface-to-ambient temperature differences of the experiment ranged from about 2.5 to 30°C.

Data Reduction

The procedures used to determine cylinder heat transfer coefficients, Nusselt numbers, and Rayleigh numbers from the measured thermocouple emfs, power input, and barometric pressure will now be described. The starting point of the data reduction procedure is the definition of the average heat transfer coefficient for the cylinder (including both the cylindrical surface and the circular end face)

$$h = Q/A(T_w - T_\infty) \tag{1}$$

where Q is the rate of heat transfer by natural convection from the cylinder to the air, and A is the total exposed surface area

$$A = \pi DL + \pi D^2/4 \tag{2}$$

In this equation, D and L respectively represent the diameter and length of the cylinder, numerical values for which have already been given for the two cylinders used during the course of the experiments.

Typically, the readings of the various thermocouples installed in the cylinder differed by no more than 1 μV (i.e., <1/60°C), and the average of the thermocouple emfs was used to evaluate T_w in equation (1). For T_∞, the temperature of the ambient air at the elevation of the cylinder was employed. In this regard, it may be noted that virtually no stratification was observed, with typical ambient temperature variations between the elevations of the highest and lowest cylinder attachment points (35 cm, 14 in.) being confined to the $1 - 2$ μV range.

With regard to Q, the balancing of the cylinder and plate temperatures nulls out conduction heat transfer between the cylinder and the plate. Therefore, the electric power input to the cylinder is equal to the sum of the rates of heat transfer from the cylinder by natural convection and by radiation. If E and I respectively denote the measured voltage and current for the cylinder heater and Q_r is the radiation heat transfer from the cylinder, then

$$Q = EI - Q_r \tag{3}$$

Owing to the highly polished surface finish of the cylinders, Q_r was always very small compared with the input power EI. At the highest power input, corresponding to $(T_w - T_\infty) \simeq 30°C$ (54°F), calculations showed that $Q_r/EI \sim 5$ percent. At the low power extreme, where $(T_w - T_\infty) \simeq 2.3°C$ (4.1°F), $Q_r/EI \sim 8$ percent. Notwithstanding the minor role of radiation, it was calculated with care for each case. The analytical basis for the radiation calculation will now be described.

To facilitate the radiation analysis, it is convenient to shift the scale of T^4 (T = absolute temperature). To this end, let

$$\theta^4 = T_w^4 - T^4 \tag{4}$$

so that

$$\theta_\infty^4 = T_w^4 - T_\infty^4, \qquad \theta_w^4 = T_w^4 - T_w^4 = 0 \tag{5}$$

It should also be noted that T_∞ denotes both the temperature of the air and the temperature of the walls of the laboratory. Furthermore, the laboratory room closely fulfills all the requirements of a blackbody enclosure. Therefore, the radiant energy flux streaming through the room is blackbody radiation corresponding to T_∞^4 or, in the transformed scale, to θ_∞^4.

The simplification afforded by the T^4 shift, equation (4), is that neither the cylinder nor the plate emits thermal radiation. Rather, in terms of θ^4, these surfaces are at zero temperature. The laboratory room is filled with blackbody radiation $\sigma\theta_\infty^4$ per unit time and area. An analysis will now be carried out to determine, under these circumstances, how much radiation is absorbed by the cylinder. The magnitude of the thus-absorbed radiant energy is equal to the radiation heat transfer Q_r from the cylinder under the actual operating conditions (i.e., prior to the shift of the T^4 scale).

The energy absorbed by the cylinder can be regarded as having two components. One of these stems from the blackbody radiant flux $\sigma\theta_\infty^4$ that is directly incident on the cylinder. The other stems from the reflection of $\sigma\theta_\infty^4$ by the plate onto the cylinder. These two contributions to Q_r will be respectively designated as Q_{rd} (direct) and Q_{rr} (reflected). Furthermore, owing to the mirror-like surface finish of the plate, it can be regarded as a specular reflector.

To further facilitate the analysis, it is convenient to envision a black surface S in a form of a tent whose base is the vertical plate. The exact shape of S is arbitrary but it must extend beyond the tip of the cylinder (i.e., the cylinder is wholly within the tent-like surface). If S emits radiation $\sigma\theta_\infty^4$ per unit time and area, then it is completely equivalent to the radiant flux $\sigma\theta_\infty^4$ which streams through the laboratory.

If A_{cc} and A_{ct} respectively denote the areas of the cylindrical and tip surfaces of the cylinder and A_s is the area of the fictive surface S, then the direct component Q_{rd} of the absorbed radiation is

$$Q_{rd} = \alpha(\sigma\theta_\infty^4 A_s F_{s-cc} + \sigma\theta_\infty^4 A_s F_{s-ct}) \tag{6}$$

where F_{s-cc} and F_{s-ct} are angle factors for radiation travelling between S and cc and between S and ct, and α is the absorptivity of the cylinder surface. When angle factor algebra is employed, e.g., $A_s F_{s-cc} = A_{cc} F_{cc-s}$, and note is taken of the fact that $F_{ct-s} = 1$, it follows that

$$Q_{rd} = \alpha\sigma\theta_\infty^4(A_{cc}F_{cc-s} + A_{ct}) \tag{7}$$

Furthermore, if F_{cc-p} denotes the angle factor for radiation travelling from A_{cc} to the plate, it is apparent from angle factor algebra that

$$F_{cc-s} = 1 - F_{cc-p} \tag{8}$$

With regard to the component Q_{rr}, it may be noted that the black body radiation from S which arrives at the cylinder via specular reflection from the plate appears to originate at the plate surface. However, owing to the fact that the plate is not a perfect reflector, $\sigma\theta_\infty^4$ is derated by ρ_p, the reflectivity of the plate. Therefore

$$Q_{rr} = \alpha\sigma\theta_\infty^4\rho_p A_p F_{p-cc} \tag{9}$$

where note has been taken of the fact that $F_{p-ct} = 0$. When angle factor algebra is employed, equation (9) becomes

$$Q_{rr} = \alpha\sigma\theta_\infty^4\rho_p A_{cc} F_{cc-p} \tag{10}$$

Equations (7) and (10) may now be added together to yield Q_r, with account being taken of equation (8) and of the fact that the plate and cylinder have the same emissivity ϵ (where $\alpha = \epsilon$ and $\rho_p = 1 - \epsilon$), so that

$$Q_r = \epsilon\sigma(T_w^4 - T_\infty^4)(A_{cc}(1 - \epsilon F_{cc-p}) + A_{ct}) \tag{11}$$

An expression for F_{cc-p} has been derived in Appendix B of [4]. When the cylinder is positioned in the central aperture in the plate, $F_{cc-p} = 0.3485$ and 0.4230, respectively for the longer and shorter cylinders. The corresponding numerical values for the cylinder positioned adjacent to either the leading and trailing edges of the plate are 0.2024 and 0.3074.

Equation (11) enables the evaluation of Q_r for both the shorter and longer cylinders. On the basis of [5] and [6], ϵ was taken to be 0.04. Auxiliary computations, to be reported shortly, were made for $\epsilon = 0.05$ to examine the sensitivity of the resulting natural convection heat transfer coefficients to the value of ϵ.

With the determination of Q_r, the convective heat transfer rate Q follows from equation (3) and the heat transfer coefficient h is then evaluated from (1).

The h values will be reported in dimensionless form via the Nusselt number

$$\mathrm{Nu} = hD/k \tag{12}$$

The Nusselt number results will be parameterized by the Rayleigh number

$$\mathrm{Ra} = g\beta\rho^2 c_p D^3(T_w - T_\infty)/\mu k \tag{13}$$

It may be noted that the cylinder diameter D has been used as the characteristic dimension. Since both test cylinders have the same diameter, this choice enables comparisons of Nusselt numbers for the two cylinders to be regarded as direct comparisons of heat transfer coefficients. Furthermore, as can be shown from the results, the use of the cylinder length as a characteristic dimension instead of the diameter leads to a less compact correlation of the results.

Equations (12) and (13) contain a number of thermophysical properties. Aside from β, these were evaluated at the reference temperature T_r suggested in [7]

$$T_r = T_w - 0.38(T_w - T_\infty) \tag{14}$$

and $\beta = 1/T_\infty$. The measured barometric pressure was used in the determination of the density ρ.

Results and Discussion

Physical Aspects of the Plate-Cylinder Interaction. In the presentation which follows, various possible manifestations of the interaction between the buoyant flows induced by the plate and the cylinder will be examined. It is well known that the boundary layer on a heated vertical plate grows thicker along the height of the plate. Along with the increase in thickness, both the velocity and temperature of the fluid within the boundary layer increase with height.

From the standpoint of a plate-attached horizontal cylinder, the up-moving boundary layer flow induced by the plate appears similar to an oncoming forced convection flow. The existence of such an oncoming flow reinforces the buoyant flow that is induced by the cylinder itself. The thus-augmented velocity field should give rise to higher heat transfer coefficients for the cylinder. Furthermore, owing

to the increase of the flat-plate-induced velocities with height, the velocity-related enhancement of the heat transfer coefficient should be greater as the cylinder is positioned increasingly farther from the leading edge.

In direct conflict with the aforementioned velocity-related enhancement is the preheating effect due to the plate. Owing to the heat transfer from the plate to the air that passes along it, the temperature of the plate-induced airflow that arrives at the cylinder is higher than the ambient temperature. Thus, the effective cylinder-to-air temperature difference is less than the temperature difference between the cylinder and ambient, and this tends to degrade the heat transfer coefficient. The extent of the degradation should be greater when the cylinder is positioned at higher elevations along the plate, since the preheating effect of the plate increases with height.

The foregoing discussion sets forth the conflicting effects of the presence of the plate on the cylinder heat transfer coefficient. Since both the opposing effects are stronger at greater elevations along the plate surface, it is not evident, a priori, whether increasing elevation will favor the triumph of one or the other.

Another factor, related to the foregoing velocity and preheating effects, but still a separate issue, is the extent of the cylinder surface that is washed by the flat plate boundary layer. For a cylinder of given length more and more of the surface will be affected by the flat plate boundary layer as the cylinder is positioned at higher elevations. Furthermore, since the thickness of the flat plate boundary layer varies inversely with the quarter power of the plate-to-ambient temperature difference, a greater portion of the cylinder surface will be affected by the presence of the flat plate when the temperature difference is small. In the present experiments, the magnitude of the temperature difference is reflected by the numerical value of the Rayleigh number, so that small Rayleigh numbers should give rise to greater plate-cylinder interactions. Finally, at a given position of attachment and temperature difference, a shorter cylinder should be more affected by the presence of the flat plate than a longer cylinder.

The foregoing discussion sets the stage for the presentation of results. As motivated by that discussion, the effects of three factors on the cylinder Nusselt number will be set forth: (*a*) Rayleigh number, (*b*) height at which the cylinder is attached to the plate, and (*c*) cylinder length. A fourth focus of the presentation is a comparison of the present results with literature correlations for the single, long horizontal cylinder (presumably without end effects).

Nusselt Numbers. The cylinder Nusselt number results are presented in Figs. 2–4 as a function of the Rayleigh number. The first of these figures conveys results for the shorter cylinder, while the second pertains to the longer cylinder. Figures 2 and 3 are each made up of two parts. In the upper part, the experimental data are compared with various literature correlations for a single, long cylinder without end effects. The lower part shows the data plotted as Nu/2 in order to obtain a presentation separate from that of the upper part. The straight lines that appear in the lower part represent least-squares power-law fits of the data. As seen in the key at the lower right of Figs. 2 and 3, the different data symbols identify the position x_c/D at which the cylinder is attached to the plate, where x_c is the distance from the leading edge of the plate to the lower stagnation point of the cylinder and D is the cylinder diameter. The Nusselt number data for the shorter and longer cylinders are brought together and compared in Fig. 4, as will be discussed shortly.

The Nusselt number results presented in Figs. 2–4 correspond to a data reduction procedure in which the emissivity of the polished aluminum surfaces was taken to be 0.04. Nusselt numbers corresponding to an emissivity of 0.05 were from 1.2 to 2.3 percent lower than those of the figures.

Attention will first be focused on the results presented in the lower parts of Figs. 2 and 3. To begin, consideration may be given to the effect of the position x_c/D at which the cylinder is attached to the plate. This effect may be identified by taking note of the spread among the three data points, each corresponding to a different x_c/D, that are clustered at the various Rayleigh numbers at which the experiments were performed.

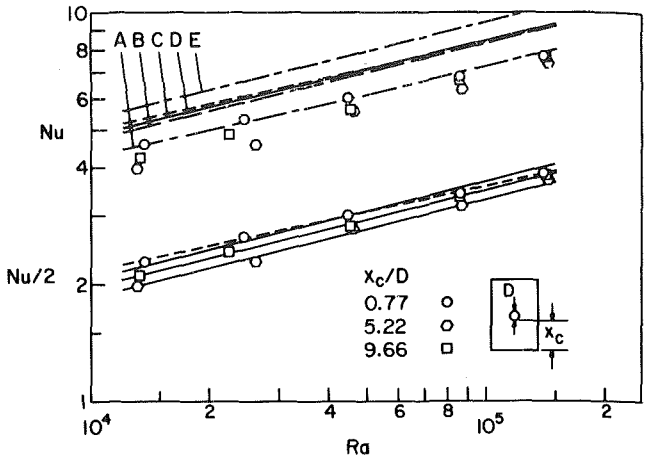

Fig. 2 Average Nusselt number results for the shorter cylinder ($L/D = \frac{1}{2}$). The literature correlations A, B, C, D, and E are identified in the text

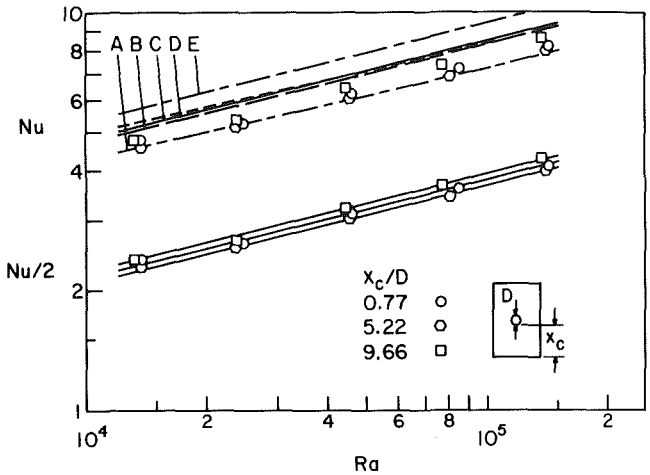

Fig. 3 Average Nusselt number results for the longer cylinder ($L/D = 1$). The literature correlations A, B, C, D, and E are identified in the text

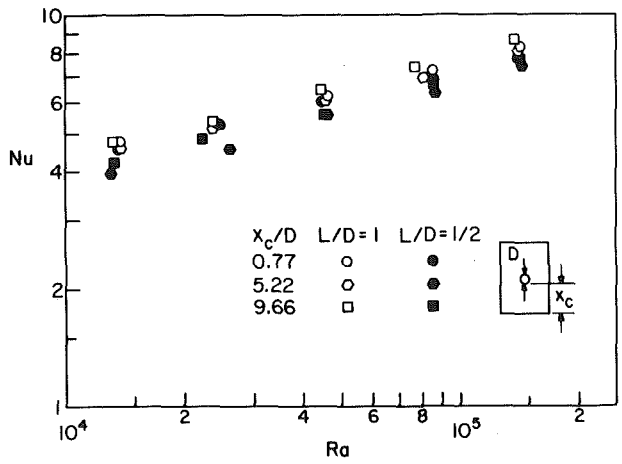

Fig. 4 Comparison of Nusselt number results for the shorter and longer cylinders

Such an examination reveals that at a given Rayleigh number, the cylinder Nusselt number is surprisingly insensitive to the position (i.e., the elevation) at which the cylinder is attached to the plate. The largest position-related variations are in the 15 percent range and these occur at the lower Rayleigh numbers for the shorter cylinder. At the higher Rayleigh numbers for the shorter cylinder and for all Rayleigh numbers for the longer cylinder, the data spread is in the 5–7 percent range. Furthermore, the lowest Nu values are encountered

with the cylinder at the middle position, $x_c/D = 5.22$, signalling a nonmonotonic variation of Nu with x_c/D.

The aforementioned tendency toward lesser sensitivity of Nu to x_c/D with increasing Rayleigh number and greater cylinder length is physically reasonable. In both instances, a lesser fraction of the cylinder is washed by the flat plate boundary layer, so that the cylinder is less affected by the presence of the plate.

The general insensitivity of the Nu values to x_c/D is worthy of special note. This insensitivity will appear even more remarkable shortly, when the significant increases with elevation of the temperature, velocity, and boundary layer thickness of the flat-plate-induced flow are displayed. Considering the already-discussed enhancing effect on Nu of the flat-plate-induced flow and the degrading effect of the plate-related preheating of the air, it must be concluded that the net balance between these effects is little influenced by the position of the cylinder. Furthermore, the net balance is only modestly affected by Rayleigh number (i.e., temperature difference) for the shorter cylinder and is independent of Rayleigh number for the longer cylinder. Such insensitivity has to be regarded as unexpected.

These unexpected findings stimulate curiosity about the influence of cylinder length, and Fig. 4 may be examined in this regard. Here, the Nusselt number data for the two cylinders are plotted as a function of the Rayleigh number. Black and open symbols are used to distinguish the two sets of data. As seen in the figure, the Nusselt numbers for the longer cylinder are somewhat higher than those for the shorter cylinder. Since the plate-cylinder interactions are smaller for the former than for the latter, it may be concluded that the net effect of the presence of the plate is to diminish the cylinder heat transfer coefficient. Further evidence of this tendency will be displayed shortly.

The differences between the two sets of Nusselt numbers are modest. The typical differences are in the 10 to 15 percent range, except when the cylinder is at the lowest position, where the typical differences are about five percent. Considering the coverage of the cylinders by the flat plate boundary layer (to be displayed shortly), larger differences might have been expected.

Nusselt Number Correlations and Literature Comparisons. A correlation of the Nusselt numbers was sought in the form

$$\mathrm{Nu} = C\mathrm{Ra}^n \tag{15}$$

where C and n may depend on the position at which the cylinder is situated on the host plate, as well as on the L/D of the cylinder. Table 1 lists the C and n values for the various cases investigated, as determined from a least-squares fit.

Inspection of Table 1 indicates that the exponent n is quite close to the value 0.25, which is the commonly encountered exponent for external natural convection flow when the laminar boundary layer regime prevails. Therefore, an alternative fit of the data was sought in the form

$$\mathrm{Nu} = C_1\mathrm{Ra}^{1/4} \tag{16}$$

with C_1 values listed in Table 2.

The solid lines passing through the data in Figs. 2 and 3 correspond to equation (16) and Table 2. A dashed line has also been plotted in Fig. 2 portraying equation (15) and Table 1 for the case of $x_c/D = 0.77$ and $L/D = \frac{1}{2}$. Aside from this case, the lines corresponding to equations (15) and (16) are hardly distinguishable.

Table 2 enables certain conclusions to be drawn about the effects of cylinder position x_c/D and cylinder aspect ratio L/D on the Nusselt number. It is evident from the table that the deviations between the $L/D = \frac{1}{2}$ and $L/D = 1$ cylinders increase as x_c/D grows larger, ranging from about 4 percent to 13 percent. Also evident is the nonmonotonic behavior of Nu with x_c/D for a given aspect ratio.

It is also of interest to compare the present Nusselt number results with literature values for horizontal cylinders. There is a large amount of available data for the horizontal cylinder, as witnessed by the compilation of Morgan [8]. Notwithstanding the size of the data bank or, perhaps, because of it, there are a number of competing correlations in the literature for the horizontal cylinder. Five of the most

Table 1 Values of C and n for equation (15)

	$L/D = \frac{1}{2}$		$L/D = 1$	
x_c/D	C	n	C	n
0.77	0.572	0.219	0.486	0.238
5.22	0.328	0.261	0.456	0.241
9.66	0.399	0.248	0.410	0.257

Table 2 Values of C_1 for equation (16)

	$L/D = \frac{1}{2}$	$L/D = 1$
x_c/D	C_1	C_1
0.77	0.411	0.426
5.22	0.371	0.415
9.66	0.391	0.442

accepted correlations have been evaluated for the operating conditions of the present experiments. These include: (*a*) Churchill ([9], equation (6)), (*b*) Fand ([10], equation (17)), (*c*) Morgan ([8], Table II), (*d*) Raithby ([11], equation (32)), and (*e*) McAdams ([12], equation (7–6*a*)). Among these, Morgan and McAdams specify that all participating thermophysical properties be evaluated at the film temperature, while Churchill and Raithby employ the same specification, except that $\beta = 1/T_\infty$. Fand's correlation employs properties evaluated at a reference temperature equal to $(T_w - 0.68(T_w - T_\infty))$.

The results obtained from the literature correlations have been rephrased in terms of common thermophysical properties evaluated on the basis of equation (14) and $\beta = 1/T_\infty$. The thus-rephrased results are plotted in the upper parts of Figs. 2 and 3 along with the present data. The designations A–E assigned to the curves are those of the preceding paragraph.

Among the correlations, that of McAdams originally dates from 1933 and is, therefore, based on limited data. The Churchill correlation is contemporary but, by examining Fig. 1 of [9], it is seen that the correlating line lies consistently below the data on which the correlation is based. The Morgan correlation is based on the largest sample of the presently available data. The near congruence of the Morgan, Raithby, and Fand correlations, taken together with the foregoing remarks about the other correlations, suggests that they be accepted as the best representation of the natural convection Nusselt number for the horizontal cylinder.

Figures 2 and 3 show that the present Nusselt number results for relatively short, wall-attached horizontal cylinders fall below those for the single isolated cylinder. This confirms the previously stated conclusion that the net effect of the presence of the plate is to degrade the cylinder Nusselt number. The deviations are greater for the shorter cylinder than for the longer cylinder, as is physically reasonable. For the shorter cylinder, the present data lie about 20 percent below that for the isolated cylinder, while the deviation is only 10 percent for the longer cylinder. These deviations are moderate, especially when viewed relative to the spread between the McAdams and Churchill correlations. For many design purposes, it would appear adequate to use the isolated cylinder correlation.

Further Perspectives on the Results. To provide insights into the nature of the approach flow which washes the cylinders, velocity and temperature profiles for the heated vertical plate have been evaluated from [13] and are plotted in Figs. 5, 6, and 7. Figure 5 shows both velocity and temperature profiles for the smallest temperature difference of the experiment, namely, $T_w - T_\infty = 2.5°\mathrm{C}$. Profiles are plotted for the x_c values corresponding to the lowest and highest positions of the cylinder on the host plate. Also appearing in the figure are heavy vertical lines which depict the cylinder length, respectively two and four cm. Figures 6 and 7 respectively display the boundary layer velocity and temperature profiles corresponding to the largest temperature difference investigated, i.e., $T_w - T_\infty = 30°\mathrm{C}$. These figures contain results for the same two x_c as in Fig. 5, and the lengths of the cylinders are also indicated.

These figures display the marked increase of the boundary layer thickness with position along the plate, as well as the substantial increases of the temperature and velocity of the fluid within the

boundary layer. When account is taken of these height-dependent variations and of the indicated lengths of the cylinders (heavy vertical lines in Figs. 5–7), the experimentally determined insensitivity of the cylinder Nusselt number to height is truly remarkable. A similar assessment relates to the effect of $T_w - T_\infty$, where the thinning of the boundary layer and the sharp increases of both the fluid temperature and velocity would be expected to affect the Nusselt number to a greater extent than is reflected in the data.

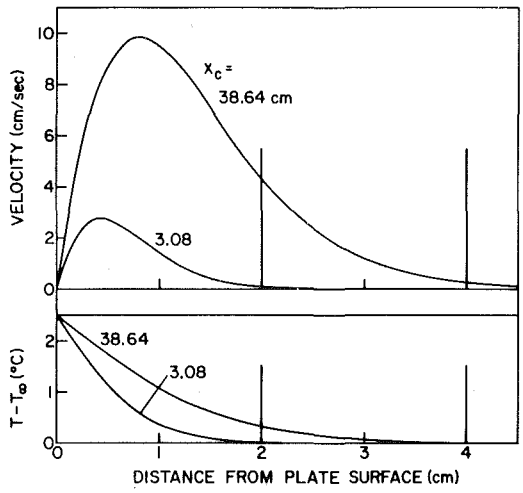

Fig. 5 Velocity and temperature profiles in the flat plate boundary layer at x_c = 3.08 and 38.64 cm, $T_w - T_\infty$ = 2.5°C

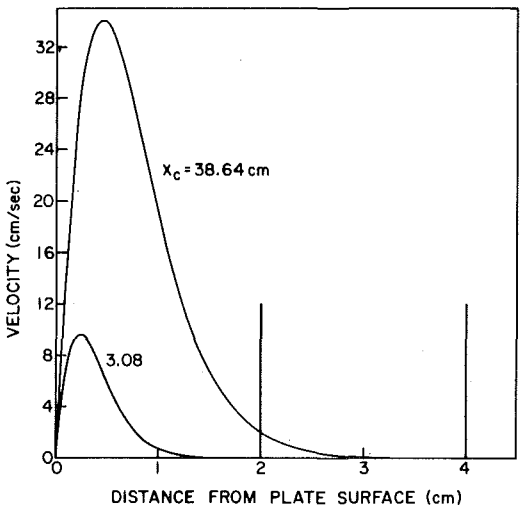

Fig. 6 Velocity profiles in the flat plate boundary layer at x_c = 3.08 and 38.64 cm, $T_w - T_\infty$ = 30°C

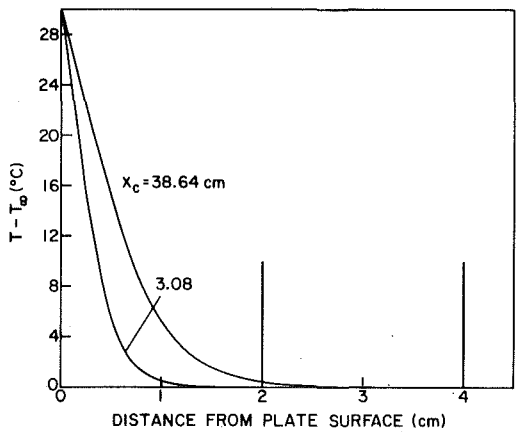

Fig. 7 Temperature profiles in the flat plate boundary layer at x_c = 3.08 and 38.64 cm, $T_w - T_\infty$ = 30°C

As a final perspective on the results, attention is drawn to the fact that the reported Nusselt numbers encompass the average heat transfer performance of both the cylindrical surface and the circular end face (i.e., the tip) of the cylinder. It is desirable to estimate the relative rates of heat transfer at the two zones. However, in view of the extreme complexity of the problem, if any estimate is to be made, it must be based on a very simple model.

To estimate the end-face heat transfer, it will be assumed that the face behaves like an isolated vertical circular plate situated in an otherwise quiescent fluid. Interactions with the cylindrical surface and with the flat plate boundary layer are, thereby, ignored, with this liberty being somewhat justified by the findings conveyed by Figs. 2–4. For the calculation, it is assumed that the heat transfer along any narrow vertical strip of the end face depends only on the distance from the lower edge of the strip and that, furthermore, the dependence is the same as that for an isothermal vertical plate in air [14]. If the end face is regarded as being made up of an array of such strips, then the rate of heat transfer Q_{ct} is ($ct \sim$ cylinder tip)

$$Q_{ct} = 0.425kD(T_w - T_\infty)\mathrm{Ra}^{1/4} \tag{17}$$

To compare this estimate with the measured overall rate of convective heat transfer Q from the cylinder, the power law correlation (16) may be used along with mean values of $C_1 = 0.39$ and 0.46 for the shorter and longer cylinders (from Table 2). This gives rise to corresponding values of $Q_{ct}/Q = 0.46$ and 0.25. If A_{ct} denotes, as before, the area of the tip of the cylinder and A is the total area of the cylinder, then $A_{ct}/A = \frac{1}{3}$ and $\frac{1}{5}$ for the two cylinders.

By comparing Q_{ct}/Q with A_{ct}/A, it appears that the end face of the shorter cylinder carries a disproportionate share of the overall heat load, while for the longer cylinder the end face heat load is more in accord with its proportionate area. The relatively large end-face heat load for the shorter cylinder suggests that the heat transfer at the cylindrical surface is degraded by the presence of the plate boundary layer. For the longer cylinder, this effect should be smaller, and the comparison of Q_{ct}/Q with A_{ct}/A bears out this expectation.

Concluding Remarks

In the experiments performed here, three physical parameters were varied with a view toward influencing the natural convection interaction between the boundary layer on a vertical isothermal plate and a short equi-temperature horizontal cylinder attached to the plate. The varied parameters included the elevation at which the cylinder is attached to the plate, the cylinder length, and the surface-to-fluid temperature difference (i.e., the cylinder Rayleigh number).

With regard to the cylinder Nusselt number, it tends to be enhanced by the flat-plate-induced approach flow and to be degraded by the plate-related preheating of the approach flow. The net balance between these conflicting effects was found to be quite insensitive to all of the varied parameters. At a fixed Rayleigh number, over most of the Rayleigh number range of the experiments, the elevation-related spread of the data fell in the 5–7 percent range, with a somewhat larger spread at the lower Rayleigh numbers for the shorter cylinder. The variation of the cylinder Nusselt number with elevation was not monotonic.

The net effect of the presence of the flat plate boundary layer is to degrade the cylinder Nusselt number, as witnessed by the fact that the Nusselt numbers for short wall-attached cylinders are lower than those for the single isolated cylinder without end effects. For the shorter cylinder, the data lie about 20 percent below the correlation for the isolated cylinder, while for the longer cylinder the deviations from the correlation are about 10 percent.

The data, which cover the Rayleigh number range from 1.4×10^4 to 1.4×10^5, could be correlated by the relation $\mathrm{Nu} = C_1\mathrm{Ra}^{1/4}$, where C_1 is a weak function of both cylinder elevation and cylinder length. An average value of $C_1 = 0.409$ correlates the data to within ±8 percent.

References

1 Eckert, E. R. G., and Soehngen, E. E., "Studies on Heat Transfer in Laminar Free Convection with the Zehnder-Mach Interferometer," AF Technical Report 5747, United States Air Force, Air Material Command, Wright-Patterson Air Force Base, Ohio, 1948.

2 Lieberman, J., and Gebhart, B., "Interactions in Natural Convection from an Array of Heated Elements, Experimental," *International Journal of Heat and Mass Transfer*, Vol. 12, 1969, pp. 1385–1396.

3 Marsters, G. F., "Arrays of Heated Horizontal Cylinders in Natural Convection," *International Journal of Heat and Mass Transfer*, Vol. 15, 1972, pp. 921–933.

4 Chrysler, G. M., "Natural Convection Heat Transfer Coefficients for a Short Horizontal Cylinder Attached to a Vertical Plate," Thesis, Department of Mechanical Engineering, University of Minnesota, Minneapolis, Minn., 1981.

5 Gubareff, G. G., Janssen, J. E., and Torborg, R. H., *Thermal Radiation Properties Survey*, Second Edition, Honeywell Research Center, Minneapolis, Minn., 1960.

6 Sparrow, E. M., and Cess, R. D., *Radiation Heat Transfer*, Hemisphere Publishing Corporation, Washington, 1978.

7 Sparrow, E. M., and Gregg, J. L., "The Variable Fluid Property Problem in Free Convection," *Trans. ASME*, Vol. 80, 1958, pp. 878–886.

8 Morgan, V. T., "The Overall Convective Heat Transfer from Smooth Circular Cylinders," in *Advances in Heat Transfer*, Vol. 11, Academic Press, New York, 1975, pp. 199–264.

9 Churchill, S. W., and Chu, H. H. S., "Correlating Equations for Laminar and Turbulent Free Convection from a Horizontal Cylinder," *International Journal of Heat and Mass Transfer*, Vol. 18, 1975, pp. 1049–1053.

10 Fand, R. M., Morris, E. W., and Lum, M., "Natural Convection Heat Transfer from Horizontal Cylinders to Air, Water and Silicone Oils for Rayleigh Numbers between 3×10^2 and 2×10^7," *International Journal of Heat and Mass Transfer*, Vol. 20, 1977, pp. 1173–1184.

11 Raithby, G. D., and Hollands, K. G. T., "Laminar and Turbulent Free Convection from Elliptic Cylinders, with a Vertical Plate and Horizontal Circular Cylinder as Special Cases," ASME JOURNAL OF HEAT TRANSFER, Vol. 98, 1976, pp. 72–80.

12 McAdams, W. H., *Heat Transmission*, third edition, McGraw-Hill, New York, 1954.

13 Ostrach, S., "An Analysis of Laminar Free-Convection Flow and Heat Transfer about a Flat Plate Parallel to the Direction of the Generating Body Force," NACA Report 1111, Washington, 1953.

14 Sparrow, E. M., and Husar, R. B., "Free Convection from a Plane Vertical Surface with a Non-Horizontal Leading Edge," *International Journal of Heat and Mass Transfer*, Vol. 12, 1969, pp. 365–369.

Effect of Vertical Separation Distance and Cylinder-to-Cylinder Temperature Imbalance on Natural Convection for a Pair of Horizontal Cylinders

E. M. Sparrow
Fellow ASME

J. E. Niethammer
Department of Mechanical Engineering,
University of Minnesota, Minneapolis, Minn. 55455

Experiments were performed to study the interactive natural convection from a pair of heated horizontal cylinders situated one above the other in a vertical plane. Prime attention was focused on how the heat transfer characteristics of the upper cylinder are affected by the presence of the lower cylinder. The vertical center-to-center separation distance between the cylinders was varied from two to nine cylinder diameters. The cylinder-to-cylinder temperature imbalance was also varied independently and systematically, with the wall-to-ambient temperature difference for the lower cylinder ranging from zero to three times that for the upper cylinder. Experiments were carried out for upper-cylinder Rayleigh numbers from 20,000 to 200,000. It was found that for a given temperature imbalance and upper-cylinder Rayleigh number, the upper-cylinder Nusselt number takes on a maximum value as a function of separation distance. The separation distance for which the maximum occurs is in the range of seven to nine cylinder diameters. The enhancement or degradation of the upper-cylinder Nusselt number relative to that for a single cylinder is strongly dependent on the separation distance, with degradation of the Nusselt number being more common at small separations and enhancement prevailing at larger separations. With regard to the temperature imbalance, its effect on the Nusselt number is of major importance at small separations but not at large separations.

Introduction

Natural convection heat transfer from a single horizontal cylinder has been intensively investigated in the past, as witnessed by extensive reviews [1, 2]. There are numerous applications, however, where heating (or cooling) is accomplished by the use of two or more horizontal cylinders. Examples of such applications include space heating (e.g., baseboard heating), heating of oils, and heating or cooling of fluids in process plants. When the buoyancy-induced fluid flow from one of the cylinders washes others in the array, the impinged cylinders can no longer be assigned heat transfer coefficients from the available data bank for the single cylinder. There is, in fact, an uncertainty as to whether the multiple-cylinder heat transfer coefficients are larger or smaller than those for the single cylinder.

The research described here is concerned with the natural convection interaction between horizontal cylinders, with specific consideration being given to a pair of horizontal cylinders situated one above the other in the same vertical plane. If both cylinders are heated, buoyant plumes will rise upward from each of them. The upward-moving plume from the lower cylinder will impinge on the upper cylinder and will affect its heat transfer characteristics via two distinct mechanisms.

First, the fact that the fluid arriving at the upper cylinder is in motion (due to the buoyancy created by the lower cylinder) means that the upper cylinder is situated in what appears to be a forced convection flow. Consequently, on this account, the presence of the lower cylinder should enhance the heat transfer coefficient at the upper cylinder relative to that for the single cylinder. On the other hand, the heat transfer at the lower cylinder tends to raise the temperature of the fluid which arrives at the upper cylinder to a value that is higher than that of the ambient fluid. Thus, with respect to the upper cylinder, the lower cylinder acts as a preheater. This preheating effect tends to decrease the heat transfer coefficient of the upper cylinder compared with that which would exist if the lower cylinder were absent.

From the foregoing, it can be seen that the presence of the lower cylinder gives rise to effects which tend to have opposite influences on the heat transfer coefficients at the upper cylinder. It is important to note that the relative strengths of these effects vary with the vertical separation distance between the cylinders, both for laminar and turbulent plumes. In either case, the preheating effect should diminish as the separation distance increases. With regard to the fluid flow which is induced by the lower cylinder and impinges on the upper cylinder, the velocity of impingement increases with increasing separation distance when the plume is laminar but is independent of the separation distance when the plume becomes turbulent.

The aforementioned conflicting influences of the preheating and the velocity of approach make it uncertain whether the upper-cylinder heat transfer coefficient will be higher or lower than that of a corresponding single cylinder. Indeed, considering the differences in the strengths of these effects at different separation distances, it is possible that the presence of the lower cylinder enhances the upper-cylinder coefficients at certain separation distances and degrades the coefficients at other separation distances. These considerations suggest the possibility of an optimum separation distance where the heat transfer coefficient is a maximum.

Another factor which has been tacitly left open in the foregoing discussion is the relative temperatures of the two cylinders. Whereas idealized operation in many applications gives rise to the same temperature for both cylinders, the realities are often otherwise. Physical reasoning suggests that the existence of cylinder-to-cylinder temperature differences can significantly influence the upper-cylinder heat transfer coefficient.

The preceding paragraphs set the stage for the research to be reported in this paper. The experiments will have two major foci. One is to systematically examine the effect of cylinder-to-cylinder separation distance on the upper-cylinder heat transfer coefficient, while

Contributed by the Heat Transfer Division for publication in the JOURNAL OF HEAT TRANSFER. Manuscript received by the Heat Transfer Division April 6, 1981.

the other is to systematically investigate the influence of cylinder-to-cylinder temperature imbalances. The experimental program was conducted in a manner so as to clearly delineate the separate roles of the separation distance and temperature imbalance, and the results will be presented in a manner so as to highlight the effects of these parameters.

The operating conditions encompassed upper-cylinder Rayleigh numbers between 2×10^4 and 2×10^5 and separation distances (center-to-center) ranging from two to nine times the cylinder diameter. The wall-to-ambient temperature difference at the lower cylinder was varied from zero to as much as three times that of the upper cylinder. Since the experiments were performed in air, the Prandtl number was constant at a value of approximately 0.7.

Interacting horizontal cylinders in natural convection have been studied experimentally [3–5], but there is no overlap between what has gone before and the work presented here. An important factor in the prior work is that the temperatures of the various participating cylinders were not independently controlled. In particular, when the separation distance was varied, the temperature imbalance between the cylinders also varied, but in a manner dictated by the heat transfer and fluid flow processes themselves [4, 5]. Thus, trends exhibited there as a function of separation distance are affected by the accompanying variation of the temperature imbalance. Therefore, the separate effects of separation distance and temperature difference were not identified. Another distinctive difference between the present work and the work referred to [4, 5] is the level of the Rayleigh number. In [4], the Rayleigh number was about 10^{-2}, while in [5] the maximum Rayleigh number was 2000. As already noted, the present Rayleigh numbers ranged from about 2×10^4 to 2×10^5.

Reference [3] was, in essence, a demonstration experiment which yielded only a single data point; in addition, all of the relevant operating conditions of the experiment were not reported.

The Experiments

Experimental Apparatus. A schematic pictorial view of the experimental apparatus is presented in Fig. 1. The essential components of the apparatus include a pair of thick-walled internally heated aluminum cylinders, a frame (not shown), which positions and supports the cylinders, instrumentation for measurement of the cylinder surface temperature and the ambient temperature, a power supply for heating the cylinders, and side baffles for eliminating transverse fluid motions associated with possible end effects.

Both cylinders shared a common length and diameter, which were fixed throughout the experiments, while the center-to-center vertical spacing S was varied parametrically. The upper cylinder will be designated as cylinder 2, while the lower is designated as 1. The electrical system was designed to enable the power supplied to the respective cylinders to be varied independently, thereby providing a means for establishing any desired temperature imbalance.

Each of the two test cylinders had a finished outside diameter D = 3.787 cm and a length L = 76.2 cm. The cylinder length was the largest that could be employed consistent with the machine tools available for fabrication. Selection of the diameter was based on the desire to achieve relatively high Rayleigh numbers and also to allow a tube wall of sufficient thickness to ensure an isothermal surface boundary condition. The resulting 20 to 1 length-to-diameter ratio is believed to closely approximate an infinite-cylinder situation, especially in view of the measures employed to minimize end effects.

The cylinders were heated electrically by dissipating electric power through a resistance heating element. A two-part cylinder design was chosen to facilitate the installation of the resistance wire. Each cylinder consisted of an inner brass tube, which served as a core for the heating wire, and an outer aluminum tube.

The inner brass tube had an outer diameter of 2.54 cm with a 0.318 cm wall thickness and was cut to a length of 71.76 cm. Eight equally spaced longitudinal grooves were milled into its surface to receive and hold the heating wire, with circumferential grooves at the respective ends of the surface to facilitate series winding of the wire. The wire was 0.0254-cm diameter chromel clad with 0.00762-cm teflon insulation, the choice of wire type and size being based on maintaining the maximum anticipated current level below one ampere.

The outer tube was of aluminum with an original outer diameter of 3.81-cm and a 0.635-cm wall thickness. Each tube was 76.2 cm in length. The bore of the aluminum tube was honed to facilitate the insertion of the heater core, and continuous low-resistance thermal contact was ensured by a coating of copper oxide cement which was applied just before the core was inserted.

Tube wall temperatures were measured by seven thermocouples. Three of these were distributed around the circumference at an axial location midway between the ends of the cylinder. The other four were positioned along the top of the cylinder at axial distances of 17.8 and 34.9 cm from the aforementioned mid-plane and to either side of it. To facilitate the installation of the thermocouples, a radial hole was drilled through the aluminum-brass assembly at each thermocouple location. Then, aluminum plugs, fabricated to the proper dimensions for a press fit into the radial holes, were each equipped with a thermocouple. The thermocouple leads for each plug were threaded through the drilled hole and passed through the bore of the heater and out one end (see Fig. 1). The plugs were pressed into the holes to a predetermined depth, subsequent to which the outer diameter of the tube was turned and then polished to the finished dimension (3.787 cm). As a result of these operations, the exposed surface of each plug blended perfectly into the remainder of the aluminum surface, so that

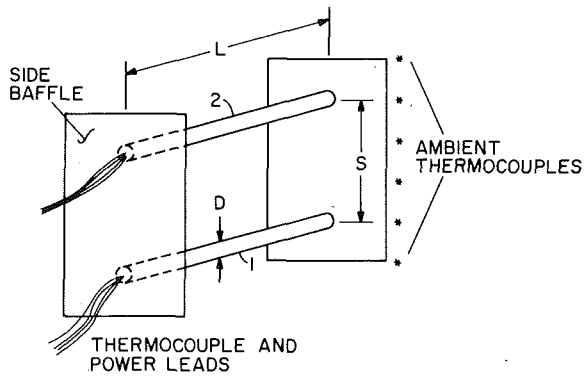

Fig. 1 Pictorial schematic view of the experimental apparatus

Nomenclature

A = cylinder surface area
D = cylinder diameter
F = radiation angle factor
g = gravitational acceleration
h = average cylinder heat transfer coefficient
k = thermal conductivity
L = cylinder length
Nu = Nusselt number, hD/k
Nu_0 = single-cylinder Nusselt number
Pr = Prandtl number
Q_{conv} = convective heat transfer rate
Q_r = radiation heat transfer rate
Ra = Rayleigh number, $(g\beta(T_w - T_\infty)D^3/\nu^2)$Pr
S = center-to-center cylinder separation distance
T_f = film temperature, $\frac{1}{2}(T_w + T_\infty)$
T_w = cylinder surface temperature
T_∞ = ambient air temperature
β = thermal expansion coefficient
ϵ = radiative emissivity
Θ^4 = scaled temperature variable, equation (2)
ν = kinematic viscosity
σ = Stefan-Boltzmann constant

Subscripts

1 = lower cylinder
2 = upper cylinder

the plug locations could not be detected with the naked eye. The thermocouple junctions were situated 0.05 cm from the surface of the aluminum cylinder.

To minimize conduction end losses via the thermocouple leads, which were led out of the apparatus, a low conductivity, small diameter wire was employed—0.0127-cm dia iron and constantan with a 0.0076-cm thick teflon cladding. In order to minimize the role of radiation heat transfer, the surface of each aluminum cylinder was subjected to a painstaking polishing procedure. The end result was a surface finish which can be characterized as "highly polished" from the standpoint of thermal radiation properties.

The frame that was designed to support and position the cylinders was of generally open construction (to avoid interfering with the flow), but possessed strength, stability, and adjustment capability. The upper cylinder was stationary with respect to the frame, with its horizontal alignment being accomplished by the leveling of the base plate of the frame. On the other hand, the position of the lower cylinder could be adjusted both vertically and horizontally, thereby enabling the two cylinders to be aligned parallel to each other in the same vertical plane. The design was such that the vertical center-to-center separation distance between the cylinders could be varied continuously over a range of nine cylinder diameters. The minimum distance between the lower cylinder and the floor of the laboratory was 80 cm.

Care was taken to minimize the thermal communication between the cylinders and the frame. This was accomplished by supporting the cylinders by point contact with a plexiglass finger inserted into the bore of the cylinder at each end. The fingers were 0.953-cm dia plexiglass rods which were shaped with a file to leave an up-pointing pyramidal protrusion on which the cylinder rested.

The side baffles illustrated in Fig. 1 were installed as an additional protection against end losses and also to eliminate extraneous transverse fluid motions associated with the finite length of the cylinders. The baffles were made of resilient fiberglass insulation, one-cm thick, and hung in a vertical plane without further support. During the course of the experiments, as the separation distance between the cylinders was increased, the fiberglass curtain was lengthened. At any separation distance, the length of the curtain extended at least 15 cm below the lower cylinder and 7.5 cm above the upper cylinder.

A vertical array of six thermocouples, deployed over a height of 50 cm, was attached to the frame in order to measure the air temperature and to detect possible stratification. The thermocouples were made of the same small-diameter iron and constantan wire that had been used for the cylinder-wall thermocouples. In the installation of the thermocouple array, care was taken to shield the thermocouple junctions from radiation interaction with the cylinders.

Thermal Environment. It is well known that natural convection is extremely sensitive to extraneous flows and disturbances in the environment. Therefore, to ensure consistent and highly accurate natural convection heat transfer data, it is necessary that the test environment be unusually quiescent and disturbance free.

The experimental apparatus was situated in a laboratory room of dimensions 3.7 × 6.1 × 3.1 m, which possessed remarkable thermal isolation and stability characteristics. The laboratory is, in fact, a room within a room. Its walls, ceiling, and floor are each backed by a 46-cm thickness of cork, which provides excellent thermal isolation. There are no ducts, grilles, vents, or heating pipes in the laboratory. The temperature of the air in the laboratory, as measured by the aforementioned fine thermocouple wires, is altogether devoid of fluctuations and is also very steady over long periods of time. Thermal stratification, even after long data runs, was negligible. To ensure the absence of disturbances in the laboratory, all instrumentation and power supplies were situated in a room adjacent to the laboratory, the laboratory being sealed throughout the entire duration of each data run.

Instrumentation and Procedure. Electric power was provided by a regulated a-c supply which maintained a constant voltage to within four significant figures during the course of a data run. The output of the supply was fed to two variable auto-transformers, one for each of the cylinders. The current flow to the respective cylinders was measured as a voltage drop through a calibrated shunt, while the voltage drop across the heating elements were determined with the aid of small-diameter voltage taps soldered to the respective ends of the heater wire. Both the power-related a-c voltages and the d-c thermocouple voltages were read to four significant figures (the latter to 1 μV) with a Hewlett-Packard 3465A multimeter. The same meter had been used for the calibration of the thermocouples.

An important aspect of the experimental procedure was the alignment of the cylinders and the setting of the vertical separation distance. The latter was accomplished with the aid of a hairline-equipped optical cathetometer with a smallest vertical scale division of 0.005 cm. The alignment of one cylinder above the other was verified and adjusted by comparison with a vertical reference consisting of a weight suspended on a length of monofilament nylon line. This reference line was held against the two cylinders on both sides, at both ends, and at the middle, and the lower cylinder was moved in its horizontal adjustment slots until the line hung tangent to both cylinders at all locations.

At each fixed vertical separation distance, several sets of data runs were performed. Each set of runs was characterized by a fixed value of the upper-cylinder Rayleigh number, while the temperature of the lower cylinder was varied parametrically, such that its wall-to-ambient temperature difference ranged from zero to three times that for the upper cylinder. Four such fixed upper-cylinder Rayleigh numbers were investigated: 20, 60, 100, and 200 thousand. The center-to-center vertical separation distance between the cylinders was varied from two to nine cylinder diameters.

Data Reduction

In this section, the procedures used for evaluating heat transfer coefficients, Nusselt numbers, and Rayleigh numbers from the measured temperatures, electric power inputs, and ambient pressures are described. The data reduction was carried out for both the upper and lower cylinders, but primary attention is focused on the upper cylinder because the lower-cylinder Nusselt numbers were found to be indistinguishable from those for a single cylinder. In addition, Nusselt and Rayleigh numbers were evaluated for single-cylinder data runs which were performed prior to the initiation of the two-cylinder runs.

The average cylinder heat transfer coefficient was determined from the definition

$$h = Q_{\text{conv}}/A(T_w - T_\infty) \tag{1}$$

in which Q_{conv} is the rate of convective heat transfer from the cylinder surface to the ambient, and A is the surface area. With regard to the cylinder wall temperature T_w, thermocouple measurements verified that the desired spatial uniformity was very nearly achieved. The circumferential temperature variations were ≤0.1°C at the highest power inputs ($T_w - T_\infty \sim 40$°C) and were not detectable within the 1 μV resolution of the instrumentation at lower powers. Axial variations were limited to about 2½ percent of $T_w - T_\infty$, with the temperature decreasing from the midpoint of the cylinder to the ends. These slight nonuniformities were averaged out by first fitting a second-degree polynomial to the measured temperatures and then averaging the polynomial fit over the length of the cylinder. This average value was assigned to T_w in equation (1).

Next, turning to the ambient temperature T_∞ in equation (1), it may be noted that the variation among the six ambient thermocouples (Fig. 1) was typically a few tenths of a percent of ($T_w - T_\infty$). These thermocouples extended over a half meter of height while the maximum center-to-center separation distance was 34 cm. Thus, stratification was negligible, and T_∞ was obtained by direct averaging of the outputs of the ambient thermocouples.

The convective heat transfer rate Q_{conv} needed for the evaluation of equation (1) is equal to the electric power input to the cylinder minus the extraneous heat losses due to radiation and conduction. Attention will first be turned to the rate of heat loss by radiation, after which the conduction loss will be discussed.

For the radiation analysis, both cylinders are assumed gray with the same emissivity ϵ, with respective (absolute) temperatures T_{w1}

and T_{w2} for the lower and upper cylinders. The laboratory room is very large compared with the apparatus, and the walls of the room are isothermal and equal to the air temperature T_∞ (also in absolute units). Therefore, the room closely fulfills all the requirements of a blackbody enclosure, so that the radiation streaming through the room is σT_∞^4 per unit area.

The analysis is significantly simplified by introducing scaled fourth-power temperatures Θ_1, Θ_2, and Θ_∞ defined as

$$\Theta_1^4 = T_{w1}^4 - T_\infty^4, \quad \Theta_2^4 = T_{w2}^4 - T_\infty^4, \quad \Theta_\infty^4 = T_\infty^4 - T_\infty^4 = 0 \quad (2)$$

Thus, in terms of the Θ scale, the ambient is at absolute zero. The radiosity approach based on equation (3–22) of [6] is then used to formulate the radiation problem. Once the radiosity B_2 of the upper cylinder has been solved, it is introduced into the heat transfer equation, (3–19) of [6], to yield Q_{r2} as follows

$$\frac{Q_{r2}}{A_2} = \frac{\epsilon(1-(1-\epsilon)F^2)\sigma\Theta_1^4 - \epsilon^2 F\sigma\Theta_2^4}{1-(1-\epsilon)^2F^2} \quad (3)$$

The quantity F is the cylinder-to-cylinder angle factor. By setting $F = 0$, equation (3) is applicable for the evaluation of the radiative loss from cylinder 2 when cylinder 1 is absent. It also can be used to calculate the heat loss from cylinder 1 by interchanging the subscripts 1 and 2. For an ϵ value of 0.05, Q_{r2} (or Q_{r1}) was 5–7 percent of the electric power input.

The conduction heat losses from the ends of the cylinder are believed to be negligible in this experiment. This judgment is based on the fact that the only contact between the cylinder and the supporting frame was a point contact with a plexiglass support. An additional defense against conduction losses was provided by the insulation at each end of the cylinder. Further support for the neglect of conduction will be provided later when the single-cylinder Nusselt number results are presented and compared with the published literature. Differentiation of the second-degree polynomial fitted to the measured temperature distribution along the cylinder was not used to estimate the conduction end losses because of the expected low numerical accuracy of the derivative.

Thus, in light of the foregoing, Q_{conv} was evaluated as

$$Q_{\text{conv}} = EI - Q_r \quad (4)$$

where E and I respectively represent the heater voltage drop and current. Equation (4) was then used as input to equation (1).

For a dimensionless presentation, the Nusselt and Rayleigh numbers are employed according to their definitions

$$\text{Nu} = hD/k, \quad \text{Ra} = (g\beta(T_w - T_\infty)D^3/\nu^2)\text{Pr} \quad (5)$$

Aside from the thermal expansion coefficient β, all of the thermophysical properties appearing in equation (5) have been evaluated at the film temperature $T_f = \frac{1}{2}(T_w + T_\infty)$. With regard to β, it was set equal to $1/T_\infty$ in accordance with the perfect gas law, as demonstrated in [7]. The density ρ (i.e., $\nu = \mu/\rho$) was evaluated using the perfect gas law, using T_f and the measured barometric pressure as inputs.

Results and Discussion

Single-Cylinder Results. As a point of departure for the presentation of results, the present experimentally determined single-cylinder Nusselt numbers will be compared with the literature. This comparison is shown in Fig. 2. In the figure, data points are plotted at five Rayleigh numbers in the range between 2×10^4 and 2×10^5. The unshaded data symbols correspond to a radiation correction based on an assumed emissivity of the cylinder surface of 0.06, whereas the shaded symbols are for an emissivity value of 0.04. The literature predictions, which are shown as lines of various types, will now be discussed.

There is a large amount of experimentally based Nusselt number data in the literature for natural convection about a horizontal cylinder, as witnessed by the compilation of Morgan [1]. These data have formed the basis of a number of competing correlations. Five of the most accepted correlations have been evaluated for the operating conditions of the present experiments. These include: (A) Churchill ([2], equation (6)), (B) Fand ([8], equation (17)), (C) Morgan ([1], Table II, (D) Raithby ([9], equation (32)), and (E) McAdams ([10], equation (7–6a)), where the designations A–E correspond to the labels on the curves of Fig. 2. Among these, Morgan and McAdams specify that all participating thermophysical properties be evaluated at the film temperature, while Churchill and Raithby employ the same specification, except that $\beta = 1/T_\infty$. Fand's correlation employs properties evaluated at a reference temperature equal to $(T_w - 0.68(T_w - T_\infty))$.

The results obtained from the literature correlations have been rephrased in terms of common thermophysical properties evaluated at the film temperature and with $\beta = 1/T_\infty$. It is the rephrased results that have been plotted in Fig. 2.

Among the correlations, that of McAdams originally dates from 1933 and is, therefore, based on limited data. The Churchill correlation is contemporary but, by examining Fig. 1 of [2], it is seen that the correlating line lies consistently below the data on which the correlation is based. The Morgan correlation is based on the largest sample of the presently available data. The very close consensus of the Morgan, Raithby, and Fand correlations, taken together with the foregoing remarks about the other correlations, suggests that this consensus be accepted as the best representation of the natural convection Nusselt number for the horizontal cylinder.

Examination of Fig. 2 reveals that the present data are in excellent agreement with the aforementioned literature consensus. For the most part, the data are within five percent of the consensus correlation, with a tendency to lie slightly low. The excellence of the agreement is underscored when note is taken of the extensive scatter that is encountered when the totality of the literature is examined, as in [1].

The agreement between the data and the literature consensus lends strong support to the apparatus, instrumentation, and experimental technique. It also supports the neglect of conduction end losses since, if such losses had been appreciable and no correction made, the data would have fallen well above the consensus. The data corresponding to the 0.04 emissivity fall about $2\frac{1}{2}$ percent above those which correspond to an emissivity of 0.06. Therefore, the specifics of the radiation correction do not significantly affect the Nusselt numbers for the single cylinder.

Multiple-Cylinder Results. Attention will now be turned to the Nusselt numbers for the interacting pair of horizontal cylinders. With regard to the lower cylinder, its Nusselt number was found to be essentially identical to that for the single cylinder, even for the closest center-to-center distance investigated ($S/D = 2$). Therefore, in what follows, only the upper-cylinder Nusselt numbers will be reported.

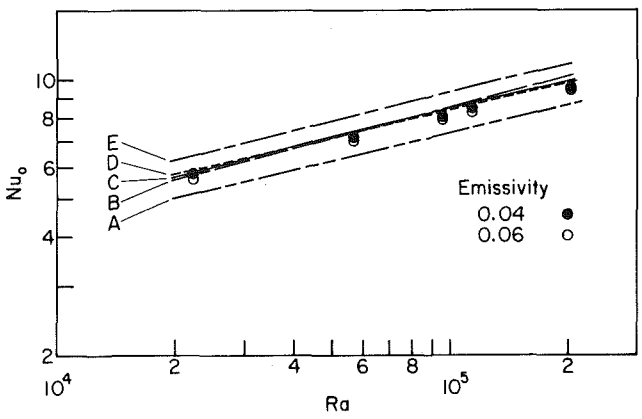

Fig. 2 Single-cylinder Nusselt number results. Curves A through E are correlations whose sources are identified in the text.

Figures 3 through 6 present upper-cylinder Nusselt numbers in a format designed to highlight the departures from the single-cylinder results. The ordinate of each figure is a ratio of Nusselt numbers. The numerator is the Nusselt number Nu for the upper cylinder with the lower cylinder in place, while the denominator is the Nusselt number Nu_0 for a single cylinder. Both Nu and Nu_0 correspond to the same Rayleigh number. The departure of Nu/Nu_0 from one is a measure of the degree to which the interaction between the cylinders either enhances or degrades the heat transfer performance relative to that of a single cylinder. When $Nu/Nu_0 > 1$, enhancement occurs, while $Nu/Nu_0 < 1$ signals degradation. Results are presented for upper-cylinder Rayleigh numbers of 20,000, 60,000, 100,000, and 200,000, with different symbols used to identify the various cases.

The abscissa characterizes the degree of temperature imbalance between the cylinders. The numerator, $(T_w - T_\infty)_1$, is the wall-to-ambient temperature difference for the lower cylinder, while $(T_w - T_\infty)_2$ in the denominator is the corresponding temperature difference for the upper cylinder. Values of the abscissa less than one indicate that the temperature of the upper cylinder is higher than that of the lower cylinder, while abscissa values greater than one correspond to the case where the lower cylinder is at a temperature higher than that of the upper cylinder. The zero abscissa value represents the case of no heating at the lower cylinder, and for that case the measured upper cylinder Nusselt number coincided with that for the single cylinder.

In each figure, lines have been faired through the data to provide continuity. The successive figures correspond to separation distances $S/D = 2$, 3, 5, and 9. The role of radiation in the data reduction is assessed in certain of the figures by a presentation which shows results for emissivity values of 0.04 and 0.06. In view of the minor differences that were encountered, the other figures were prepared using an emissivity value of 0.05 in the radiation correction.

From an overall examination of Figs. 3–6, it can be seen that the degree of enhancement or degradation of the heat transfer from the upper cylinder is strongly dependent on the cylinder-to-cylinder separation distance. For the smaller separation distances, degradation ($Nu/Nu_0 < 1$) is generally the rule, while at larger separation distances enhancement ($Nu/Nu_0 > 1$) predominates. At $S/D = 9$, the largest separation distance examined, enhancement prevails for the entire range of operating conditions.

This finding has immediate applications to practice. For example, for a two-cylinder unfinned baseboard heater, the desired heat transfer task can be accomplished with cylinder wall temperatures that are lower when the cylinders are widely spaced. If the cylinders are heated by hot water or condensing steam, the temperature of those fluids can be lower, with a resulting decrease of transmission line

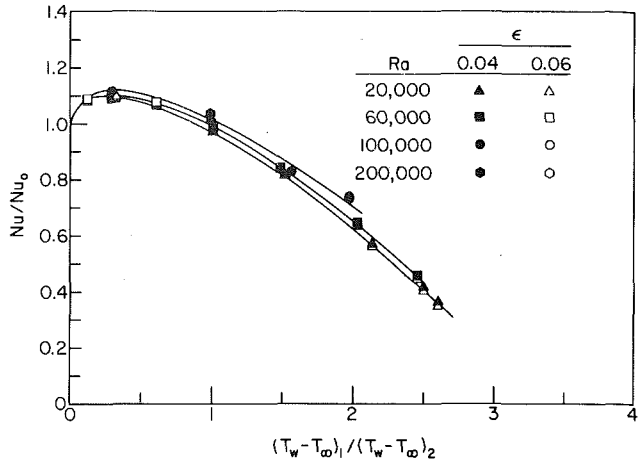

Fig. 4 Effect of cylinder-to-cylinder interaction on the upper-cylinder Nusselt number for $S/D = 3$

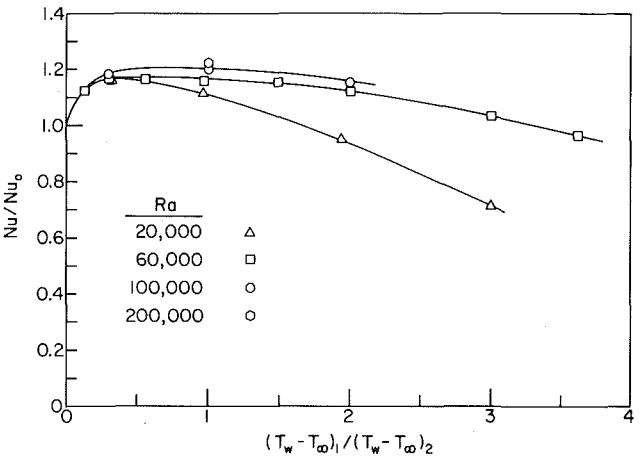

Fig. 5 Effect of cylinder-to-cylinder interaction on the upper-cylinder Nusselt number for $S/D = 5$ ($\epsilon = 0.05$ for radiation correction)

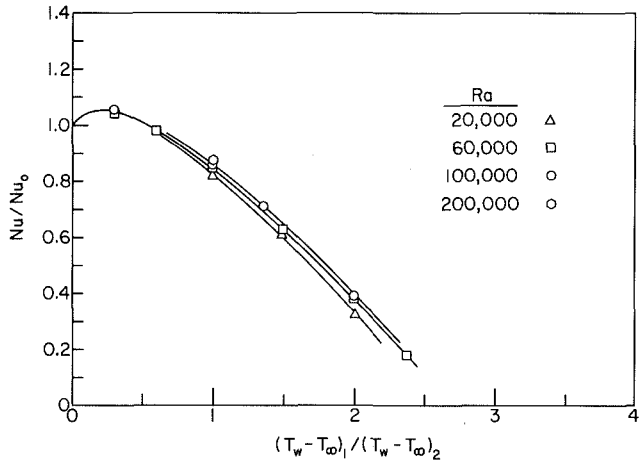

Fig. 3 Effect of cylinder-to-cylinder interaction on the upper-cylinder Nusselt number for $S/D = 2$ ($\epsilon = 0.05$ for radiation correction)

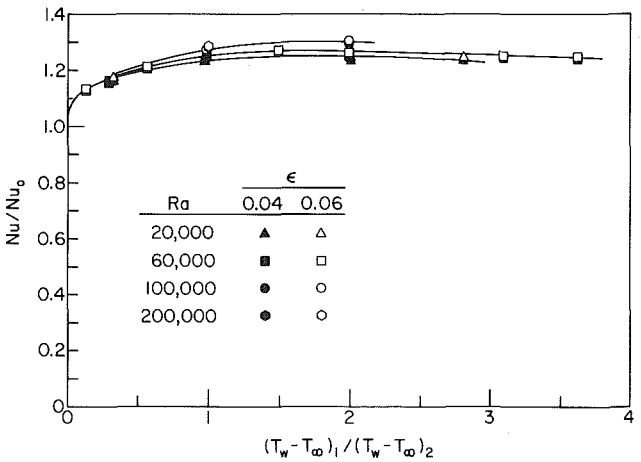

Fig. 6 Effect of cylinder-to-cylinder interaction on the upper-cylinder Nusselt number for $S/D = 9$

losses.

Another global observation can be made by looking at the effect of the temperature ratio $(T_w - T_\infty)_1/(T_w - T_\infty)_2$. At the smaller separation distances (Figs. 3, 4), there is a strong effect of the temperature ratio on Nu/Nu_0. The intermediate spacing case, Fig. 5, reflects a lesser dependence. Finally, at the largest separation distance, Fig. 6, Nu/Nu_0 is nearly independent of the temperature ratio.

A final overall observation is that in the range investigated, the Rayleigh number does not have a very significant effect on Nu/Nu_0. The one exception to this behavior is seen in Fig. 5. There, the results for the lowest Rayleigh number are separated from those for the higher Rayleigh numbers. Since, as already indicated, Fig. 5 portrays a transitional behavior between dependence and independence of the results on the temperature ratio, the just noted exception can be interpreted as a lag in the transitional process. To verify the accuracy of the results of Fig. 5, the data were retaken, with special care being given to the vertical alignment of one cylinder above the other. The second set of data was within two percent of the first set, which is typical of the general level of reproducibility of the experiments as a whole.

The figures will now be examined individually, beginning with Fig. 3. In Fig. 3, it is seen that the largest value of Nu/Nu_0 is about 1.05. Beyond this maximum, Nu/Nu_0 decreases sharply with the temperature ratio. The value of Nu/Nu_0 when the two cylinders are the same temperature (i.e., abscissa value of one) is about 0.85. It is interesting to note that if the curves were to be extrapolated to higher temperature ratios, negative values of Nu/Nu_0 would be obtained. Such negative values would mean that there is a heat flow from the air to the upper cylinder, even though the cylinder temperature remains above that of the ambient air. In order to achieve these conditions, it would be necessary to cool the upper cylinder. The aforementioned heating effect at the upper cylinder is due to the preheating of the air at the lower cylinder coupled with the close proximity of the cylinders.

Whereas Fig. 3 showed results which were dominated by the preheating effect due to the lower cylinder, Fig. 4 demonstrates the spacing-related growing importance of the counteracting influence of the buoyancy that is imparted to the fluid by the lower cylinder. The velocities induced by this buoyancy appear to the upper cylinder to be similar to a forced convection flow, with a corresponding tendency towards heat transfer enhancement. Therefore, the values of Nu/Nu_0 in Fig. 4 are always higher than the corresponding values in Fig. 3.

The growing importance of the buoyancy imparted by the lower cylinder and the waning influence of its preheating effect are in evidence in Figs. 5 and 6. The falloff of the curves with increasing temperature ratio disappears and larger values of Nu/Nu_0 are obtained. For example, in Fig. 6, at a temperature ratio of one, Nu/Nu_0 has a value of about 1.25. This further underscores the significant enhancement that occurs at large separation distances.

Summarizing Figures and Concluding Remarks

To further underscore the effect of separation distance on the Nusselt number ratio, crossplots have been prepared in which Nu/Nu_0 is plotted as a function of S/D. The crossplots are presented in Figs. 7–9, respectively, for the Rayleigh numbers 20,000, 60,000, and 100,000 (there was insufficient data available for the highest Rayleigh number of 200,000 to enable a crossplot to be made). Each figure contains results for two different temperature ratios, one and two, respectively. Curves have been passed through the crossplotted data to provide continuity. It should be noted that data were taken at additional values of S/D for Ra = 60,000 in order to better define the shape of the Nu/Nu_0 versus S/D dependence. The curves faired through the Ra = 60,000 data served to guide the curve shapes fitted to the Ra = 20,000 and Ra = 100,000 data.

From an overall examination of these figures, it is seen that at small separation distances, the Nusselt number increases sharply with increasing separation distance. With further increases of separation distance, the Nusselt number increase becomes more and more gradual, with the ultimate attainment of a maximum. The maximum appears to occur in the range of S/D between seven and nine. The occurrence of this maximum has significant practical ramifications. For optimum performance of heating systems, it would be appropriate to place the upper cylinder in the aforementioned range of S/D. In the often-encountered case of a temperature ratio of one (i.e., both cylinders at the same temperature), the value of Nu/Nu_0 at the maximum is about fifty percent greater than the value at S/D of two. Even more dramatic enhancement would be realized when the tem-

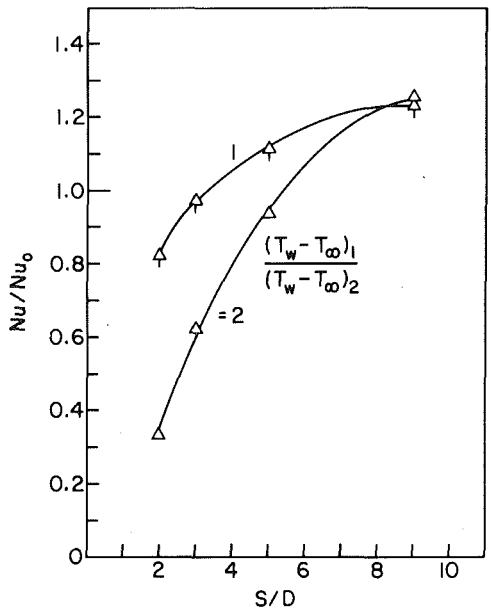

Fig. 7 Effect of cylinder-to-cylinder separation distance on the upper-cylinder Nusselt number for Ra = 20,000 and for $(T_w - T_\infty)_1/(T_w - T_\infty)_2$ = 1 and 2

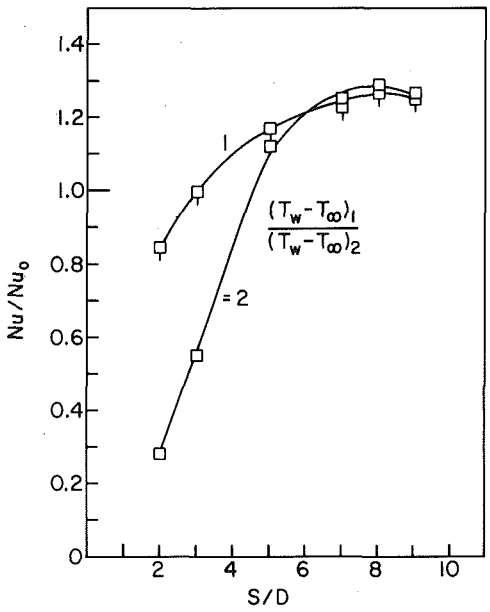

Fig. 8 Effect of cylinder-to-cylinder separation distance on the upper-cylinder Nusselt number for Ra = 60,000 and for $(T_w - T_\infty)_1/(T_w - T_\infty)_2$ = 1 and 2

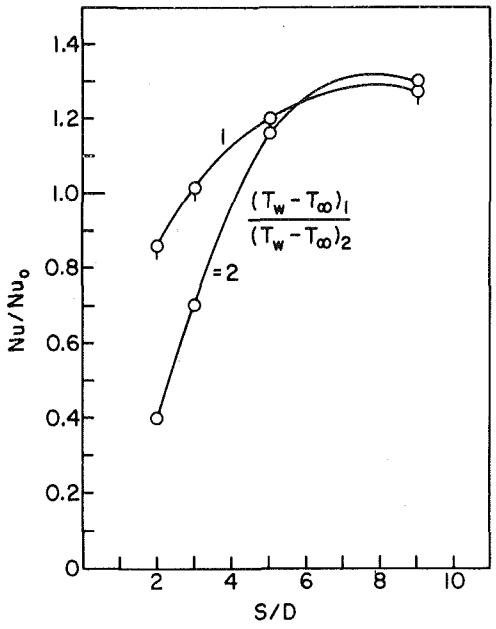

Fig. 9 Effect of cylinder-to-cylinder separation distance on the upper-cylinder Nusselt number for Ra = 100,000 and for $(T_w - T_\infty)_1/(T_w - T_\infty)_2 = 1$ and 2

perature ratio is greater than one. For the temperature ratio of two, the maximum Nusselt number is about three and one-half times that at $S/D = 2$.

The general trends in Figs. 7–9 are consistent with the physical ideas discussed in the Introduction. The conflict between the enhancing effect of the buoyancy imparted to the flow by the lower cylinder and the degrading effect of the preheating are major factors in establishing the trends.

Dimensional analysis indicates that the upper cylinder Nusselt number depends on the Rayleigh number of the cylinder and on $(T_w - T_\infty)_1/(T_w - T_\infty)_2$, S/D, and Pr. The first three of these dimensionless parameters were varied during the course of the investigation, while the Prandtl number was that of air (~0.7). Aside from the Prandtl number restriction, the results should be applicable to all similar geometrical situations which fall within the parameter ranges investigated.

References

1 Morgan, V. T., "The Overall Convective Heat Transfer from Smooth Circular Cylinders," in *Advances in Heat Transfer*, Vol. 11, Academic Press, New York, 1975, pp. 199–264.

2 Churchill, S. W., and Chu, H. H. S., "Correlating Equations for Laminar and Turbulent Free Convection from a Horizonal Cylinder," *International Journal of Heat and Mass Transfer*, Vol. 18, 1975, pp. 1049–1053.

3 Eckert, E. R. G., and Soehngen, E. E., "Studies on Heat Transfer in Laminar Free Convection with Zehnder-Mach Interferometer," AF Technical Report 5747, United States Air Force, Air Material Command, Wright-Patterson Air Force Base, Ohio, 1948.

4 Lieberman, J., and Gebhart, B., "Interactions in Natural Convection from an Array of Heated Elements, Experimental," *International Journal of Heat and Mass Transfer*, Vol. 12, 1969, pp. 1385–1396.

5 Marsters, G. F., "Array of Heated Horizontal Cylinders in Natural Convection," *International Journal of Heat and Mass Transfer*, Vol. 15, 1972, pp. 921–933.

6 Sparrow, E. M., and Cess, R. D., *Radiation Heat Transfer*, Hemisphere Publishing Corp., Washington, 1978.

7 Sparrow, E. M., and Gregg, J. L., "The Variable Fluid Property Problem in Free Convection," *Trans. ASME*, Vol. 80, 1958, pp. 879–886.

8 Fand, R. M., Morris, E. W., and Lum, M., "Natural Convection Heat Transfer from Horizontal Cylinders to Air, Water, and Silicone Oils for Rayleigh Numbers between 3×10^2 and 2×10^7," *International Journal of Heat and Mass Transfer*, Vol. 20, 1977, pp. 1173–1184.

9 Raithby, G. D. and Hollands, K. G. T., "Laminar and Turbulent Free Convection from Elliptic Cylinders, with a Vertical Plate and Horizontal Circular Cylinder as Special Cases," ASME JOURNAL OF HEAT TRANSFER, Vol. 98, 1976, pp. 72–80.

10. McAdams, W. H., *Heat Transmission*, 3rd ed., McGraw-Hill, New York, 1954.

Y. Zvirin[1]
Nuclear Safety and Analysis Department,
Electric Power Research Institute,
Palo Alto, Calif. 94303

P. R. Jeuck III
Mechanical Research
Program, Engineering Sciences Laboratory,
SRI International
Menlo Park, Calif.

C. W. Sullivan
R. B. Duffey
Nuclear Safety and Analysis Department,
Electric Power Research Institute,
Palo Alto, Calif. 94303

Experimental and Analytical Investigation of a Natural Circulation System with Parallel Loops

A theoretical and experimental study of a natural circulation loop is presented. The analysis is based on a one-dimensional model in which the continuity, momentum, and energy equations are given and solved. Expressions for the steady-state and transient flow rates and temperature distributions are derived. The apparatus consisted of an electrically-heated section and two parallel loops with heat exchangers. Steady-state and transient experiments were conducted to study the effects of core flow resistance, power distribution and upper plenum design. Flow oscillations were observed under certain conditions, which were accompanied by instabilities and flow reversals. Reasonable agreement (±30 percent) is obtained between the analytical and experimental results.

1 Introduction

Natural circulation loops (thermosyphons) have various engineering applications and appear in some geophysical phenomena. Japikse [1] reviewed some technological aspects of thermosyphon applications. The most common is the natural circulation solar water heater, which has been studied experimentally and theoretically [2–5]. Torrance [6] investigated an open thermosyphon with geothermal applications.

It has recently been realized that natural circulation may also play an important (and even crucial) role in long-term cooling of light-water nuclear reactors (LWRs). A simplified treatment of a single phase loop of a nuclear reactor which yields an estimate of the steady-state flow rate and core temperature difference, is presented by Lewis [7]. However, recent work on nuclear applications of thermosyphons is mainly concerned with transient behavior and stability of liquid metal fast breeder reactor loops (LMFBRs), cf. [8–9].[2]

Simple loops have also been studied in order to better understand basic phenomona in thermosyphons. Steady-state, transient behavior and stability characteristics have been investigated in toroidal and vertical loops [10–14], including the effects of a throughflow. This latter case may be important in a nuclear reactor loop when cold makeup water must be added.

Most of the work on thermosyphons has been concerned with single flow path loops. Some applications, for example the cooling systems of pressurized water reactors (PWRs), involve parallel loops. Chato [15] investigated a parallel-channel system of vertical tubes between two constant-temperature reservoirs. His results show that such systems can exhibit instabilities due to multiple steady-state solutions.

The present work is an analytical and experimental investigation of a natural circulation system with two parallel once-through heat exchangers. The analysis (Section 2) is based on existing one-dimensional modelling methods for thermosyphons. The coupled momentum and energy equations for the fluid in the loop are solved to yield the steady-state flow rate and temperatures and the transient behavior of the loop. The experimental apparatus, (Section 3), included an electrically-heated core and two parallel loops with once-through heat exchangers. Both steady-state and transient experiments were performed with heat removal from either or both heat exchangers (Section 4); comparison with the analysis shows relatively good agreement.

Strong oscillations, implying an instability, were discovered for a transition between two steady one-loop operations, where the initial condition had a valve shutting off the primary flow in one loop.

2 Analysis

2.1 Derivation of the Governing Equations. To describe natural circulation in the loop (see Fig. 1), we follow conventional one-dimensional formulations utilizing mass, momentum and energy conservation. In the theory, the only spatial coordinate, s, runs around the loop. It is assumed that the average cross-sectional temperature (T) is equal to the mixed mean temperature. Use is made of the Boussinesq approximation, i.e. the density, ρ, is considered constant (having a reference value ρ_ℓ) in the governing equations except for the buoyancy force term. The other fluid properties are considered constant, which is justified for the small temperature variations here. It follows from these assumptions that the loop flow rate $Q(t)$, and mean velocity, $u(t)$, are uniform and depend only on the time, t.

The momentum equation can now be written in the following manner (for a flow in the positive s direction), cf. [10–14]:

$$\rho_\ell \frac{\partial u}{\partial t} = -\frac{\partial p}{\partial s} - \rho g \mathbf{e}_z \cdot \mathbf{e}_s - F_s \tag{1}$$

Integrating equation (1) around the loop, the pressure term vanishes and the momentum equation for the whole loop is obtained as:

$$\rho_\ell a \frac{dQ}{dt} = -g \oint \rho dz - \frac{1}{2}\rho_\ell \oint f u^2 \frac{ds}{D(s)} \tag{2}$$

where f is the friction coefficient such that $F_s ds = \frac{1}{2}\rho_\ell\, ds/D\, fu^2$. Equation (2) can also be rewritten as:

$$\rho_\ell\, a \frac{dQ}{dt} = -g \oint \rho dz - \frac{1}{2}\rho_\ell R Q^2 \tag{3}$$

where R is the total flow resistance parameter, defined by the usual

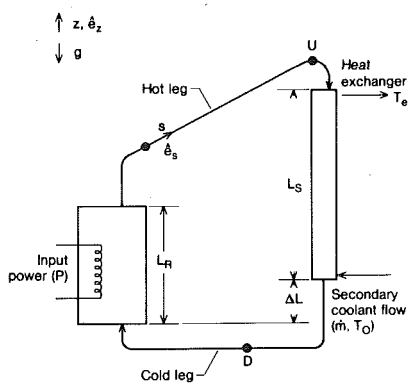

Fig. 1 A natural circulation loop—general representation and coordinate system

[1] On leave from the Faculty of Mechanical Engineering, Technion, Haifa, Israel.

[2] In a totally independent and parallel study, A. K. Agrawal, et al. (ASME Paper No. 80-WA/HT-41) analysed and reviewed LMFBR plant data. Their results are similar to those presented here.

Contributed by the Heat Transfer Division for publication in the JOURNAL OF HEAT TRANSFER. Manuscript received by the Heat Transfer Division March 17, 1980.

sum of the frictional and form losses:

$$R \equiv \oint \frac{fds}{DA^2} \equiv \sum_{i_{\text{tubes}}} f_i \frac{L_i}{D_i A_i^2} + \sum_{j_{\text{form}}} \frac{K_j}{A_j^2} \tag{4}$$

In this expression, the friction coefficients in tubes are f_i, L_i are the lengths, and K_j the form losses in the various components of the loop. The friction coefficients and factors depend on the Reynolds number of the flow and the component geometry, and for laminar flow the last term in equation (3) will be proportional to Q (rather than Q^2). While equation (3) was derived for a single loop, parallel loops can be treated in a straightforward manner, using appropriate distribution of flow rates and overall friction parameters.

The energy equation is written separately for each component of the loop:

$$\rho_\ell c A\left(\frac{\partial T}{\partial t} + u\frac{\partial T}{\partial s}\right) = q \tag{5}$$

where q is P/L_R for the heated section, $h\pi D_s(T - T_{\text{II}})$ for the heat sink and zero for the (insulated) pipes.

The coupled momentum and energy equations (3) and (5) govern the flow in the loop. These must be solved simultaneously, subject to the condition that the temperature is continuous around the loop. For the transient solutions appropriate initial conditions must be specified.

2.2 Steady-State Motions. At steady-state all the time dependent terms disappear and equations (3–5) reduce to:

$$\frac{1}{2}\rho_\ell R Q^2 = -g \oint \rho dz \tag{6}$$

$$\rho_\ell c Q \frac{\partial T}{\partial s} = \begin{cases} P/L_R & \text{heat source,} \quad (7a) \\ -h\pi D_s (T - T_{\text{II}}) & \text{heat sink,} \quad (7b) \\ 0 & \text{pipes.} \quad (7c) \end{cases}$$

The solution of the last equation yields uniform temperatures in the connecting pipes, which requires, then, that the hot leg temperature is equal to the core outlet and heat exchanger inlet (and similarly for the cold leg).

The coupled steady-state equations can be solved as follows: first, equations (7a, 7b) are solved for the temperature distributions. The flow rate Q is a constant parameter, which is still unknown at this stage. The results for the temperature are then used, together with an equation for $\rho(T)$, to evaluate the integral in equation (6), resulting in an algebraic equation for the flow rate. The solution Q can now be used to calculate the temperature distribution. It is noted that this approach is more general than the formulation of Lewis [7]. In the latter, an overall heat balance on the core was employed rather than the formal energy equation. Instead of the density integral in the momentum equation, an equivalent "driving head" was taken, with two distinct values of the densities (for the hotter and colder portions of the loop).

The exact solution of equation (7a) for a uniformly distributed input power is a linear temperature profile in the core:

$$T = T_c + \frac{P}{\rho_\ell c Q}\frac{s}{L_R} \quad 0 \leqslant s \leqslant L_R \tag{8}$$

where s is the distance from the bottom of the heated section. This relation yields the temperature difference of the core (or between the hot and cold legs):

$$\Delta T_R = T_H - T_c = \frac{P}{\rho_\ell c Q} \tag{9}$$

An approximate method is used for solving equation (7b). Integration of this equation along the heat sink yields:

$$\rho_\ell c Q(T_H - T_c) = h\pi D_s L_s\ (T_{\text{I}} - T_{\text{II}}) \tag{10}$$

It is assumed that the temperature distribution of the primary fluid in the heat exchanger is linear:

$$T = T_H - \Delta T_R s/L_s \quad 0 \leqslant s \leqslant L_s \tag{11}$$

where s is measured from the top of the heat sink. The solutions (8) and (11) are used now to integrate equation (6), where the density is written as $\rho = \rho_\ell\,[1 - \beta(\mathrm{T} - T_\ell)]$:

$$-g \oint \rho dz = \beta g \rho_\ell \oint T dz = \beta g \rho_\ell \Delta T_R \times \left[\frac{1}{2}(L_s - L_R) + \Delta L\right] \equiv \beta g \rho_\ell \Delta T_R \Delta z. \tag{12}$$

where ΔL is the elevation of the bottom of the heat sink above that of the heat source. Δz, as defined in equation (12), is the equivalent driving head; it is also equal to the difference in elevation between the center of the heated section and that of the heat sink. The subscript ℓ is omitted in the following, and ρ denotes the constant reference liquid density.

Using equations (12) and (6), the following expressions are obtained for the flow rate and the temperature difference:

$$Q = \left[\frac{2\beta g \Delta z P}{\rho c R}\right]^{1/3};\ \Delta T_R = \left(\frac{P}{\rho c}\right)^{2/3}\left(\frac{R}{2g\beta\Delta z}\right)^{1/3},\ \text{turbulent flow.} \tag{13}$$

For laminar flow, the friction force in equation (6) can be written as $\rho r Q$, resulting in:

$$Q = \left[\frac{2\beta g \Delta z P}{\rho c r}\right]^{1/2},\ \Delta T_R = \left(\frac{rP}{2\beta g \Delta z \rho c}\right)^{1/2},\ \text{laminar flow.} \tag{14}$$

Nomenclature

A = cross-sectional area
A^H = heat transfer area of the heat exchanger
a = geometrical parameter, $a = \int ds/A(s)$
c = specific heat
D = diameter
$\mathbf{e}_s, \mathbf{e}_z$ = unit vectors in the s and z directions, Fig. 1.
F_s = friction force per unit volume
f = friction coefficient
Gz = Graetz number, RePrD/L
g = acceleration of gravity
H = heat transfer parameter, $H = hA^H$
h = heat transfer coefficient
K = friction factor
L = length
$\dot{m}$ = secondary coolant mass flow rate
P = input power
Pr = Prandtl number
p = pressure
Q = volumetric primary flow rate
q = heat flux
R = overall friction factor, turbulent flow
Ra = Rayleigh number, $g\beta D^3\Delta T/(\nu\alpha)$
Re = Reynolds number
r = overall friction factor, laminar flow
s = spatial coordinate, running around the loop
T = temperature
T_ℓ = reference temperature
t = time
u = velocity
V = volume of primary fluid
z = vertical coordinate
Δz = driving head, equation (12)
α = thermal diffusivity
β = thermal expansion coefficient
ν = kinematic viscosity
ρ = density
ρ_ℓ = reference density
τ = time constant

Subscripts

c = cold leg
D = bottom of core
e = secondary flow outlet
H = hot leg
P = end steady-state conditions for primary side
R = core (heated section)
s = heat exchanger
UP = upper plenum
o = secondary flow inlet
I = primary side
Ii = initial conditions for primary side
II = secondary side

Once Q and ΔT_R have been determined, equations (9, 10) can be used to calculate the temperatures T_H and T_c, with reference to the secondary side temperature T_{II}.

It can be shown that a more accurate solution of the energy equation (7*b*), employing an average heat transfer coefficient, yields an exponential temperature distribution. This will modify the expression (12) for Δz as follows:

$$\Delta z = L_s \left[\frac{1}{1-e^{-\phi}} - \frac{1}{\phi}\right] - \frac{1}{2}L_R + \Delta L \tag{15}$$

where $\phi = H/\rho cQ$. In general, then, equation (6) must be solved numerically and the dependence of the heat transfer parameter on the flow rate Q has to be taken into account. However, for the range of the present experiments, it was found that $\phi \approx 0.45$, which would modify the value of Δz by 12 percent, and the results for Q and ΔT_R, (equations (13) or (14)) by less than 6 percent. It is noted that Zvirin, et al. [4] compared the results of thermosyphon models based on linear temperature distributions with more exact solutions and showed that the deviations are small, thus justifying the approximation.

2.3 Transient Behavior. The objective of the transient analysis is mainly to estimate the characteristic time constant of the system. For this, the energy equation is written as an overall balance:

$$\rho cV\frac{dT_I}{dt} = P - \dot{m}\,c\,(T_e - T_0) \tag{16}$$

where thermal inertia of the secondary flow was neglected compared to the primary. The average primary temperature T_I is taken as: $T_I = (T_H + T_c)/2$ and $T_e(t)$ is the secondary outlet temperature. Another equation is derived from a heat balance on the heat exchanger:

$$hA^H\,(T_I - T_{II}) = \dot{m}\,c\,(T_e - T_0) \tag{17}$$

where the average secondary side temperature is $T_{II} = (T_e + T_0)/2$. The last relationships yield an expression for T_e:

$$T_e = [HT_I + (\dot{m}\,c - H/2)\,T_0]/[\dot{m}\,c + H/2] \tag{18}$$

which leads to the following equation when inserted into equation (16), where the inlet secondary temperature T_0 is considered constant:

$$\rho cV\frac{d}{dt}(T_I - T_0) + \frac{\dot{m}\,c\,H}{\dot{m}\,c + H/2}(T_I - T_0) = P \tag{19}$$

The solution of this equation is:

$$T_I = T_P + (T_{Ii} - T_P)\,e^{-t/\tau} \tag{20}$$

where the time constant and the final steady-state temperature are,

$$\tau = \frac{\rho V\,(\dot{m}\,c + H/2)}{\dot{m}\,H},\quad T_p = T_0 + \frac{P\,(\dot{m}\,c + H/2)}{\dot{m}\,c\,H}. \tag{21}$$

It is interesting to note the two limits on heat withdrawal from the heat exchanger. For the case of a very low heat transfer coefficient or small heat transfer area, $H \ll \dot{m}\,c$, equations (21) yield:

$$\tau \approx \rho cV/H,\quad T_P \approx T_0 + P/H \tag{22}$$

Both the steady-state temperature and the time constant are large and controlled by the heat transfer parameter. For the other limiting case, $\dot{m}\,c \ll H$, we obtain:

$$\tau \approx \rho\,V/2\dot{m},\quad T_P \approx T_0 + P/2\dot{m}c \tag{23}$$

with τ and T_P controlled by the secondary side flow $\dot{m}$ as can be expected. It is noted that if there is boiling on the secondary side (i.e., steam generator), the heat removal capability will be governed by the two-phase level location [16].

Finally, it is noted that the behavior of the average system temperature is governed by the heat transfer in the heat sink, while the flow rate and the temperature difference over the heat section are governed by the flow resistance. The time constant of the system can be evaluated by the transient behavior of the average temperature. Thus, steady and transient experiments allow us to evaluate these effects, and this was the purpose of the experimental investigation.

3 The Experimental Loop

The experimental system is shown in Figs. 2 and 3. The heated section consisted of two concentric transparent acrylic tubes, with the heat source and an orifice plate installed in the inner (core). The annular gap between the core and the vessel served as a downcomer, directing the water from the cold legs (entering at the same elevation as the hot legs) to the bottom of the core.

Two transparent acrylic tubes connected the core to the hot legs. Eight 0.13 mm holes were drilled in these tubes in the downcomer annulus, to represent, for example, a gap existing between the hot leg and the downcomer of a nuclear reactor at low temperatures.

Two identical parallel loops were constructed of copper tubing, consisting of a heat exchanger, a hot leg and a cold leg. The secondary flow channels in the heat exchangers were made by wrapping and soldering approximately 7.6 m of 6.35 mm dia copper tubing around the 5.04 cm tube. The loops were insulated by premolded fiberglass. Two different heater designs were used for the heat source, each with a 3 kW capacity, to test the effect of the heat distribution. The first was a single immersion electric heater, shown in Figs. 2 and 3. The second have five spiral elements, evenly spaced from bottom to top in the core.

An orifice plate was located above the heater and below the outlets to the hot legs (see Fig. 1). It was designed to impose varying flow resistance of the heated section. Four configurations of the plate were used in the experiments (see Fig. 4(*a*)). Two different geometries of the upper plenum (above the orifice plate) were also tested (see Fig. 4(*b*)). In the second design, another acrylic sleeve was inserted inside the upper plenum. This sleeve had holes, designed to create motion towards the hot legs in the otherwise more stagnant plenum. A small expansion tank located on top of the stand pipe (see Figs. 2 and 3) was used to maintain complete water filling of the system under atmospheric pressure and compensated for the thermal expansion of the water.

Temperatures were measured (by mercury thermometers and thermocouples) in the heated section, the hot and cold legs, and inlets and outlets of the secondary cooling water, as shown in Fig. 2. The secondary cooling water flow rates were measured by rotameters independently calibrated by volume measurements. The electric power input, controlled by a variable transformer, was also measured. In selected tests, a video tape recorded the movement of dye in both cold legs in order to estimate the water velocity.

Tests were performed for validating the estimate of the friction losses parameter using forced circulation, with the pump in loop A (see Fig. 2). Stagnation probes were used to measure pressure differences between the top of the straight vertical section of the cold leg and the bottom of the heat exchanger. The flow rate, measured by a rotameter at the outlet of the pump, was varied to obtain data in both laminar and turbulent flows.

The experimental uncertainties involved in the measurements are estimated at 0.2°C for the temperatures and 3 percent for the secondary flow rates $\dot{m}$. The errors involved in calculating the flow rate Q by equation (9) and the heat transfer parameter H by equation (17) are mainly due to heat losses from the system, as discussed in Section 4.1.1.

A natural circulation run consisted usually of establishing an initial and final steady-state of one- and/or two-loop operation, and recording the transient between them. After venting the trapped air and noncondensible gases formed during the heating of the system, the input power was adjusted [to near 2.9 kW or 1.45 kW]. The one- and two-loop operations were established by secondary cooling flow through either or both of the heat exchangers.

4 Results and Discussion

4.1 Natural Circulation Steady State.

4.1.1 General Behavior. The conditions of all the tests, with the various configurations of the input power distribution, orifice plate and upper plenum design, are summarized in Table 1. An example of the steady-state experimental results is presented in Table 2; Figs. 5 and 6 contain all the steady-state data.

The heat removal rate by the secondary coolant flow was calculated

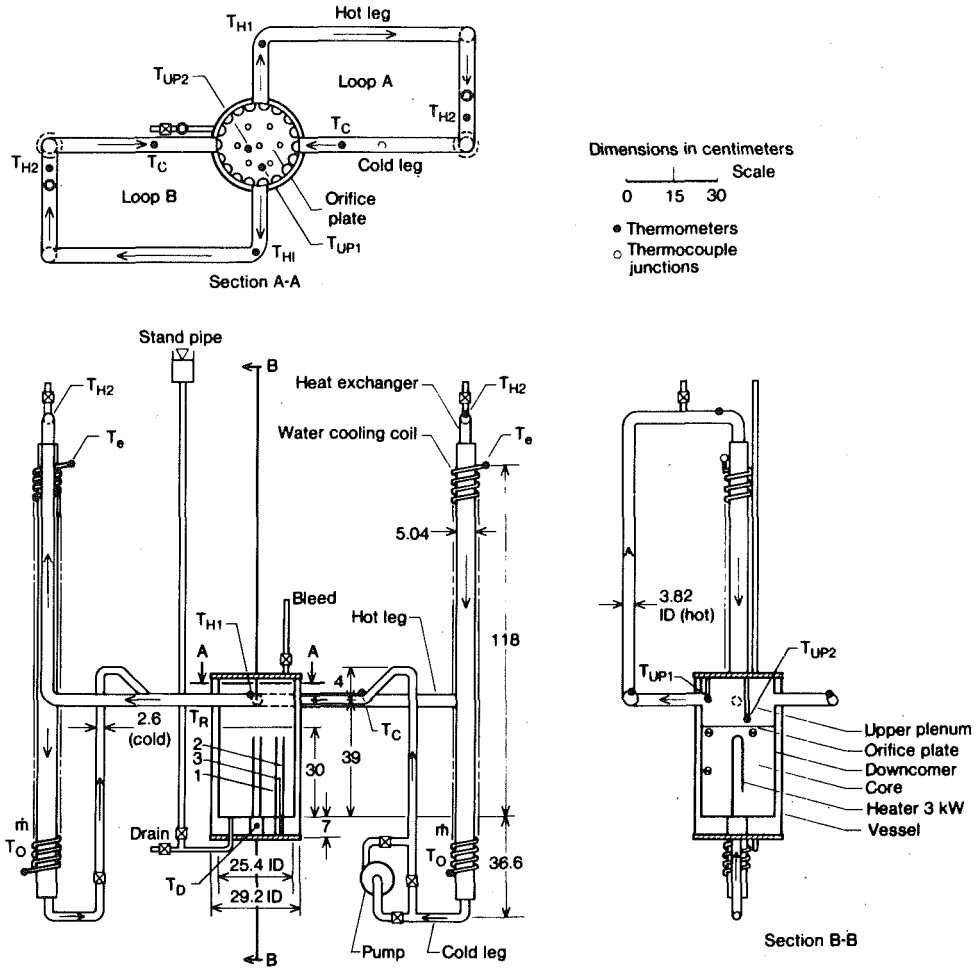

Fig. 2 Schematic arrangement of the experimental natural circulation loop

Table 1 Summary of tests conditions

Run No.	1	2	3	4	5	6	7	8	9	10	11
Heater Configuration I—cylindrical II—stacked spirals	I	I	I	I	I	I	II	II	II	II	II
Orifice Plate Fig. 4(*a*)	I	I	II	III	III	III	III	III	III	IV	IV
Upper Plenum Design-Fig. 4(*b*)	I	I	I	I	I	I	I	I	I	I	II

Input power 2.88 ± 0.06 kW except for run No. 9 (1.44 kW)
Secondary coolant flow 0.050–0.063 kg/s in each active loop, at inlet temperature of 11–15°C
Runs No. 2 and 5—one loop only

Table 2 Steady-state experimental results and the calculations of flowrate and temperature difference, runs 4 and 10

	Secondary Coolant Flow						Primary Coolant										
	Loop A			Loop B							Loop A		Loop B			Esti-mated (equation (12))	
Run No.	$\dot{m}$ 10^2 kg/s	T_0 °C	T_e °C	$\dot{m}$ 10^2 kg/s	T_0 °C	T_e °C	T_D °C	T_{R3} °C	T_{R1} °C	T_{R2} °C	T_C °C	T_H °C	T_C °C	T_H °C	ΔT_R °C	Q_R $10^5 m^3/s$	Remarks
4	5.4	12	18	6.0	12	17.5	23.9	23.9	36.1	37.8	23.9	37.5	23.3	37.5	13.9	4.97	Measurements of velocities in the cold leg by tracing dye movements (see Table 3).
10	5.5	12.5	25	0	24	24	33.0	37.8	50.8	52.5	33.6	51.7	34.4	49.4	18.1	3.87	
	5.2	13.5	25.5	0	29	29	40.6	45.7	45.6	50.6	33.6	52.8	51.7	52.8	19.2	3.57	
	5.2	13	20	6.3	13.5	19	26.1	31.1	31.1	36.3	25.6	38.6	25.0	38.6	13.3	5.23	

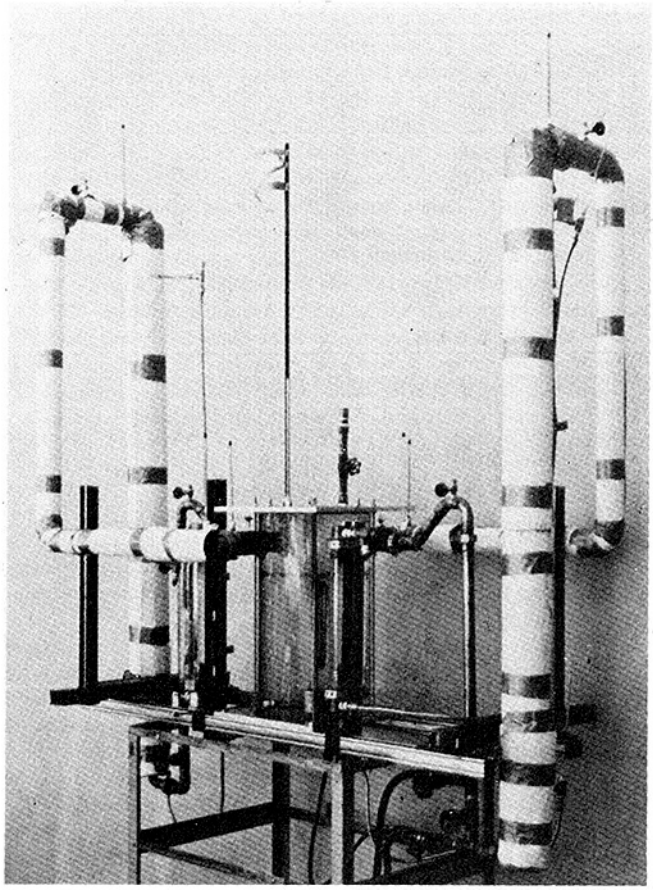

Fig. 3 The natural circulation experimental loop

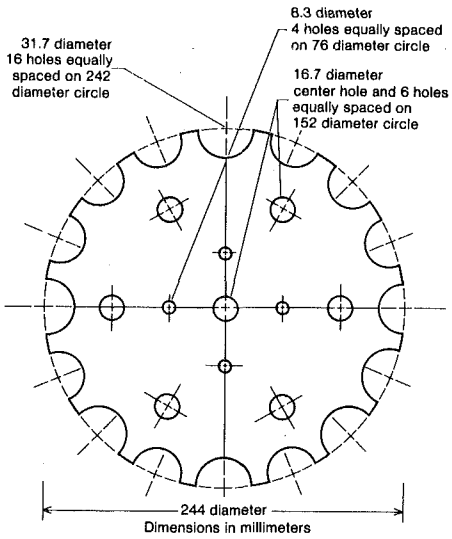

Fig. 4(*a*) Orifice plate detail. All four designs included the outside openings. I—Just the seven 16.7 mm holes, No 8.3 mm holes. II—The four 8.3 mm holes replace the center 16.7 mm hole. All 16.7 mm holes plugged, leaving the 8.3 mm holes. IV—All holes plugged

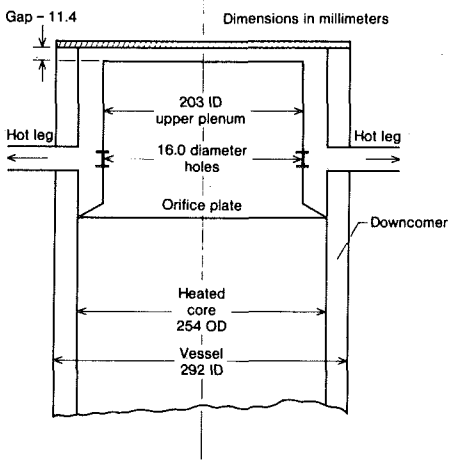

Fig. 4(*b*) Upper plenum arrangement—Design II. Design I does not have the innermost sleeve

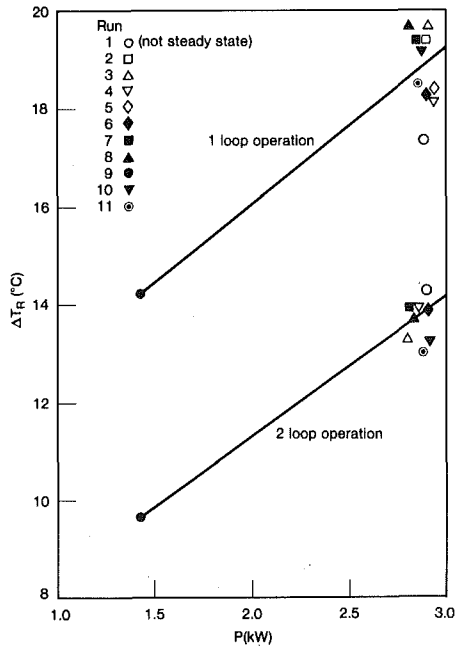

Fig. 5 Steady-state temperature difference over the vessel as a function of the input power

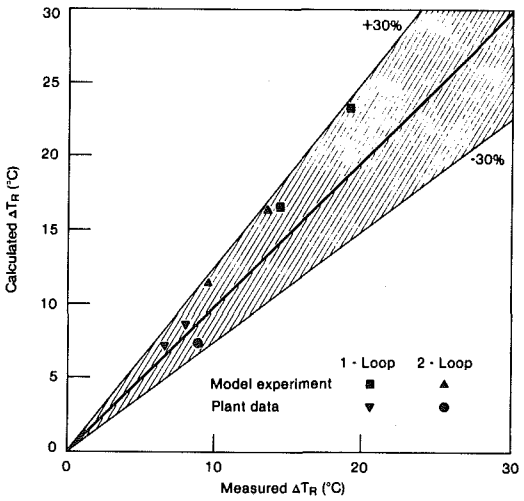

Fig. 6 Comparison of experimental and plant data and theoretical calculations

Table 3 Comparison of average experimental and theoretical values of flow rates and temperature differences and velocities (1l and 2l = one- and two-loop operations)

Power kW	Mode	Average System Temperature °C	Experimental ΔT_R °C	Q_R $10^5 m^3/s$	u_c m/s	Re_c	Theoretical ΔT_R °C	Q_R $10^5 m^3/s$
2.88	1l	42	19.0	3.62	0.068	2790	23.4	2.94
	2l	31	13.5	5.10	0.048	1590	16.6	4.16
1.44	1l	33	14.2	2.42	0.046	1580	16.6	2.08
	2l	25	9.7	3.55	0.033	960	11.7	2.94

			Measured u_c	Estimated u_c
2.93	1l	Run No. 4	0.086	0.073
2.89	2l		0.074	0.047

for every run from the measured values of the flow rates ($\dot{m}$) and the inlet and outlet temperatures. This was found to be typically 96 percent of the input power for two-loop steady-state operation and 93 percent for one-loop operation, where all the temperatures in the system were higher. For the latter case, most of the heat losses were from the inactive loop, which implies that there was some weak flow in this branch. Observations confirm, indeed, this conclusion. On the other hand, the errors involved in calculating Q and H by equations (9) and (17) are small, as mentioned above, probably less than 3 percent. Moreover, the low losses justify the assumptions made in the analysis which are therefore small and can be neglected.

The most important parameter which can serve to characterize the system behavior at steady-state is the temperature difference over the heated section, which is directly related to the flow rate in the loop, equation (9). Figure 5 shows all the data of ΔT_R; the variation (for the same power) is quite small—1.5°C for one-loop and 1.1°C for two-loop operations. The conclusion is that the configuration of the vessel-heaters, upper plenum and orifice plate was not the dominant parameter affecting the flow, but rather the flow resistance of the tubing in the loop governed the steady-state behavior. Calculations of the flow resistances yield the same results. However, the systematic deviations between the data points in Fig. 5 are significant enough to enable examination of the vessel geometry effects.

4.1.2 Visual Observations. Convection currents were clearly visible due to the refraction of light in density gradients and the motion of small dust particles in the flow. Flow patterns were non-uniform: a clear upward buoyant plume formed centrally for the axial immersion heater, which the orifice plate smoothed out. A cold "waterfall" effect with an expanding mixing zone could be seen in the downcomer as cooled water returned from the cold legs, indicating incomplete mixing of the returning water. Where the leakage paths existed at the hot leg connections as explained above, flow jets could be clearly seen emanating from the holes, retaining their identity for 10–20 hole diameters. The conclusion from the visual observations was that the flows were three-dimensional and were never hydrodynamically fully-developed.

4.1.3 Effect of Orifice Plate. In runs 1–3, the orifice plate had the same flow area, see Fig. 4(a) and Table 1. As can be seen from Fig. 5, and considering the change in power between runs 2 and 3, the effect on ΔT_R is indeed very small. In runs 4–6, the orifice plate created a higher flow resistance. For two-loop operation, ΔT_R was higher than in the previous cases as could be expected. For one-loop operation, however, ΔT_R was lower, implying a higher flow rate than before. This can be attributed to a recirculation region in the upper plenum (in runs 1–3) caused by the observed jets rising through the center holes. The partial elimination of these jets in runs 4–6 reduced this region in the nonsymmetrical one-loop operation, enhancing the flow towards the hot leg. Similarly, the results of runs 10 and 11, where the orifice plate had the outside openings only, show a decrease of ΔT_R (compared to runs 7 and 8 with the same heater configuration). This demonstrates that most of the flow passes through the outside of the plate, leading to recirculation in the upper plenum and a reduction of the flow rate.

4.1.4 Upper Plenum Design. The effect of the second configuration of the upper plenum (Fig. 4(b)), with a better connection to the hot legs (run 11), was exhibited by a marked decrease of the temperature difference (and increase of the flow rate) as can be expected, see Fig. 5.

4.1.5 Input Power Distribution. The change to stacked spiral heaters (runs 7 and 8 with the same orifice plate as runs 4–6) caused only a slight change of ΔT_R for two-loop operation, while a significant increase was obtained for one-loop operation (see Fig. 5). This behavior can be attributed partly to the increased flow resistance of the stacked heaters, and partly to the skewed temperature and velocity distributions formed by the uniform heating in the core and non-symmetrical flow through only one loop.

4.1.6. Effect of Power Variation. Run 9 (see Table 1 and Fig. 5) was performed at half power compared to all other tests. The ratio of the average temperature differences for full- and half-power tests is 1.33 for one-loop and 1.41 for two-loop operation. This agrees well with the analytical calculations, equation (14), for laminar flow, where ΔT_R is proportional to $P^{1/2}$. As shown in the following discussion, the range of Reynolds number corresponded, indeed, to laminar flow. The flow was near the transition region in the cold leg during one-loop tests at full power; even in this case, the flow was laminar in the rest of the loop. The same conclusion can also be drawn by comparing the results of the one-loop and two-loop tests (Fig. 5). For turbulent flow $R_{2\text{loop}} \approx \frac{1}{4}(R_{1\text{loop}})$, while for laminar flow, $r_{2\text{loop}} \approx \frac{1}{2}(r_{1\text{loop}})$. The ratios of ΔT_R (1.38 − 1.47) are closer to $2^{1/2}$ than to $4^{1/3}$ (see equations (13) and (14)).

4.1.7 Comparison of Experimental and Theoretical Results. The average values of the temperature difference ΔT_R for all the one- and two-loop experiments for both input powers are listed in Table 3. The flow rates in the heated section, Q_R, were estimated by equation (9); for two-loop operation, the flow rate in each loop is half of Q_R. The mean velocities in the cold leg, u_c, where calculated from these values of Q_R. The table also includes a comparison with the cold leg velocities measured by tracing dye movement by a video tape recorder, run 4. For the one-loop operation, the agreement is quite good; for the two-loop operation, the estimated average velocity is considerably lower than the measured value. This is most probably because the latter represents the conditions near the center of the tube. For one-loop operation, the flow is near the transition to the turbulent flow regime and the transverse velocity profile is flat. For two-loop operation, the flow is laminar and the velocity near the center is much higher than the average. Taking into consideration these arguments, the agreement between the estimated and measured velocities is reasonably good.

Table 3 also includes the analytical results of ΔT_R and Q_R. The Reynolds number range implies laminar flows and equations (14) were used. The equivalent "driving head" is $\Delta z = 0.366$ m (see Fig. 2). The flow resistance parameter for one loop, $r = 3600\ (\text{ms})^{-1}$, was obtained from the pressure-drop measurements; this value agrees well with textbook friction loss correlations. It can be shown that for parallel flow through both loops, r for one complete loop (one-half of the flow) is given by $r = r_{\text{loop}} + 2\,r_R$. As mentioned above, the resistance of the vessel was much smaller than that of the loop and can be neglected.

The comparison between the measured and calculated temperature differences is also shown in Fig. 6, which includes nuclear power plant data and the results of calculations carried out by the same method. The plant is a 2500 MWt PWR with two loops having once-through

steam generators. The data for the natural circulation flows are for about 0.1 percent of full power, cf references [17–18].

The differences between the measured and calculated values of the temperature difference ΔT_R is between 17 and 23 percent. The discrepancies are mainly due to the multidimensional and developing nature of the flow affecting the loop resistance. As mentioned above, these effects were also observed visually during the experiments. Developing jet-type behavior and internal areas of recirculating flows in and between the heated section and the upper plenum could be detected.

4.2 Transient Behavior of the Natural Circulation Loop.

4.2.1 General Behavior. Most of the tests were performed as transient flows between two steady end conditions of one and two-loop operation. The behavior in all cases except for run No. 5, discussed below, were quite similar: initial short-term transient followed by a longer term stabilization of the temperature distribution. The results for runs 10 and 11 (both from one to two-loop operations) are shown in Fig. 7. The hot leg temperatures were very close in both loops, and one curve for T_H is illustrated. The behavior of cold leg temperatures, however, was different. Initially, T_{cB} in the inactive loop B was close to T_H. It sharply decreased immediately following the activation of the heat exchanger in this loop (by initiating secondary coolant flow). This can be explained by the heat removal in the previously stagnant loop. Accordingly, the characteristic transient time of this process should be the time it takes for a "fluid particle" to complete one circulation of the loop. This will be given by L/u where L is the total circulation length (5.9 m—see Fig. 2) and u is a characteristic average velocity. Since the flow rate during this initial transient is close to one-loop operation, the estimated average cold leg velocity is 0.073 m/s (Table 3), and u is found to be 0.034 m/s, which yields a value of 2.9 min for the first transient time. It can be seen from Fig. 7, indeed, that the time for T_{cB} to reach the value of T_{cA} is about 3 min.

The effect of the upper plenum configuration on the transient behavior of the system can be seen from Fig. 7. The decrease of the average system temperature (represented by T_{r1}) is more rapid with the second design of the upper plenum (run 11), which had a better connection to the hot legs (see Fig. 4(*b*)). This effect is more pronounced in the initial stages of the transient because of the reduction of the stagnant region above the orifice plate.

4.2.2 Comparison with the Analysis. The mean system temperature, given by equations (20) and (21) as a function of time, is also plotted in Fig. 7–run 10 (see also Table 2). The average primary temperature at the end steady-state, T_P = 31°C, calculated by equation (21), is very close to the measured value. The overall heat transfer parameter for the heat exchanger, H = 0.195 kW/°C, was calculated from a heat balance, equation (17). The heat transfer coefficient h (and then H) can also be estimated by basic convective heat transfer considerations assuming the primary side to be limiting. For developing laminar forced flow in a tube, the heat transfer coefficient $\bar{h}$ (or the Nusselt number $\overline{\mathrm{Nu}}$) is given as a function of the Graetz number. The effect of natural convection, which is very significant in the flow under consideration, can be accounted for by the following empirical expression, e.g., reference [19]:

$$h = \left[1 + 0.072 \frac{\left(\mathrm{Ra}\frac{D}{L}\right)^{3/4}}{\mathrm{Gz}}\right]^{1/3} \bar{h} \tag{24}$$

where the Rayleigh number is based on the average temperature difference between the primary and secondary sides. The result for the heat transfer parameter is H = 0.153 kW/°C. The deviation from the estimate of 0.195 kW/°C is 21 percent, the same order of magnitude as that in the flow resistance coefficients. As mentioned above, these deviations are due to the multidimensional flow patterns in the natural circulation loop.

The estimated value of H yields τ = 20.6 min (equation (21)). The time constant obtained from the experimental curve for $T_{R1}(t)$ is approximately 16 min., with a deviation, again, of 25 percent from the theory. The agreement between the analysis, based on the estimated for H from equation (17), and the data (Fig. 7) is quite good, considering the simplified approach.

4.2.3 Oscillatory Behavior. In run No. 5, the initial steady-state condition was a one-loop operation where the primary flow in loop B was shut off by a valve. The transient caused by opening this valve, with secondary coolant flow in loop A only, is illustrated in Fig. 8. It can be observed that an initial short-term transient of about one minute took place, during which the hot leg temperature near the vessel T_{HB1} increased, while the cold leg temperature dropped to a value close to that of the stagnant secondary fluid, indicating a flow from the core into the hot leg. Thus, the initial temperature distribution in the completely stagnant loop B had a minimum with a value near T_{II} at the bottom of the heat exchanger, see Fig. 8. It is concluded,

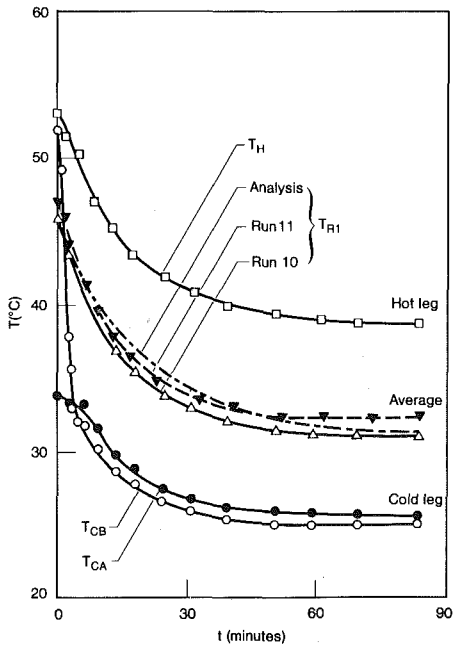

Fig. 7 Transient behavior of the system; hot and cold legs and average core temperatures, run 10; the latter compared with the analysis and with run 11

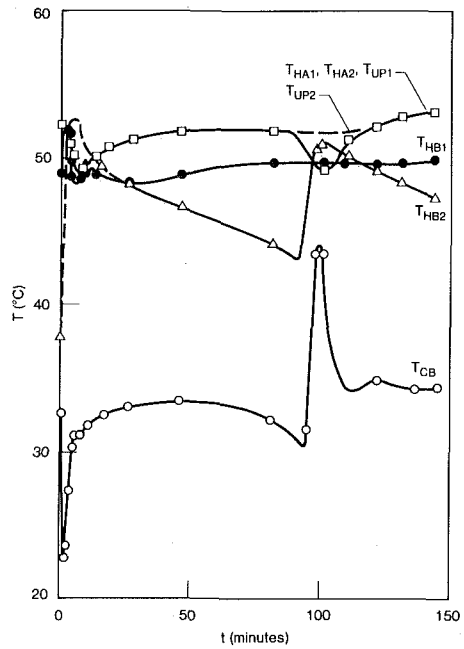

Fig. 8 Oscillatory behavior of the loop—run No. 5.

then, that when a loop was maintained inactive just by no secondary flow in the heat exchanger, some weak flow existed due to heat losses.

The short-term transient discussed above was followed by some fluctuations of the temperatures; these decayed after about 15 min. It appeared as if the system approached a stable steady state. As can be seen from Fig. 8, however, the temperature at the top of the heat exchanger in the inactive loop was continuously decreasing (at a constant rate) due to heat losses. At about 90 min, a critical condition was reached, as indicated by the sharp oscillations. The temperature at the top of the B-loop heat exchanger (T_{HB2}) increased rapidly, accompanied by a sharp increase of the cold leg temperature. At the same time, T_H in the active loop and the temperature T_{UP1} in the upper plenum near the B-loop inlet decreased. This is clearly an indication that a flow reversal occurred in the B-loop, caused by the density difference in the vertical section of the hot leg: heavier liquid, at a lower temperature, on top and lighter liquid near the vessel ($T_{HB2} < T_{HB1}$). After about 10–15 min, the temperatures stabilized again, but a decrease of T_{HB2} could be observed at the same rate as before. This could mean that another oscillation would occur had the experiment not terminated.

Finally, it is worthwhile to calculate the Rayleigh number in the rising section of the cold leg at the start of the reversed flow. The relevant temperature difference was $T_{HB1} - T_{HB2} = 6°C$ and $L = 0.94$ m, yielding $Ra_c = 2.7 \times 10^{11}$. It is noted that this Rayleigh number is of quite different order than that associated with the classical Benard-Rayleigh convection instabilities of a large horizontal liquid layer heated from below.

5 Conclusions

Natural circulation in a model loop relevant to a PWR has been shown to be an effective means of heat removal. By comparing a one-dimensional analysis with results of the experiments and available plant data, it has been demonstrated that simple analytical modeling is capable of describing the steady-state and transient behavior.

Various parameters, such as the core flow resistance, input heat distribution, and upper plenum geometry, have been shown to give rise to three-dimensional flow effects. These contribute to the overall uncertainty of order 30 percent, between the analysis and the data. It is noted that both the experimental uncertainties and the approximations introduced in the one-dimensional analysis (Boussinesq and linear temperature distribution in the heat exchangers) can only account for about 10 percent deviations between the theoretical and experimental results. Finally, the experiments showed that certain loop conditions, which give rise to inverted density profiles, can cause instabilities of the flow.

Acknowledgment

The authors wish to thank Mr. P. M. Newgard and Dr. R. L. Kiang of SRI International for their assistance during all stages of the experimental work.

References

1 Japikse, D., "Advances in Thermosyphon Technology," in *Advances in Heat Transfer*, edited by T. F. Irvine, Jr. and J. P. Hartnett, Vol. 9, Academic Press, New York, 1973, pp. 1–111.

2 Ong, K. S., "A Finite Difference Method to Evaluate the Thermal Performance of a Solar Water Heater," *Solar Energy*, Vol. 16, 1974, pp. 137–147.

3 Shitzer, A., Kalmanoviz, D., Zvirin, Y., and Grossman, G., "Experiments with a Flat-Plate Solar Water Heating system in Thermosyphonic Flow," *Solar Energy*, Vol. 22, 1979, pp. 27–35.

4 Zvirin, Y., Shitzer, A., and Grossman, G., "The Natural Circulation Solar Heater-Models with Linear and Nonlinear Temperature Distributions," *International Journal Heat Mass Transfer*, Vol. 20, 1977, pp. 997–999.

5 Zvirin, Y., Shitzer, A., and Bartal-Bornstein, A., "On the Stability of the Natural Circulation Solar Heater," *Proceedings of the 6th International Heat Transfer Conference*, Toronto, Canada, Vol. 2, 1978, pp. 141–145.

6 Torrance, K. E., "Open Loop Thermosyphon with Geological Applications," ASME *JOURNAL HEAT TRANSFER*, Vol. 101, 1979. pp. 677–683.

7 Lewis, E. E., *Nuclear Power Reactor Safety*, Wiley, New York, 1977, p. 345.

8 Gillette, J. L., Singer, R. M., Tokar, J. V., and Sullivan, J. E., "Experimental Study of the Transition from Forced to Natural Circulation in EBR-II at Low Pressure and Flow," ASME Paper No. 79-HT-10, 1979.

9 Gregory, C. V., Bell, R., Brown, G., Dawson, C. W., Henderson, J. D. C., and Hampshire, R., "Natural Circulation Studies in Support of the Dounreay Prototype Fast Reactor (PFR)," ANS/ENS International Meeting on Fast Reactor Safety Technology, Seattle, Washington, Aug. 1979.

10 Welander, P., "On the Oscillatory Instability of a Differentially Heated Fluid Loop," *Journal Fluid Mechanics*, Vol. 29, 1967, pp. 17–30.

11 Creveling, H. F., DePaz, J. F., Baladi, J. Y., and Schoenhals, R. J., "Stability Characteristics of a Single-Phase Free Convection Loop," *Journal Fluid Mechanics*, Vol. 67, 1975, pp. 65–84.

12 Zvirin, Y., and Greif, R., "Transient Behavior of Natural Circulation Loops: Two Vertical Branches with Point Heat Source and Sink," *International Journal Heat Mass Transfer*, Vol. 22, 1979, pp. 499–504.

13 Greif, R., Zvirin, Y., and Mertol, A., "The Transient and Stability Behavior of a Natural Circulation Loop," ASME JOURNAL HEAT TRANSFER, Vol. 101, 1979, pp. 684–688.

14 Zvirin, Y., "On the Behavior of a Natural Circulation Loop with a Through-flow," *Proceedings of the 14th Intersociety Energy Conversion Engineering Conference*, Boston, Mass., 1974–1978, Aug 1979.

15 Chato, J. C., "Natural Convection Flows in Parallel-Channel Systems," ASME JOURNAL OF HEAT TRANSFER, Vol. 85, 1963, pp. 339–345.

16 Duffey, R. B., Kalra, S. P., Merilo, M., Sun, K. H., and Zvirin, Y., "Beyond the Large LOCA: Current Heat Transfer Aspects of LWR Safety Analysis," *Proceedings International Seminar on Nuclear Reactor Safety Heat Transfer*, Dubrovnik, Yugoslavia, Aug 1980.

17 Yeung, M. R., Meadows, A. H., and Turner, K. W., "Reactor Coolant System Coastdown and Natural Circulation," ANS/ENS Thermal Reactor Safety Meeting, Knoxville, Tenn, Apr 1980.

18 Denver, D. J., Harrison, J. F., Jr. and Trikouros, N. G., "RETRAN Natural Circulation Analyses During the Three Mile Island Unit 2 Accident," ANS/ENS Thermal Reactor Safety Meeting, Knoxville, Tenn, Apr 1980.

19 McAdams, W. H., *Heat Transmission*, McGraw-Hill, New Hork, 1954, p. 233.

Refilling and Rewetting of a Hot Horizontal Tube

Part III: Application of a Two-Fluid Model to Analyze Rewetting

A. M. C. Chan[1]
S. Banerjee[2]
Mem. ASME

Department of Engineering Physics,
McMaster University,
Hamilton, Ontario L8S 4M1, Canada

Experiments on rewetting and refilling of hot horizontal tubes [1] indicate that a liquid "tongue" initially runs along the bottom causing significant precooling. The rewetting front follows this tongue, with the bottom of the tube rewetting before the top. Very little precooling is observed at the top and rewetting apparently occurs at quite high temperatures. Rewetting velocities generally decrease with increases in inlet water temperature, initial tube wall temperature and power input into the tube. Rewetting velocities increase with increases in injection flow rate. The data cannot be explained in terms of a conduction controlled rewetting model. Also the rewetting temperature varies considerably between the top and bottom of the tube, and along the tube. The phenomena appear to be hydrodynamically controlled and are well predicted by a two fluid model with reasonable constitutive equations for wall and interfacial friction, and heat transfer. The transverse gravitational force has to be incorporated in the model to account for flow stratification. The most critical constitutive relationship is with regard to the transition from film boiling to a rewet surface at the bottom of the tube. A model based on interfacial instability to signal this transition predicts the experimental results.

Introduction

Rewetting and refilling is a very complicated thermalhydraulic process [1]. To model it, the simple conduction controlled rewetting model [2] is clearly inadequate as discussed previously [1]. Physically, rewetting is the re-establishment of water contact with a hot surface. In the case of a moving quench front, highly nonequilibrium processes occur. For example, sputtering exists at, and violent boiling exists behind, the quench front. These processes determine the rewetting rates and cannot usually be "frozen" as assumed in the conduction controlled model through the assumption of a constant quench velocity. Instead the process is strongly affected by the local flow parameters, such as pressure, heat transfer coefficient, water flow rate and subcooling. Thus, to better model the flow situation, a nonequilibrium two-fluid model is needed. This two-fluid model approach is especially necessary for stratified flow in horizontal channels.

A simplified two-fluid model which can be used to study the refilling and rewetting process in a hot horizontal tube has been developed in a previous paper [3]. The model has been used to predict the refilling of a cold tube.

In the present paper (which is the last in a series of three papers), the refilling and rewetting of a hot horizontal tube is analyzed using the simplified two-fluid model. Results are compared with experimental data presented previously [1].

Numerical Procedures

The governing equations [3] are solved numerically using a computer code (REWET). The code solves the hydraulic and thermal equations using an upwind finite difference characteristic method and an explicit finite difference technique, respectively [3]. A flow diagram of the code is given in Fig. 1. The computational steps are shown.

Twenty-four cells are normally used to represent the heated test section. Six cells are used to simulate the inlet and outlet tubing, respectively. More cells have been used for spatial convergence studies. Uniform mesh sizes are used for the present investigation, however, nonuniform meshes can be incorporated into the code with minor modifications.

Since explicit numerical schemes are used, the time step size (Δt) is limited by stability considerations. The stability conditions are not the same for the hydraulic and thermal equations. It has been found that in general, the gravity wave velocity in the hydraulic equations tends to limit Δt [4]. Therefore, Δt is determined by the stability condition of the hydraulic equations and is given by

$$\Delta t \leq \min\left\{\frac{\Delta z}{|U_L + c|}, \quad \frac{\Delta z}{|U_L - c|}\right\} \tag{1}$$

Different time step sizes have also been used for temporal convergence studies.

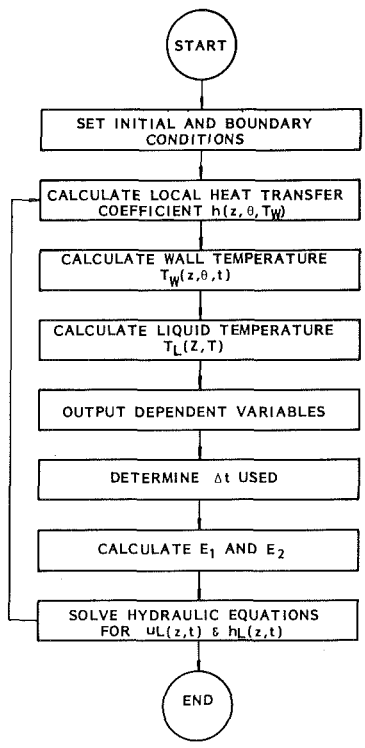

Fig. 1 Flow diagram of computer code REWET

[1] Current address: Mechanical Research Department, Ontario Hydro, 800 Kipling Avenue, Toronto, Ontario M8Z 5S4.
[2] Current address: Department of Chemical and Nuclear Engineering, University of California, Santa Barbara, CA. 93106.

Contributed by the Heat Transfer Division for publication in the JOURNAL OF HEAT TRANSFER. Manuscript received by the Heat Transfer Division January 2, 1981.

The heat transfer mechanisms during the refilling and rewetting transients are very complicated. Different modes of heat transfer exist along the channel depending on the local water level and wall temperature. The effective heat transfer coefficient (h) is, in most cases, the sum of the coefficients of a number of heat transfer processes. The local heat transfer model used is given in Table 1. The correlations for the coefficients of different heat transfer processes are also given.

Constitutive models are required to obtain the interfacial transfer terms which appear on the right hand side of the hydraulic equations (i.e., in E_1 and E_2). Some constitutive models for one-dimensional two-phase flows are given by Hughes, et al. [6] for different flow regimes. The models used in the REWET code are summarized in Table 1. Stratified flow is assumed.

Surface Rewetting

In order that the REWET code can predict the right quench behaviour, the appropriate local heat transfer coefficients have to be supplied as a function of time. Since quenching is associated with high heat transfer and since it is always preceded by stable film boiling except maybe in the region close to the top in a horizontal channel, it is clear that the high heat transfer follows breakdown of stable film boiling to transition or nucleate boiling. The conditions under which such transitions take place are not well understood. However, they are of paramount importance in the understanding of the rewetting processes. A transition model based on stability considerations will be described. The model is capable of predicting the right quenching conditions for our experiments.

Necessary and Sufficient Conditions for Surface Rewetting. In film boiling, the heated surface is blanketed by a thin film of vapor. Surface rewetting may be initiated by instabilities at the liquid-vapor interface. It should be emphasized here that the breakup of the interface does not automatically lead to surface rewetting. For example, breakup of an extended liquid mass boiling over a very hot surface into a number of smaller masses does not necessarily result in rewetting. When the interface breaks up, regions of enhanced heat transfer (rewet spots) may form on the heating surface. This provides the necessary conditions for surface rewetting. However, if the surface is highly conductive and has a high heat capacity. these regions of enhanced heat transfer will dry up rapidly and film boiling is restored. Therefore, the sufficient condition for surface rewetting would require that the rewet spots could grow or spread.

A process which has been widely observed experimentally leading to surface rewetting is the so called Leidenfrost transition [12]. The surface temperature at the transition point is known as the Leidenfrost or rewetting temperature. Rewet spots will form when the surface temperature drops to the rewetting temperature and the thrust due to vapor generation can no longer support a continuous liquid-vapor interface. Provided the rewet spots can grow, the decrease of the surface temperature to the rewetting temperature provides, in general, the necessary and sufficient conditions for surface rewetting. Since the spread or decay of the rewet spots is expected to be locally conduction controlled, this would explain why the rewetting temperature has been found to depend on the physical properties of the heating surface as well as the surface finish.

It should be pointed out here that the concept of a Leidenfrost or rewetting temperature is not always tenable. Wachters, et al. [13] has shown that under carefully designed experimental conditions, liquid drops can exist without wetting the surface even when the surface is below the saturation temperature of the liquid. This can happen when an intact vapor layer can be maintained.

The existence of intermittent solid-liquid contacts or rewet spots in stable film boiling has been detected by Bradfield [14] and Kovalev [15]. Their results give strong experimental support to the fact that interface breakup or the formation of rewet spots on the heating surface does not, in general, provide sufficient conditions for surface rewetting if the surface temperature is high enough.

However, if the heat capacity of the hot surface is low, e.g., a thin walled tube, rewet spots can spread once formed even if the temperature is high. Thus, the break up of the liquid-vapor interface will provide both necessary and sufficient conditions for surface rewetting. In other words, rewetting can occur independent of the surface temperature.

This has been found to be the case for our refilling and rewetting experiments which used a thin walled test section, 0.898 mm thick. It was found that rewetting can occur at wall temperatures much higher than the corresponding Leidenfrost temperature and the apparent quench temperature can be quite different at different axial locations [1]. Instability of the liquid-vapor interface in film boiling may therefore be the dominant mechanism that results in surface quenching in our experiments. The mechanism that, in turn, leads to instability of the liquid-vapor interface will now be examined.

Instability in Film Boiling. The mechanism proposed is based on the instability of a wave at the liquid vapor interface. The instability is hydrodynamic in nature, the wall temperature affects it indirectly through the velocity and the thermophysical properties of the vapor. The use of interfacial stability in analyzing transition from film boiling was first proposed by Chang [16] and later developed by Zuber [17]. The existence of capillary waves (or ripples) on the interface in film boiling has been observed experimentally, for example,

Nomenclature

A = area
c = gravity wave velocity, wave velocity
C_p = heat capacity
D = diameter
D_h = hydraulic diameter
e = surface emissivity
f = friction factor
g = gravitational force
Gr = Grashof number
h = enthalpy, heat transfer coefficient
h_L = liquid level
h_q = effective quench level
h_{fg} = heat of evaporation
k = thermal conductivity
m = wave number, friction force multiplier
$\dot{m}$ = rate of interfacial mass transfer
M = total mass of liquid inventory in the system
p = pressure
Pr = Prandtl number
QV = liquid volumetric flow rate
Q_{in} = energy input from channel wall
Q_{out} = energy lost by channel wall in terms of losses in heat capacity
r = radial direction
Re = Reynolds number
t = time
T = temperature
u, U = velocity
V = rewetting velocity
y = vertical distance
y_h = hydraulic depth
z = axial direction, axial distance
α = void fraction, thermal diffusivity
β = fraction of energy input used for evaporation
γ = weighting factor in the determination of the interface velocity
δ = vapor film thickness
ΔM = mass difference
Δt = time step size
ΔT = wall superheat
Δz = mesh size
ϵ = channel wall thickness
θ = angular position
λ = wavelength
ρ = density
σ = surface tension
ϕ = two phase friction multiplier

Subscripts

B = bottom of channel
CHF = critical heat flux
crit = critical
F = fluid
G = vapor phase
i = interphase
in = inlet
k = phase k
L, f = liquid phase
r = relative
sat = saturation
S = mid-side of channel
T = top of channel
z = axial direction
w = channel wall

Table 1 Constitutive relations used in REWET

Constitutive Relations	Equations Used	Reference
Interfacial Mass Transfer	$\dot{m}_L = \frac{\beta Q}{h_{fg}}$ where $\beta = 1$ Film Boiling Region; $= 0$ Quenching Region	Chan [4]
Wall Shear -Liquid Phase	$F_{WL} = \frac{1}{2} f_L u_L \lvert u_L \rvert \rho_L a_L / \alpha_L A_o$ where $f_L = mf$ Inlet Feeder Region; $= f$ $h_L = D$; $= \phi f$ Quenching Region; $= 0$ Film Boiling Region; and $f = 0.0791/Re^{0.25}$, $m = F(u_L^o)$, $\phi = 60$	Chan [4]

by Bromley [18] and by Westwater and Santangelo [19]. Therefore, they are worth examining for an explanation of rewetting of thin tubes.

Hydrodynamically, when two fluids, in contact with each other, are in relative motion, then if the relative velocity is high enough, a Kelvin-Helmholtz instability [20] would set in. The amplitude of the capillary waves on the interface would grow under favorable conditions.

For a flat interface for which we consider the effect of surface tension, the propagation equation for a small disturbance as derived by Lamb [20] and adopted by Zuber [17] is given by

$$c^2 = \frac{\sigma m}{\rho_L + \rho_G} - \frac{\rho_L \rho_G}{(\rho_L + \rho_G)^2}(U_G - U_L)^2 \tag{2}$$

The condition for instability is that the disturbance or wave can grow. That is, c should have an imaginary part. The stability criterion can be obtained for c to be wholly real as

$$U_{\text{rel}} = U_G - U_L \leq \left[\frac{\sigma m}{\rho_L \rho_G}(\rho_L + \rho_G)\right]^{1/2} \tag{3}$$

When this criterion is not satisfied, the interface becomes unstable and the necessary conditions for a transition from film boiling and subsequent surface rewet are present. It should be emphasized again that these may not be sufficient conditions except for very thin walled tubes. Sufficient conditions would require that the localized high heat transfer regions (rewet spots) could grow.

Vapor Flow in Film Boiling. Film boiling occurs when a continuous layer of vapor is generated at the liquid-vapor interface due to the heat conducted through the vapor film from the heating surface. Considerable experimental and analytical work has been done on film boiling under different physical situations, e.g. by Bromley [18], Chang [12], Berenson [10], Hamill and Baumeister [22], Breen and Westwater [23], Kruger and Rohsenow [24] and others. In all these investigations, the primary objective was to obtain heat transfer coefficients. The vapor flow in the vapor film has not received much attention. Since the vapor velocity in the vapor film may determine the stability of the film if Kelvin-Helmholtz instabilities are considered, it is one of the most important parameters in predicting boiling transition and subsequent quenching of the surface in thin walled test sections. A detailed analysis of the vapor flow in the vapor film for stratified flows in horizontal systems is given by Chan [4]. Only a brief description will be presented here.

The flow model used is shown in Fig. 2. The liquid is separated from the tube wall by a thin vapor film. The thickness of the vapor film (δ) can vary under the influence of vapor generation and thrust, hydrostatic pressure and pressure drop due to vapor flow. The flow of vapor is assumed to be one-dimensional as shown, i.e. it is assumed that it will vent upwards and then flow along the channel in the vapor space above the liquid.

Table 1 continued

Constitutive Relations	Equations Used	Reference
Wall Shear - Vapor Phase	$F_{WG} = \frac{1}{2} f_G u_G \lvert u_G \rvert \rho_G a_G / \alpha_G A_o$ where $f_G = 0.005$	Wallis [5]
Interfacial Shear	$F_{GL} = \frac{1}{2} f_i u_r \lvert u_r \rvert \rho_G a_i / A_o$ where $u_r = u_G - u_L$, $f_i = 0.005$	Wallis [5]
Momentum Transfer	$T_m = \dot{m}_L u_i$ where $u_i = \gamma u_G + (1-\gamma) u_L$ and $\gamma = 0.5$	Hughes et al [6]
Local Heat Transfer Model	(i) $h_L = 0$: $\bar{h} = h_{VF} + h_{FC} + h_{RAD}$ $0 \leq y \leq D$ (ii) $0 < h_L < (h_L)_{crit}$: $\bar{h} = h_{FB} + h_{FC} + h_{RAD}$ $0 < y < h_L$; $\bar{h} = h_{VF} + h_{FC} - h_{RAD}$ $h_L \leq y \leq D$ (iii) $(h_L)_{crit} \leq h_L < D$: $\bar{h} = h_{VF} + h_{FC} + h_{RAD}$ $h_L < y < D$; $\bar{h} = h_{FB} + h_{FC} + h_{RAD}$ $h_q < y \leq h_L$; $\bar{h} = h_Q + h_{FC} + h_{RAD}$ $0 \leq y \leq h_q$ where $h_Q = h_{TB}$ $T_w \geq T_{CHF}$; $= h_{NB}$ $T_{sat} < T_w < T_{CHF}$; $= h_{LF}$ $T_w \leq T_{sat}$ (iv) $h_L = D$ and $T_w < T_{sat}$: $\bar{h} = h_{LF} + h_{FC} + h_{RAD}$ $0 \leq y \leq D$	Chan [4]
Free Convection Heat Transfer Coefficient	$h_{FC} = 0.525(Gr\,Pr)^{0.25} k_f / D_h$	McAdams [7]
Radiation Heat Transfer Coefficient	$h_{RAD} = \sigma\varepsilon(T_w^4 - T_f^4)/(T_w - T_f)$	Bird et al [8]
Vapor Phase Heat Transfer Coefficient	$h_{VF} = 0.023\left(\frac{\rho_g u_G D_h}{\mu_g}\right)^{0.8} \frac{k_g}{D_h}$	Sissom and Pitts [9]
Liquid Phase Heat Transfer Coefficient	$h_{LF} = 0.023\left(\frac{\rho_f u_L D_h}{\mu_f}\right)^{0.8} \left(\frac{C_p \mu}{k}\right)_f^{0.4} \frac{k_f}{D_h}$	Sissom and Pitts [9]
Film Boiling Heat Transfer Coefficient	$h_{FB} = 0.425\left\{\frac{k_g^3 h_{fg} \rho_g g(\rho_f - \rho_g)}{\mu_g \Delta T \sqrt{g/g(\rho_f - \rho_g)}}\right\}^{0.25}$	Berenson [10]
Transition Boiling Heat Transfer Coefficient	$h_{TB} = 9 \times 10^3 \exp(-0.0054\,\Delta T_w)$	Tong [11]
Nucleate Boiling Heat Transfer Coefficient	$h_{NB} = \frac{\exp(P/630)}{(0.072)^2} \Delta T_w$	Tong [11]

Considering the vapor channel, we can write down the mass and momentum conservation equations for the vapor phase:

Mass Conservation

$$\rho_G \frac{\partial \delta}{\partial t} + \rho_G \frac{\partial}{\partial x}(\delta \cdot U_G) = \frac{k \Delta T}{h_{fg}} \frac{1}{\delta} \tag{4}$$

where constant vapor density is assumed and heat transport is assumed to be by molecular conduction across the vapor film only, i.e., $h = k/\delta$. U_G is the vapor velocity in the vapor channel.

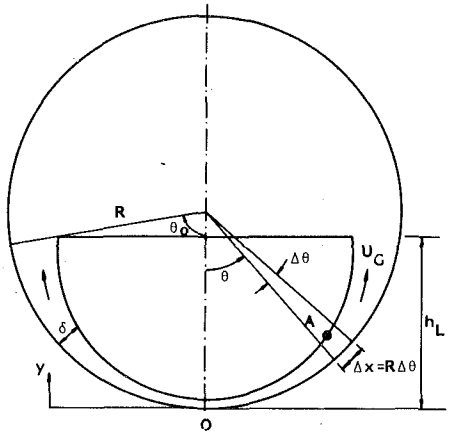

Fig. 2 Film boiling model

Momentum Conservation

$$\frac{\partial}{\partial t}(\delta \cdot U_G) + \frac{\partial}{\partial x}(\delta \cdot U_G{}^2) = -\frac{1}{\rho_G}\frac{\partial}{\partial x}(\delta \cdot P) - \frac{1}{\rho_G}(\tau_G + \tau_i) + \frac{k\Delta T}{\rho_G h_{fg}}\frac{U_i}{\delta} \quad (5)$$

Where P is the local pressure and can be shown given by

$$P - P_0 = \rho_L g(h_L - y) - \frac{1}{\rho_G}\left(\frac{k\Delta T}{h_{fg}}\frac{1}{\delta}\right)^2 - \sigma\left[1 + \left(\frac{\partial\delta}{\partial x}\right)^2\right]^{-3/2}\frac{\partial^2\delta}{\partial x^2} \quad (6)$$

P_{HH} P_{VT} P_{ST}

The terms are respectively contributions from hydrostatic head (P_{HH}), vapor thrust (P_{VT}) and surface tension (P_{ST}). P_{HH} is maximum at $y = 0$ and equals zero at $y = h_L$. P_{VT} results from mass transfer. P_{ST} is usually small except near $\theta = 0$ and can be ignored. P_0 is the system pressure above the liquid and is considered constant.

Equations (4) and (5) can be simplified if the time derivatives are assumed to be small. The set of equations are then solved numerically using an explicit finite different technique for δ and U_G. It was found that δ is nearly constant in the first half of the vapor channel and opens up rapidly after that. U_G rises linearly from zero at the origin, gets to a maximum at the point where δ starts to increase rapidly. It then decreases due to an increase in flow area as δ increases [4].

Film boiling heat transfer coefficients at the bottom of the tube are also obtained by this analysis and are in agreement with the correlation given in Table 1.

Onset of Instability. The instability criterion for boiling transition as given by equation (3) can be reduced to

$$U_G \geq \left[\frac{2\pi\sigma}{\rho_G\lambda}\right]^{1/2} \quad (7)$$

because $\rho_L \gg \rho_G$ in our experiments, and U_L is very small in the assumed direction of flow in the vapor film.

From equation (7), it is clear that the stability of the vapor film is determined by λ and U_G. λ is the wavelength of the Kelvin-Helmholtz instability and is dependent on the system geometry. For the flow situation shown in Fig. 2, the two lowest modes of oscillation are given in Fig. 3. Higher order harmonics may be excited at later stages of the boiling transition when U_G can become large locally. However, at the onset of instability, only the fundamental mode and its first harmonic are considered. It is not clear which of the two modes will be excited, because it is not clear whether the vapor channel length should be taken as the entire liquid-vapor interface length or just half of that due to symmetry.

Assuming the wavelength, λ, equals the vapor channel length, the critical vapor velocity (U_{crit}) for the onset of the Kelvin-Helmholtz instability can thus be calculated using equation (7). Results for the fundamental mode and its first harmonic are plotted in Fig. 4 for

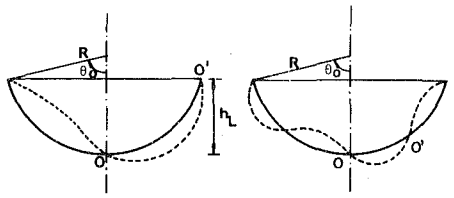

Fig. 3(a) cfn = 0, $\lambda = 2R\theta_0$ Fig. 3(b) $n = 1$, $\lambda = R\theta_0$

Fig. 3 Possible modes of oscillation

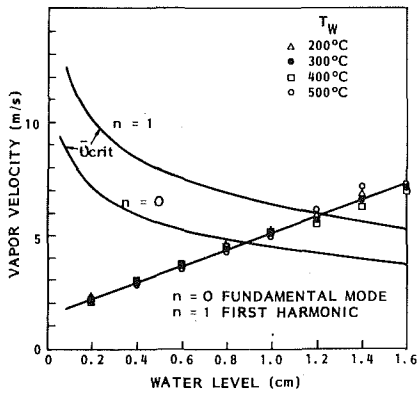

Fig. 4 Critical and average vapor velocities versus water level

different water levels (h_L). It can be seen that U_{crit} is always higher for the first harmonic.

The average vapor flow velocity in the vapor channel is also plotted in Fig. 4. Results for different wall superheats (ΔT) are shown. Averaged vapor velocities are used here instead of the local values because the growth of the interfacial wave will be affected by the vapor flow over a distance equal to half of wavelength.

The critical water level for the outset of instability can be readily obtained from the figure. This is the water level at which $\overline{U}_G$ equals U_{crit}. Since $\overline{U}_G$ is essentially independent of ΔT, $(h_L)_{crit}$ is also independent of ΔT. It should be noted that $(h_L)_{crit}$ is higher for the first harmonic.

From the above analysis, it is obvious that $(h_L)_{crit}$ so deduced is only good to a first approximation because there are uncertainties with regard to λ and $\overline{U}_G$. Also the initiation of an interfacial instability may not always lead to rewetting as mentioned before, though for very thin walled systems, it might provide both necessary and sufficient conditions. More precise values may be obtained empirically by comparing numerical results with experimental data. The procedure will be described in the next section.

The Quench Model

The computer code, REWET requires the use of a quench model which can predict boiling transitions under different thermalhydraulic conditions. As discussed above, the mechanism suggested for boiling transition in the present situation is a Kelvin-Helmholtz type of hydrodynamic instability. A critical water level, $(h_L)_{crit}$ can be derived. A simple quench model based on $(h_L)_{crit}$ is proposed in Fig. 5 where the tube wall level (h_q) at which boiling transition occurs is plotted against h_L, the water level. It can be seen that no transition takes place at the lower portion of the tube covered by water until $(h_L)_{crit}$ is reached. At this point, the vapor film becomes unstable, and boiling transition is postulated to occur at the bottom. It is not clear how h_q changes with h_L. However, it is certain that h_q would rise as h_L increases. At $h_L = D$, i.e. when the tube is filled to the top, boiling transition at the top will occur simultaneously i.e., $h_q = D$. This can be shown to occur due to an axial interfacial instability of the Kelvin-Helmholtz type.

A linear function is used in Fig. 5 relating h_q and h_L between $(h_L)_{crit}$ and D. However, this need not be the case. Other functions may be possible. Examples are shown in broken lines in the figure. Since the

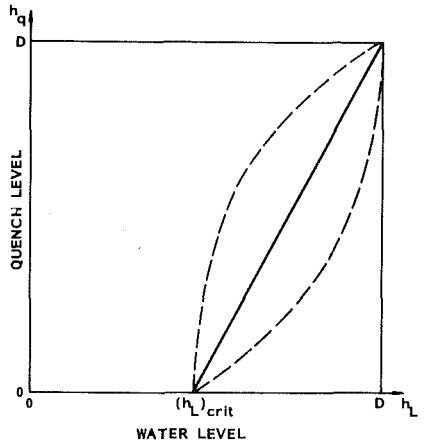

Fig. 5 Quench model

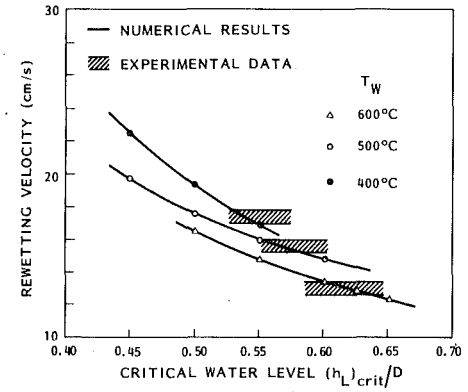

Fig. 6 Rewetting velocity ($\bar{V}_B$) versus critical water level $(h_L)_{crit}$

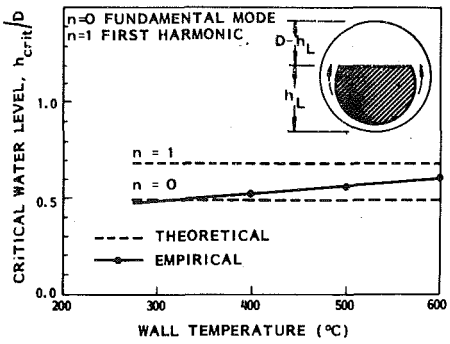

Fig. 7 Comparison of theoretical and empirical water level for vapor film instability

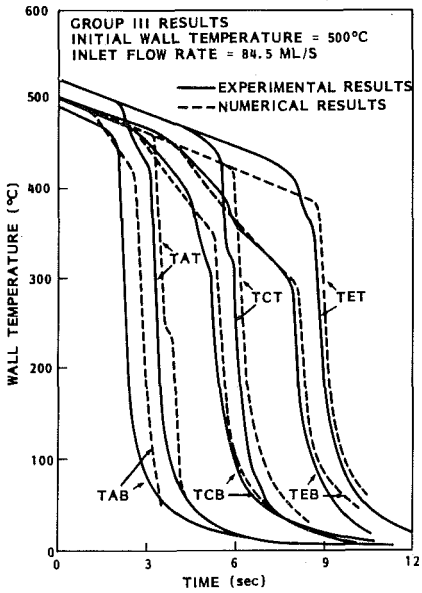

Fig. 8 Transient top and bottom wall temperatures—comparison of experimental and numerical results

way the surface is quenched is not known in detail, a straight line function is used in REWET for simplicity. The results are not very sensitive to the form of the function.

In order to use the quench model, $(h_L)_{crit}$ has to be known. Theoretically, $(h_L)_{crit}$ is obtainable using the hydrodynamic instability model. It is of interest to compare the theoretically predicted value of $(h_L)_{crit}$ with those determined from experiments.

Numerical studies indicate that since $(h_L)_{crit}$ determines the onset of surface quenching for the bottom or lower portion of the tube, it has a first order effect on the advancement of the leading edge of the quench front. $(h_L)_{crit}$ can be adjusted till the experimentally measured values of $\bar{V}_B$ match the numerical results obtained from the code REWET. For fixed initial and boundary conditions, REWET is run with different $(h_L)_{crit}$ values. Results are then compared with the corresponding experiments. The value that gives the closest agreement is chosen.

The results of such a numerical procedure are shown in Fig. 6 for different initial wall temperatures. The experimental data bands are also shown. It can be seen that $\bar{V}_B$ decreases as $(h_L)_{crit}$ increases and intercepts the data bands. The $(h_L)_{crit}$ values that give $\bar{V}_B$ which are within the data bands are obtained. It should be noted that $(h_L)_{crit}$ so deduced are essentially empirical. Their accuracy depends on the accuracy of the experimental data used. In general, $(h_L)_{crit}$ can be determined to within 0.025D as can be seen in the figure.

The empirical curve for $(h_L)_{crit}$ is given in Fig. 7 together with the theoretically predicted values. The agreement between the theoretical and empirical results are good. The instability theory can predict $(h_L)_{crit}$ reasonably well. A weak wall temperature dependence is observed in the empirical curve. This means that the wall temperature can have some effect on the boiling transition, which is to be expected physically. However in view of the relative simplicity of the instability model the agreement is good.

Results

Using the quench model discussed and the constitutive relations as given in Table 1, the refilling and rewetting processes in a hot horizontal channel can be predicted using the computer code REWET.

It should be noted that the constitutive models used have been kept as simple as possible. For example, the friction factor, f_G and f_i assume constant values of 0.005 in the wall and interfacial shear terms. The film boiling heat transfer coefficients in the table also correspond to those obtained from the detailed analysis of vapor flow in film boiling. β is assumed to have constant values of unity and zero in the film boiling and quenching regions respectively in the interfacial mass transfer model. Changes in these and other assumptions may change the numerical results somewhat. This will be discussed later. The best estimates of $(h_L)_{crit}$ obtained in the previous section are usually used in the following analysis.

Typical quenching results obtained using REWET are shown in Fig. 8. The corresponding experimental results are superimposed for direct comparison. Only top and bottom wall temperatures at three locations (A, C, E) are shown for simplicity. It can be seen that the agreement between the numerical and experimental results is good. The computer code can predict the quench of the channel in reasonable detail, especially for the bottom of the channel. The apparent quench temperatures correspond very well. This means that the quench model and the $(h_L)_{crit}$ used are physically realistic. Also the proposed quench mechanism (interfacial instability) on which the quench model and $(h_L)_{crit}$ are based may indeed be the dominant mechanism that leads to surface rewetting for our system. The slopes of the numerical temperature curves in different regions are also close

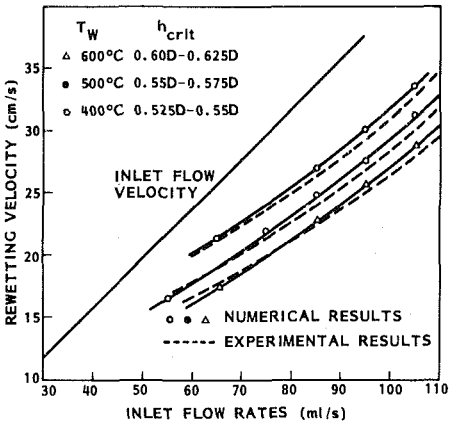

Fig. 9 Average rewetting velocity ($\bar{V}_s$) versus inlet flow rate—comparison of experimental and numerical results

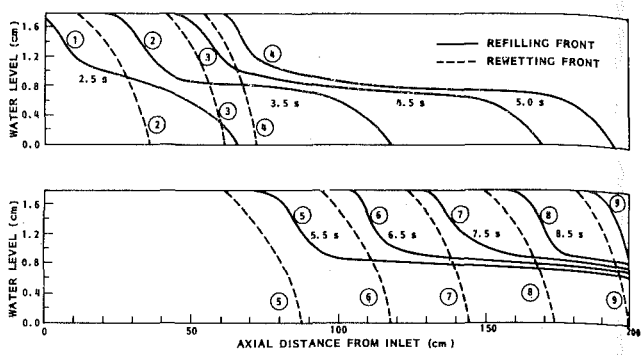

Fig. 10 Propagation of refilling and rewetting fronts—numerical results (initial wall temperature = 500°C, inlet flow rate = 85 ml/s)

to those observed in the experiments. This means that the heat transfer coefficients used in REWET are close to the actual values in the physical situation.

Average Rewetting Velocities. The REWET code has been used to study the refilling and rewetting experiments under different initial and boundary conditions. The operating conditions for Group III experiments [2] were used. The results are shown in Fig. 9. The experimental results are also shown in broken lines. Good agreement is again obtained. The analytical results are "predictive" in the sense that they have not been "tuned" to fit the data by varying the constitutive equations.

Effects of other parameters on the average rewetting velocity have also been studied, for example, effects of inlet water subcooling and test section insulation. Results obtained are consistent with experimental data [4].

Refilling and Rewetting Fronts. In the refilling and rewetting processes, we can define two moving fronts: one with respect to the quenching of the tube, the rewetting front, and the other with respect to the filling of the tube, the refilling front (liquid tongue). In general, the refilling front always precedes the rewetting front, because quenching can occur only under given hydraulic conditions when there is liquid present.

The movements of these fronts during transients are of practical interest, because they affect the mode of heat transfer and consequently the tube wall temperatures. In principle, their movements can be deduced experimentally from wall temperature measurements. However, this would require many wall temperature measurements, along and around the tube so that the detailed motion of the fronts may be traced.

The locations of the refilling and rewetting fronts at any instant are, however, readily obtainable from the numerical calculations. By following the motion of these fronts along the tube, a clear picture of the refilling and rewetting processes can be obtained. An example is shown in Fig. 10.

The liquid level, h_L is plotted along the tube at different times after the initiation of the transient. The refilling fronts are defined by the solid lines in the figure whereas the broken lines define the rewetting fronts. Refilling water in the form of a liquid tongue is observed numerically extending far downstream. This is in agreement with photographic studies [4] as well as measurements with other instruments [1].

Sensitivity Tests. In order to assess its performance, the REWET code has been subjected to a series of sensitivity tests. The tests are for: (i) spatial and temporal convergence and (ii) sensitivity to constitutive relations. The tests in the second category are useful in assessing the relative importance of the constitutive models used. They also provide information on how the code can be improved by adopting more accurate constitutive relations.

The results of the convergence tests are summarized in Table 2. The average rewetting velocities, $\Delta M/M$ and Q_{in}/Q_{out} ratios are compared. $\Delta M/M$ and Q_{in}/Q_{out} are measures of how well mass and energy are conserved in the calculations. It can be seen that the results are good for all three cases. Therefore, we may conclude that converged results are obtained when 24 nodes and Δt as given by equation (1) are used. It can also be seen that the code conserves mass and energy well for all cases.

Table 2 Convergence tests—computer code REWET

	$\Delta t = \Delta t$		$\Delta t = \Delta t/2$
	24 Nodes	35 Nodes	24 Nodes
$\bar{V}_B$ (cm/s)	27.1	27.0	28.7
$\bar{V}_s$ (cm/s)	28.0	27.6	28.1
$\bar{V}_T$ (cm/s)	27.6	27.4	28.0
$\lvert\Delta M\rvert_M$	1.2%	1.8%	2.0%
Q_{in}/Q_{out}	0.97	0.97	0.96%

Table 3 Sensitivity studies

Changes in Constitutive Relations	$\bar{V}_B$ (cm/s)	$\bar{V}_s$ (cm/s)	$\bar{V}_T$ (cm/s)
Reference Case (constitutive relations in Table 1 are used)	25.4	24.9	25.0
Liquid to wall shear (i) m = 5.0; ϕ = 50. (ii) m = 1.0; ϕ = 10. (iii) m = 3.0; ϕ = 210.	24.8 25.1 24.4	25.0 24.7 24.6	25.5 25.2 25.1
Vapor to wall and Interfacial shear (i) f_i = 0.001; f_G = 0.001	26.0	26.5	26.2
Interfacial mass transfer (i) β = 0 for both film boiling and quenching region	25.7	25.5	25.9

Results of the sensitivity tests are summarized in Table 3. A case with an initial wall temperature of 500°C and a constant inlet flow of 85 ml/s is used as a reference against which other test results can be compared. A friction factor multiplier of 2.5 is used in the liquid to wall friction factor in the inlet feeder region in the reference case.

The constitutive relations are changed as shown in the table, one at a time. Other constitutive relations are kept the same as in the reference case. The average rewetting velocities are listed for comparison. No significant changes in the rewetting rates are observed in all cases. This means that the numerical results are relatively insensitive to the interfacial transfer terms. However, they are sensitive to $(h_L)_{crit}$ as shown previously in Fig. 6.

This result is very important, because, in the simplified two-fluid model used, the vapor phase velocity is not solved in detail. Had the numerical results been more sensitive to the interfacial transfer terms, a more accurate vapor velocity calculation would have been needed. Thus, the simplified model would no longer apply in this hypothetical situation.

Conclusion

The refilling and rewetting processes in a hot horizontal tube have been analyzed using the generalized one-dimensional two-fluid model. It has been shown that the two-fluid model approach provides a powerful structure for analyzing such flow situations, and the formulation used can still be relatively simple and close to the real physics of the situation.

To predict the transition of heat transfer mode from film boiling or the occurrence of quenching at the bottom of the tube, a quench model based on a critical water level, $(h_L)_{crit}$, is used. $(h_L)_{crit}$ is obtained from a model based on initiation of a Kelvin-Helmholtz type of instability at the vapor film-liquid interface in the film boiling region. The values agree reasonably well with those deduced from experimental results.

The initiation of the interfacial instability is believed to be the governing mechanism that leads to surface rewetting. However, this is only a necessary condition. The sufficient condition will require that the rewet spots formed on the hot surface can grow. For thin walled tubes, because of the low heat capacity, rewet spots can probably grow once they are formed. Therefore, interfacial instability appears to be both necessary and sufficient for rewetting in these cases.

Several experiments have been conceived to investigate the more fundamental aspects of surface rewetting. A relatively simple experiment would be to refill and rewet a uniformly-heated horizontal tube with high heat capacity patches. Copper blocks can be used to produce the patches. It is expected that surface quenching will occur downstream of a high heat capacity patch when the patch is still dry. Detailed temperature measurements in the block and other locations would be used to determine the correctness of our postulate that instability of the vapor film is a necessary but not sufficient condition for surface rewetting. The most interesting phenomenon would be if the high heat capacity patch was actually colder than the upstream and downstream sections, but did not rewet. This would support our model strongly.

The simple quench model has been found to be quite successful in predicting quenching characteristics and rewetting rates. Numerical results were found to be relatively insensitive to the interfacial transfer models used. This is because the refilling and rewetting processes are dominated by the liquid flow which is in turn affected primarily by the inlet flow rate and the hydrostatic pressure head behind the stratified quench front.

References

1 Chan, A. M. C., and Banerjee, S., "Refilling and Rewetting of a Hot Horizontal Tube—Part I: Experiments," ASME JOURNAL OF HEAT TRANSFER, Vol. 103, No. 2, 1981, pp. 281–286.

2 Yamanouchi, A., "Effect of Core Spray Cooling in Transient State After Loss of Coolant Accident," *Journal of Nuclear Science and Technology*, Vol. 5, 1968, pp. 547–558.

3 Chan, A. M. C., and Banerjee, S., "Refilling and Rewetting of a Hot Horizontal Tube—Part II: Structure of a Two-Fluid Model," ASME JOURNAL OF HEAT TRANSFER, Vol. 103, No. 2, 1981, pp. 287–292.

4 Chan, A. M. C., "Transient Two Phase Flows: Refilling and Rewetting of a Hot Horizontal Tube," Ph.D. Thesis, Dept. of Engineering Physics, McMaster, 1980.

5 Wallis, G. B., *One Dimensional Two-Phase Flow*, McGraw Hill, New York 1969, Chapter 2.

6 Hughes, E. D., Lyczkowski, R. W., and McFadden, J. H., "An Evaluation of State-of-the-Art Two-Velocity Two-Phase Flow Models and Their Applicability to Nuclear Reactor Transient Analysis," EPRI Report NP-143, 1976.

7 McAdams, W. H., *Heat Transmission*, McGraw Hill, New York, 1954, 3rd ed., pp. 172–176.

8 Bird, R. B., Stewart, W. E., and Lightfoot, N. E., *Transport Phenomena*, McGraw Hill, New York, 1972.

9 Sissom, L. E., and Pitts, D. R., *Elements of Transport Phenomena*, McGraw Hill, New York, 1972.

10 Berenson, P. J., "Film Boiling Heat Transfer from a Horizontal Surface," ASME JOURNAL OF HEAT TRANSFER, Vol. 83, 1961, pp. 351–358.

11 Tong, L. S., "Heat Transfer Mechanisms in Nucleate and Film Boiling," *Nuclear Engineering and Design*, Vol. 21, 1972, pp. 1–25.

12 Hsu, Y. Y., and Graham, R. W., *Transport Processes in Boiling and Two-Phase Systems*, Hemisphere Publishing, 1976, Chapter 4.

13 Watchers, L. H. J., Bonne, H., and Van Nouhius, H. J., "The Heat Transfer from a Hot Horizontal Plate to Sessile Water Drops in Spheroidal State," *Chemical Engineering Science*, Vol. 2, 1966, pp. 923–926.

14 Bradfield, W. S., "Liquid Solid Contact in Stable Film Boiling," *Industrial and Engineering Chemistry Fundamentals*, Vol. 5, 1966, pp. 200–204.

15 Kovalev, S. A., "An Investigation of Minimum Heat Fluxes in Pool Boiling of Water," *International Journal of Heat Mass Transfer*, Vol. 9, 1966, pp. 1219–1226.

16 Chang, Y. P., "A Theoretical Analysis of Heat Transfer in Natural Convection and in Boiling," *Trans. ASME*, Vol. 79, 1957, pp. 1501–1513.

17 Zuber, N., "Stability of Boiling Heat Transfer," *Trans. ASME*, Vol. 80, 1958, pp. 711–720.

18 Bromley, L. A., "Heat Transfer in Stable Film Boiling," *Chemical Engineering Progress*, Vol. 46, 1950, pp. 221–227.

19 Westwater, J., and Santangelo, J. G., "Photographic Study of Boiling," *Industrial Engineering Chemistry*, Vol. 47, 1955, pp. 1605–1610.

20 Lamb, H., *Hydrodynamics*, Dover Publications, New York, 1955, Sixth ed., p. 445.

21 Chang, Y. P., "Wave Theory of Heat Transfer in Film Boiling," ASME JOURNAL OF HEAT TRANSFER, Vol. 81, 1959, pp. 1–12.

22 Hamill, T. D., and Baumeister, K. J., "Film Boiling Heat Transfer from a Horizontal Surface as an Optimal Boundary Value Process," *Proceedings 3rd International Heat Transfer Conference*, 1966, Vol. 4, pp. 59–64.

23 Breen, B. P., and Westwater, J. W., "Effect of Diameter of Horizontal Tubes on Film Boiling Heat Transfer," *Chemical Engineering Progress Symposium Series*, Vol. 58, 1962, pp. 67–72.

24 Kruger, R. A., and Rohsenow, W. M., "Film Boiling Inside Horizontal Tubes," *Proceedings 3rd International Heat Transfer Conference*, 1966, Vol. 5, pp. 60–68.

M. K. Jensen
Department of Mechanical Engineering,
The University of Wisconsin-Milwaukee,
Milwaukee, Wisc. 53201,
Assoc. Mem. ASME

A. E. Bergles
Department of Mechanical Engineering and
Engineering Research Institute,
Iowa State University,
Ames, Iowa 50011,
Fellow ASME

Critical Heat Flux in Helically Coiled Tubes

A study of boiling R-113 in electrically heated coils of various diameters is reported. Subcooled critical heat flux (CHF) is lower with coils than with straight tubes. The difference increases as mass velocity and ratio of tube diameter to coil diameter (d/D) increases. On the contrary, quality CHF is enhanced and increases with d/D; CHF initially increases with increasing mass velocity, but decreases after a maximum is reached. Operational problems, in particular upstream dryouts, can occur if a coiled tube is operated with low to moderate subcooling near the inlet and with moderately high heat fluxes.

Introduction

Many industries use helically and spirally coiled heat exchanger tubes for single-phase, evaporating, and condensing flows. Coils are used in chemical reactors, agitated vessels, storage tanks, and in some nuclear stream generators. In a new application, a coiled tube has been proposed [1] for the receiver of a concentrating-type solar collector in a large-scale power generation system.

With evaporating flows, the emphasis has been on once-through vaporization and the critical heat flux (CHF) condition. However, few studies have dealt with the subcooled region or the transition from the subcooled to the quality region. This region is of particular interest during system startup and when the heat exchanger is operating with near zero inlet quality and with moderately high heat fluxes.

Various investigators, e.g., [2–9], have concluded that the differences in the heat transfer and pressure drop characteristics between flow in coils and in straight tubes can be attributed to the formation of a secondary flow superimposed on the main flow. A pair of generally symmetrical vortices arises due to the centrifugal force, which occurs because of the coil geometry. Some of the findings of these investigations are as follows: CHF in coils occurs at different bulk steam qualities at different circumferential locations, with the coiled tubes, in most cases, having higher qualities at which a particular circumferential location exhibits the CHF condition and higher *average* critical qualities at a particular axial location (obtained by averaging the qualities required to initiate the CHF condition at different circumferential locations) than vertical straight tubes at the same heat flux and tube length, and that the CHF condition usually occurs at the inside surface (the surface closest to the coil axis) first. The circumferential location of the initiation of the CHF condition appears to be determined by the balance of centrifugal and gravitational forces. Because of stronger centrifugal forces and secondary flow, a smaller radius coil gives higher critical qualities at the same heat flux, mass velocity, and tube length. In general, at a fixed critical quality in the high quality region, an increase in mass velocity results in an increase in average CHF, which is the reverse of the situation usually found with straight tubes. (As will be demonstrated, increasing the mass velocity in coils does not always result in higher CHF's.) When the CHF condition occurs, the surface temperatures are much smaller than those in a straight tube. To help explain forced convection boiling behavior, hydrodynamic studies, e.g., [10, 11], have investigated adiabatic two-phase flow behavior in coils. One interesting observation is that at high gas flow rates the liquid tends to collect at the inside surface of the tube (film inversion). A more detailed literature review can be found in [12].

Few studies have been performed in the subcooled region. Miropol'skiy, et al. [3, 13] found that in the subcooled region the CHF is lower in a coil than in a straight tube, but around zero quality a reversal occurs; over a small quality change, the CHF in the coil changes from being lower to being higher than that in a straight tube. No adequate explanation was given for this phenomenon. Hughes and Olson [14] investigated subcooled CHF in a curved rectangular channel with only one side heated at a time. However, their results probably cannot be extrapolated to actual coiled tube performance.

Since little information is available concerning the subcooled CHF or the transition from the subcooled to quality region, the present study was initiated to determine the coiled tube CHF-x_{cr} behavior from the highly subcooled region to the high quality region. A straight, horizontal tube was tested to provide the reference data for direct evaluation of the coil performance. Since there is strong interest for using helically coiled tubes in vapor generators in power plants, it seemed appropriate to perform the experiments at a pressure level comparable to that which might be used in a power plant. R-113 was chosen as the working fluid since, on the basis of scaling laws suggested by Barnett [15] for straight tubes, 6.9 MPa water can be modeled by 0.94 MPa R-113, with the CHF for R-113 being only about 4 percent that of water. (The scaling parameters were not verified by comparison of the present data to water data.) In addition, there is strong interest in Rankine cycle boilers using refrigerants as working fluids.

Experimental Apparatus

A schematic of the closed flow loop is shown in Fig. 1. R-113 (dissolved gases <0.05 ppm by volume) was delivered by a variable-speed pump to the tube side of the preheater/recuperator (P/R) while some fluid was bypassed back to the surge tank. The liquid temperature at the outlet of the P/R was controlled by adjusting the flow rate and pressure of the fluid on the shell side of the P/R. Electric preheaters downstream of the P/R were used to set the required test-section inlet temperature. A flow control valve (F3 or F4) at the test-section inlet was used to eliminate thermal-hydraulic flow instabilities; F5 or F9 was used to maintain the test-section outlet pressure. The electrically (d-c) heated test sections were enclosed in a transite box. The space between the test section and walls of the box was filled with insulation so as to reduce the heat loss to a negligible value. The flow was mea-

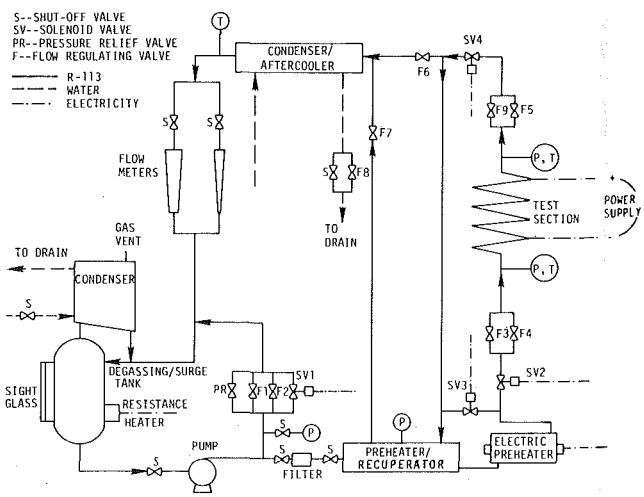

Fig. 1 Schematic layout of test loop

Contributed by The Heat Transfer Division for publication in the JOURNAL OF HEAT TRANSFER. Manuscript received by The Heat Transfer Division June 16, 1980.

sured with rotameters. All temperatures were measured with 30ga copper-constantan thermocouples. The thermocouple outputs as well as the voltage drops and currents supplied to the test sections were automatically monitored with a Hewlett-Packard data acquisition system.

One straight, horizontal tube and three coiled tubes with vertical coil axes were tested (see Table 1). The tube material was 316 stainless steel. Generally, two lengths (63.5 cm and 127 cm) were used for both straight and coiled test sections so as to cover a range of outlet enthalpy. After coiling a tube, if inspection revealed ripples on the inside surface, the coil was discarded since roughness in the tube wall could bias the results. Some deformation in tube diameter was experienced which resulted in a slightly oval tube, but generally the difference between the major and minor diameters was on the order of only 0.05 mm.

For the straight test sections, a straight entrance length of 40 cm preceded the heated section. Fourteen thermocouples were spaced along the upper tube wall. The wall temperatures of the coiled test sections were measured at both axial and circumferential locations. For the longer test sections, 14 axial locations were used; for the shorter, ten axial stations were used. The axial locations each had four thermocouples positioned 90 deg apart around the circumference, with 0 deg being at the top of the tube and 270 deg being closest to the helix axis.

The experimental conditions covered in this investigation were: P: 0.94 ± 0.04 MPa (at test-section outlet); G: 570–5470 kg/m^2 s; q'': 54,000–800,000 W/m^2; x_{cr}: −0.55–0.94; and inlet subcooling: 0–110 K.

Table 1 Test section dimensions

Test Section No.	Inside Tube Diameter cm	Coil Diameter cm	$\frac{d}{D}$	Heated Length cm	Total Coil Length cm	Approx. No. of Coils in Heated Length	Helix Angle deg.	Pitch cm/Coil	Tube Wall Thickness mm
1	0.762	(straight)	-	63.5	-	-	-	-	0.152
2	0.762	(straight)	-	127.0	-	-	-	-	0.152
3	0.744	40.96	0.0182	129.5	762.0	1	1.78	2.540	0.254
4	0.744	40.96	0.0182	63.5	762.0	1/2	1.78	2.540	0.254
5	0.762	21.59	0.0353	127.0	640.1	2	1.68	1.588	0.152
6	0.762	21.59	0.0353	125.7	501.7	2	1.68	1.270	0.152
7	0.762	21.59	0.0353	63.5	502.9	1	1.68	1.270	0.152
8	0.762	21.59	0.0353	63.5	393.7	1	1.68	1.270	0.152
9	0.762	11.75	0.0649	127.0	294.6	3 1/2	3.87	1.270	0.152
10	0.762	11.75	0.0649	63.5	296.6	1 3/4	3.87	1.588	0.152
11	0.762	11.75	0.0649	63.5	348.0	1	3.87	1.588	0.152

Experimental Procedure

Operating Procedure and Data Reduction. As an initial check of the experimental apparatus and procedure, single-phase heat transfer tests were performed with the coils and compared to correlations [16, 17] found in the literature. Agreement was excellent for the majority of the Reynolds number range (7100 < Re < 120,000), with most Nusselt numbers being within ±10 percent of the predictions.

Testing began after degassing the R-113. The test-section flow rate, pressure level, and inlet fluid temperature were set at their required levels and the test-section power was increased in small steps. After the power was increased, if one or more wall temperatures rose rapidly relative to the other wall temperatures, data were taken quickly and test-section power than was either rapidly reduced to a low level or shut-off completely. Generally, the temperature rise during this time was in the range of 16 to 50°C. If damage (carbon scaling caused by decomposition of R-113) was indicated during subsequent operating checks, the test section was discarded and a new one was prepared. Even for a small carbon deposit, changes in the boiling characteristics occurred. This problem was not evident in the straight tube tests.

The inside wall temperature and nonuniform heat flux distribution were determined by solving the steady-state heat conduction problem for a circular tube, modified to take into account the circumferential variation in wall thickness, resulting from the bending process, as well as changes in heat and electrical conduction lengths and areas. The inputs to the data reduction program were the measured outside wall temperatures, voltage drops, and currents. The wall thicknesses and temperature drops were small enough so that the property variations due to the temperature gradients were negligible. Circumferential conduction was found to be insignificant because of the thin tube wall, low metal thermal conductivity, and high heat transfer coefficient. Details of the operating procedure and data reduction can be found in [12].

Identification of CHF Condition. In the present system the temperature profile was obtainable during the CHF tests. For the straight tube, as the test-section power was slowly raised, before the CHF condition occurred (with its rapidly increasing wall temperature at the exit wall thermocouple location), there was a change in the slope of the temperature profile, $(T_w - T_{sat})$ versus L, near the outlet. This was a stable condition indicating a slight degradation in the heat transfer coefficient. It appeared as if intermittent vapor blanketing was occurring before the CHF condition was reached. With each increase in power, the slope increased slightly until a drastic reduction in the heat transfer coefficient occurred and the outlet wall temperature rose rapidly. Power was then reduced or shut off.

Generally, when the final power level was reached, only the last two thermocouples indicated this drastic temperature rise, with the second-to-last thermocouple not showing as steep a temperature rise as the last thermocouple. At lower mass velocities and heat fluxes, the elevation in temperature extended 12 to 15 cm along the tube. Even if the power was not reduced immediately, the post-CHF (dryout) zone did not appear to propagate upstream past the last or sometimes the second-to-last thermocouple location. In those cases where there was an elevation in wall temperature at several thermocouples, the CHF condition (local heat flux and quality) was identified by noting the thermocouple location with a 17°C rise in wall temperature. The validity of this procedure was demonstrated in a study by Bennett, et al. [18].

In the subcooled region for $G \leq 1000$ kg/m^{2}s in the horizontal tube, some upstream CHF conditions occurred; but the wall was apparently rewetted downstream of the CHF location. The CHF condition was identified at the upstream location. Generally, upstream departures from nucleate boiling were relatively stable; and, although the temperature fluctuated at times as much as 5 to 10°C, the temperature level remained approximately constant. These dryout zones were

Nomenclature

a = radial acceleration, m/s^2
Bo = boiling number $(q''/H_{fg}G)$
d = inside tube diameter, cm
D = coil diameter, tube axis to tube axis, cm
g = gravitational acceleration, m/s^2
G = mean mass velocity, kg/m^{2}s
Gr = Grashof number $(gd^3 (\rho_\ell - \rho_v) \rho_\ell/\mu_{sv}^2)$
H_{fg} = heat of vaporization, J/kg
L = heated length, cm
p = pressure, MPa
q'' = heat flux, W/m^2
Re = Reynolds number (Gd/μ)
T = temperature, °C
V = mean axial velocity, m/s
x = thermodynamic quality
ρ = density, kg/m^3
μ = dynamic velocity, Ns/m^2

Subscripts

c = coiled
calc = calculated
cr = critical
exp = experimental
in = inlet
ℓ = liquid
s, sat = saturated
str = straight
v = vapor
w = wall

short in length and were followed by a normal nucleate boiling section. In several runs, this dryout and rewet occurred several times along the tube. This has been observed previously (e.g., [19]).

The identification of the coiled tube CHF condition was basically the same as for the straight tube tests. No steady-state circumferential temperature profiles were obtained at the CHF condition. However, transient profiles obtained about 0.5 s into the event indicated that once the CHF condition was reached at one circumferential location, the dryout zone did not necessarily spread around the tube. Only the initial occurrence of the CHF condition was recorded in this study. Upstream CHF conditions occurred in the coils also, but the temperature profiles could not be ascertained.

Data from 93 straight tube and 172 coiled tube test runs are reported. Uncertainties associated with the variables are suggested to be: q'', ± 2.5 percent; x, ± 6.6 percent; and G, ± 2.1 percent. Tabular data, including inlet subcooling and critical length, are available from the first author.

CHF in Straight, Horizontal Tubes

General Characteristics. The CHF data obtained from the two straight horizontal test sections exhibit the same characteristics and trends as found in previous studies performed either with water or refrigerants, e.g., [19–21]. The data are plotted in Fig. 2, where "negative quality" is used as an indication of the liquid subcooling and is defined as $(H-H_{sat})/H_{fg}$. The general trend is a monotonic decrease in CHF with increasing x_{cr}; this latter dependent variable was changed by changing the inlet temperature. Slightly more scatter is evident at lower mass velocities. Since these data are typical (relative to the scatter) of all the data taken, only faired-in curves will be shown on composite figures for the remainder of the data. Although not verified by altering both the heated length and subcooling, it is felt that the "local conditions hypothesis" is applicable. That is, the CHF depends only on local quality for a given pressure level, mass velocity, and tube diameter. (The applicability of this concept has been shown most recently by Katto [22].) In the subcooled and low quality regions, the CHF increases with increasing mass velocity and decreases with decreasing subcooling. At low quality an inversion occurs, and the CHF then decreases with increasing quality and mass velocity. Griffel and Bonilla [21] suggest that this reversal occurs because of different mechanisms for the CHF in bubbly and annular flow.

Buoyancy can be used to explain the upstream CHF conditions and the erratic wall temperature profiles obtained at low mass velocities. Various studies, e.g., [19, 23–27] for water and refrigerants in vertical downflow and in horizontal flow, have shown that buoyancy reduces the CHF when compared to vertical upflow, with the main influence being in the subcooled and bubbly flow regimes. As the mass velocity increases, the differences between vertical upflow and horizontal flow diminish, and at high mass velocities the data are indistinguishable.

Correlation of CHF Data. Merilo [27] developed a correlation for the CHF condition in horizontal tubes using water and R-12 data. The bulk of that data was in the high quality region ($0.2 < x_{cr} < 0.7$). His correlation consistently underpredicted the present data by 15–55 percent, with the average being about 35 percent low. The deviations tended to increase with increasing flow rate and subcooling. The low predictions may be because most of the present data are in the subcooled and low quality (<15 percent) regions. Therefore, a more accurate correlation against which the coiled tube data could be compared was developed.

For horizontal flow, the influence of buoyancy on the CHF is determined by the relative magnitudes of the buoyancy and inertia forces. If the boiling number, Bo, is plotted as a function of the liquid Reynolds number, Re_s, with the critical quality as a parameter, there should be a change in the slope of the resulting curves due to CHF degradation caused by buoyancy.

Data from six of the seven mass velocities were curve fit as linear functions of x_{cr}. The lowest mass velocity data were not used because of excessive scatter caused by buoyancy, as mentioned previously.

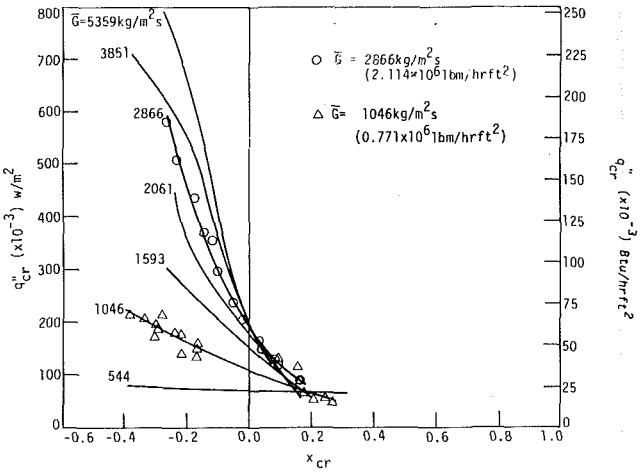

Fig. 2 Composite of straight, uniformly heated horizontal tube CHF data

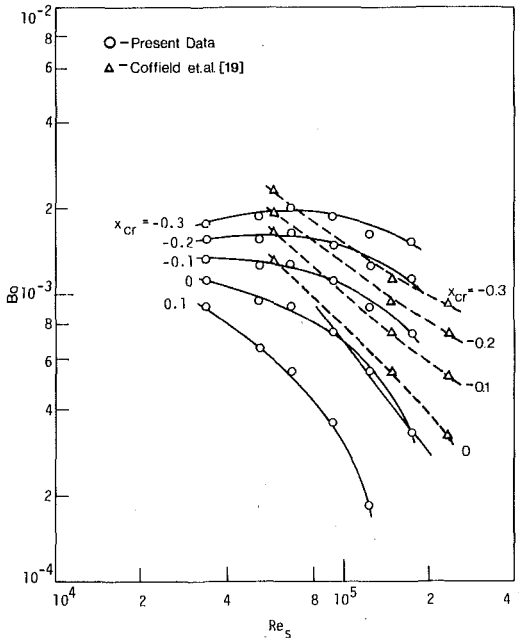

Fig. 3 Variation in boiling number with Reynolds number and quality

These equations were used to cross-plot the data as shown in Fig. 3. For the different qualities, straight lines can be drawn through the highest three mass velocities. It is quite evident that there is a definite change in slope of the lines around $Re_s = 75{,}000$, which corresponds to $G \simeq 2050$ kg/m^2 s. Also shown are R-113 data from Coffield, et al. [20], obtained with a 1.02 cm dia vertical test section at the same pressure as the present study. As can be seen, no corresponding downturn in the curves is evident as the Reynolds number decreases.

The nondimensional correlation developed for the highest three mass velocities where buoyancy apparently had little effect is

$$Bo = \frac{q''_{cr,\,str}}{H_{fg}\,G} = Re_s^{-0.6}\,[1.234 - 3.873 \times 10^{-6}\,Re_s + (-1.367 - 3.150 \times 10^{-6}\,Re_s)x] \quad (1)$$

Equation (1) can be extended to include the effect of buoyancy on the present data by using the ratio of bubble buoyancy to inertia forces (Gr/Re_s^2). (The tube diameter is used for the bubble diameter, thus referring to the onset of plug flow.) Bertoni, et al. [26] used the inverse of this to correlate the effect of buoyancy in vertical downflow. The ratio (Bo_{exp}/Bo_{calc}) was plotted (see Fig. 4) as a function of Gr/Re_s^2. No trend could be discerned for the effect of quality. The correction

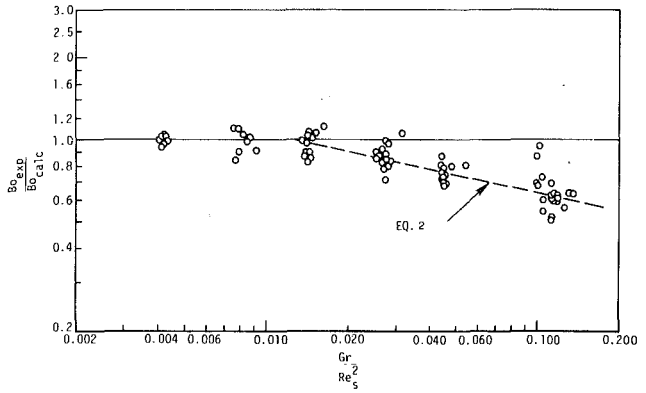

Fig. 4 Effect of buoyancy on the boiling number

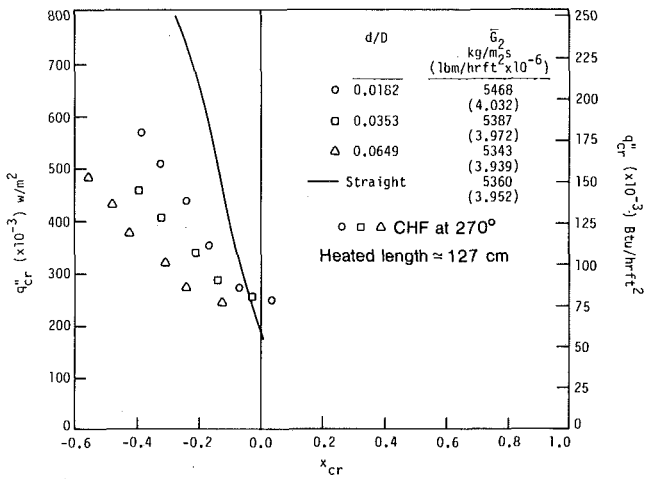

Fig. 5 Local CHF data for coiled tubes, $\bar{G} \simeq 5400$ kg/m² s

factor by which equation (1) is multiplied to account for buoyancy-induced degradation is

for $Gr/Re_s^2 \geq 0.0127$

$$C = 0.4\,(Gr/Re_s^2)^{-0.21}$$

for $Gr/Re_s^2 < 0.0127$

$$C = 1.0 \qquad (2)$$

C is about 0.6 at $G = 1000$ kg/m² s. It should be noted that the variation in Gr/Re_s^2 is caused mainly by the Reynolds number variation.

Taking into account the parameteric distortion (thus ensuring that the heat balance equation is not violated), the average absolute percent deviation (AAPD) of the predicted data from the experimental data is 3.9 percent, with the maximum deviation being 16.6 percent. The R-113 data from [20] were also compared using a pressure function ($_e - 0.783\ p/p_{cr}$) developed in their study. With C set equal to unity, the APPD was 10.5 percent with the maximum deviation being 29.6 percent.

CHF in Helical Coils

General Characteristics of the Data. Examples of the coiled tube CHF data are shown on Fig. 5. Composite figures of all the coiled tube curves are shown in Figs. 6–8. Again, the "local conditions hypothesis" seems to apply. Generally, the temperature rise associated with the CHF condition occurred first at the inside of the coil. However, as the mass velocity decreased, the CHF location shifted from the inside of the coil to the top. In the high quality region, the long tubes were used to obtain the CHF data in all cases; in the subcooled, high mass velocity region, again the long tubes were used. In the subcooled, low mass velocity region, the short tubes were used to obtain the CHF data, while in the subcooled, intermediate mass velocity region both long and short tubes were used.

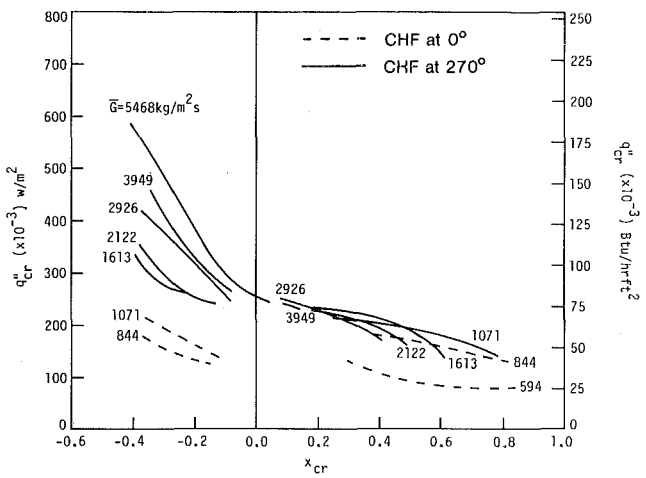

Fig. 6 Composite of local CHF data for 41 cm dia coil

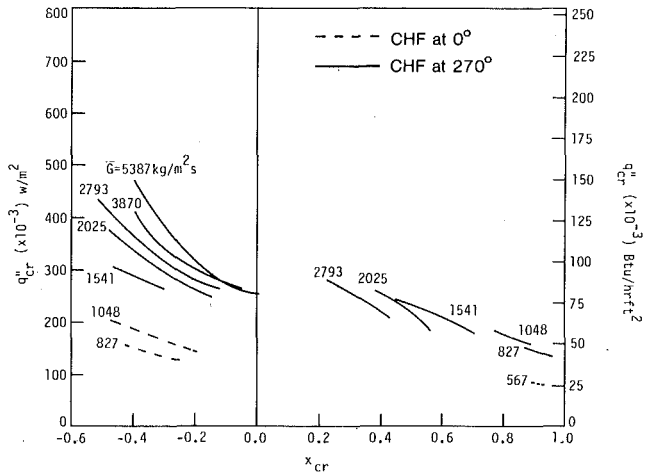

Fig. 7 Composite of local CHF data for 21.6 cm dia coil

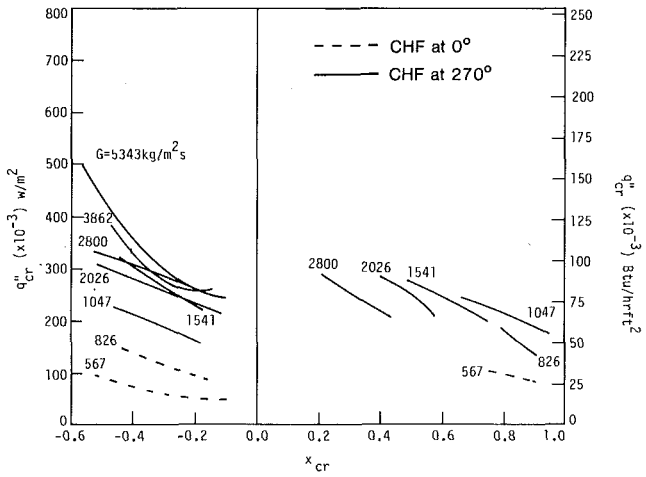

Fig. 8 Composite of local CHF data for 11.7 cm dia coil

No subcooled CHF data were obtained at the lowest mass velocity for the 22 cm and 41 cm coils. Erratic wall temperature profiles (similar to those experienced with the straight tube) were observed which made identification of the CHF condition difficult, if not impossible. The low mass velocity problem in the subcooled region (for coils and straight horizontal tubes) probably is due to a nearly horizontal CHF-x_{cr} curve. The shallower the slope, the more chance that upstream dryouts and erratic temperature profiles will be encountered.

As can be seen from the three composite figures, for each mass velocity there is a region in which no data could be obtained. Schematically (Fig. 9) this "forbidden zone" can be explained as follows. Assume the CHF-x_{cr} curve for a coiled tube is line ABCD. The dashed lines are operating lines. The CHF condition will occur at several locations in a tube if a horizontal line at the CHF intercepts the CHF-x_{cr} curve at qualities higher than the inlet quality associated with a particular operating line. Only an exit CHF condition would occur at $x_{in} = 0$ and $x_{in} = x_1$. However, if the inlet quality is reduced to x_2, an upstream CHF condition will occur since the CHF conditions are satisfied for both the exit and some point upstream. Additional upstream CHF conditions will occur until x_N is reached, after which only exit CHF conditions would be experienced. Points on the curve from C to C' would be unobtainable without length and/or inlet quality changes; the curve from B to C cannot be obtained without upstream CHF conditions.

Waters, et al. [28] found similarly shaped CHF-x_{cr} curves for tests with very high mass velocities (6700–9500 kg/m^2 s). Aladyev, et al. [29] obtained similar curves with a compressible volume upstream of the test section. Bergles, et al. [30] generated a similar curve in horizontal low-pressure water flows. The controlling mechanism for this behavior in coiled-tube flow appears to be different from the mechanism suggested in [28–30]. This is discussed in the next section.

The problem of upstream CHF conditions was most severe with the 22 cm coil. Few data points in the quality region at the lower mass velocities could be obtained. As the mass velocity increased to 1500 kg/m^2 s and greater, muuch more data were obtainable. By examining the parametric trends, an explanation for this phenomenon can be offered. The shape of the curve in Fig. 9 varies with mass velocity and d/D ratio. Refer to Figs. 6–8 to note that point B tends to be lower and farther to the left as the mass velocity and coil diameter decrease. The difference in heat flux between B and C decreases with increasing mass velocity and coil diameter. The same inlet conditions that cause an upstream CHF condition in the 22 cm coil might not cause a CHF condition in the 41 cm coil since point B for the 41 cm coil occurs at too high a heat flux. Similarly, for the 12 cm coil, point B occurs at a low enough quality and heat flux so that much of the curve from B to C is at a quality below the inlet quality that causes the upstream CHF conditions in the 22 cm coil.

Discussion of CHF Results. Consider first the subcooled region. There are major differences between the straight horizontal tube and coiled tube subcooled CHF. The differences are consistent regardless of the value of d/D but are not consistent with varying mass velocity. In the subcooled region, the CHF-x_{cr} curves decrease monotonically with decreasing subcooling. The coiled tube data are lower than those of the straight tube, with the curves converging as the subcooling decreases. With decreasing d/D (see Fig. 10) and mass velocity, the coiled tube data approach the straight tube data. Similar trends have been observed previously [3, 13]. However, a mechanism for the subcooled CHF in coiled tubes has not been suggested in the literature.

At lower mass velocities, buoyancy effects are evident. For $G \leq 1000$ kg/m^2 s, generally the CHF condition occurred at the top of the tube instead of at the inner wall. At 1000 kg/m^2 s for the 12 cm coil, dryout occurred at the inner surface, while for the two larger coils it occurred at the top of the tube. The present low velocity results are confirmed by the observations of Ünal [31]. Using high speed photography, he noted that at about 15.9 MPa, when the mass velocity of water in bubbly flow was reduced from 1500 to 760 kg/m^2 s, bubbles climbed toward the top of the tube. Thus, a locally high void fraction could occur at the top of the tube and lead to a CHF condition.

The differences between the subcooled CHF condition in coiled and straight horizontal tubes appear to be attributable to the existence of centrifugal forces in the coil flow which tend to preferentially collect the vapor at the inner surface, where the circumferential heat flux is the highest, thus causing a locally high void fraction and initiating the CHF condition at a lower heat flux than in a straight tube. At the lower mass velocities and larger coil diameters, the weaker centrifugal forces reduce the strength of the secondary flow. The vapor is not as greatly affected by the weaker forces; hence, less preferential clotting

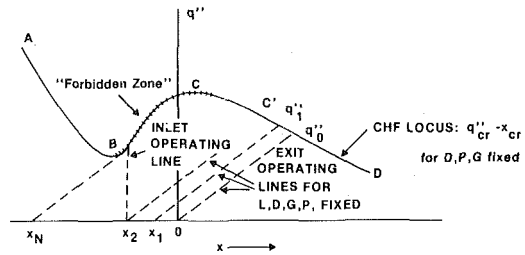

Fig. 9 Schematic representation of "forbidden zone"

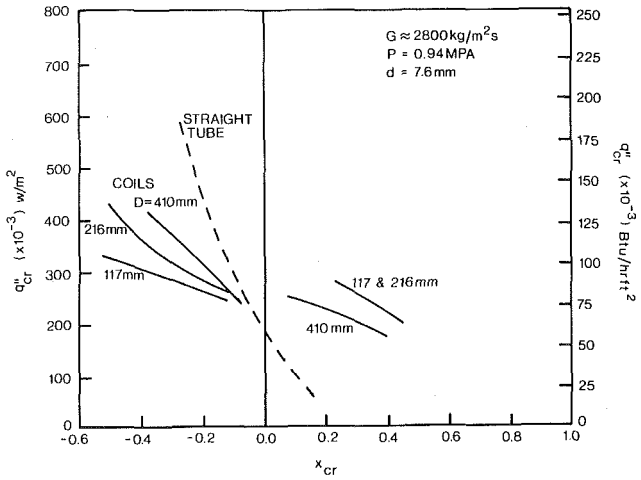

Fig. 10 Effect of curvature ratio (d/D) on CHF

at the inner surface occurs. At some critical mass velocity/coil diameter combination, the buoyancy force overcomes the inertial and centrifugal forces resulting in vapor clotting at the top of the tube and little difference between the straight and coiled tube CHF.

In the quality region, the CHF level is enhanced as a result of the radial acceleration. While the present straight tube reference data are limited to the low quality region, it is apparent that substantial gains in the CHF can be realized. The data show a consistent increase in CHF with an increasing d/D ratio. For a given quality, the CHF initially increases with increasing mass velocity, then decreases after reaching a maximum at about 1000 kg/m^2 s. This mass velocity effect has also been noted in several studies [2, 3, 6] and has occurred in the range of 800 to 2000 kg/m^2 s. No explanations have been offered previously as to why this happens.

As in the subcooled region, buoyancy effects (with the CHF occurring at the top of the tube) were apparent between 840 and 1000 kg/m^2 s for the largest coil and between 540 and 800 kg/m^2 s for the two smaller coils. Previous experiments, e.g., [2, 3], have indicated that the quality region dryout occurs first at the inside of the coil followed by the top and bottom. However, other studies, e.g., [4, 32, 33], indicate that the top and bottom of the tube tend to dryout first, followed by the inner wall. It should be pointed out that the range of the mass velocities in [2] (380–1900 kg/m^2 s) and [3] (110–2670 kg/m^2 s) overlap the range of this experiment (570–5470 kg/m^2 s), while in [4] the range was 70–490 kg/m^2 s, in [32] it was 30–310 kg/m^2 s, and in [33] it was 45–123 kg/m^2 s. The mass velocity level has a strong effect on the location of the initiation of the CHF condition. The discrepancies among the different investigations might be caused by the different mass velocity levels.

Using the experiment evidence, it is possible to speculate on the various controlling mechanisms involved in the different regions where the CHF behavior varies with mass velocity, d/D ratio, quality, etc. In the lower mass velocity range at a level above which buoyancy effects are negligible a possible explanation of the CHF condition is as follows: In straight tubes, increasing the flow rate causes increased turbulence in the vapor core. The liquid entrainment rate begins to exceed the redeposition rate with a resulting decrease in liquid film

thickness. The larger the mass flow rate, the faster the film becomes depleted and the lower the critical heat flux becomes [21]. In coils, the flow regime quickly becomes annular at low quality; centrifugal force causes a separation of the phases, with the liquid being concentrated at the wall. The secondary circulation spreads the liquid film over the perimeter ensuring a wetted wall. With increasing mass flow, centrifugal effects become stronger and any entrained liquid will quickly be deposited on the tube wall and circulated along the perimeter [32]. Hence, the resulting higher liquid film flow rate causes the CHF in coils to be larger than that in straight tubes. At the lowest mass velocities, buoyancy effects cause the liquid film to grow thinner at the top of the tube. This liquid flows to the inside surface delaying dryout there, but contributing to an earlier dryout at the top of the tube.

As the mass velocity and quality increase, perhaps the effect of the secondary circulation decreases. Hendricks and Simon [34] and Rippel, et al. [35] observed less secondary circulation when two phases are present in helical coil flow. Hopwood [36] calculated nonevaporating droplet trajectories for a mass velocity of 1000 kg/m^2 s for several pressures and droplet diameters. As the pressure increased and droplet diameter decreased, the angular trajectory, measured in degrees from where a drop left the inner wall to where it struck the outer wall, increased. From this analysis, several things can be inferred. As droplets decrease in size due to evaporation and turbulence associated with higher mass velocities, there will be less of a tendency for the drops to wet the walls since their trajectories will be longer. With fewer drops reaching the tube wall, the liquid film flow rate would decrease. At some critical combination of conditions, the continuous beneficial effect of the increased centrifugal force, because of increased mass velocity, will be balanced and overcome by the fragmentation of the droplets because of this same increase in mass velocity. Hence, the CHF would initially increase with mass velocity, reach a maximum, and then decrease with further increases in mass velocity.

The transition zone between the subcooled region with its CHF mechanism and the quality region with its much different mechanism appears to be determined approximately by the change from the bubbly flow regime, with a locally high wall void fraction, to the annular flow regime. In the straight tube, the transition from subcooled CHF to quality CHF is accomplished smoothly, as evidenced by the data (Fig. 2). For the coiled tubes, if the linear portions of the subcooled CHF curves were extended to low quality, the lines would converge at about the same location as for the straight tube. This suggests that the flow regime transition, if unaffected by the coil effect, would proceed just as in the straight tube. However, the coiled tube curves start deviating from the linear generally around $x_{cr} = -0.1$ to -0.2. At this point the void fraction becomes large enough to affect the flow regime and the beneficial characteristics of the quality coil flow begin to predominate over the detrimental subcooled CHF characteristics. A comparison of straight and coiled tube slug to annular flow transition was performed [12] for both the present R-113 data and the water data from Miropol'sky [3]. This analysis tended to support the conclusion that the minimum in the CHF-x_{cr} curve is, indeed, fixed by the transition from slug flow to annular flow.

Correlation of CHF Data.

Subcooled CHF. The difference in the CHF condition between the straight and coiled tubes can be attributed to the presence of a centrifugal force in the coil. The centrifugal force is characterized by a nondimensionalized radial acceleration $(a/g) = V^2/gD$ where V is based on the mass velocity and local liquid temperature. The range of radial acceleration in the present experiment was 0.097 to 14.5. Only those data below $x_{cr} = -0.10$ were considered so that the flow regime transition effects discussed in the preceding section could be avoided. The resulting equation for the circumferentially local CHF, with $q_{cr,\,str}$ from equation (1), is

$$\frac{q''_{cr,\,c}}{q''_{cr,\,str}} = K = 0.769(a/g)^{-0.26} \quad \text{for } \frac{(a/g)}{(d/D)} > 10$$

$$\text{and } K = 1 \quad \text{for } \frac{(a/g)}{(d/D)} \le 10 \qquad (3)$$

Comparing the calculated with the experimental CHF, the AAPD = 7.4 percent, with the maximum deviation being 45.3 percent.

Quality CHF. Since few data points are available from this study for the quality region straight tube CHF, the quality coiled tube CHF data were not correlated as a ratio as were the subcooled CHF data. Dimensional analysis indicates that the dimensionless groups of importance are: Bo, x, d/D, and Re. (Many of the dimensionless groups suggested by Ahmad [37] were eliminated since, with only one pressure used, these groups were constants in this experiment.) Since there is a reversal in the behavior of the data because of the mass velocity effects, the data were separated into two groups, with the break point being 950 kg/m^2 s. Not enough data were available to set the break more precisely. Also, only the data greater than $x_{cr} = 0.1$ were used to avoid transition effects.

The equations obtained for the circumferentially local CHF are

for $G > 950$ kg/m^2 s

$$Bo = 17126\,\mathrm{Re}^{-1.143x-0.436}\,(d/D)^{0.31}$$

for $G \le 950$ kg/m^2 s

$$Bo = 0.00000409\,\mathrm{Re}^{0.50x-0.460}\,(d/D)^{0.17} \qquad (4)$$

where the Reynolds number is based on the saturated vapor viscosity. The AAPD = 3.0 percent, with the maximum deviation being 14.1 percent.

Conclusions

An experimental study has been conducted to determine the effects of mass velocity, exit subcooling/quality, and curvature ratio on the CHF in forced convection boiling in helically coiled tubes. The following conclusions can be drawn from the investigation.

1 CHF in straight, horizontal, uniformly heated tubes decreases monotonically with decreasing subcooling at a given mass velocity and increases with increasing mass velocity at a given subcooling. At low quality, a reversal occurs and CHF then increases with decreasing mass velocity. At low mass velocities, buoyancy causes a decrease in CHF relative to a straight vertical tube.

2 The subcooled CHF in helically coiled tubes is lower than that in a straight, horizontal tube. The CHF, relative to a straight tube, decreases with increasing d/D and mass velocity. The centrifugal acceleration, which depends on the axial fluid velocity and coil diameter, is sufficient to correlate the differences between the straight and coiled tube CHF for the present data.

3 The CHF in the quality region in coils is higher than that in a straight, horizontal tube. At a given mass velocity and quality, the CHF increases with increasing d/D. At a given quality and d/D, the CHF first increases with mass velocity, then, after reaching a maximum, decreases with mass velocity.

4 Undesirable upstream dryouts could occur if a helical coil is operated with low inlet qualities. This "forbidden zone" is the result of the minimum in the CHF-x_{cr} curve.

More data need to be obtained, particularly at other pressures, to extend the ranges of validity of the proposed correlations. Further work is required to define the "forbidden zone" and to develop correlations to describe the problem area.

Acknowledgments

The investigation was supported by the Department of Mechanical Engineering and Engineering Research Institute of Iowa State University and by the U.S. Department of Energy under contract No. EG-78-S-02-4649.

References

1 Clements, L. D., "Design Considerations for the Energy Receiver in a Fixed Mirror-Distributed Focus (FMDF) Solar Energy System," Miami International Conference on Alternate Energy Sources, Miami, Fla, 1977.

2 Carver, J. R., Kakarala, C. R., and Slotnik, J. S., "Heat Transfer in Coiled Tubes in Two Phase Flow," Babcock and Wilcox Company Research Report 4438, July 1964.

3 Miropol'skiy, Z. L., and Pikus, V. Y., "Critical Boiling Heat Fluxes in Curved Channels," *Heat Transfer—Soviet Research*, Vol. 1, 1969, pp. 74–79.

4 Kozeki, M., Nariai, H., Furukawa, T., and Kukrosu, K., "A Study of Helically-Coiled Tube Once-Through Steam Generator," *Bulletin of the JSME*, Vol. 13, No. 66, 1970, pp. 1485–1494.

5 Babarin, V. P., Sevasty'yanov, R. I., Alad'yev, J. T., Khuydyakov, V. F., and Tkachev, V. A., "Critical Heat Fluxes in Tubular Coils," *Heat Transfer—Soviet Research*, Vol. 3, No. 4, 1971, pp. 85–90.

6 Cumo, M., Farello, G. E., and Ferrari, G., "The Influence of Curvature in Post Dry-out Heat Transfer," *International Journal of Heat and Mass Transfer*, Vol. 15, 1972, pp. 2045–2062.

7 Naitoh, M., Nakamura, A., and Ogasawara, H., "Dryout in Helically Coiled Tubes of Sodium Heated Steam Generator," ASME Paper No. 74-WA/HT-48, 1974.

8 Alad'yev, I. T., Petrov, V. I., Rzayev, A. I., and Khudyakov, V. F., "Heat Transfer in a Sodium-Potassium Heat Exchanger (Potassium Boiler) Made of Helically Coiled Tubes," *Heat Transfer—Soviet Research*, Vol. 8, No. 3, 1976, pp. 1–16.

9 Campolunghi, F., Cumo, M., Ferrari, G., and Palazzi, G., "Full Scale Tests and Thermal Design Correlations for Coiled Once-Through Steam Generators," Comitato Nazionale Energia Nucleare, Report No. RT/ING (75)11, 1975.

10 Banerjee, S., Rhodes, E., and Scott, D. S., "Film Inversion of Co-Current Two-Phase Flow in Helical Coils," *AIChE Journal*, Vol. 13, 1967, pp. 189–191.

11 Whalley, P. B., "Air-Water Two-Phase Flow in a Helically Coiled Tube," *International Journal of Multiphase Flow*, Vol. 6, 1980, pp. 345–356.

12 Jensen, M. K., "Boiling Heat Transfer and Critical Heat Flux in Helical Coils," Ph.D. Dissertation, Iowa State University, 1980.

13 Miropol'skiy, Z. L., Picus, V. J., and Shitsman, M. E., "Regimes of Deteriorated Heat Transfer at Forced Flow of Fluids in Curvilinear Channels," *Proceedings Third International Heat Transfer Conference*, Chicago, Vol. 2, pp. 97–101; New York, AIChE, 1966.

14 Hughes, T. F., and Olsen, D. R., "Critical Heat Fluxes for Curved Surfaces During Subcooled Flow Boiling," *Transactions of the CSME*, Vol. 3, No. 3, 1975, pp. 122–130.

15 Barnett, P. G., "An Experimental Investigation to Determine the Scaling Laws of Forced Convection Boiling Heat Transfer, Part I," AEEW Report R-363, 1964.

16 Seban R. A., and McLaughlin, E. F., "Heat Transfer in Tube Coils with Laminar and Turbulent Flow," *International Journal of Heat and Mass Transfer*, Vol. 6, 1963, pp. 387–395.

17 Mori, Y., and Nakayama, W., "Study on Forced Convection Heat Transfer in Curved Pipes (Second Report, Turbulent Region)," *International Journal of Heat and Mass Transfer*, Vol. 10, 1967, pp. 37–59.

18 Bennett, A. W., Hewitt, G. F., Kearsey, H. A., and Keeys, R. K. F.,"Heat Transfer to Steam-Water Mixtures Flowing in the Uniformly Heated Tubes in Which the Critical Heat Flux Has Been Exceeded," AERE Report No. R-5373, 1967.

19 Merilo, M., "Crtical Heat Flux Experiments in a Vertical and Horizontal Tube with Both Freon-12 and Water as Coolant," *Nuclear Engineering and Design*, Vol. 44, 1977, pp. 1–16.

20 Coffield, R. D., Jr., Rohrer, W. M., Jr., and Tong, L. S., "A Subcooled DNB Investigation of Freon-113 and Its Similarity to Subcooled Water DNB Data," *Nuclear Engineering and Design*, Vol. 11, 1969, pp. 143–153.

21 Griffel, J., and Bonilla, C. F., "Forced Convection Boiling Burnout for Water in Uniformly Heated Tubular Test Sections," *Nuclear Engineering and Design*, Vol. 2, 1969, pp. 1–35.

22 Katto, Y., "On the Heat Flux/Exit-Quality Type Correlation of CHF of Forced Convection Boiling in Uniformly Heated Vertical Tubes," *International Journal of Heat and Mass Transfer*, Vol. 24, 1981, pp. 533–539.

23 Rounthwaite, C., and Clouston, M., "Heat Transfer During Evaporation of High Quality Water-Steam Mixtures Flowing in Horizontal Tubes," *Second International Heat Transfer Conference-Boulder*, ASME, New York, 1961, pp. 200–211.

24 Papell, S. S., "Buoyancy Effects on Forced Convection Boiling," ASME Paper No. 67-HT-63, 1967.

25 Styrikovich, M. A., and Miropolskii, Z. L., *Doklady Akademii NAUK SSSR*, Vol. 71, No. 2, 1950.

26 Bertoni, R., Ciprianai, R., Cumo, M., and Palazzi, G., "Upflow and Downflow Burnout," Comitato Nazionale Energia Nucleare, Report No. RT/ING (76) 24, 1976.

27 Merilo, M., "Fluid-to-Fluid Modeling and Correlation of Flow Boiling Crisis in Horizontal Tubes," *International Journal of Multiphase Flow*, Vol. 5, 1979, pp. 313–325.

28 Waters, E. D., Anderson, J. K., Thorns, W. L., and Batch, J. M., "Experimental Observations of Upstream Boiling Burnout," *Chemical Engineering Progress Symposium Series*, No. 57, Vol. 61, 1964, pp. 230–237.

29 Aladyev, I. T., Miropolsky, Z. L., Doroshchuk, V. E., and Styrikovich, M. A., "Boiling Crisis in Tubes," *Second International Heat Transfer Conference-Boulder*, ASME, New York, 1961, pp. 237–243.

30 Bergles, A. E., Lopina, R. F., and Fiori, M. P., "Critical Heat Flux and Flow Pattern Observations for Low-Pressure Water Flowing in Tubes," ASME JOURNAL OF HEAT TRANSFER, Vol. 89, 1967, pp. 69–74.

31 Ünal, H. C., "Determination of Void Fraction, Incipient Point of Boiling, and Initial Point of Net Vapor Generation in Sodium-Heated Helically Coiled Steam Generator Tubes," ASME JOURNAL OF HEAT TRANSFER, Vol. 100, 1978, pp. 268–274.

32 Owhadi, A., Bell, K. J. and Crain, B., Jr., "Forced Convection Boiling Inside Helically—Coiled Tubes," *International Journal of Heat and Mass Transfer*, Vol. 11, 1968, pp. 1779–1793.

33 Crain, B. Jr., and Bell, K. J., "Forced Convection Heat Transfer to a Two-Phase Mixture of Water and Steam in a Helical Coil," *AIChE Symposium Series No. 131*, Vol. 69, 1973, pp. 30–36.

34 Hendricks, R. C., and Simon, F. E., "Heat Transfer to Hydrogen Flowing in a Curved Tube," *ASME Multi-phase Flow Symposium*, Philadelphia, Penn., Nov. 1963, ASME, New York, 1963, pp. 90–93.

35 Rippel, G. R., Eidt, C. M., Jr., and Jordan, H. B., Jr., "Two-Phase Flow in a Coiled Tube," *I&EC Process Design and Development*, Vol. 5, 1966, pp. 32–39.

36 Hopwood, P. F., "Pressure Drop, Heat Transfer and Flow Phenomena For Forced Convection Boiling in Helical Coils—A Literature Review," AEEW Report R-757, 1972.

37 Ahmad, S. Y., "Fluid-to-Fluid Modeling of CHF: A Compensated Distortion Model," *International Journal of Heat and Mass Transfer*, Vol. 16, 1973, pp. 641–662.

A Nondimensional Analysis of Boiling Dry a Vertical Channel with a Uniform Heat Flux

K. H. Sun
Mem. ASME

R. B. Duffey
C. Lin

Nuclear Safety and Analysis Department,
Electric Power Research Institute,
Palo Alto, Calif. 94303

A thermal-hydraulic model has been developed for describing the phenomenon of hydrodynamically-controlled dryout, or the boil-off phenomenon, in a vertical channel with a spatially-averaged or uniform heat flux. The use of the drift flux correlation for the void fraction profile, along with mass and energy balances for the system, leads to a dimensionless closed-form solution for the predictions of two-phase mixture levels and collapsed liquid levels. The physical significance of the governing dimensionless parameters are discussed. Comparisons with data from single-tube experiments, a 3 × 3 rod bundle experiment, and the Three Mile Island nuclear power plant show good agreement.

Introduction

Boiling water in a vertical channel at very low inlet flows causes the channel to empty of two-phase mixture. A discrete, although unsteady and uneven, two-phase level is formed as in a domestic kettle or saucepan. The emptying of the channel has been called "boil-off"; and for nuclear reactor applications "core uncovery" if the fuel rods are progressively exposed [1, 2].

The analysis of the level position proceeds by solving the one-dimensional continuity and energy equations for imcompressible flow, together with a local void fraction relationship linking the vapor content with the vapor flux.

The numerical solution of these simultaneous equations was carried out [1] and a simplified and approximate analytical solution was derived for the special case of uniform heat flux and zero inlet flow. This paper extends and generalizes the treatment by systematically identifying the appropriate dimensional quantities, and providing an exact analytical solution.

Physical Model

The physical system under consideration is a vertical open channel of length L and cross-sectional flow area A_c, filled with liquid and vapor mixture at a height z_2. The coexistence of the vapor and liquid in the channel is the result of power input to the channel $\dot{Q}$ which is uniformly distributed along the channel wall. At the bottom of the channel, liquid at temperature T_0 is fed into the channel at a constant mass flow rate $\dot{M}_i$. The problem of interest is to determine the transient variation of the mixture level z_2, subject to the given conditions of channel length and flow area (L, A_c), power ($\dot{Q}$), the inlet subcooling (T_0), the inlet flow rate ($\dot{M}_i$), and system pressure. A schematic illustration of the boiling flow is shown in Fig. 1.

The present physical model is similar to that described in reference [1], but simplified for uniform heat flux and constant inlet flow. The simplification renders the problem to a closed-form and exact solution for the mixture level.

Governing Equations. There are five key parameters in the boil-off process; the vapor and liquid flows as a result of vaporization, the void fraction for given flow conditions, the transient mass inventory, and the two-phase mixture level which is related to the mass inventory and the void fraction. As discussed in reference [1], the present analysis assumes that the system is at quasi-steady state, i.e., the void fraction does not change with time. The governing equations associated with these five parameters are as follows.

The energy equation which calculates the vapor flow rates from the heat input and the inlet enthalpy, is expressed by the relation

$$j_g(z) = \frac{\dot{Q}}{A_c L} \cdot \frac{z}{\rho_g h_{fg}} - \frac{\dot{M}_i C_p (T_s - T_0)}{A_c \rho_g h_{fg}} \quad z \geq z_{sat} \tag{1}$$

where z is the coordinate starting from the bottom of the channel, j_g is the volumetric vapor flux, and ρ_g, h_{fg}, T_s, are the vapor density, the latent heat of vaporization, and the saturation temperature, respectively.

The void fraction in the channel, α, as a function of the vapor flow rate along the vertical distance, can be calculated from the Drift Flux correlation [3] for the two-phase flow region,

$$\alpha(z) = \frac{j_g(z)}{C_0[j_g(z) + j_f(z)] + V_{gj}} \tag{2}$$

where j_f is the local volumetric liquid flux, C_0 is the distribution parameter, and V_{jg} is the so-called drift velocity. It should be noted that the effect of different void fraction correlations, e.g. the Cunningham and Yeh correlation [4] and the Wilson correlation [5], was discussed in detail in reference [1]. Only the Drift Flux correlation is used in the present analysis because it renders a closed-form solution of general interest.

The mass inventory is the sum of the mass of liquid and vapor below the two-phase mixture level and can be characterized by the collapsed liquid level, z_1, which is defined as follows; provided $\rho_g \ll \rho_f$,

$$z_1 \equiv z_{sat} + \int_{z_{sat}}^{z_2} (1 - \alpha)\, dz \tag{3}$$

where z_{sat} is the elevation, at which the bulk liquid becomes saturated, calculated from the simple energy balance relation

$$z_{sat} = \frac{L\dot{M}_i C_p (T_s - T_0)}{\dot{Q}} \tag{4}$$

It should be noted that in equation (3) the small amount of vapor mass is neglected. The subcooled boiling region, which was discussed in detail in reference [1], was also neglected because its effect is very small at low inlet flow conditions.

The collapsed liquid level z_1 is also related to z_2 through the mass conservation relation which is expressed as

$$\frac{dz_1}{dt} = -\frac{\dot{Q} z_2}{A_c L \rho_f h_{fg}} + \frac{\dot{M}_i}{A_c \rho_f}\left[1 + \frac{C_p(T_s - T_0)}{h_{fg}}\right] \tag{5}$$

The physical meaning of equation (5) is that the depletion of the inventory is caused by heat input to the two-phase pool subtracting the energy required to heat the inlet subcooled water to the saturation temperature.

We must still evaluate the volumetric liquid flux $j_f(z)$ in equation (2). This can be considered by dividing the pool into two regions. For the region below the bulk boiling elevation z_{sat}, the gross vapor flow is zero, i.e. $j_g = 0$ for $0 < z \leq z_{sat}$, and j_f can be simply obtained by the "cold-fill" relation

[1] Present Address: Department of Nuclear Engineering, University of California, Berkeley, Calif. 94720.

Contributed by the Heat Transfer Division and presented at the Winter Annual Meeting of The American Society of Mechanical Engineers, Nov. 15–20, 1981, Washington, D.C. Manuscript received by the Heat Transfer Division March 20, 1981. Paper No. 81-WA/HT-60.

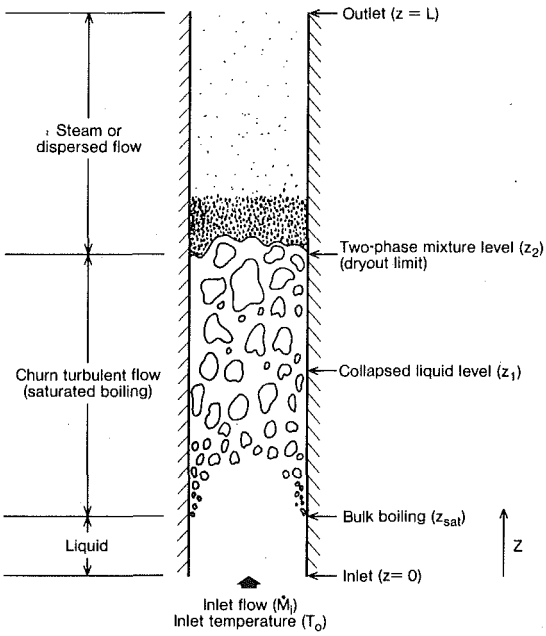

Fig. 1 A schematic illustration of the boiloff phenomenon in a flow channel

$$j_f(z) = \frac{\dot{M}_i}{A_c\rho_f} = \text{constant}, \quad z < z_{sat} \tag{6}$$

For $z \geq z_{sat}$, this constant liquid velocity, as calculated by equation (6) is decreased as a result of vaporization. From mass balance considerations, it can be obtained that

$$j_f(z) = \frac{\dot{M}_i}{A_c\rho_f} - \frac{\rho_g j_g(z)}{\rho_f} \text{ for } z \geq z_{sat} \tag{7}$$

The combination of equation (7) with equation (1) leads to the expression that, for $z \geq z_{sat}$

$$j_f(z) = \frac{\dot{M}_i}{A_c\rho_f} - \left[\frac{\dot{Q}z}{A_cL\rho_f h_{fg}} - \frac{\dot{M}_i C_p(T_s - T_0)}{A_c\rho_f h_{fg}}\right] \tag{8}$$

Equations (1–3, 5) and (8) are the five equations to solve for j_g, j_f, α, z_1, and z_2.

Inserting equation (7) into equation (2), the void fraction α, can be represented as a function of j_g given by

$$\alpha = \frac{j_g}{C_0\left(\frac{\dot{M}_i}{A_c\rho_f} - \frac{\rho_g}{\rho_f}j_g + j_g\right) + V_{gj}} = \frac{j_g}{C_0 j_g + V^*_{gj}} \tag{9}$$

where

$$V^*_{gj} \equiv V_{gj}\left(1 + C_0\frac{\dot{M}_i}{A_c\rho_f V_{gj}}\right) \tag{10}$$

and it is assumed that $\rho_g \ll \rho_f$.

Now, equations (1, 3, 5), and (9) are sufficient to solve for j_g, α, z_1, and z_2.

Solutions. Inserting equation (9) into equation (3), z_1 is expressed as

$$z_1 = z_2 - \int_{z_{sat}}^{z_2}\left(\frac{j_g}{C_0 j_g + V^*_{gj}}\right)dz \tag{11}$$

Since j_g is a function of z only, as indicated in equation (1), equation (11) can be integrated directly to become

$$z_1 = z_2 - \frac{1}{C_0}(z_2 - z_{sat}) + \frac{V^*_{gj}A_cL\rho_g h_{fg}}{C_0^2\dot{Q}} \times \ln\left[1 + \frac{C_0}{V^*_{gj}}\left(-\frac{\dot{M}_i C_p(T_s - T_0)}{A_c\rho_f h_{fg}} + \frac{Qz_2}{A_cL\rho_g h_{fg}}\right)\right] \tag{12}$$

Since it is assumed that the inlet flow and subcooling are constant, $dz_{sat}/dt = 0$. By taking the derivative of equation (12) and equating it with equation (5), the following relation is obtained.

$$-\frac{\dot{Q}z_2}{A_cL\rho_f h_{fg}} + \frac{\dot{M}_i}{A_c\rho_f}\left[1 + \frac{C_p(T_s - T_0)}{h_{fg}}\right] = \frac{C_0 - 1}{C_0}\frac{dz_2}{dt} + \frac{1}{C_0\left[1 + \frac{C_0}{V^*_{gj}}\left(-\frac{\dot{M}_i C_p(T_s - T_0)}{A_c\rho_g h_{fg}} + \frac{\dot{Q}z_2}{A_cL\rho_g h_{fg}}\right)\right]}\frac{dz_2}{dt} \tag{13}$$

Equation (13) is a first-order nonlinear ordinary differential equation for z_2 as a function of t, and therefore, can be solved with a single initial condition,

$$z_2 = z_{2o} \text{ at } t = 0 \tag{14}$$

where z_{2o} is the initial two-phase mixture level.

To simplify the algebraic forms and to facilitate physical interpretations of the solutions, the following dimensionless parameters are introduced. They are the dimensionless time, θ, where

$$\theta \equiv \frac{\dot{Q}t}{A_cL\rho_f h_{fg}} \tag{15}$$

and the dimensionless two-phase mixture level, Z_2, where

$$Z_2 \equiv \frac{z_2}{z_{2o}} \tag{16}$$

For further simplification we let

$$N_q \equiv \frac{\dot{Q}z_{2o}}{A_cL\rho_g h_{fg}V^*_{gj}} = \frac{z_{2o}}{L}\frac{\dot{Q}/\rho_g A_c h_{fg}}{V^*_{gj}} \tag{17}$$

which is the ratio of the vapor to phase-separation velocities;

$$N_m \equiv \frac{\dot{M}_i}{A_c\rho_g V^*_{gj}} = \frac{\rho_f}{\rho_g}\frac{\dot{M}_i/\rho_f A_c}{gj}\frac{1}{\left[1 + C_0\left(\frac{\dot{M}_i/A_c\rho_f}{V_{gj}}\right)\right]} \tag{18}$$

Nomenclature

A_c = cross-sectional area of flow in a channel
C_0 = the distribution parameter in Zuber and Findlay's correlation
C_p = thermal capacity
h_{fg} = latent heat of vaporization
j_f = volumetric flux of liquid
j_g = volumetric flux of vapor
L = length of the flow channel
$\dot{M}_i$ = mass flow rate of inlet feed at the bottom of channel
N_m = a dimensionless number defined in equation (18)
N_q = a dimensionless number defined in equation (17)
N_s = the dimensionless subcooling parameter, as defined in equation (19)
$\dot{Q}$ = total heat input along the channel
t = time
T_0 = inlet feed water temperature
T_{sat} = saturation temperature
V_{gj} = the drift velocity in Zuber and Findlay's correlation
V^*_{gj} = a modified drift velocity, as defined in equation (10)
z = the vertical coordinate
z_1 = the collapsed liquid level
z_2 = the two-phase mixture level
z_{2o} = the initial two-phase mixture level
z_{sat} = elevation at which the bulk fluid reaches saturation temperature
Z_1 = the dimensionless collapsed liquid level, z_1/z_{20}
Z_2 = the dimensionless two-phase mixture level, z_2/z_{20}
Z_{sat} = the dimensionless elevation at which the bulk fluid reaches saturation, z_{sat}/z_{20}
α = the void fraction
θ = the dimensionless time as defined in equation (15)
ρ_f = the density of liquid
ρ_g = the density of vapor

a measure of the liquid inlet to vapor phase-separation velocities; and

$$N_s \equiv \frac{C_p(T_s - T_0)}{h_{fg}} \tag{19}$$

the subcooling number.

Now Equation (13) can be rewritten in a convenient dimensionless form,

$$-Z_2 + \frac{N_m(1+N_s)}{N_q} = \frac{C_0 - 1}{C_0}\frac{dZ_2}{d\theta} + \frac{1}{C_0}\frac{1}{1 - C_0N_mN_s + C_0N_qZ_2}\frac{dZ_2}{d\theta} \tag{20}$$

and the initial condition, Equation (14) written as

$$Z_2 = 1 \text{ at } \theta = 0 \tag{21}$$

Equations (20) and (21) can be solved in exact form to yield the following solution of Z_2 as a function of θ only:

$$\theta = -\frac{C_0 - 1}{C_0} ln \left[\frac{Z_2 - \frac{N_m(1+N_s)}{N_q}}{1 - \frac{N_m(1+N_s)}{N_q}}\right] - \frac{1}{C_0(1+C_0N_m)} ln \left[\frac{Z_2 - \frac{N_m(1+N_s)}{N_q}}{1 - \frac{N_m(1+N_s)}{N_q}}\right] - \frac{1}{C_0(1+C_0N_m)} ln \left[\frac{1 - C_0N_mN_s + C_0N_qZ_2}{1 - C_0N_mN_s + C_0N_q}\right] \tag{22}$$

According to the same dimensionless analysis, equations (4) and (12) can be cast into the dimensionless form that

$$Z_{sat} \equiv \frac{Z_{sat}}{Z_{2o}} = \frac{N_mN_s}{N_q} \tag{23}$$

and

$$Z_1 \equiv \frac{Z_1}{Z_{2o}} = \frac{C_0 - 1}{C_0}(Z_2 - Z_{sat}) + Z_{sat} + \frac{1}{C_0^2N_q} ln\,[1 + C_0N_q(Z_2 - Z_{sat})] \tag{24}$$

It is evident from equations (22) and (24) that once Z_2 is calculated as a function of θ from equation (22), Z_1 can be easily calculated from equation (24).

Special Solutions for the Case of No Inlet Flow. For the special case of no inlet flow, the liquid state is saturated, and therefore, $\dot{M}_i = 0$, and $T_0 = T_{sat}$. This leads to the relation that

$$N_m = N_s = 0$$

and equations (22) and (24) can be simplified to the forms

$$\theta = -ln\left[\frac{Z_2}{\left(\frac{1 + N_qC_0Z_2}{1 + N_qC_0}\right)^{1/C_0}}\right] \tag{25}$$

and

$$Z_1 = \frac{C_0 - 1}{C_0}Z_2 + \frac{1}{C_0^2N_q} ln\,(1 + C_0N_qZ_2) \tag{26}$$

Further approximations for the cases of $N_q \gg 1$ and $Z_2 \approx 0(1)$ reduce equations (25) and (26) to the expressions

$$Z_2 = \exp\left(-\frac{C_0}{C_0 - 1}\theta\right) \tag{27}$$

and

$$Z_1 = \frac{C_0 - 1}{C_0}Z_2 + \frac{ln\,(C_0N_qZ_2)}{C_0^2N_q} \tag{28}$$

where equation (27) is identical to the approximate solution given in reference [1]. It is noted from this approximation that the parameter C_0 in the void fraction correlation is a sensitive parameter in the predictions, particularly at the low pressure conditions where V_{gj} and j_f are generally small compared to j_g, as seen from equation (2).

Results and Discussion

General Solutions. The exact solutions obtained in equations (22) and (24) provide a functional relationship among the dimensionless two-phase mixture level, Z_2, the dimensionless collapsed liquid level, Z_1, and the dimensionless time, θ. There are three other dimensionless parameters N_q, N_m, N_s which characterize the heat flux, the inlet feed flow, and the inlet subcooling, respectively.

For given system conditions, i.e., the channel geometry, the heat flux, the inlet flow and temperature, and the system pressure, the parameters N_q, N_m, and N_s are known and Z_1 and Z_2 can be calculated. For practical interest, the range of N_q varies from 0 to $0(10^2)$, N_m from 0 to 0(10), and N_s from 0 to $0(10^{-1})$. Sample results of the general solutions are illustrated in Figs. 2 to 6.

Figures 2 and 3 show the sensitivity of N_q for given N_m and N_s. A higher N_q represents a higher heat flux, and results in a faster boil-off rate. In Fig. 3, with an expanded time scale and smaller N_q values, it

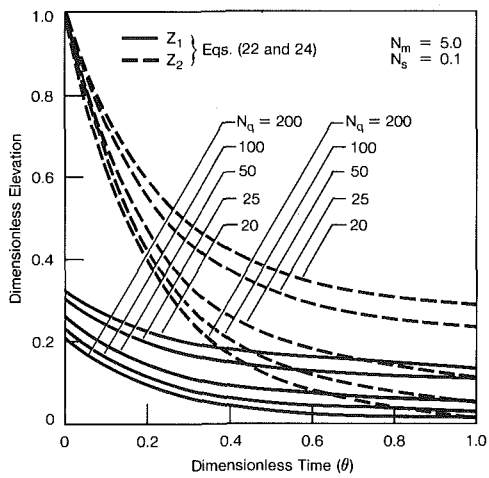

Fig. 2 The variation of Z_1 and Z_2 as a function of θ with N_q as a varying parameter

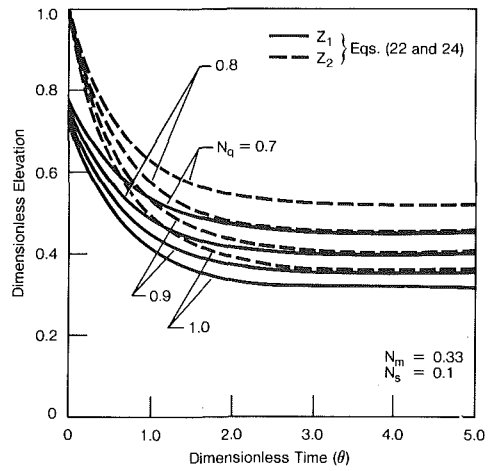

Fig. 3 The variation of Z_1 and Z_2 as a function of θ with N_q as a varying parameter

is shown that the boil-off reaches an asymtotic state when the evaporation, as characterized by N_q, is balanced by the inlet flow embedded in the parameter N_m.

Figures 4 and 5 depict the effect of N_m on the boil-off rate for given N_q and N_s. The sensitivity of N_m on Z_1 and Z_2 indicates the strong effect of inlet liquid flow of the boil-off transient. This is because a small amount of liquid inlet, due to the large difference of densities between the liquid and the vapor, can turn into a sizable steam flow at the two-phase interface. In fact, for a sufficiently large inlet flow, the channel wall will not be uncovered. The process is then referred to as reflooding [6]. For smaller N_m values, as shown in Fig. 5 on a expanded time scale, the boil-off process eventually reaches a steady state when the mass loss due to vaporization is balanced by the inlet flow. Figure 6 illustrates the influence of the subcooling parameter N_s on the boil-off process. As N_s increases, which means the inlet subcooling is higher, the vaporization rate decreases, causing a slower boil-off rate. Since N_s is a function of pressure only, it does not have the variability like N_q and N_m. In general, the value of N_s is not greater than 0.2.

The special solutions for the case of no feed flow are given in equations (25) and (26), in which only the parameter N_q has an effect on the boil-off process. A sample calculation is shown in Fig. 7. The overall trend is similar to the cases presented in Figs. 2 and 3.

Comparison with Data. The comparison of numerical models with experimental data from simulated reactor rod bundles with nonuniform power profiles was discussed in detail in reference [1]. In the present paper, comparisons are limited to the special cases of uniform or averaged heat flux which is the basis for the present model. Specifically, recent data from Seban and Kharraazi [7] and Chon [8] are used for qualification of the model. Then, the analysis is extended to the boil-off condition occurred in the Three Mile Island accident [1, 8].

The experimental investigation of Seban and Kharraazi [7] is the most comprehensive basic study of the boil-off phenomenon to date. From their single-tube test facility, seven tests with different powers were conducted to provide a wide range of boil-off rate, a factor of 10 in the parameter N_q. Reflooding tests were first run and the boil-off transient was initiated by termination of inlet flow at prescribed conditions. Temperature readings at various elevations along the 12 ft (3.66 m) long tube provided the time of tube dryout, an indication of the passage of the two-phase mixture level. A pressure reading for the mass in the tube provided the transient variation of the collapsed liquid level. Presented in Fig. 8 are the data of Seban and Kharraazi in the form of elevation with respect to the time of dryout at the

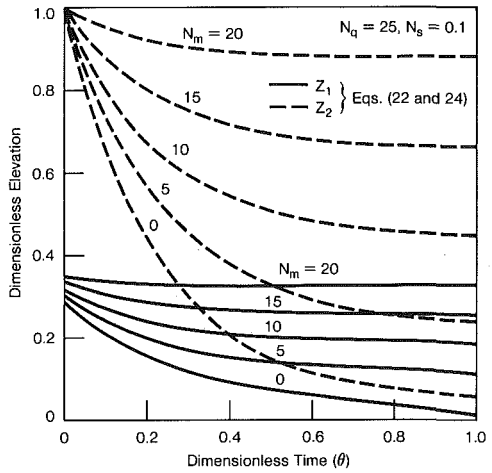

Fig. 4 The variation of Z_1 and Z_2 as a function of θ with N_m as a varying parameter

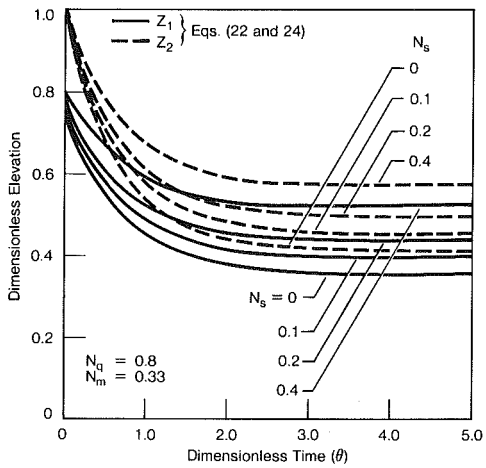

Fig. 6 The variation of Z_1 and Z_2 as a function of θ with N_s as a varying parameter

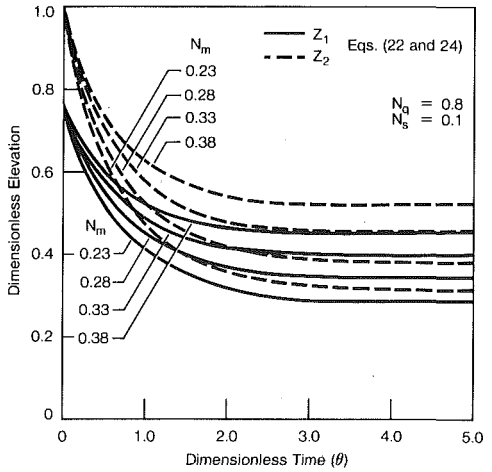

Fig. 5 The variation of Z_1 and Z_2 as a function of θ with N_m as a varying parameter

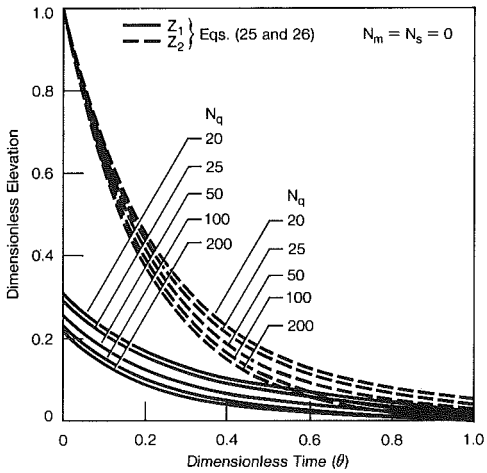

Fig. 7 The variation of Z_1 and Z_2 as a function of θ with N_q as a varying parameter for the case of no feed flow (N_m = N_s = 0)

specific elevations. It is clear from the figure that the higher the power, the less time it takes to boil-off the liquid in the tube.

The data of Chon [8] were obtained from a 3 × 3 rod bundle test section. Similar to the data in reference [7], there were two tests with different powers, which provided transient variation of the two-phase mixture levels and the collapsed liquid levels. Both sets of data [7, 8] were obtained at atmospheric pressures with no inlet feed flow.

To compare the present analysis with data, the parameter N_q has to be evaluated first. Aside from the geometric factors and fluid properties, there are two ingredients which are inherent from the drift flux correlation for the void fraction [3]; the distribution parameter C_0 and the drift velocity V_{gj}. Since the sensitivity of C_0 on boil-off was evaluated in detail in reference [1], we shall adapt $C_0 = 1.25$ as recommended in reference [1]. For the drift velocity, we take the Zuber and Findlay expression for the churn-turbulent flow,

$$V_{gj} = 1.41 \left[\frac{\sigma g\,(\rho_f - \rho_g)}{\rho_f^2}\right]^{1/4} \tag{29}$$

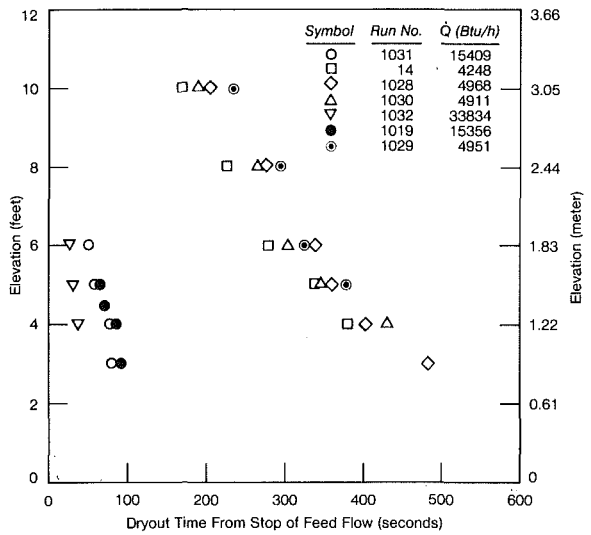

Fig. 8 The dryout times at various elevations from the single-tube boiloff tests of Seban and Kharraazi [7]

which is a function of pressure only for a given fluid. For the case of water, V_{gj} varies from 0.72 ft/s (0.22 m.s.) at atmospheric pressure to 0.56 ft/s (0.17 m/s) at 1000 psia (68 bars).

Once C_0 and V_{gj} are known, the parameter N_q can be evaluated for each test condition. The initial conditions, i.e., the initial elevations of the two-phase mixtures, for the single tube case are the locations where the temperature readings register the dryout first. For the 3 × 3 bundle case, the top of the bundle is chosen as the initial two-phase mixture level due to the lack of sufficient temperature readings.

Figure 9 illustrates the comparison of Equation (25) with the data of [7] and [8] in dimensionless form. In the dimensionless elevations, the initial two-phase mixture level for each run corresponds to the highest dryout location as shown in Fig. 8. It is shown that data from wide range of power levels and different channel geometries can be correlated very well by the present analysis.

To compare the measured collapsed liquid level with theory, we use equation (26) which provides a relationship between Z_1 and Z_2 and is theoretically invariant with time. The measured collapsed liquid levels are usually continuous readings from the pressure transducers, while the two-phase mixture levels are discrete dryout locations. Therefore, for each two-phase level, the collapsed liquid level measured as the same time can be used for comparison with the result from equation (26). Figure 10 shows the comparison of equation (26) with the data [7, 8] which agree well with theory at later times, i.e., lower elevations, but deviate from the theory at early times, i.e., higher elevations. With the two-phase levels calculated from equation (25), first, the collapsed liquid levels calculated from equation (26) underpredict the 3 × 3 bundle data [7] and overpredict the single-tube data [6]. This discrepancy cannot be adjusted by changing the C_0 values common to both cases. The cause of this is probably associated with the functional and stylized relationship of the Drift Flux correlation. The comparatively high liquid inventory in the 3 × 3 rod bundle suggests that the spacer grid and the bundle tie-plate probably act as flow blockage. This may cause liquid fall back from the upper plenum in the bundle [8], which would lead to a higher measured mass inventory, i.e. Z_1.

The nuclear core in the Three Mile Island Unit 2 (TMI-2) plant was partially uncovered during the March 1979 accident due to insufficient coolant flow and subsequent boiling dry [1, 2]. The accident scenario has been discussed in detail [2] and the analyses made by various models were presented in reference [1]. In this paper, the TMI-2 core uncovery transient is analyzed with an average heat flux approximation. This approximation is reasonable since the TMI-2 core power was nearly uniform along its length except for the short regions of about 1.8 ft (0.55 m) near the two ends. With the system

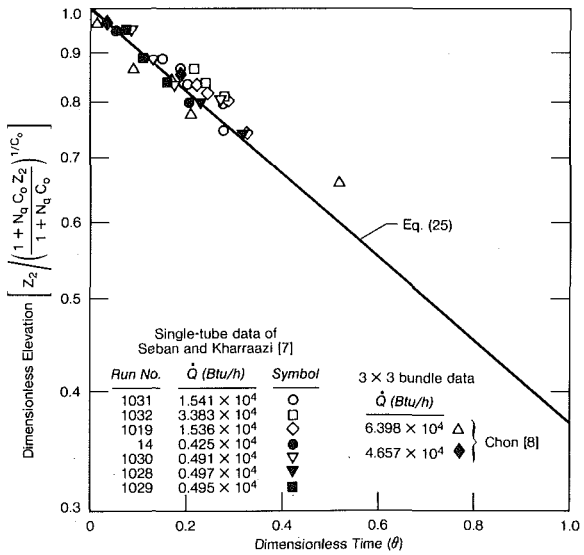

Fig. 9 The comparison of the calculated two-phase levels with data from single-tube tests [7] and 3 × 3 bundle tests [8]

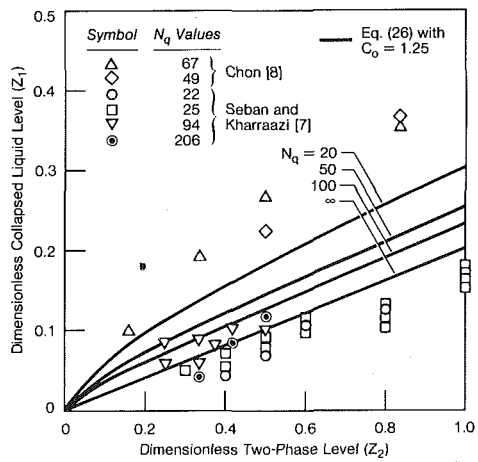

Fig. 10 The comparison of calculated relationship between Z_1 and Z_2 with data from single-tube tests [7] and 3 × 3 bundle test [8]

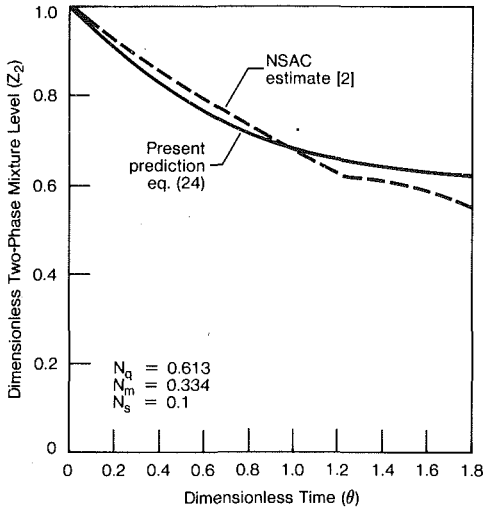

Fig. 11 The comparison of present analysis of TMI-2 core uncovery transient with the estimated plant transient of NSAC [2]

pressure of approximately 750 psia (51 bars) and the estimate of core power at 9.5×10^7 Btu/hr (27.8 MW), the inlet feed flow at 5.8×10^4 lb/hr (7.3 Kg/s), and an average subcooling of 60°F (33°C), the governing dimensionless parameters are $N_q = 0.613$, $N_m = 0.334$, and $N_s = 0.1$. Figure 11 shows the comparison of present calculation of the two-phase mixture level during the TMI-2 accident with the estimated plant transient response [2] for the first 30 min. of the core uncovery transient. The agreement of the present model with data shown in Figs. 9, 10, and 11, except for the 3×3 bundle whose data are somewhat doubtful, has demonstrated the applicability of the present model not only to the conditions of the simple geometries at lower pressures, but also to the conditions of full-scale nuclear plants.

Conclusions

With the assumptions of a uniform heat flux and a constant inlet flow rate, a closed-form dimensionless solution calculates the two-phase mixture level and the collapsed liquid level during boiling dry a vertical channel.

From the solutions, three governing dimensionless parameters are identified for the boiling dry phenomenon. They are N_q, N_m, and N_s to characterize the heat flux, the inlet feed flow, and the inlet subcooling, respectively.

For a given channel geometry and a system pressure, the parameter N_m exerts the most pronounced effect among the three parameters, indicating that the inlet flow rate is the most sensitive parameter in the boil-off transient.

The theory is in reasonably good agreement with available single tube, rod bundle and the estimated large plant transient response.

References

1 Sun, K. H., Duffey, R. B., and Peng, C. M., "The Prediction of Two-Phase Mixture Level and Hydrodynamically-Controlled Dryout Under Low Flow Conditions," presented at the ASME-AIChE 19th National Heat Transfer Conference, Orlando, Fla, July 27–30, 1980, Symposium HTD-Vol. 7, "Experimental and Analytical Modeling of LWR Safety Experiments," pp. 1–10, to appear in *International Journal of Multiphase Flow*.

2 NSAC, 1979, "Analysis of the Three-Mile Island-Unit 2 Accident," Electric Power Research Institute, Report NSAC-1, NSAC, 1980, Report NSAC-1 (revised). (Also, personal communications with D. Cain.)

3 Zuber, N., and Findlay, J. A., "Average Volume Concentration in Two-Phase Flow Systems," ASME JOURNAL OF HEAT TRANSFER, 1965, pp. 453–468.

4 Cunningham, J. P., and Yeh, H. C., "Experiments and Void Correlation for PWR Small-Break LOCA Conditions," *Transactions of the American Nuclear Society*, Vol. 17, 1973, p. 269.

5 Wilson, J. F., Grenda, R. T., and Patterson, J. F., "The Velocity of Rising Steam in a Bubbling Two-Phase Mixture," *Transactions of the American Nuclear Society*, Vol. 5, 1962, pp. 151–152.

6 Sun, K. H., "High Temperature Heat Transfer Applications to Nuclear Power Safety—Reflooding and Core Uncovery Phenomena," presented at the Japan-U.S. Heat Transfer Joint Seminar, Sept. 29–Oct. 2, 1980, Tokyo, Japan.

7 Seban, R. A., and Kharraazi, A., "Single-Tube Reflood with Subsequent Boiling Dry Because of Termination of the Feed," EPRI Report NP-80-4-LD, Aug. 1980.

8 Chon, W. Y., Addabbo, C., and Liao, N. S., "Combined Bottom and Top Reflooding Experimental Plan," EPRI Report NP-1331, Feb. 1980. (Also, personal communications, 1980–1981.)

An Analytical and Experimental Investigation of Bubble Waiting Time in Nucleate Boiling

Ameer Ali
Graduate Student.

R. L. Judd
Professor.
Mem. ASME

Mechanical Engineering Department,
McMaster University,
Hamilton, Ontario,
Canada L854L7

In as much as bubble nucleation theory formulated on the basis of transient conduction to the liquid in the vicinity of the heat transfer surface predicted results for bubble waiting time that were inconsistent with experimental data, a bubble nucleation theory incorporating both conductive and convective heat transfer to the liquid in the wake of a rising bubble was developed. The bubble waiting time results predicted by this theory agreed very well with experimental observations and therefore the evidence suggests that the convective heat transfer contribution is a significant feature of bubble nucleation particularly for subcooled boiling conditions.

Conduction Controlled Nucleation

A unique characteristic of nucleate boiling is the presence of active sites on the heat transfer surface which have the ability to nucleate and support the growth of vapour bubbles. Nucleation sites have been demonstrated conclusively to be tiny cavities, scratches and other imperfections in the heat transfer surface [1–4]. The rate of heat transfer in nucleate boiling depends upon the number of active sites per unit area; as the temperature of the heat transfer surface is raised above the liquid saturation temperature the number of active sites increases with accompanying increases in the rate of heat transfer.

The time elapsed between two consecutive bubble departures at a given site is the bubble period which in turn is comprised of two parts: the waiting period t_w, which is the time from the last bubble departure to the beginning of the next bubble formation and the growing period t_g, which is the time from the beginning of the bubble formation to its departure or collapse. Bubble emission frequency f, which is the inverse of bubble period, assumes importance in boiling heat transfer correlations, such as that proposed by Rohsenow [5], in which the rate of heat transfer is related to the amount of energy transported per bubble emitted.

In 1961, Han and Griffith [6] investigated the behaviour of the thermal boundary layer adjacent to the heat transfer surface with respect to bubble emission in nucleate boiling and concluded that a bubble emission cycle consisted of the following stages.

- growth of the thermal boundary layer
- bubble nucleation and growth
- detachment of the bubble from the heating surface

Bubble detachment at the end of the growth period is invariably followed by the destruction of the thermal layer as relatively cold liquid from the bulk rushes in to fill the void left behind by the departing bubble. A new cycle begins as the thermal layer starts to recover.

Hsu [7] proposed a model for bubble nucleation which assumed that a nucleus sits at the mouth of a cavity of favourable geometry as discussed by Bankoff [8] at the beginning of an emission cycle. The nucleus is assumed to be the residual vapour left behind by the preceding bubble and is surrounded by relatively cold bulk liquid at temperature T_∞. As time passes, the cold liquid is heated by transient conduction and the local thermal boundary layer thickness increases; when it grows to the extent that the liquid surrounding the nucleus becomes warmer than the vapour in the nucleus, the bubble waiting time ends and the bubble begins to grow. Figure 1 shows that bubble growth commences when

$$T(b, t) - T_\infty = \theta(b, t) = \theta_v = T_v - T_\infty \tag{1}$$

After achieving sufficient size, the bubble detaches from the heat transfer surface and leaves a residue of vapour behind that will serve as the nucleus for the formation of the next bubble. As the bubble leaves the heating surface, bulk liquid at temperature T_∞ rushes in and fills the void left behind thus destroying the local thermal boundary layer. The nucleus is once again surrounded by relatively cold bulk liquid and another bubble cycle begins.

If Hsu's bubble nucleation model is correct and transient conduction to the thermal boundary layer is the sole means of heat transfer, then it can be shown that the temperature distribution in the thermal boundary layer can be approximated by

$$\frac{T(y, t) - T_\infty}{T_w - T_\infty} = \frac{\theta(y, t)}{\theta_w} = \operatorname{erfc}\left(\frac{y}{2\sqrt{\kappa_\ell t}}\right) \tag{2}$$

when surface temperature is assumed constant. Figure 2 taken from reference [9] presents an analysis of the thermal boundary layer thickness measurements of Best, et al. [10] which demonstrates that equation (2) seriously underestimates the growth of the thermal boundary layer.

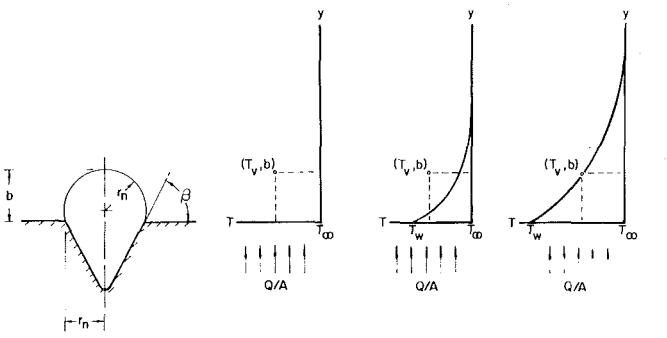

Fig. 1 History of bubbling waiting time

Contributed by the Heat Transfer Division for publication in the JOURNAL OF HEAT TRANSFER. Manuscript received by the Heat Transfer Division September 22, 1980.

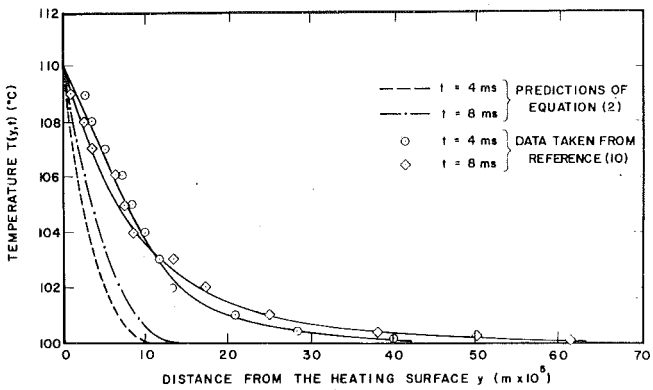

Fig. 2 Temperature distribution in a liquid layer adjacent to the heating surface at 4 ms and 8 ms after bubble departure

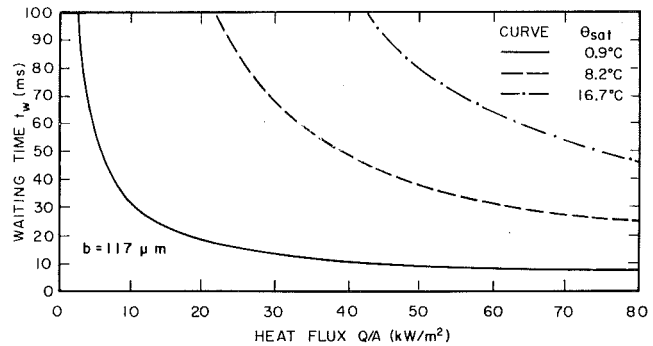

Fig. 3 Plot of bubble waiting time as a function of heat flux according to conduction controlled bubble nucleation

For the case of constant heat flux in which conduction is assumed to be the only mode of heat transfer, it can be shown that

$$\frac{T(y,t)-T_\infty}{(Q/A)\sqrt{\kappa_\ell t}/k_\ell}=\frac{\theta(y,t)}{\theta_w(t)}=2\,\text{ierfc}\left(\frac{y}{2\sqrt{\kappa_\ell t}}\right) \tag{3}$$

When equation (1) the criterion equation for bubble growth is satisfied, the waiting time comes to an end. Substitution of equation (3) into equation (1) after having set $y = b$ and $\theta_v = \theta_{sat} + A/r_n$ yields

$$\theta_{sat}+\frac{A}{r_n}=2\,\frac{(Q/A)\sqrt{\kappa_\ell t}}{k_\ell}\,\text{ierfc}\left(\frac{b}{2\sqrt{\kappa_\ell t}}\right) \tag{4}$$

When it is assumed that $b \simeq 2r_n$ because of the small contact angles associated with organic liquids, the solution of equation (4) for $t = t_w$ yields a family of curves such as that shown in Fig. 3. According to this model,

- Bubble waiting time decreases with increasing heat flux.
- Bubble waiting time increases with increasing subcooling.

While the first result is consistent with the experimental results presented in the next section, the second result contradicts the data. Further evidence is therefore provided to suggest that conduction alone is not capable of accounting for the transfer of heat between the heating surface and the bulk liquid in bubble nucleation.

Experimental Investigation

At the commencement of the research, experimental apparatus constructed by Voutsinos [11] to investigate microlayer evaporation at various levels of heat flux and subcooling already existed, which was quite adequate in meeting the requirements of the present investigation. A sectional view is shown in Fig. 4. In the present investigation, dichloromethane was boiled at atmospheric pressure on a borosilicate glass heating surface at six levels of heat flux ranging from 25 kW/m^2 to 63 kW/m^2 and three levels of subcooling 0.9, 8.2 and 16.7°C, respectively. The heat transferred was generated by passing a direct current through a thin layer of stannic oxide deposited on the surface of the borosilicate glass in contact with the liquid, thereby establishing a constant heat flux boundary condition. Throughout the course of the experiment, the surface superheat varied little with changes in the level of heat flux or subcooling investigated as customarily happens with this type of boiling phenomenon. A detailed description of the experimental apparatus, test conditions, test procedure and the full range of thermometric and waiting time data is presented in reference [9].

High speed motion pictures were taken from beneath the boiling vessel at a framing rate of approximately 1000 frames/s and the film strips obtained were analyzed for bubble waiting time. Figures 5 and 6 show plots of bubble waiting time t_w versus the impressed heat flux Q/A with liquid subcooling ($T_{sat} - T_\infty$) as a parameter for two of the 12 sites investigated.

Conduction/Convection Controlled Nucleation

Best et al. [10] suggested that hydrodynamic effects are involved in the transient bulk heating process. Accordingly, it is proposed to reformulate the bubble nucleation problem to incorporate the effect of convection in the wake of the rising bubbles and to examine the predictions of this model in light of the experimental observations. Our intention is not to promote a new bubble nucleation theory but rather to introduce a plausible procedure for adapting conventional nucleation theory to account for the deficiencies associated with the prediction of bubble waiting time under subcooled boiling conditions.

The flow which is established in the wake of a rising bubble is very complicated and only recently has it become possible to predict the unsteady velocity components adjacent to the surface from which a bubble is rising with any confidence [10]. However, in this study an approximate analysis will be used since there is as yet no analytical solution for the transient temperature distribution. The derivation which follows predicts the development of the unsteady velocity and

Nomenclature

A = physical property parameter $A = 2\sigma T_{sat}/\rho_v h_{fg}$
b = height of bubble nucleus above point of contact of liquid vapour interface with heat transfer surface
C = specific heat
f = bubble emission frequency
h_{fg} = latent heat of vaporization
k = thermal conductivity
Q/A = heat flux
r = radial coordinate
r_n = bubble nucleus radius
T = temperature
t = time
t_c = time constant
t_g = bubble growing time
t_w = bubble waiting time
u = horizontal component of velocity
U = velocity of flow at the bubble base
V_∞ = bubble rise velocity
y = axial coordinate
β = contact angle
δ = wake thickness
Δ = penetration distance
η = dimensionless distance $\eta = y/\Delta(t)$
θ = temperature difference $\theta = T - T_\infty$
θ_{sat} = liquid subcooling $\theta_{sat} = T_{sat} - T_\infty$
κ = thermal diffusivity
ξ = dimensionless distance $\xi = y/\delta(t)$
ϕ = dimensionless penetration distance $\phi = \Delta(t)/\sqrt{\kappa_\ell t_c}$
ρ = density
σ = surface tension
τ = dimensionless time $\tau = t/t_c$
χ = dimensionless wake thickness $\chi = \delta(t)/\sqrt{\kappa_\ell t_c}$

Subscript

ℓ = liquid
n = nucleus
sat = saturated
v = vapor
w = wall
∞ = bulk

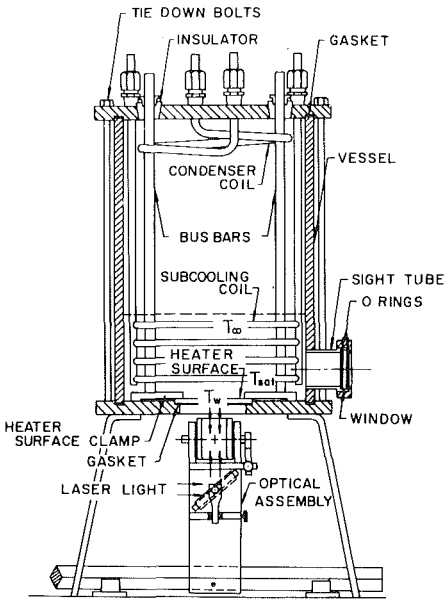

Fig. 4 Sectional view of experimental apparatus

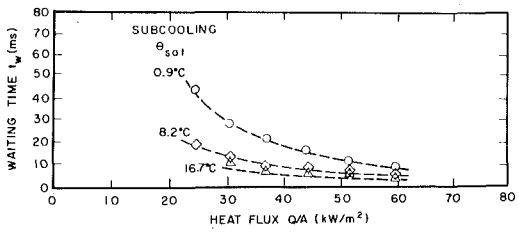

Fig. 5 Bubble waiting time results for site A

temperature fields in the wake of a bubble moving away from a horizontal heating surface.

Consider a bubble of hemispherical shape rising in an incompressible liquid of constant properties at temperature T_∞ moving away from a heat transfer surface that is subjected to a net heat flux Q/A. An idealized hemispherical shape is assumed for simplicity in the analysis, although bubbles of this shape have actually been observed experimentally [12]. As the bubble rises, liquid moves in with a horizontal velocity component $u(r, y, t)$ to fill the void that is left behind and an unsteady flow field is therefore set up in the vicinity of the surface. One of the features of this flow field is the formation and growth of a wake region whose thickness is shown as $\delta(t)$ in Fig. 7. As a result of conduction to the liquid from the heat transfer surface and convective energy transport induced by the flow behind the bubble, a thermal boundary layer whose thickness is shown as $\Delta(t)$ in Fig. 7 develops in the wake region. The hydrodynamic boundary conditions are

$$u(r, 0, t) = 0 \tag{5a}$$

$$u(r, \delta, t) = U(r,t) \tag{5b}$$

the thermal boundary conditions are

$$T(0, t) = T_w(t) \tag{6a}$$

$$T(\Delta,t) = T_\infty \tag{6b}$$

and the initial conditions associated with the problem are

$$\delta(0) = 0 \tag{7a}$$

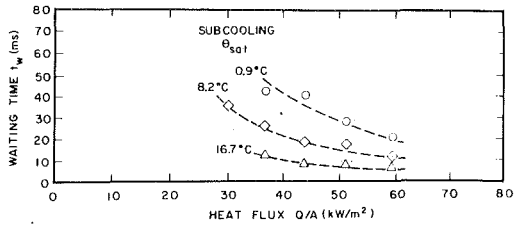

Fig. 6 Bubble waiting time results for site B

$$\Delta(0) = 0 \tag{7b}$$

The analysis begins by developing the mass conservation equation appropriate to the present flow system. With reference to the cylindrical shell of liquid shown in Fig. 7, with inner radius r, outer radius $r + dr$, and height $\delta(t)$ under the bubble base, the mass flowrate into the shell may be written

$$\dot{m}_{in} = 2\pi\rho_\ell \left\{ r \int_0^{\delta(t)} u(r, y, t)dy \right\} \tag{8}$$

and the mass flowrate out of the shell may be written

$$\dot{m}_{out} = 2\pi\rho_\ell \left\{ r \int_0^{\delta(t)} u(r, y, t)dy + \frac{\partial}{\partial r}\left[r \int_0^{\delta(t)} u(r, y, t)\right]dr \right\} \tag{9}$$

The rate of growth of the shell as a result of bubble departure from the surface is

$$\dot{m}(t) = 2\pi\rho_\ell r \frac{d\delta(t)}{dt} dr \tag{10}$$

In accordance with the conservation of mass principle

$$\frac{1}{r}\frac{\partial}{\partial r}\left[r \int_0^{\delta(t)} u(r, y, t)dy \right] = -\frac{d\delta(t)}{dt} \tag{11}$$

To solve equation (11) it is first necessary to be able to specify the velocity distribution $u(r, y, t)$ and the thickness $\delta(t)$. A suitable expression for the velocity distribution which satisfies the hydrodynamic boundary conditions is

$$u(r, y, t)/U(r, t) = (2\xi - 2\xi^3 + \xi^4) \tag{12}$$

where $\xi = y/\delta(t)$. Substitution of equation (12) into the integral which appears on the left-hand side of equation (11) yields

$$\int_0^{\delta(t)} u(r, y, t)dy = \tfrac{7}{10} U(r, t)\delta(t) \tag{13}$$

From a simple force balance on a bubble rising in a semi-infinite liquid, Best et al. [10] determined that an expression of the form

$$V(t) = V_\infty(1 - e^{-t/t_c}) \tag{14}$$

would represent the velocity at which a bubble moves away from the surface on which it formed, where V_∞ and t_c are unspecified constants which have to be determined empirically. Consequently, in the wake region, it was assumed that

$$\delta(t) = \text{Constant}\,[\tau - (1 - e^{-\tau})] \tag{15}$$

where equation (15) was obtained by integrating equation (14) after defining $V(t)$ as $d\delta(t)/dt$ and setting $\delta(0) = 0$. The ratio t/t_c has been replaced by τ. The constant is simply a scale factor which has no particular significance. Substitution of equations (13) and (15) into equation (11) leads to

$$\frac{1}{r}\frac{\partial}{\partial r}[rU(r, t)] = -\frac{10}{7}\frac{1}{\delta(t)}\frac{d\delta(t)}{dt} = -\frac{10}{7}\frac{1}{t_c}\frac{(1 - e^{-\tau})}{[\tau - (1 - e^{-\tau})]} \tag{16}$$

The energy conservation equation can be developed similarly. With reference to the cylindrical shell of liquid depicted in Fig. 7, the energy equation can be shown to be

$$\rho_\ell C_\ell \left\{\frac{\partial}{\partial t}\int_0^{\Delta(t)} \theta(y,t)dy + \frac{1}{r}\frac{\partial}{\partial r}\left[r\int_0^{\Delta(t)} u(r,y,t)\theta(y,t,)dy\right]\right\} = \frac{Q}{A} \tag{17}$$

The solution of equation (17) requires a knowledge of the temperature distribution $\theta(y, t)$ which was assumed to be independent of the radial coordinate because the heat flux is uniform over the heating surface. This assumption would be valid if the analysis were applied to a semi-infinite domain, but in as much as the present analysis is confined to the finite domain in the wake of a rising bubble, the assumption is not strictly correct. However, the region of particular interest so far as the nucleation phenomenon is concerned, lies on the axis where radial variation ought to be least significant, and as a consequence, an expression of the form

$$\frac{T(y,t)-T_\infty}{T_w(t)-T_\infty} = \frac{\theta(y,t)}{\theta_w(t)} = (1-3\eta+3\eta^2-\eta^3) \tag{18}$$

where $\eta = y/\Delta(t)$ was used to represent the temperature distribution for the sake of convenience. Substitution of equation (18) into the integrals which appear on the left-hand side of equation (17) yields

$$\frac{\partial}{\partial t}\int_0^{\Delta(t)} \theta(y,t)dy = \frac{1}{4}\frac{d}{dt}[\theta_w(t)\Delta(t)] \tag{19}$$

and

$$\int_0^{\Delta(t)} u(y,t)\theta(y,t)dy = U(r,t)\theta_w(t)\Delta(t) * \left[\frac{1}{10}\left(\frac{\Delta}{\delta}\right) - \frac{1}{70}\left(\frac{\Delta}{\delta}\right)^3 + \frac{1}{280}\left(\frac{\Delta}{\delta}\right)^4\right] \tag{20}$$

and furthermore

$$\frac{Q}{A} = -k_\ell\left[\frac{\partial\theta(y,t)}{\partial y}\right]_{y=0} = +\,3k_\ell\frac{\theta_w(t)}{\Delta(t)} = \text{Constant} \tag{21}$$

because of the assumption that a constant heat flux is impressed at the boiling heat transfer surface. As a consequence of this relationship

$$\theta_w(t) = \frac{1}{3}\frac{Q}{A}\frac{\Delta(t)}{k_\ell} \tag{22}$$

Substitution of equations (19) and (20) into equation (17) and rearrangement of the resulting expression gives

$$\rho_\ell C_\ell\left\{\frac{1}{4}\frac{d}{dt}[\theta_w(t)\Delta(t)] + \theta_w(t)\Delta(t)\left[\frac{1}{10}\left(\frac{\Delta}{\delta}\right) - \frac{1}{70}\left(\frac{\Delta}{\delta}\right)^3 + \frac{1}{280}\left(\frac{\Delta}{\delta}\right)^4\right] * \frac{1}{r}\frac{\partial}{\partial r}[rU(r,t)]\right\} = \frac{Q}{A} \tag{23}$$

The use of equation (16) to eliminate

$$\frac{1}{r}\frac{\partial}{\partial r}[rU(r,t)],$$

and equation (22) to eliminate $\theta_w(t)$ leads to

$$\frac{d\phi^2}{d\tau} - \frac{1-e^{-\tau}}{[\tau-(1-e^{-\tau})]}\phi^2\left[\frac{4}{7}\left(\frac{\phi}{\chi}\right) - \frac{4}{49}\left(\frac{\phi}{\chi}\right)^3 + \frac{1}{49}\left(\frac{\phi}{\chi}\right)^4\right] = 12 \tag{24}$$

where

$$\phi = \Delta(t)/\sqrt{\kappa_\ell t_c}$$

and

$$\chi = \delta(t)/\sqrt{\kappa_\ell t_c} = \text{Constant}[\tau-(1-e^{-\tau})]/\sqrt{\kappa_\ell t_c}$$

Solution of equation (24) subject to the initial condition $\Delta(0) = 0$ yields the dimensionless time τ at which a dimensionless thermal layer of thickness ϕ is attained as the result of conduction and convection in the liquid adjacent to the boiling heat transfer surface. If the flow induced contribution were to become insignificant, as occurs when the ratio ϕ/x approaches zero implying that the bubble is so far removed from the heating surface that the influence of its wake upon transient heating process is negligible, then equation (24) would become

$$\frac{d\phi^2}{d\tau} = 12 \tag{25}$$

which can be solved by direct integration to give

$$\Delta(t) = 12\sqrt{\kappa_\ell t} \tag{26}$$

Substitution of equation (26) into equation (22) and subsequent combination with equation (18) yields

$$\frac{T(y,t)-T_\infty}{(Q/A)\sqrt{\kappa_\ell t}/k_\ell} = \frac{\sqrt{12}}{3}\left[1-3\left(\frac{y}{\sqrt{12\kappa_\ell t}}\right) + 3\left(\frac{y}{\sqrt{12\kappa_\ell t}}\right)^2 - \left(\frac{y}{\sqrt{12\kappa_\ell t}}\right)^3\right] \tag{27}$$

which closely approximates equation (3), as demonstrated by Fig. 8, thereby substantiating the validity of the approximate solution technique.

Nucleation occurs and the bubble waiting time comes to an end when equation (1), the criterion equation for bubble growth is satisfied. Substitution of equation (18) into equation (1) after having set

$$y = b, \quad \theta_w(t) = \frac{1}{3}\frac{Q/A}{k_\ell}\Delta(t) \quad \text{and} \quad \theta_v = \theta_{\text{sat}} + A/r_n \text{ yields}$$

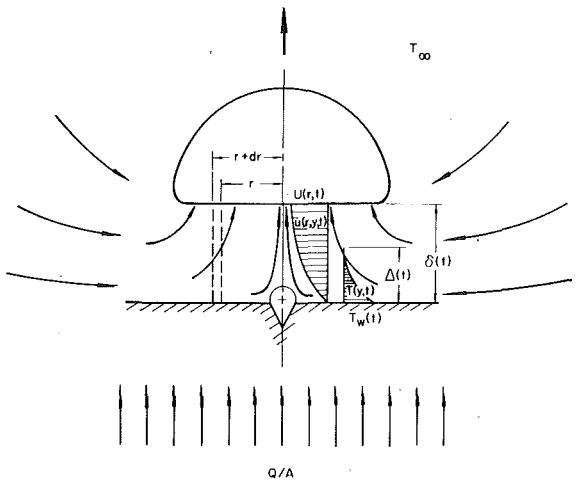

Fig. 7 Representation of the region in the wake of a rising bubble

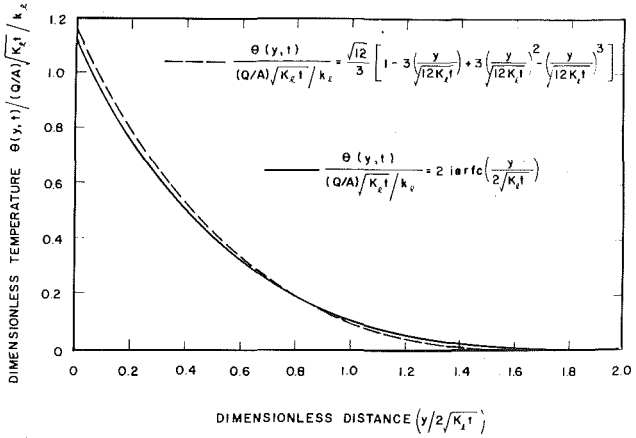

Fig. 8 Plot of dimensionless temperature versus dimensionless distance for a liquid receiving heat by conduction

$$\theta_{sat} + \frac{A}{r_n} = \frac{1}{3}\frac{Q/A}{k_\ell}\Delta(t)\left[1 - 3\left(\frac{b}{\Delta(t)}\right) + 3\left(\frac{b}{\Delta(t)}\right)^2 - \left(\frac{b}{\Delta(t)}\right)^3\right] \quad (28)$$

where $\Delta(t)$ is obtained from the solution of equation (24). Computer solution of equation (28) for $t = t_w$ yields a family of curves such as that shown in Fig. 9. According to this model, it is possible for the bubble waiting time to decrease with increasing subcooling in accordance with the experimental results depending upon the choice of the time constant.

Correlation of Experimental Results

Given that $b \simeq 2r_n$, equations (24) and (28) which must be solved simultaneously to obtain the predictions for the conduction/convection controlled nucleation model involving five variables: nucleus radius r_n, time constant t_c, liquid subcooling θ_{sat}, heat flux Q/A and bubble waiting time t_w. Out of these five variables, only the latter three could be measured in the experimental part of the investigation. Since both nucleus radiation r_n and time constant t_c were unknowns, testing of the model predictions required an indirect approach.

The situation is such that for a single set of experimental data comprised of measurements of bubble waiting time versus heat flux at a single level of subcooling, there is only one equation to solve for the two unknowns time constant and nucleus radius. The problem would be insoluable except for the additional information obtained by reasoning that although nucleus radius might vary from site to site depending on the size and geometry of the cavities, the nucleus radius at a particular site would not change as subcooling changed. Accordingly, the procedure employed involved assuming different values of time constant and fitting the three sets of bubble waiting time/heat flux results corresponding to the three levels of subcooling investigated for a particular site until a single value of nucleus radius was obtained. The procedure was repeated for all 12 nucleation sites visible within the field of view of the high speed camera which were active at more than one level of subcooling.

In the course of applying this technique to the various data sets pertaining to the different nucleation sites, it was observed that the time constant was dependent on only the level of subcooling and independent of the site characteristics, viz: $t_c = 0.1$ ms at $\theta_{sat} = 0.9°C$, $t_c = 1.50$ ms at $\theta_{sat} = 8.2°C$ and $t_c = 20.0$ ms at $\theta_{sat} = 16.7°C$. The value associated with the approximately saturated boiling condition is very small and the convection term in equation (24) is not significant, which implies that the experimental results are essentially conduction controlled. However, as subcooling increases, the convection term assumes increasingly greater importance in order to develop the enhanced heat transfer rates which the experimental results seem to require. The observed variation of time constant with subcooling is reasonable, since bubbles accelerate more slowly as the degree of subcooling increases; bubbles detaching from the surface begin to condense as soon as they move into the subcooled liquid and the buoyancy force tending to accelerate them away from the surface decreases as subcooling increases. If the subcooling were great enough, the bubbles would not move away from the surface at all, which would imply that the time constant were infinite. The fact that the values of time constant obtained by fitting the theory to the data are not completely arbitrary but tend to assume unique values at each level of subcooling for all 12 nucleation sites investigated denotes significant agreement between theory and experiment in a global context.

The extent of the agreement between the predictions of the model and the experimental results is demonstrated in Figs. 9 and 10. Similar agreement was observed for the other sites which were visible within the field of view of the high speed camera. Furthermore, it can be seen that the theoretically determined values of waiting time become very large at a heat flux of the order of 20 kW/m^2. The implication of this observation is that boiling should cease around this level of heat flux and although precise experimental data is lacking, this is essentially what was observed to happen.

Concluding Remarks

On the basis of the experimental measurements obtained, it would seem that conduction controlled nucleation theory is not capable of predicting bubble waiting time in subcooled nucleate boiling. The growth of the thermal boundary layer and subsequent bubble nu-

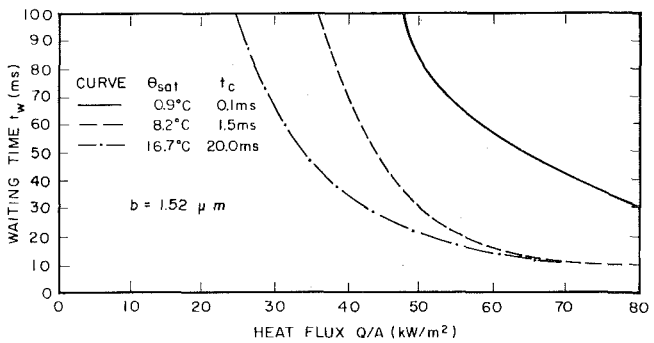

Fig. 9 Plot of bubble waiting time as a function of heat flux according to conduction/convection controlled bubble nucleation

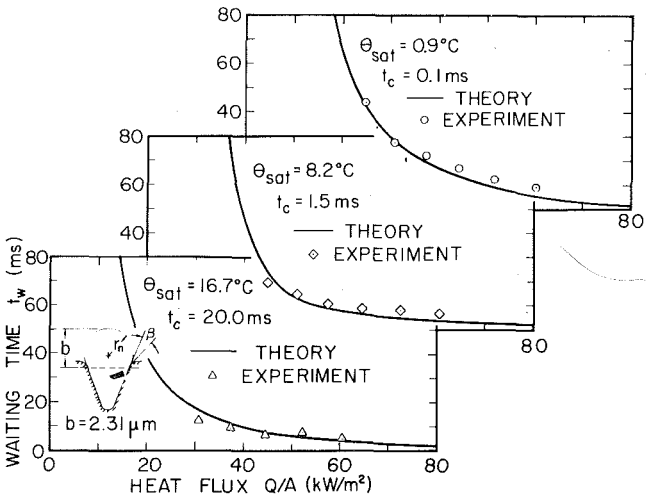

Fig. 10 Agreement between theory and experiment for site A

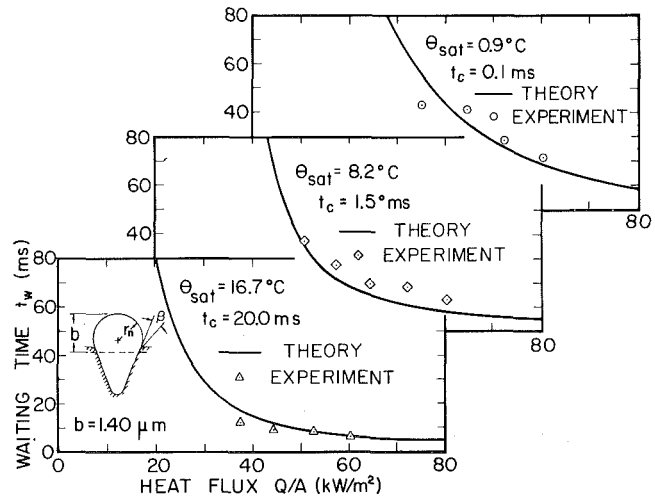

Fig. 11 Agreement between theory and experiment for site B

cleation appears to be governed by some other mechanism and it is thought that the combined effect of conduction and convection is responsible. While it is undeniable that the model developed is a simple representation of the actual physical phenomenon, the success of the conduction/convection controlled nucleation theory in correlating the experimental results is sufficient to encourage further research.

Acknowledgment

The authors wish to acknowledge the support of the National Science and Engineering Research Council of Canada through grant A4362.

References

1 Griffith, P., and Wallis, J. D., "The Role of Surface Conditions in Nucleate Boiling," *Chemical Engineering Progress Symposium Series*, Vol. 55, 1959, pp. 49–63.

2 Clark, H. B., Strenge, P. S., and Westwater, J. W., "Active Sites for Nucleate Boiling," *Chemical Engineering Progress Symposium Series*, Vol. 55, 1959, pp. 103–110.

3 Nix, G. H., Vachon, R. I., and Hall, D. M., "A Scanning Electron Microscopy Study of Pool Boiling Surfaces," *Proceedings of the Fourth International Heat Transfer Conference*, Paris-Versailles, 1970.

4 Nail, J. P., Vachon, R. I., and Morehouse, J., "An SEM Study of Nucleation Sites in Pool Boiling from 304 Stainless Steel," ASME JOURNAL OF HEAT TRANSFER, May 1974, pp. 132–137.

5 Rohsenow, W., "A Method for Correlating Heat Transfer Data for Surface Boiling of Liquids," *Trans. ASME*, Aug. 1952, pp. 969–976.

6 Hsu, Y. Y., and Graham, R. W., "An Analytical and Experimental Study of the Thermal Boundary Layer and Ebullition Cycle in Nucleate Boiling," NASA TN D-594, 1961.

7 Hsu, Y. Y., "On the Size Range of Active Nucleation Cavities on a Heating Surface," ASME JOURNAL OF HEAT TRANSFER, Aug. 1962, pp. 207–216.

8 Bankoff, S. G., "Entrapment of a Gas in the Spreading of a Liquid over a Rough Surface," *AIChE Journal*, Vol. 4, No. 1, Mar. 1958, pp. 24–26.

9 Ali, A., "An Analytical and Experimental Investigation of Bubble Waiting Time in Nucleate Boiling," M. Eng. Thesis, McMaster University, 1980.

10 Best, R., Burow, P., and Beer, H., "Die Warmeubertragung beim Sieden under dem Einfluss Hydrodynamischer Vorgange," *International Journal of Heat and Mass Transfer*, Vol. 18, 1975, pp. 1037–1047.

11 Voutsinos, C. M., "Laser Interferometric Investigation of Microlayer Evaporation for Various Levels of Subcooling and Heat Flux," Mechanical Engineering Thesis, McMaster University, 1976.

12 Johnson, M. A., de la Pena, J., and Mesler, R. B., "Bubble Shapes in Nucleate Boiling," *Chemical Engineering Progress Symposium Series*, Vol. 62, No. 64, 1966, pp. 1–5.

13 Judd, R. L., and Hwang, K. S., "A Comprehensive Model for Nucleate Boiling Heat Transfer Including Microlayer Evaporation," ASME JOURNAL OF HEAT TRANSFER, Nov. 1976, pp. 623–629.

Convective Heat Transfer to Turbulent Droplet Flow in Circular Tubes

A. G. Rane[1]
Senior Engineer,
Westinghouse Electric Corp.
Research and Development Center,
Pittsburgh, Pa 15235
Assoc. Mem. ASME

Shi-Chune Yao
Assoc. Professor,
Department of Mechanical Engineering
Carnegie-Mellon University
Pittsburgh, Pa 15213
Mem. ASME

Turbulent droplet flow heat transfer is analyzed for the thermal entrance region of a circular tube. Calculations are performed considering droplet size variation, vapor acceleration and dilution of droplet number density until the single-phase fully developed conditions is reached. Effect of the relevant dimensionless groups on the heat transfer results is studied. The analytical results are compared with the available experimental data. These comparisons show good agreement between the experimental data and the predictions.

Introduction

There has been substantial development in the analytical ability to handle single pass flow heat transfer problems. However, the current understanding of the two-phase flow heat transfer is not mature enough to perform analysis with similar accuracy. Therefore, experimental techniques are still predominantly used to understand the two-phase flow heat transfer phenomena. Along with the experimental studies, there have been many attempts made to formulate the two-phase flow heat transfer in a complete and general form. These attempts usually result in large numbers of complicated equations due to interfacial phenomena between the phases.

One component two-phase flow and single phase flow heat transfer problems are generally similar in nature. When heat is transfered to these flows, both approach the same fully developed single-phase condition. Due to this similarity, analysis of two-phase flow heat transfer attracts many researchers. Koizumi, et al. [1] have analyzed turbulent droplet flow heat transfer by assuming that the flow field is one dimensional, and that the heat transfer occurs from wall to vapor, vapor to droplets and from wall to droplets. They used wall to vapor heat transfer coefficients given by the Dittus-Boelter correlation for the single phase flow. Although their analysis matches the experimental data with reasonable accuracy, this type of approach overlooks the coupling between the wall to vapor heat transfer, and the vapor to droplet heat transfer. The coupling between these mechanisms influences the thermal boundary layer, which is two-dimensional in nature.

In view of a more reasonable approach, authors have adopted a model which considers the evaporating droplets as distributed heat sinks in the flow field. Following this approach, the laminar flow heat transfer in the thermal entrance region of circular tubes has been studied by Yao [2] considering constant droplet size and constant droplet number density. This analysis has been extended by Rane and Yao [3] for constant droplet size, but decreasing droplet number density along the stream due to the evaporation of droplets in low pressure systems. A more complete investigation of the evaporating laminar droplet flow by Yao and Rane [4] explores the heat transfer behavior of such flows till all the droplets are evaporated and single phase flow conditions are reached.

In the present study, turbulent droplet flow heat transfer analysis is performed. When the thermal eddy diffusivity expression for the turbulent flow is changed to molecular thermal diffusivity, the problem formulation resembles the one presented in reference [4]. Also, when the evaporating droplets are not included in the formulation, it becomes a classical turbulent single phase heat transfer formulation. Hence, the analysis presented in this paper is general in nature. In the later sections, results generated from the analysis are compared with the experimental data. This comparison shows good agreement between the analytical and the experimental results, and hence the analytical model could be extended to handle other two-phase flow problems.

Model and Formulation

Generally dispersed flow is characterized by its high void fraction. In dispersed flow heat transfer, the vapor is superheated by the heat transferred from the hot wall, but the evaporating droplets are at saturation temperature. Since this one component two-phase mixture is in a thermally nonequilibrium state, the droplets evaporate and generate saturated vapor.

In the present study, one component two-phase flow in the post dry-out region is analyzed. The unique features of the physical model are stated in detail in the references [5, 6]. The assumptions made in the following formulation are:

1 negligible thermal radiative and droplet-wall contact heat transfer

2 monodispersed flow at the thermal entrance and strong radial mixing downstream. Therefore the droplet number density n is not a function of radius. Conductive heat transfers between vapor and small droplets.

3 high flow quality (>0.5) and constant fluid properties

4 The turbulent velocity and diffusivity radial variations are not affected by the presence of droplets.

The coordinate system used in the present study is shown in Fig. 1. The heat sink effect due to evaporating droplets is represented in

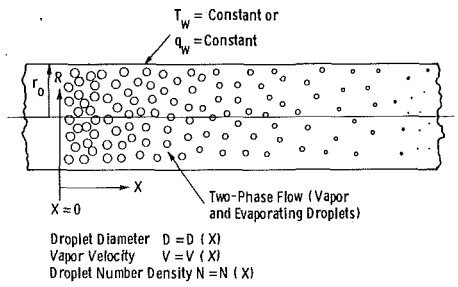

Fig. 1 A geometric and physical description of the droplet flow in the thermal entrance region of a circular tube

[1] This work was done when the author was with the Department of Mechanical Engineering, Carnegie-Mellon University, Pittsburgh, Pa 15213.

Contributed by the Heat Transfer Division for publication in the JOURNAL OF HEAT TRANSFER. Manuscript received by The Heat Transfer Division January 19, 1981.

terms of the heat transferred from the superheated vapor to the saturated droplets, and the heat required to heat up the generated vapor to the local vapor temperature.

Following the derivation in references [5, 6], the energy balance on a fluid element with this equivalent heat sink term gives the following energy equation for the vapor phase.

$$VU(r)\frac{\partial T}{\partial x} = \frac{1}{r}\frac{\partial}{\partial r}\left[e(r)r\frac{\partial T}{\partial r}\right] - \left[\frac{n\pi d^2 h_p}{\rho_v C_p}\right](T - T_s) \quad (1)$$

where $U(r)$ and $e(r)$ are the velocity and the diffusivity expressions. The initial and boundary conditions for this equation are

$$T = T_s \text{ at } x = 0 \quad (2)$$

$$\frac{\partial T}{\partial r} = 0 \text{ at } r = 0 \quad (3)$$

and

$$T = T_w \text{ at } r = r_0 \text{ for constant wall temperature} \quad (4)$$

or

$$k\frac{\partial T}{\partial r} = q_w \text{ at } r = r_0 \text{ for constant wall heat flux} \quad (5)$$

The mean vapor velocity V in equation (1) varies along the stream due to vapor generation from the evaporating droplets.

For a steady-state flow with small droplets, the number of droplets passing through any tube cross section is equal to the value at the tube inlet. Even after a droplet has been evaporated, an imaginary droplet with zero volume is still considered conceptually. Hence, assuming the same mean velocity for droplets and the vapor, the local mean velocity for the vapor can be related to the local droplet number density as follows.

$$Vn = V_0 n_0 \quad (6)$$

The variation in the droplet number density can be related to the change in the droplet size in the following manner:

$$\frac{1}{2}\rho_1 n\pi d^2 d(d) = -\rho_v \frac{dV}{V} \quad (7)$$

$$= -\rho_v \frac{dn}{n} \quad (8)$$

with the initial condition

$$n = n_0 \qquad \text{when } d = d_0 \quad (9)$$

Equation (8) can be solved using the initial condition given by (9) to obtain the following expression.

$$\frac{1}{n} = \frac{1}{n_0} + \frac{\pi}{6}\left[\frac{\rho_1}{\rho_v}\right](d_0^3 - d^3) \quad (10)$$

Assuming that the difference between the mean vapor velocity and mean droplet velocity is negligible for small droplets, and using $V = dx/dt$, the energy balance on a droplet gives the following equation.

$$-\frac{1}{2}\rho_1 h_{fg}\pi d^2 V\frac{dd}{dx} = \pi d^2 h_d(Tm - Ts) \quad (11)$$

with initial condition

$$d = d_0 \qquad \text{at } x = x_0 \quad (12)$$

where mean vapor temperature is used for the average heat transfer to a droplet. The variations of mean vapor velocity and droplet number density given by equations (6, 10), and (11) can be used to solve equation (1). These equations can be nondimensionalized and the resulting dimensionless equations are

$$[1 + A(1 - D^3)]U(R)\frac{\partial\theta}{\partial X} = \frac{1}{R}\frac{\partial}{\partial R} \times \left[E(R)R\frac{\partial\theta}{\partial R}\right] - S\left[\frac{D}{1 + A(1 - D^3)}\right]\theta \quad (13)$$

with initial and boundary conditions

Nomenclature

A = liquid loading parameter, defined as $\frac{\pi}{6}[n_0 d_0^3]\left[\frac{\rho_1}{\rho_v}\right]$

C = wall superheat parameter, defined as $\frac{C_p(T_w - T_s)}{h_{fg}}$ for constant wall temperature condition, as $\frac{C_p q_w r_0}{k h_{fg}}$ for constant wall flux condition

C_p = specific heat for vapor

d_0 = droplet diameter at the thermal entrance

d = droplet diameter or differential notation

D = dimensionless droplet diameter (d/do)

e = thermal diffusivity for turbulent flow

E = normalized thermal diffusivity for turbulent flow

h_{fg} = latent heat of evaporation

h_d = heat transfer coefficient for evaporating droplets

h_p = heat transfer coefficient for nonevaporating droplet or sphere

k = thermal conductivity of vapor

M_{l0} = liquid mass flow rate at the thermal entrance

M_{v0} = vapor mass flow rate at the thermal entrance

M_t = total mass flow rate, $(M_{v0} + M_{l0})$

n = droplet static number density

n_0 = droplet static number density at the thermal entrance

N = dimensionless droplet number density, (n/n_0)

Nu_∞ = fully developed Nusselt number for single-phase flow, $h2r_0/k$

Nu_x = local Nusselt number, defined as $\frac{2q_w r_0}{k(T_w - T_s)} = \frac{2}{\theta_w - \theta_m}$ for constant heat flux condition, as $\frac{2q_w r_0}{k(T_w - T_m)} = \frac{2}{1 - \theta_m}$ $\left.\frac{\partial\theta}{\partial R}\right|_{R=1}$ for constant temperature condition

Pr = Prandtl number for vapor, $\frac{\mu C_p}{k}$

q_w = wall heat flux

r = radial coordinate

r_0 = radius of circular tube

R = dimensionless radial coordinate (r/r_0)

Re = Reynolds number for single phase flow

Re_0 = vapor Reynolds number at the thermal entrance, $\frac{2\rho_v V_0 r_0}{\mu}$

Re_∞ = vapor Reynolds number for fully developed droplet flow, $(1 + A)\mathrm{Re}_0$

S = heat sink parameter, defined as $\pi n_0 d_0 r_0^2\left(\frac{h_p d_0}{k}\right)$

t = time

T = vapor temperature

T_m = vapor bulk mean temperature $\frac{2}{r_0^2}\int_0^{r_0} TU(r)rdr$

T_s = saturation temperature

T_w = wall temperature

u = local time mean axial velocity, is a function of r and x

U = dimensionless axial velocity, (u/V)

V = mean vapor velocity, is a function of x only

V_0 = mean vapor velocity at the thermal entrance

x = axial coordinate

X = dimensionless axial coordinate, $(x/r_0)/\mathrm{Re}_0\mathrm{Pr}$

θ = dimensionless vapor temperature, defined as $\frac{T_w - T_s}{T_w - T_s}$ for constant wall temperature condition, $\frac{k(T - T_s)}{q_w r_0}$ for constant heat flux condition

θ_m = dimensionless vapor bulk mean temperature, $2\int_0^1 \theta U(R)RdR$

θ_w = dimensionless wall temperature

μ = dynamic viscosity of vapor

ν = kinematic viscosity of vapor

ρ_1 = liquid density

ρ_v = vapor density

$$\theta = 0 \quad \text{at } X = 0 \tag{14}$$

$$\frac{\partial \theta}{\partial R} = 0 \quad \text{at } R = 0 \tag{15}$$

and

$$\theta = 1 \quad \text{at } R = 1 \text{ for } T_w = \text{constant} \tag{16}$$

or

$$\frac{\partial \theta}{\partial R} = 1 \quad \text{at } R = 1 \text{ for } q_w = \text{constant} \tag{17}$$

where the dimensionless droplet size D is determined by solving equation (11) using equation (12), which takes the following nondimensional form.

$$D[1 + A(1 - D^3)]\frac{dD}{dx} = -\frac{2S}{3A}\left[\frac{\theta_m}{\frac{1}{C} + \theta_m}\right] \tag{18}$$

with initial condition

$$D = 1 \quad \text{at } X = 0 \tag{19}$$

The dimensionless velocity expression $U(R)$ and the thermal diffusivity expression $E(R)$ are derived from expressions suggested by Deissler [7], and are outlined in reference [5].

A finite difference scheme with marching technique was used to solve the set of equations. The details of the grid system and the numerical calculations are presented by the author in references [5] and [6]. The numerical results are presented and discussed in the following sections.

Results and Discussion

Turbulent Droplet Flow Heat Transfer. The present heat transfer analysis for turbulent single phase flow in the thermal entrance region shows good agreement with the investigations and experimental data reported in literature [7–9]. The details are presented in the reference [6].

The turbulent droplet flow heat transfer results were obtained parametrically for both constant wall heat flux and constant wall temperature condition considering droplets size variation. For laminar flow, the heat transfer results are independent of Reynolds and Prandtl numbers when axial heat conduction is neglected, while for turbulent flow, heat transfer results are influenced by both Reynolds and Prandtl numbers.

As identified in the literature [3, 6], dispersed flow heat transfer depends strongly on three dimensionless groups, which are heat sink parameter, S, liquid loading parameter, A, and wall superheat parameter, C. All of these parameters are evaluated at the thermal entrance. When heat is transferred to the dispesed flow, the liquid evaporates and the flow eventually becomes single phase flow. Hence, if the inlet vapor Reynolds number is Re_0 and the liquid loading is A at the thermal entrance, then the Reynolds number for the resulting single phase flow (Re_∞) is given by

$$\mathrm{Re}_\infty = (1 + A)\mathrm{Re}_0 \tag{20}$$

This resulting single phase Reynolds number (Re_∞) is fixed at 2.0×10^5, in our parametric study, to maintain a constant mass flow rate, and the effect of the dimensionless groups S, A, and C is studied for $\mathrm{Pr} = 0.7$.

(*a*) *Constant Wall Heat Flux.* The droplet diameter variation is generally parabolic in nature. For high S values, the droplet diameter D reduces rapidly due to the high degree of liquid dispersion. The droplet diameter variations for different values of the wall superheat parameter C indicate that low wall heat flux reduces the rate at which the droplets evaporate. Figure 2 shows the effect of the liquid loading parameter A on the droplet size variation which is consistent with the expected behavior.

For the region in which the droplet flow has reached single phase, and the resulting single phase flow has reached fully developed conditions, the mean vapor temperature can be written as

$$2\pi r_0 q_w = (M_{v0} + M_{l0})C_P(T_m - T_s) + M_{l0}h_{fg} \tag{21}$$

This equation can be nondimensionalized and expressed as

$$\theta_m = (4CX - A)/C(1 + A) \tag{22}$$

For single phase flow, the liquid loading parameter A is equal to zero, and the above relationship reduces to

$$\theta_m = 4X \tag{23}$$

Equation (22) gives a family of straight lines for various values of A and C. Substituting equation (22) in the definition of Nu_∞ we obtain

$$\theta_w = \frac{2}{\mathrm{Nu}_\infty} + \left[\frac{4CX - A}{C(1 + A)}\right] \tag{24}$$

This equation can be rearranged and expressed as follows

$$\theta_w = \left[\frac{4}{\mathrm{Re}_\infty \mathrm{Pr}}\right]\left[\frac{x}{r_0}\right] + \left[\frac{2}{\mathrm{Nu}_\infty} - \frac{A}{C(1 + A)}\right] \tag{25}$$

Here, Nu_∞ is the fully developed Nusselt number for a single phase flow with Reynolds number Re_∞ and Prandtl number Pr.

Equation (25) confirms that for the resulting fully developed single phase flow, the slope of the wall temperature variation remains unchanged irrespective of whether the original flow is single phase or two-phase as long as the mass flow rate is the same. The differences occur in the intercepts of these asymptotic straight lines on the θ_w axis. These intercepts are function of Nu_∞, A and C.

Generally for large S values, or for large degree of liquid dispersion, the heat sink effect is strong and the wall temperature at a given axial location is low. When A and C are held constant, all the curves merge to a straight line given by equation (25) sooner or later depending upon whether S is large or small, respectively. The effect of the liquid loading parameter A on the wall temperature variation is shown in Fig. 3. For high liquid loading, the wall temperature rises to a high value and then approaches a straight line given by equation (25) with a dip in between. This drop in wall temperature occurs approximately in the same region where droplet size is reducing relatively fast, that is just before they evaporate completely. The dashed lines are just the extension of the final straight lines to indicate the same slope as single phase results. The effect of wall superheat parameter C is also important. In the region where droplets are evaporating, the wall temperature is insensitive to changes in C. But the effect of C is strong in the region where droplets are completely evaporated, which one would expect by inspecting equation (25). In droplet flow heat transfer at constant wall heat flux, the linear rise in wall temperature is delayed and this delay can be quantified with the help of equation (25).

The local Nusselt numbers Nu_x for different values of S and A are presented in Figs. 4 and 5. At a fixed value of Re_∞, the local Nusselt numbers for single phase flows with various Re_0's are also shown in

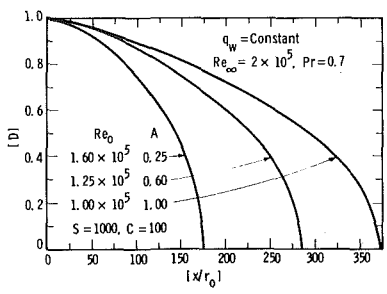

Fig. 2 Variation of droplet diameter in the thermal entrance region with constant wall heat flux: $S = 1000$; $A = 0.25, 0.6, 1.0$; $C = 100$

these figures. For any case, Re_0 can be obtained from equation (20) once the value of A is fixed. Figure 4 shows curves for different values of S. The local Nusselt numbers are large for large values of S in the region where two-phase flow exists. The effect of liquid loading on the local Nusselt numbers is shown in Fig. 5 for various values of A. Generally, heat transfer to the turbulent droplet flow is enhanced compared to the single phase flow heat transfer with the same Re_0 in the thermal entrance region of a circular tube.

(*b*) *Constant Wall Temperature.* In general, the results for turbulent droplet flow heat transfer at constant wall temperature are similar to those for constant wall heat flux. The detail heat transfer results for this case are given in the author's thesis [6]. The local Nusselt number calculations show that if the degree of liquid dispersion, S, is increased keeping all other parameters unchanged, the local Nusselt number increases. When droplets are present in the flow field, the local Nusselt numbers are always higher than those for single phase flow with the same inlet vapor Reynolds number Re_0.

Figure 6 shows the variation of the mean vapor temperature in the thermal entrance region for different values of S. The arrows show the locations where droplets are completely evaporated. For high S values, the mean vapor temperature increases slowly due to fine dispersion of liquid. But, as soon as all the liquid is evaporated completely, the mean vapor temperature rises sharply and approaches the curve for single phase flow with the same mass flow rate.

Comparison with the Experimental Data. Many experimental investigations have been performed in the past to study the dispersed flow heat transfer. The experimental data available in the literature is abundant. Since most of these studies do not report all of the information vital to the comparison between the experimental data and the present results, the data reported by Koizumi, et al. [1], and Forslund and Rohsenow [10, 11] was selected because it was the most complete. The data reported by Koizumi, et al., contains important information such as droplet size distribution and liquid loading at the thermal entrance, but this information does not extend to large axial distances where droplets evaporate completely. On the other hand, experimental data obtained by Forslund and Rohsenow [11] contains information for large axial distances. However, these authors do not report droplet size distribution and liquid loading at the thermal entrance.

The experimental data reported in the literature [1, 11] and the corresponding parameters for the present analysis are given in Table 1. In the experiments performed by Koizumi, et al. [1], there was always a wet tube region upstream of the dryout zone. Since the present calculations for the turbulent droplet flow heat transfer start at the dryout point, the starting point of the dryout zone is identified by the sharp rise in the wall temperature. The data from Koizumi, et al.'s having a wall heat flux of 7.14×10^4 w/m^2 was selected for comparison. Figure 7 shows the comparison between the data, the present analysis with droplet size variation, and author's previous work [5, 6] considering constant droplet size. This comparison shows good agreement between the data and the present analyses.

Forslund and Rohsenow [11] obtained data from dispersed flow film boiling of nitrogen in a vertical tube. To find suitable experimental runs to compare with the present analysis, the mean droplet size, liquid loading, and fluid properties at the thermal entrance are necessary. For comparison with Forslund and Rohsenow's [11] data, the liquid loading at the thermal entrance is estimated from the reported wall heat flux and exit equilibrium quality using an energy balance. Runs 259, 262, and 282 were selected for comparisons, because they have the lowest liquid loadings at the thermal entrance among all the reported runs. Forslund and Rohsenow estimated the mean droplet size at the thermal entrance using visual studies along with the droplet break-up and the droplet heat transfer mechanisms. Due to the un-

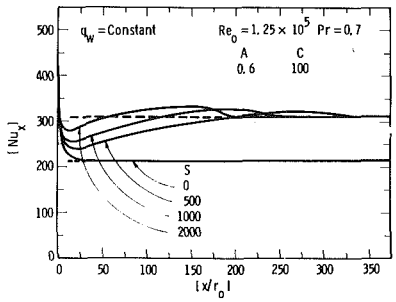

Fig. 4 Variation of local Nusselt number in the thermal entrance region with constant wall heat flux. S = 500, 1000, 2000; A = 0.6; C = 100

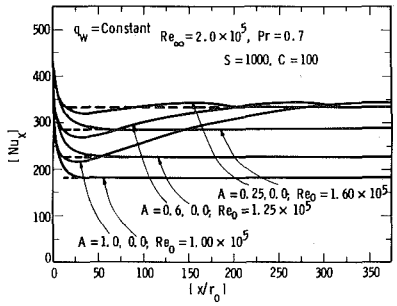

Fig. 5 Variation of local Nusselt number in the thermal entrance region with constant wall heat flux: S = 1000; A = 0.25, 0.6, 1.0; C = 100

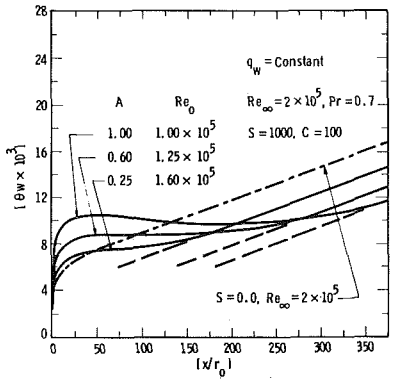

Fig. 3 Variation of wall temperature in the thermal entrance region with constant wall heat flux: S = 1000; A = 0.25, 0.6, 1.0; C = 100

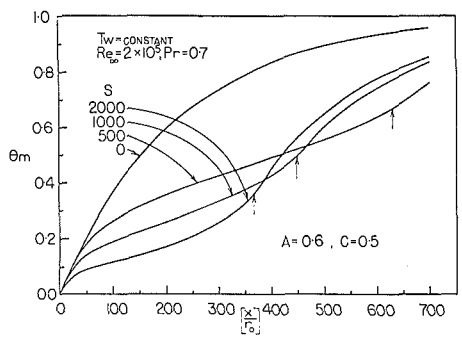

Fig. 6 Variation of mean vapor temperature in the thermal entrance region with constant wall temperature: S = 2000, 1000, 500; A = 0.6; C = 0.5

Table 1 Basic parameters for comparison with the experimental data

Koizumi, Ueda and Tanaka's [1]. Experimental Data for R-113

Experimental Data Tube radius r_0 = 5 mm					Corresponding Parameters for Present Analysis					
P_s bar	q_w W/m^2	M_{l0} kg/hr	M_{v0} kg/hr	d_0 μm	Re_0	Re_∞	Pr	S	A	C
3.08	*8.41×10^4*	*86.3*	*165*	*30*	*5.1×10^5*	*7.8×10^5*	*0.8*	*2615*	*0.523*	*207*

Forslund and Rohsenow's [11]. Experimental Data for Nitrogen

Experimental Data Saturation pressure P_s = 1.694 bar					Corresponding Parameters for Present Analysis					
Run No.	r_0 mm	q_w W/m^2	M_t kg/hr	M_{l0}/M_{v0} estimated	Re_0	Re_∞	Pr	S	A	C
259	4.1	4.9×10^4	18.2	7.2	1.67×10^4	1.37×10^5	0.84	2000	7.2	153
262	4.1	1.6×10^4	18.2	7.6	1.59×10^4	1.37×10^5	0.84	625	7.6	49
282	2.9	3.3×10^4	9.0	7.3	1.15×10^4	9.50×10^4	0.84	1100	7.3	72

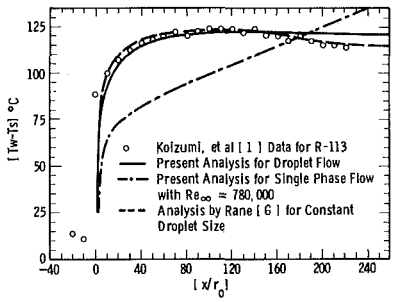

Fig. 7 Comparison of wall temperatures in the thermal entrance region with Koizumi, et al.'s [1] experimental data. Re_∞ = 780,000; S = 2615; A = 0.523; C = 207

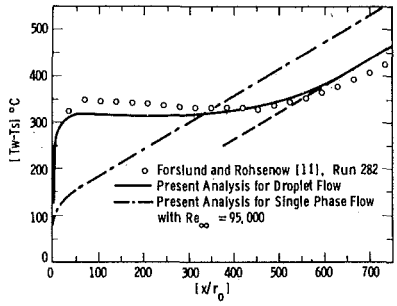

Fig. 8 Comparison of wall temperatures in the thermal entrance region with Forslund and Rohsenow's [11] experimental data. Re_∞ = 95,000; S = 1100; A = 7.3; C = 72 (Run 282)

certainty associated with these estimations, the mean droplet sizes at the thermal entrance are re-evaluated in the present analysis. Calculations have been made for reported values of C, A, Re_0, Pr. The most appropriate heat sink parameter S which agrees with the experimental data is determined from a range of initial droplet size. The relevant experimental data and the corresponding values of the parameters used in the present calculations are presented in Table 1.

Figures 8 and 9 show the comparison between the measured wall temperatures and those predicted by the present analysis for Runs 282, and 259, respectively. These curves finally merge to a straight line given by equation (25). In these figures, the wall temperature variation for single phase flow with the same mass flow rate M_t is also shown. These solid straight lines are extended by dashed lines to show that they are parallel to the straight line for the corresponding single phase flow. In general, these figures show favorable agreement between the measured and the predicted wall temperatures.

For Run 282, the results show that all the droplets are completely evaporated which was also observed in their experiment (i.e., "few fine droplets"). The experimental results for Run 262 are predicted very well for $(x/r_0) > 200$ [6]. In the region $0 < (x/r_0) < 200$, the wall temperatures are overpredicted. This may be due to the liquid contact with the wall, because, here, the liquid loading is highest and at the same time the wall heat flux is the lowest among the selected three runs. For this run, Forslund and Rohsenow [11] observed droplets present in the flow at $(x/r_0) = 600$, and similar prediction has been made by the present analysis. The experimental results for Run 259 are predicted accurately for all (x/r_0)'s. Again, their observation of "few fine droplets at the tube exit, barely detectable" is consistent with the present prediction.

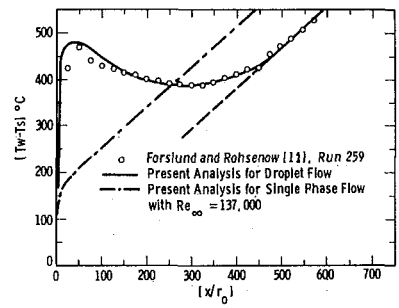

Fig. 9 Comparison of wall temperatures in the thermal entrance region with Forslund and Rohsenow's [11] experimental data. Re_∞ = 137,000; S = 2000; A = 7.2; C = 153 (Run 259)

Conclusions

From the present study and the author's previous work [3–6] it is evident that dispersed flow heat transfer in circular tubes can be calculated accurately using the distributed heat sink approach where the heat sink accounts for the droplet heat transfer in the superheated vapor stream. It is also important to point out that this approach can be used to analyze droplet flow heat transfer in other application areas with reasonable degrees of confidence. This method of analyzing one-component dispersed flow heat transfer problems forms the basis of a generalized theory of convective heat transfer, where single phase heat transfer analysis becomes a special case of this more general formulation.

References

1 Koizumi, V., Ueda, T., and Tanaka, H., "Post Dryout Heat Transfer to R-113 Upward Flow in a Vertical Tube," *International Journal of Heat Mass Transfer*, Vol. 22, May 1979, pp. 669–678.

2 Yao, S. C., "Convective Heat Transfer of Laminar Droplet Flow in Thermal Entrance Region of Circular Tubes," ASME JOURNAL OF HEAT TRANSFER, Vol. 101, No. 3, 1979, pp. 480–483.

3 Rane, A., and Yao, S. C., "Heat Transfer of Evaporating Droplet Flow in Low Pressure Systems," The Canadian Journal of Chemical Engineering, Vol. 58, June 1980 pp. 303–308.

4 Yao, S. C., and Rane, A. G., "Heat Transfer of Laminar Mist Flow in Tubes," ASME JOURNAL OF HEAT TRANSFER, Vol. 102, No. 4, Nov. 1980, pp. 678–683.

5 Yao, S. C. and Rane, A. G., "Numerical Study of Turbulent Droplet Flow Heat Transfer," ASME Winter Annual Meeting, Paper No. 80-WA/HT-48, Nov. 1980 (accepted for publication in *International Journal of Heat Mass Transfer*).

6 Rane, A. G., "Dispersed Flow Heat Transfer in Circular Tubes," Ph.D. Thesis, Carnegie-Mellon University, May 1980.

7 Deissler, R. G., "Analysis of Turbulent Heat Transfer, Mass Transfer, and Friction in Smooth Tubes at High Prandtl and Schmidt Numbers," National Advisory Committee for Aeronautics, NACA Report 1210, Washington, D.C., 1955.

8 Sparrow, E. M., Hallman, T. M., and Seigel, R., "Turbulent Heat Transfer in the Thermal Entrance Region of a Pipe with Uniform Heat Flux," *Applied Science Research*, Ser. A, Vol. 7, 1957, pp. 37–52.

9 Wolf, H., and Lehman, J., Private Communication by reference [11], Project Squid Research, *Jet Propulsion Center*, Purdue Univesity.

10 Forslund, R. P., and Rohsenow, W. M., "Dispersed Flow Film Boiling," ASME JOURNAL OF HEAT TRANSFER, Nov. 1968, pp. 399–407.

11 Forslund, R. P., and Rohsenow, W. M., "Thermal Non-Equilibrium in Dispersed Flow Film Boiling in a Vertical Tube," MIT Report No. 75312-44, Nov. 1966.

Steam Condensation on Various Gold Surfaces

D. W. Woodruff[1]

J. W. Westwater
Mem. ASME

Department of Chemical Engineering,
University of Illinois,
Urbana, Ill. 61801

Gold surfaces were investigated as promoters of dropwise condensation (DWC) of steam at atmospheric pressure. Very high heat fluxes at low ΔT's may be achieved in this manner. Seven gold electroplating baths, one electroless immersion gold bath, and vacuum vapor deposition of gold were used. Five surface preparations for pure gold were tested. Gold deposits ranged in thickness up to 20,000 A.U. Auger electron spectroscopy and scanning electron microscopy were used to describe the surfaces chemically and physically.

Deposits from the bright pure gold plating baths and the "acid, hard" baths promoted DWC. Deposits from alloyed baths, the ultrapure bath, and vapor deposition gave mixed or filmwise condensation. Two surface preparations on solid gold gave DWC, one gave mixed, and two gave filmwise condensation. The results indicate that gold provides an oxide-free surface which adsorbs trace organics from the surroundings. These promote DWC.

Introduction

Dropwise condensation of steam has been a subject of study for fifty years [1]. For all but the last fifteen, the standard method of promotion has been the application of a promoting agent, typically an organic substance which lowers the surface energy of the condensing surface. These organic-type promoters have the inherent disadvantage of washing off the surface rather rapidly.

Since 1965, gold (and other noble metals) have been praised as surfaces for dropwise condensation [2–6]. No organic promoter need be added to the gold. Gold surfaces have the advantages of permanence, high thermal conductivity, and resistance to corrosion. The cost disadvantage can be kept to a minimum by depositing very thin layers of the gold onto the condenser surface. Previous work by the present authors [7] showed the dependence of the mode of condensation on the thickness of the promoting gold electrodeposit. It was shown that a 1000 A.U. deposit (the equivalent of 500 layers of gold atoms) from a proprietary gold-sulfite plating bath was required to produce dropwise condensation of steam.

It is known that electrodeposits of the same material can have widely different properties depending on the composition of the electroplating bath and the various electroplating parameters (current, substrate geometry, agitation rate, etc.). The object of this experimental study [8] was to investigate various types of gold electroplating baths and the ability of their respective electrodeposits to promote dropwise condensation. A major point of interest was whether or not 1000 A.U. deposits from all these baths would promote dropwise condensation. In addition, vapor deposition was used as an alternate method of deposition. As an additional experiment, a sample of pure, solid gold was also tested for mode of condensation using various surface cleaning techniques prior to condensation.

In support of this program, Auger Electron Spectroscopy (AES) and Scanning Electron Microscopy (SEM) were used to study the condenser surfaces. AES gives the analysis of the chemical elements in a surface layer (approximately the top 10 A.U.). It is a powerful analytical tool for phenomena involving surface properties. It has one drawback in that it does not show whether elements are present as chemical compounds or as free elements. The present study is the first to use AES to gain an insight into dropwise condensation.

Background

Since 1965, gold layers have been considered as promoters for dropwise condensation. Erb [3] first described its use in a study of metal sulfides as promoters. In this study, silver was observed to be a better promoter than its sulfide. This led to the investigation of gold and other noble metals, which were subsequently found to promote dropwise condensation. In the same year Umur and Griffith [9] reported the use of a gold deposit to prevent corrosion of their condenser surface. It was found that this gold-plated surface needed no added organic promoter in their system, and they attributed this behavior to organic contamination in their system.

Since that time a number of investigators have used gold deposits as promoters. Erb and co-workers published a number of papers [2–6, 10–12] in support of gold as a promoter. Tower and Westwater [13] used a gold-promoted system in their study of the effect of condenser surface inclination. Wilkins, Bromley, and Read [14] showed results which have made promotion by gold questionable. In their tests, a pure, gold tube and a gold-plated tube did not exhibit dropwise condensation. They claimed that their system was simply cleaner than others whose systems were dropwise. Since that time, a number of authors have also observed dropwise behavior on gold [7, 8, 15, 16, 17].

It is interesting to note that a parallel disagreement exists among physical chemists concerning the appropriate contact angle of water on a clean, gold surface. Claims have centered around inferred cleanliness, but with no actual surface cleanliness measurements until recently. Reference [8] gives a review of this dispute.

Experimental

Condensation tests were performed on the flat circular face of a copper test piece, see Fig. 1(c). A careful surface preparation was used to get "clean" surfaces. The face was polished first to a mirror finish, using silicon-carbide abrasive paper followed by three grades of polishing alumina suspended in deionized water. The final polish was with 0.05 μm grade. The polishing was done on a variable-speed polishing wheel using Buehler Microcloth.

To remove all machining oils and all finger oils, the test piece next

[1] Present address: General Electric Company, Schenectady, New York.

Contributed by the Heat Transfer Division and presented at the National Heat Transfer Conference, Milwaukee, Wis., August 1981. Manuscript received by the Heat Transfer Division 22 July 1981. Paper No. 81-HT-15.

underwent vigorous cleaning procedure. It was soaked in ethylene dichloride, followed by a soak in methanol. Next it was soaked in a boiling alkaline bath, followed by a rinse of deionized water. Next, the piece was cleaned cathodically in another alkaline bath, and then rinsed copiously with deionized water.

In order to maintain similarity to the earlier work [7], the piece was again polished, but this time clean cotten gloves were used to avoid finger oil contamination. Between the soak in ethylene dichloride and the electron microscope work, the test pieces were not touched by human hands.

After the final 0.05 μm polish, the sample was rinsed in deionized water and placed immediately in the electroplating cell. This was a Teflon cell which held approximately 50 ml of gold-plating solution. The cathode (copper test piece) and the stainless steel anode were approximately 5 cm apart, and the solution was stirred by a magnetic, Teflon-coated stirring bar.

The control of the plating thickness was accomplished by plating at the appropriate current while observing the output of a stripchart recorder monitoring the output of a current integrator. When the output reached the level indicating the appropriate thickness, the circuit was broken. The time of current flow was recorded on a stopwatch, and the current was recorded as well. The product of measured current and time agreed quite closely with the current flow measured with the current integrator. At the completion of plating, the cell was disassembled and the test piece removed and rinsed. It was immediately mounted in the condensing cell.

The thickness was one of the variables observed. The other was the nature of the plating bath. Eight different baths were used in this study. They are described below and briefly in Table 1, as communicated by the manufacturer.

Bath A was the same sulfite bath used in the earlier study [7]. It contained gold sulfite as the gold salt, and sodium sulfite as the conducting salt, with the sodium salt of arsenic oxide in minute concentration as the brightener. No organic compounds were present in this bath.

The role of a brightener in an electroplating bath is to produce a shiny, mirror-like surface. The mechanism is unknown, but brighteners may be likened to surface active agents which improve the spread of gold on the base metal. Bath B was a cyanide bath that contained no brightener. It produced a pure, satin-bright deposit.

Bath C was a cyanide bath brightened with cobalt. Bath D was quite similar, but was brightened with nickel. Both were considered acid baths, producing bright, hard deposits.

Bath E was a solution of the purest gold potassium cyanide available, with potassium cyanide, phosphate, and carbonate as conducting salts. It contained no brighteners, and produced a pure, dull gold deposit.

Bath F was one which contained silver an an alloying metal. This was a cyanide bath, and produced a bright deposit.

Bath G was heavily alloyed with copper and cadmium and was cyanide based as well. Deposits were stated to be approximately 65 percent gold, 25 percent copper, and 10 percent cadmium.

Bath H was an electroless immersion bath, that is, no external electrical current was supplied to drive the deposition. The test piece was simply immersed into a beaker of the bath for the appropriate length of time. The maximum thickness obtainable was approximately 1000 A.U. after about 15 minutes immersion, according to the manufacturer.

In addition to the eight electroplating preparations, the method of vapor deposition was also used. After the test piece was polished, cleaned, and rinsed, it was taken immediately to facilities for vapor deposition in a nearby campus laboratory. This deposition was performed in an evacuated bell jar using 100 percent pure gold wire heated in a tungsten wire boat as the vapor source. The sample was stationary almost directly below the hot source. Upon completion of deposition, the sample was immediately returned for condensation tests.

Beside these tests of thin, gold deposits on polished, copper substrates, five tests were performed on a pure, solid-gold test piece, 6.35 mm thick. Five different cleaning techniques were tested. The first was the alkaline cleaning described previously for the copper test pieces. The specimen was handled identically through the electrolytic cleaner and the final 0.05 μm polish. It was then rinsed and placed immediately in the condensing cell.

The second treatment was a plasma cleaning technique. The gold sample was prepared as above through the second fine polish and rinse. It was then rinsed in methanol, dried, and placed in a plasma cleaning apparatus. A vacuum was applied and a voltage applied which created the plasma (ionized oxygen). This atmosphere is very reactive and should burn off all organic molecules. The piece was cleaned in this manner for approximately four and one-half hours. At the completion, the test piece was removed and taken immediately to the condensation cell.

For the third treatment, the sample was dipped in full strength aqua regia (1 part nitric acid, 2 parts hydrochloric acid) twice, for about 1 second each dip, and then was immediately rinsed and placed in the condenser.

The fourth cleaning was a high-temperature heat treatment. The gold sample was cleaned through the second fine polish and rinsed. It was rinsed in methanol and dried. The sample was then placed in an electrically heated furnace at 866 K in air to oxidize any organics present. After one hour the sample was removed with gold-plated forceps and quenched immediately in deionized water. It was immediately placed in the condensing cell.

Heat Treatment II (the fifth method) was similar to the previous method except that after the final polish and rinse, the sample was polished on a clean piece of Microcloth using only deionized water, but no alumina polish. This was done to remove any entrapped alumina from the surface. This was followed by a heat treatment as described above.

Following any particular preparation, the test piece was placed in the condensing cell for heat transfer tests. The condensing cell is shown in Fig. 1(b). It was nearly identical to that used previously [7] except for minor modifications to accommodate the new test piece geometry.

Steam was provided at atmospheric pressure from a four liter stainless steel boiler heated with two 400 W immersion heaters. Steam was delivered to the condensing cell via flexible stainless steel hose. Excess steam exited to an auxiliary condenser where it was condensed and measured. The condensate from the test condenser was collected through a U-tube exit which prevented back-up of air into the system. The system was "once-through", with boiling makeup water added to the boiler as needed and condensate lines going to the drain. The entire set-up was well insulated with glass wool.

Teflon gaskets were used throughout, so the steam was in contact with only stainless steel, Teflon, glass, and the gold-copper test piece. The entire apparatus was thoroughly cleaned with a hot alkaline bath similar to that used for the test pieces. Special effort was taken to avoid any organic contamination of this system. The steam system is shown in Fig. 1(a).

Heat transfer measurements included the steam temperature, the two condensate flow rates, the cooling water flow-rate, the cooling water temperatures at the cooling chamber inlet and outlet, and the temperature at 1.59 mm from the rear in the test piece. These data allowed two calculations of heat flux (condensate and cooling water) and extrapolation to calculate the surface temperature.

The heat transfer experiments took place immediately after surface preparation of the various samples. The samples were always put into

Nomenclature

The thickness of electroplated deposits are given in Angstrom units (A.U.) in this paper. This is useful, because the gold atom has a dia of 2 A.U. Note that 1 A.U. = 10^{-10} m.

flowing steam. Data were taken after four to five hours of continuous condensation. During this waiting period, photographs were taken of the condenser surface to record the progress of the promotion of dropwise condensation. After photography was completed, the cell window was insulated and heat transfer data were recorded. Runs were made in order of increasing ΔT by increasing the cooling water flowrate.

At the completion of the run, the test piece was removed from the system and was stored in a covered pyrex culture dish. The pieces were stored for a period of days to weeks before the Auger surface analysis was performed, followed by the electron microscopy. Auger spectra were taken at three positions (minimum) on each sample.

Auger Electron Spectroscopy. Auger Electron Spectroscopy (AES) requires that the solid sample be placed in a chamber with a ultrahigh vacuum ($\sim 10^{-9}$ torr). The sample is excited by an impinging electron beam of typically 5keV. Due to the interactions of this beam with the surface atoms, a fraction of the electrons which leave the surface have discrete energies which are identified with the atom of their origin. These Auger electrons are created in the sample as deep as the electron beam penetrates (on the order of microns), but because the returning electrons also interact with the solid substrate atoms, only the very top Auger electrons keep their chemical identity. The

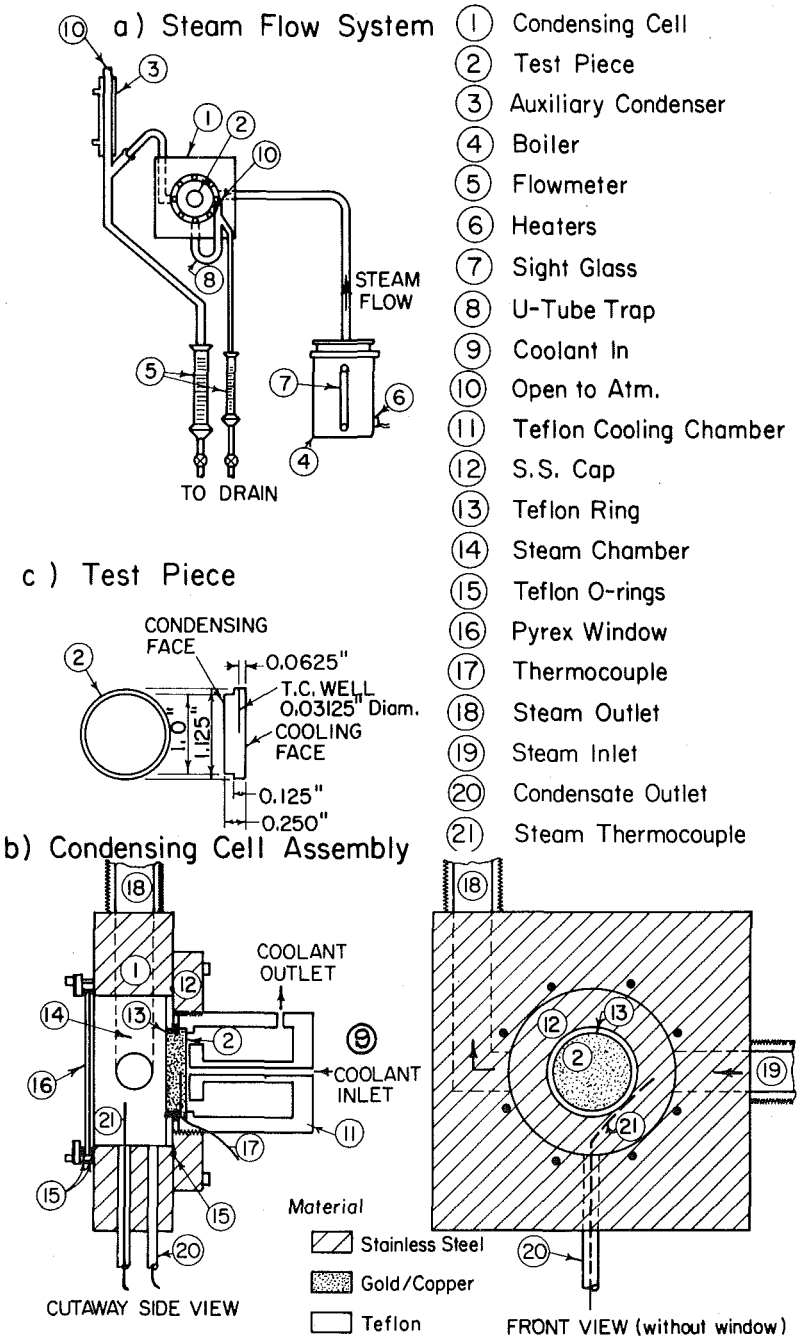

Fig. 1 Sketch of condensation test apparatus

result is a number of electrons with discrete energies from the topmost layer of the substrate, typically the top 10 A.U. These have a low count compared to the background continuum of electrons, so the signal is electronically differentiated to enhance the signal. Thus, an Auger spectrum is a plot of dN/dE versus Electron Energy, where N is the number of electrons with energy E. The position of the peak identifies the source atom. For example gold has an important peak at 2028 eV, whereas silver has one at 356 eV. The concentration of an element is determined by the height of its peak. Auger electron spectroscopy is non-destructive, and the sample is recovered unaltered.

Presentation of Results

The results of the heat transfer experiments are presented in Fig. 2. Figure 2(a) includes the heat flux curves for the baths which gave deposits that promoted dropwise condensation satisfactorily. These are Baths A–D. The dashed lines for the 900 A.U. deposit from Bath A indicate that transitions between dropwise and filmwise condensation occurred with this thickness as the cooling water flow rate was altered. The results with the pure, solid-gold test piece are also presented in Fig. 2(a). Deposits from Baths E–H, and from the vapor deposition are presented in Fig. 2(b). These promoted only partial dropwise (mixed) condensation, or did not promote dropwise condensation even for their thickest deposits. The dropwise area from Fig. 2(a) is the shaded region in 2(b) included for comparison.

Figure 2 demonstrates the attraction of dropwise condensation. The heat fluxes are very high, even at low ΔT. For example at ΔT =3K, the highest flux for dropwise condensation is 380 kW/m^2. For filmwise condensation at ΔT = 3K, the flux is about 25 kW/m^2.

Figure 3 shows photographs of progression of promotion during the 3.6 hours from the start of condensation; in Fig. 3(a) are photographs for the 2000 A.U. deposit from Bath A. In every test which showed dropwise condensation, the promotion always began at the edge and progressed steadily inward. In Fig. 3(a), the heat transfer coefficient was 26 kW/m^{2}K, and in Fig. 3(d) it had increased to 74. The rate of advance of the promoted areas and the pattern of dropwise and filmwise areas varied from bath to bath.

Figure 4 presents photographs of the mode of condensation on the thickest deposit tested from each of the plating baths and the vapor deposition tests. These were each taken at approximately 3.5 hours into the test. At the completion of the heat transfer test of the 1000 A.U. deposit from Bath B, the surface demonstrated 100 percent dropwise condensation. The final conversion occurred after insulation was put over the window and the heat transfer data were recorded. In Fig. 4, the best performance is for Fig. 4(c), which had a heat flux of 471 kW/m^2 at a ΔT of 3.2 K. The poorest is Fig. 4(g) with a flux of 326 at 28.9 K.

The five tests on the pure, solid-gold test piece are shown in Fig. 5. When prepared by alkaline cleaning or the plasma cleaning techniques, the surface supported dropwise condensation. The acid treatment and the two heat treatments resulted in filmwise condensation, although the second heat treatment had a small amount of dropwise condensation on the edges. In Fig. 5, the best results are for Fig. 5(a) with a flux of 356 kW/m^2 at a ΔT of 4.6 K. The worst are for Fig. 5(d) with a flux of 292 at a ΔT of 27 K. Table 2 presents an overview of these results, with plating bath, deposit thickness, and mode of condensation.

A typical Auger spectrum taken from the 1000 A.U. deposit from Bath A is presented in Fig. 6. This was taken after condensation tests were completed. The main spectral lines of the major components are labeled gold, copper, carbon, and oxygen. The major peaks are marked by asterisks, and the computed concentrations are indicated as atomic percentages. These concentrations are calculated from the peak heights using the knowledge of the machine sensitivities and the elemental sensitivities taken from Reference [18]. A different multiplier is needed for each element.

Figure 7 was constructed by plotting the surface analysis for gold, copper, oxygen, and carbon for all tests with the eight baths, the vapor deposits, and the pure, solid-gold specimens. The data points for carbon are shown. The data points for the other elements are omitted for clarity; they have scatter similar to the scatter for carbon. Figure 7 shows the heat transfer coefficient h, at ΔT = 8.3 K.

A strong correlation exists between the heat transfer performance and the surface composition. The predominance of gold and carbon at the expense of copper and oxygen on the surface favor the occurence of dropwise condensation. This same trend was observed when mixed condensation was observed. The Auger analysis at positions which

Table 1 Gold plating baths used in this study

Bath	Descriptor	Gold Electrolyte	Brightener	Trade Name[1]
A	Sulphite	Sulfite	Arsenic	Techni-Gold 25
B	Pure, satin-bright	Cyanide	None	Orotemp 24
C	Cobalt-brightened	Cyanide	Cobalt	Orosene 999
D	Nickel-brightened	Cyanide	Nickel	Orotherm HT
E	Pure, dull	Cyanide	None	Industrial 24 K
F	Silver-alloyed	Cyanide	**	HG Gold
G	Cu/Cd/Ag-alloyed	Cyanide	**	Oroclad
H	Electroless	Cyanide	**	Oromerse BR

[1] All baths manufactured by Technic, Inc.
** No information given

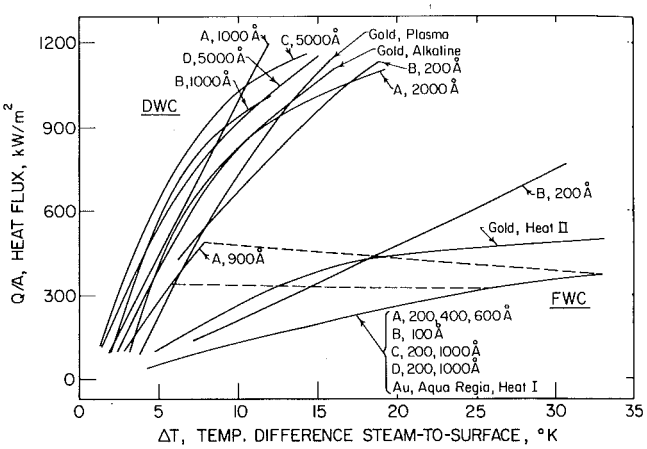

Fig. 2a Part of the heat transfer results for different gold surfaces. Dropwise condensation is DWC, and filmwise condensation in FWC. Other symbols are explained in Table 1.

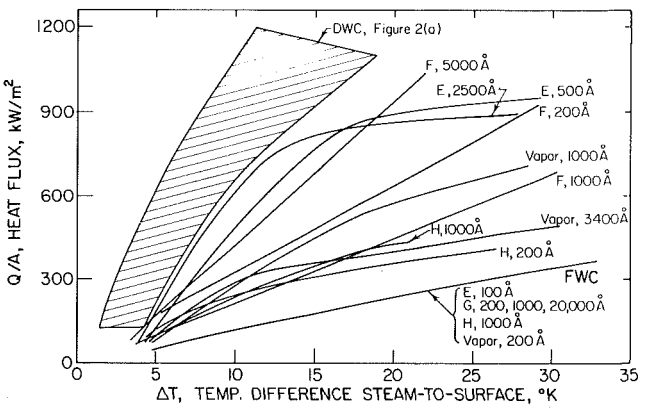

Fig. 2b Remaining heat transfer results

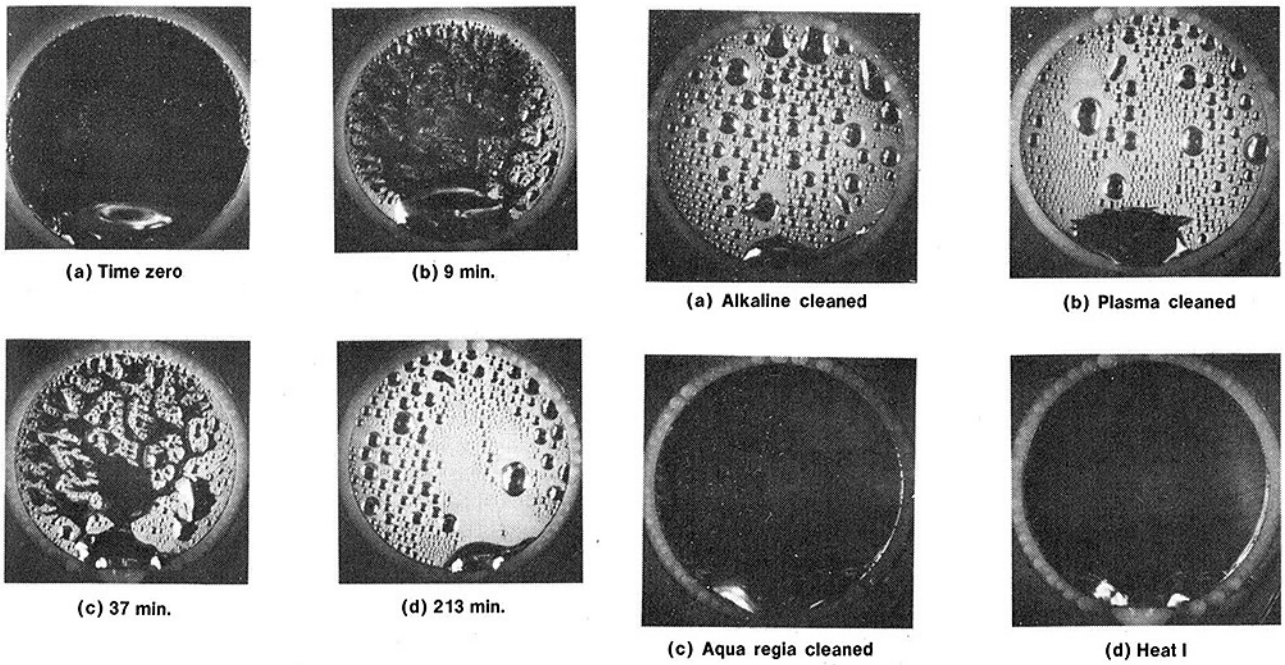

Fig. 3 Development of dropwise condensation on 2000 A.U. gold deposit from Bath A

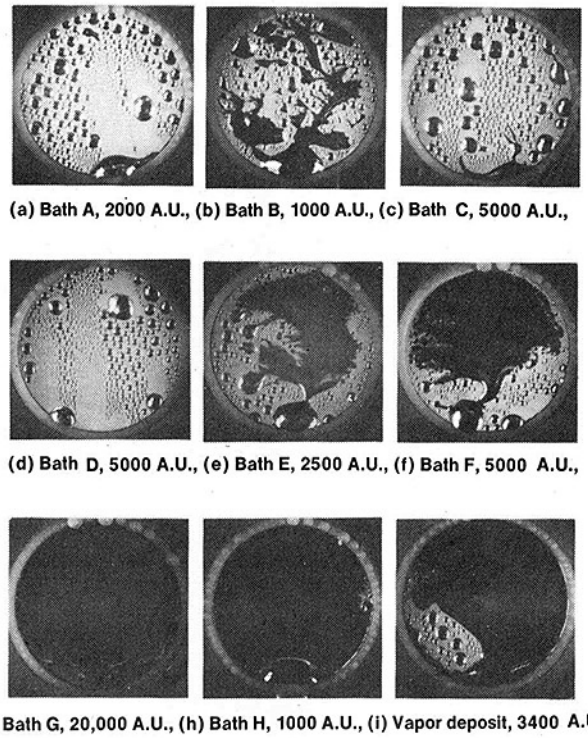

Fig. 4 Contrasting appearance of steady-state condensation on various gold surfaces after 3.5 hours

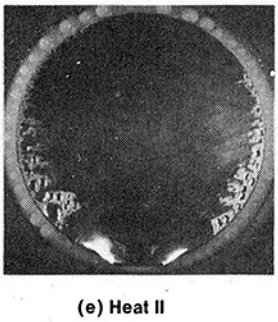

Fig. 5 Contrasting appearance of steady-state condensation on pure solid gold specimen

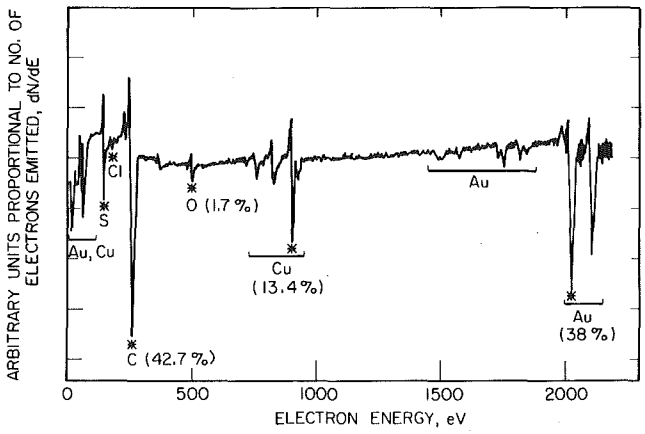

Fig. 6 Auger spectrum for 1000 A.U. electroplated gold from Bath A on copper

Table 2 Summary of condensation results for gold surfaces D = dropwise condensation, F = filmwise, M = mixed

	Deposit thickness, A.U.											
	100	200	400	500	600	900	1000	2000	2500	3400	5000	20,000
Bath A		F	F		F	M	D	D				
Bath B	F	M, D					D					
Bath C		F					F				D	
Bath D		F					F				D	
Bath E	F			M					M			
Bath F		M					M				M	
Bath G		F					F					F
Bath H		M					F, M					
Vapor Deposit		F					M			M		

pure solid gold:	alkaline cleaning	−D
	plasma cleaning	−D
	aqua regia cleaning	−F
	heat I	−F
	heat II	−M

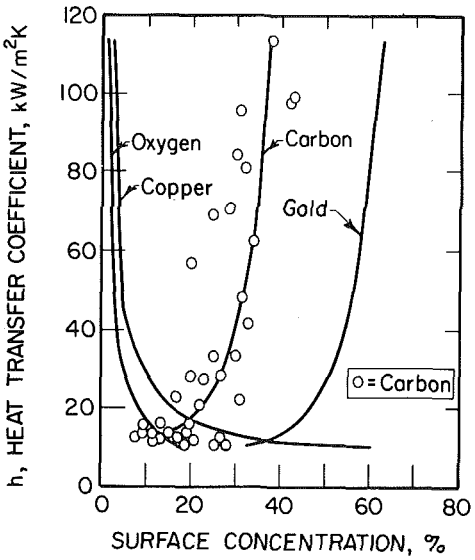

Fig. 7 The effect of surface composition on the condensation heat transfer coefficient h at a ΔT of 8.3 K. All runs are included.

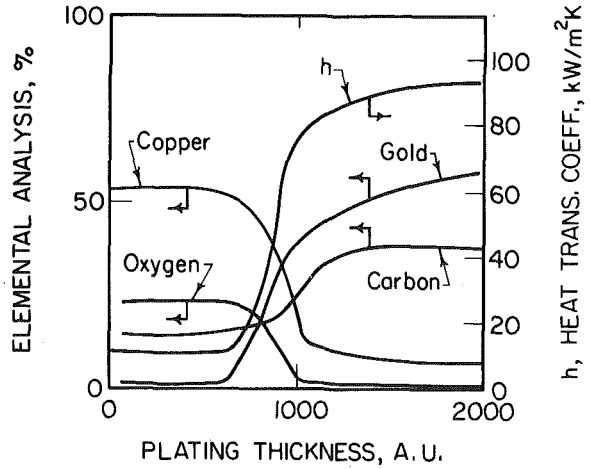

Fig. 8 Effect of thickness of gold plating on the surface composition and the condensation heat transfer coefficient at a ΔT of 8.3 K. Runs with Bath A.

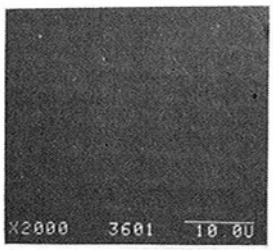

(a) 2000 A.U. thick from Bath A, see Fig. 3(d)

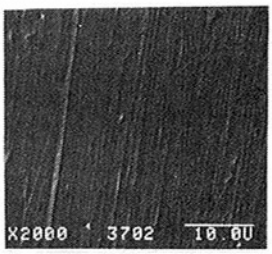

(d) Pure gold, alkaline cleaned, see Fig. 5(a)

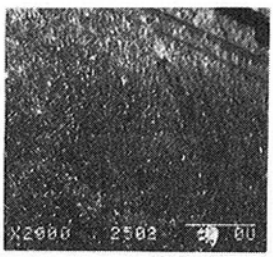

(b) 2500 A.U. from Bath E, see Fig. 4(e)

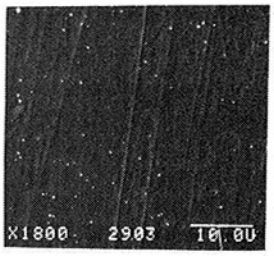

(e) Pure gold, Heat Treatment II, see Fig. 5(e)

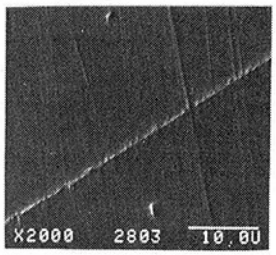

(c) 1000 A.U. Vapor Deposit

Fig. 9 Scanning electromicrographs of gold condenser surfaces. The scale indicates 10 μm

demonstrated dropwise condensation on a mixed surface were higher in gold and carbon, and lower in carbon and oxygen, relative to positions on the same sample which demonstrated filmwise condensation. The concentrations of trace elements such as chlorine and sulfur were quite constant throughout.

The critical thickness in the deposit growth can be seen by comparing the Auger analyses from the six deposits from Bath A. Figure 8 presents the composition of the four major elements and the heat transfer coefficient at $\Delta T = 8.3$ K as a function of deposit thickness. Between 600 A.U. and 1000 A.U. a dramatic change occurs both in the surface chemistry and in the promotional ability of the Bath A deposit. This change in surface composition was seen for all baths tested, though the change in the heat transfer coefficient was less dramatic for those baths which did not produce dropwise condensation.

Scanning electron micrographs of five surfaces are presented in Fig. 9. These were taken after the Auger analyses were completed. They show the surface topography representative of the various types of deposits. Figure 9(a) is a bright 2000 A.U. deposit from Bath A. The appearance is typical of those seen from Baths A–D, F, and H, and the 200 A.U. and 1000 A.U. Bath G deposits. Figure 9(b) is an unbrightened, 2500 A.U. deposit from Bath E and is similar in appearance to the 20,000 A.U. deposit from Bath G.

Figure 9(c) is of the 1000 A.U. vapor-deposited surface. It has a strikingly different surface texture from the electrodeposited surfaces. Figure 9(d) and (e) are of the pure, solid-gold surfaces. Figure 9(d) is of the alkaline cleaned surface and is similar to the plasma-cleaned, gold surface. Figure 9(e) is of the second heat treated surface, representing the aqua regia treatment and the first heat treatment also. These surfaces show the polishing markings clearly. Note that the alumina polishing remnants (the small, white spots) are more prevalent on the latter surfaces. The electron microscope provides no information regarding adsorbed organic molecules.

The final test performed in this program was a promoter lifetime study of a 2000 A.U. deposit from Bath A. At the writing of this paper, this sample has demonstrated perfect dropwise condensation for 2500 continuous hours followed by a shift to filmwise condensation on about 25 percent of the surface and 75 percent dropwise elsewhere which has persisted for an additional period of over 2500 hours.

Discussion

It has been shown here that all gold surfaces are not equivalent in their ability to promote dropwise condensation. The pure, bright deposits from Baths A and B were superior in their ability to promote dropwise condensation. Each required a 1000 A.U. deposit for promotion. The cobalt and nickel brightened Baths C and D produced promoting deposits, but at a greater required thickness (5000 A.U. for each). The pure, dull deposit from Bath E did promote dropwise condensation at the edges. It is believed that because of its roughness, see Fig. 9(b), this deposit was considerably slower to promote.

The alloyed plating Baths F and G, the electroless Bath H, and vapor deposition produced layers which did not promote satisfactory dropwise condensation. The Auger analysis revealed that Bath H was also alloyed with a small amount of silver. This is discouraging, because one would hope that alloying might be an appropriate method of reducing the gold content (and thus cost) of a gold-plated condenser surface. However, the present study indicates that the purer and brighter a gold deposit, the better it will perform as a promoter for dropwise condensation of steam.

The vapor deposit failed as a promoter because of incomplete coverage, as indicated by the micrograph Fig. 9(c) and the Auger analysis. Methods of oscillating the sample during deposition and of obtaining a cleaner vacuum might improve this. It should be noted that less than 1 percent of the total gold evaporated was actually deposited on the sample. As a commercial method of depositing gold for promotion of dropwise condensation, vapor deposition seems unsuitable at this time.

It has also been shown that the promotional ability of a pure, solid-gold piece is dependent on its surface preparation. The difference between promotion and non-promotion was seen both with the Auger analysis and the electron microscopy: the surfaces which were non-promoters had more polishing alumina remnants present on the surface. It appears that some alumina is trapped below the surface level during polishing, and that the aqua regia dissolved enough gold to expose this alumina. Apparently the heat treatments also brought the alumina to the surface. This exposed alumina appears to prevent or hinder promotion of dropwise condensation.

It is interesting to note that the Auger analyses of these gold condenser surfaces show that none of the samples tested approached the ideal situation of a pure, gold surface, not even the solid, pure, gold sample. Thus gold surfaces are as much a product of their environment and history as of the bulk properties beneath. It is indeed questionable whether an ideal pure gold surface is a practical possibility.

Two observations indicate that an organic species is responsible for the promotion of dropwise condensation on gold. First, promotion on gold surfaces is not immediate. The dropwise areas always started at the edge of the test piece and progressed inward as seen in Fig. 3. This is interpreted to mean that a promoting agent was adsorbing on the surface, starting at the edges, and migrating towards the center. There was some concern that the small Teflon ring around the test piece was the source of this promoter. In a special test with a Teflon plug fitted in the center of a gold-plated test piece, nonwettability began at both the inner and outer metal-Teflon edges. It is not clear whether the cause was the chemical discontinuity or the mechanical discontinuity at these borders. In a separate test, a Teflon piece was purposefully touched to a gold-plated condenser surface; no additional or premature promotion was observed at the place of contact. Additionally, no fluorine was detected in the Auger analyses taken on these condenser surfaces. It does not appear that Teflon was the promoting agent. Note that whatever the source of promoter, it was effective only for thicker gold surfaces and not for thin gold layers or for copper alone.

The second observation is that the Auger analysis presented in Fig. 7 shows a positive correlation between promotion and the amount of carbon on the gold surfaces. This indicates that an organic compound is present on the surface and is responsible for the promotion. The strong association of carbon with the gold surfaces also indicates that gold surfaces attract organics from the surroundings, in spite of heroic efforts to prevent it. The negative correlation of heat transfer coefficient (and carbon concentration) with oxygen concentration indicates that the role of the gold may be to provide an oxide-free surface for organic adsorption. A recent paper by Smith [19] also shows the association between carbon concentration (as detected by Auger analysis) and the nonwettability of gold surfaces.

From all of this evidence, it is concluded that an organic species of unknown origin is responsible for the promotion of dropwise condensation on gold-plated or pure gold surfaces. Further, the adsorbed promoter is tenacious, lasting thousands of hours continuously in a once-through steam flow system.

Conclusions

It has been shown that all gold electrodeposits do not perform equivalently as promoters of dropwise condensation. Pure, bright electrodeposits are superior promoters, and alloyed or dull deposits are inferior. The vapor deposits tested were also inferior for promotion. The deposits which did promote did not always do so at the same deposit thickness. Two cleaning preparations of a pure gold sample promoted dropwise condensation, three did not.

Auger electron spectroscopy provided elemental analysis of the condenser surfaces. Promotion of dropwise condensation is associated with high concentations of gold and carbon, and with low concentrations of copper and oxygen. The carbon appears automatically with the gold plate, even if the plating solutions are organic-free. Dropwise condensation always starts at the edge of the sample and moves inward. It is concluded that an unidentified organic species is responsible for promotion of dropwise condensation on gold surfaces. The amount of organic material present may be as little as about one-third of a monomolecular layer.

Acknowledgment

Financial support was provided partially by the U.S. Department of Energy under Contract US-DOE-DE-AC02-80ER10596. Fellowship support was furnished by the Atlantic Richfield Foundation.

References

1 Schmidt, E., Schurig, W., and Sellschopp, W., "Versuche uber die Kondensation von Wasserdampf in Film und Tropfenform," *Tech. Mech. u Thermodynam.*, Vol. 1, 1930, pp. 53–63.

2 Erb, Robert A., "Wettability of Metals under Continuous Condensing Conditions," *Journal of Physical Chemistry*, Vol. 69, 1965, pp. 1306–1309.

3 Erb, Robert A., and Thelen, Edmund, "Dropwise Condensation on Hydrophobic Metal and Metal-Sulphide Surfaces," *Chemical Engineering News*, Vol. 43, No. 15, 1965, p. 72.

4 Erb, Robert A., and Thelen, Edmund, "Promoting Permanent Dropwise Condensation," *Ind. Engr. Chem.*, Vol. 57, 1965, pp. 49–52.

5 Erb, Robert A., and Thelen, Edmund, "Dropwise Condensation," Presented at the First International Symposium on Water Desalination, Wash. D.C., 1965.

6 Erb, Robert A., "Heterogeneous Nucleation on Single-Crystal Silver and Gold Substrates in Cyclic Condensation of Water Vapor," Ph.D. Thesis, Temple University, 1965, 98 pages.

7 Woodruff, David W., and Westwater, J. W., "Steam Condensation on Electroplated Gold: Effect of Plating Thickness," *International Journal of Heat Mass Transfer*, Vol. 22, 1979, pp. 629–632.

8 Woodruff, David W., "Gold Surfaces for Dropwise Condensation," Ph.D. Thesis, University of Illinois, 1980.

9 Umur, A., and Griffith, P., "Mechanism of Dropwise Condensation," JOURNAL OF HEAT TRANSFER, Vol. 87, 1965, pp. 275–284

10 Erb, Robert A., "The Wettability of Gold," *Journal of Physical Chemistry*, Vol. 72, No. 7, 1968, pp. 2412–2417.

11 Erb, Robert A., Haigh, Thomas I., and Downing, Thomas M., "Permanent Systems for Dropwise Condensation for Distillation Plants," *Symposium on Enhanced Tubes for Desalination Plants*, U. S. Dept. of Interior, Wash., D.C. July 1970, pp. 177–201.

12 Erb, Robert A., "Dropwise Condensation on Gold," *Gold Bulletin*, Vol. 6, No. 1, 1973, pp. 2–6.

13 Tower, R. E., and Westwater, J. W., "Effect of Plate Inclination of Heat Transfer During Dropwise Condensation of Steam," *Chemical Engineering Progress Symposium Series*, Vol. 66, No. 102, 1970, pp. 21–25.

14 Wilkins, David G., Bromley, Leroy A., and Read, Stanley M., "Dropwise and Filmwise Condensation of Water Vapor on Gold," *AIChE Journal*, Vol. 19, No. 1, 1973, pp. 119–123.

15 Abdelmessih, A. J., Neumann, A. W., and Yang, S. W., "The Effect of Surface Characteristics on Dropwise Condensation," *Letters in Heat and Mass Transfer*, Vol. 2, 1975, pp. 285–292.

16 Detz, Clifford M., and Vermesh, Robert J., "Nucleation Effects in the Dropwise Condensation of Steam on Electroplated Gold Surfaces," *AIChE Journal*, Vol. 22, No. 1, 1976, pp. 87–93.

17 Woodruff, David W, "Electroplated Gold Surfaces for Dropwise Condensation: The Effect of Plating Thickness," M.S. Thesis, University of Illinois, 1978.

18 Davis, Lawrence E., MacDonald, Noel C., Palmberg, Paul W., Riach, Gerald E., and Weber, Roland E., *Handbook of Auger Electron Spectroscopy*, Physical Electronics Industries, Inc., Eden Prarie, Minnesota, 1972.

19 Smith, Tennyson, "The Hydrophilic Nature of a Clean Gold Surface," *Journal of Colloid and Interface Sciences*, Vol. 75, No. 1, 1980, pp. 51–55.

Heat-Exchanger Effectiveness in Thermoelectric Power Generation[1]

M. S. Bohn

Solar Energy Research Institute, Golden, Colo. 80401

This paper presents a method for calculating the electrical power generated by a thermoelectric heat exchanger. The thermoelectric heat exchanger transfers heat from a hot fluid to a cold fluid through a thermoelectric generator located in the heat-exchanger wall separating the two fluid streams. The method presented here is an extension of the NTU method used to calculate heat-exchanger heat-transfer effectiveness. The effectiveness of thermoelectric power generation is expressed as the ratio of the actual power generated to the power that would be generated if the entire heat-exchanger area were operating at the inlet fluid temperatures. This method collapses results for several heat-exchanger configurations and allows a concise presentation of the results. It is shown that the NTU method of calculating heat-exchanger heat-transfer effectiveness can be modified in a similar way.

Introduction

Thermoelectric power generation has been used for many years, primarily in applications requiring high reliability, quiet operation, or the ability to operate on a wide variety of fuels. Examples of such devices include radioisotope-heated generators for deep space probes [1] and fossil-fueled generators for military field power requirements [2]. Most recently, the use of thermoelectric generators has been proposed for Ocean Thermal Energy Conversion (OTEC) [3].

Thermoelectric generation makes use of a bulk phenomenon: the Seebeck effect. A temperature gradient across any material tends to drive charge carriers from the hot side to the cold side, producing a voltage across the material. Specially-designed semiconductor thermoelectric alloys produce several hundred microvolts per degree Kelvin temperature difference across the material. For a detailed description of the thermoelectric effect, see reference [4].

The fuel source for thermoelectric generators (such as those described in references [1] and [2]) provides a heat reservoir at a specified temperature, and heat is rejected by the thermoelectric device either by radiation (space applications) or by forced convection with cooling fins. Analyses of most thermoelectric generators in the literature [5] generally assume a hot-junction temperature, and the cold-junction temperature is either assumed or calculated on the basis of cooling-fin performance [6].

Another method of "fueling" the thermoelectric generator is by the transfer of heat from a hot fluid stream to a cold fluid stream. This is the technique proposed in reference [3] for the OTEC application. Here, cold seawater from the ocean depths is pumped to the ocean surface and through one side of a heat exchanger. Warm surface seawater is pumped through the other side of the heat exchanger. Thermoelectric elements placed in the interface separating the two fluid streams generate electrical power as the heat flows through the interface (Fig. 1). Other examples of thermoelectric power generation using fluid-to-fluid heat transfer, as suggested in reference [7], include solar ponds, geothermal sources, and waste-heat recovery. Applications in which fuel costs are low appear to be economically feasible.

To exploit the temperature difference between two fluid streams for thermoelectric power generation, a heat exchanger clearly is needed to keep the fluid streams separate and to channel the heat flow from the hot stream through the thermoelectric device and into the cold stream. In addition, the heat exchanger protects the thermoelectric elements from the heat transfer fluids and provides a rigid structure for the thermoelectric elements.

Thermal performance of the heat exchanger can be calculated given the overall thermal conductance (which must account for the presence of the thermoelectric elements), fluid flow rates, inlet temperatures, heat capacities, heat exchanger area, and flow configuration. A convenient procedure is given in reference [8], in which the effectiveness of heat exchange is given as a function of dimensionless heat-exchanger size for a variety of heat-exchanger configurations. This method of presenting heat-exchanger effectiveness is called the NTU (number of transfer units) method. Heat-exchanger effectiveness is given as the ratio of actual heat-transfer to the thermodynamically maximum possible heat transfer.

Unfortunately, that heat-exchanger effectiveness cannot be used to predict electrical power generation of a thermoelectric heat exchanger. As shown in the next section, local power generation depends on a nonlinear function of temperature difference, while the heat-exchanger effectiveness is calculated from a linear function of temperature difference.

The purpose of this paper is to extend the NTU method so that effectiveness of thermoelectric power generation can be easily determined once the fluid properties, flow rates, and flow configuration are known. The effectiveness of thermoelectric power generation will be given as a dimensionless ratio of actual power generated to the maximum possible power generation.

In the following sections, an expression for local steady-state power generation per unit area is developed. Power output of the heat exchanger is then given as an integral of that expression over the heat-exchanger area, and then the effectiveness in power generation, ξ_p, is defined. Results for several heat-exchanger configurations are given as graphs of ξ_p versus dimensionless heat-exchanger size, and an example of using the results is given.

Electrical Power Generated per Unit of Heat-Exchanger Area

The electrical power output per unit of heat exchanger area is proportional to the product of the heat flowing through the heat exchanger and the Carnot efficiency seen at the hot and cold junctions of the thermoelectric generator:

$$P = Kq\left(1 - \frac{T_{cj}}{T_{hj}}\right) \tag{1}$$

We take the proportionality constant K to be a material property. Although K is a function of temperature (see Appendix), errors due to using the value of K at an average operating temperature are not large [9] if the heat exchanger is operated at low to moderate temperature differences ($1 - T_c/T_h < 0.5$).

As seen in Fig. 2, the heat flow is through three thermal resistances in series. The thermal resistance from the hot fluid to the thermoelectric hot junction is R_{fh}, and that from the thermoelectric cold function to the cold fluid is R_{fc}. Thermal resistance of the thermoelectric material is R_{te}. The resistances R_{fh} and R_{fc} must, in general, include fouling resistance, fin efficiencies, thermal conductivity of the heat-exchanger plate, and thermal contact resistance. Thermal resistance of the thermoelectric generator, R_{te}, must include Peltier

[1] Prepared for the U.S. Department of Energy, Contract No. EG77C014042.

Contributed by the Heat Transfer Division for publication in the JOURNAL OF HEAT TRANSFER. Manuscript received by the Heat Transfer Division September 10, 1980.

and Joule heating effects (see Appendix) and is computed assuming zero heat transfer through any insulation used to isolate the thermoelectric elements. All thermal resistances are referred to the heat-exchanger base area.

From Fig. 2, the junction temperatures may be eliminated by using

$$q = \frac{T_{hj} - T_{cj}}{R_{te}} = \frac{T_h - T_c}{R_{fh} + R_{fc} + R_{te}} [1 + 0\{K(1 - T_c/T_h)\}] \quad (2)$$

$$\frac{T_h - T_{hj}}{R_{fh}} = \frac{T_h - T_c}{R_{fh} + R_{fc} + R_{te}} [1 + 0\{K(1 - T_c/T_h)\}]. \quad (3)$$

The approximation in the above equations expresses the difference in heat flow through the three resistances due to energy removal in the form of electrical power. A conversion efficiency of 20 percent ($K = 0.2$) would represent the maximum efficiency from current thermoelectric materials. For such a device operating with a maximum available temperature difference $1 - T_c/T_h = 0.5$ (probably the upper limit for most practical applications of thermoelectric generators, [7]), the error term in equations (2) and (3) would be 0.10. Since these conditions represent the worst possible case, we neglect this error term in the analysis. Note that for applications involving large temperature differences, errors due to neglecting this term and due to temperature dependence of K may not be negligible.

Using equations (2) and (3) in equation (1), we may write

$$P = \frac{KT_h\epsilon^2 R_{te}}{[R_{fc} + R_{fh} + R_{te} - R_{fh}\epsilon][R_{fh} + R_{fc} + R_{te}]}, \quad (4)$$

where we use $\epsilon = 1 - T_c/T_h$, the Carnot efficiency based on the available fluid temperature difference. In reference [11], an equation similar to equation (4) was used to determine the fluid temperature distribution within the heat exchanger that would yield maximum power output. Thickness of the thermoelectric element, as a function of location in the heat exchanger, which gives the desired temperature distribution, was then determined.

Specifying the thickness distribution of the thermoelectric element in the heat exchanger does not appear to be the most practical approach, especially for mass-produced thermoelectric heat exchangers as proposed in reference [3]. A more practical approach is to assume constant thermoelectric element thickness and calculate the power generated by the heat exchanger, given fluid inlet temperatures, fluid properties, and heat-exchanger dimensions.

Assumption of a constant thermoelectric element thickness will allow determination of the thickness that will maximize local power generation. This is possible because, within manufacturing constraints, R_{te} is a quantity that we may vary at will. Maximizing equation (4) with respect to R_{te}, we find the value R_{te}* that yields maximum power output is

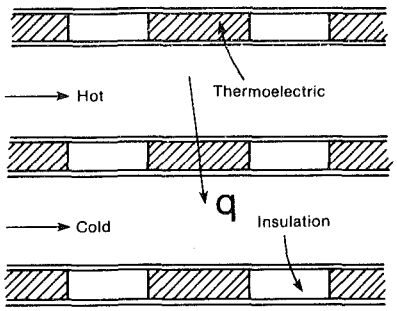

Fig. 1 Detail of heat-exchanger/thermoelectric-generator combination

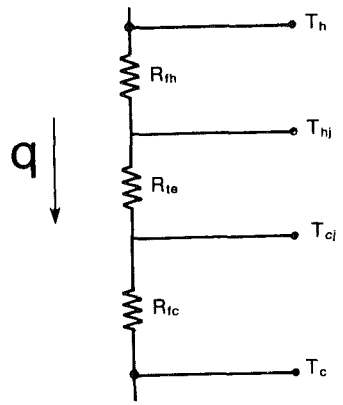

Fig. 2 Thermal resistance network

$$R_{te}^* = (R_{fc} + R_{fh}) \left(1 - \frac{\epsilon R_{fh}}{R_{fc} + R_{fh}}\right)^{1/2}. \quad (5)$$

Since ϵ varies through the heat exchanger (the resulting variation in R_{te}* is small) we must choose one value in order to calculate one value for R_{te}*. The most reasonable value is ϵ_0, which we define as ϵ calculated at the fluid inlet temperatures, T_{hm} and T_{cm}. Using ϵ_0 in equation (5), substituting R_{te}* for R_{te} in equation (4), and defining the thermal resistance ratio,

Nomenclature

A = heat exchanger base area, cm^2
C_c = heat capacity rate (specific heat × mass flow rate) on cold side, W/K
C_h = heat capacity rate on hot side, W/K
C_{min} = smaller of C_c and C_h, W/K
C_{max} = larger of C_c and C_h, W/K
K = thermoelectric device conversion efficiency
Ntu = number of transfer units
Ngu = number of generation units
P* = electrical power generated per unit heat exchanger base area, W/cm^2
P_0* = P* evaluated at inlet fluid temperatures, W/cm^2
P_{out} = heat exchanger electrical power output, W
q = heat flux from hot fluid, W/cm^2
q_{max} = thermodynamically maximum possible heat exchanged, W
r = ratio of heat capacity rates, C_c/C_h
r' = r if $r > 1$, 1 if $r \leq 1$
R_{fc} = thermal resistance from cold fluid to thermoelectric cold junction, K-cm^2/W
R_{fh} = thermal resistance from hot fluid to thermoelectric hot junction, K-cm^2/W
R_{te} = thermoelectric thermal resistance, K-cm^2/W
R_{te}* = the value of R_{te} that gives maximum P*, K-cm^2/W
T_c = local cold fluid temperature in the heat exchanger, K
T_{cj} = thermoelectric cold junction temperature, K
T_{cm} = value of T_c at heat exchanger inlet, K
T_h = local hot fluid temperature in the heat exchanger, K
T_{hj} = thermoelectric hot junction temperature, K
T_{hm} = value of T_h at heat exchanger inlet, K
$T_{h,out}$ = hot fluid outlet temperature, K
U = overall thermal conductance $(R_{fc} + R_{fh} + R_{te})^{-1}$, W/cm^2-K
α = thermal resistance ratio $R_{fh}/(R_{fh} + R_{fc})$
ϵ = Carnot efficiency based on local fluid temperatures in the heat exchanger
ϵ_0 = ϵ based on inlet fluid temperatures
ξ = heat exchanger effectiveness
ξ' = modified heat exchanger effectiveness
ξ_p = heat exchanger effectiveness in thermoelectric power generation

$$\alpha \equiv \frac{R_{fh}}{R_{fh} + R_{fc}}, \tag{6}$$

we find the maximum power generated per unit area is then

$$P^* = \frac{KT_h\epsilon^2}{R_{fh} + R_{fc}} \frac{(1 - \alpha\epsilon_0)^{1/2}}{[1 + (1 - \alpha\epsilon_0)^{1/2}][1 - \alpha\epsilon + (1 - \alpha\epsilon_0)^{1/2}]}, \tag{7}$$

and the required thermoelectric thermal resistance is

$$R_{te} = (R_{fc} + R_{fh})(1 - \alpha\epsilon_0)^{1/2}. \tag{8}$$

The electrical power generated by the entire heat-exchanger area A is then given by

$$P_{\text{out}} = \int_A P^* dA. \tag{9}$$

Effectiveness of Thermoelectric Power Generation

To express the results in a convenient form it is necessary to make equation (9) dimensionless. The quantity we use to nondimensionalize equation (9) is P_0^*A, which is the electrical power that would be generated if the entire heat-exchanger area were operating at the maximum available temperature difference; i.e., the inlet fluid temperatures. We may calculate P_0^* from equation (7) by substituting T_{hm} for T_h and ϵ_0 for ϵ:

$$P_0^* = \frac{KT_{hm}\epsilon_0^2}{R_{fh} + R_{fc}} \frac{(1 - \alpha\epsilon_0)^{1/2}}{[1 + (1 - \alpha\epsilon_0)^{1/2}][1 - \alpha\epsilon_0 + (1 - \alpha\epsilon_0)^{1/2}]}. \tag{10}$$

We may now calculate the effectiveness of thermoelectric power generation from

$$\xi_p = \int_A \frac{P^*}{P_0^*} \frac{dA}{A}. \tag{11}$$

Substituting equations (7) and (10) into equation (11), we find

$$\xi_p = \int_A \left(\frac{\epsilon}{\epsilon_0}\right)^2 \left(\frac{T_h}{T_{hm}}\right) \left\{\frac{1 - \alpha\epsilon_0 + (1 - \alpha\epsilon_0)^{1/2}}{1 - \alpha\epsilon + (1 - \alpha\epsilon_0)^{1/2}}\right\} \frac{dA}{A}. \tag{12}$$

The effectiveness ξ_p may be calculated from equation (12) given the temperature distribution in the heat exchanger. The temperature distribution may be determined from a heat balance equation, which will depend on the heat-exchanger configuration. Parallel flow, for example, gives

$$U(T_h - T_c) = C_c \frac{dT_c}{dA} = -C_h \frac{dT_h}{dA}. \tag{13}$$

Consistent with previous arguments, we have neglected errors of $0\{K(1 - T_c/T_h)\}$ in equation (13).

Given inlet conditions, equation (13) may be solved to give the temperature distribution in the heat exchanger. Equation (12) may then be solved for ξ_p. The solution of equation (13), which gives the heat exchanger effectiveness ξ, results in two dimensionless quantities UA/C_h and C_h/C_c. Therefore, the effectiveness of thermoelectric power generation is a function of four quantities;

$$\xi_p = \xi_p\left(\frac{UA}{C_h}, \frac{C_h}{C_c}, \epsilon_0, \alpha\right). \tag{14}$$

We choose to call the first independent variable Ngu (number of generation units), and the second independent variable r. The number of generation units is a dimensionless heat-exchanger size. Comparing Ngu with Ntu [8]:

$$\text{Ntu} = UA/C_{\min}; \tag{15}$$

therefore,

$$\text{Ngu} = \text{Ntu when } r \leq 1;$$
$$\text{Ngu} = \text{Ntu}/r \text{ when } r > 1.$$

The reason for using a new variable Ngu instead of Ntu is the nonlinearity in equation (12). If we were to express heat-exchanger effectiveness in terms of Ngu, we would find

$$\xi(\text{Ngu} \cdot r, 1/r) = \xi(\text{Ngu}, r), \tag{16}$$

so that a symmetry exists due to the linearity of equation (13); i.e., it does not matter whether the hot fluid or the cold fluid has the largest capacity rate. Therefore, it is possible to consider ξ to be only a function of $UA/C_{\min}$ and $C_{\min}/C_{\max}$, i.e., $r \leq 1$. Because equation (12) is nonlinear, an expression like equation (16) does not exist for ξ_p. Therefore, it is necessary to consider both $r \leq 1$ and $r > 1$.

The effectiveness of thermoelectric power generation, ξ_p, expresses how effectively the heat exchanger utilizes the heat-transfer area in generating electrical power. A heat exchanger with a low ξ_p is generating a small amount of electrical power per unit of heat-exchanger area. Consider, for example, a parallel-flow heat exchanger (in which the inlet area is operating at essentially the maximum available fluid-temperature difference). A very short parallel-flow heat exchanger would have an ξ_p near unity. As we lengthen the heat exchanger, the local fluid-temperature difference decreases, less power is generated per unit area, and the ξ_p for the heat exchanger will be less than unity.

Note the difference between this type of effectiveness and that used to define ξ, the heat-exchanger effectiveness [8]:

$$\xi \equiv \frac{q}{q_{\max}} = \frac{C_h(T_{hm} - T_{h,\text{out}})}{C_{\min}(T_{hm} - T_{cm})}. \tag{17}$$

The effectiveness given by equation (17) expresses how efficiently the heat exchanger transfers heat. Clearly, the longer the parallel-flow heat exchanger is, the more heat it will transfer and the closer to unity ξ will be.

Defining ξ_p as an area effectiveness serves two purposes. First, the nondimensionalization of equation (7) by P_0^* minimizes the number of parameters upon which ξ_p depends. Second, in a fluid loop using a thermoelectric heat exchanger, one of the major costs may be the heat exchanger. Therefore, generation of maximum electrical power per unit of heat-exchanger area is important. Defining ξ_p according to equation (11) gives an effectiveness that describes how well the heat-exchanger area is being utilized. As explained in the Appendix, heat-exchanger effectiveness ξ may also be expressed as an area utilization effectiveness.

Calculation Procedure

For most heat-exchanger configurations, solutions of heat-exchanger effectiveness exist. Reference [8] discusses several of these solutions. The solution of equation (12), however, requires the temperature distribution in the heat-exchanger; not just inlet and outlet temperatures. Since equation (12) is nonlinear, a numerical integration is appropriate.

For each heat-exchanger configuration, a heat-balance equation similar to equation (13) was written. In most cases a closed-form solution was found. This solution was used to calculate heat-exchanger effectiveness from reference [8], which may be written as

$$\xi = r' \frac{T_{hm} - T_{h,\text{out}}}{T_{hm} - T_{cm}}, \tag{18}$$

where $r' = r$ if $r > 1$, and $= 1$ if $r \leq 1$.

As a check on the calculation, this value of ξ was compared to that given in reference [8] for the same values of Ntu and $C_{\min}/C_{\max}$.

The temperature distribution was then inserted into equation (12) and the solution for ξ_p found by trapezoidal rule integration. Errors due to the numerical integration were much smaller than those due to the approximation expressed in equations (2) or (3).

Results

Effectiveness ξ_p was calculated for the following heat-exchanger configurations: (i) parallel flow, (ii) counterflow, (iii) crossflow—no mixing, (iv) crossflow—hot side mixed, (v) crossflow—cold side mixed, and (vi) parallel counterflow—shell side mixing.

The range of independent variables is $0 \leq \text{Ngu} < 5$; $0 \leq r \leq 4$; $0.1 \leq \epsilon_0 \leq 0.5$; $0.1 \leq \alpha \leq 0.9$.

The results show a very weak dependence of ξ_p upon either the thermal resistance ratio, α, or the heat-exchanger configuration. Varying α from 0.1 to 0.9 with ϵ_0, r, and Ngu remaining unchanged resulted in a change in ξ_p of less than 0.015. Therefore, all results were

computed with $\alpha = 0.5$.

A comparison of the six heat-exchanger configurations showed that parallel flow gave the smallest ξ_p and counterflow gave the largest ξ_p; the differences, however, were always less than 0.02. Therefore, we will present results for parallel flow only.

Results are plotted in Figs. 3, 4, and 5 for Carnot efficiency $\epsilon_0 = 0.1$, 0.3, 0.5, respectively. Comparing the three graphs, the effectiveness apparently depends weakly on Carnot efficiency. For small values of capacity ratio, the largest change in ξ_p, as Carnot efficiency is changed from 0.1 to 0.5, is about 0.05.

The graphs also show that the effectiveness is greater than 0.5 only for Ngu < 1. If the previous comments on the appropriateness of using an area utilization effectiveness for thermoelectric heat exchangers hold true, then it is clear most such devices will be designed with Ngu < 1.

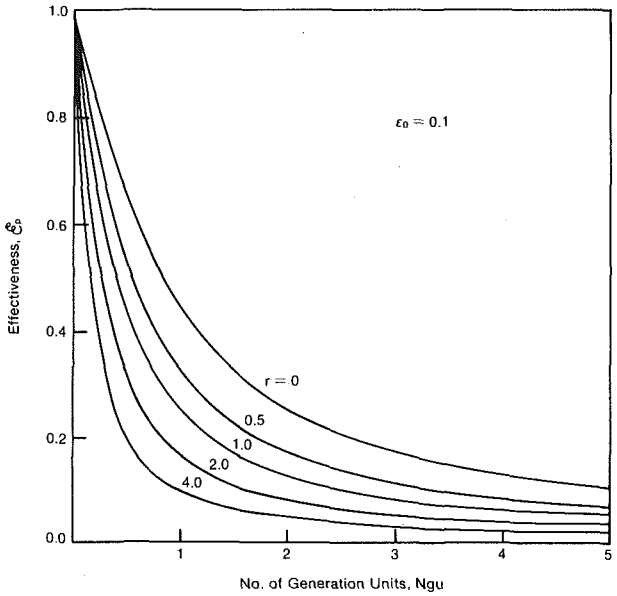

Fig. 3 Effectiveness of thermoelectric power generation for Carnot efficiency = 0.1

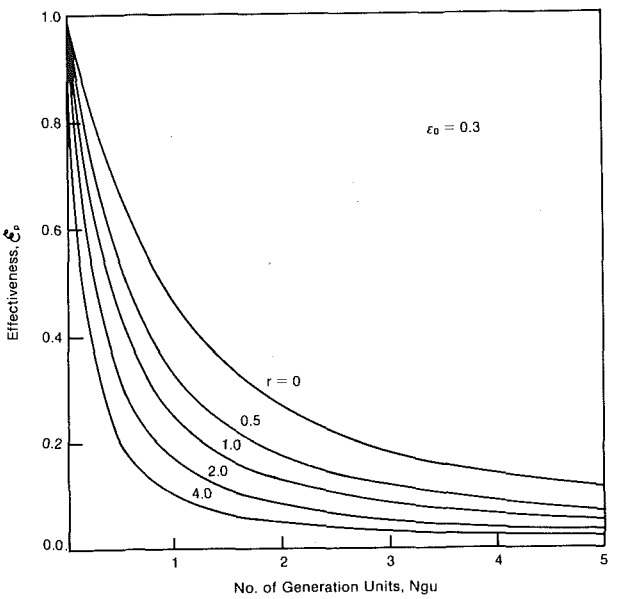

Fig. 4 Effectiveness of thermoelectric power generation for Carnot efficiency = 0.3

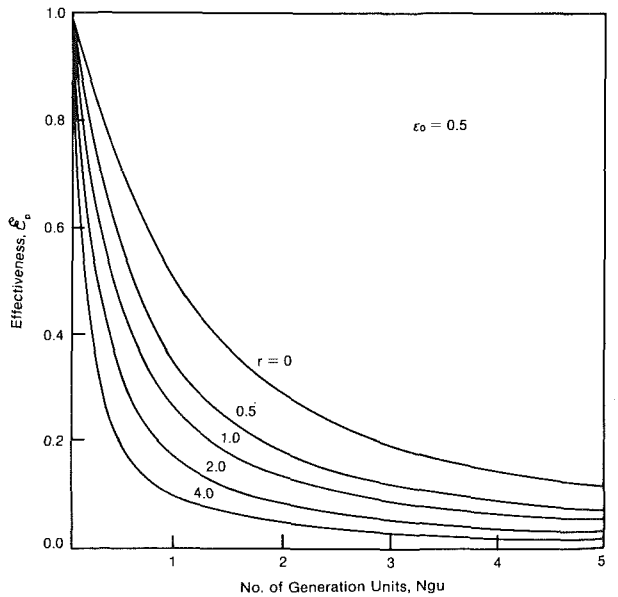

Fig. 5 Effectiveness of thermoelectric power generation for Carnot efficiency = 0.5

Example

In this section we present an example thermoelectric heat-exchanger performance calculation. We will follow the example presented in reference [8], in which heat-transfer performance and pressure drop are computed for an air-to-water gas turbine intercooler. The intercooler has 90,900 kg/h air flow (inlet temperature = 127°C) cooled by 181,800 kg/h water (inlet temperature 16°C). The crossflow configuration has a finned, flat-tube surface with cooling water flow through the tubes. Total base (cold side) heat-transfer area is 66 m^2. Heat-exchanger dimensions are 1.63 m × 0.61 m × 0.48 m.

The required thermoelectric element thickness may be calculated using equation (5) and the thermal resistances on the hot side and cold side, $R_{fc} = 1.13$, $R_{fh} = 8.29$°C cm^2/W.

The Carnot efficiency is $\epsilon_0 = 0.28$. From equation (8), $R_{te} = 8.16$°C cm^2/W.

From the Appendix, the required thickness of thermoelectric material would be 0.22 cm for 100 percent, area coverage if the thermoelectric material is Bi_2Te_3 (see reference [3]). Adding this thermal resistance increases the overall thermal resistance to $U^{-1} = 17.58$°C cm^2/W, reducing the number of transfer units from Ntu = 2.73 to 1.46. Heat-transfer effectiveness is reduced from $\xi = 0.90$ to 0.75 (see Fig. 2–14, [8]).

Since the hot side has the minimum capacity rate Ngu = Ntu, r = 0.122, from Fig. 4 the effectiveness of thermoelectric power generation is $\xi_p = 0.32$. Assuming a thermoelectric conversion efficiency $K = 0.18$, equation (10) gives $P_0^* = 1721$ W/m^2. Therefore, electrical power output would be $P_{out} = 36{,}350$ W. For comparison, the pumping power required for both fluid sides is computed from reference [8] to be 19,790 W.

It should be noted that each application must be optimized for the best performance. In this example we used the flow rates given in the original example [8]. If the desired result was maximum net power output, then these flow rates are not necessarily optimum. An iterative scheme would be needed to find the flow rate that gives maximum power. A similar procedure was followed in the OTEC application [3], where heat-exchanger flow length (Ngu), hot-water flow rate, and cold-water flow rates were adjusted until minimum plant cost resulted. The results presented in this paper give the link between heat-exchanger size, flow rates, and electrical power output needed for such optimizations.

References

1 Gayek, H. W., "Power Conditioning for Thermoelectric Generators," *IECEC Record*, 1968, pp. 669–679.

2 Guazzoni, G., Angello, J., and Herchakowski, A., "Regenerative Burner System for Thermoelectric Power Sources," *Proceedings, Second International Conference on Thermoelectric Energy Conversion*, Arlington, TX, Mar. 1978. IEEE 78CH1313-6.

3 Bohn, M., Benson, D., and Jayadev, T., "Thermoelectric Ocean Thermal Energy Conversion," ASME *Journal of Solar Energy Engineering*, Vol. 102, May 1980, pp. 119–127.

4 Ioffe, A. F., "Semiconductor Thermoelements and Thermoelectric Cooling," Infosearch Ltd., London, 1957, pp. 36–44.

5 Richards, J., and Nystrom, T. L., "Procedure for the Design of a Thermoelectric Converter and Comparison with Test Results Obtained on a High Power Density Device," Society of Automotive Engineers, Paper 680395, 1968.

6 Oftedal, T., and Thoresen, P., "Thermoelectric Generator Based on Compressed Charcoal Fuel," *Proceedings, Second International Conference on Thermoelectric Energy Conversion*, Arlington, TX, Mar. 1978. IEEE 78CH1313-6.

7 Benson, D., and Jayadev, T., "Thermoelectric Energy Conversion," *Proceedings Seventh Energy Technology Conference*, Washington D.C., Mar. 24–26, 1980.

8 Kays, W., and London, A., *Compact Heat Exchangers*, McGraw-Hill, New York, 1964.

9 Sherman, B., Heikes, R., and Ure, R., "Calculation of Efficiency of Thermoelectric Devices," *Journal of Applied Physics*, Vol. 31, 1960.

10 Nottage, H. B., Starrett, P., and Winksell, P. L., "Thermoelectric Generators with Surface Heat Loss," ASME JOURNAL OF HEAT TRANSFER, Vol. 4, Aug. 1962, pp. 193–206.

11 Swanson, B. W., and Somers, E., "Optimization of a Conventional Fuel Fired Thermoelectric Generator," ASME JOURNAL OF HEAT TRANSFER, Vol. 81, Aug. 1959, pp. 245–248.

12 Raag, V., Hankins, L., and Swerdling, M., "Design Concepts of Solar Thermoelectric Generators in Space Applications," *Proceedings, Second International Conference on Thermoelectric Energy Conversion*, Arlington, TX, Mar. 1978. IEEE 78CH1313-6.

APPENDIX

Thermoelectric Conversion Efficiency and Thermal Resistance. From reference [4] we may derive expressions for the thermoelectric conversion efficiency K and thermal resistance R_{te}. For thermoelectric elements with constant properties

a	Seebeck coefficient	(V/K)
σ	Electrical conductivity	(1/ohm-cm)
k_{te}	Thermal conductivity	(W/cm-K)
t_{te}	element thickness	(cm),

the efficiency, defined as the ratio of useful electrical energy delivered to the external load to the energy consumed from the heat source, is

$$\eta = \frac{1 - \dfrac{T_{cj}}{T_{hj}}}{2\left[1 + \dfrac{2}{T_{hj}z} - \dfrac{1}{4}\left(1 - \dfrac{T_{cj}}{T_{hj}}\right)\right]} \tag{19}$$

when external load resistance is matched to internal electrical resistance for maximum power delivery. Reference [4], equation (31), and equation (32) also give an expression for η under maximum efficiency operation. The quantity z is known as the thermoelectric material figure of merit,

$$z = \frac{a^2\sigma}{k_{te}}, \tag{20}$$

and typically has values less than $3.5 \times 10^{-3}\ K^{-1}$.
From our definition of K we see that

$$K = \frac{1}{2\left[1 + \dfrac{2}{T_{hj}z} - \dfrac{1}{4}\left(1 - \dfrac{T_{cj}}{T_{hj}}\right)\right]} \tag{21}$$

For a given heat exchanger, equation (21) may be used to compute the variation of K in the heat exchanger and to determine if using a mean value of K will introduce unacceptable errors.

The heat drawn from the heat source per unit cross-sectional area of thermoelectric element from reference [4] is

$$q = \left(k_{te} + \frac{\sigma a^2}{2}T_{hj} - \frac{\sigma a^2}{2}\frac{T_{hj} - T_{cj}}{4}\right)\frac{T_{hj} - T_{cj}}{t_{te}}. \tag{22}$$

The thermoelectric thermal resistance is then

$$R_{te} = \frac{t_{te}}{k_{te} + \dfrac{\sigma a^2}{2}T_{hj} - \dfrac{\sigma a^2}{2}\dfrac{T_{hj} - T_{cj}}{4}}. \tag{23}$$

Given the required R_{te} from equation (5), material properties, and average operating temperatures, the required thickness of the thermoelectric material is determined. Equation (23) may also be used to determine a mean value of R_{te} in the heat exchanger and the magnitude of errors thus introduced.

Modified Heat-Exchanger Effectiveness. Heat-exchanger effectiveness ξ can be redefined so that it too expresses an area utilization effectiveness, ξ'. This may be a more useful definition for heat-exchanger applications in which the heat exchanger has more

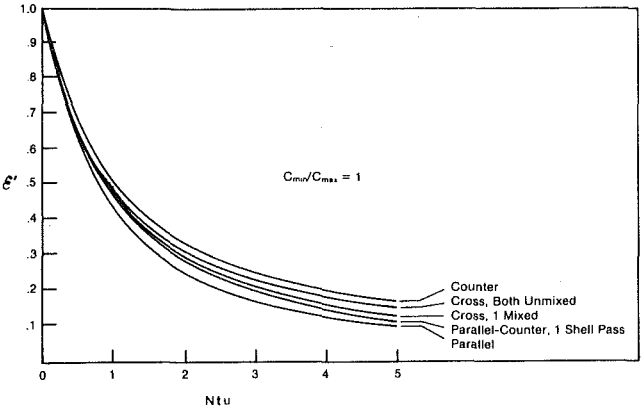

Fig. 6 Modified heat-exchanger effectiveness for different heat-exchanger configurations

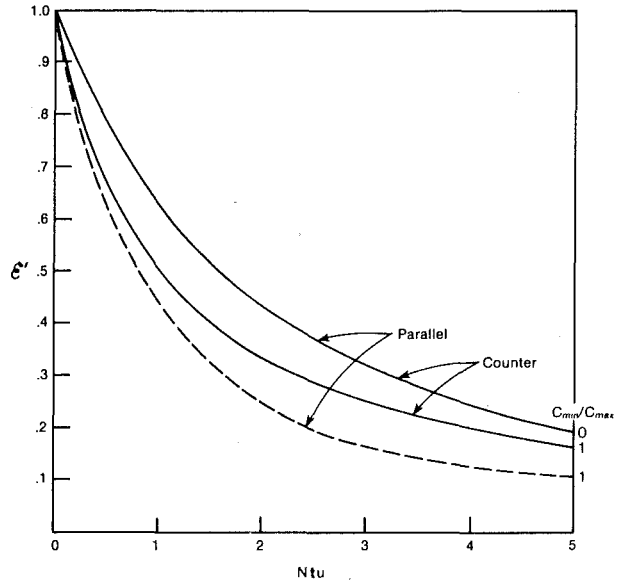

Fig. 7 Modified heat-exchanger effectiveness for capacity rate variation

value than the energy being transferred, e.g., in waste heat recovery. If the actual heat transferred is made nondimensional with the heat that would be transferred if the entire heat exchanger area were operating at the maximum available temperature difference, equation (17) would be modified to

$$\xi' = \frac{C_h(T_{hm} - T_{h,\text{out}})}{UA(T_{hm} - T_{cm})} \tag{24}$$

The relation between the two effectivenesses is simple:

$$\xi' = \xi/\text{Ntu}. \tag{25}$$

Like the power generation effectiveness, ξ' tends to unity as Ntu approaches zero and decreases for increasing Ntu.

The result of this type of nondimensionalization is shown in Figs. 6 and 7. Apparently, when heat exchanger effectiveness is based on area utilization, heat exchanger configuration does not strongly influence effectiveness. The largest variation in effectiveness is 0.1, whereas, for the original definition of effectiveness, the largest difference is 0.5 (see Fig. 2–25, [8]).

A General Extended Surface Analysis Method

A. D. Snider
College of Natural Sciences

A. D. Kraus
College of Engineering,
Fellow, ASME
University of South Florida,
Tampa, Fla

An earlier paper by the authors presented an algorithm for analyzing certain arrays of extended surface, in terms of the heat transfer properties and geometries of the individual fins comprising the array. This paper identifies the subclass of arrays susceptible to such analysis as trees, in the graph theoretic sense, and extends the technique by deriving general equations for efficiently analyzing a perfectly arbitrary configuration of fins.

Introduction

In an earlier paper [1], the authors presented a new scheme for evaluating certain arrays of extended surface. The present paper will demonstrate how some basic techniques from graph theory can be used to establish a perfectly general set of equations which efficiently solve the extended surface problem for an *arbitrary* configuration of fins.

For expository convenience, it is best to begin by summarizing the results of [1].

For concreteness, consider the single pass cross flow heat exchanger core depicted in Fig. 1. It is assumed that the exchanger is operated under the idealized conditions listed in [1], usually attributed to Murray [3] and Gardner [4]. Roughly, this means that the heat flow in each fin is treated as one-dimensional and time-independent and that the source (hot fluid) and environment (coolant) remain at constant and uniform temperatures. In such a case, one can utilize symmetry to reduce the problem to the analysis of the heat flow in the repeating section shown in Fig. 2. Observe that symmetry dictates adiabaticity at the tips of fins 6 and 9. (Previous analyses of this triple stack have been based on other choices of the repeating section [5], but this one is best for illustrating the technique. In a general case, of course, there would be no symmetry and the entire array must be used).

The heat transfer characteristics of any individual fin in the array can be expressed in one of two ways. First, identify one end of the fin as the base and the other as the tip. Denote the base and tip temperature excesses (i.e., fin temperature minus environmental temperature) by θ_b and θ_t, and denote the base and tip heat flows by q_b and q_t, respectively, in accordance with the sign conventions indicated in Fig. 3. Then

i for each fin with finite (non-zero) tip width, i.e., a *regular* fin, there is a 2×2 *thermal transmission matrix*, Γ, which relates tip conditions to base conditions via

$$\begin{bmatrix}\theta_t\\ q_t\end{bmatrix} = [\Gamma]\begin{bmatrix}\theta_b\\ q_b\end{bmatrix} = \begin{bmatrix}\gamma_{11} & \gamma_{12}\\ \gamma_{21} & \gamma_{22}\end{bmatrix}\begin{bmatrix}\theta_b\\ q_b\end{bmatrix} \tag{1}$$

ii For each fin with zero tip width, i.e. a *singular fin*, there is a single *thermal transmission ratio* μ which governs the base conditions via the equation

$$\frac{q_b}{\theta_b} = \mu \tag{2}$$

The Γ and μ parameters for most of the commonly manufactured fin shapes are given in [1] and [6].

These are situations in which a regular fin can be regarded as having a fixed, known value of q_b/θ_b, as, for instance, if the tip is adiabatic, or isolated and exposed to the environment. In such cases, the two equations displayed in (1) can be reduced to a single equation like (2) and the regular fin inherits a thermal transmission ratio and can be treated as singular (cf. [1]).

With the individual fins thus characterized, [1] advocates analyzing an *array* of fins by establishing the $q{:}\theta$ ratios at the tips of the extreme fins (which are either adiabatic or exposed), and using (1) and (2) and continuity conditions to work back through each fin until the source, or "base surface," is reached. A glance at Fig. 2 exposes the inadequacy of this technique; the appearance of a loop in the fin configuration foils the method, as there is no unique path back to the source.

Therefore, the algorithm described in [1] (and subsequently extended in [2]) is restricted to arrays that contain no loops, i.e., trees, in the graph theoretical sense. Nonetheless, the techniques espoused therein can be useful in reducing more general arrays, as will be seen in subsequent sections of this paper.

The Thermal Admittance Matrix

For the convenience of the general analysis it's convenient to recast (1) into the form

$$\begin{bmatrix}q_b\\ q_t\end{bmatrix} = [Y]\begin{bmatrix}\theta_b\\ \theta_t\end{bmatrix} = \begin{bmatrix}y_{11} & y_{12}\\ y_{21} & y_{22}\end{bmatrix}\begin{bmatrix}\theta_b\\ \theta_t\end{bmatrix} \tag{3}$$

where the elements of the *thermal admittance matrix* Y can be computed from the elements of the thermal transmission matrix Γ:

$$y_{11} = -\gamma_{11}/\gamma_{12} \quad y_{12} = 1/\gamma_{12}$$

$$y_{21} = -\det[\Gamma]/\gamma_{12} \quad y_{22} = \gamma_{22}/\gamma_{12}$$

For singular fins, one can verify that the equations of the form (3) still hold with

$$Y = \begin{bmatrix}\mu & 0\\ 0 & 0\end{bmatrix} \tag{4}$$

Thus, the distinction between regular and singular fins is unnecessary with the admittance matrix formulation.

Elementary Connections

Before turning to the fully general algorithm, it is worthwhile to discuss some preliminary reductions that can be performed on an array to simplify its analysis. In particular, it is possible to treat a pair of fins as one single fin if the pair is connected in one of three basic ways. The exposition of these "elementary connections" will help place the results of [1, 2] in perspective.

In the *cascade* connection, the base of fin 2 is connected to the tip of fin 1 (Fig. 4). Continuity requires that

$$\theta_b{}^{(2)} = \theta_t{}^{(1)};\ q_b{}^{(2)} = q_t{}^{(1)} \tag{5}$$

The resulting composite thermal transmission matrix is then the product of the individual thermal transmission matrices:

$$\begin{bmatrix}\theta_t{}^{(2)}\\ q_t{}^{(2)}\end{bmatrix} = [\Gamma_2]\begin{bmatrix}\theta_b{}^{(2)}\\ q_b{}^{(2)}\end{bmatrix} = [\Gamma_2]\begin{bmatrix}\theta_t{}^{(1)}\\ q_t{}^{(1)}\end{bmatrix} = [\Gamma_2\Gamma_1]\begin{bmatrix}\theta_b{}^{(1)}\\ q_b{}^{(1)}\end{bmatrix} \tag{6}$$

(Equivalently, one can express base conditions in terms of tip conditions, using the matrix $T = \Gamma^{-1}$; then the composite T equals T_1T_2. The advantage of Γ is that it arises directly as a solution of the heat flow equation and has been tabulated [1, 6]).

In the *parallel* connection, the fins are connected at the base *and* at the tip (Fig. 5). The continuity conditions become [7]

$$\theta_b{}^{(1)} = \theta_b{}^{(2)} \equiv \theta_b;\ \theta_t{}^{(1)} = \theta_t{}^{(2)} \equiv \theta_t \tag{7}$$

Contributed by The Heat Transfer Division for publication in the JOURNAL OF HEAT TRANSFER. Manuscript received by the Heat Transfer Division April 30, 1980.

Because the heat flows add, the resulting composite thermal admittance matrix is the sum of the individual thermal admittance matrices:

$$\begin{bmatrix} q_b{}^{(1)} + q_b{}^{(2)} \\ q_t{}^{(1)} + q_t{}^{(2)} \end{bmatrix} = [Y_1] \begin{bmatrix} \theta_b{}^{(1)} \\ \theta_t{}^{(1)} \end{bmatrix} + [Y_2] \begin{bmatrix} \theta_b{}^{(2)} \\ \theta_t{}^{(2)} \end{bmatrix} = [Y_1 + Y_2] \begin{bmatrix} \theta_b \\ \theta_t \end{bmatrix} \quad (8)$$

In the *cluster* connection, the fins are joined at the base only, with both tips free of further connections (Fig. 6). As mentioned in the foregoing this implies that each fin, singular or not, can be characterized by an effective thermal transmission ratio. The continuity condition is

$$\theta_b{}^{(1)} = \theta_b{}^{(2)} = \theta_b \quad (9)$$

and inasmuch as the heat flows add at the base, the resulting composite thermal transmission ratio is the sum of the individual thermal transmission ratios:

$$\frac{q_b{}^{(1)} + q_b{}^{(2)}}{\theta_b} = \frac{q_b{}^{(1)}}{\theta_b{}^{(1)}} + \frac{q_b{}^{(2)}}{\theta_b{}^{(2)}} \quad (10)$$

When the fin configuration contains no loops, (6) and (10) can be *employed iteratively to solve the array; this is the thesis of [1].* The occurrence of isolated loops can be handled using (8), but a configuration like Fig. 2 can only be reduced, not solved completely, by these elementary connections. A more powerful algorithm is necessary.

The General Array Algorithm

To analyze an arbitrary fin configuration (with or without the preprocessing discussed in the previous section) one first represents the array by a labeled, directed graph with its edges (branches) corresponding to the individual fins and its nodes corresponding to the connection points. The orientation arrows point from base to tip on each individual fin. The graph of the repeating section in Fig. 2 is displayed in Fig. 7.

Now consider the mathematical problem of solving for the heat flows and temperatures. For a rough count, disregard any singular fins. Each regular fin carries four unknowns; for e fins there are $4e$ unknowns. The transmission matrices (1) account for $2e$ relations. At each node there is one heat-flow-balance equation and $(l_i - 1)$ temperature balance equations, if l_i fins adjoin the ith node. For n nodes the total number of equations is therefore

$$2e + \sum_{i=1}^{n} (1 + l_i - 1) = 4e \quad (11)$$

($\Sigma l_i = 2e$ because every regular fin adjoins two nodes).

The classical strategy [5] is to work from these $4e$ equations in $4e$ unknowns. Inasmuch as $e = 7$ in Fig. 7 (disregarding the effectively singular fins 6 and 9), the reader will appreciate the efficiency of the graph-theoretical algorithm to be described; it gives a direct formulation of this problem with five equations and five unknowns! To express the continuity equations systematically and efficiently, one uses an *incidence matrix*, Ω, to describe the physical connections, that is, the *topology* of the configuration. Ω is defined as follows: Ω has *one* row for each node and *two* columns for each edge of the graph. If the

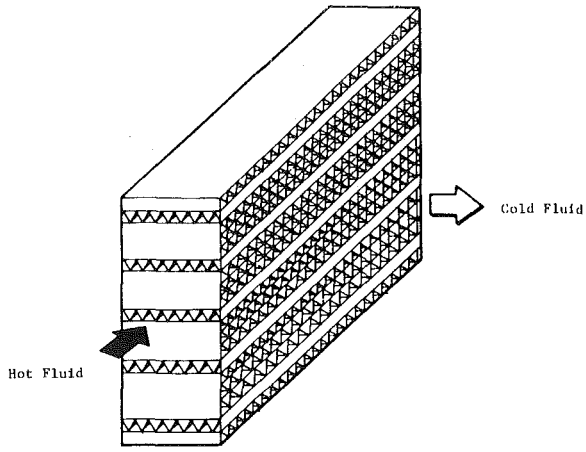

Fig. 1 Cross-flow heat exchanger (Courtesy, Airesearch Division of Garrett Corporation)

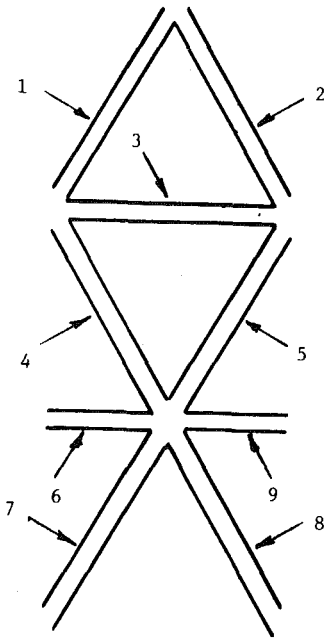

Fig. 2 Repeating section of triple stack on one side of cross-flow heat exchanger

Nomenclature

A = oriented incidence matrix
a = elements of A
e = number of edges
J = combination of matrices ($J = \Omega S Y_g \Omega^T$)
l = number of fins adjoining a node
n = number of nodes
Q = source heat flow, Btu/hr (watts)
q = heat flow, Btu/hr (watts); can refer to a heat flow vector
$\mathbf{q}$ = heat flow vector
r = rank of matrix
S = sign correcting matrix
T = temperature, °F (°C)
Y = thermal admittance matrix
Y_g = fin-graph admittance matrix
y = elements of Y
α = corner element of J^{-1}
β = corner element of J^{-1}
Γ = thermal transmission matrix
γ = elements of Γ
δ = corner element of J^{-1}
ϵ = corner element of J^{-1}
θ = temperature excess, °F (°C)
μ = thermal transmission ratio, Btu/hr-°F (watts/°C)
Υ = inverse of Γ ($\Upsilon = \Gamma^{-1}$)
Ω = fin incidence matrix
ω = elements of Ω

Subscripts

a = a particular value
b = base conditions; also designates a particular value
i = an index
t = tip conditions

graph has e edges and n nodes, Ω is n by $2e$. The first column corresponding to a given edge indicates to which node the base of that edge is attached and the second column identifies the node attached to the tip. Formally, the elements of Ω are $\omega_{i,2j-1} = 1$ if the j^{th} base adjoins the i^{th} node; $\omega_{i,2j} = 1$ if the j^{th} tip adjoins the i^{th} node; and $\omega_{rs} = 0$ otherwise. For example, for the fin graph in Fig. 7 Ω is given by

$$
[\Omega] = \text{Nodes}
\begin{array}{c}
\\ 1 \\ 2 \\ 3 \\ 4 \\ 5 \\ 6 \\ 7 \\ 8
\end{array}
\begin{array}{c}
\overbrace{}^{1} \overbrace{}^{2} \overbrace{}^{3} \overbrace{}^{4} \overbrace{}^{5} \overbrace{}^{6} \overbrace{}^{7} \overbrace{}^{8} \overbrace{}^{9} \\
\text{Edges}
\end{array}
\begin{bmatrix}
1\,0 & 1\,0 & 0\,0 & 0\,0 & 0\,0 & 0\,0 & 0\,0 & 0\,0 & 0\,0 \\
0\,1 & 0\,0 & 0\,1 & 1\,0 & 0\,0 & 0\,0 & 0\,0 & 0\,0 & 0\,0 \\
0\,0 & 0\,1 & 1\,0 & 0\,0 & 1\,0 & 0\,0 & 0\,0 & 0\,0 & 0\,0 \\
0\,0 & 0\,0 & 0\,0 & 0\,1 & 0\,1 & 1\,0 & 1\,0 & 1\,0 & 1\,0 \\
0\,0 & 0\,0 & 0\,0 & 0\,0 & 0\,0 & 0\,1 & 0\,0 & 0\,0 & 0\,0 \\
0\,0 & 0\,0 & 0\,0 & 0\,0 & 0\,0 & 0\,0 & 0\,1 & 0\,0 & 0\,0 \\
0\,0 & 0\,0 & 0\,0 & 0\,0 & 0\,0 & 0\,0 & 0\,0 & 0\,0 & 0\,1 \\
0\,0 & 0\,0 & 0\,0 & 0\,0 & 0\,0 & 0\,0 & 0\,0 & 0\,1 & 0\,0
\end{bmatrix} \tag{12}
$$

Now the continuity conditions for heat flow state that, at every node, the heat going out to each incident fin base must be balanced by the heat coming in from each incident fin tip, plus the heat input from the sources if there are any. Thus at the i^{th} node

$$\Sigma\, q_b{}^{(j)} - \Sigma\, q_t{}^{(j)} = Q_i \tag{13}$$

where the first sum extends over the fins with base incident to node i and the second extends over those with tip incident to node i; Q_i is the source input at the i^{th} node.

One can read off from the +1 entries of the i^{th} row of Ω precisely which terms come into the sum (13). If the heat flows are arranged into a column vector as

$$\mathbf{q} = [q_b{}^{(1)}, -q_t{}^{(1)}, q_b{}^{(2)}, -q_t{}^{(2)}, \ldots, q_b{}^{(e)}, -q_t{}^{(e)}]^T \tag{14}$$

then the continuity conditions for heat flow can be expressed as

$$\Omega\mathbf{q} = Q \tag{15}$$

with $Q = [Q_1, Q_2, \ldots, Q_n]^T$

Continuity conditions for the temperatures simply state that all θ's attached at a given node are equal. Forming the vector

$$\theta = [\theta_b{}^{(1)}, \theta_t{}^{(1)}, \theta_b{}^{(2)}, \theta_t{}^{(2)}, \ldots, \theta_b{}^{(e)}, \theta_t{}^{(e)}]^T \tag{16}$$

one observes that the node to which a given base (tip) is attached can be found by looking for the +1 entry in the corresponding column of Ω. Thus, if one constructs a column vector, $\boldsymbol{\theta}$, whose i^{th} component is the common value of the temperature excesses at node i

$$\boldsymbol{\theta} = [\theta_1, \theta_2, \ldots, \theta_n]^T \tag{17}$$

then the continuity conditions for the temperatures can be expressed as

$$\theta = \Omega^T\boldsymbol{\theta} \tag{18}$$

Finally, one can mathematically assemble all of the thermal admittance equations, one for each fin, into a *single* matrix equation:

$$
\begin{bmatrix}
q_b{}^{(1)} \\ q_t{}^{(1)} \\ q_b{}^{(2)} \\ q_t{}^{(2)} \\ \vdots \\ q_b{}^{(e)} \\ q_t{}^{(e)}
\end{bmatrix}
=
\begin{bmatrix}
y_{11}^{(1)} & y_{12}^{(1)} & 0 & 0 & \cdots & 0 & 0 \\
y_{21}^{(1)} & y_{22}^{(1)} & 0 & 0 & \cdots & 0 & 0 \\
0 & 0 & y_{11}^{(2)} & y_{12}^{(2)} & \cdots & 0 & 0 \\
0 & 0 & y_{21}^{(2)} & y_{22}^{(2)} & \cdots & 0 & 0 \\
 & & & \cdots\cdots & & & \\
0 & 0 & 0 & 0 & \cdots & y_{11}^{(e)} & y_{12}^{(e)} \\
0 & 0 & 0 & 0 & \cdots & y_{21}^{(e)} & y_{22}^{(e)}
\end{bmatrix}
\begin{bmatrix}
\theta_b{}^{(1)} \\ \theta_t{}^{(1)} \\ \theta_b{}^{(2)} \\ \theta_t{}^{(2)} \\ \\ \theta_b{}^{(e)} \\ \theta_t{}^{(e)}
\end{bmatrix}
$$

i.e.,

$$q = Y_g\theta \tag{19}$$

where Y_g is the (tridiagonal) *fin-graph admittance matrix* and q is the column vector of heat flows.

Then combining (15, 18) and (19) results in the node equations for the n nodal temperature excesses

$$\Omega S Y_g \Omega^T\boldsymbol{\theta} = \mathrm{Q} \tag{20}$$

where S is a "sign correcting" matrix relating $\mathbf{q}$ and q via $\mathbf{q} = Sq$:

$$
[S] = \begin{bmatrix}
1 & 0 & 0 & 0 & \cdots & 0 & 0 \\
0 & -1 & 0 & 0 & \cdots & 0 & 0 \\
0 & 0 & 1 & 0 & \cdots & 0 & 0 \\
0 & 0 & 0 & -1 & \cdots & 0 & 0 \\
 & & & \text{------} & & & \\
 & & & \text{------} & & & \\
0 & 0 & 0 & 0 & \cdots & 1 & 0 \\
0 & 0 & 0 & 0 & \cdots & 0 & -1
\end{bmatrix} \tag{21}
$$

The awkward appearance of $[S]$ in the node equations (20) could be eliminated by reversing the sign convention for q_t (Fig. 3), but this would fly in the face of tradition (cf. [5]), as well as cause difficulty elsewhere (e.g., the cascade procedure [1]).

The node equations can be constructed directly from the fin graph and are quite few in number: one for each node. Preprocessing by exploiting the elementary connections may reduce this number still further, and a special "trick" to be described in the next section allows one to discount nodes occurring at isolated fin tips, such as nodes 5 and 7 in Fig. 7. As promised, a subsequent example will show that the repeating section leads to only five node equations. Thus, the algorithm expressed by (20) would appear to be the method of choice for the analysis of general finned arrays.

Comments on the Node Equations

1 If the tip of a particular fin has no other fins or sources connected to it, as fins 6 and 9 in Fig. 7, the corresponding node equations can be obviated by the following device. Observe that, inasmuch as the fin is effectively singular, its contribution to the fin-graph admittance matrix Y_g produces a row of zeroes because of (4). Thus, the equation is redundant and the associated node temperature excess does not appear in the system (20).

Of course there is no loss of information because the performance of such a fin does not depend on its tip temperature, as demonstrated by (2). To take advantage of this, one can delete the fin from consideration, replacing it in the fin-graph by an equivalent negative heat source at its *base* node, injecting heat *into* the node at a rate (in accordance with (2))

$$Q_i = -\mu\theta_i \tag{22}$$

This substitution introduces no new unknowns and preserves the linearity of the node equations. It can be used whenever a subgraph of the fin graph contains no loops.

2 The similarity of the node equations (20) to the node equations for an electrical network is tempting but misleading. The temperature excesses θ are not "across variables" like voltage; the operating characteristics of a fin depend on *both* θ_b and θ_t and not merely on their difference. Thus, for instance, one cannot treat any of the nodes as a datum. Moreover, the heat flows differ at the base and tip; q is not a "through variable". Consequently, there is no thermal analogy to the loop currents of circuit theory. A partial analogy with electrical two-part theory does exist and will be exploited in a future paper.

3 The matrix Ω contains precisely the same information as the customary n by e oriented incidence matrix A (cf. [8]):

$$a_{ij} = \begin{cases} +1 \text{ if the base of fin } j \text{ adjoins node } i \\ -1 \text{ if the tip of fin } j \text{ adjoins node } i \\ 0 \text{ otherwise} \end{cases}$$

This leads one to suspect that the algorithm could be formulated in terms of A, but the present authors are doubtful on this point. Certainly A can be linearly expressed in terms of Ω, because the columns of the former are combinations of the columns of the latter; but Ω cannot be obtained linearly from A, because the rank of Ω exceeds the rank of $[A]$ ($r(\Omega) = n$, $r(A) = n - 1$).

Example

The technique will now be applied to the fin configuration in Fig. 2, whose fin graph is depicted in Fig. 7.

First of all observe that fins 6 and 9 form a cluster. Thus their effective μ's can be added. Also fins 7 and 8 are connected in parallel (because they have the same base and tip temperatures). Thus their Y's can be added. These preliminary simplifications reduce the graph to Fig. 8, with fins 6 and 7 appropriately modified. The location of the heat sources is also shown (recall Fig. 2).

As mentioned in remark 1 in the previous section, node 5 and fin 6 can be replaced by an effective heat source feeding node 4 at the rate $Q_4 = -\mu_6\theta_4$. The incidence matrix for the fin graph then becomes

$$\Omega = \begin{array}{c} \text{node} \\ 1 \\ 2 \\ 3 \\ 4 \\ 6 \end{array} \begin{array}{c} \text{fin} \\ \begin{bmatrix} 1\,0 & 1\,0 & 0\,0 & 0\,0 & 0\,0 & 0\,0 \\ 0\,1 & 0\,0 & 0\,1 & 1\,0 & 0\,0 & 0\,0 \\ 0\,0 & 0\,1 & 1\,0 & 0\,0 & 1\,0 & 0\,0 \\ 0\,0 & 0\,0 & 0\,0 & 0\,1 & 0\,1 & 1\,0 \\ 0\,0 & 0\,0 & 0\,0 & 0\,0 & 0\,0 & 0\,1 \end{bmatrix} \\ 1 \quad 2 \quad 3 \quad 4 \quad 5 \quad 7 \end{array}$$

The fin graph admittance matrix has the form

$$[Y_g] = \begin{bmatrix} [Y_1] & [0] & [0] & [0] & [0] & [0] \\ [0] & [Y_2] & [0] & [0] & [0] & [0] \\ [0] & [0] & [Y_3] & [0] & [0] & [0] \\ [0] & [0] & [0] & [Y_4] & [0] & [0] \\ [0] & [0] & [0] & [0] & [Y_5] & [0] \\ [0] & [0] & [0] & [0] & [0] & [Y_7] \end{bmatrix}$$

Assembling the components of (20) and identifying the sources results in

$$[\Omega S Y_g \Omega^T] \begin{bmatrix} \theta_1 \\ \theta_2 \\ \theta_3 \\ \theta_4 \\ \theta_6 \end{bmatrix} = \begin{bmatrix} Q_a \\ 0 \\ 0 \\ -\mu_6\theta_4 \\ Q_b \end{bmatrix} \tag{23}$$

If T_a and T_b are specified, then θ_1 and θ_6 are known and (23) expresses five linear equations in the unknowns θ_2, θ_3, θ_4, Q_a, and Q_b. If desired flow rates Q_a and Q_b are specified, then (23) expresses linear equations for the θ_i, from which T_a and T_b can be calculated.

A single performance index for the array could be defined by assuming it is loaded symmetrically, so that $\theta_1 = \theta_6$, and using (23) to

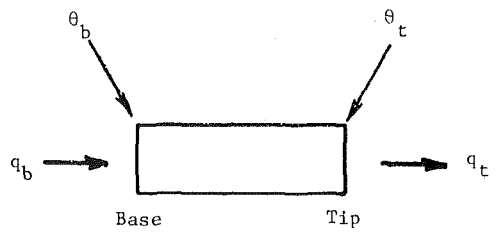

Fig. 3 Sign conventions for fin analysis

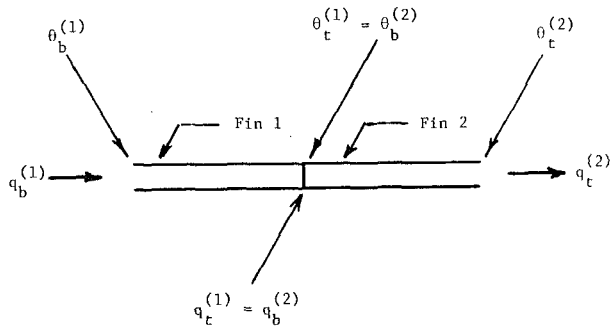

Fig. 4 Cascade connection

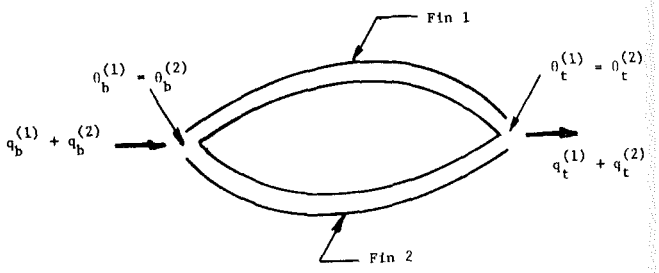

Fig. 5 Parallel connection

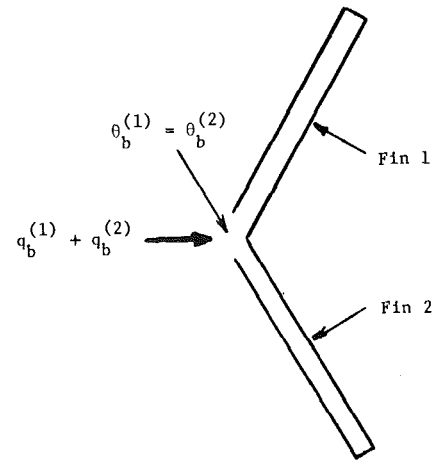

Fig. 6 Cluster connection

compute the ratio of total heat dissipated to base temperature excess $(Q_a + Q_b)/\theta_1$. To carry this out, observe that if μ_6 is added to the (4,4) entry of $\Omega S Y_g \Omega^T$, and the result is called J, then (22) becomes

$$[J]\begin{bmatrix}\theta_1\\ \theta_2\\ \theta_3\\ \theta_4\\ \theta_6\end{bmatrix} = \begin{bmatrix}Q_a\\ 0\\ 0\\ 0\\ Q_b\end{bmatrix}$$

Observe further that if the "corner" elements of J^{-1} are labeled α, β, δ, and ϵ,

$$[J]^{-1} = \begin{bmatrix}\alpha & \cdots & \beta\\ \cdot & & \cdot\\ \cdot & & \cdot\\ \cdot & & \cdot\\ \delta & \cdots & \epsilon\end{bmatrix}$$

then $\theta_1 = \alpha Q_a + \beta Q_b$, $\theta_6 = \delta Q_a + \epsilon Q_b$. And a little algebra shows that, when $\theta_1 = \theta_6$, $(Q_a + Q_b)/\theta_1 = (\alpha - \beta + \epsilon - \delta)/(\alpha\epsilon - \beta\delta)$.

Clearly, any other relevant parameters can similarly be extracted from the equations represented by (22). The elements of J^{-1} can be identified as cofactors, but the fact that Y_g is nondiagonal inhibits the development of convenient topological formulas (analogous to Kirchhoff's third and fourth laws). In any event, it is usually better numerically to solve equations than compute inverses.

Example

In [1] an unsymmetrically loaded 11.1 plain plate fin heat exchanger with splitter plates (a double stack or double sandwich) was analyzed with the aid of a mathematical artifice which appeared somewhat ad hoc. The solution will now be repeated using the general array algorithm; it is more straightforward (but admittedly longer). The units of Btu/hr and °F are employed for comparison with [1].

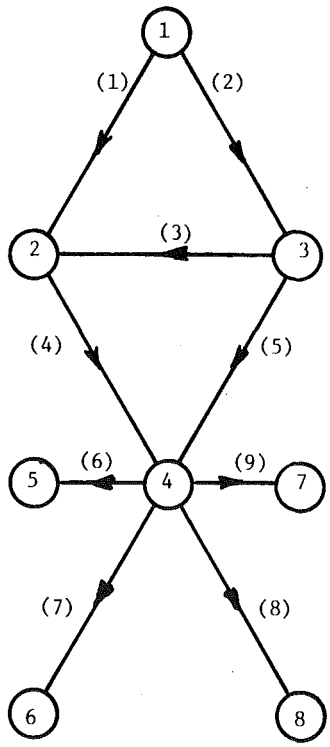

Fig. 7 Graph of repeating section shown in Fig. 2. Numbers in parentheses indicate edges

The configuration is shown in Fig. 9 with the oriented graph of the repeating section displayed as Fig. 10. Pertinent dimensions may be extracted from [1].

In accordance with (3), the thermal admittance matrices for each of the fins are calculated to be

$$[Y_1] = [Y_4] = \begin{bmatrix}2.54 & -2.34\\ 2.34 & -2.54\end{bmatrix}$$

$$[Y_2] = [Y_3] = \begin{bmatrix}21.95 & -21.91\\ 21.91 & -21.95\end{bmatrix}$$

The relevant matrices become

$$[\Omega] = \begin{bmatrix}1&0&0&0&0&0&0&0\\ 0&1&1&0&1&0&1&0\\ 0&0&0&0&0&0&0&1\\ 0&0&0&1&0&0&0&0\\ 0&0&0&0&0&1&0&0\end{bmatrix}$$

$$[Y_g] = \begin{bmatrix}2.54&-2.34&0&0&0&0&0&0\\ 2.34&-2.54&0&0&0&0&0&0\\ 0&0&21.95&-21.91&0&0&0&0\\ 0&0&21.91&-21.95&0&0&0&0\\ 0&0&0&0&21.95&-21.91&0&0\\ 0&0&0&0&21.91&-21.95&0&0\\ 0&0&0&0&0&0&2.54&-2.34\\ 0&0&0&0&0&0&-2.34&-2.54\end{bmatrix}$$

For this particular application 10 Btu/hr were injected into the base of fin 1, and 8 Btu/hr into the tip of fin 4. Therefore

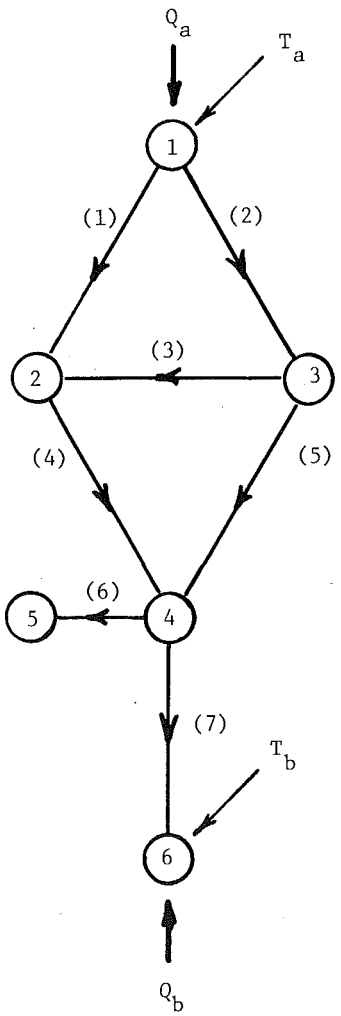

Fig. 8 Fin graph of Fig. 7 with preliminary simplifications

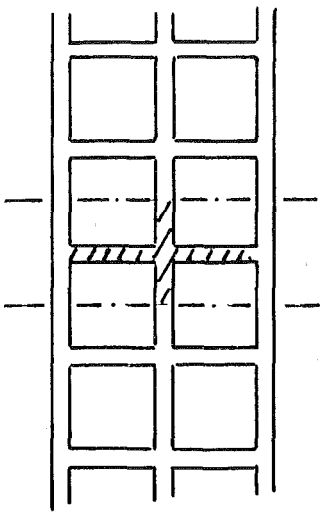

Fig. 9 Double stack arrangement of compact heat exchanger surfaces. The cross hatched area is a repeating section for analysis.

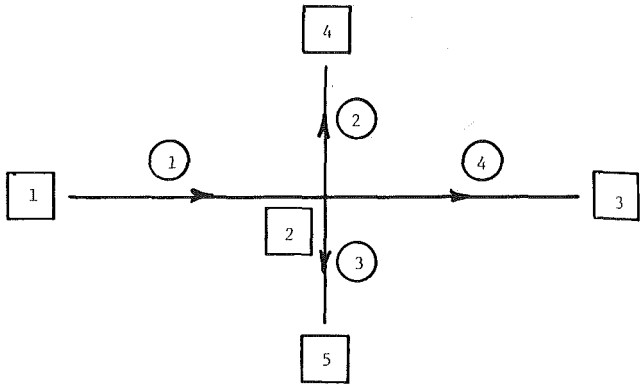

Fig. 10 Oriented graph for repeating section in Fig. 9. Numerals in circles represent fins, numerals in boxes represent node points.

$$[Q] = \begin{bmatrix} 10 \\ 0 \\ 8 \\ 0 \\ 0 \end{bmatrix}$$

The foregoing matrices, along with $[S]$, are multiplied in accordance with (20), resulting in

$$\begin{bmatrix} 2.54 & -2.34 & 0 & 0 & 0 \\ -2.34 & 48.97 & -2.34 & -21.91 & -21.95 \\ 0 & -2.34 & 2.54 & 0 & 0 \\ 0 & -21.91 & 0 & 21.95 & 0 \\ 0 & -21.91 & 0 & 0 & 21.95 \end{bmatrix} \begin{bmatrix} \theta_1 \\ \theta_2 \\ \theta_3 \\ \theta_4 \\ \theta_5 \end{bmatrix} = \begin{bmatrix} 10 \\ 0 \\ 8 \\ 0 \\ 0 \end{bmatrix}$$

By Gauss elimination or other appropriate method the following results are obtained:

$$[\theta] = \begin{bmatrix} 20.15 \\ 17.63 \\ 19.36 \\ 17.59 \\ 17.59 \end{bmatrix} (°F)$$

Here it is observed that $\theta_1 = 20.15°F$ and $\theta_3 = 19.36°F$, in agreement with [1].

Summary and Conclusion

This paper has described a new technique for systematically and efficiently analyzing a general array of extended surface. The algorithm is based on principles of graph theory, employing a novel kind of incidence matrix.

The results of previous work [1, 2] have been placed in perspective; they are applicable (and recommended) when the array is a tree, and in more general configurations they furnish useful rules for preliminary simplifications. The transmission matrices and ratios defined therein find their way into the general algorithm through the thermal admittance matrices (3).

A rather spectacular—and quite realistic—example, plus the experience gleaned from electrical network theory [8] lead to the conclusion that the present technique is the method-of-choice for analyzing a general array.

Acknowledgment

Support to A. D. Kraus by the National Science Foundation under grant ENG 77-01297 is gratefully acknowledged.

References

1 Kraus, A. D., Snider, A. D., and Doty, L. F., "An Efficient Algorithm for Evaluating Arrays of Extended Surface," ASME JOURNAL OF HEAT TRANSFER, Vol. 100, May 1978, pp. 288–293.

2 Razelos, P., discussion of "An Efficient Algorithm for Evaluating Arrays of Extended Surface," ASME JOURNAL OF HEAT TRANSFER, Vol. 102, Feb. 1980, pp. 185–186.

3 Murray, W. M., "Heat Dissipation Through an Annular Disk or Fin of Uniform Thickness," *Journal of Applied Mechanics*, J:A7B, 1938.

4 Gardner, K. A., "Efficiency of Extended Surfaces," *Trans ASME*, Vol. 67, 1945, p. 621.

5 Kern, D. Q., and Kraus, A. D., *Extended Surface Heat Transfer*, McGraw-Hill, New York, 1972.

6 Kraus, A. D., and Snider, A. D., "New Parameterizations for Heat Transfer in Fins and Spines," ASME JOURNAL OF HEAT TRANSFER, Vol. 102, Aug. 1980, pp. 415–419.

7 Kraus, A. D., *Analysis of Arrays of Extended Surface*, NSF Grant Report, Grant No. ENG 77-01297.

8 Johnson, D. E., and Johnson, J. R., *Graph Theory with Engineering Applications*, Ronald Press, New York, 1972.

Prediction of Heat Transfer Coefficients in Gas Flow Normal to Finned and Smooth Tube Banks

J. C. Biery
Los Alamos Scientific Laboratory,
Los Alamos, N.M.
and
Chairman,
Department of Chemical Engineering,
University of Florida
(Deceased)

A new method is presented to predict heat transfer coefficients for gas flow normal to smooth and finned tube tanks with triangular pitch. A transformation from the actual tube bank to an equivalent equilateral triangular pitch infinite smooth tube bank (ETP-I-STB) is made. A function of C_h ($C_h = N_{ST}N_{PR}{}^{2/3}N_{Re}0.4$) versus $(X_t\ D_0)_\Delta$, ratio of transverse pitch to tube diameter for the ETP-I-STB, was developed. The C_h for the equivalent ETP-I-STP then applies to the actual tube bank. The method works with circular finned tubes, smooth tubes, continuous finned tubes, and segmented finned tubes with any triangular pitch. Also, fair predictions were made for in-line tubes with high Reynolds numbers.

Introduction

Until recently, prediction of heat transfer and heat transfer coefficients in gas flow normal to tube banks has been done without the assistance of any general correlations. For instance, in the description of such heat transfer phenomena in Kays and London [1] and Fraas and Ozisik [2] much data are presented for specific cases of heat transfer particularly over bare and finned tubes. The suggested procedure is to find an experimental set of data for conditions similar to those being designed to predict the proper heat transfer coefficients.

Recently, Mirkovic [3] has presented a very fine set of data concerning heat transfer to gases flowing normal to finned tube banks. Also, the experiments were designed to generate an overall correlation that takes into account the transverse and longitudinal tube bank pitch in addition to the fin spacing and fin length for triangular pitch tube banks. The correlation is specific to triangular pitch finned tubing and is not applicable to smooth, flattened, continuous finned tube arrays.

In an attempt to provide a general predictive method for heat transfer in gases in normal flow over tube banks with varying geometries and finning, the following transformation method was developed and is presented below. The procedure presented allows for the prediction of much of the heat transfer data presented in Kays and London, Fraas and Ozisik, and Mirkovic by a transformation method that appears to be useful for finned tubes, smooth tubes, flattened tubes in triangular pitch and, in some cases, for the same in-line configurations.

General Development of the Transformation Method

The method given below for the prediction of heat transfer coefficients for smooth tube, finned tube, flattened tube, continuous-fin and segmented-fin tube banks in triangular pitch was somewhat suggested by the development in Kays and London [1]. In that development, they had observed that the general correlation given in equation (1) applied for gas flow normal to smooth tube banks with only a relatively small variation in the C_h coefficient. Unfortunately, C_h was a function of the longitudinal and transverse pitch of the tube bank, and, therefore, a general correlation was not presented.

$$N_{ST}N_{PR}{}^{2/3} = C_hN_{RE}{}^{-0.4} \tag{1}$$

In this new transformation method, the main task is to find an *equilateral triangular pitch infinite smooth tube bank* (ETP-I-STB) that has the same D_h/D_0, hydraulic diameter divided by a characteristic diameter, as the tube bank being considered. The heat transfer coefficient for this ETP-I-STB is that desired for the real bank. For instance, to predict the heat transfer for a smooth tube bank with a 1.5–2.0 transverse and longitudinal pitch (the numbers refer to the X_t divided by D_0 and X_1 divided by D_0 for the tube bank), an equivalent ETP-I-STB should be found that has the same D_h/D_0 of the non-equilateral pitch smooth tube bank. (For the 1.5–2.0 bank, D_h/D_0 equals 1.27. The (X_t/D_0) for the equivalent bank is 1.68.) The hydraulic diameter utilized in this development is that of Kays and London [1] and is given in equation (2).

$$D_h = 4r_h = \frac{4A_cX_1}{A_{HT}} \tag{2}$$

The minimum flow area, A_c, many times will be in the transverse direction to flow. However, for tube banks with a short X_1 compared to X_t the minimum flow area may well be along the diagonal of the triangular pitched bank.

Figure 1 shows a diagram of the triangular array with the flow normal to the tubes. In this case the fin tubes are shown. However, the same dimensions and configurations are utilized for the triangular pitch smooth tube arrays. By applying the formula for the hydraulic diameter in equation (2) to a triangular pitch smooth tube array, the ratio of the hydraulic diameter divided by the diameter of the tube is given in equation (3).

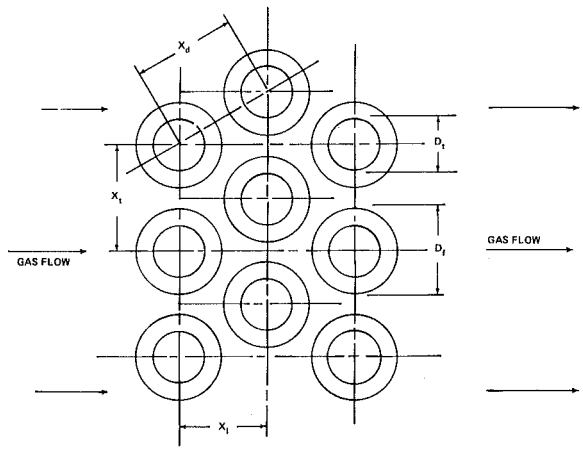

Fig. 1 Triangular layout of the tube bank with normal gas flow

Contributed by the Heat Transfer Division for publication in the JOURNAL OF HEAT TRANSFER. Manuscript received by the Heat Transfer Division, September 15, 1980.

$$\frac{D_h}{D_0} = 4\left[\frac{X_{\min}}{D_0} - 1\right]\left(\frac{X_1}{D_0}\right)\Big/\pi \tag{3}$$

$X_{\min}$ is utilized in equation (3) and is the smaller of the two numbers of X_t and X_d. If the array is an equilateral triangular array, then the ratio of D_h diameter to D_0 is given in equation (4), and, of course, is only a function of $(X_t/D_0)_\Delta$.

$$\left(\frac{D_h}{D_0}\right)_\Delta = 4\left[\left(\frac{X_t}{D_0}\right)_\Delta - 1\right]\left[0.866\left(\frac{X_t}{D_0}\right)_\Delta\right]\Big/\pi \tag{4}$$

Thus, when an equivalent ETP-I-STB array is being sought, the hydraulic diameters given by equations (3) and (4) are equated. First, the hydraulic diameter for the array being designed is calculated by equation (3). It is then substituted into equation (4) for the hydraulic diameter of the ETP-I-STB. As a result, the new pitch-to-diameter ratio for the ETP-I-STB is calculated via equations (5) and (6).

$$A = \left(\frac{D_h}{D_0}\right)\left[\frac{\pi}{4(0.866)}\right] \tag{5}$$

$$\left(\frac{X_t}{D_0}\right)_\Delta = \frac{+1 + (4A+1)^{1/2}}{2} \tag{6}$$

Then, if C_h for ETP-I-STB is known as a function of the ratio of $(X_t/D_0)_\Delta$, then C_h is also known for the array being considered.

To find the C_h function of $(X_t/D_0)_\Delta$, the data of Kays and London [1] and Grimison [4] and the data of Pierson [5] from Fraas and Ozisik [2] were analyzed by the above procedure. The data were converted into the form of equation (1). The C_h for each configuration was thus calculated. The $(X_t/D_0)_\Delta$ of the equivalent ETP-I-STB was determined by equations (2–6) and the results were then plotted in Figs. 2 and 3.

The transformation does have the property of bringing all of the various configurations onto one curve. The two sets of data shown in Figs. 2 and 3 generated similar and almost identical C_h versus $(X_t/D_0)_\Delta$ curves with empirical curve fitting. The function of C_h versus $(X_t/D_0)_\Delta$ given in equation (7) resulted.

$$C_h = 0.2818\left(\frac{X_t}{D_0}\right)_\Delta - 0.1282 - \frac{0.08263\left[1.20 - \left(\frac{X_t}{D_0}\right)_\Delta\right]}{\left[\left(\frac{X_t}{D_0}\right)_\Delta - 0.8924\right]} \tag{7}$$

Thus, the procedure for predicting Stanton numbers and heat transfer coefficients for triangular pitch smooth tube arrays other than equilateral configurations has been completed with the generation of the C_h function. By obtaining the hydraulic diameter, dividing it by the diameter of the tube, and finding then an equivalent ETP-I-STB with the same hydraulic diameter to diameter of tube ratio, a new characteristic dimension of this array is developed, $(X_t/D_0)_\Delta$. By insertion of this dimension into the C_h function, equation (1), C_h is thus generated for the desired array.

The hydraulic diameter characteristic of the array being studied is, of course, incorporated in the Reynolds number. Also, the Stanton number includes a mass flow term, which is the gas flow rate through the minimum flow area whether diagonal or transverse. An interesting result of the above correlation and transformation is that if the hydraulic diameter calculated on the transverse dimension is utilized in both the transformation calculation and in the Reynolds number, the C_h function, equation (7), produces the correct C_h for the particular hydraulic radius being utilized. However, in all cases, even though the hydraulic diameter may not be calculated on the minimum flow area, the G mass flow rate is always calculated on the minimum flow area, whether diagonal or transverse. Data are presented in Figs. 1 and 2 for the three possible cases of D_h being calculated on the minimum flow area or the frontal flow area or the diagonal flow area. Again, comparable results are produced in all three cases with the transformation being utilized.

The main reason for the developing this transformation is the hope that it will be applicable to other configurations that involve finned tubing.

Application of Transformation Method to Finned Tube Data

The data for gas flow normal to a series of circular finned tube banks as presented in Kays and London [1] in Figs. 10-75 through 10-82 were analyzed with the above outlined transformation method. Also, included in the Kays and London set of graphs were a series of data taken by Jameson [6]. Initially, the characteristic diameter, D_0, of the finned tubes was taken to be the tube diameter, D_t. The results, however, from the transformation with this particular characteristic diameter gave only partially satisfactory results. Then, by trial and error and empirical fitting, a better characteristic diameter, that was 0.8 of the distance from the root of the fin to the tip of the fin, was discovered to give very satisfactory predictions of C_h. The results of

Nomenclature

A = dimensionless factor defined by equation (5)

A_{HT} = total heat transfer surface area, including fin surface and edges of fins, per unit length of tube

A_C = minimum flow area for gas per unit length of tube (note: area can be transverse to flow or diagonal to flow; see Fig. 1)

C_h = dimensionless coefficient defined in equation (1)

C_p = specific heat of gas at constant pressure

D_h = hydraulic diameter; defined in equation (2)

D_f = diameter of fins

D_t = diameter of tube with fins

D_0 = diameter of smooth circular tube

D_x = transverse dimension of flattened tube

D_f = characteristic diameter defined by equation (10)

$D_{0.8}$ = characteristic diameter defined by equation (10) with $F = 0.8$

de_t = hydraulic diameter used by Mirkovic'

$$\frac{2A_{HT}}{I_k} = \frac{D_t(1 - T_hF_{\text{in}}) + D_f(T_hF_{\text{in}})}{(D_f - D_t)F_{\text{in}} + 1} + \frac{\frac{1}{2}(D_f{}^2 - D_f)^2F_{\text{in}}}{(D_f - D_t)F_{\text{in}} + 1}.$$

D_y = longitudinal dimension of flattened tube

f = fin efficiency as defined by Kays and London [1]

ETP-I-STB = equilateral triangular pitch infinite smooth tube bank

F_{in} = number of fins per unit length

F = dimensionless factor in D_F equation, equation (10)
= defined as a function of fin spacing, in equation (12)

G = gas mass flow rate through minimum flow area, A_c

G_f = geometrical factor in K_T, equation (11)
$= K_T/(N_{\text{Nu}}N_{\text{PR}}{}^{-0.33})$

h = heat transfer coefficient
h is utilized in $q = hA_{HT}\epsilon_f(T_g - T_s)$

I_K = projected perimeter of tube per unit length

k = thermal conductivity of gas at bulk stream conditions

K_T = dimensionless parameter, used by Mirkovic' and defined by equation (11)

N_{NU} = Nusselt number = hD_h/k

N_{PR} = Prandtl number = C_p/k

N_{RE} = Reynolds number = GD_h/μ (note: for other publications cited, N_{RE} and N_{NU} defined with other diameters such as D_0, de_t)

N_{ST} = Stanton number = h/C_pG

q = rate of heat transfer to a unit length of tube

r_h = hydraulic radius = A_CX_1/A_{HT}

S_{BF} = spacing between fins

T_h = thickness of fin

T_g = temperature of mixed gas stream flowing past tube surface

T_s = temperature of outside tube surface, at base of fins if tubing finned

μ = viscosity of gas at bulk stream conditions

X_d = diagonal distance between tubes, center to center, in triangular array

X_1 = longitudinal distance between rows, centerline to centerline

X_t = transverse distance between tubes, center to center, in a row

$X_{\min}$ = smaller of X_d and X_t

$(X_t/D_0)_\Delta$ = dimensionless transverse distance between tubes in equivalent ETP-I-STB

the data analysis of the Kays and London and the Jameson data are presented in Fig. 4.

The calculation of the hydraulic diameter is made via the equation (2). Equations (8) and (9), however, give the detailed calculation in reference to the tube diameter, fin diameter, longitudinal pitch, transverse pitch, and fin thickness. The characteristic diameter, $D_{0.8}$ is calculated via equation (10*b*).

$$D_h = 4r_h = \frac{4A_cX_1}{A_{HT}} = \frac{4[(X_{\min} - D_t) - (D_f - D_t)F_{in}T_h]x_1}{\pi[D_t(1 - T_hF_{in}) + D_f(T_hF_{in}) + \frac{1}{2}(D_f^2 - D_t^2)F_{in}]} \quad (8)$$

$$X_{\min} = \text{smaller of} \begin{Bmatrix} X_t \\ X_d \end{Bmatrix} \quad (9)$$

$$D_F = D_t + F(D_f - D_t) \quad (10a)$$

$$D_{0.8} = D_t + 0.8(D_f - D_t) \quad (10b)$$

The predictive method is similar to that outlined for the smooth tube calculations. First, the hydraulic diameter, D_h, is calculated and is then divided by $D_{0.8}$. The parameter "A" then is calculated from equation (5) with the new $(D_h/D_{0.8})$ substituted for the smooth tube (D_h/D_0). The $(X_t/D_0)_\Delta$ for the equivalent ETP-I-STB is determined from equation (6). The $(X_t/D_0)_\Delta$ is then entered into the equation (7) to predict the C_h factor for the desired finned tube bank.

The data from Kays and London [1] and Jameson [6] are plotted in Fig. 4. A more detailed comparison of these data with the predicted transformation is given in Table 1. The overall results of the 39 values and their prediction is an average of 0.5 percent error with a standard deviation of 12.5 percent. The prediction method appears to be quite satisfactory for estimating the C_h value for the data being studied. Most of the data have a ±5 percent and possibly greater experimental error. Therefore, the transformation estimates that are generally within ±10 percent of the experimental data appear to be surprisingly good.

As indicated previously, Mirkovic' [3] published in 1974 a fine set of data for heat transfer across helical finned tubes. In addition, he presented an overall correlation for prediction of heat transfer coefficients with a consideration for the geometry of the bank and the structure of the finned tubing. The above transformation method was tested point by point with the experimental data as generated by Mirkovic' and published in the above reference [3]. The results are given in Fig. 5. The data as shown in Fig. 5 utilized the $D_{0.8}$ as the characteristic diameter, and the hydraulic diameter as previously outlined. The C_h predictive method estimated the values of C_h as compared with experimental values of C_h with an average error of +5.4 percent. The standard deviation was 8.5 percent.

The data of Mirkovic' were taken on a tube bank which had eight rows in it. As indicated in Kays and London [1], the overall average transfer coefficient for an eight-row bank should be approximately 92 percent of the heat coefficient for an infinite tube bank. Since the Kays and London data were extrapolated to an infinite tube bank, the data from Mirkovic' should have been approximately 8 percent low. As compared to the transformation method predictions, they were an average of 5.4 percent low. Therefore, the predictions and the Mirkovic' data agree quite well.

$$K_T = N_{NU}N_{PR}^{-0.33}\left[\frac{X_t - D_t}{D_t}\right]^{-0.1}\left[\frac{x_1 - D_t}{D_t}\right]^{+0.15} \times \left[\frac{1 - F_{in}T_h}{\frac{1}{2}F_{in}(D_f - D_t)}\right]^{-0.25} = 0.224\, N_{RE}^{0.66} \text{ (Note: } de_t \text{ used in } N_{RE} \text{ and } N_{NU}) \quad (11)$$

The Mirkovic' correlation, which is given in equation (11), was utilized to analyze the Mirkovic' data [3] and also the Kays and London [1] and Jameson [6] data. The overall results of the use of the equation on Mirkovic's own data gave very fine results as should be expected since these data produced the parameters and coefficients for the correlation. The overall result gave an average error of +0.3 percent with a standard deviation of 3.6 percent.

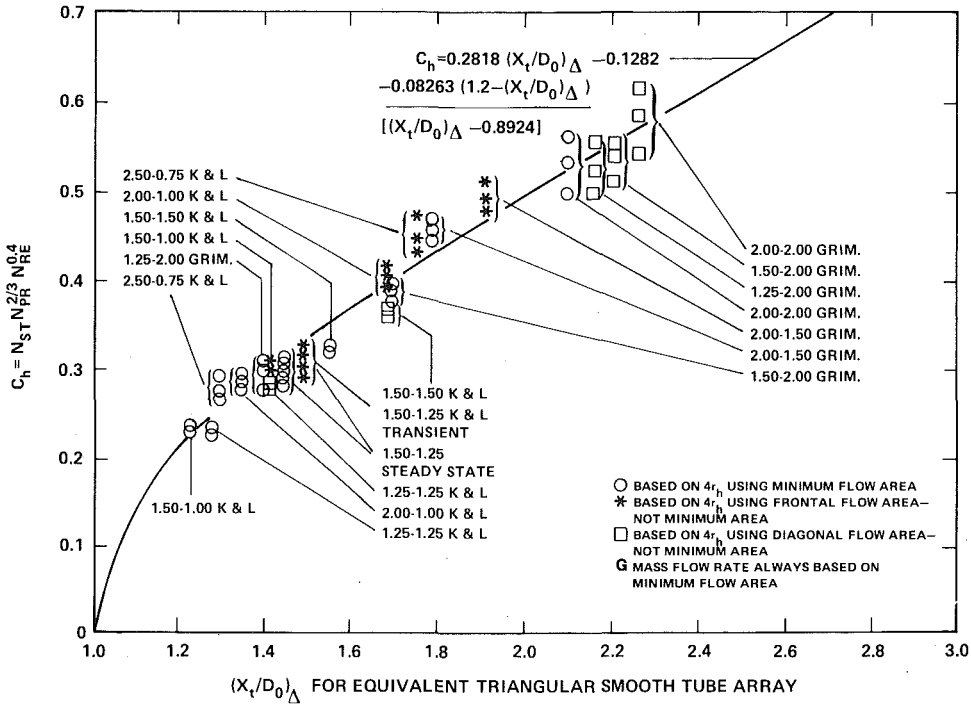

Fig. 2 Transformation of smooth tube data from Kays and London [1] and Grimison [4]

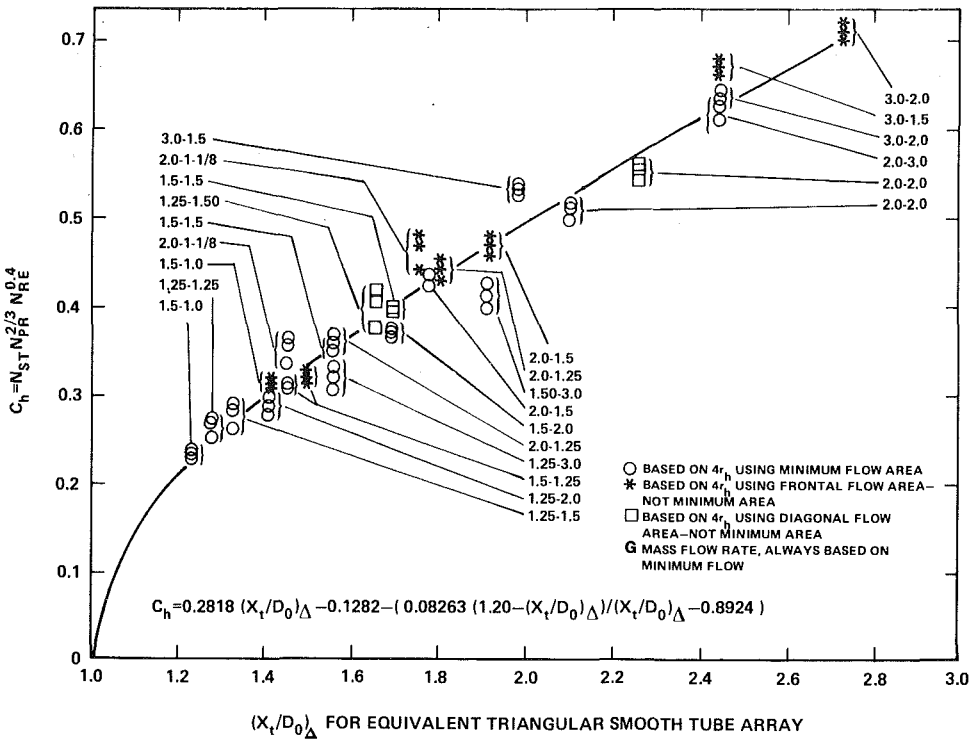

Fig. 3 Transformation of smooth tube data from Pierson [5] in Fraas and Ozisik [2]

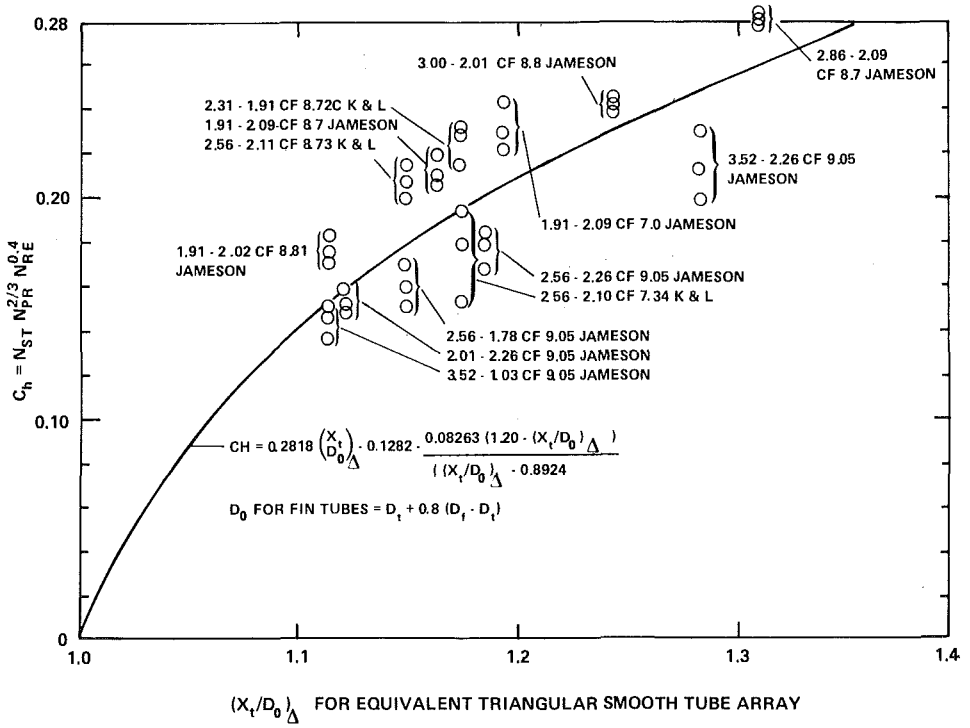

Fig. 4 Transformation of circular fin tube data from Kays and London [1] and Jameson [6]

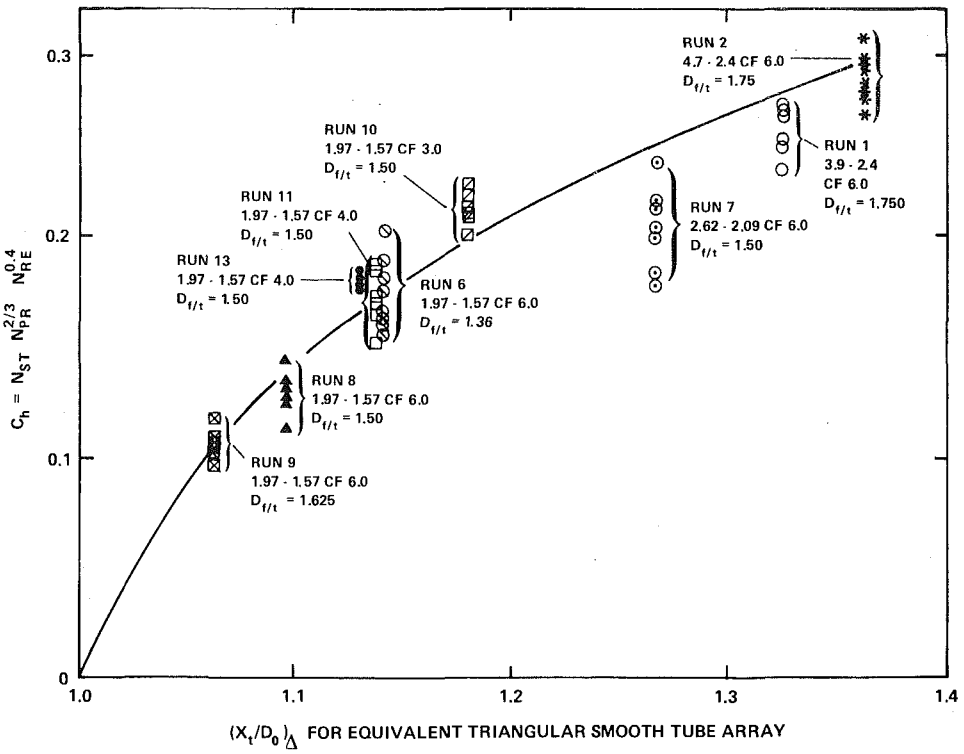

Fig. 5 Transformation of helical fin tube data from Mirkovic' [3]

The Mirkovic' correlation was also utilized to analyze the data of Kays, London and Jameson. The results are summarized in Table 1. Overall, the Mirkovic' prediction was quite good except for one run of the Jameson data.

The overall result not including this one Jameson run in Fig. 10-81-*D* [1] was an underprediction: a −5.6 percent average error for 36 data points with a standard deviation of 12.1 percent.

The comparison of the Mirkovic' correlation with the Jameson run indicated, however, a flaw in the formulation. The geometrical factor includes a term that subtracts the diameter of the tube from the longitudinal pitch. In a triangular pitch bank, where the transverse pitch is large and the longitudinal pitch small, the longitudinal pitch can approach and sometimes be smaller than the diameter of the tube. In the run from Fig. 10-81-*D* of Jameson as taken from Kays and London [1], the ratio of the longitudinal pitch to the diameter is 1.03. In this case, the geometrical term utilized in the Mirkovic' correlation gave a very unsatisfactory and unrealistic prediction. As a result, the Mirkovic' correlation predicted heat transfer coefficients that were between 80 and 90 percent too large.

A more detailed analysis of the experimental C_h from Mirkovic [3], versus the predicted C_h from the transformation is presented in Figs. 6 and 7. Each run of the Mirkovic' data is presented with C_h displayed as a function of the Reynolds number as based on the hydraulic diameter. If the transformation method were perfect, the C_h would be a constant value and would not be a function of the Reynolds number. In many cases the results give a fairly constant value of C_h. However, for the tube banks with very wide separation such as Run 5, where the diameter X_t/D_t and X_1/D_t were 4.3 and 3.1, the constant value of C_h was not achieved until a Reynolds number of approximately 10,000 was reached. Thus, some droop was indicated at the beginning of the C_h curves for the runs with the wide spacing between the tubes. Such early droop in the C_h value was evidenced in Runs 1, 3, 4, and 5. The slight early decrease in C_h would indicate a possible nonuniformity in the turbulent field surrounding the tubes. However, as the velocity was increased, the uniformity reached a consistancy such that C_h remained constant. The data indicate that the 0.4 coefficient on the Reynolds number gives nearly constant values of C_h at higher Reynolds number.

Mirkovic' did study the effect of varying the number of fins per unit length on the tube and the effect of this variation on the heat transfer coefficient. As indicated in Figs. 6 and 7, the transformation method handles quite well a variety of fin dimensions and fin spacing. However, Runs 10, 11, and 13, which have wider fin spacing, give C_h values that are a few percent above the predicted curve, while most of the other data were a few percent below the curve as would be expected with the smaller number of rows in the tube bank. The wider the spacing between the fins, the more freely the gas can circulate between the fins. Therefore, the characteristic diameter would be expected to decrease as the spacing between the fins increases. This trend was indicated very well in Run 10 where the spacing between the fins was approximately 7 mm. In most of the data from Kays and London, [1] and Jameson, [6] and Mirkovic' [3], the spacing was approximately 3 mm between fins.

Therefore, a minor modification of the transformation method was indicated by the Mirkovic' data. The characteristic diameter should be decreased somewhat as the spacing increases between the fins. With very wide spacing, of course, the characteristic diameter should approach the tube diameter of the finned tubing. An estimate for this changing percentage of the fins to be included in the characteristic diameter is presented as equation (12). This equation has the characteristic of giving a 0.8 factor for a spacing between fins of 3 mm. The factor goes to 1 as the spacing drops to 0 and approaches a 0 factor as the spacing goes to 9 mm.

The equation cannot be used with a space between fins greater than 9 mm. For Run 10 of the Mirkovic' data with S_{BF}(mm) equal to 7.2 mm, F equals 0.33 from equation (12), and the characteristic diameter is 59 mm as compared to 71.1 mm with F equal to 0.8. With this change, the prediction now is 1.4 percent high where it was 7 percent low. The modification is minor as indicated but seems to move the data in the correct direction for fins with wider spacing.

$$F = 1.35 - 0.183\, S_{BF(\text{mm})} - \left[\frac{3.0 - S_{BF(\text{mm})}}{S_{BF(\text{mm})}^{+8.57}}\right] \qquad (12)$$

Prediction of Heat Transfer for Segmented Fins

In 1978 Weierman, et al. [7] presented a paper describing heat transfer for in-line and staggered tube tanks with long segmented fins. The transformation method was tested on the staggered tube bank data. The results of these data are summarized in Table 2. With the use of the $D_{0.8}$ as the characteristic diameter, the estimate of the C_h transformation was approximately 20 percent low. If the diameter of the tube was used as a characteristic diameter, the estimate became 16 to 17 percent high. By trial and error, the best characteristic diameter for these segmented fins was shown to be the diameter at the root of the segmented cuts. With the use of the root diameter as the characteristic diameter, the estimate was approximately 2 percent high.

The use of the smaller characteristic diameter for this particular tube with segmented fins makes sense in that the segmented cuts in the fin tubing allows intercommunication of the gas flow streams from one fin space to another. Therefore, the characteristic diameter would then become smaller since the gas between the fins has more mobility. The use of the Mirkovic' correlation [3] gave an estimate that is between 23 and 32 percent too low. Thus, with the proper selection of a characteristic diameter, the transformation method gives a very fine estimate of the heat transfer performance of these segmental finned tubes. However, as indicated, the change of the characteristic diameter from D_t all the way to D_f gave an error range of −20 to +16 percent. Any one of these numbers would be quite satisfactory for an initial estimate of the heat transfer performance. However, with the use of the root diameter, the heat transfer coefficient is estimated quite accurately with the transformation method.

Use of Transformation Method with Continuous Fin and Finned Tubing with Flattened Tubes

The transformation method seems to satisfactorily predict the heat transfer coefficients for staggered banks of smooth and finned tubes. The method was, therefore, tested to determine whether or not it could predict heat transfer coefficients for continuous fin circular tubing and for flattened fin tubing with continuous fins. Of course, with these configurations a new choice for the characteristic diameter must be made since the fins are continuous and the $D_{0.8}$ formulation has no meaning. The data from Kays and London, and Trane presented in the Kays and London [1] were analyzed using the trans-

Table 1 Comparison of C_h transformation method and Mirkovic' correlation in predicting heat transfer coefficients for experimental circular fin tube data from Kays and London [1] and Jameson [6]

Data from Graphs		C_h Estimate				K_T Estimate—Mirkovic			
N_{RE} Based on D_h	$N_{ST}N_{PR}^{2/3}$	C_h(exp) Calculated from data	C_h(est) Est. from $(X_t/D_0)_\Delta$ Function	% Error C_h(exp)/ C_h(est)	N_{RE} Based On d_{e_t}	Geom. Factor, G_f	$N_{ST}N_{PR}^{2/3}$ = 0.224 $N_{RE}^{-0.34}$ G_f	% Error est./Exp.	
600	0.01506	0.195	0.196	+ 0.8	1980	1.193	0.01421	− 5.7	Fig. 10-75
2000	0.00860	0.180		+ 9.1	6600		0.00944	+ 9.7	CF-754
10000	0.00388	0.155		+26.9	33000		0.00546	+40.7	K & L
500	0.0180	0.216	0.180	−16.9	2000	1.255	0.01346	−22.1	Fig. 10-76
1500	0.0108	0.201		−10.7	6000		0.00927	−14.2	CF-8.72
6000	0.00645	0.209		−14.1	24010		0.00579	−10.3	K & L
500	0.01915	0.230	0.195	−15.1	1750	1.180	0.01499	−18.3	Fig. 10-77
2000	0.01035	0.217		− 9.8	7000		0.00935	− 9.6	CF-8.72 (C)
8000	0.00638	0.232		−15.9	28000		0.00584	− 8.5	K & L
1500	0.0120	0.223	0.207	− 7.4	4770	1.184	0.01063	−11.5	Fig. 10-79
3000	0.0094	0.231		−10.5	9540		0.00839	−10.7	Jameson
8000	0.0067	0.244		−15.2	25440		0.00601	−10.3	CF-7.0
1500	0.0112	0.209	0.189	− 9.6	5880	1.126	0.00933	−16.3	Fig. 10-80 A
3000	0.00855	0.210		−10.2	11770		0.00769	−10.1	Jameson
8000	0.00605	0.220		−14.3	31380		0.00528	−12.7	CF-8.7
2000	0.0134	0.280	0.263	− 6.3	3680	1.169	0.01175	−12.3	Fig. 10-80 B
5000	0.0094	0.284		− 8.4	9210		0.00861	− 8.5	Jameson
10000	0.00715	0.285		− 7.8	18410		0.00680	− 4.9	CF 8.7
1500	0.0082	0.153	0.161	+ 5.0	8020	1.414	0.00745	− 9.1	Fig. 10-81 A
3000	0.0061	0.150		+ 7.1	16040		0.00589	− 4.4	Jameson
6000	0.0049	0.159		+ 1.1	32080		0.00465	− 5.1	CF 9.05
2000	0.0081	0.169	0.202	+19.6	6700	1.354	0.00827	+ 2.1	Fig. 10-81 B
4000	0.0065	0.179		+12.9	13410		0.00653	+ 0.5	Jameson
8000	0.00515	0.186		+ 8.7	26810		0.00516	+ 0.2	CF 9.05
2000	0.0095	0.199	0.251	+26.3	4050	1.291	0.01030	+ 8.4	Fig. 10-81 C
5000	0.0071	0.214		+17.3	10130		0.00754	+ 6.2	Jameson
10000	0.0058	0.231		+ 8.8	20270		0.00596	+ 2.7	CF 9.05
1500	0.0074	0.138	0.156	+13.0	8500	0.750	0.01379	+86.4	Fig. 10-81 D
3000	0.0060	0.148		+ 5.4	16990		0.01090	+81.6	Jameson
6000	0.0047	0.153		+ 2.0	33980		0.00861	+85.1	CF-9.05
1500	0.0082	0.153	0.181	+18.0	6380	1.259	0.00905	+10.3	Fig. 10-81 E
3000	0.00655	0.161		+12.1	12800		0.00715	+ 9.1	Jameson
6000	0.00525	0.170		+ 6.2	25500		0.00565	+ 7.6	CF-9.05
1500	0.0093	0.173	0.157	− 9.5	8710	1.385	0.00740	−20.5	Fig. 10-82 A
3000	0.00715	0.176		−11.1	17420		0.00585	−18.3	Jameson
8000	0.0050	0.182		−14.0	46450		0.00419	−16.3	CF-8.81
2000	0.0115	0.241	0.232	− 3.7	5050	1.280	0.00964	−16.2	Fig. 10-82 B
4000	0.0088	0.243		− 4.4	10120		0.00761	−13.5	Jameson
10000	0.00615	0.245		− 5.2	25240		0.00558	− 9.2	CF-8.81

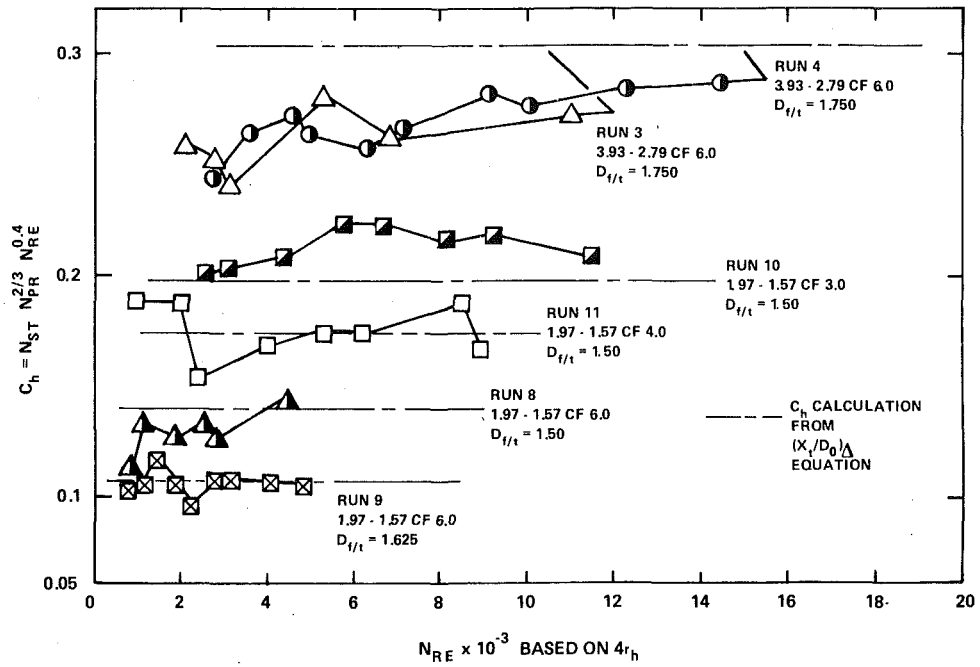

Fig. 6 Helical fin tube data from Mirkovic' [3] comparison of C_h experimental with C_h estimated from transformation versus Reynolds number

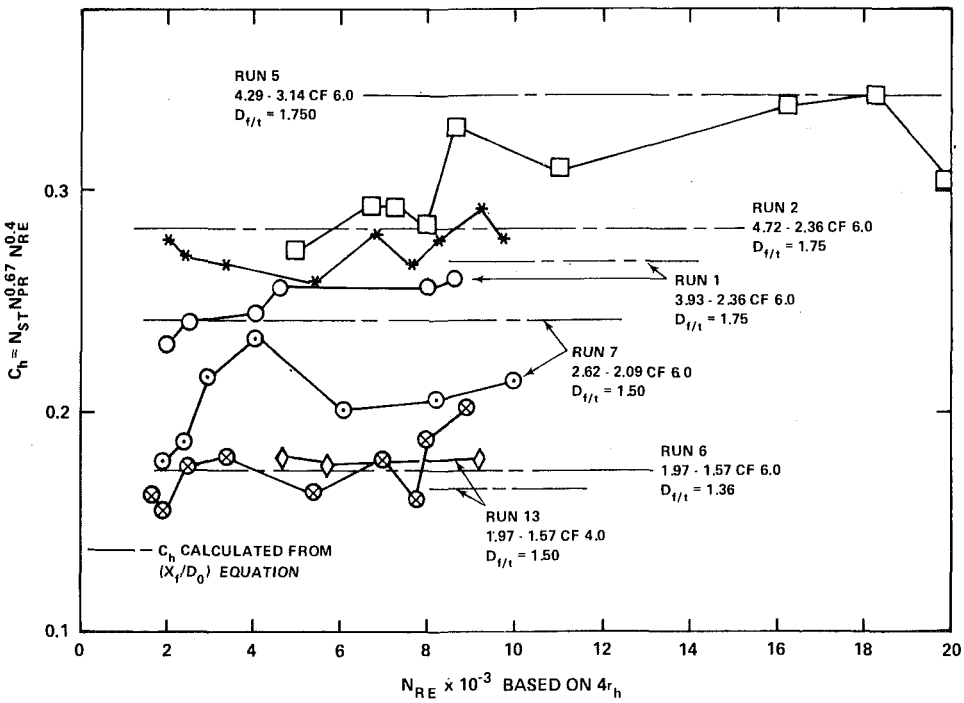

Fig. 7 Helical fin tube data from Mirkovic' [3] comparison of C_h experimental with C_h estimated from transformation versus Reynolds number

Table 2 Prediction of heat transfer coefficients for segmented fin tube data of Wierman, [7] using C_h Transformation method and Mirkovic' correlation [3]

Estimate with Transformation Method with Various Characteristic Diameters

N_{Re} Based on D_t	$N_{ST}N_{PR}^{2/3}$	N_{Re} Based on D_h	C_h exp.	C_h est. Based on $D_{0.8}$	% Error Est. / Exp	C_h (est) Based on D_t	% Error Est. / Exp.	C_h (Est) Based on Root of Slot	% Error Est. / Exp.
4000	0.0111	652	0.148	0.119	−19.6	0.167	+12.8	0.152	+2.7
7000	0.0089	1142	0.149		−20.1		+12.0		+2.0
18000	0.0059	2952	0.144		−17.4		+16.0		+5.5
36000	0.00485	5871	0.156		−23.7		+ 7.0		−2.6

Estimate with Mirkovic Correlation $G_f = 1.654$

N_{Re} Based on d_{et}	$N_{ST}N_{PR}^{2/3} = 0.224\ N_{RE}^{-0.34}$ / G_f	% Error
4934	0.00751	−32.4
8630	0.00621	−30.3
22330	0.00449	−23.9
44400	0.00356	−26.7

Table 3 Estimation of in-line tube bank heat transfer with C_h transformation method—smooth and flattened data from Kays and London [1] and Grimison [4]

Table No. In [1]	X_t/D_0	X_l/D_0	D_h/D_0	Based on D_h N_{RE}	$N_{ST}N_{PR}^{2/3}$ (Exp)	C_h (exp.)	C_h (est.) Eq. (7)	% Error
Fig. 10–12	1.50	1.25	0.796	10000	0.0073	0.291	0.330	+14
K & L				4200	0.010	0.281		+17
Fig. 10-13	1.50	1.25	0.796	10000	0.0071	0.283	0.330	+17
K & L				4500	0.0100	0.289		+14
Fig. 10-14	1.25	1.25	0.398	8200	0.0059	0.217	0.250	+14
K & L				2100	0.0100	0.213		+17
Fig. 10-15A	1.25	1.50	0.477	20000	0.0050	0.263	0.270	+ 3
Grimison				4000	0.0100	0.276		− 2
Fig. 10-15B	1.25	2.00	0.637	26000	0.0050	0.292	0.303	+ 4
Grimison				5100	0.0100	0.304		− 1
Fig. 10-15C	1.50	1.50	0.955	39000	0.0050	0.343	0.355	+ 3
Grimison				7000	0.0100	0.345		+ 3
Fig. 10-15D	1.50	2.00	1.273	50000	0.0050	0.379	0.397	+ 5
Grimison				9100	0.0100	0.383		+ 4
Fig. 10-16A	2.00	1.25	1.591	60000	0.0050	0.408	0.434	+ 6
Grimison				10000	0.0083	0.330		+31
Fig. 10-16B	2.00	1.50	1.910	70000	0.0050	0.433	0.467	+ 8
Grimison				10000	0.0090	0.358		+30
Fig. 10-16C	2.00	2.00	2.547	100000	0.0051	0.510	0.525	+ 3
Grimison				10000	0.0125	0.498		+ 6

Flattened In-Line Tubes

Figure No.	D_x/D_y	X_t/D_y	X_l/D_y	D_h/D_y	N_{RE} (Based on D_h)	$N_{ST}N_{PR}^{2/3}$ (Exp)	$N_{RE}^{0.4}$	C_h (exp)	C_h (est)	% Error
Fig. 10-17	0.403			0.545	10000	0.0055	39.81	0.219	0.284	+ 3
K & L					6000	0.0060	32.45	0.195		+ 46
					4000	0.0049	27.59	0.135		+110
Fig. 10-18	0.403	0.705	1.092	0.597	10000	0.0058	39.81	0.231	0.295	+ 27
K & L					5000	0.0060	30.17	0.199		+ 48

formation method. The characteristic diameters chosen are as follows:

1 For the continuous finned circular tubing, the D_f equivalent was chosen to be the minimum of X_t or X_1. The characteristic diameter was then chosen to be $D_{0.8}$ and was calculated using this definition of D_f.

2 For the finned flattened tubing, the D_f equivalent was chosen to be the diameter expressed in equation (13). This equivalent fin diameter is the dimension of the tube in the longitudinal direction plus the length of the fins between adjacent tubes in the transverse direction. The equivalent diameter then for the finned flattened tubing was taken to be that as expressed in equation (14). Equation (14) is similar to the normal $D_{0.8}$ equation with longitudinal diameter of the flattened fin tubing being the diameter of the tubes.

$$D_f = D_y + (X_t - D_x) \tag{13}$$

$$D_{0.8} = D_y + 0.8\,(D_f - D_y) \tag{14}$$

With the choice of the above equivalent fin diameters and the characteristic diameters for the continuous finned circular tubing and the continuous finned flattened tubing, the transformation then

produced the results as shown in Fig. 8. The results again were very satisfactory with the C_h grouping around the predictive curve in a ±15 percent band.

Use of Transformation of In-Line Smooth Tube Banks

As indicated by Weierman, et al. [7], the heat transfer coefficients for in-line tube banks may be substantially less than those for comparable staggered tube banks. The reason for the lower heat transfer is the nonhomogeneity of the turbulent field and the very wide variation of gas temperatures around the in-line tubes. Gas streaming can occur between the tubes with a subsequent smaller amount of heat transfer occurring. However, at high and very high Reynolds numbers where the turbulent field becomes more homogeneous, the transformation method as described here does give reasonable estimates of the heat transfer coefficients. The data of Kays and London, and Grimison as presented in Kays and London Figs. 10-12 through 10-16 [1] were analyzed with the transformation method to determine its applicability. The results of the prediction are given in Table 3. In general, for Reynolds numbers above 10,000, the prediction appears to be quite adequate for the in-line banks studied. The transformation method does tend to predict between 10 to 20 percent too high in many instances for in-line bank data. However, as a first guess at heat transfer coefficients for in-line tube banks, the transformation can be utilized.

For lower Reynolds numbers and banks with very wide spacing, the method may well predict C_h's that are substantially too high. The method was used on the flattened in-line tubes as shown in Figs. 10-17 and 10-18 in Kays and London [1]. The results were definitely unsatisfactory. In this case, the C_h estimates were approximately 30 percent high with Reynolds numbers at approximately 10,000. Again, for Reynolds numbers near 100,000 the estimate possibly would be quite satisfactory.

One set of in-line data from Weierman [7] were estimated by the transformation. For the segmental finned tubes with wide spacing, the error was very great and no satisfactory application of the transformation method could be made for this set of data. The error was approximately 130 percent too high.

Summary and Conclusion

A new transformation method is presented for the prediction of heat transfer coefficients for gas flowing normal to staggered tube banks. The method seeks out an equivalent equilateral triangular pitched infinite smooth tube bank (ETP-I-STB) with the same ratio of hydraulic diameter to characteristic diameter. The C_h factor from the ETP-I-STB is utilized as the C_h value for the bank being studied. (C_h is defined in equation (1).)

The method appears to have broad applicability. For the data analyzed it satisfactorily predicted heat transfer coefficients for triangular pitched smooth tube banks, for circular finned tube banks with triangular pitch, and for continuous finned tube banks for both circular and flattened tubes. In addition, one set of segmented fin tube data was satisfactorily simulated. The estimates were in general within ±15 percent of the experimental data. For systems with high Reynolds numbers, well above 10,000, the transformation method predicted quite satisfactorily the heat transfer coefficients for in-line smooth tube and finned tube banks. Thus, with use of the transformation method, a general procedure can be inserted into simulation programs for the study of a variety of smooth tube and finned tubes with a variety of geometric pitches to determine comparative heat transfer behavior.

References

1 Kays, W. M., and London, A. L., *Compact Heat Exchangers*, McGraw-Hill, New York, 2nd ed., 1964, Vol. 7, pp. 127–128, 164–227.

2 Fraas, A. P., and Ozisik, M. N., *Heat Exchanger Design*, Wiley, New York, 1965, pp. 326–332.

3 Mirkovic', Z., "Heat Transfer and Flow Resistance Correlation for Helically Finned and Staggered Tube Banks in Crossflow," in *Heat Exchangers: Design and Theory Source Book*, N. H. Afgan and E. U. Schlunder, eds., McGraw-Hill, New York, 1974, Chapter 20, pp. 559–584.

4 Grimison, E. D., "Correlation and Utilization of New Data on Flow Resistance and Heat Transfer for Cross-Flow Resistance and Heat Transfer for Cross Flow of Gases Over Tube Banks," *Trans ASME*, Vol. 59, 1937, pp. 583–594.

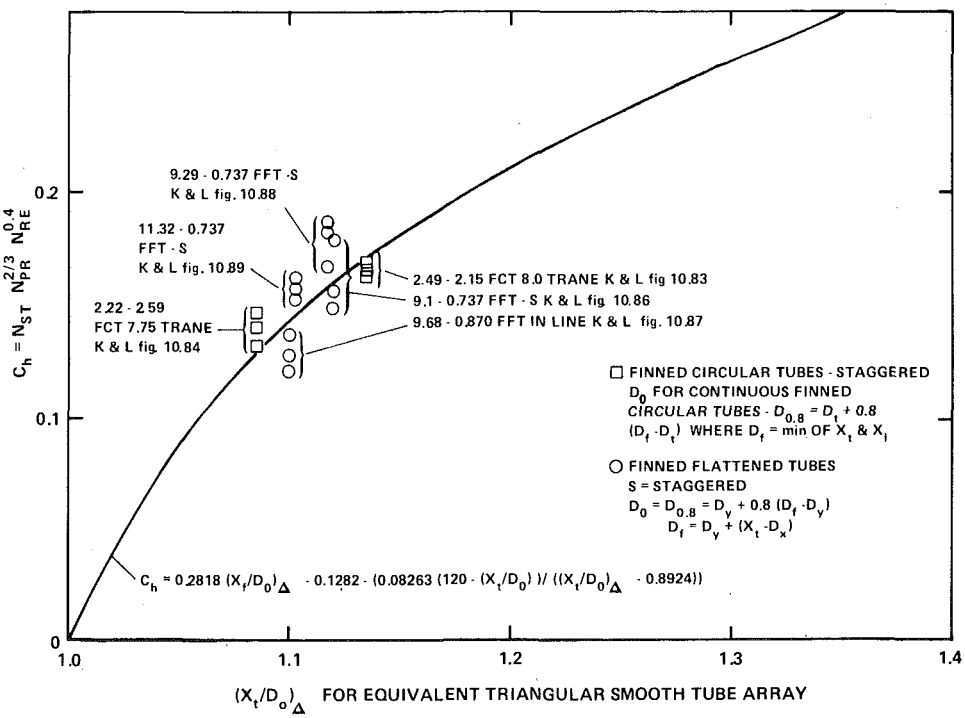

Fig. 8 Transformation of continuous fin circular and flattened tube data from Kays and London [1] and Trane

5 Pierson, O. L., "Experimental Investigation of the Influence of Tube Arrangement on Convection Heat Transfer and Flow Resistance in Cross Flow of Gases Over Tube Banks," *Trans. ASME*, Vol. 59, 1957, pp. 563–572.
6 Jameson, S. L., "Tube Spacing in Finned-Tube Banks," *Trans. ASME*, Vol. 67, 1945, pp. 633–642.
7 C. Weierman, Taborek, J., and Marner, W. J., "Comparison of the Performance of In-Line and Staggered Banks of Tubes with Segmented Fins," in *Heat Transfer Research and Applications*, J. C. Chen, ed., AIChE Symposium Series, 1978, No. 174, Vol. 74, AIChE, New York, pp. 39–46.

Modeling of a Rotary Dry Cooling Tower

J. A. Valenzuela

L. R. Glicksman

Mem. ASME

Department of Mechanical Engineering, Massachusetts Institute of Technology, Cambridge, Mass. 02139

A novel design of a rotary heat exchanger to be used as a dry cooling tower is described. The heat exchanger consists of a matrix of thin steel disks which rotate between a hot water bath and a forced draft air stream. On top of the water floats a 2 cm thick layer of oil which coats the rotating disks and thus eliminates evaporation. An analytical model of the heat exchanger was developed and validated with experimental measurements taken on a 1.5 m dia test section. The model was then used to determine the net effect of the oil on the heat transfer performance. Although the oil film that coats the disks presents an additional resistance to the transfer of heat, it also contributes to the heat capacity of the disks. It was found that the reduction in the overall heat transfer rate due to the presence of the oil is small, of the order of 5 to 10 percent.

Introduction

The Rotary Dry Cooling Tower (RDCT) analyzed in this paper is proposed as an alternative to the conventional finned-tube dry cooling tower. The RDCT would normally operate as a dry tower, but it would be possible to increase its heat rejection capacity during peak load periods by transferring some of the heat through evaporation.

A conceptual design of the RDCT is shown in Fig. 1. It consists of a matrix of thin annular metal disks mounted on a rotating shaft. The lower section of the disks is immersed in a water trough through which the condenser cooling water circulates in a closed loop. Ambient air is blown across the upper portions of the disks. Any given section of a disk absorbs heat as it rotates through the water bath and is later cooled by the air stream in a periodic fashion.

The RDCT can be operated in either a dry or a wet/dry mode. In the first case a layer of oil approximately 2 cm thick is floated on the water surface. As they rotate, the disks take on a thin oil film that, in turn, effectively suppresses evaporation. To operate the RDCT in a wet/dry mode the oil layer is drained off; water beads then adhere to the rotating disks and some evaporation takes place. In this mode of operation, the heat rejection capacity of the RDCT can be increased by as much as 50 to 100 percent [1].

The RDCT has significant potential for use in regions with scarce water supply. Its real impact will depend on the relative cost of the RDCT as compared with alternative technologies, such as conventional finned-tube dry cooling towers and Phase Change Ammonia Loop cooling towers. Preliminary cost studies [2] indicate that the RDCT, operating strictly as a dry tower, is cost competitive with the conventional finned-tube cooling tower. The ability of the RDCT to increase its heat rejection capacity during peak demand periods by operating in a wet/dry mode makes the comparison even more favorable.

In this paper a simplified analytical model of the RDCT is described. The model is then used for a parametric study of the RDCT performance and for the evaluation of the decrease in performance that results from the oil film coating the disks. The model predictions are also compared with experimental results.

Analytical Model

In principle the RDCT is similar to other periodic heat exchangers, such as those used to transfer heat between inlet and exhaust air streams. There are, however, some important differences between the RDCT and other periodic heat exchangers; specifically: the RDCT transfers heat between a gas stream and a liquid stream rather than between two gas streams; the flow direction of the water and air streams in the RDCT is perpendicular to the axis of rotation, rather than aligned with it; and there is in the RDCT a low conductivity oil film between the fluid streams and the rotating metal disks. Because of these differences the existing regenerative exchanger analysis, such as those given in references [3] and [4], are not applicable to the RDCT.

The flow conditions in an RDCT vary with position on the surface of the rotor. Not only is the rotor exposed to different fluids in different regions, but also within each region the fluid temperature and velocity relative to the disk change with position. A rigorous analysis of the RDCT would therefore require the subdivision of the rotor surface into infinitesimally small regions. The overall heat transfer rate would then be obtained by integrating the local rate over the entire surface. The inherent uncertainty in the prediction of the local flow conditions and film coefficients, however, does not warrant such rigorous treatment. A good approximation of the RDCT performance can be obtained by considering only a few regions which have more or less uniform flow characteristics, and using average values for the film coefficients in each region.

Experimental measurements [1] indicate that the water temperature is fairly uniform throughout the trough owing to the mixing induced by the rotating disks. There is, however, a small region of higher temperature in the vicinity of the inlet port. The water side was therefore modeled as two well-mixed heat exchangers in series.

Because of their annular configuration, most of the air flow across the disks is in a radial direction; that is, in crossflow with the rotor. Near the top of the rotor the disks and the air are in counterflow, but this region is too small to justify separate analysis. Since the disks are thin (~0.3mm) conduction in the rotor can be neglected. There are, moreover, no barriers to prevent the cross-mixing of the air stream. The air side was therefore modeled as two cross-flow heat exchangers in series with the air stream well mixed.

The subdivision of the RDCT into four heat exchangers interconnected by the rotor is shown in Fig. 2. The additional coupling between the two water-side heat exchangers was introduced in order to model the circulating water flow pattern set up by the rotation of the disks.

In modeling the RDCT three steps were involved: first, an effective heat transfer coefficient at the rotor surface was derived in order to account for the temperature gradient across the oil film; then, the flow in each region was modeled to obtain average film coefficients; and finally, the standard cross-flow and counter-flow effectiveness relations, which describe the performance of the individual heat exchangers, were combined to obtain an analytical expression for the overall effectiveness of the RDCT.

Effective Heat Transfer Coefficient. The oil film coating the metal disks plays an important role in the heat transfer process. Owing to its low thermal conductance, the oil film presents an additional resistance to the transfer of heat between the fluid streams and the metal disk. The oil, however, also contributes to the heat capacity of the rotor. The relative magnitude of these effects is a strong function of the oil film thickness.

Contributed by the Heat Transfer Division and presented at the 19th Annual AIChE/ASME Heat Transfer Conference, Orlando, Fla., July 27–30, 1980. Revised manuscript received by the Heat Transfer Division October 17, 1980. Paper No. 80-HT-95.

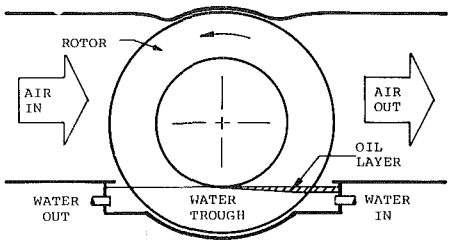

Fig. 1 Conceptual design of the Rotary Dry Cooling Tower

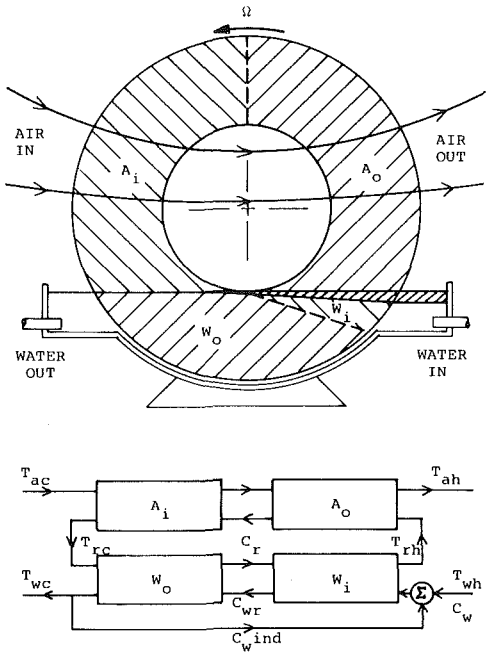

Fig. 2 Heat exchanger subsystems for the RDCT model

The oil film thickness distribution on the surface of the disk was determined theoretically and then verified experimentally. The average oil film thickness on the air side is given by [5]:

$$\delta_0 = \frac{8}{3}\left[\frac{\Omega R \nu_0}{g}\right]^{1/2}\left[\frac{(1-\eta)^{1/2}}{2^{3/2}(1+\eta)} - \frac{(1-\eta)^{3/2}}{2^{5/2}(1+\eta)}\right] \tag{1}$$

where η is the ratio of the inner to the outer radius of the rotor. For the typical operating conditions of the RDCT (see Appendix) the average oil film thickness is about 0.15 mm. Since the oil coats the disks on both sides, the total thickness of the oil film is roughly equal to the thickness of the metal. When the oil layer covers the entire surface of the trough, the oil film on the water side is two to three times thicker than the film on the air side. It was found, however, that the oil on the trough surface is driven towards the side where the disks rotate out of the water, as shown in Fig. 1. Under this operating condition, the disks cannot pick up additional oil as they enter the water, and consequently, the average oil film thickness on the water side is equal to that on the air side. That is the normal mode of operation of the RDCT.

The heat transfer process in the rotor is analogous to the problem of transient heat conduction in a composite wall subject to convective boundary conditions. Three heat transfer mechanisms are involved: (1) forced convection between the fluid and the oil surface; (2) conduction through the oil film; and (3) conduction within the metal disk. The relative importance of these mechanisms depends on the magnitude of the conductances associated with them. Some typical values for these conductances are:

Air-side film coefficient	$h_{fa} \sim 60$ W/m^2°C
Water-side film coefficient	$h_{fw} \sim 10^3$ W/m^2°C
Oil heat conductance	$h_0 = k_0/\delta_0 \sim 500$ W/m^2°C
Metal heat conductance	$h_m = k_m/\delta_m \sim 10^5$ W/m^2°C

Since the metal conductance is several orders of magnitude larger than the others, it is reasonable to assume a uniform temperature throughout the thickness of the disk. The other conductances, however, are comparable in magnitude and must all be considered in the analysis.

The rotor is not, strictly speaking, a lumped heat capacity system. Not only are there temperature gradients in the oil film, but also the magnitude of the oil and metal temperature excursions are different (the oil is hotter than the metal in the water side and cooler in the air side). The analysis of the individual heat exchangers, however, requires that a single temperature be assigned to the rotor at each point. One can account for the temperature gradients in the oil film by defining an effective heat transfer coefficient U that matches the heat transfer rates at the rotor surface, that is:

$$U(T_r - T_f) = h_f(T_s - T_f) \tag{2}$$

where the rotor mean temperature is given by:

$$T_r = \left[\frac{1}{n+1}\right]\overline{T}_0 + \left[\frac{n}{n+1}\right]T_m \tag{3}$$

and n is the metal-to-oil heat capacity ratio; T_m is the local metal temperature; $\overline{T}_0$ is the local average oil film temperature; T_s is the local oil surface temperature; and h_f is the local film coefficient. If the temperature profile in the oil film is approximated by a quadratic polynomial, an expression for the effective heat transfer coefficient can be obtained from equation (2) and (3) as:

$$U = \left[\frac{1}{1 + \mathrm{Bi}\left[\dfrac{3n(n+1)+1}{3(n+1)^2}\right]}\right]h_f \tag{4}$$

where the oil film Biot number is defined as $\mathrm{Bi} = h_f\delta_0/k_0$. Using the effective heat transfer coefficient defined in equation (4), the rotor can be modeled as a lumped capacity system with a total heat capacity equal to the sum of the metal and the oil film heat capacities. To verify the accuracy of this approximation, this lumped capacity analysis of

Nomenclature

A = area, m^2
Bi = Biot number
C = heat capacity rate, W/°C
g = acceleration of gravity, m/s^2
h = heat transfer conductance, W/m^2°C
h_f = heat transfer film coefficient, W/m^2°C
k = thermal conductivity, W/m°C
n = disk to oil heat capacity ratio
NTU = number of heat transfer units
RDCT = rotary dry cooling tower
Q_t = total heat transfer rate, W
R = radius, m
rpm = revolutions per minute
T = temperature, °C
U = heat transfer coefficient, W/m^2°C
δ_m = disk thickness, m
δ_0 = average oil film thickness, m
ϵ = heat exchanger effectiveness
η = ratio of the inner to outer radius of the disk
ν_0 = oil viscocity, m^2/s
Ω = angular velocity, rad/s

Subscripts

a = air
av = average
c = cold
f = fluid
h = hot
i = inlet
ind = induced
m = metal
o = outlet, oil
r = rotor
s = surface
w = water
wr = water recirculation

the composite wall was compared to the exact solution given in reference [6]. In the range of Bi and n likely to be found in the RDCT ($1 \le \text{Bi} \le 10$; $0.1 \le n \le 1$) the solutions were within 0.1 percent of each other.

Heat Exchanger Submodels. In computing the local film coefficients, two types of surfaces were considered: smooth surfaces and surfaces with repeated rib roughness. McAdams' [7] correlation was used for the smooth surfaces and Han's [8] correlation for the roughened surfaces. On the air side the film coefficient was modified to include entrance effects in the form suggested in reference [9].

Air Side. The flow in the two air-side heat exchangers was modeled as flow between parallel plates of rectangular shape. Owing to the annular configuration of the rotor, the air flow pattern is a combination of horizontal and radial flows, as shown in Fig. 3. An equivalent channel length was therefore defined as the average between the mean flow lengths obtained for purely radial and purely horizontal flows. The height of the channel was adjusted to make the total area of the rectangular heat exchangers equal to the air-side area of the rotor. The air stream heat capacity rate was obtained directly from the specified inlet flow conditions.

Expressions for the effectiveness of several standard heat exchanger configurations can be found in reference [3]. For the inlet air-side heat exchanger the effectiveness is given by:

$$\epsilon_{ai} = \frac{C_{\max(a,r)}}{C_r}\left[1 - \exp(-\Gamma C_r/C_a)\right]$$

$$\text{with } \Gamma = 1 - \exp(-\text{NTU}_{ai} C_{\min(a,r)}/C_r)$$

$$\text{and } \text{NTU}_{ai} = (A_{ai}U_{ai})/C_{\min(a,r)} \tag{5}$$

Substitution of NTU_{ao} for NTU_{ai} in equation (5) yields the expression for ϵ_{ao}.

Water Side. A simple model of the water circulation pattern was used to obtain the local flow conditions in the water-side heat exchangers. The details of the water circulation model can be found in reference [5]. Average film coefficients for each water-side heat exchanger were calculated by numerical integration of the local film coefficients. By integrating the local water flow rate across the boundary between the two water-side heat exchangers, the heat capacity rate of the recirculating water flow was obtained.

To account for its well-mixed condition, each water-side heat exchanger was modeled as a counter-flow exchanger with a water recirculation loop of infinite heat capacity rate, as shown in Fig. 4. The inlet heat exchanger effectiveness is defined as:

$$\epsilon_{wi} = \frac{Q_{wi}}{C_{\min(wr,r)}(T_{wrh} - T'_r)} \tag{6}$$

and similarly,

$$\epsilon' i = \frac{Q_{wi}}{C_{\min(i',r)}(T'_i - T'_r)} \tag{7}$$

An energy balance on the water streams yields:

$$Q_{wi} = C_{wr}(T_{wrh} - T'_{wr}) = C'_i(T'_i - T'_{wr}) \tag{8}$$

Combining equations (6–8) we obtain:

$$\epsilon_{wi} = \left[\frac{C_{\min(i',r)}/C_{\min(wr,r)}}{1 + \epsilon'_i C_{\min(i',r)}(1/C_{wr} - 1/C'_i)}\right]\epsilon'_i \tag{9}$$

In the limit as C_i' goes to infinity, ϵ_i' is given in reference [3] as: $\epsilon_i' = 1 - \exp(-\text{NTU}_{wi})$; where $\text{NTU}_{wi} = A_{wi}U_{wi}/C_r$. Equation (9) then becomes:

$$\epsilon_{wi} = \frac{C_r}{C_{\min(wr,r)}}\left[\frac{1 - \exp(-\text{NTU}_{wi})}{1 + \frac{C_r}{C_{wr}}\left[1 - \exp(-\text{NTU}_{wi})\right]}\right] \tag{10}$$

The expression for the outlet water-side heat exchanger effectiveness is obtained by substituting NTU_{wo} for NTU_{wi} in equation (10).

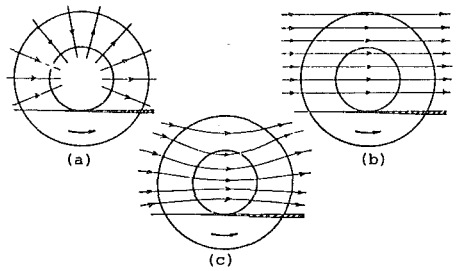

Fig. 3 Air side flow pattern: (*a*) radial flow; (*b*) horizontal flow; (*c*) real flow

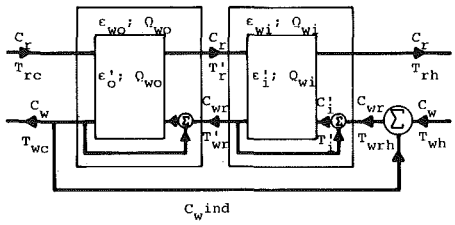

Fig. 4 Modelling of water-side well-mixed heat exchangers

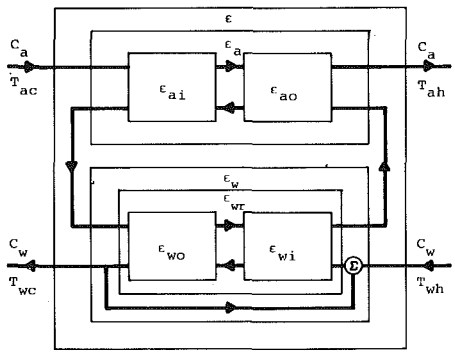

Fig. 5 Combination of individual heat exchanger effectiveness to obtain overall effectiveness of the RDCT

Overall Heat Transfer Effectiveness. The expressions for the individual effectiveness can be combined to obtain the overall effectiveness of the RDCT defined as:

$$\epsilon = \frac{Q}{C_{\min(a,w)}(T_{wh} - T_{ac})} \tag{11}$$

The steps followed in that derivation are illustrated in Fig. 5. First ϵ_{ai} and ϵ_{ao} are combined to obtain ϵ_a and similarly ϵ_{wi} and ϵ_{wo} are combined to obtain ϵ_{wr}. The water recirculation loop is then added to ϵ_{wr} to obtain ϵ_w. Finally, ϵ_a and ϵ_w are combined to obtain ϵ. Each one of these steps involves combining equations similar to equations (6–8). The complete derivation can be found in reference [5].

The overall heat transfer effectiveness of the RDCT was obtained as:

$$\epsilon \approx \left[\frac{C_{\min(a,w)}}{C_{\min(a,r)}}\frac{1}{\epsilon_a} + \frac{C_{\min(a,w)}}{C_{\min(w,r)}}\frac{1}{\epsilon_w} - \frac{C_{\min(a,w)}}{C_r}\right]^{-1} \tag{12}$$

where

$$\epsilon_a = \frac{C_a C_r(\epsilon_{ai} + \epsilon_{ao}) - C_{\min(a,r)}\epsilon_{ai}\epsilon_{ao}(C_a + C_r)}{C_a C_r - C^2_{\min(a,r)}\epsilon_{ai}\epsilon_{ao}} \tag{13}$$

$$\epsilon_w = \left[\frac{C_{\min(wr,r)}/C_{\min(w,r)}}{1 + \epsilon_{wr}C_{\min(wr,r)}(1/C_w - 1/C_{wr})}\right]\epsilon_{wr} \tag{14}$$

and

$$\epsilon_{wr} = \frac{C_{wr}C_r(\epsilon_{wi} + \epsilon_{wo}) - C_{\min(wr,r)}\epsilon_{wi}\epsilon_{wo}(C_{wr} + C_r)}{C_{wr}C_r - C^2_{\min(wr,r)}\epsilon_{wi}\epsilon_{wo}} \tag{15}$$

Parametric Analysis of Heat Transfer Performance

The overall effectiveness of the RDCT is a function of twelve parameters, as indicated by equations (5–15). Formally one can express the effectiveness as:

$$\epsilon = \epsilon(C_a, C_w, C_{wr}, C_r, A_{ai}, A_{ao}, A_{wi}, A_{wo}, U_{ai}, U_{ao}, U_{wi}, U_{wo}) \quad (16)$$

It is convenient to express this relationship in terms of nondimensional combinations of the independent parameters. Both air-side heat exchangers have the same areas and heat transfer coefficients, and therefore two of these variables can be eliminated. In addition, it was found that changing the relative size of the two water side heat exchangers has little effect on the heat transfer rate (less than 5 percent). Therefore, in order to simplify the graphical representation of the results, A_{wi} was set equal to zero in these calculations, and C_{wr} and U_{wi} were eliminated along with A_{wi}. The remaining variables can be arranged into four nondimensional groups. While there are numerous choices for the nondimensional groups, we will use the ones suggested in reference [3] for coupled heat exchangers:

$$\epsilon = \epsilon\left[\frac{C_a}{C_w}, \frac{C_r}{C_{\min(a,w)}}, \mathrm{NTU}_0, \frac{(AU)_a}{(AU)_w}\right] \quad (17)$$

where

$$\mathrm{NTU}_0 = \frac{1}{C_{\min(a,w)}}\left[\frac{1}{1/(AU)_a + 1/(AU)_w}\right]$$

Figure 6 shows graphically the dependence of the overall effectiveness on these parameters.

The conductance ratio, $(AU)_a/(AU)_w$, appears to have a very small effect on the overall effectiveness for a range of values between 0.2 and 8. A similar result was obtained in the analysis of coupled heat exchangers given in reference [3]. This result is significant because it implies that the effectiveness is mostly dependent on three nondimensional groups: C_a/C_w, $C_r/C_{\min(a,w)}$ and NTU_0. This does not mean, however, that the actual value of the heat conductance ratio is unimportant. It bears a direct relationship to the total disk surface area required to transfer heat at a specified rate. Given the het capacity rates and the NTU_0, there is for each heat transfer coefficient ratio, U_a/U_w, an optimum area ratio, A_a/A_w, which will yield the minimum total area required. The optimum area ratio can be obtained from the definition of NTU_0 and is given by:

$$A_a/A_w = [U_w/U_a]^{1/2} \quad (18)$$

This condition can be easily implemented in the RDCT by specifying the inner and outer diameters of the annular disks.

Net Effect of the Oil Film on the Heat Transfer Performance

While the oil layer floating on top of the water trough provides an effective means of controlling evaporation, it also affects the heat transfer process in three ways: (1) the heat transfer coefficient between the fluid streams and the metal disk is reduced; (2) the rotor heat capacity rate is increased; and (3) the angular velocity of the rotor is limited to 2–3 rpm. (At higher angular velocities small water beads are carried over to the air side on the surface of the disks, resulting in significant evaporation). The relative importance of these three effects depends strongly on the disk thickness, as shown in Fig. 7. For thin disks at lower angular velocities, the increased rotor capacity rate outweighs the decrease in the heat transfer coefficient, and the performance of the oil covered disks is actually better than that of the bare metal disks. This situation is reversed, however, at higher angular velocites where further increases in the rotor heat capacity rate have no bearing on the overall effectiveness.

To evaluate the net effect of the oil on the heat transfer performance, the heat transfer rate for the oil coated disk operating at the maximum allowable angular velocity, must be compared to the heat transfer rate of the bare metal disk operating at infinite angular velocity. An empirical correlation for the maximum angular velocity was used in these calculations [5]. The results are given in Table 1.

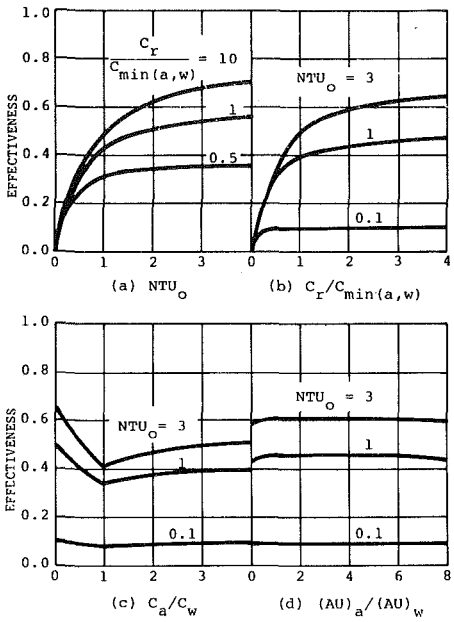

Fig. 6 Overall effectiveness curves. The parameters which are held constant in each graph have the values: $C_r/C_{min(a,w)} = 1.25$; $C_a/C_w = 0.4$; $(AU)_a/(AU)_w = 0.1$

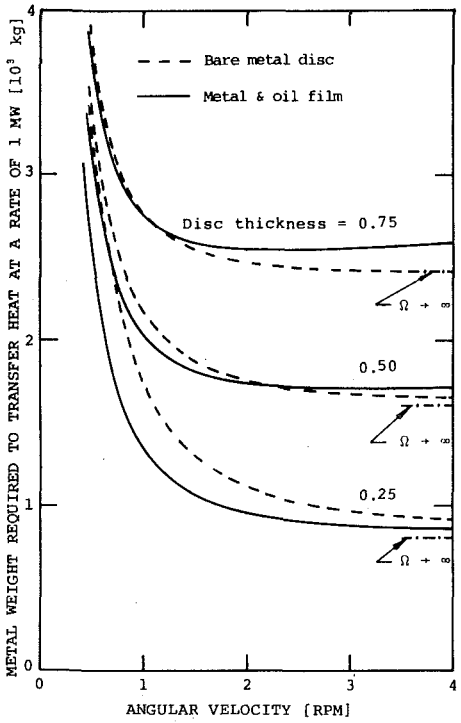

Fig. 7 Effect of the oil on the heat transfer performance

Table 1 Effect of the oil system on the total metal mass required to transfer heat at a rate of 1 MW.

	Rotor mass per megawatt transferred [10^3kg]		
δ_m[mm]	Bare Metal	Metal and Oil Film	Percent Increase
0.25	2.03	2.26	11.5
0.50	4.04	4.34	7.3
0.75	6.07	6.43	5.9

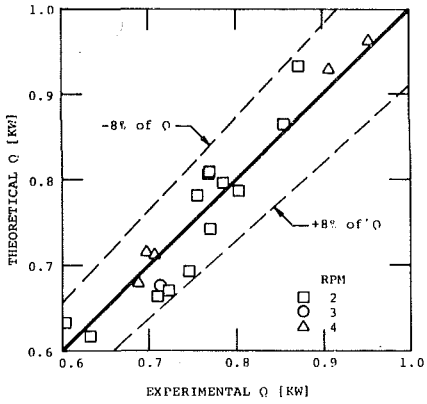

Fig. 8 Comparison between the experimentally measured heat transfer rate and that predicted by the theoretical model

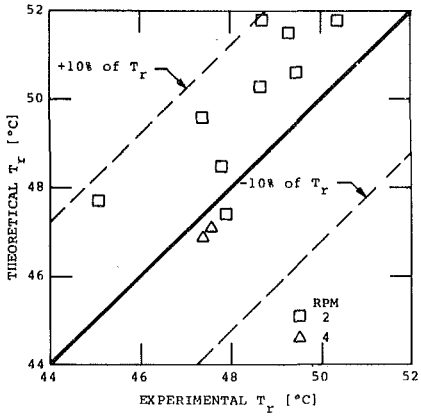

Fig. 9 Comparison between the experimentally measured average rotor temperature and that predicted by the theoretical model

It can be seen that the net effect of the oil on the RDCT performance is small—of the order of 5 to 10 percent. Since the total rotor mass required to transfer heat at a specified rate is proportional to the disk thickness, the disks should be as thin as the structural integrity of the rotor will permit.

Empirical Validation of the Model

The theoretical model was compared with the experimental results of Dong [1]. Those measurements were taken in an RDCT model which had eight 1.5 m dia disks. The range of parameters studied in these experiments was the following:

Air inlet temperature	22–31	°C
Air velocity	0.7–1.5	m/s
Water inlet temperature	54–58	°C
Water volume flow rate	2.2–7.7	l/min-disk
Rotor angular velocity	2–4	rpm

To evaluate the agreement btween the analytical model and the experimental results, two quantities were compared: (1) the total heat transferred per disk, and (2) the average disk (metal) temperature. The first one compares the overall agreement, and the second one, the relative magnitudes of the air and water side heat transfer coefficients. It can be seen from Figs. 8 and 9 that theory and experiment differ by less than 10 percent. These results indicate good agreement between the theoretical model and the experimental apparatus, particularly since the model has no adjustable constants.

Conclusion

The RDCT has significant potential for use in regions with scarce water supply. As a dry tower, it is cost competitive with the conventional finned-tube cooling tower. In addition, the RDCT has the advantage of allowing increased heat rejection capacity during peak demand periods by operating in a wet/dry mode.

Although the RDCT is a fairly complex system, it was shown that it can be adequately modeled as four interconnected heat exchangers. The model so developed has no adjustable constants and predicts the experimental results within ± 10 percent.

The oil film coating the disks plays an important role in the heat transfer process. Although there are temperature gradients across the oil film, it was found that a lumped heat capacity approach was still applicable. An effective heat transfer coefficient was derived to account for the temperature gradients and energy storage in the oil film. It was found that the reduction in overall heat transfer rate due to the presence of the oil is small—of the order of 5 to 10 percent.

References

1 Dong, J. W., "Experimental Performance of the Full Scale Periodic Cooling Tower," M. S. Thesis, M.I.T. Dept. of Mechanical Engineering, 1976.

2 ESEERCO Project EP 2-3, "Design and Cost Investigation of Rotary Disc Dry Cooling Tower," 1979.

3 Kays, W. M., and London, A. L., *Compact Heat Exchangers*, McGraw-Hill, New York, 1964, pp. 27–30.

4 Mueller, A. C., "Heat Exchangers," in *Handbook of Heat Transfer*, W. M. Rohsenow and J. P. Harnett, McGraw-Hill, New York 1973, pp. 18.67–18.81.

5 Valenzuela, J. A., "Hydrodynamics of Oil Used to Suppress Evaporation from a Periodic Cooling Tower and its Effect on the Heat Transfer Performance," MS Thesis, M.I.T. Dept. of Mechanical Engineering, M.S. Thesis, M.I.T. Dept. of Mechanical Engineering, 1977.

6 Harris, R. S., Jr., and Davidson, J. R., "An Analysis of Exact and Approximate Equations for the Temperature in an Insulated Thick Skin Subject to Aerodynamic Heating," NASA TN D-519, Washington, D.C., Jan. 1961.

7 McAdams, W. H. *Heat Transmission*, 3rd ed., McGraw-Hill, New York 1954.

8 Han, J. C., "Convective Heat Transfer Augmentation in Channels using Repeated Rib Roughness," Doctor of Science Thesis, M.I.T. Dept. of Mechanical Engineering, 1976.

9 Boelter, L. M. K., Young, G., Inversen, H. W., "An Investigation of Aircraft Heaters XXVII-Distribution of Heat Transfer Rate in the Entrance Region of a Circular Tube," NASA TN 1451, Washington, D.C., July 1948.

APPENDIX

Typical Operating Conditions of the RDCT

Water inlet temperature	55°C
Water volume flow rate	4.4 l/min-disk
Air inlet temperature	24°C
Air velocity	4.6 m/s
Water level (R_i/R_0)	0.4
Water feed height (F/R_0)	0.3
Spacing between disks	1.3 cm

Surface roughness characteristics:

e/D_h	0.05
P/e	10
angle of attack	45 deg
rib shape angle	60 deg

Oil properties:

density	0.84×10^3 kg/m^3
viscosity	1.3×10^{-5} m^2/s
specific heat	2.0×10^3 J/kg°C
thermal conductivity	0.13 W/m°C

Metal properties:

density	7.8×10^3 kg/m^3
specific heat	0.47×10^3 J/kg°C
thermal conductivity	43 W/m°C

Heat Transfer and Interface Motion During Melting and Solidification around a Finned Heat Source/Sink

A. G. Bathelt[1]
R. Viskanta

Heat Transfer Laboratory,
School of Mechanical Engineering,
Purdue University,
West Lafayette, Ind. 47907

The effectiveness of extended surfaces on a horizontal, cylindrical heat source/sink was studied experimentally during solid-liquid phase change heat transfer. Melting and freezing experiments were performed in a test cell suitable for photographic and shadowgraphic observations using a circular cylinder with three rectangular fins parallel to the axis and evenly distributed around the circumference of the heat exchanger. Results are reported for n-heptadecane as the phase change material. Orientation of fins on the heat exchanger with respect to the gravitational field are found to have more influence on the melting than on the freezing processes. The use of fins was found to be more effective for melting than for freezing. The instantaneous local and circumferentially averaged heat transfer coefficients at the heat source surface for melting from a cylinder with fins were usually within ±20 percent of those for melting from a bare cylinder. During solidification the degree of heat transfer enhancement due to finning is greatest when the frozen layer is thin and decreases as the layer grows thicker.

Introduction

Commercial acceptance and the economics of solar energy, conservation, "waste" heat utilization, and other alternate energy technologies are tied to the design and development of efficient and cost effective thermal energy storage systems (TES). The latent heat-of-fusion energy storage concept has the primary advantage of performing the storage function at nearly constant temperature and a large specific storage capacity [1]. Unfortunately, there is little information on heat transfer coefficients, solid-liquid interface motion, and other technical data applicable to design of latent heat-of-fusion TES systems under realistic demand conditions for charging and discharging the storage. Good understanding of heat transfer processes involved is essential for predicting the storage system performance with accuracy and avoiding costly system overdesign.

Available experiment data [2–6] have established that during melting natural convection in the liquid aids heat transfer. However, during freezing the development of natural convection in the melt can greatly reduce and even completely stop the process if the liquid is superheated [7, 8]. In addition, the solid layer formed on the cooled surface increases the thermal resistance and can greatly reduce the heat transfer rate, particularly for materials that have low thermal conductivity. A standard method for enhancing heat transfer, if the dominant resistance is on the fluid side, is to use extended surfaces [9]. The purpose of this paper is to report on a study aimed at obtaining understanding of heat transfer processes during solid-liquid phase change from a heat source/sink with extended surfaces and to determine the effectiveness of fins during melting and freezing of a material. Use of fins in thermal energy storage units for spacecraft thermal control purposes have been reported [10, 11], but detailed heat transfer processes and solid-liquid interface motion were not investigated in these system performance studies. The use of fins to enhance heat conduction in latent heat-of-fusion energy storage systems has been reported [12] since the present paper was submitted for publication. A two-dimensional integral method of solution has been used to analyze the problem of solidification in a rectangular enclosure in which the end wall temperature is fixed and the side walls are conducting [13]. Freezing experiments on a vertical, finned tube have been performed [14][2] and will be discussed later.

Heat transfer from a cylindrical heat exchanger with longitudinal fins embedded in a phase change material during melting and freezing was studied because a class of storage units given serious consideration is a standard shell and tube exchanger in which the PCM is on the shell side. The solid-liquid interface position during phase change was recorded photographically and the local heat transfer coefficient measured by a shadowgraphic method. Instantaneous local and circumferentially averaged, as well as time and circumferentially averaged, heat transfer coefficients are reported for a paraffin (n-heptandecane, $C_{17}H_{36}$, $T_f = 22.2°C$) as the phase change material during melting. The effects of fin orientation with respect to the gravitational field on the melt and solid volume formed during melting and freezing are also determined.

Experiments

Test Apparatus. The experimental apparatus employed here is an adaptation of that of [6], thereby obviating the need for detailed exposition. The description of the apparatus is facilitated by reference to the schematic diagram of the system shown in Fig. 1. The test apparatus used in the experiments consisted of a light source, a con-

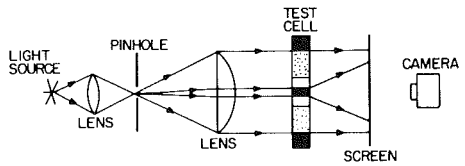

Fig. 1(*a*) Schematic of shadowgraph system

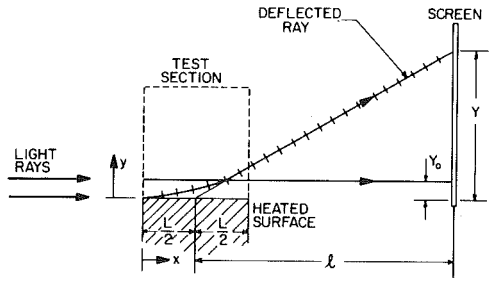

Fig. 1(*b*) Displacement of light beam grazing heated surface

Fig. 1 Schematic diagram of the test apparatus

[1] Now at Dornier-System GMBH, 7990 Friedrichshafen, West Germany.

[2] The authors are grateful to Professor E. M. Sparrow for providing a copy of the paper prior to its publication.

Contributed by the Heat Transfer Division and presented at the 19th AIChE/ASME National Heat Transfer Conference, Orlando, Fla., July 27–30, 1980 of The American Society of Mechanical Engineers. Revised manuscript received by the Heat Transfer Division, October 17, 1980. Paper No. 80-HT-10.

denser lens and a pinhole, a collimating lens, the test cell, and a screen. During melting experiments the system served for shadowgraphic as well as photographic observations. For solidification experiments the test arrangement was used only for photographic observations of the solid-liquid interface motion because the light rays grazing the interface were deflected into the solid (thus precluding shadowgraphic observation). A Mach-Zehnder interferometer would have been preferred over a shadowgraph system. Unfortunately, the high sensitivity of the index of refraction of paraffins to temperature results in too large interference fringe density for accurate interpretation [15, 16], and therefore could not be used for reasonable heat exchanger surface minus fusion temperature differences.

The melting and freezing experiments were performed in a test cell which allowed for optical and photographic observation of the phase change processes. The inside dimensions of the rectangular test cell were 35.5 × 25.5 × 7.5 cm. A U-shaped aluminum frame. 7.5 cm thick, was attached to a rectangular base plate which was adjustable in the vertical direction (at its four corners) in order to obtain a precision leveling of the test cell. The front and back sides of the cell were made of 0.6 cm thick plate glass to allow for visualization, photography, and optical observation of the phenomena taking place during phase transformation. To reduce heat gains (or losses) from the test cell a second glass plate was installed parallel to the first to form a 1.2 cm wide vertical air gap. The thickness of the air gap between the vertical glass plates was so chosen as to minimize natural convection, the heat transfer between the test cell, and the ambient environment. The top of the test cell was closed with a Plexiglass cover. When needed, a frosted glass screen could be lowered into position between the test heat source/sink and the camera for photographing the shadowgraphic images and the location of the phase change boundary. The heat exchanger, a brass cylinder with three longitudinal fins, was installed in the test cell. The faces of the test cell were covered with removable styrofoam insulation. The insulation could be replaced immediately after the photographs were taken.

The test cell was well instrumented, with provisions made to install a total of 45 thermocouples from the aluminum sides of the cell. Each thermocouple was placed in a 0.1 cm i.d. and 18 cm long stainless steel tube with the thermocouple junction exposed at one end. The tube was fitted tightly through a hole along the axis of a bolt. The stainless steel tube with the thermocouple inside it was then positioned horizontally in the test cell.

The test heat exchanger consisted of a 2.5 cm o.d. by 7.0 cm long cylinder with three rectangular, longitudinal fins distributed uniformly around the perimeter of the cylinder. The brass fins had a cross-section of 0.5 × 2.5 cm. They were installed in milled grooves and then soldered. The fins increased the heat transfer area of the heat source/sink by 190 percent and its volume by 76 percent. Two holes drilled in the center provided the connection for the inlet and outlet tubes for circulating a working fluid through the heat exchanger from a constant temperature bath. Holes were drilled axially into the cylinder every 45 deg with their axis on a 1.5 cm dia circle. The holes were selectively connected by grooves and closed by disks on each end of the cylinder. One disk was provided with three holes for connecting the inlet and outlet tubes and for bringing out the thermocouple lead wires.

Four thermocouples were located in the cylindrical part of the heat exchanger at $\theta = 0, 90, 180$ and 270 deg. Two thermocouples were installed in each fin to measure the temperature at the midsection of the heat source/sink at the center of the fin and at a distance of 0.08H from the tip of the fin. A hole was drilled through the inner glass plate of the test cell for bringing out the fluid supply tubes and the thermocouple wires. After installation of the cylinder the hole was sealed with silicone-rubber to prevent the leakage of the liquid PCM from the test cell.

Test Procedure. Prior to each experiment the phase change material was degasified by heating the liquid to be temperatures above 110°C until gas could no longer be observed. The liquid was cooled to about 5°C above the fusion temperature and carefully syphoned into the test cell in order not to entrap gas. The ambient air temperature in the laboratory was controlled in order to insure that only a small temperature difference existed between the air and the fusion temperature of the PCM. After the test cell was filled with the liquid paraffin the optical system was aligned. The Chromel-Constantan thermocouples were connected to an automatic integrating digital microvoltmeter and a high speed printer which scanned the selected channels automatically at a rate of one per second and printed the emf output at pre-programmed time intervals.

In both melting and solidification experiments, great care was taken to establish a uniform temperature of the PCM with very little subcooling or superheating, respectively. For example, before melting was initiated in the experiment, ethylene glycol was circulated through the heat exchanger at a temperature of about 5°C below the fusion temperature of the phase change material to assure a firm, solid PCM around the heat exchanger. After all of the PCM was solidified, the temperature of the circulating fluid was raised close to the fusion temperature of the material for the purpose of equilibrating the solid and eliminating subcooling as a parameter on the melt shape and heat transfer. When the thermocouples throughout the test cell indicated a temperature of the PCM within 0.2°C of the imposed cylinder surface temperature, the preheating process was terminated. The initial condition, a uniform temperature of the solid PCM close to the fusion temperature, was then assumed to be established and the experiment begun.

During solidification experiments the ambient air temperature was maintained slightly above the fusion temperature of the phase change material. Once the test cell was filled with the liquid PCM it was left

Nomenclature

A_h = heat source/sink surface area including fins
c = specific heat
D_0 = diameter of the cylinder
E_s = stored energy defined by equation (5)
Fo = Fourier number, $\alpha_\ell t/R_0^2$
g = gravitational constant
Gr = Grashof number, $g\beta(T_w - T_f)D_0^3/\nu_\ell^2$
h = local heat transfer coefficient
Δh_f = latent heat-of-fusion
k = thermal conductivity
ℓ = distance between the center of the test cell and screen, see Fig. 1(*b*)
L = length of the heat source/sink, see Fig. 1(*b*)
n = index of refraction
Nu = Nusselt number, hD_0/k_ℓ
Pr = Prandtl number, ν_ℓ/α_ℓ
r = radial distance
R_0 = radius of the cylinder
Ra = Rayleigh number, Gr · Pr
S_c = subcooling parameter, $c_s(T_f - T_i)/\Delta h_f$
Ste = Stefan number, $c_\ell(T_w - T_f)/\Delta h_f$ for melting and $c_s(T_f - T_w)/\Delta h_f$ for solidification
t = time
T = temperature
T_F = film temperature, $(T_w + T_f)/2$
V_ℓ = melt volume
V_s = solidified volume
V_0 = volume of the heat source/sink
y = direction perpendicular to heat source surface, see Fig. 1(*b*)
Y = distance perpendicular to the heat source surface by which the light rays are deflected on the screen, see Fig. 1(*b*)
α_ℓ = thermal diffusivity, $k_\ell/\rho_\ell c_\ell$
β = thermal expansion coefficient
θ = angle, see Fig. 2
ρ = mass density
τ = dimensionless time, Ste · Fo
ν = kinematic viscosity

Subscripts

f = fusion (melting)
i = initial
ℓ = liquid
s = solid
w = wall

Superscripts

$-$ = circumferentially averaged heat transfer coefficient
$*$ = averaged over the time period from $t = 0$ to $t = t$
$\sim$ = time and circumferentially averaged heat transfer coefficient, see equation (7)

undisturbed to reach a uniform ambient temperature throughout the test cell. Then the working fluid, cooled to a predetermined temperature, was circulated through the heat exchanger.

Heat sink/source surface temperatures were recorded at desired time intervals, ranging from every 2 min at the beginning of the experiment to every 30 min at later times. Photographs were taken with a 6 × 6 cm still camera (Mamiya C 300 Professional with a 250 mm, f6.3 telelens) to record both the solid-liquid interface position and the maximum beam deflection (shadowgraph).

Shadowgraphic Observations. A shadowgraphic system (Fig. 1) was employed to study heat transfer during solid-liquid phase change and to obtain detailed information on heat transfer coefficients. This optical method involves an identification of a light ray and recording of the deflection after its passage through the test cell. The deflection of the rays results from the variation of the index of refraction with temperature of the test fluid. Detailed description of the system and its theoretical basis are available in the literature [17, 18].

Temperature measurements have confirmed that because of effective heat transfer the temperature along the heat exchanger and fins is nearly uniform. For a system where a change in the index of refraction and temperature in the axial direction, e.g. along the direction of propagation of light ray, are negligible in comparison to the transverse direction, the distance Y on the screen of the deflected light beam grazing the heat source surface (see Fig. 1(b)) can be calculated from the geometrical optics theory [18] as

$$Y = \frac{1}{n}\frac{dn}{dT}\frac{dT}{dy}\ell L \tag{1}$$

The local Nusselt number, based on the cylinder diameter as a characteristic length, can be expressed in terms of known and measured quantities as

$$\mathrm{Nu} = \frac{hD_0}{k} = -\frac{D_0(\partial T/\partial y)_w}{(T_w - T_f)} = -\left[\frac{D_0 nY}{\ell L(T_w - T_f)}\right]\Big/\frac{dn}{dT} \tag{2}$$

The maximum deflection Y on the screen of the light rays grazing the heat source surface is determined from the photographs made of the shadowgraph images during the melting process. To aid in the data reduction from the shadwograph images, both sides of each fin were radially divided into four sections, yielding five points (indicated by the symbols B, MB, M, MT, and T, respectively, as shown in Fig. 2).

Two different orientations of the vertical fin (at either $\theta = 0$ deg or $\theta = 180$ deg), referred to either as arrangements A or B, respectively, have been used in the experiments. The same heat exchanger was used for both arrangements in order to eliminate errors not related to heat transfer processes but which are specific to the construction of the heat exchanger (e.g., installation of thermocouples, fluid circulations inside the cylinder, etc.).

The heat transfer parameters were based on the diameter of the cylinder as a characteristic length. This permitted comparison of results between the cylinder without and with extended surfaces. The surface temperature was averaged over the cylindrical part of the heat source/sink and used in determining the Grashof number for the melting process. The thermophysical properties were evaluated at the film temperature.

Results and Discussion

Heat Transfer During Melting.

Cylinder and Fin Surface Temperatures. About 180 s after the working fluid from the constant temperature bath started to circulate through the heat exchanger, the cylindrical part and the rectangular fins reached almost constant surface temperatures. Because of heat conduction in the fins from the warmer base (B) to the cooler tip (T) the surface temperature of the fin located at $\theta = 0$ deg was smaller than that of the fin at $\theta = 120$ deg and indicated the greatest temperature difference between the base and the tip. The differences between $1'B$ and $1'T$ were 0.75°C and 3.0°C for Ste = 0.058 and Ste = 0.178, respectively.

For arrangement B the heat source was rotated by 60 deg in the clockwise direction from that of arrangement A. Again, the cylindrical part of the heat source surface reached an almost constant wall temperature in about 180 s after the start of heating, but temperature variation with angular position of the cylindrical part was not observed. This is attributed partly to the fact that the melted PCM in the region -60 deg $\le \theta \le 60$ deg was trapped between the two lower fins and the bottom of the cylinder. In this region the liquid is gravitationally stable, and heat transfer is by conduction. For Ste = 0.262 the temperature differences between the base and the tip of the fins were 3.5°C for the fin at $\theta = 60$ deg and about 2.5°C for the fin at $\theta = 180$ deg.

Melt Shape. The solid-liquid interface position was photographed during the phase change process at different times. The interface locations in Fig. 3 were traced directly from the photographs. The two arrangements of fins on the heat exchanger result in distinctly different melt shapes for the two experiments. This is attributed to natural convection in the melt region, which was clearly observed.

It appears from Fig. 3 that only for very short times ($\tau < 0.025$) is heat transfer primarily by conduction, as evidenced by a liquid layer of constant thickness around the heat source. Due to the extension of the fins in vertical direction, the characteristic length for the finned cylinder should be different than that for the cylinder without fins. However, the diameter of the cylindrical part of the finned heat exchanger was chosen as a characteristic length to demonstrate the effect of the fins on heat transfer from the source.

Natural convection was observed first to occur at the top of the finned heat exchanger and was due to thermal instability induced by the temperature differences along the fins and the hot surface of the cylinder (120 deg $\le \theta \le$ 240 deg in Fig. 3(a) and 60 deg $\le \theta \le$ 300 deg in Fig. 3(b)) [15]. As in the case of bare cylinder [5], there was more melting above the heat source and very little below. This is clearly demonstrated by the results of Fig. 3. The strong upward trust of the melting zone above the finned cylinder is caused by natural convection. The circulation conveys the hot liquid to the upper part of the melt zone and in this manner continues to support the upper movement of the solid-liquid interface.

The effectiveness of the extended surface in comparison to the bare cylinder in melting the PCM is clearly demonstrated in Fig. 4. The ordinate in Fig. 4 was arbitrarily chosen to be (V_ℓ/V_0)/Ste in order to collapse the experimental data on one curve for the particular heat source arrangement. The volume of the PCM melted in the two arrangements of the finned cylinder was higher than for the bare cylinder. As expected, arrangement A proved to be more effective than

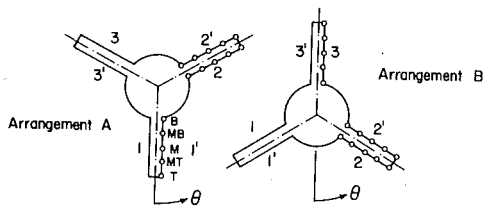

Fig. 2 Physical model and coordinate system for cylinder with extended surfaces

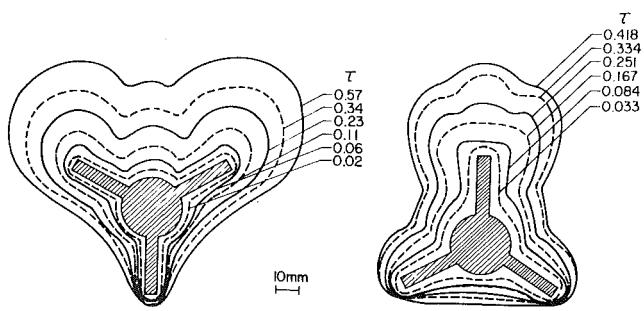

Fig. 3(a) Arrangement A, Ste = 0.179

Fig. 3(b) Arrangement B, Ste = 0.262

Fig. 3 Experimentally determined liquid region contours during melting

Table 1 Local heat transfer results, $Nu/Ra^{1/4}$, at the fin surface for arrangement *A*: Ste = 0.058, Ra = 1.28×10^6

Fin	τ	0.019	0.037	0.074	0.111	0.148	0.500
	T	0.487	0.557	0.508	0.544	0.544	0.584
	TM	0.523	0.557	0.508	0.544	0.508	0.584
1′	*M*	0.544	0.557	0.508	0.544	0.438	0.584
	MB	0.551	0.540	0.508	0.466	0.425	0.498
	B	0.557	0.525	0.466	0.438	0.375	0.498
	T	0.535	0.678	0.508	0.398	0.398	0.498
	TM	0.571	0.656	0.508	0.398	0.398	0.498
2	*M*	0.589	0.636	0.508	0.398	0.398	0.453
	MB	0.593	0.463	0.508	0.386	0.412	0.437
	B	0.636	0.450	0.508	0.375	0.425	0.424
	T	0.535	0.593	0.466	0 398	0.318	0.453
	TM	0.523	0.574	0.466	0.358	0.318	0.453
2′	*M*	0.544	0.517	0.466	0.358	0.358	0.453
	MB	0.551	0.463	0.466	0.386	0.375	0.437
	B	0.557	0.412	0.466	0.412	0.390	0.424

Table 2 Local heat transfer results, $Nu/Ra^{1/4}$, at the fin surface for arrangement *B*: Ste = 0.169, Ra = 4.42×10^6

Fin	τ	0.108	0.162	0.216	0.270	0.324
	T	0.265	0.244	0.237	0.219	0.219
	TM	0.282	0.244	0.237	0.219	0.219
2	*M*	0.282	0.244	0.237	0.219	0.215
	MB	0.263	0.247	0.247	0.224	0.225
	B	0.244	0.237	0.240	0.229	0.234
	T	0.354	0.332	0.306	0.237	0.215
	TM	0.311	0.295	0.287	0.248	0.213
2′	*M*	0.289	0.277	0.270	0.248	0.224
	MB	0.265	0.256	0.247	0.236	0.224
	B	0.244	0.237	0.227	0.218	0.234
	T	0.314	0.280	0.341	0.289	0.269
	TM	0.303	0.261	0.313	0.287	0.240
3	*M*	0.277	0.246	0.240	0.206	0.184
	MB	0.187	0.171	0.192	0.188	0.149
	B	0.172	0.158	0.177	0.174	0.141

arrangement *B*. This is due to the more intense natural convection circulation in the melt. For arrangement *B* the stable temperature gradients along the fins and the hot cylindrical surface produced a gravitationally stable liquid region between the two lower fins where heat transfer was by conduction only.

Local Heat Transfer. In the radial direction, the surface of the fins was divided into four regions of equal width parallel to the cylinder axis, yielding five distinct points (see Fig. 2). The base point *B* was assumed to be at the same temperature as the cylindrical part adjacent to it. With only two thermocouples installed in each fin, the surface temperatures at the points *MB* and *MT* were interpolated between *T*, *M*, and *B*, and taken into account in the data reduction procedure. It was difficult to determine the distance of the deflected light rays in the vicinity of point B because the deflections from the cylindrical part and from the fin surface adjacent to it were superimposed. In addition, the dark shadow of the thermal boundary layer sometimes made it impossible to evaluate the deflection at that point. Local heat transfer results at the fin surface, determined experimentally using the shadowgraph method, are summarized in Tables 1 and 2 for arrangements *A* and *B*, respectively. It should be emphasized that the nature of the shadowgraph technique allows determination of only the average surface temperature gradient, $(\partial T/\partial y)_w$, over the entire length of the heat source, see equation (1). Therefore, any nonuniformities in the gradient along the heat exchanger axis as a result of heat losses from the test cell walls are already accounted for, and the Nusselt numbers given in the paper should be considered as average values over the cylinder length.

A comparison of local heat transfer results[3] between the two arrangements of the finned cylinder and the cylinder without extended surface, for similar Stefan numbers, is shown in Fig. 5 (for the cylindrical part of the heat source only). The missing data for the cylinder with extended surfaces are due to the location and the physical thickness of the fins. In order to compare the heat transfer results, both the Nusselt and Rayleigh numbers were based on the diameter of the cylinder as characteristic length, even in the case of the cylinder with extended surfaces. As pointed out earlier, this may not be appropriate. The variation of the local heat transfer parameter $Nu/Ra^{1/4}$ with angular position and time for the finned and unfinned cylindrical heat sources are similar. The results for early times, $\tau < 0.05$, could not be obtained using a shadowgraph system because the melt layer was too thin to allow the deflected ray grazing the heat exchanger surface to leave the test cell. It is during the early time when heat transfer is predominantly by conduction that the heat transfer coefficient decreases sharply with time [3, 5]. The modification of the natural convection flow field around the source by the fins produces different trends in both the angular and timewise dependence of the

[3] In Figs. 5 and 6 the experimental data points are joined by solid lines for the sake of clarity.

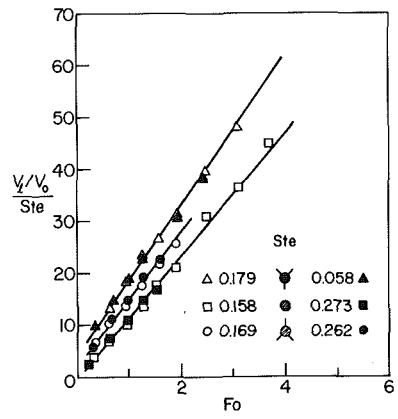

Fig. 4 Comparison of melt volumes for finned cylinder arrangements *A* and *B* and the bare cylinder

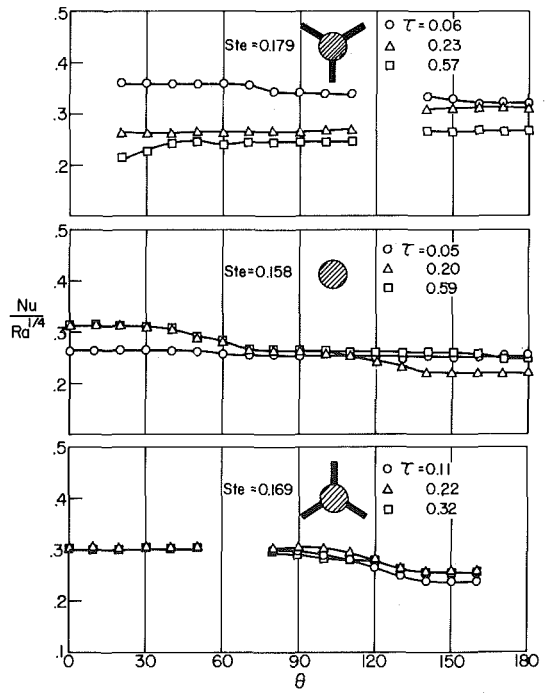

Fig. 5 Effect of time on local heat transfer for arrangements *A* and *B* and for cylinder without fins

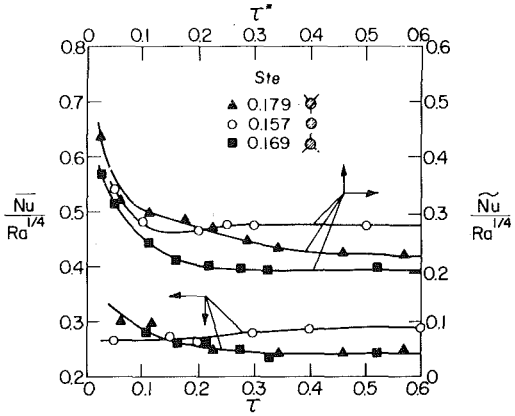

Fig. 6 Dependence of the circumferentially averaged heat transfer on dimensionless time: $Ra_l = 4.15 \times 10^6$

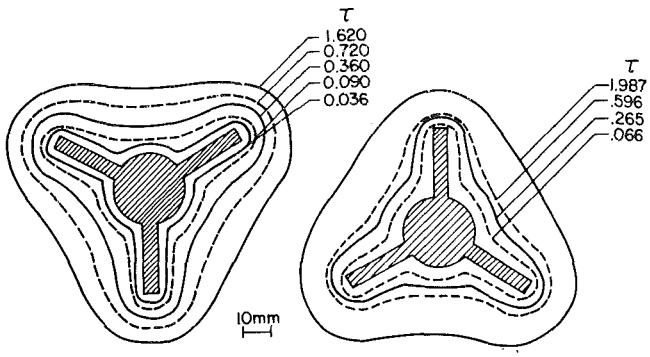

Fig. 7(a) Arrangement A, Ste = 0.251, $Ra_l = 2.5 \times 10^4$

Fig. 7(b) Arrangement B, Ste = 0.185, $Ra_l = 7.2 \times 10^4$

Fig. 7 Experimentally determined solid region contours

heat transfer coefficient, but the differences in $Nu/Ra^{1/4}$ between the finned and bare cylinder is usually with ±20 percent. The results shown in the figure also indicate that a nearly quasi-steady melting rate is reached most rapidly for arrangement B where the liquid is stable over the lower third of the heat exchanger.

Average Heat Transfer. A circumferentially averaged instantaneous Nusselt number was also calculated. This average was based on area weighted average Nusselt numbers for the fins and the cylindrical part,

$$\overline{Nu} = w_{fin}\overline{Nu}_{fin} + w_{cyl}\overline{Nu}_{cyl} \tag{3}$$

where $w_{fin} = 0.7$ and $w_{cyl} = 0.3$ are weighting factors based on the effective heat transfer areas. The fins contributed 70 percent and the cylindrical part 30 percent of the total transfer area. Since the heat source in arrangements A and B was symmetrical about a vertical plane through the cylinder axis, the instantaneous circumferentially averaged Nusselt numbers $\overline{Nu}_{fin}$ and $\overline{Nu}_{cyl}$ were based on local Nusselt numbers for the fin (e.g., as given in Tables 1 and 2) and local Nusselt numbers for the cylindrical part (e.g., as shown in Fig. 5), respectively. In order to compare the heat transfer results with the cylinder without fins, the Rayleigh number was based on $(T_w - T_f)$ with T_w as the wall temperature of the cylindrical part of the heat source at $\theta = 180$ deg. The comparison of results for arrangements A and B with those for the cylinder without fins is shown in Fig. 6. In all cases, a time-independent heat transfer coefficient is reached after a sufficiently long time. Unfortunately, no data could be obtained for early times ($\tau <$ 0.05) when the melt layer around the heat source is relatively thin.

As an alternative to the tedious determination of the heat transfer coefficient by the shadowgraph technqiue, particularly for a cylinder with extended surface, is the use of an energy balance method on the phase change material. Hereby, the average heat transfer coefficient is based on the variation of the melted volume of the PCM with time. Assuming that the heat losses (gains) from the solid and liquid PCM to the ambient laboratory environment are negligible in comparison to the heat input at the heat source and that the only mode of heat transfer from the heat source surface to the PCM is by natural convection, the transient energy balance on the material can be expressed as

$$\frac{dE_s}{dt} = \bar{h}A_h(T_w - T_f) \tag{4}$$

where the energy stored in the PCM (based on the initial temperature of the solid as the reference condition) is given by

$$E_s \simeq \int_{T_i}^{T_f} \rho_s V_s c_s dT + \rho_\ell V_\ell \Delta h_f + \int_{T_f}^{T_F} \rho_\ell V_\ell c_\ell dt \tag{5}$$

and $\bar{h}$ is the instantaneous circumferentially averaged heat transfer coefficient at the heat source surface. If the time to reach a constant surface temperature is small compared with the duration of the experiment, the wall temperature T_w can be considered to be constant and integration of equation (4) between $t = 0$ and $t = t$ yields

$$E_s = \tilde{h}A_h(T_w - T_f)t^* \tag{6}$$

where $\tilde{h}$ is the time and circumferentially averaged heat transfer coefficient defined as

$$\tilde{h} = \frac{1}{t^*}\int_0^{t^*}\left[\frac{1}{A_h}\int_{A_h} h dA\right]dt \tag{7}$$

Since the temperature difference between the heat source and the melting point is relatively small, the dependence of the physical properties on temperature can be neglected and the time and circumferentially averaged Nusselt number can be obtained by combining equations (5) and (6) to form a Nusselt number,

$$\tilde{Nu} = \frac{\tilde{h}D_0}{k} = \frac{1}{\tau^*}\left[1 + \frac{1}{2}Ste - \frac{1}{2}(\rho_s/\rho_\ell)S_c\right]\frac{4V_\ell}{A_h D_0} \tag{8}$$

A similar approach was used by Marshall [19] to determine natural convection heat transfer coefficients during melting of a PCM contained in rectangular enclosures.

Qualitatively, the trends in the heat transfer results based on the shadowgraph technique and the PCM energy balance method are similar (Fig. 6). The method could not be used for measuring the heat transfer coefficient at very early times ($\tau < 0.04$) because, as previously mentioned, the melt layer was too thin to allow the deflected ray to leave the test cell. For this reason results could not be obtained. Available results [3, 5] show that the heat transfer coefficient decreases very sharply at early times, reaches a minimum, and then increases slightly before reaching a nearly constant value. For the cylinder without fins heat transfer results for $\tau > 0.1$ differ only by about 5 percent, while the maximum difference between the two methods of reducing data was 16 percent, and occurred for arrangement B. Higher values were expected to result with the energy balance method at early times ($\tau < 0.1$) because of the time averaging effect on the heat transfer coefficient. As expected, the data for arrangements A and B do not fall on a single curve. This is partly due to the natural convection circulation pattern in the melt and its effect on the melt shape and volume. The melt volume is a critical parameter in determining the average Nusselt number $\tilde{Nu}$. The results of Fig. 6 show that after quasi-steady melting has been reached ($\tau \gtrsim 0.14$ and $\tau^* \gtrsim 0.2$), the heat transfer coefficient is higher than either of the two finned cylinder arrangements. This clearly indicates that at later times the fins do not increase the circumferentially averaged heat transfer coefficient over that for a bare cylinder, but that the presence of fins enhances total heat transfer from a finned cylindrical source and increases the rate of melting of the material.

Heat Transfer During Solidification.

Cylinder and Fin Surface Temperature. The surface temperature of the cylindrical part of the heat exchanger was independent of the heat sink arrangements A or B, i.e., the location of the fins ($\theta = 0$, 120, 240 deg or $\theta = 60$, 180, 300 deg, respectively) and of the Stefan number, showed no variation with angular position. However, in contrast to the melting experiments, it took considerably longer to reach a constant value of the wall temperature. In addition, all three fins showed

the same temperature variation between the tip (T) and the base (B). This was expected since the only mode of heat transfer from the heat sink surface to the solid PCM was by heat conduction. Typically, temperature differences between the tip and the base of the fin were about 1°C and about 0.25°C between points T and MT on the fin for Ste = 0.251.

Solid-Liquid Interface Motion. Almost immediately after the cooling process was initiated, $t \simeq 2$ s, the heat sink surface was covered with a frosty layer of solid paraffin. The thickness of this layer increased very rapidly at early times. The progression of the phase change boundary with time is illustrated in Fig. 7 for arrangements A and B, respectively. The Rayleigh number, the parameter controlling natural convection around the solid-liquid interface, was based on the outside diameter of the cylinder as the characteristic length and was defined as $\mathrm{Ra} = g\beta(T_\infty - T_f)D_0^3/\nu_\ell\alpha_\ell$.

For early times ($\tau < 0.04$) heat transfer at the solid-liquid interface was predominantly by conduction and resulted in the formation of a solid layer of practically constant thickness around the heat sink. Later, natural convection in the liquid appeared to increase in importance, caused the solidification process to slow down, and produced a solid layer of nonuniform thickness around the finned heat exchanger.

The results for arrangement A (Fig. 7(a)) indicate the same solidified volume as the results for arrangement B (Fig. 7(b)) but at only 80 percent of the dimensionless time. This clearly indicates the effect of the initial superheat ($T_\infty - T_f$) in the liquid on the rate of solidification. The superheat was 1.6°C and 4.6°C, for the results given in Figs. 7(a) and 7(b), respectively. In addition, arrangement B may be conducive for more intense natural convection flow along the solid-liquid interface. For arrangement A (Fig. 7(a)) the cooler liquid adjacent to the phase-change boundary is located above the warmer liquid (in the region between $\theta = -130$ deg and $\theta = 130$ deg), producing a counter-clockwise circulation cell in the liquid to the right and below the center of the heat sink and a clockwise circulation cell in the liquid to the left and below the center of the heat sink. The liquid region above the nearly horizontal phase change boundary (130 deg $< \theta <$ 230 deg) was observed to be relatively stable. In this region heat transfer from the liquid to the solid was primarily by conduction.

For arrangement B (Fig. 7(b)) the liquid underneath the heat sink ($-70 < \theta < 70$ deg) is unstable because the temperature of the fluid in contact with the solid-liquid interface is at the fusion temperature T_f. It was observed that even for the small initial superheats in the liquid, a plume had developed from the bottom two fins, and descended toward the bottom of the test cell producing natural convection circulation in the test cell.

From the sequence of photographs taken during the solidification process the volume of the solidified PCM was measured with a planimeter and compared with data for the cylinder without fins. It was found that the rate of solidification decreased sharply with time for $\tau < 0.2$ and then leveled off due to the increasing resistance to heat transfer by conduction in the solid and development of natural convection at the solid-liquid interface [15]. This trend has also been observed in experiments with the cylindrical heat exchanger without an extended surface [7]. It was determined that for similar Stefan numbers, initial conditions, and freezing time, arrangement A yields a higher solidified volume (V_s/V_0) than the cylinder without fins.

When the results are plotted as in Fig. 8, the data for the volume of the solidified material fall along straight lines, which can be approximated by

$$V_s/V_0 = C_s(\mathrm{Ste} \cdot \tau)^{0.5} \tag{9}$$

The constant C_s depends on the arrangement and the Stefan number. The initial superheat of the liquid was purposely kept small to eliminate it as an independent parameter, but the volume of the material frozen is expected also to depend on the superheat (i.e., buoyancy force) because it influences natural convection flow in the liquid and heat transfer at the interface. The results shown in Fig. 8 clearly indicate that for a fixed Rayleigh number the degradation in heat transfer is greater for lower values of the temperature difference (i.e., lower Stefan number) across the frozen layer.

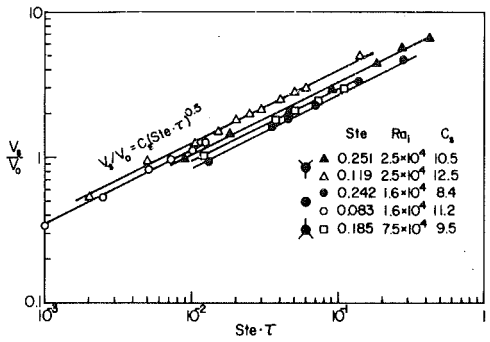

Fig. 8 Volume of solid formed around cylinders with and without extended surfaces

It is interesting to note that the results of this work are consistent with those for freezing on a vertical finned cylinder reported recently [14]. For conduction-controlled solidification the volume (mass) of material frozen is proportional to the freezing time t as $t^{0.5}$ for a finned tube and as $t^{0.634}$ for the unfinned tube. The results in Fig. 8 indicate a similar time dependence but show no difference between a finned and a bare horizontal cylinder. This is attributed, at least in part, to the difference in orientation of the heat sink with respect to the gravitational field. There was significant variation in the frozen layer thickness with height for the vertical finned tube and negligible variation in the frozen layer thickness with the axial distance for the horizontal finned and bare cylinder.

Conclusions

Solid-liquid interface motion and heat transfer during melting and freezing from a horizontal cylindrical heat exchanger with longitudinal fins embedded in a paraffin has been studied experimentally. Based on the experimental results obtained it has been concluded that:

- Use of extended surfaces on a heat source/sink enhances the rate of melting and freezing in comparison to that without fins.
- Orientation of fins with respect to the gravitational field on a horizontal cylindrical heat exchanger is important for taking full advantage of natural convection effects, to enhance melting, and not to create quiescent melt regions where natural convection circulation may be suppressed.
- The effectiveness of fins is greatest during solidification at early times when the frozen layer formed on the heat sink is thin and decreases as the layer grows thicker. The degree of enhancement is generally greater than the volume ratio of the finned and bare cylinders.
- For the experimental conditions considered, the presence of natural convection in the melt retarded freezing only by a relatively little amount.

No attempts were made in the study to either optimize the fin geometry of the fin orientation with respect to the gravitational field on heat transfer during solid-liquid phase change. An optimization would be essential if efficient and cost effective shell and tube type latent heat-of-fusion energy storage units using finned tubes are to be designed.

Acknowledgments

This work was supported by the National Science Foundation Heat Transfer Program under Grant No. ENG-7811686. The authors are indebted to Professor W. Leidenfrost for many helpful discussions.

References

1 Lorsch, H. G., Kauffman, K. W., and Denton, J. C., "Thermal Energy Storage for Heating and Off-Peak Air Conditioning," *Energy Conversion*, Vol. 15, 1975, pp. 1–8.

2 White, R. D., Bathelt, A. G., Leidenfrost, W., and Viskanta, R., "Study of Heat Transfer and Melting From a Cylinder Imbedded in a Phase Change Material," ASME Paper No. 77-HT-42, 1977.

3 Sparrow, E. M., Schmidt, R. R., and Ramsey, J. W., "Experiments on the Role of Natural Convection in the Melting of Solids," ASME JOURNAL OF HEAT TRANSFER, Vol. 100, 1978, pp. 11–16.

4 Hale, N. W., and Viskanta, R., "Photographic Observation of the Solid-Liquid Interface Motion During Melting of a Solid Heated from an Isothermal Vertical Wall," *Letters in Heat Hass Transfer*, Vol. 5, 1978, pp. 329–337.

5 Bathelt, A., Viskanta, R., and Leidenfrost, W., "An Experimental Investigation of Natural Convection in the Melted Region Around a Heated Horizontal Cylinder," *Journal of Fluid Mechanics*, Vol. 90, Part 2, 1979, pp. 227–239.

6 Bathelt, A. G., Viskanta, R., and Leidenfrost, W., "Latent Heat-of-Fusion Energy Storage: Experiments on Heat Transfer from Cylinders During Melting," ASME JOURNAL OF HEAT TRANSFER, Vol. 101, 1979, pp. 453–458.

7 Bathelt, A. G., Van Buren, P. D., and Viskanta, R., "Heat Transfer During Solidification Around a Cooled Horizontal Cylinder," *AIChE Symposium Series*, No. 189, Vol. 75, 1979, pp. 103–111.

8 Sparrow, E. M., Ramsey, J. W., and Kemink, R. G., "Freezing Controlled by Natural Convection," ASME JOURNAL OF HEAT TRANSFER, Vol. 101, 1979, pp. 578–584.

9 Eckert, E. R. G., and Drake, R. M., *Analysis of Heat and Mass Transfer*, McGraw-Hill, New York, 1972.

10 Humphries, W. R., and Griggs, E. I., "A Design Handbook for Phase Change Thermal Control and Energy Storage Devices," NASA Technical Paper 1074, NASA, Washington, DC, 1977.

11 Abhat, A., Dietrich, G., and Hage, M., "Study and Design of a Modular Phase Change Material Thermal Capacitor for Application to Spacelab Payloads," AIAA Paper 78-887, 1978.

12 Henze, R. H., and Humphrey, J. A. C., Enhanced Heat Conduction on Phase-Change Thermal Energy Storage Devices," ASME Paper No. 80-WA/HT-45.

13 Griffin, F. P., and Smith, R. N., "Approximate Solution for Freezing Adjacent to an Extended Surface," ASME Paper No. 80-HT-8.

14 Sparrow, E. M., Larson, E. D., and Ramsey, J. W., "Freezing on a Finned Tube for Either Conduction-Controlled or Natural-Convection-Controlled Heat Transfer," *International Journal of Heat and Mass Transfer*, (in press).

15 Bathelt, A. G., "Experimental Study of Heat Transfer During Solid-Liquid Phase Change Around a Horizontal Heat Source/Sink," Ph.D. Thesis, Purdue University, 1979.

16 Van Buren, P.D., and Viskanta, R., "Interferometric Measurement of Heat Transfer During Melting from a Vertical Plate," *International Journal of Heat and Mass Transfer*, Vol. 23, 1980, pp. 568–571.

17 Hauf, W., and Grigull, W., "Optical Methods in Heat Transfer," in *Advances in Heat Transfer*, J. P. Hartnett and T. F. Irvine, Jr., eds., Academic Press, New York, 1970, Vol. 6, pp. 133–366.

18 Goldstein, R. J., "Some Measurement Techniques in Heat Transfer," in *Heat Transfer 1978*, National Research Council of Canada, Ottawa, 1978, Vol. 6, pp. 495–508.

19 Marshall, R. H., "Natural Convection Effects in Rectangular Enclosures Containing a Phase Change Material," in *Thermal Storage and Heat Transfer in Solar Energy Systems*, F. Kreith, R. Boehm, J. Mitchell, and R. Bannerot, eds., ASME, New York, 1978, pp. 61–69.

T. R. Hsu
Professor.

G. Pizey
Senior Research Associate.

Department of Mechanical Engineering,
University of Manitoba,
Winnipeg, Manitoba, Canada R3T 2N2

On the Prediction of Fusion Rate of Ice by Finite Element Analysis

A finite element algorithm including phase change is presented for the prediction of the rate of freezing of fresh water under general ambient conditions. This method has shown to be highly versatile in dealing with multi-phase materials of complicated geometries. Experiments were performed to verify the code prediction on the fusion of fresh water and a case with oil inclusion. Close agreement was observed between the predicted and measured values.

Introduction

The rapid increase of oil and gas explorations in the Arctic region in recent years has stimulated a renewed interest in the development of more accurate analytical models for the prediction of the thermal and mechanical behavior of ice. The application of ice covers in this region for transportation and shelter purposes [1] has necessitated a thorough understanding of the response of these covers when subjected to varying thermomechanical inputs. Although there are a number of publications available on the mechanical properties and strengths of ice [2, 3], including prediction of the thermal regime and thickness of an ice sheet and the effect of these variables on load bearing capacity [4], most work is empirical and based on rather restrictive shapes and conditions. The analysis presented here provides a method for predicting the temperature distribution and rate of freezing of an ice sheet subjected to varying thermal inputs. A comparison with results obtained from a pure water freezing experiment indicates that accurate estimates of ice sheet thickness can be obtained with this procedure. The flexibility of the method is further demonstrated by an accurate prediction of the multidimensional ice/water phase front migration in the presence of an oil inclusion.

The cooling of a large body of fresh water can be described as convective until the body reaches a uniform temperature of 4°C, at which point the density extremum has been reached and convective circulation ceases [5]. Further cooling with eventual ice growth occurs by unidirectional heat conduction. A vertical section through an ice covered body of water reveals a temperature gradient varying from some temperature less than 0°C at the top of the ice sheet, to 0°C at the phase front to 4°C at some location beneath the ice, a region called the thermocline. Below the thermocline the water is isothermal at 4°C. Any ice thickness prediction model must incorporate these physical features.

The estimation of ice growth under either fixed or variable thermal conditions has been analyzed by a number of authors using either analytical [6, 7] or numerical [8, 9] methods. A relatively new numerical technique which has gained widespread interest involves the application of the finite element method to heat transfer problems [10]. The finite element procedure can accommodate complex geometries with fixed or variable temperature or heat flux boundary conditions. It also can be used for compound materials with nonlinear thermal properties. In addition, solution accuracy can be improved with refined meshes in the analysis.

Although the use of finite element thermal analysis has increased rapidly, only a few authors [11, 12] have included the feature of phase change and the analyses are confined to constant boundary conditions. The purpose of this study is to develop a finite element model for the prediction of ice thickness in an ice/water mixture subject to a general thermal environment, which may involve the prescribed surface temperature and convective boundary conditions.

Finite Element Formulation

The essence of the finite element method is to replace the continuous body by a finite number of elements of certain shapes interconnected at the apex or nodes. For the analysis of conduction of heat in a solid, an interpolation function is assumed for the temperature field within each element. Thermal equilibrium equations are then derived at nodal points in the discretized system.

The analysis begins by assuming the temperature in an element to be related to its nodal temperatures by the following relation:

$$T_m(\mathbf{r}, t) = \{b_m(\mathbf{r})\}^T \{T(t)\} \tag{1}$$

where $T_m(\mathbf{r}, t)$, $\{T(t)\} \equiv$ temperatures in the element and at nodal points respectively; r = spatial coordinates; and $\{b_m(\mathbf{r})\} \equiv$ interpolation function.

Temperature gradients are given by:

$$\{T_{m,i}(\mathbf{r}, t)\} = \{a_m(\mathbf{r})\}^T \{T(t)\}$$

where

$\{T_{m,i}(\mathbf{r}, t)\} \equiv$ element temperature gradient

$$\{a_m(\mathbf{r})\}^T = \{b_{m,i}(\mathbf{r})\}^T$$

In order to insure the continuity of the temperature across the nodal points for the neighboring elements, the first variation of the functional proposed by Gurtin [13] with respect to $\{T(t)\}$ has yielded the following heat balance equation for the discretized solid [10]:

$$[C]\,(\{\dot{T}(t)\} - \{\dot{T}(0)\}) + [K] \cdot \{T(t)\} = \{Q(t)\} \tag{2}$$

in which $[C] = \sum_{m=1}^{M} [C^m]$

$$[K] = \sum_{m=1}^{M} [K^m]$$

$$\{Q(t)\} = \sum_{m=1}^{M} \{Q_m(t)\} \tag{3a}$$

are the corresponding overall heat capacitance, conductivity and thermal force matrices, and

$$[C^m] = \int_{V_m} \rho_m(\mathbf{r})\, C_m(\mathbf{r})\, \{b_m(\mathbf{r})\}^T \{b_m(\mathbf{r})\}\, dV_m$$

$$[K^m] = \int_{V_m} \{a_m(\mathbf{r})\}\, [K_m(\mathbf{r})]\, \{a_m(\mathbf{r})\}^T\, dV_m$$

$$\{Q_m(t)\} = \int_{V_m} \rho_m(\mathbf{r}) \cdot q_m(\mathbf{r}, t)\, \{b_m(\mathbf{r})\}^T\, dV_m + \int_{S_m} Q_i{}^m(\mathbf{r}, t) n_i \{b_m(\mathbf{r})\}^T\, dS_m \tag{3b}$$

where $\rho_m, C_m, K_{ij}{}^m \equiv$ mass density, specific heat, and thermal conductivity in an element; $q_m \equiv$ heat generation rate per unit mass in an element; $Q_i{}^m \equiv$ prescribed heat flux conditions on the boundary of an element; $V_m, S_m \equiv$ volume and boundary surface of an element; $n_i \equiv$ unit vector normal to the element surface S_m; and $M \equiv$ total number of elements in the system.

It is clear that equation (2) is nonlinear since the material properties $K_m(\mathbf{r})$, $\rho_m(\mathbf{r})$ and $Q_m(\mathbf{r}, t)$ and hence the matrices $[K]$, $[C]$ and $\{Q\}$ are all dependent on the element temperature T.

Contributed by the Heat Transfer Division for publication in the JOURNAL OF HEAT TRANSFER. Manuscript received by the Heat Transfer Division October 7, 1980.

By rewriting equation (2) into the following form:

$$[C]\{\dot{T}\} + [K]\{T\} = \{Q\}$$

and expressing the above equation at time instants t and $t + \Delta t$, the difference of the thermal equilibrium states between these two instants with constant thermal properties is:

$$[C](\{\dot{T}_{t+\Delta t}\} - \{\dot{T}_t\}) + [K](\{T_{t+\Delta t}\} - \{T_t\}) = \{Q_{t+\Delta t}\} - \{Q_t\} \quad (4)$$

The forward explicit finite difference scheme provides that:

$$\{\dot{T}_{t+\Delta t}\} = \frac{\{T_{t+\Delta t}\} - \{T_t\}}{\Delta t}$$

or

$$\{\dot{T}_{t+\Delta t}\} - \{\dot{T}_t\} = (\{T_{t+\Delta t}\} - \{T_t\})/\Delta t - \{\dot{T}_t\}$$

Equation (4) can thus be expressed as:

$$\left(\frac{[C]}{\Delta t} + [K]\right)\{\Delta T_t\} = [C]\{\dot{T}_t\} + \{\Delta Q_t\} \quad (5)$$

where

$$\{\Delta T_t\} = \{T_{t+\Delta t}\} - \{T_t\} \text{ and}$$

$$\{\Delta Q_t\} = \{Q_{t+\Delta t}\} - \{Q_t\}.$$

Now, since $\{\dot{T}_t\} = \dfrac{\{T_t\} - \{T_{t-\Delta t}\}}{t - (t - \Delta t)}$

$$\{\dot{T}_t\} = \frac{\{T_t\} - \{T_{t-\Delta t}\}}{\Delta t}$$

Finally, with $\{\Delta T_{t-\Delta t}\} = \{T_t\} - \{T_{t-\Delta t}\}$, one may express equation (5) in the form:

$$[K^*]\{\Delta T_t\} = \{Q_t^*\} \quad (6)$$

where the equivalent conductivity matrix,

$$[K^*] = \frac{[C]}{\Delta t} + [K]$$

and the equivalent thermal force matrix

$$\{Q_t^*\} = \frac{[C]}{\Delta t}\{\Delta T_{t-\Delta t}\} + \{\Delta Q_t\}$$

Implementation of Phase Change

Direct integrations of the element heat capacity and conductivity matrices in equation (3) are feasible with the material's thermophysical properties varying moderately within each time increment. For the cases of melting or freezing process where these properties may vary drastically as shown in Fig. 1, problems likely will occur in the region of the phase change temperature, T_f. The latent heat required for the phase change is mathematically represented by a Dirac function type variation of heat capacity of the material. This drastic change of material properties often causes serious numerical stability problems in the computation.

This difficulty may be overcome by the technique proposed in [14] and adopted herein that the integral of heat capacity with respect to temperature is a smooth function of temperature even during the phase transformation. Hence the enthalpy of the material which is defined as:

$$H(T) = \int_{T_0}^{T} \rho C(T) dT$$

is introduced in the computation. Having thus established an $H-T$ curve, it is reasonable to interpolate the enthalpy in any element containing a phase boundary as follows:

$$H_m(\mathbf{r}, t) = \{b_m(\mathbf{r})\}^T \{H(t)\} \quad (7)$$

where $H_m(\mathbf{r}, t)$, $\{H(t)\} \equiv$ enthalpy in the element and at nodal points, respectively.

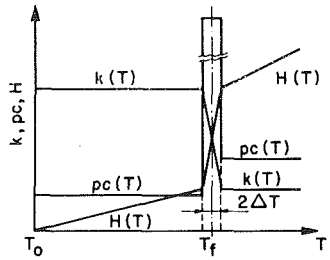

Fig. 1 Graphic representation of material property variations through phase change

Further, since by definition

$$\rho C = dH/dT$$

the values of heat capacity at the particular integrating points for the phase transition element can be approximated by determining the enthalpy gradient with respect to temperature as:

$$\langle \rho C \rangle_{x,y,z} \simeq \frac{1}{3}\left(\frac{\partial\{H_m\}}{\partial x}\Big/\frac{\partial\{T_m\}}{\partial x} + \frac{\partial\{H_m\}}{\partial y}\Big/\frac{\partial\{T_m\}}{\partial y} + \frac{\partial\{H_m\}}{\partial z}\Big/\frac{\partial\{T_m\}}{\partial z}\right) \quad (8)$$

Thus, for an element containing a phase boundary, the heat capacity $\rho_m C_m$ can be determined by the following procedures: (i) Determine the nodal values of enthalpy $\{H(t)\}$ corresponding to the nodal temperatures $\{T(t)\}$ from the temperature-enthalpy $(H-T)$ curve; (ii) Evaluate equation (8) for $\langle \rho C \rangle_{x,y,z}$ using the relationships:

$$\frac{\partial}{\partial \mathbf{r}_i}\{H_m(\mathbf{r})\} = \frac{\partial}{\partial \mathbf{r}_i}\{b_m(\mathbf{r})\}^T \{H(t)\}$$

$$\frac{\partial}{\partial \mathbf{r}_i}\{T_m(\mathbf{r})\} = \frac{\partial}{\partial \mathbf{r}_i}\{b_m(r)\}^T \{T(t)\} \qquad i=1,2,3$$

(iii) The element heat capacity can thus be evaluated by using equation (8) and the following integral:

$$[C^m] = \int_{V_m} \langle \rho C \rangle_{x,y,z} \{b_m(\mathbf{r})\}\{b_m \mathbf{r}\}^T dV_m \quad (9)$$

Thermal Boundary Conditions

Most freezing and melting of ice is caused by heat flows across the free surface. In addition to the prescribed surface temperature condition, the present analysis also handles other more general cases: e.g., natural and forced convective and radiative boundary conditions. Various boundary conditions can be accounted for in the analysis either by including the second integral in equation (3*b*) in the derivation of the $\{Q_m(t)\}$ matrix or by appropriate modifications to the $\{Q(t)\}$ matrix in equation (3*a*) at a later stage. Since the present paper only dealt with the cases involving natural convection and prescribed temperature boundary conditions, only these two types of thermal boundary conditions will be presented as follows:

Natural Convection. This condition applies when the air surrounding the contact ice surface is stagnant, or moving at a very low velocity. The heat flow across a boundary layer at the surface of the ice in the thermal force matrix is given by:

$$Q = ah(T_e - T_s)$$

where a = area of the contact surface; h = heat transfer coefficient by natural convection; T_e = temperature of the bulk fluid; and T_s = temperature of the contact surface.

If the contact surface is between nodes i and j, in a finite element analysis, heat transfer across the surface may be approximated by concentrating the total heat flow through the boundary at the nodes i and j. If the temperature of the contact surface is taken as $(T_i + T_j)/2$, then

$$Q_i = b_c(T_e - T_i) \quad (10a)$$

$$Q_j = b_c(T_e - T_j) \quad (10b)$$

where $b_c = Lth\,[T_e - (T_i + T_j)/2]/2$; t = thickness of the element average (circumference of the surface ij in the axisymmetric case); and L = linear distance between nodes i and j.

The additional heat flow across the boundary elements evident from equation (10) requires modification of both the conductivity and thermal force matrix in equation (2) by adding the following:

$$K'_{ii} = K_{ii}^* + b_c$$
$$K'_{jj} = K_{jj}^* + b_c$$
$$Q'_i = Q_i^* + b_c T_e$$
$$Q'_j = Q_j^* + b_c T_e$$

where K'_{ii}, K'_{jj} = diagonal terms corresponding to nodes i and j, respectively, in the modified overall conductivity matrix; K_{ii}^*, K_{jj}^* = diagonal terms corresponding to nodes i and j, respectively, in the conductivity matrix; Q'_i, Q'_j = rate of heat flow at nodes i and j, respectively, in the modified heat flow matrix, and; Q_i^*, Q_j^* = rate of heat flow at nodes i and j, respectively, in the corresponding nodes i and j, respectively. This procedure can be applied repeatedly for all the free convection boundary elements.

Prescribed Surface Temperature. This boundary condition can be handled by assuming an imaginary super-conductive element connected to the node for which the temperature is specified. Suppose the temperature at node i is prescribed to be T_i^0, then the appropriate modifications are:

$$K'_{ii} = e \tag{11a}$$

$$Q'_i = eT_i^0 \tag{11b}$$

where $e = \Sigma_{m=1}^{N} (K_{mm}^* \times 10^6)$; $N \equiv$ total number of nodes with prescribed temperature in the system; and $K_{mm}^* \equiv$ diagonal elements in the overall conductivity matrix.

Solution Procedures

The procedures of the numerical solution for the finite element formulations is similar to that outlined in [10] except for the phase change algorithm. A certain change of the computational sequences were also made for the convenience of coupling with the mechanical analyses, although the mechanical analysis was not involved in the present investigation. The procedure for the thermal analysis can be outlined as follows: (1) initialize nodal temperatures; (2) form $[K]$, $[C]$ and $\{Q\}$ matrices according to equation (3) with the selected thermal material properties based on the element temperatures obtained from the previous step. For elements undergoing phase change, the element heat capacity matrix $[C]$ must be computed according to equations (7, 8) and (9); (3) form the equivalent conductivity matrix $[K^*]$ in equation (6); (4) triangularize $[K^*]$; (5) modify $[K^*]$ for prescribed surface temperature condition following equation (11); (6) calculate the equivalent thermal force matrix $\{Q_t^*\}$ from equation (5); (7) modify $\{Q_t^*\}$ for applicable boundary condition, e.g., in equation (10); (8) adjust $[K^*]$ corresponding to Step (7); (9) solve for the nodal temperature increment at time t, $\{\Delta T_t\}$ from equation (6); (10) calculate the nodal temperature $\{T_t\} = \{T_{t-\Delta t}\} + \{\Delta T_t\}$; (11) repeat the same procedure for the next time increment.

Results and Discussion

The finite-element formulations outlined above have been implemented into an existing thermoelastic-plastic stress analysis code TEPSA. This code handles simplex elements of axisymmetric and plane geometries. The detail description of this code can be found in [15–17].

The revised code was first used to reproduce the analytical results described in [14] for the fusing of ice with prescribed surface temperature. Identical thermophysical properties, model and element sizes were used. The TEPSA code gave essentially identical results to those derived in [14].

In order to further check the validity of the TEPSA code, two experiments were performed to verify the results predicted by the code.

In the first experiment, the water was placed in a thermally insulated cylindrical container with its top surface exposed to the air at 6.8°F in a cold room as illustrated in Fig. 2. Temperatures at five stations along the axis of the cylinder including one on the ice/air interface were measured at various intervals. The measured surface temperature and the corresponding surface heat transfer coefficient h are given in Table 1. Both T_s and h were used as separate boundary conditions in the finite element analysis.

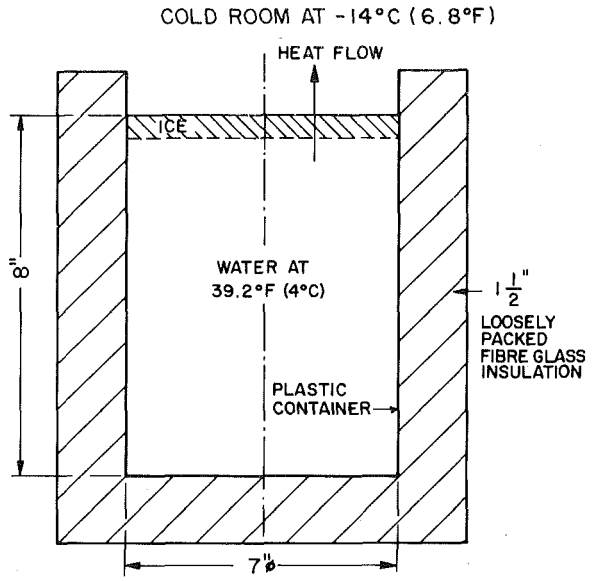

Fig. 2 Sample for ice fusion experiment

Table 1 Measured ice surface temperature and heat transfer coefficient

Time (hours)	Surface Temperature T_s (°F)	Heat Transfer Coefficient h (BTU/in s °F) × 10^{-6}
0	27.3	7.8
6	25.9	7.6
17	23.9	7.0
23	23.0	6.1
29	21.9	6.1
40	21.0	5.9
47	20.5	5.7
54	19.8	5.9
64	18.7	6.0
71	18.3	5.9
77	18.0	5.9
88	14.7	8.8

Ambient temperature = 6.8°F

Since the container was considered to be perfectly insulated with no radial heat flow, a simple one-dimensional finite element idealization was used first as illustrated in Fig. 3. Other input information to the finite element analysis included the thermal properties of ice and water as shown in Fig. 4. The locations of the phase front within any element was obtained by extrapolating the temperature gradients from the closest ice element. Since quadrilateral elements of the size of 0.5 in. × 0.5 in. were used in this analysis, comparison of the numerical and experimental results begins only after a thin layer of ice of one element thickness had been formed. The nodal temperature variation in the ice/water mixture at this state is given in Fig. 3. This "pre-freezing" was necessary as the present analysis has not yet been modified to handle the natural convection of water before reaching the density extremum temperature.

In Fig. 5 the comparison of the analytical results obtained by the TEPSA codes and the measured ice thickness at various instances is shown. It is interesting to observe that both types of boundary conditions, i.e. using prescribed surface temperature, T_s in Table 1; and the convective conditions with h and the surrounding air temperature 6.8°F gave virtually identical results. The predicted results with the assumed thermally insulated condition for the sides and bottom

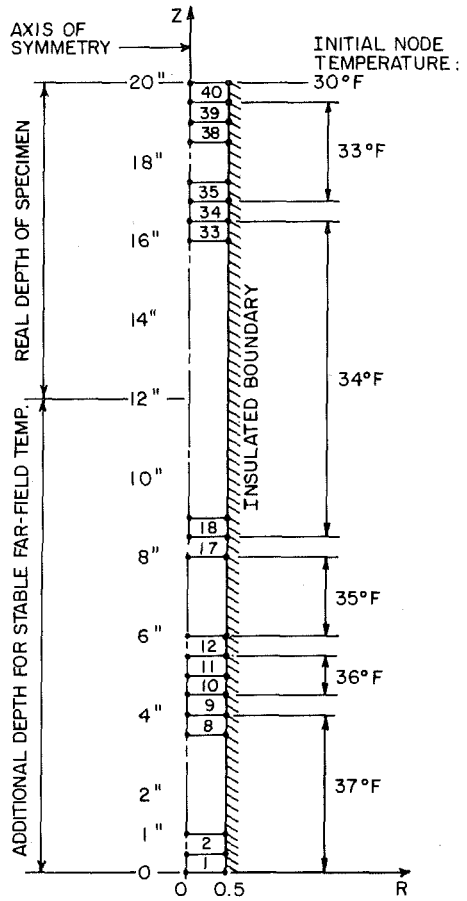

Fig. 3 Finite element idealization for one-dimensional fusion of ice

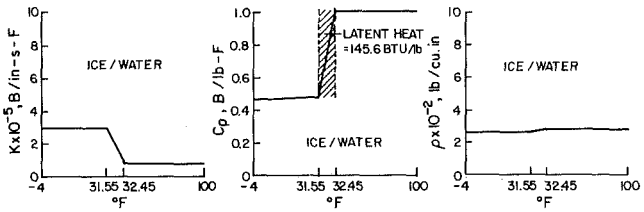

Fig. 4(*a*) Properties of ice and water

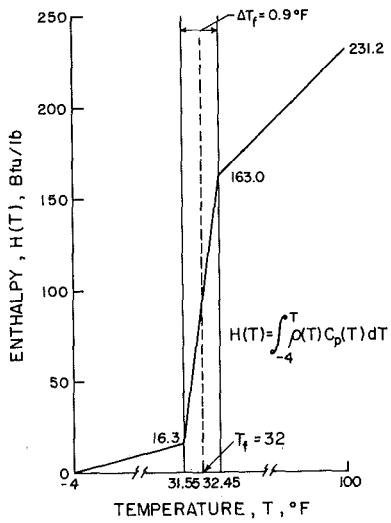

Fig. 4(*b*) Variation of enthalpy of ice during phase change

Fig. 4 Thermophysical properties of ice and water

agreed well with the measured values up to the first 48 h into the experiment. Significant discrepancies however began to develop thereafter. These discrepencies were due largely to the fact that heat lost through the sides and bottom of the plastic container became significant when more ice was formed in the container. This phenomenon violated the perfect thermal insulation boundary condition used throughout the entire analysis.

An attempt was then made to account for this heat loss by extending the finite element model in Fig. 3 in the radial direction to include the thermal insulation material as illustrated in Fig. 6. The initial condition, element size and the axial dimension of the model remained unchanged. However, a slight reduction in the radial dimension to the real specimen was made in the model in order to reduce the total number of elements used in the computation. The loss of heat through the insulation material in the radial direction was accounted for by applying a small convective heat transfer coefficient of 10^{-8} Btu/in^2-s-°F. The properties of the insulation material were assigned to be: thermal conductivity: 5×10^{-6} Btu/in-s-°F; specific heat: 0.25 Btu/lb-°F density: 0.025 lb/in.^{3}.

The computed ice thickness at various instants are shown in dotted line in Fig. 5, which correlate extremely well with the measured values except at the very end of the experiment.

Since TEPSA code was primarily developed to handle multi-dimensional analysis, a numerical and experimental study involving the presence of an oil slick in the ice fusion was conducted. Figure 7 depicts the experimental arrangement of the case. Ice was to be formed in a rectangular tank of 11 in. × 24 in. × 12 in. deep. The tank

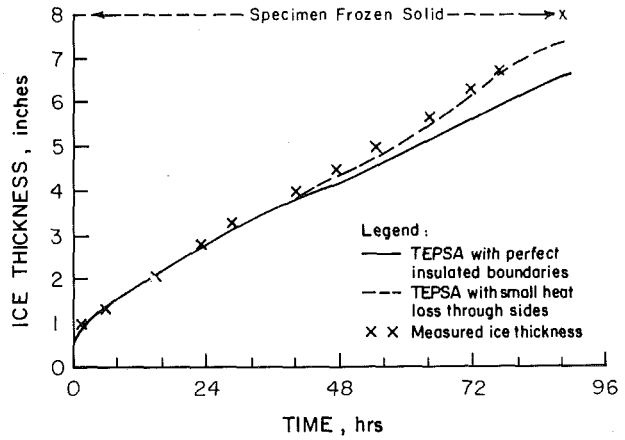

Fig. 5 Comparison of results on ice fusion rate

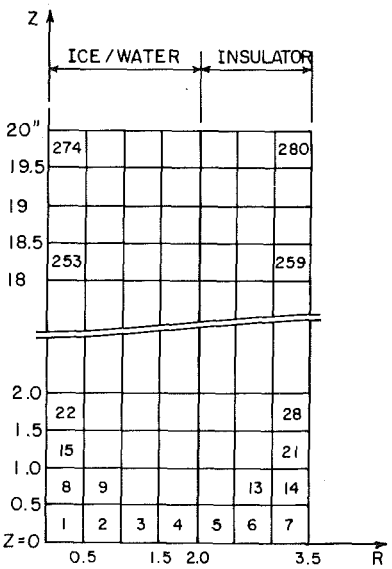

Fig. 6 Finite element idealization for ice fusion with radial heat loss

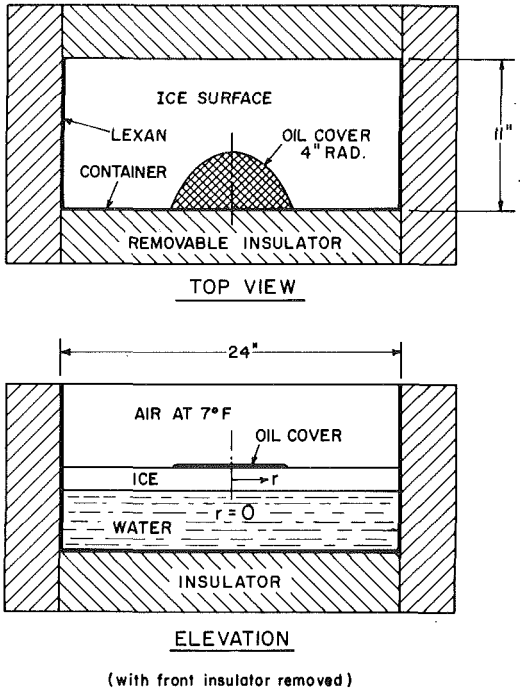

Fig. 7 Experimental set-up for ice fusion with oil cover

was made of lexan plastic and was thermally insulated by 10 in. thick styrofoam panels on the sides. A portion of the front insulation panel could be removed so that the position of ice/water phase front could be visually measured. An initial 1 inch thick ice was grown in the container and then a small amount of No. 1 crude oil was poured onto the ice surface in a half circle configuration such that its diameter coincided with the front edge of the tank. Figure 8 shows the finite element idealization of the experimental configuration. The input initial nodal temperatures indicated in Fig. 8 and the prescribed surface temperatures for TEPSA code were obtained from the experimental measurements. The thermophysical properties for the oil used in the analysis are shown in Fig. 9. As indicated in Fig. 10, the calculated ice thickness show excellent agreement with the experimentally measured values at the locations directly beneath (r = 0 in.) and away from (r = 10 in.) the oil slick.

It was found in the present investigation that among several factors which affect the accuracy of the analysis, the time step size and the size of the phase transition temperature are most critical. However, due to the rather long-term characteristics of the freezing problems observed experimentally, a relatively large time step size of 60 min was used for all numerical solutions obtained in this paper. In addition, a 0.9°F width was chosen for the temperature-enthalpy phase transition zone such that, with the above-noted time step and element sizes, the maximum change of any nodal temperature for an element was less than the phase transition width. This ensured that the enthalpy values at the integrating points for any element in the model would follow the H-T curve through the phase transition zone. The temperature changes for elements undergoing phase change were such that the spacial enthalpy and temperature derivatives at the start of any time step closely approximated the slope of the H-T curve in the transition zone as shown in Fig. 4(b). Thus for the given thermal load, time step and element size in this analysis, a proper phase transformation heat balance was preserved and accurate results were obtained. It was felt that the marginal increase in the accuracy for the phase front prediction by using a smaller time step size and a reduced width of the phase transition zone was not warranted as far as the computing costs were concerned. The three time step solution mentioned in [14] was adopted initially for the solution procedure here. However, as noted in [18] and also observed here, the temperature oscillations were such that the three time step algorithm had to be abandoned, and the time step procedure as described previously was employed.

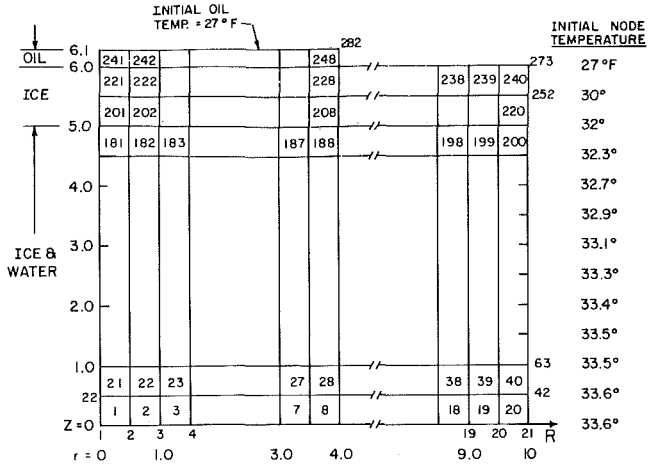

Fig. 8 Finite element idealization for ice fusion with oil cover

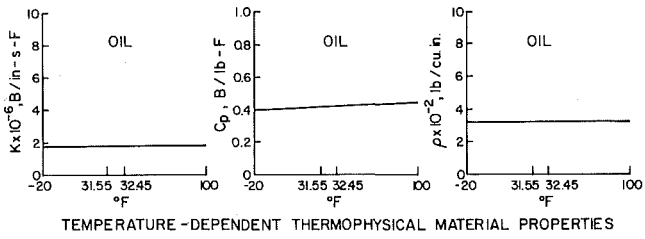

Fig. 9 Thermophysical properties of No. 1 crude oil

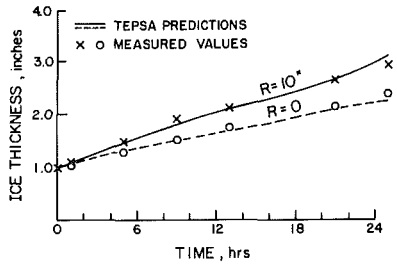

Fig. 10 Comparison of results on ice fusion with oil cover

The extension of the finite element model in Fig. 3 was necessary to ensure that the far field temperature would not vary significantly during the freezing of water in the container. Significant variation of the far field temperature had shown to cause numerical instability. Much smaller element size, time steps and phase change temperature zone would have to be used, which undoubtedly would drastically increase both the computational cost and effort.

Acknowledgment

The authors wish to acknowledge the contribution made by a former Research Associate, Mr. R. Wu in the early stage of this development. Thanks are due to Mr. D. Fedorowich for his valuable contributions in the preparation and performance of the experiments. Generous financial support to this project by the Natural Sciences and Engineering Research Council Canada under Grant Number G0220 is appreciated.

References

1 Gold, L. W., "Use of Ice Covers for Transportation," *Canadian Geotechnical Journal*, Vol. 8, 1971, pp. 170–181.

2 Frederking, R. M. W., and Gold, L. W., "The Bearing Capacity of Ice Covers under Static Loads," *Canadian Journal of Civil Engineering*, Vol. 3, 1976, pp. 288–293.

3 Gold, L. W., "Elastic and Strength Properties of Fresh-Water Ice," *Proceedings of Conference on Ice Pressure Against Structures*, Laval Univ., 1966, pp. 13–23.

4 Hutter, K., and Williams, F. M., "Theory of Floating Ice Sheets," *Physics and Mechanics of Ice*, ed. by Per Tryde, Springer-Verlag, 1980, pp. 147–162.
5 Pounder, E. R., *Physics of Ice*, Pergamon Press, London, 1965.
6 Stefan, J., "Über die Theorie der Eisbildung, insbesondere über die Eisbildung im Polarmeere," Vol. XCVIII, No. IIa, Sitzunysberuhte der Mathematisch-Natururssensihaftluhen Classe der Kaiserbihen Akademie der Wissenschaften, Wien, 1890, pp. 965–983.
7 Luikov, A. V., *Analytical Heat Diffusion Theory*, Academic Press, New York, 1968.
8 Murray, W. D., and Landis, F., "Numerical and Machine Solutions of Transient Heat Conduction Problems Involving Melting and Freezing," *Trans. ASME*, Vol. 81, pp. 106–112, 1959.
9 Atthery, D. R., "A Finite Difference Scheme for Melting Problems Based on the Method of Weak Solutions," *Moving Boundary Problems in Heat Flow and Diffusion*, ed. by Ockender J. R. and Hodgkins, W. R., Clarendon Press, Oxford, 1975.
10 Wilson, E. L., and Nickell, R. E., "Application of the Finite Element Method to Heat Conduction Analysis," *Nuclear Engineering and Design*, Vol. 4, 1966, pp. 276–286.
11 Hibbit, H. D., and Marcal, P. V., "A Numerical, Thermo-Mechanical Model for the Welding and Subsequent Loading of a Fabricated Structure," *Computers and Structures*, Vol. 3, 1973, pp. 1145–1174.
12 Friedman, E., "Thermomechanical Analysis of the Welding Process Using the Finite Element Method," ASME *Journal of Pressure Vessel Technology*, 1975, pp. 206–213.
13 Gurtin, M. E., "Variational Principles for Linear Initial-Value Problems," *Quarterly Journal of Applied Mathematics*, Vol. 22, 1964, p. 252.
14 Comini, G., Del Guidice, S., Lewis, R. W., and Zienkiewicz, O. C., "Finite Element Solution of Non-Linear Heat Conduction Problems with Special Reference to Phase Change," *International Journal of Numerical Methods for Engineering*, Vol. 8, 1974, pp. 613–624.
15 Hsu, T. R., Bertel, A. W. M., Banerjee, S., and Harrison, W. C., "Theoretical Basis for a Transient Thermal Elastic-Plastic Stress Analysis of Nuclear Reactor Fuel Elements," Atomic Energy of Canada Ltd., Rep. AECL-5233, 1976.
16 Hsu, T. R., and Bertels, A. W. M., "Propagation and Opening of a Through Crack in a Pipe Subject to Combined Cyclic Thermomechanical Loadings," *ASME Journal of Pressure Vessel Technology*, Feb., 1976, pp. 17–25.
17 Noor, A. K., "Survey of Computer Programs for Solution of Nonlinear Structural and Solid Mechanics Problems," *Journal of Computers and Structures*, V. 13, 1981, pp. 425–465.
18 Morgan, K., Lewis, R. W., and Zienkiewicz, O. C., "An Improved Algorithm for Heat Conduction Problems with Phase Change," *International Journal of Numerical Methods for Engineering*, Vol. 12, 1978, pp. 1191–1195.

An Experimental Investigation of Ice Formation around an Isothermally Cooled Cylinder in Crossflow

K. C. Cheng
Mem. ASME
Hideo Inaba[1]
R. R. Gilpin
Assoc. Mem. ASME
Department of Mechanical Engineering,
University of Alberta,
Edmonton, Alberta,
Canada T6G 2G8

The problem of steady-state, two-dimensional ice formation around an isothermally cooled circular cylinder in a crossflow is studied experimentally for the ranges of Reynolds numbers, Re_d, 2.3×10^2 to 8.6×10^4 and cooling temperature ratios, θ_c, 6.3 to 75.8. The local and average heat transfer coefficients at the ice-water interface are obtained from measured ice profiles by using a series solution of the Laplace equation in the ice. Correlation equations for the average heat transfer are obtained for three regimes of Reynolds numbers. A correlation is also obtained for the cooling capacity that can be stored in the ice layer around a cylinder.

1 Introduction

The classical Stefan problems or free boundary problems in which the diffusive processes control the change of phase of a material occur in many scientific and engineering problems involving natural phenomena and industrial processes. Recent extensions of the Stefan problem motivated largely by practical applications consider such real effects as convection (free and/or forced), flow regime (laminar or turbulent), maximum density, supercooling, geometrical configurations, multidimensionality and other physical effects involving either external or internal flow situations. Because of the difficulty in obtaining the analytical solutions for some of these free boundary problems, numerical solutions using either finite-difference or finite element technique have increasingly been used.

For many of the more difficult free boundary problems not even numerical techniques are entirely adequate and one must resort to experimental investigations. This appears to be particularly true of the problems where a flow separation, transition to turbulence or a turbulent flow may exist. In such situations [1–4] new phenomena such as unstable behavior, not anticipated by theoretical calculations have been observed. Extensive experimental investigations of ice formation in the presences of forced convection flows in pipes [3, 5, 6] and along flat plates [2, 7, 8] have been reported. In contrast, only a very limited number of experimental results have been reported for the case of freezing around a cooled pipe in cross flow [9, 10] and these results exist only at rather low Reynolds numbers—less than 10^3. Theoretical predictions of ice growth around a cylinder exist only for the case of conduction heat transfer [11–13]. On the other hand, forced convection around a horizontal circular cylinder without phase change is one of the basic problems in convective heat transfer and has been studied extensively by many investigators.

When an isothermally cooled long horizontal circular pipe with a wall temperature below the freezing temperature ($T_w < 0°C$) is immersed in a flowing water at a uniform temperature $T_\infty > 0°C$, the two-dimensional transient solidification problem arises. In this initial process, the latent heat of fusion is released at the ice-water interface and the ice thickness increases until a steady-state is reached. For the range of experimental conditions in this study, the steady state condition is approached within the order of hours after the initiation of cooling process. In the transient process, the latent heat, the convective heat at the interface and the heat removal to subcool the ice are conducted through the solid into the cooling pipe wall. A steady-state is reached when the convective heat transfer is balanced by the conduction heat transfer at the interface. It is the shape of this steady state interface and the convective heat transfer rate at it that will be studied here.

[1] Present address: Department of Mechanical Engineering, Kitami Institute of Technology, Hokkaido, Japan.

Contributed by the Heat Transfer Division for publication in the JOURNAL OF HEAT TRANSFER. Manuscript received by The Heat Transfer Division December 31, 1980.

2 Experimental Apparatus and Procedure

Experiments were conducted in a closed loop water tunnel having a test section in a form of rectangular plexiglas channel, measuring 25.4 cm wide, 45.7 cm high and 213.4 cm long [4]. A smooth converging entrance section provides a uniform flow to the section and the velocity can be varied in the range $U_\infty = 1$ cm/s to 5 m/s. The temperature of the water can be controlled at any value between room temperature and near 0°C by means of a refrigeration and heat exchanger system. The copper test cylinder (38.1 mm o.d., wall thickness 1.5 mm and length 254 mm) was placed horizontally in the test section. A schematic of the test cylinder details is shown in Fig. 1. To promote turbulence of the coolant (a mixture of glycol, alcohol and water) in the test cylinder for high heat transfer, a coiled spring was inserted in the annular space. The coolant was circulated at a high velocity between the test cylinder and a temperature controlled bath with a temperature range $0 \sim -25°C$. The inlet and outlet temperatures of the coolant at the test cylinder were within 0.1°C. The two-dimensionality of the flow and temperature fields around the horizontal cylinder were confirmed by the observations that the ice contour around the cylinder was axially uniform except for a small region near the wall of the rectangular test section.

The calming section with screens is located at a distance 3 m upstream of the test cylinder. Three sizes of screens, $M = 22$ mm, $d_g = 1.5$ mm, $M = 3.5$ mm, $d_g = 0.7$ mm, and $M = 0.6$ mm, $d_g = 0.15$ mm, where M = mesh size and d_g = wire diameter, were employed in the present experiments. The free stream velocity and turbulence level

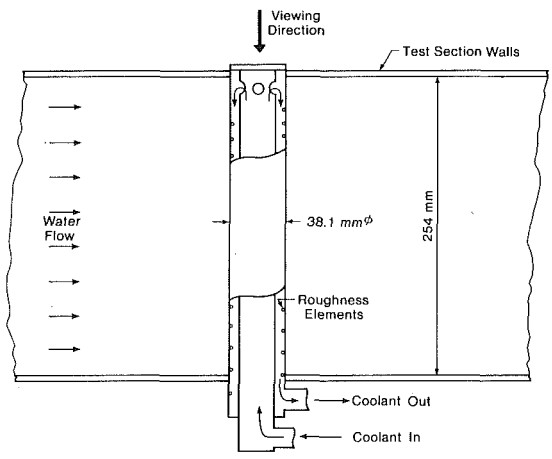

Fig. 1 Test cylinder

were measured at a location about 10 cylinder diameters upstream of the test cylinder using a laser Doppler anemometer system (15 mW). The turbulent intensity $Tu = (U'^2)^{1/2}/U_\infty$ was estimated from the streamwise component of the free stream velocity fluctuation. The free stream temperature was also measured at the same location.

After reaching a steady state for the given experimental conditions (coolant temperature or the cylinder surface temperature, free stream velocity and temperature), the ice contour was recorded photographically. The data reduction for the local heat transfer coefficient at the ice-water interface and other heat transfer results is based on the photographic record of the ice profile. In this study, the ranges of the experimental conditions were (see Table 1): free stream velocity $U_\infty = 1.02 \sim 397$ cm/s; free stream turbulence intensity $Tu = 0.3 \sim 4.0$ percent; free stream water temperature $T_\infty = 0.25 \sim 2.7°C$; cylinder surface temperature $T_w = -5.8 \sim -24.2°C$; Reynolds number based on cylinder outside diameter $Re_d = 2 \times 10^2 \sim 9 \times 10^4$; and cooling temperature ratio $\theta_c = 6.3 \sim 75.8$.

3 Analysis of Temperature Field in Ice Layer and the Determination of Local Heat Transfer Coefficient at the Ice-Water Interface

By noting that the cylinder surface temperature T_w and the freezing temperature $T_f = 0°C$ are known, the two-dimensional temperature field of the steady state ice layer can be obtained by a point-matching technique using the exact solution of the Laplace equation in polar coordinates. Past experience [14] suggests that the simple point-matching method will yield sufficiently accurate approximate solution for the present Dirichlet problem involving annular geometrical configuration with a circular inner boundary and a fairly compact outer boundary.

Defining the dimensionless quantities $\theta = (T - T_w)/(T_f - T_w)$ and $r = R/R_1$ for temperature and radial coordinate, the Laplace equation becomes (see Fig. 2)

$$\frac{\partial^2\theta}{\partial r^2} + \frac{1}{r}\frac{\partial\theta}{\partial r} + \frac{1}{r^2}\frac{\partial^2\theta}{\partial\phi^2} = 0. \tag{1}$$

The boundary conditions are:

$$\begin{aligned} &\theta = 0\ (T = T_w) \text{ at } r = 1 \text{ (cylinder surface)} \\ &\theta = 1\ (T = T_f) \text{ at } r = R_2/R_1 \text{ (interface).} \end{aligned} \tag{2}$$

Assuming symmetry of the ice layer profile with respect to the horizontal axis, only the upper half of the ice layer needs consideration. Using the exact series solution of equation (1) given in [15] for the present problem and satisfying the boundary condition at the cylinder surface ($R = R_1$) exactly, the solution can be shown to be

$$\theta = b_0 \log r + \sum_{n=1,2,3,\ldots}^{\infty} [a_n(r^n - r^{-n}) \cos n\phi]. \tag{3}$$

The unknown coefficients b_0, a_n for the complementary solution in equation (3) can be obtained by a point-matching method satisfying the boundary condition $\theta = 1$ at the ice-water interface at twenty equally angular spaced points along the upper ice profile AB (see Fig. 2). For the solution of Laplace equation, it is known that the maximum error occurs at the boundary. Calculations were made for $n = 20$, 30 and 40. In view of the rather small difference in results among the three cases, $n = 20$ was selected in this study. With $n = 20$, the maximum boundary errors for θ at the interface were found to be less than 10^{-6} for some extreme cases. In most cases the maximum boundary errors were negligibly small, being the order of 10^{-9} or less whereas the exact boundary value is $\theta = 1$. This observation confirms the convergence of the solution.

With the temperature field for the annular ice layer available, the local and average heat transfer coefficients at both the ice-water interface and the cylinder surface can be computed readily. At steady-state, a heat balance at the interface gives

$$h\,(T_\infty - T_f) - k_i \left.\frac{\partial T}{\partial n}\right|_{R=R_2} = 0. \tag{4}$$

In terms of the dimensionless quantities θ and r defined earlier, the local heat transfer coefficient $h_{n,\phi}$ can be written as

$$h_{n,\phi} = k_i \frac{(T_f - T_w)}{(T_\infty - T_f)} \frac{1}{R_1} \left[\frac{\sin(\psi - \theta)}{r_2} \left.\frac{\partial\theta}{\partial\phi}\right|_{r=r_2} + \cos(\psi - \phi) \left.\frac{\partial\theta}{\partial r}\right|_{r=r_2} \right] \tag{5}$$

where the angle ψ is defined in Fig. 2. The direction of the external normal n at any point on the ice-water interface was determined by

Symbols	T_∞, °C	θ_c	U_∞, cm/s	Re_d	Tu, %	Re_{Ds}	Re_{Dmax}
○	2.72	7.1	1.0	2.26×10^2	0.30	3.44×10^2	4.07×10^2
●	1.41	10.9	9.6	2.08×10^3	0.36	3.62×10^3	4.18×10^3
◑	0.67	21.6	14.1	3.04×10^3	1.49	6.53×10^3	7.46×10^3
◐	0.69	29.2	23.2	5.01×10^3	1.22	1.07×10^4	1.24×10^4
◓	0.48	44.8	35.3	7.64×10^3	0.80	1.99×10^4	2.14×10^4
◒	0.55	36.4	35.6	7.69×10^3	3.51	1.62×10^4	1.89×10^4
□	0.42	50.8	50.9	1.10×10^4	0.76	2.67×10^4	2.98×10^4
■	0.92	6.3	60.4	1.31×10^4	0.84	1.52×10^4	1.79×10^4
◨	0.64	34.6	77.5	1.67×10^4	3.02	3.03×10^4	3.44×10^4
◧	0.28	75.8	87.0	1.88×10^4	1.72	4.49×10^4	5.02×10^4
◓	0.72	25.2	101.0	2.18×10^4	1.01	3.25×10^4	3.87×10^4
◒	0.46	50.6	110.0	2.37×10^4	0.63	4.84×10^4	5.21×10^4
◩	0.84	22.6	112.0	2.41×10^4	0.40	3.46×10^4	3.91×10^4
◪	0.46	50.3	129.0	2.79×10^4	0.67	5.23×10^4	6.12×10^4
◪	0.30	67.1	131.0	2.82×10^4	4.11	5.49×10^4	5.61×10^4
◩	0.45	54.0	158.0	3.41×10^4	4.01	5.90×10^4	6.61×10^4
△	0.43	52.8	222.0	4.79×10^4	2.45	7.75×10^4	7.78×10^4
▲	0.31	68.4	230.0	4.97×10^4	0.80	9.33×10^4	9.94×10^4
▽	0.45	41.8	253.0	5.46×10^4	1.40	7.89×10^4	8.07×10^4
▼	0.31	63.2	271.0	5.82×10^4	1.77	9.35×10^4	8.57×10^4
◇	0.44	43.8	397.0	8.57×10^4	1.72	1.17×10^5	1.09×10^5

Table 1 Range of parameter values for experiments

Nomenclature

A_s = cross-sectional area of ice
a_n, b_0 = coefficients of series solution in equation (3)
c_p = specific heat
Ds = effective diameter of ice near forward stagnation point
D_{max} = maximum diameter of ice layer profile
d = cylinder diameter
Gr_{Ds} = Grashof number based on Ds
H = height of rectangular test section
h_m, $h_{n,\phi}$ = average and local heat transfer coefficients
k_i, k_w = thermal conductivities for ice and water
L = latent heat of fusion per unit volume
Nu_d, Nu_{Ds} = Nusselt numbers, $h_m d/k_w$ (average), and $(h)_{\phi=0}Ds/k_w$ (stagnation point)
Pr = Prandtl number
Q = cooling capacity stored in ice layer per unit axial length
Q' = nondimensional cooling capacity
R, R_1, R_2 = radial coordinate, outside radius of cylinder and radial coordinate of ice-water interface
Re_d, Re_{Ds} = Reynolds numbers, $U_\infty d/\nu$, $U_\infty Ds/\nu$
r = dimensionless radial coordinate, R/R_1
T = temperature
T_f, T_w, T_∞ = freezing temperature of water, surface temperature of cylinder and free stream temperature
Tu = longitudinal (streamwise) turbulence intensity, $(U'^2)^{1/2}/U_\infty$
U_∞ = free stream velocity
$(U'^2)^{1/2}$ = rms—value of longitudinal fluctuating velocity component
γ_s = density of ice
θ = dimensionless temperature, $(T - T_w)/(T_f - T_w)$
θ_c = cooling temperature ratio, $(T_f - T_w)/(T_\infty - T_f)$
ν = kinematic viscosity
ϕ = angular position measured from forward stagnation point
ψ = angle defined in Fig. 2

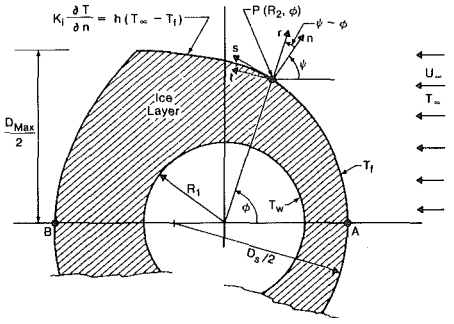

Fig. 2 Definition of variables and coordinates used

considering the cord subtended by the two neighboring points located at ±2.5 deg from an angle ϕ. By using equation (3) the heat transfer rate through the cylinder surface ($R = R_1$) can be found by integration. On the other hand, the heat transfer rate through the ice-water interface can be obtained by using Simpson's rule for integration. The agreement between the two results was found to be within 1 percent in all cases confirming the accuracy of the present method of determining the local heat transfer coefficient. Precision in measuring the ice layer thickness is an important factor in the present method for determining the temperature field of the ice layer. In order to minimize the measuring errors the photographs of the ice layer were enlarged two to three times the actual size.

4 Experimental Results and Discussion

4.1 Steady-State Ice Layer Profile and Local Heat Transfer at the Ice-Water Interface. Photographs in Fig. 3 show the shape of the steady-state ice buildup on the cylinder for three different conditions of flow and temperature, Re_d and θ_c. They represent typical results for (*a*) "low", (*b*) "moderate", and (*c*) "high" Reynolds numbers in the range accessible to the present experiment. Since the ice was symmetrical only one half, the upper half, of the ice layer is shown in each case.

To understand the shape of the ice profile it is useful to simultaneously look at the variation of local heat transfer around the cylinder that it implies. Figure 4 shows the calculated local heat transfer rate obtained by solving the Laplace equation in the ice layer as described previously. The three results shown are for the same conditions as existed in the photographs in Fig. 3. The ice layer profiles measured from the photographs are also plotted on this figure for reference.

By examining the ice layer profiles and by comparing the variation in local heat transfer with that observed in a circular cylinder some speculations can be made about the implied flow regimens around the ice. At the lowest Reynolds number, $Re_d = 2.08 \times 10^3$, the flow field is quite simple. From the front stagnation point, $\phi = 0$, to $\phi \simeq 120$ deg appears to represent a laminar boundary layer development. At $\phi \simeq 120$ deg this boundary layer separates and the region $\phi = 120$ to 180 deg represents the wake flow. The laminar separation was always very clearly evident on the ice surface because it resulted in a sharp line on the ice surface where an apparently discontinuous change in the slope of ice layer occurred.

For a circular cylinder the laminar separation point would occur around $\phi = 80$ deg. It is, however, rather meaningless to compare the angular positions on the ice cylinder with those of a circular cylinder since the ice grossly distorts the cylinder from a circular shape. In fact the ice surface in the laminar flow region shapes up more like a parabolic cylinder than a circular one. A more meaningful comparison may be made on the basis of the angle ψ in Fig. 2—the angle between the local normal to the ice and U_∞. For the ice surface just upstream from the separation point $\psi \approx 82$ deg which is very similar to the case for the circular cylinder.

At higher Reynolds numbers the flow regimens are more difficult to interpret. Examining the variation of the local heat transfer for the highest Reynolds number, $Re_d = 5.82 \times 10^4$, and again comparing with the results for a circular cylinder [16] would suggest the following. From $\phi = 0$ to 70 deg a laminar boundary layer exists. At $\phi = 70$ deg a laminar separation occurs followed by a separation bubble from $\phi = 70$ to 100 deg. At $\phi \simeq 100$ deg the flow reattaches as a turbulent boundary layer which develops along the ice until $\phi \simeq 140$ deg where it separates. By way of comparison it is interesting to note that for flow on an ice layer grown on a flat plate the transition from laminar to turbulent flow also occurred, except for very thin ice layers, via a separation bubble [2].

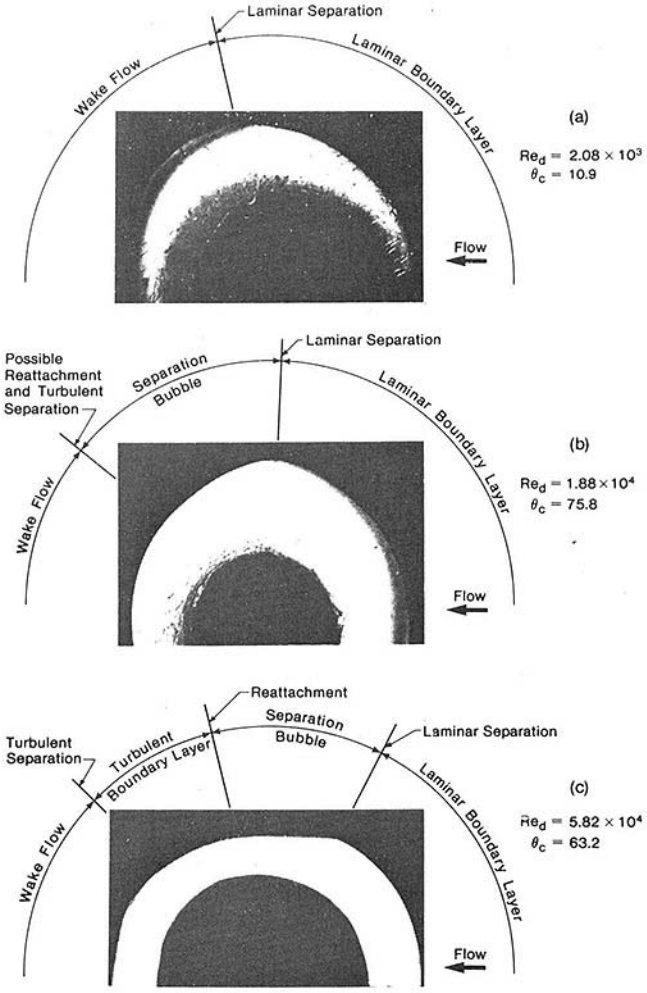

Fig. 3 Photographs of ice layer (light coloured region) around the cylinder at various Reynolds numbers. Flow regions indicated were obtained by an interpretation of the local heat transfer coefficient variation around the cylinder

The intermediate Reynolds number, $Re_d = 1.88 \times 10^4$, is approximately the lowest Reynolds number for which a reattachment of the flow as a turbulent boundary layer is implied by the ice profile shape. For this condition the variation of local heat transfer rate with increasing ϕ undergoes a sharp change in slope and possible short period of decrease near $\phi = 130$ deg which may indicate a possible reattachment before the wake region develops. For a circular cylinder one would normally not expect that a turbulent boundary layer would exist below a Reynolds number of about 4×10^5. Even using the maximum diameter of the ice to calculate the Reynolds number, $Re_{D\max}$, the value is only 3.9×10^4 when a turbulent boundary layer is implied on the ice. This is quite consistent with the observations for transition on a flat plate with ice growth in that there the transition was also observed to occur at as much as an order of magnitude lower Reynolds numbers than for a plate without ice [2]. The reason for this appears to be related to the fact that the transition on the ice occurs

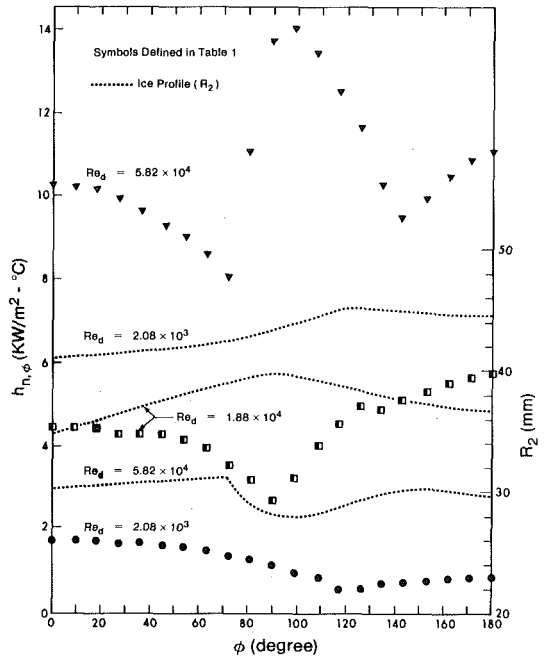

Fig. 4 Variation around the cylinder of the thickness of the ice layer and the local heat transfer coefficient that was calculated from it

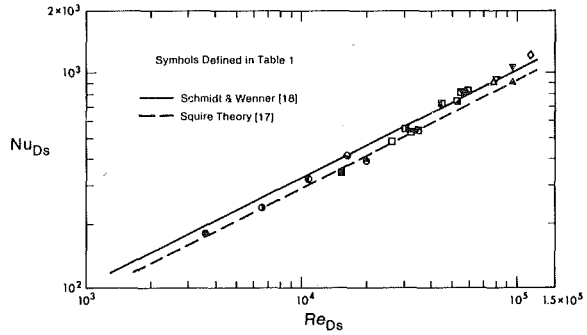

Fig. 5 Comparison of the heat transfer rate at the forward stagnation point on the ice with results for a circular cylinder

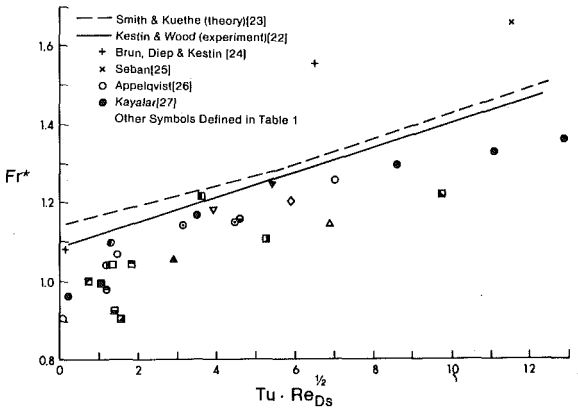

Fig. 6 The effect of free stream turbulence on heat transfer at the forward stagnation point

via a separation bubble. The "trigger" for the separation, a sharp change in the ice profile, is produced by the change in local heat transfer coefficient that occurs at the separation point. The separation is thus a self-reinforcing phenomenon that can induce a transition on the ice surface at Reynolds numbers considerably lower than what are usually required for a transition on a smooth surface.

4.2 Local Heat Transfer around the Forward Stagnation Point. From the photographic results of the ice layer profile around the isothermally cooled cylinder, it is found that the ice-water interface can be approximated by a circle near the forward stagnation point with a maximum deviation of ±1.5 percent within the angular position $\phi \leq 45$ deg. In this region the heat transfer rates may be compared to those for a circular cylinder. Forced convection from a circular cylinder with constant wall temperature has been studied by Squire [17] and Schmidt and Wenner [18] and many others. Schmidt and Wenner [18] provide the following experimental correlation equation for the local heat transfer coefficient near the forward stagnation point

$$\frac{hd}{k} = 1.14\left(\frac{U_\infty d}{\nu}\right)^{1/2} \mathrm{Pr}^{0.4}\left[1-\left(\frac{\phi \text{ deg}}{90}\right)^3\right], \quad \phi < 80 \text{ deg} \qquad (6)$$

The stagnation point Nusselt numbers $(\mathrm{Nu})_{Ds} = (h)_{\phi=0}\, Ds/k_w$, Ds = diameter of a circle near the forward stagnation point, from the present experiments are shown in Fig. 5 and the results are compared with theory [17] and correlation equation (6) [18]. Although some scatter of the experimental data exists depending on the experimental conditions, the present results are in very good agreement with those in [17, 18].

At this point it is of interest to consider the various factors which might contribute to the scatter in the present results and to differences in results among various investigations.

(*a*) *Variable Property Effects.* Since the temperature difference between the ice surface (0°C) and the free stream is less than 2.7°C in the present investigation, one would not expect the effect of variable viscosity to be significant [19]. The main problem comes in comparing the present results with other results obtained using air as a working medium. Scaling the data used $\mathrm{Pr}^{0.4}$ as opposed to a $\mathrm{Pr}^{1/3}$ correlation results in a 20 percent difference in the predictions with the former giving the best agreement.

(*b*) *Channel Blockage Effect.* The blockage ratio $D_{\max}/H$ where $D_{\max}$ is the maximum diameter of the ice and H is the height of the test section reached a maximum value of 0.23. When the results are plotted against blockage ratios no significant trend in the data could be observed.

(*c*) *Free Convection Effect.* The buoyancy effect in mixed laminar convection around the horizontal cylinder can be estimated using the parameter $|\mathrm{Gr}|/\mathrm{Re}^2$ [20]. Using the lowest free stream velocity U_∞ = 1.02 cm/s and the maximum ΔT = 2.7°C in this study, the value for $|(\mathrm{Gr})_{Ds}|\mathrm{Re}^2_{Ds}$ is found to be 0.64 and the effect of free convection on heat transfer result is estimated to be less than one percent. It is noted that the free convection effect becomes significant when the parametric value is greater than 1.92 [20].

(*d*) *The Effect of Longitudinal Vortices.* In the range of Reynolds numbers Re_{Ds} considered in this study, one may expect the appearance of the longitudinal vortices near the forward stagnation point [21]. However, the visual observation shows that no traces of the longitudinal vortices on the ice surface can be detected.

(*e*) *The Effect of Free Stream Turbulence.* The effect of free stream turbulence on stagnation point heat transfer result for the present problem has been studied by Kestin and Wood [22], Smith and Kuethe [23], Brun, et al. [24], Seban [25], Appelqvist [26], Kayala [27] and others. The results from this study and previous results are plotted in Fig. 6 in the form of modified Frössling number $\mathrm{F_r}^* = (Nu)_{Ds}/\mathrm{Re}_{Ds}{}^{1/2}/(\mathrm{Pr})^{0.4}$ versus the parameter involving turbulent intensity $Tu(\mathrm{Re})_{Ds}{}^{1/2}$ for comparison. The modified Frössling number is used in order to compare the present data with the existing data for air. It appears that the empirical correlation of Kestin and Wood [22] and the semiempirical correlation of Smith and Kuethe [23] predict the general qualitative trend for the present data and the present data are consistent with previous data when turbulence is accounted for.

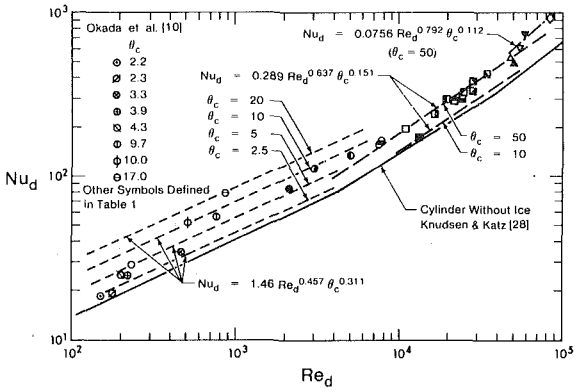

Fig. 7 The influence of the ice layer on the average heat transfer rate to the cylinder

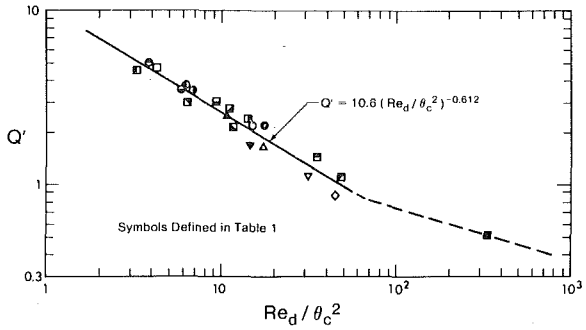

Fig. 8 The nondimensional cooling capacity stored in a steady state ice layer around a cylinder

4.3 Average Heat Transfer. The average Nusselt number Nu_d as a function of Reynolds number is shown in Fig.7 where the results from Okada, et al. [10] for low Reynolds number range are also plotted for reference. The experimental correlation equations for the average Nusselt number Nu_d using the parameters Re_d and θ_c are obtained by using the least square method. The results are:

$$Nu_d = 1.46\ Re_d^{0.457}\theta_c^{0.311},\ 2 < \theta_c < 20,\ Re_d < 5 \times 10^3 \quad (7)$$

$$Nu_d = 0.289\ Re_d^{0.637}\theta_c^{0.151},\ 6 < \theta_c < 76,\ 5 \times 10^3 < Re_d < 5 \times 10^4 \quad (8)$$

$$Nu_d = 0.0756\ Re_d^{0.792}\theta_c^{0.112},\ 40 < \theta_c < 65,\ Re_d > 5 \times 10^4 \quad (9)$$

In the low Reynolds number range $Re_d < 5 \times 10^3$ the standard deviation of the experimental data from equation (7) is ±11 percent. In the range $5 \times 10^3 < Re_d < 5 \times 10^4$, where the influence of the turbulent boundary layer appears, the experimental data deviation from equation (8) is 7 percent. For $Re_d > 5 \times 10^4$, one lacks sufficient experimental data, but the data agree with equation (9) within ±5 percent.

Also shown on Fig. 7 is the standard correlation used for cylinders without ice [28]. It can be seen that this value is reached for $\theta_c = 2$ in equation (7) and $\theta_c \approx 10$ in equation (8). These values of θ_c represent the lower limit of the applicability of these correlations.

4.4 The Amount of Ice Growth around the Cylinder. In applications where cooling capacity is stored by growing ice, for example in some types of water chillers, an important factor to know is the total amount of cooling capacity stored in the ice. The storage, Q, per unit length of pipe is then

$$Q = \gamma_s L\, A_s \quad (10)$$

where A_s is the cross-sectional area of ice. In this equation the sensible heat storage has been neglected as it is usually small compared to the latent heat of fusion. Equation (10) can be rewritten in a dimensionless form as

$$Q' = \frac{4Q}{\pi d^2 \gamma_s L} = \frac{4\,A_s}{\pi d^2} \quad (11)$$

In Fig. 8, Q' has been plotted as a function of the parameter Re_d/θ_c^2. This parameter would be expected to be a precisely valid correlation parameter only if the flow was entirely laminar [7]; however, it appears to be reasonably effective in this case as well. The correlation equation is given by

$$Q' = 11.2\ (Re_d/\theta_c^2)^{-0.612}. \quad (12)$$

In the range $3 < Re_d/\theta_c^2 < 50$ the standard deviation between the experimental data and equation (12) is ±11 percent.

For the values of Re_d/θ_c^2 much greater than 50 the ice layer becomes too thin for accurate measurement; however, the one data point that was taken at a value of 300 suggests that the correlation will underpredict the extent of ice growth for very thin layers. At the other limit that is $Re_d/\theta_c^2 \to 0$ ($Re_d \to 0$ or $\theta_c \to \infty$) one must consider free convection effects. If required the mean ice cylinder diameter can be calculated from equations (11) and (12).

Concluding Remarks

It was found that the local and average heat transfer rates at the ice-water interface of an ice layer grown on a circular cylinder could be determined directly from a photograph showing the shape of the ice layer. The calculation involved first solving for the temperature field in the ice using a point matching method and then extracting the temperature gradients and heat transfer rates at the ice-water interface. The method was simple and convenient to use and thus may find application for other geometries where ice growth is studied.

Using the rather simple technique results were obtained for the variation in local heat transfer over the ice surface in various Reynolds number regimes between $Re_d = 2.3 \times 10^2$ to 8.6×10^4. The local heat transfer results can be used to imply points of flow separation and transition on the ice. From the present results it would appear that a laminar to turbulent boundary layer transition occurs on the ice layer around a cylinder at Reynolds numbers as much as an order of magnitude lower than it would for a circular cylinder without ice. This observation is consistent with previous observations of transition on an ice layer grown on a flat plate and appears to be due to the interaction of the flow and the shape of the ice layer.

Correlations were obtained for the average heat transfer coefficient to a cylinder with ice growth and for the total quantity of cooling capacity that could be stored in the ice.

Acknowledgment

This work was supported by the Natural Sciences and Engineering Research Council of Canada.

References

1 Ashton, G. D., and Kennedy, J. F., "Ripples on Underside of River Ice Covers," *Journal of Hydraulic Division*, ASCE 98, 1972, pp. 1603–1624.

2 Hirata, T., Gilpin, R. R., and Cheng, K. C., "The Steady State Ice Layer Profile on a Constant Temperature Plate in a Forced Convection Flow. II The Transition and Turbulent Regimes," *International Journal of Heat Mass Transfer*, Vol. 22, 1979, pp. 1435–1443.

3 Gilpin, R. R., "The Morphology of Ice Structure in a Pipe at or Near Transition Reynolds Numbers," AIChE Symposium Series No. 189, Vol. 75, 1979, pp. 89–94.

4 Gilpin, R. R., Hirata, T., and Cheng, K. C., "Wave Formation and Heat Transfer at an Ice-Water Interface in the Presence of a Turbulent Flow," *Journal of Fluid Mechanics*, Vol. 99, 1980, pp. 619–640.

5 Zerkle, R. D., and Sunderland, J. E., "The Effect of Liquid Solidification in a Tube upon Laminar-Flow Heat Transfer and Pressure Drop," ASME JOURNAL OF HEAT TRANSFER, Vol. 90, 1968, pp. 183–190.

6 Mulligan, J. C., and Jones, D. D., "Experiments on Heat Transfer and Pressure Drop in a Horizontal Tube with Internal Solidification," *International Journal of Heat Mass Transfer*, Vol. 19, 1976, pp. 213–219.

7 Hirata, T., Gilpin, R. R., Cheng, K. C., and Gates, E. M., "The Steady State Ice Layer Profile on a Constant Temperature Plate in a Forced Convection Flow. I Laminar Regime," *International Journal of Heat Mass Transfer*, Vol.

22, 1979, pp. 1425–1433.

8 Savino, J. M., and Siegel, R., "Experimental and Analytical Study of the Transient Solidification of a Warm Liquid Flowing Over a Chilled Flat Plate," NASA TN D-4015, 1967.

9 Carlson, F. M., "An Investigation of the Solidification of a Flowing Liquid on a Circular Cylinder in Crossflow," Ph.D. Thesis, University of Connecticut, 1975.

10 Okada, M., Katayama, K., Terasaki, K., Akimoto, M., and Mabune, K., "Freezing Around a Cooled Pipe in Crossflow," *Bulletin of the JSME*, Vol. 21, No. 160, 1978, pp. 1514–1520.

11 London, A. L., and Seban, R. A., "Rate of Ice Formation," *Trans. ASME*, Vol. 65, 1943, pp. 771–778.

12 Tien, L. D., and Churchill, S. W., "Freezing Front Motion and Heat Transfer Outside an Infinite, Isothermal Cylinder," *AIChE Journal*, Vol. 11, 1965, pp. 790–793.

13 Shih, Y. P., and Tsay, S. Y., "Analytical Solution for Freezing a Saturated Liquid Inside or Outside Cylinders," *Chemical Engineering Science*, Vol. 26, 1971, pp. 809–816.

14. Cheng, K. C., and Hwang, G. J., "Laminar Forced Convection in Eccentric Annuli," *AIChE Journal*, Vol. 14, 1968, pp. 510–512.

15 Hildebrand, F. B., *Advanced Calculus for Applications*, Prentice-Hall, New York, 1962, p. 435.

16 Giedt, W. H., "Investigation of Variation of Point Unit Heat-Transfer Coefficient Around a Cylinder Normal to an Air Stream," *Trans. ASME*, Vol. 71, 1949, pp. 375–381.

17 Squire, H. B., *Modern Developments in Fluid Dynamics*, Vol. 2, Oxford University Press, 1938, p. 632.

18 Schmidt, E., and Wenner, K., "Heat Transfer Over the Circumference of a Heated Cylinder in Transverse Flow," NACA TM No. 1050, Oct. 1943.

19 Perkins, H. C., and Leppert, G., "Local Heat-Transfer Coefficients on a Uniformly Heated Cylinder," *International Journal of Heat Mass Transfer*, Vol. 7, 1964, pp. 143–158.

20 Mucoglu, A., and Chen, T. S., "Analysis of Combined Forced and Free Convection Across a Horizontal Cylinder," *Canadian Journal of Chemical Engineering*, Vol. 55, 1977, pp. 265–271.

21. Sutera, S. P., Maeder, P. F., and Kestin, J., "On the Sensitivity of Heat Transfer in the Stagnation Point Boundary Layer to Free Stream Vorticity," *Journal of Fluid Mechanics*, Vol. 16, 1963, pp. 497–520.

22 Kestin, J., and Wood, R. T., "The Influence of Turbulence on Mass Transfer from Cylinders," ASME JOURNAL of HEAT TRANSFER, Vol. 93, 1971, pp. 321–327.

23 Smith, M. C., and Kuethe, A. M., "Effects of Turbulence on Laminar Skin Friction and Heat Transfer," *Physics Fluids*, Vol. 9, 1966, pp. 2337–2344.

24 Brun, E. A., Diep, G. B., and Kestin, J., "Sur un Nouveau Types des Tourbillons Longitudinaux dan l'Écoulement autor dún Cylindre. Influence de lÁngle d'Attaque et de la Turbulence du Courant Libre," *Comptes Rendus de l'Academie des Sciences*, Vol. 263, 1966, pp. 742–745.

25 Seban, R. A., "The Influence of Free Stream Turbulence on the Local Heat Transfer from Cylinders," ASME JOURNAL OF HEAT TRANSFER, Vol. 82, 1960, pp. 101–107.

26 Appelqvist, B., "The Influence of Turbulence on the Local Heat Transfer from a Cylinder Normal to an Air Stream, Including Further Development of a Method for Local Heat Transfer Measurements," Doctoral Dissertation, Chalmers University of Technology, Gotherburg, 1965.

27 Kayalar, L., "Experimentelle und Theoretische Untersuchungen über den Einfluss des Turbulenzgrads auf den Wärmeübergang in der Umgebung des Staupunkts eines Kreiszylinders," *Forschung im Ingenieurwesen*, Vol. 35, pp. 157–167, 1969.

28 Knudsen, J. D., and Katz, D. L., *Fluid Dynamics and Heat Transfer*, McGraw-Hill, New York, 1958.

B. Vick
M. N. Özişik
Mem. ASME

Mechanical and Aerospace Engineering Department,
North Carolina State University,
Raleigh, N. C. 27650

Quasi-Steady-State Temperature Distribution in Periodically Contacting Finite Regions

Heat transfer across two surfaces which make and break contact periodically according to a continuous regular cycle is investigated theoretically and exact analytical solutions are developed for the quasi-steady-state temperature distribution for a two-region, one-dimensional, periodically contacting model. The effects of the Biot number, the thermal conductivity and thermal diffusivity of the materials and the duration of contact and break periods on the interface temperature and the temperature distribution within the solids are illustrated with representative temperature charts.

Introduction

The subject of heat transfer across metallic surfaces held in contact permanently has been extensively explored both experimentally and theoretically [1–7]. However, information on heat transfer across solids which are brought into contact and then separated in a continuous cycle is not readily available, despite the importance of this problem in numerous engineering applications. Examples of heat transfer across solids include: heat transfer from the exhaust valve of an internal combustion engine, which travels via seating; the heat transfer between workpiece and die in repetitive hot metal deformation processes; the temperature behavior of the walls of internal combustion engines, and many others.

Very little work is available in the literature on the theoretical investigation of heat transfer across periodically contacting surfaces. An analog computer method of solution was used to analyze the one-dimensional model, first, for perfect thermal contact condition [8] and later for imperfect thermal contact condition [9] during contact. An approximate method of analysis was applied [10] to solve the problem considered in reference [8] under quasi-steady-state conditions. More recently [11], the finite integral transform technique was successfully applied to reduce the analysis of the quasi-steady state heat transfer problem of a single region to the solution of a system of matrix equations for the transform of the temperature.

In the present analysis, we apply the finite integral transform technique to solve the problem for two finite periodically contacting regions, with imperfect thermal contact at the interface.

Mathematical Formulation

We consider two surfaces which are undergoing a continuous, regular cycle of contact and separation with the cycling process continued sufficiently long for the quasi-steady-state conditions to be established. Figure 1 illustrates the geometry and the coordinates for the two parts of the cycle, with the regions open during period-1 and closed during period-2. The surfaces remain separated for a time period of t_1 and come into contact for an amount of time t_2. We assume that: the bars are insulated laterally so that no heat transfer takes place from the sides; the two bars have identical cross-sectional areas; the bars may have different but uniform thermal and physical properties; when the bars are brought together, there may be a thermal contact resistance between the surfaces; when the surfaces are separated by a small distance, a convective heat transfer takes place with an environment at a specified temperature; at the two noncontacting ends of the bars, heat transfer is by convection; and the quasi-steady-state condition is established.

Our interest in this problem is in the determination of the temperature distribution through the bars and the temperature of the contacting surfaces as a function of time during both the open and the closed cycles.

The mathematical formulation of this problem given below includes, for generality, heat generation within the bars. The governing differential equations and the boundary conditions for the open and closed periods are now summarized.

Equations for Period-1, $0 \le t \le t_1$, (open)

$$\frac{\partial^2 T_i^{(1)}}{\partial x^2} + \frac{1}{k_i} g_i^{(1)}(x,t) = \frac{1}{\alpha_i} \frac{\partial T_i^{(1)}(x,t)}{\partial t}, \quad \text{in } L_{i-1} < x < L_i \tag{1a}$$

$$-k_i \frac{\partial T_i^{(1)}(L_{i-1},t)}{\partial x} + a_i^{(1)} T_i^{(1)}(L_{i-1},t) = u_i^{(1)}(t) \tag{1b}$$

$$k_i \frac{\partial T_i^{(1)}(L_i,t)}{\partial x} + b_i^{(1)} T_i^{(1)}(L_i,t) = v_i^{(1)}(t) \tag{1c}$$

$$T_i^{(1)}(x,0) = F_i^{(1)}(x) \tag{1d}$$

where the subscripts $i = 1$ and 2 refer to the first and second region, and the superscript (1) refers to period-1.

Equations for Period-2, $0 \le t \le t_2$, (closed)

$$\frac{\partial^2 T_i^{(2)}}{\partial x^2} + \frac{1}{k_i} g_i^{(2)}(x,t) = \frac{1}{\alpha_i} \frac{\partial T_i^{(2)}(x,t)}{\partial t}, \quad \text{in } L_{i-1} < x < L_i \tag{2a}$$

$$-k_1 \frac{\partial T_1^{(2)}(0,t)}{\partial x} + a_1^{(2)} T_1^{(2)}(0,t) = u_1^{(2)}(t) \tag{2b}$$

$$-k_i \frac{\partial T_i^{(2)}(L_1,t)}{\partial x} = h\left[T_1^{(2)}(L_1,t) - T_2^{(2)}(L_1,t)\right] \tag{2c}$$

$$k_2 \frac{\partial T_2^{(2)}(L_2,t)}{\partial x} + b_2^{(2)} T_2^{(2)}(L_2,t) = v_2^{(2)}(t) \tag{2d}$$

$$T_i^{(2)}(x,0) = F_i^{(2)}(x) \tag{2e}$$

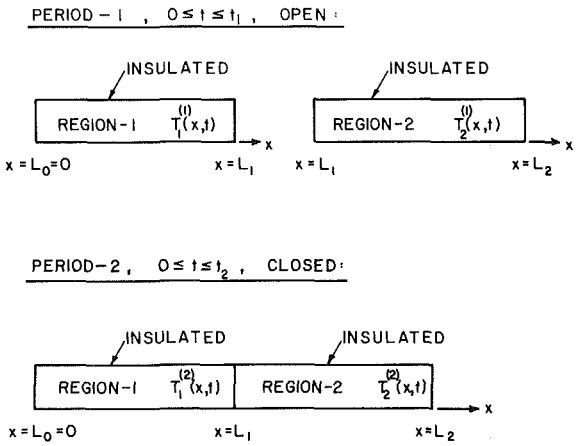

Fig. 1 Geometry and coordinates for the open and closed cycles

Contributed by the Heat Transfer Division for publication in The JOURNAL OF HEAT TRANSFER. Manuscript received by The Heat Transfer Division January 30, 1981.

where the subscripts $i = 1$ and 2 refer to the first and second regions and the superscript (2) refers to period-2.

For the quasi-steady-state condition to exist, the temperature distribution within the rods at the end of one period must be equal to the initial temperature distribution in the rods at the beginning of the next period. Therefore, the functions $F_i^{(1)}(x)$ and $F_i^{(2)}(x)$ are related to the temperature distribution in the rods at the end of the periods by the relation

$$T_j^{(i)}(x, t_i) = F_j^{(3-i)}(x), \text{ in } L_{j-1} < x < L_j \tag{3}$$

where $i, j = 1$ or 2.

If the initial condition functions, $F_j^{(3-i)}(x)$, for $i, j = 1$ or 2, are known at the beginning of each cycle, the temperature distributions $T_i^{(1)}(x, t)$ and $T_i^{(2)}(x, t)$, for $i = 1$ or 2, can subsequently be calculated from the solution of the system of equations (1) and (2). Therefore, in the following analysis we are concerned with the development of relations needed for the solution of these initial condition functions or their integral transforms.

Analysis

The finite integral transform technique described in the references [11–13] is now applied in order to transform the problem defined by equations (1–3) into a system of matrix equations for the determination of the integral transforms $\overline{F}_{\text{in}}^{(1)}$ and $\overline{F}_n^{(2)}$ of the initial condition functions $F_j^{(3-i)}(x)$. The basic steps in the analysis are as follows: the systems (1) and (2) are formally solved, by the application of the finite integral transform, and the quasi-steady-state condition (3) is applied in order to express the $F_j^{(3-i)}(x)$ functions in terms of the transforms $\overline{F}_{\text{in}}^{(1)}$ and $\overline{F}_n^{(2)}$. When the integral transforms of the resulting equations are taken, matrix equations are obtained for the determination of the functions $\overline{F}_{\text{in}}^{(1)}$ and $\overline{F}_n^{(2)}$. Once these transforms are known, the temperature distribution in the medium is readily determined from the solution of the equations (1) and (2) which were obtained by the integral transform technique. We now present this analysis in detail.

Solution for Period-1. The temperature distributions $T_1^{(1)}(x, t)$ and $T_2^{(1)}(x, t)$, defined by equations (1) for period-1 are uncoupled, hence the temperatures can be solved for each region independently. The eigenvalue problems appropriate for the solution of the systems defined by equations (1) are taken as

$$\frac{d^2X_{\text{in}}^{(1)}(x)}{dx^2} + \frac{\beta_{\text{in}}^2}{\alpha_i} X_{\text{in}}^{(1)}(x) = 0, \quad \text{in } L_{i-1} < x < L_i \tag{4a}$$

$$-k_i \frac{dX_{\text{in}}^{(1)}(L_{i-1})}{dx} + a_i^{(1)} X_{\text{in}}^{(1)}(L_{i-1}) = 0 \tag{4b}$$

$$k_i \frac{dX_{\text{in}}^{(1)}(L_i)}{dx} + b_i^{(1)} X_{\text{in}}^{(1)}(L_i) = 0 \tag{4c}$$

for $i = 1, 2$.

The eigenfunctions $X_{\text{in}}^{(1)}(x)$, $n = 1, 2, 3, \ldots$, satisfy the following orthogonality relation

$$\frac{k_i}{\alpha_i} \int_{L_{i-1}}^{L_i} X_{\text{im}}^{(1)}(x) X_{\text{in}}^{(1)}(x) dx = \begin{cases} 0 & \text{for } m \neq n \\ N(\beta_{\text{in}}) & \text{for } m = n \end{cases} \tag{5a}$$

where

$$N(\beta_{\text{in}}) = \frac{k_i}{\alpha_i} \int_{L_{i-1}}^{L_i} [X_{\text{in}}^{(1)}(x)]^2 dx \tag{5b}$$

The finite integral transform pair for the function $T_i^{(1)}(x, t)$ is defined as

$$\text{Transform:} \quad \overline{T}_{\text{in}}^{(1)}(t) = \frac{k_i}{\alpha_i} \int_{L_{i-1}}^{L_i} T_i^{(1)}(x, t) X_{\text{in}}^{(1)}(x) dx \tag{6a}$$

$$\text{Inversion:} \quad T_i^{(1)}(x, t) = \sum_{n=1}^{\infty} \frac{1}{N(\beta_{\text{in}})} \overline{T}_{\text{in}}^{(1)}(t) X_{\text{in}}^{(1)}(x) \tag{6b}$$

$$\text{in } L_{i-1} < x < L_i, \quad \text{for } i = 1, 2$$

We now take the integral transform of the system defined by equations (1) by the application of the transform (6a). That is, we operate on both sides of equation (1a) with the operator $k_i \int_{L_{i-1}}^{L_i} X_{\text{in}}^{(1)}(x) dx$, and utilize the boundary conditions (1b,c) and the eigenvalue problem (4). After a lengthy, but straightforward series of manipulations, the partial differential equation (1a) is transformed into an ordinary differential equation for the integral transform, $\overline{T}_{\text{in}}^{(1)}(t)$, of the function, $T_i^{(1)}(x, t)$. The initial condition needed for the solution of this ordinary differential equation is obtained by taking the integral transform of the initial condition (1d).The ordinary differential equation for $\overline{T}_{\text{in}}^{(1)}(t)$ is solved subject to the tansformed initial condition $\overline{F}_{\text{in}}^{(1)}$ and the resulting transform is inverted by the inversion formula (6b) to obtain the solution for the temperature functions, $T_i^{(1)}(x, t)$, for period-1, in the form

$$T_i^{(1)}(x, t) = \sum_{n=1}^{\infty} \frac{1}{N(\beta_{\text{in}})} e^{-\beta^2_{in} t} X_{\text{in}}^{(1)}(x) \cdot \left[\overline{F}_{\text{in}}^{(1)} + \int_0^t A_{\text{in}}^{(1)}(t') e^{\beta^2_{in} t'} dt' \right], \tag{7}$$

$$\text{in } L_{i-1} \leq x \leq L_i, \, 0 \leq t \leq t_1$$

where

$$N(\beta_{\text{in}}) = \frac{k_i}{\alpha_i} \int_{L_{i-1}}^{L_i} [X_{\text{in}}^{(1)}(x)]^2 dx \tag{8a}$$

$$\overline{F}_{\text{in}}^{(1)} = \frac{k_i}{\alpha_i} \int_{L_{i-1}}^{L_i} F_i^{(1)}(x) X_{\text{in}}^{(1)}(x) dx \tag{8b}$$

$$A_{\text{in}}^{(1)}(t) = u_i^{(1)}(t) X_{\text{in}}^{(1)}(L_{i-1}) + v_i^{(1)}(t) X_{\text{in}}^{(1)}(L_i) + \overline{g}_{\text{in}}^{(1)}(t) \tag{8c}$$

Nomenclature

$a_j^{(i)}$ = heat transfer coefficient at left boundary of region-j for period-i
A = ratio of thermal diffusivities
$A_{\text{in}}^{(1)}(t)$ = boundary condition and generation contributions in region-i for period-1
$A_n^{(2)}(t)$ = boundary condition and generation contributions for period-2
$b_j^{(i)}$ = heat transfer coefficient at right boundary of region-j for period-i
Bi = Biot number
$f_j^{(i)}(\eta)$ = dimensionless initial temperature in region-j, period-i
$\overline{F}_{\text{in}}^{(1)} = n^{\text{th}}$ transform of initial temperature in region-i, period-1
$\overline{F}_n^{(2)} = n^{\text{th}}$ transform of initial temperatures for period-2
$g_j^{(i)}(x, t)$ = heat generation function in region-j, period-i
h = contact conductance at contacting surfaces
k_i = thermal conductivity in region-i
K = ratio of thermal conductivities
L_i =lengths of the regions
L = ratio of lengths of regions
$N(\beta_{\text{in}}) = n^{\text{th}}$ normalization integral in region-i for period-1
$N(\lambda_n) = n^{\text{th}}$ normalization integral for period-2
t = time variable
t_1, t_2 = duration of the open and closed periods
$T_j^{(i)}(x, t)$ = temperature of region-j, period-i
$\overline{T}_{\text{in}}^{(1)}(t) = n^{\text{th}}$ transform of temperature in region-i for period-1
$\overline{T}_n^{(2)}(t) = n^{\text{th}}$ transform of temperatures for period-2
$u_j^{(i)}(t)$ = nonhomogenius portion of boundary condition at left end of region-j in period-i
$v_j^{(i)}(t)$ = nonhomogenius portion of boundary condition at right end of region-j in period-i
x = axial coordinate
$X_{jn}^{(i)}(x) = n^{\text{th}}$ eigenfunction for region-j, period-i
α_i = thermal diffusivity of region-i
$\beta_{\text{in}} = n^{\text{th}}$ eigenvalue for region-i, period-1
$\theta_j^{(i)}(\eta, \tau)$ = dimensionless temperature of region-j, period-i
η = dimensionless axial coordinate
$\lambda_n = n^{\text{th}}$ eigenvalue for period-2
τ = dimensionless time variable
τ_1, τ_2 = dimensionless durations of open and closed cycle

$$\bar{g}_{in}^{(1)}(t) = \int_{L_{i-1}}^{L_i} g_i^{(1)}(x,t) X_{in}^{(1)}(x)\,dx \tag{8d}$$

and $i = 1$ or 2.

Solution for Period-2. Temperatures $T_1^{(2)}(x,t)$ and $T_2^{(2)}(x,t)$, defined by equations (2) for period-2, are coupled through the boundary conditions (2c). Therefore, the appropriate coupled eigenvalue problem for the solution of the system (2) is taken as [13]

$$\frac{d^2X_{in}^{(2)}(x)}{dx^2} + \frac{\lambda_n^2}{\alpha_i} X_{in}^{(2)}(x) = 0, \quad \text{in } L_{i-1} < x < L_i \tag{9a}$$

$$-k_1 \frac{dX_{1n}^{(2)}(0)}{dx} + a_1^{(2)} X_{1n}^{(2)}(0) = 0 \tag{9b}$$

$$-k_i \frac{dX_{in}^{(2)}(L_1)}{dx} = h\,[X_{1n}^{(2)}(L_1) - X_{2n}^{(2)}(L_1)] \tag{9c}$$

$$k_2 \frac{dX_{2n}^{(2)}(L_2)}{dx} + b_2^{(2)} X_{2n}^{(2)}(L_2) = 0 \tag{9d}$$

$$\text{for } i = 1, 2.$$

The eigenfunctions $X_{1n}^{(2)}(x)$ and $X_{2n}^{(2)}(x)$ satisfy the following coupled orthogonality relation

$$\sum_{i=1}^{2} \frac{k_i}{\alpha_i} \int_{L_{i-1}}^{L_i} X_{in}^{(2)}(x) X_{im}^{(2)}(x)\,dx = \begin{cases} 0 & \text{for } m \neq n \\ N(\lambda_n) & \text{for } m = n \end{cases} \tag{10a}$$

where the normalization integral $N(\lambda_n)$ is given by

$$N(\lambda_n) = \sum_{i=1}^{2} \frac{k_i}{\alpha_i} \int_{L_{i-1}}^{L_i} [X_{in}^{(2)}(x)]^2\,dx \tag{10b}$$

The finite integral transform pair for the function $T_i^{(2)}(x,t)$ is defined as [13]

$$\text{Transform:} \quad \bar{T}_n^{(2)}(t) = \sum_{i=1}^{2} \frac{k_i}{\alpha_i} \int_{L_{i-1}}^{L_i} T_i^{(2)}(x,t) X_{in}^{(2)}(x)\,dx \tag{11a}$$

$$\text{Inversion:} \quad T_i^{(2)}(x,t) = \sum_{n=1}^{\infty} \frac{1}{N(\lambda_n)} \bar{T}_n^{(2)}(t) X_{in}^{(2)}(x) \tag{11b}$$

$$\text{in } L_{i-1} < x < L_i, \text{ for } i = 1, 2$$

We now take the integral transform of the system defined by equations (2) by the application of the transform (11a). That is, we operate on both sides of equation (2a) with the operator $k_i \int_{L_{i-1}}^{L_i} X_{in}^{(2)}(x)\,dx$, sum up the results for $i = 1$ and 2, integrate by parts twice, make use of the definition of the integral transform (11a),the boundary conditions (2b, c, d) and the eigenvalue problem (9). Finally, the partial differential equation (2a) is transformed to an ordinary differential equation for the integral transform $\bar{T}_n^{(2)}(t)$ of the functions $T_1^{(2)}(x, t)$ and $T_2^{(2)}(x,t)$. The initial condition needed for the solution of this ordinary differential equation is obtained by taking the integral transform of the initial condition (2e). This ordinary differential equation for $\bar{T}_n^{(2)}(t)$ is solved subject to the transformed initial condition, $\bar{F}_n^{(2)}$, and the resulting transform is inverted by the inversion formula (11b) to yield the solution for the temperatures, $T_i^{(2)}(x,t)$, for period-2 in the form

$$T_i^{(2)}(x,t) = \sum_{n=1}^{\infty} \frac{1}{N(\lambda_n)} e^{-\lambda_n^2 t} X_{in}^{(2)}(x) \cdot \cdot \left[\bar{F}_n^{(2)} + \int_0^t A_n^{(2)}(t') e^{\lambda_n^2 t'} dt'\right] \tag{12}$$

$$\text{in } L_{i-1} \le x \le L_i, \; 0 \le t \le t_2$$

where

$$N(\lambda_n) = \sum_{i=1}^{2} \frac{k_i}{\alpha_i} \int_{L_{i-1}}^{L_i} [X_{in}^{(2)}(x)]^2\,dx \tag{13a}$$

$$\bar{F}_n^{(2)} = \sum_{i=1}^{2} \frac{k_i}{\alpha_i} \int_{L_{i-1}}^{L_i} F_i^{(2)}(x) X_{in}^{(2)}(x)\,dx \tag{13b}$$

$$A_n^{(2)}(t) = u_1^{(2)}(t) X_{1n}^{(2)}(0) + v_2^{(2)}(t) X_{2n}^{(2)}(L_2) + \bar{g}_n^{(2)}(t) \tag{13c}$$

$$\bar{g}_n^{(2)}(t) = \sum_{i=1}^{2} \int_{L_{i-1}}^{L_i} g_i^{(2)}(x,t) X_{in}^{(2)}(x)\,dx \tag{13d}$$

and $i = 1$ or 2.

Equations for $\bar{F}_{in}^{(1)}$ and $\bar{F}_n^{(2)}$. In order to obtain the matrix equations for the determination of the functions $\bar{F}_{in}^{(1)}$ and $\bar{F}_n^{(2)}$, the quasi-steady-state condition (3) is applied to the solutions (7) and (12) and we respectively obtain

$$F_i^{(2)}(x) = \sum_{n=1}^{\infty} \frac{1}{N(\beta_{in})} e^{-\beta_{in}^2 t_1} X_{in}^{(1)}(x) \cdot \cdot \left[\bar{F}_{in}^{(1)} + \int_0^{t_1} A_{in}^{(1)}(t') e^{\beta_{in}^2 t'} dt'\right] \tag{14a}$$

$$F_i^{(1)}(x) = \sum_{n=1}^{\infty} \frac{1}{N(\lambda_n)} e^{-\lambda_n^2 t_2} X_{in}^{(2)}(x) \cdot \cdot \left[\bar{F}_n^{(2)} + \int_0^{t_2} A_n^{(2)}(t') e^{\lambda_n^2 t'} dt'\right] \tag{14b}$$

for $i = 1, 2$.

We now operate on both sides of equation (14a) with the operator

$$\frac{k_i}{\alpha_i} \int_{L_{i-1}}^{L_i} X_{im}^{(2)}(x)\,dx$$

add the results for $i = 1$ and 2, and utilize the definition of the integral transform (13b) to obtain

$$\bar{F}_m^{(2)} = \sum_{i=1}^{2} \frac{k_i}{\alpha_i} \sum_{n=1}^{\infty} \frac{1}{N(\beta_{in})} e^{-\beta_{in}^2 t_1} \times \left[\int_{L_{i-1}}^{L_i} X_{im}^{(2)}(x) X_{in}^{(1)}(x)\,dx\right] \cdot \cdot \left[\bar{F}_{in}^{(1)} + \int_0^{t_1} A_{in}^{(1)}(t') e^{\beta_{in}^2 t'} dt'\right] \tag{15a}$$

for $m = 1, 2, 3, \ldots$.

Similarly, we operate on both sides of equation (14b) with the operator

$$\frac{k_i}{\alpha_i} \int_{L_{i-1}}^{L_i} X_{im}^{(1)}(x)\,dx$$

and utilize the definition of the integral transform (8b) to obtain

$$\bar{F}_{im}^{(1)} = \frac{k_i}{\alpha_i} \sum_{n=1}^{\infty} \frac{1}{N(\lambda_n)} e^{-\lambda_n^2 t_2} \times \left[\int_{L_{i-1}}^{L_i} X_{im}^{(1)}(x) X_{in}^{(2)}(x)\,dx\right] \cdot \cdot \left[\bar{F}_n^{(2)} + \int_0^{t_2} A_n^{(2)}(t') e^{\lambda_n^2 t'} dt'\right] \tag{15b}$$

for $i = 1, 2$, and $m = 1, 2, 3, \ldots$.

Equations (15), for $m = 1, 2, 3, \ldots$, can be written in the matrix form as

$$\mathbf{F} = \sum_{i=1}^{2} (\mathbf{D}_i^{(1)} \mathbf{F}_i + \mathbf{C}_i^{(1)}) \tag{16a}$$

$$\mathbf{F}_i = \mathbf{D}_i^{(2)} \mathbf{F} + \mathbf{C}_i^{(2)} \tag{16b}$$

for $i = 1, 2$, and various matarices are defined below.

$\mathbf{F}$, $\mathbf{F}_i$, $\mathbf{C}_i^{(1)}$ and $\mathbf{C}_i^{(2)}$ are column vectors given by

$$\mathbf{F} = (\bar{F}_m^{(2)}), \; \mathbf{F}_i = (\bar{F}_{im}^{(1)}) \tag{17a,b}$$

$$\mathbf{C}_i^{(1)} = \left(\frac{k_i}{\alpha_i} \sum_{n=1}^{\infty} \frac{1}{N(\beta_{in})} e^{-\beta_{in}^2 t_1} \left[\int_{L_{i-1}}^{L_i} X_{im}(2) X_{in}^{(1)} dx\right] \cdot \cdot \left[\int_0^{t_1} A_{in}^{(1)}(t') e^{\beta_{in}^2 t'} dt'\right]\right) \tag{17c}$$

$$\mathbf{C}_i^{(2)} = \left(\frac{k_i}{\alpha_i} \sum_{n=1}^{\infty} \frac{1}{N(\lambda_n)} e^{-\lambda_n^2 t_2} \left[\int_{L_{i-1}}^{L_i} X_{im}^{(1)} X_{in}^{(2)} dx\right] \cdot \cdot \left[\int_0^{t_2} A_n^{(2)}(t') e^{\lambda_n^2 t'} dt'\right]\right) \tag{17d}$$

and $\mathbf{D}_i^{(1)}$ and $\mathbf{D}_i^{(2)}$ are square matrices defined by

$$\mathbf{D}_i^{(1)} = \left(\frac{k_i}{\alpha_i}\frac{1}{N(\beta_{in})} e^{-\beta_{in}^2 t_1}\left[\int_{L_{i-1}}^{L_i} X_{im}^{(2)} X_{in}^{(1)} dx\right]\right) \quad (17e)$$

$$\mathbf{D}_i^{(2)} = \left(\frac{k_i}{\alpha_i}\frac{1}{N(\lambda_n)} e^{-\lambda_n^2 t_2}\left[\int_{L_{i-1}}^{L_i} X_{im}^{(1)} X_{in}^{(2)} dx\right]\right) \quad (17f)$$

In the above equations, m indicates the row and n indicates the column.

Equations (16a, b) can be solved simultaneously to give

$$\mathbf{F} = \left(\mathbf{I} - \sum_{i=1}^{2} \mathbf{D}_i^{(1)}\mathbf{D}_i^{(2)}\right)^{-1} \sum_{i=1}^{2} (\mathbf{D}_i^{(1)}\mathbf{C}_i^{(2)} + \mathbf{C}_i^{(1)}) \quad (18a)$$

$$\mathbf{F}_i = D_i^{(2)}\left(\mathbf{I} - \sum_{j=1}^{2} \mathbf{D}_j^{(1)}\mathbf{D}_j^{(2)}\right)^{-1} \sum_{j=1}^{2} (\mathbf{D}_j^{(1)}\mathbf{C}_j^{(2)} + \mathbf{C}_j^{(1)}) + \mathbf{C}_i^{(2)} \quad (18b)$$

where I denotes the identity matrix.

Equations (18) are an infinite set of equations for the transforms of the initial temperature distributions, $\overline{F}_{in}^{(1)}$ and $\overline{F}_{n}^{(2)}$. However, this infinite set of equations must be truncated to a finite number of terms in order to solve for a specific case and the number of terms needed depends on the rate of convergence and the accuracy desired.

The solution of the problem is now formally complete, because knowing $\overline{F}_{in}^{(1)}$ and $\overline{F}_{n}^{(2)}$, the temperature distributions $T_i^{(1)}(x, t)$ and $T_i^{(2)}(x, t)$, for the open and closed periods, can be evaluated from equations (7) and (12), respectively.

Results and Discussion

A Special Case. We first examine the special case of two identical regions (i.e., $k_1 = k_2 \equiv k$, $\alpha_1 = \alpha_2 = \alpha$, $L_1 = L_2 - L_1 \equiv L$) with no heat generation. The boundary conditions are taken such that the surface at $x = 0$ of the region-1 is kept at a constant temperature, T_0, while the surface at $x = 2L$ of the region-2 is kept at a constant temperature, $-T_0$. The contacting surfaces at $x = L$ are assumed to be insulated (i.e., negligible heat transfer) when they are separated and have a contact conductance, h, when they are in contact. For this special case, various dimensionless quantities are defined as

$$\left.\begin{aligned} &\theta_j^{(i)}(\eta, \tau) = \frac{T_j^{(i)}(x, t)}{T_0}, f_j^{(i)}(\eta) = \frac{F_j^{(i)}(x)}{T_0} \text{ for } i, j = 1, 2. \\ &\eta = \frac{x}{L}, \tau = \frac{\alpha t}{L^2}, \\ &\tau_i = \frac{\alpha t_i}{L^2} \text{ for } i = 1 \text{ or } 2, \quad \text{Bi} = \frac{hL}{k}. \end{aligned}\right\} \quad (19)$$

This special case corresponds to the one-region problem studied in reference [1]. In order to show that our symmetric special case can indeed produce results for the one-region problem, we calculated the dimensionless temperature $f_1^{(2)}$ and $f_1^{(2)}$ at the beginning of the open and closed cycles. The results listed in Table 1 for Bi = 10 and $\tau_1 = \tau_2 = 0.078125$ correspond exactly to those given in reference [11] for the one-region problem.

Figure 2 shows the effects of the variation of the cycle time, $\tau_1 = \tau_2$, when the duration of the open and closed periods are equal. In the region-1, considered in this figure, the open period corresponds to heating and the closed period to heat removal through the contacting surface. As a result, the temperature at the end of the open cycle, which corresponds to temperature at the beginning of the closed cycle increases with increasing cycle time. Similarly, the temperature distribution at the end of the closed cycle, which corresponds to the temperature distribution at the beginning of the open cycle is lower with increasing cycle time. As a result, the difference between temperatures at the begining of the open and closed periods increases with increasing cycle time as illustrated in this figure.

Figure 3 illustrates the effects of the Biot number at the contacting surfaces for a given cycle time, $\tau_1 = \tau_2 = 0.1$. For the region-1, increasing the Biot number implies more heat loss through the contacting surface during the closed period as a result the temperature is lower at the beginning of the open period with increasing Biot number. The low initial temperature at the beginning of the open period results in a lower initial temperature at the beginning of the closed cycle.

The General Case. We now examine the more general case in which the regions have different lengths and different thermal properties. We assume that the boundary surface at $x = 0$ of region-1 is kept at a constant temperature, T_0, while the boundary surface at $x = L_2$ of the region-2 is kept at zero temperature. The contacting surfaces are assumed to be insulated (i.e., negligible heat loss) when they are separated and have a contact conductance, h, when they are in contact. We nondimensionalize all quantities with respect to the region-1, hence introduce the following dimensionless quantities

Table 1 Dimensionless temperature distributions $f_1^{(1)}$ and $f_1^{(2)}$ at the beginning of open and closed cycles in Region-1. (Bi = 10, $\tau_1 = \tau_2 = 0.078125$)

η	$f_1^{(1)}$	$f_1^{(2)}$
0.0	1.00000	1.00000
0.1	0.92022	0.91664
0.2	0.83987	0.83378
0.3	0.75816	0.75218
0.4	0.67401	0.67313
0.5	0.58605	0.59859
0.6	0.49286	0.53118
0.7	0.39335	0.47398
0.8	0.28716	0.43018
0.9	0.17502	0.40260
1.0	0.05875	0.39317

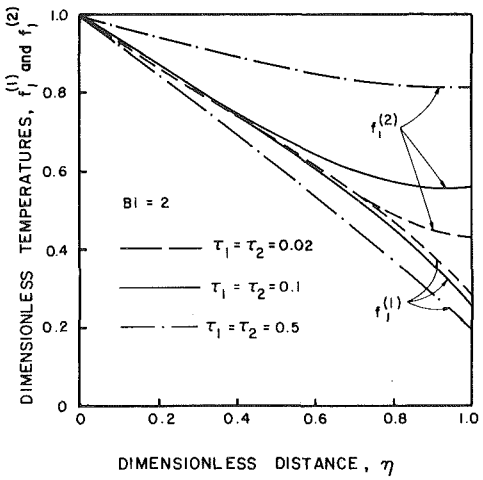

Fig. 2 Effects of the duration of contact and separation time on temperature distributions for the case of two identical regions

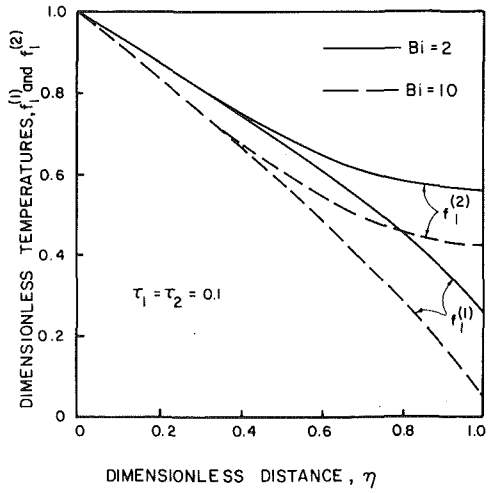

Fig. 3 Effects of Biot number on temperature distributions for the case of two identical regions

$$\left.\begin{aligned} \theta_j^{(i)}(\eta,\tau) = \frac{T_j^{(i)}(x,t)}{T_0}, f_j^{(i)}(\eta) = \frac{F_j^{(i)}(x)}{T_0}, (i,j=1,2) \\ \eta = \frac{x}{L_1}, \tau = \frac{\alpha_1 t}{L_1^2} \end{aligned}\right\} \quad (20)$$

For this more general case, the solutions will depend on the following six dimensionless parameters

$$\left.\begin{aligned} \mathrm{Bi} = \frac{hL_1}{k_1}, \tau_1 = \frac{\alpha_1 t_1}{L_1^2}, \tau_2 = \frac{\alpha_1 t_2}{L_1^2}, \\ A = \frac{\alpha_2}{\alpha_1}, K = \frac{k_2}{k_1}, L = \frac{L_2}{L_1} \end{aligned}\right\} \quad (21)$$

Figures 4–6 illustrate the effects of the variation of the thermal conductivity and the thermal diffusivity of the region-2, on the temperaure distributions at the beginning of the open and closed periods.

Figure 4 shows that increasing the thermal conductivity of the region-2 lowers the temperatures in both regions for the open and closed periods. The reason for this is as follows. Raising the thermal conductivity of region-2 reduces the overall thermal resistance for the system, hence increases the heat flow rate during the closed period. If region-1 should accommodate this increased heat flow rate with the same thermal resistance, the temperature gradient should increase or the temperature distribution should appear lower in region-1 during the closed period. As a result, the temperature distribution

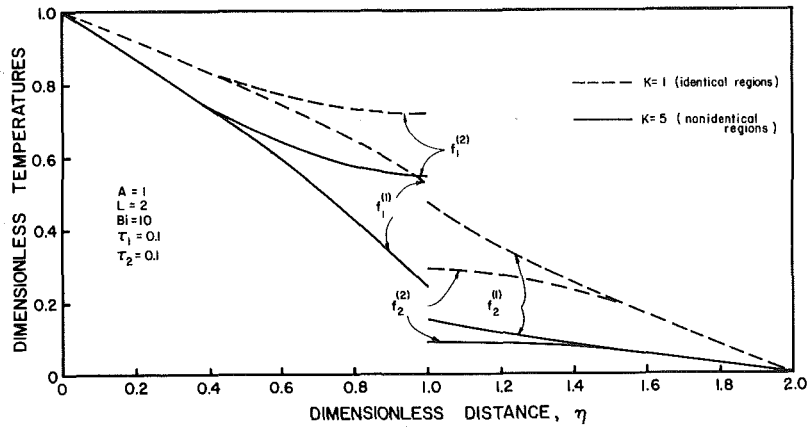

Fig. 4 Comparison of temperatures for identical and nonidentical regions (effects of thermal conductivity ratio *K*)

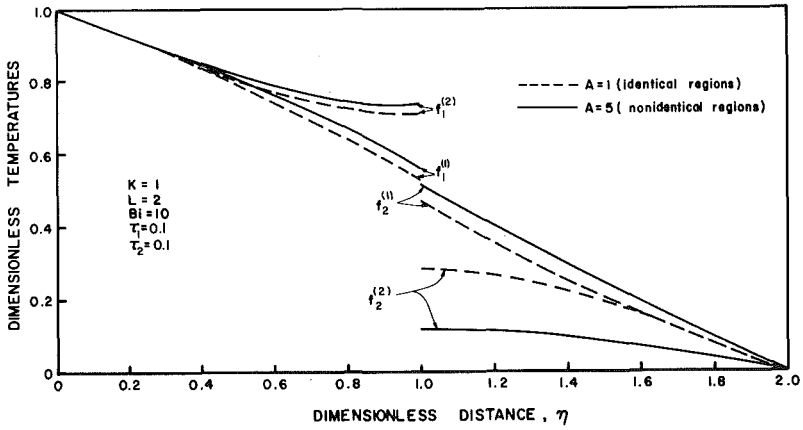

Fig. 5 Comparison of temperatures for identical and nonidentical regions (effects of thermal diffusivity ratio *A*)

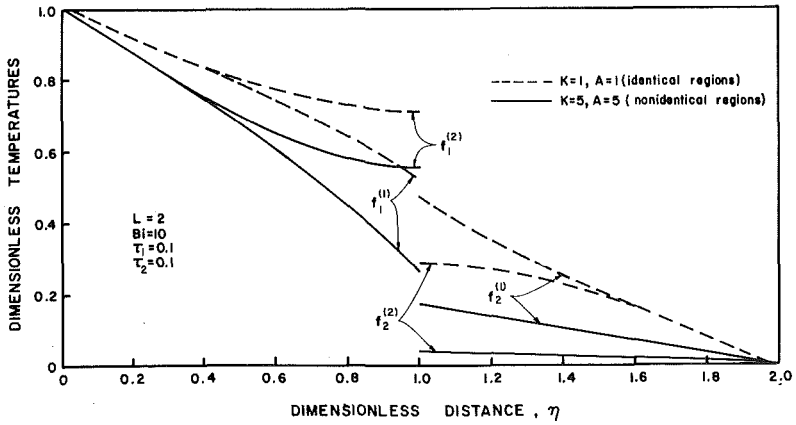

Fig. 6 Comparison of temperatures for identical and nonidentical regions (combined effects of *K* and *A*)

in region-1 is lower at the beginning of both open and closed periods. The temperatures in region-2 are lower, because the cooling rate is faster during the open period due to lower thermal resistance.

Figure 5 shows that increasing the thermal diffusivity of region-2, increases the temperatures in the region-1 for both the open and the closed periods; but in the region-2, the temperature is higher for the open period and lower for the closed period. This can be explained as follows. The larger the thermal diffusivity of a medium, the faster is its response to temperature changes. When the region-2 is heated during the closed period, its temperature will rise more rapidly when the thermal diffusivity is higher, and the temperature at the beginning of the open cycle will be higher. During the open period, the region-2 is subjected to cooling, hence it is cooled more rapidly when the thermal diffusivity is higher, and the temperature at the beginning of the closed period will be lower. The temperature of region-1 is influenced by the higher temperatue of the region-2 during the closed period. As a result, the temperature of the region-1 is higher at the beginning of both open and closed periods.

Finally, Fig. 6 shows the combined effects of increasing the thermal conductivity and thermal diffusivity of the region-2 (i.e., $K = 5$, $A = 5$). For this particular case the effects of thermal conductivity appear to be dominant, since the behavior of the curves is similar to that shown in Fig. 4.

Acknowledgment

This work was supported in part through a grant by the National Science Foundation.

References

1 Moore, C. J., Jr., and Blum, H. A., "Effects of Transient Pressure Environments on Heat Transfer in One-Dimensional Composite Slabs with Contact Resistance," *AIAA Progress in Astronautics and Aeronautics*, Vol. 21, 1968, pp. 621–636.

2 Atkins, H., "Bibliography on Thermal Metallic Contact Conductance," NASA Technical Memorandum, TMX-53227, Apr. 1965.

3 Wong, H. Y., "A Survey of Thermal Conductance of Metallic Contacts," Ministry of Technology, Aeronautical Research Council Current Papers, CP No. 973, HMSO, 1968.

4 Moore, C. J., Jr., Atkins, H., and Blum, H. A., "Subject Classification Bibliography for Thermal Contact Conductance Studies," ASME Paper No. 68-WA/HT-18.

5 Thomas, T. R., and Probert, S. D., "Correlations for Thermal Contact Conductance in Vacuo," ASME JOURNAL HEAT TRANSFER, Vol. 94, 1972, pp. 276–280.

6 Fletcher, L. S., "Thermal Contact Resistance of Metallic Interfaces," AIAA Paper No. 70-852, 1970.

7 Veziroğlu, T. N., Yüncü, H., and Kakac, S., "Analysis of Thermal Conductance of Contacts with Interstitial Plats," *International Journal of Heat Mass Transfer*, Vol. 19, 1976, pp. 959–965.

8 Howard, J. R., and Sutton, A. E., "An Analogue Study of Heat Transfer Through Per Periodically Contacting Surfaces," *International Journal Heat Mass Transfer* Vol. 13, 1970, pp. 173–183.

9 Howard, J. R., and Sutton, A. E., "The Effect of Thermal Contact Resistance on Heat Transfer Between Periodically Contacting Surfaces," ASME JOURNAL OF HEAT TRANSFER, Vol. 95, 1973, pp. 411–412.

10 Reed, J. R., and Mullineux, G., "Quasi-Steady State Temperature Distribution in Finite Regions with Periodically-Varying Boundary Conditions," *International Journal Heat Mass Transfer*, Vol. 16, 1973, pp. 2007–2012.

11 Mikhailov, M. D., "Quasi-Steady State Temperature Distribution in Finite Regions with Periodically-Varying Boundary Conditions," *International Journal Heat Mass Transfer*, Vol. 17, 1974, pp. 1475–1478.

12 Yener, Y. and Özişik, M. N., "On the Solution of Heat Conduction in Multi-Region Finite Media with Time Dependent Heat Transfer Coefficient," *Proceedings of the 5th International Heat Transfer Conference, Cu 2.5*, Tokyo, 1974, pp. 188–192.

13 Özişik, M. N., *Heat Conduction*, John Wiley and Sons, New York, 1980.

M. Imber

Professor of Mechanical Engineering, Polytechnic Institute of New York, Brooklyn, New York 11201, Mem. ASME

Thermally Symmetric Nonlinear Heat Transfer in Solids

Material thermal properties are temperature dependent, and this effect cannot be disregarded at elevated design temperatures. Based upon the principle of equivalent linearization, analytical solutions are developed for thermally symmetric planar solids. The solution method is, in turn, extended to a composite wall whose individual thermal conductivities are also temperature dependent. As a demonstration of the method's accuracy several numerical examples are shown.

Introduction

For elevated operating temperatures the usual assumption of constant thermal properties must be abandoned, since properties of materials vary with temperature, and the local thermal conductivity, $\lambda(T)$ for example, can differ a great deal from its reference value. Accordingly, the literature is rich in reported methods for the solution of the nonlinear problem, and exhaustive listings are readily available. A brief survey of representative approaches appears in [1].

Recently, approximate analytical solutions have been developed employing the concept of optimal or equivalent linearization. Vujanovic [2] derives a solution for the semi-infinite domain exposed to a constant surface temperature. Because of the optimization technique used, the method is limited in that direct extension to temporal boundary conditions is not feasible. Imber [1] presents an approach which removes this restriction thru the introduction of pseudo-heat generation terms. The analysis incorporates an iteration feature; consequently a mechanism for accuracy improvement is available. Baclic [3] introduces a variation of the method in which the minimization is performed with respect to another nonlinear differential equation. The solutions are applicable to the semi-infinite domain.

In the main, the information appearing in the literature addresses the single layer situation, and attempts to extend the results to more than one layer becomes formidable. This is particularly true for the integral approach, Yang [4], Chung [5] and Sugiyama [6], applied this method to multi-component planar solids. Numerical solutions have appeared in the literature in great numbers; however they suffer from the fact that the parametric relationships are not explicitly evident.

In what follows, approximate solutions are first obtained for a finite homogeneous planar wall whose surface is exposed to boundary conditions of the first or third kind. This is followed by an extension to a multi-component wall whose individual thermal conductivities are linear functions of temperature. As an illustration of the method's accuracy, several graphical comparisons are shown between the analytical approach and the conventional numerical solutions.

Methodology

Briefly, the method of equivalent linearization proposes to replace the original nonlinear differential system with a linear one in some optimal fashion. For the case of a homogeneous finite wall, of thickness, L, with constant specific heat, the original one dimensional nonlinear differential equation

$$\rho c \frac{\partial T}{\partial t} = \frac{\partial}{\partial x}\left(\lambda \frac{\partial T}{\partial x}\right) \tag{1}$$

is replaced by an approximate linear one, optimally selected

$$\rho c \frac{\partial T}{\partial t} = a \frac{\partial^2 T}{\partial x^2} + f(x,t) \tag{2}$$

The function, $f(x, t)$ is tentatively identified as the pseudo-heat generation contributions. In equation (2), the term, a, represents a constant parameter selected so that $I(a)$ in equation (3) is minimized:

$$I(a) = \int_0^L \int_0^t \left\{\frac{\partial}{\partial x}\left(\lambda \frac{\partial T}{\partial x}\right) - a\frac{\partial^2 T}{\partial x^2} - f(x,t)\right\}^2 dxdt \tag{3}$$

where the limits on the spatial integration coincide with the geometry under consideration. Thus the operation $dI/da = 0$ results in an explicit expression for, a:

$$a = \frac{\int_0^L \int_0^t \left[\frac{\partial}{\partial x}\left(\lambda \frac{\partial T}{\partial x}\right) - f(x,t)\right]\frac{\partial^2 T}{\partial x^2} dxdt}{\int_0^L \int_0^t \left(\frac{\partial^2 T}{\partial x^2}\right)^2 dxdt} \tag{4}$$

A trial solution, $T_0(x, t)$, is now chosen such that it satisfies the boundary conditions and the linear form of equation (1), and it replaces all the temperature terms in equation (4). Since the quantity, a, is prescribed to be a constant, any temporal contributions from numerator in equation (4) must be negated. The function, $f(x, t)$ is constructed to effect this; consequently, the aforementioned adjustment produces in a straightforward manner the result that $a = \lambda_{ref}$, the reference thermal conductivity.

For the finite layered wall, a unified mathematical description of the relevant nonlinear differential equations is

$$\rho_i c_i \frac{\partial T_i}{\partial t} = \nabla \cdot (\lambda_i \nabla T_i),\ i = 1, 2, \ldots, n \tag{5}$$

where, i, stands for the particular layer, and, n, the number of layers. The intent of the method is to replace this equation with the linear version

$$\rho_i c_i \frac{\partial T_i}{\partial t} = a_i \frac{\partial^2 T_i}{\partial x^2} + f_i(x,t) \tag{6}$$

where the continuity conditions at the interfaces are represented by

$$T_i = T_{i+1} \quad \text{and} \quad \lambda_i \nabla T_i = \lambda_{i+1} \nabla T_{i+1} \tag{7}$$

In turn, for each layer the mean square difference is formed as per equation (3),

$$I(a_i) = \int_{L_i}^{L_{i+1}} \int_0^t \{\nabla \cdot (\lambda_i \nabla T_i) - a_i \nabla^2 T_i - f_i(x,t)\}^2 dxdt,\ i = 1, 2, \ldots, n \tag{8}$$

followed by the required differentiation, $dI(a_i)/da_i = 0$. Hence,

$$a_i = \frac{\int_{L_i}^{L_{i+1}} \int_0^t [\nabla \cdot (\lambda_i \nabla T_i) - f_i(x,t)]\, \nabla^2 T_i dxdt}{\int_{L_i}^{L_{i+1}} \int_0^t (\nabla^2 T_i)^2 dxdt} \tag{9}$$

where the difference in lengths, $L_{i+1} - L_i$, represents the individual layer thicknesses. The constant term, a_i, is chosen to be the reference thermal conductivity in each layer; consequently the numerator in equation (9) must be compatible with this requirement. As shown in

Contributed by the Heat Transfer Division for publication in the JOURNAL OF HEAT TRANSFER: Manuscript received by The Heat Transfer Division November 14, 1980.

[1], several options are available in the selection of the function, $f(x, t)$; however for multilayered solids, the choice is obscured by the complexity of the trial function expressions. There is, however, an unpretentious selection available, as will now be demonstrated. When the thermal conductivity variation is written as, $\lambda(T) = \lambda_{\text{ref},i}\,(1 + \beta_i T_i)$, then equation (9) becomes

$$a_i = \frac{\int_{L_i}^{L_{i+1}} \int_0^t [\lambda_{\text{ref},i}\nabla^2 T_i + \lambda_{\text{ref},i}\beta_i T_i \nabla^2 T_i + \lambda_{\text{ref},i}\beta_i (\nabla T_i)^2 - f_i(x,t)]\,\nabla^2 T_i dx dt}{\int_{L_i}^{L_{i+1}} \int_0^t (\nabla^2 T_i)^2 dx dt} \quad (10)$$

and a choice for the function, $f_i(x, t)$, is apparent, i.e.,

$$f_i(x,t) = \lambda_{\text{ref},i}\beta_i T_i\,\nabla^2 T_i + \lambda_{\text{ref},i}\beta_i (\nabla T_i)^2 \quad (11)$$

The procedure just described greatly simplifies the approach shown in [1] in that successive iterations are no longer necessary, and the function, $f_i(x, t)$ is readily identifiable.

Unlike the homogeneous application, in the layered geometry the requirement of flux continuity at the interface must be addressed. From the preceding principles of optimization, the mean square difference in the fluxes is first formed and then differentiated. Thus

$$J(a_i) = \int_{L_i}^{L_{i+1}} \int_0^t \{\lambda_i \nabla T_i - a_i \nabla T_i - g_i(x,t)\}^2\,dx dt,\ i = 1, 2, \ldots, n \quad (12)$$

and

$$a_i = \frac{\int_{Li}^{L_{i+1}} \int_0^t [\lambda_i \nabla T_i - g_i(x,t)]\nabla T_i dx dt}{\int_{L_i}^{L_{i+1}} \int_0^t (\nabla T_i)^2 dx dt} \quad (13)$$

It therefore follows that for $a_i = \lambda_{\text{ref},i}$, and a linear variation in, $\lambda(T)$,

$$g_i(x,t) = \lambda_{\text{ref},i}\beta_i T_i \nabla T_i \quad (14)$$

Consequently the appropriate flux condition at the interface is

$$\lambda_{\text{ref},i}(\nabla T_i) + g_i = \lambda_{\text{ref},i+1}(\nabla T_{i+1}) + g_{i+1} \quad (15)$$

Equation (15) is particularly noteworthy, since the terms, g_i and g_{i+1}, are known functions formed solely by their respective trial functions. This contribution results in a linearization of the nonlinear interface condition. Though the preceding pertains to variable thermal conductivity, the method is flexible and easily extended to include contributions of temperature dependent specific heat.

Homogeneous Planar Wall. As a first application of the linearization procedure, the approximate solution will be generated for a finite slab of thickness, L, whose inner and outer surfaces are subject to conditions of no flux and constant surface temperature, respectively. For convenience, the nonlinear heat conduction equation, equation (1), is rewritten, nondimensionally, as

$$\frac{\partial \overline{T}}{\partial \tau} = (1 + \beta\overline{T})\frac{\partial^2 \overline{T}}{\partial \eta^2} + \beta\left(\frac{\partial \overline{T}}{\partial \eta}\right)^2 \quad (16)$$

where the term, $\overline{T}$, denotes the dimensionless temperature, and it is equal to the ratio in the excess of the local temperature over the initial value divided by the difference in the surface value and the initial amount. Similarly, the dimensionless spatial coordinate, η, is formed by normalizing with respect to the slab thickness, i.e., $\eta = x/L$, and the dimensionless time, τ, is $\tau = \delta_{\text{ref}}\,t/L^2$. The term, δ_{ref}, signifies the reference thermal diffusivity. The relevant boundary and initial conditions are:

$$\frac{\partial \overline{T}}{\partial \eta} = 0 \text{ at } \eta = 0,\ \overline{T}(1,\tau) = 1 \text{ and } \overline{T}(\tau, 0) = 0 \quad (17)$$

It should be noted that for the thermal conductivity variation $\lambda(\overline{T}) = \lambda_{\text{ref}}\,(1 + \beta\overline{T})$ the quantity β, represents, in this instance, the conventional coefficient multiplied by the difference of the surface and initial temperatuers, $T_s - T_{\text{in}}$. Proceeding with the derivation, the trial function, $\overline{T}_0(\eta, \tau)$, is generated so that it simultaneously satisfies the linear version of equation (16), i.e., $\beta = 0$, and the associated conditions represented by equation (17). In the linear differential system under consideration, the trial function is simply,

$$\overline{T}_0(\eta,\tau) = 1 - \frac{4}{\pi}\sum_{n=0}^{\infty}\frac{(-1)^n}{2n+1}e^{-\omega_n^2\tau}\cos\omega_n\eta \quad (18)$$

with the term, ω_n, defined as, $\omega_n = (2n + 1)\,\pi/2$. Applying the proposed simplification, equation (18) is substituted into equation (4) and the function, $f(x, t)$ formed accordingly. The result is identical to that of equation (11) when the subscripted designation is elimated. Thus it follows from equation (2) that the equivalent differential equation, in nondimensional form, is

$$\frac{\partial T}{\partial \tau} = \frac{\partial^2 T}{\partial \eta^2} + \beta\pi\sum_{n=0}^{\infty}(-1)^n(2n+1)\,e^{-\omega_n^2\tau}\cos\omega_n\eta + 4\beta\sum_{m,n=0}^{\infty}(-1)^{n+m}e^{-(\omega_n^2+\omega_m^2)\tau}\{\sin\omega_n\eta\sin\omega_m\eta - (2m + 1/2n + 1)\cos\omega_n\eta\cos\omega_m\eta\} \quad (19)$$

where an abbreviated symbol for the required multiple summation is shown. A solution now is sought for the preceding equation satisfying the boundary and initial conditions represented by equation (17). Since the resultant differential system is linear, conventional methods of solution can be applied. For brevity, the details will not be shown, and only the end result of the analysis is presented. The approximate temperature function is therefore

Nomenclature

a = constant parameter

$A = \dfrac{\lambda_{\text{ref},2}}{\lambda_{\text{ref},1}}\left(\dfrac{\delta_{\text{ref},1}}{\delta_{\text{ref},2}}\right)^{1/2}$

$B(m, n, p)$ = general coefficient, see equation (27)

c = specific heat

D_{2n} = general coefficient, see equation (13)

$f(x, t)$ = local pseudo-heat generation contributions

$g(x, t)$ = local heat flux correction

$\overline{h}$ = Biot modulus, hL/λ_{ref}

$I(a)$ = mean square difference integral of differential equations

$J(a)$ = mean square difference integral of fluxes

$k_i(n, p), K(n), K(n, p)$ = general coefficients, see equations (A1–A4)

L = wall thickness

m, n, p = summation indices

$N(n)$ = general coefficient, see equation (A5)

P_n = general coefficient, $A/\tan\omega_{1n}$

$Q(m, n)$ = general coefficient see equation (A11)

$s_i(m, n, p), S(m, n, p)$ = general coefficients, see equations (A6–A10)

T = temperature

$\overline{T}$ = dimensionless temperature

t = time

x = space variable

β = modified thermal conductivity coefficient

δ = thermal diffusivity

λ = thermal conductivity

ρ = density

τ = dimensionless time, $\delta_{\text{ref}}\,t/L^2$

η = dimensionless space coordinate, x/L

ω_n = respective Eigenvalues

Subscripts

a = ambient

i = respective location

in = initial

ref = reference value

1 = first layer

2 = second layer

$$\bar{T}(\eta,\tau) = 1 - \frac{4}{\pi}\sum_{p=0}^{\infty}\frac{(-1)^p}{2p+1}e^{-\omega_p^2\tau}\cos\omega_p\eta + \pi\beta\tau\sum_{p=0}^{\infty}(-1)^p(2p+1)e^{-\omega_p^2\tau}\cos\omega_p\eta + \frac{16\beta}{\pi^3}\sum_{m,n,p=0}^{\infty}(-1)^p\left\{\left[\frac{2n-2m}{2n+1}\right]\times\left[\frac{1}{2n-2m+2p+1}+\frac{1}{-2n+2m+2p+1}\right] + \left[\frac{2n+2m+2}{2n+1}\right]\left[\frac{1}{2n+2m+2p+3}-\frac{1}{2n+2m-2p+1}\right]\right\}\times\left\{\frac{e^{-(\omega_n^2+\omega_m^2)\tau}-e^{-\omega_p^2\tau}}{[2p+1]^2-[(2n+1)^2+(2m+1)^2]}\right\}\cos\omega_p\eta \quad (20)$$

For the second illustration of the method, the approximation solution is obtained for the preceding geometry, with a boundary condition of the third kind. Accordingly for a finite slab of thickness, L, which receives energy at its surface by convection from a sink temperature, T_a, the appropriate boundary and initial conditions are

$$\frac{\partial\bar{T}}{\partial\eta} = 0 \text{ at } \eta = 0,$$

$$-(1+\beta\bar{T})\frac{\partial\bar{T}}{\partial\eta} = \bar{h}(\bar{T}-1) \text{ at } \eta = 1, \text{ and } T(\eta,0) = 0 \quad (21)$$

where the term, $\bar{h}$, is the Biot modulus, $hL/\lambda_{\text{ref.}}$ All temperatures are normalized with respect to the ambient temperature excess; consequently, β, is now the conventional coefficient multiplied by this excess. Following the methodology presented earlier, the trial function for the linear system is

$$\bar{T}_0(\eta,\tau) = 1 - 4\sum_{n=1}^{\infty}\frac{\sin\omega_n e^{-\omega_n^2\tau}\cos\omega_n\eta}{2\omega_n+\sin 2\omega_n} \quad (22)$$

where the Eigenvalues, ω_n, are determined from the transcendental equation, $\omega_n \tan\omega_n = \bar{h}$. After substitution of equation (22) into equation (4), the resultant approximation for the original nonlinear differential equation is

$$\frac{\partial T}{\partial\tau} = \frac{\partial^2 T}{\partial\eta^2} + 4\beta\sum_{n=1}^{\infty}\frac{\omega_n^2\sin\omega_n e^{-\omega_n^2\tau}\cos\omega_n\eta}{2\omega_n+\sin 2\omega_n} + 4\beta\bar{h}^2\sum_{m,n=1}^{\infty}\frac{\omega_m\sec\omega_m\sec\omega_n e^{-(\omega_m^2+\omega_n^2)\tau}}{(\omega_m^2+\bar{h}^2+\bar{h})(\omega_n^2+\bar{h}^2+\bar{h})}\times\{\omega_n\sin\omega_m\eta\sin\omega_n\eta - \omega_m\cos\omega_m\eta\cos\omega_n\eta\} \quad (23)$$

Unlike the first example, the present illustration has a nonlinear boundary condition at the surface, $\eta = 1$. It is therefore necessary to develop an approximation for this requirement. This is achieved in the following manner. Though equations (12–15) were intended for use in composite instances, by a simple adjustment, they are also applicable for the homogeneous wall. What is required is that the indicated integrations be performed over the range from 0 to L. This in effect produces the result of

$$\lambda_{\text{ref}}(\nabla T) + g(x,t) = -h[T(x,t) - T_a] \text{ at } x = L \quad (24)$$

where the subscripted notation has been removed since the wall is now homogeneous. In terms of the dimensionless parameters, η and τ, the explicit expression for equation (24) is

$$-\left[\frac{\partial\bar{T}}{\partial\eta}+\bar{h}(\bar{T}-1)\right] = 4\beta\sum_{n=1}^{\infty}\frac{\omega_n\sin^2\omega_n e^{-\omega_n^2\tau}}{2\omega_n+\sin 2\omega_n} - 4\beta\bar{h}^3\sum_{m,n=1}^{\infty}\frac{e^{-(\omega_m^2+\omega_n^2)\tau}}{(\omega_m^2+\bar{h}^2+\bar{h})(\omega_n^2+\bar{h}^2+\bar{h})} \text{ at } \eta = 1 \quad (25)$$

The required solution for the preceding differential system is obtained by conventional linear analytical techniques though protracted algebraically because of the presence of the pseudo-heat generation quantities. The analysis presents no unusual difficulties, consequently the derivation details will not be presented at this time. The temperature function is hence

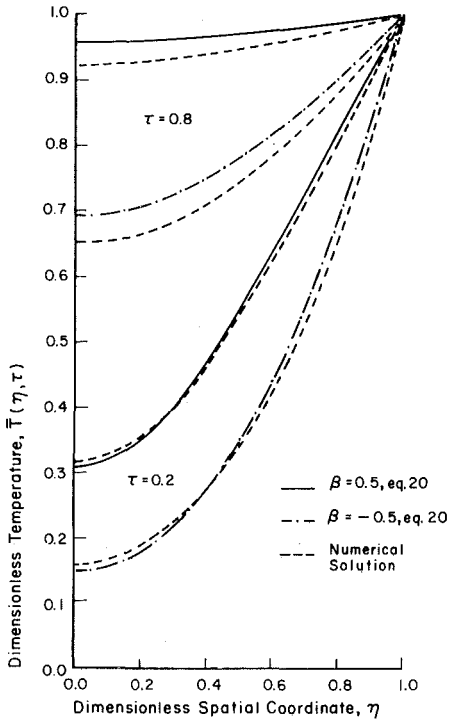

Fig. 1 Comparison of temperatures for $\beta = \pm 0.5$, $\bar{h} = \infty$

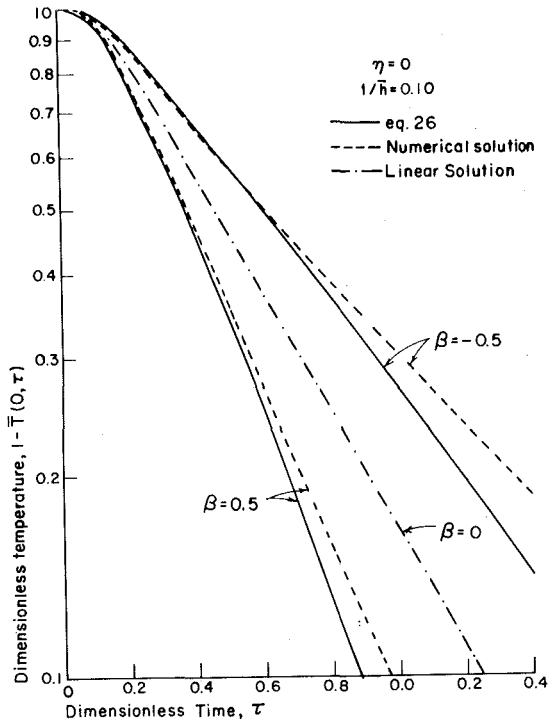

Fig. 2 Comparison of temperatures for $\beta = \pm 0.5$, $\bar{h} = 10$, $\eta = 0$

$$\overline{T}(\eta,\tau) = 1 - 4\sum_{n=1}^{\infty}\frac{\sin\omega_n e^{-\omega_n^2\tau}\cos\omega_n\eta}{2\omega_n+\sin 2\omega_n} + 2\beta\bar{h}\tau\sum_{n=1}^{\infty}\frac{\omega_n^2\sec\omega_n e^{-\omega_n^2\tau}\cos\omega_n\eta}{\omega_n^2+\bar{h}^2+\bar{h}}$$

$$- 8\beta\sum_{m,n,p=1}^{\infty}\left\{\frac{\omega_m\omega_p^2\sin\omega_m\sin\omega_n\sec^2\omega_p\cos\omega_p\eta}{[\omega_p^2+\bar{h}^2+\bar{h}][\omega_p^2-(\omega_m^2+\omega_n^2)][2\omega_m+\sin 2\omega_m][2\omega_n+\sin 2\omega_n]}\right\}\{B(m,n,p)-B(-m,n,p)\}\{e^{-(\omega_m^2+\omega_n^2)\tau}-e^{-\omega_p^2\tau}\}$$

$$- 4\beta\bar{h}\sum_{n=1}^{\infty}\left[\frac{\omega_n\sin\omega_n}{(2\omega_n+\sin 2\omega_n)(\omega_n^2+\bar{h}^2+\bar{h})}\right][\eta\sin\omega_n\eta + 2\omega_n\tau\cos\omega_n\eta]\,e^{-\omega_n^2\tau}$$

$$+ 2\beta\bar{h}\sum_{n=1}^{\infty}\left[\frac{\sin\omega_n}{(2\omega_n+\sin 2\omega_n)^2(\omega_n^2+\bar{h}^2+\bar{h})}\right][\sin 2\omega_n - 2\omega_n\cos 2\omega_n]\cos\omega_n\eta e^{-\omega_n^2\tau}$$

$$+ 4\beta\bar{h}^3\sum_{m,n=1}^{\infty}\frac{\cos\sqrt{\omega_m^2+\omega_n^2}\,\eta\,e^{-(\omega_m^2+\omega_n^2)\tau}}{(\omega_m^2+\bar{h}^2+\bar{h})(\omega_n^2+\bar{h}^2+\bar{h})(\bar{h}\cos\sqrt{\omega_m^2+\omega_n^2}-\sqrt{\omega_m^2+\omega_n^2}\sin\sqrt{\omega_m^2+\omega_n^2})}$$

$$+ 16\beta\bar{h}^2\sum_{m,n,p=1}^{\infty}\frac{\omega_p^2\sin\omega_p\cos\omega_p\eta\,e^{-\omega_p^2\tau}}{(\omega_m^2+\bar{h}^2+\bar{h})(\omega_n^2+\bar{h}^2+\bar{h})(2\omega_p+\sin 2\omega_p)(\omega_m^2+\omega_n^2-\omega_p^2)} \quad (26)$$

where the term, $B(m, n, p)$, is defined as

$$B(m,n,p) = [\omega_m+\omega_n]\left[\frac{\sin(\omega_m+\omega_n+\omega_p)}{\omega_m+\omega_n+\omega_p} + \frac{\sin(\omega_m+\omega_n-\omega_p)}{\omega_m+\omega_n-\omega_p}\right] \quad (27)$$

To generate the appropriate terms represented by, $B(-m, n, p)$, the following identity must be used, $\omega_{-m} \equiv -\omega_m$. Lastly, the general Eigenvalues, ω_i, appearing in the preceding equations are determined from the root equation associated with the trial function, $\omega_i \tan\omega_i = \bar{h}$.

Numerical Results for Homogeneous Case. For the homogeneous slab exposed to a constant surface temperature, numerical results were obtained by conventional numerical difference techniques, for a range in β values. Comparisons between the approximate solution, equation (20) and the numerical solution are presented in Fig. 1 for two values of τ, 0.2 and 0.8. In this figure, the solid curves represent the analytical results for positive values of β and the intermittent broken curves are associated with the negative values of β. In addition, the related numerical solutions are indicated as continually broken curves. The results demonstrate good correspondence between the two differing approaches for computation of the nonlinear temperature field, since the difference between the two is never larger than 5 percent anywhere in the field with the largest difference occurring at the plane of symmetry. The computations for smaller values of β, not shown, indicate a rapid diminution in any differences. Particularly, for $\beta = \pm 0.15$, the differences, for all practical purposes, were imperciptible. For convection, the numerical results are shown at the two spatial locations, $\eta = 0$ and $\eta = 1$, so as to best demonstrate the attendant accuracy. Figures 2 and 3 are the paired results for, $\bar{h} = 10$, and $\beta = \pm 0.5$. In addition, the linear solution; $\beta = 0$, is shown as an intermittent dashed curve. Similarly Figs. 4 and 5 are the paired results for, $\bar{h} = 1$, and $\beta = \pm 0.5$. As in the preceding case, for smaller values of β, all differences become insignificant, hence these values are not indicated at this time. However, as a further demonstration of the method's accuracy, additional comparisons are contained in Tables 1 and 2, which are arranged, listing in columns, the values obtained for the linear (Lin.), the finite difference (Num.), and the analytical (Approx.) solutions for other β values. In summary, for the broad range in the Biot numbers considered, the computations reveal that the approximate analytical method is successful in producing results that correspond closely to those available from the numerical procedure. This is particularly evident for weak nonlinear systems, i.e., $\beta = \pm 0.15$. As the degree of nonlinearity increases, how well the results compare is dependent upon the values of the Biot number. In the main, the equivalent linearization approach duplicates the finite difference computations closely.

Composite Planar Wall. The equivalent linearization method will now be extended to a two component wall, whose individual thermal conductivities are assumed to be linear functions of temperature. The inner surface of this wall is thermally insulated, and the outer surface is kept at a constant temperature, T_s. Introducing subscripted notation, the respective wall thicknesses are represented

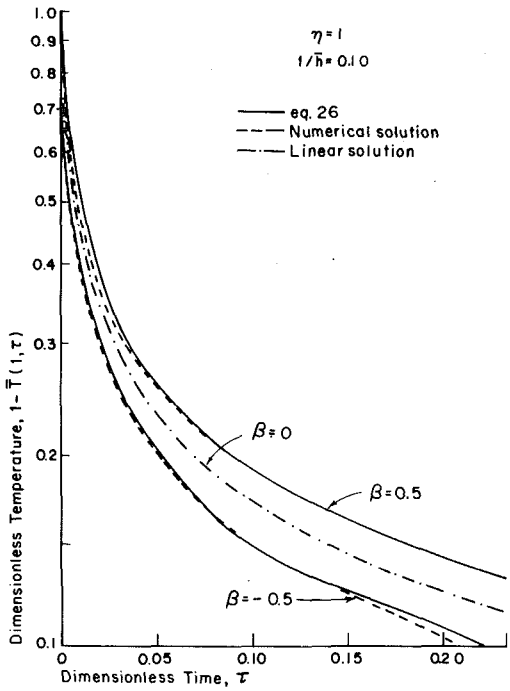

Fig. 3 Comparison of temperatures for $\beta = \pm 0.5$, $\bar{h} = 10$, $\eta = 1$

as, $L_{i+1} - L_i$, and the distance, L_1, is the position location of the insulated face in the first layer. For each layer, normalized quantities are introduced for the temperature, $\overline{T}_i = (T_i - T_{in})/(T_s - T_{in})$, the space coordinate, $\eta_i = (x - L_i)/(L_{i+1} - L_i)$, and the time, $\tau_i = \delta_{ref,i}\text{-}t/(L_{i+1} - L_i)^2$. The subscript, i, denotes the particular wall under study; consequently the generalized nonlinear differential system for a wall consisting of two layers is

$$\frac{\partial\overline{T}_i}{\partial\tau_i} = (1+\beta_i\overline{T}_i)\frac{\partial^2 T_i}{\partial\eta_i^2} + \beta_i\left(\frac{\partial\overline{T}_i}{\partial\eta_i}\right)^2, i = 1, 2. \quad (28)$$

with the boundary and initial conditions of

$$\frac{\partial\overline{T}_i}{\partial\eta_i} = 0, \eta_1 = 0, \overline{T}_2(1,\tau_2) = 1, \overline{T}_2(\eta_1, 0) = \overline{T}_2(\eta_2, 0) = 0 \quad (29)$$

and the interface requirements as

$$\overline{T}_1(1,\tau_1) = \overline{T}_2(0,\tau_2),\ \lambda_{ref,1}(1+\beta_1\overline{T}_1)\left.\frac{\partial\overline{T}_1}{\partial\eta_1}\right|_{\eta_1=1} = \lambda_{ref,2}\left(\frac{L_2-L_1}{L_3-L_2}\right)(1+\beta_2\overline{T}_2)\left.\frac{\partial\overline{T}_2}{\partial\eta_2}\right|_{\eta_2=0} \quad (30)$$

For the linear version of equation (28), the associated trial functions are

$$\overline{T}_{01}(\eta_1,\tau_1) = 1 - A\sum_{n=1}^{\infty}(\sin\omega_{1n})^{-1}D_{2n}e^{-\omega_{1n}^2\tau_1}\cos\omega_{1n}\eta_1 \quad (31)$$

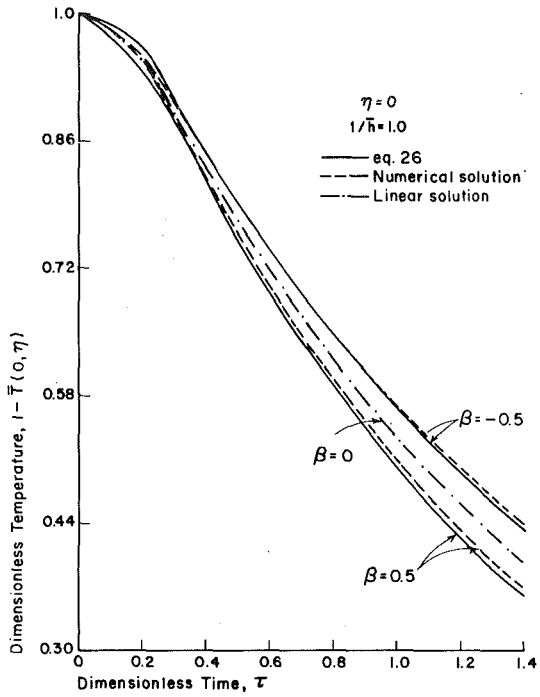

Fig. 4 Comparison of temperatures for $\beta = \pm 0.5$, $\bar{h} = 1$, $\eta = 0$

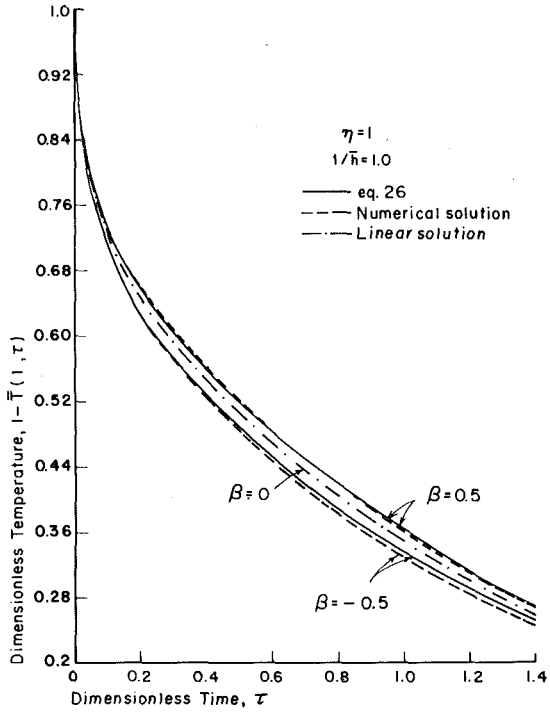

Fig. 5 Comparison of temperatures for $\beta = \pm 0.5$, $\bar{h} = 1$, $\eta = 1$

Table 1 Dimensionless temperature, $1 - \bar{T}(\eta, \tau)$, for $\bar{h} = 0.10$

	η = 0					η = 1.0				
		β = 0.5		β = - 0.5			β = 0.5		β = - 0.5	
τ	Lin.	Num.	Approx.	Num.	Approx.	Lin.	Num.	Approx.	Num.	Approx.
0	1.0000	1.0000	1.0000	1.0000	1.0000	1.0000	1.0000	1.0000	1.0000	1.0000
0.2	.9940	.9940	.9926	.9940	.9954	.9514	.9518	.9530	.9511	.9499
0.4	.9772	.9770	.9767	.9774	.9776	.9310	.9316	.9317	.9303	.9302
0.6	.9587	.9584	.9583	.9591	.9592	.9128	.9137	.9137	.9119	.9120
0.8	.9404	.9399	.9398	.9409	.9410	.8953	.8964	.8963	.8941	.8942
1.0	.9224	.9218	.9216	.9231	.9231	.8781	.8794	.8794	.8767	.8769
1.2	.9047	.9039	.9038	.9055	.9050	.8613	.8627	.8627	.8597	.8599
1.4	.8874	.8865	.8863	.8884	.8884	.8448	.8464	.8464	.8430	.8432

Table 2 Dimensionless temperature, $1 - \bar{T}(\eta, \tau)$, for $\bar{h} = 0.10$

	η = 0					η = 1.0				
		β = 0.15		β = - 0.15			β = 0.15		β = - 0.15	
τ	Lin.	Num.	Approx.	Num.	Approx.	Lin.	Num.	Approx.	Num.	Approx.
0	1.0000	1.0000	1.0000	1.0000	1.0000	1.0000	1.0000	1.0000	1.0000	1.0000
0.2	.9940	.9940	.9936	.9940	.9944	.9514	.9515	.9519	.9513	.9510
0.4	.9772	.9771	.9770	.9772	.9773	.9310	.9312	.9312	.9308	.9307
0.6	.9587	.9586	.9586	.9588	.9589	.9128	.9131	.9131	.9126	.9126
0.8	.9404	.9403	.9402	.9406	.9406	.8953	.8956	.8956	.8950	.8950
1.0	.9224	.9222	.9222	.9226	.9226	.8781	.8785	.8785	.8777	.8778
1.2	.9047	.9045	.9044	.9050	.9050	.8613	.8618	.8617	.8608	.8609
1.4	.8874	.8871	.8871	.8877	.8877	.8448	.8453	.8453	.8443	.8443

and

$$\bar{T}_{02}(\eta_2, \tau_1) = 1 - \sum_{n=1}^{\infty} [P_n \cos \omega_{2n}\eta_2 - \sin \omega_{2n}\eta_2] D_{2n} e^{-\omega_{1n}^2 \tau_1} \quad (32)$$

where the roots, ω_{1n}, are determined from the transcendental equation, $\tan \omega_{1n} \tan \omega_{2n} = A$. In these equations, the following relationships apply:

$$A = \frac{\lambda_{\text{ref},2}}{\lambda_{\text{ref},1}} \left(\frac{\delta_{\text{ref},1}}{\delta_{\text{ref},2}}\right)^{1/2} \qquad P_n = \frac{A}{\tan \omega_{1n}}, \qquad \frac{\omega_{2n}}{\omega_{1n}} = \left(\frac{L_3 - L_2}{L_2 - L_1}\right) \left(\frac{\delta_{\text{ref},1}}{\delta_{\text{ref},2}}\right)^{1/2}$$

and

$$D_{2n} = 2 \sin \omega_{1n} \cos \omega_{1n} \cos \omega_{2n} (\omega_{1n} \sin \omega_{2n} \cos \omega_{2n} + \omega_{2n} \sin \omega_{1n} \cos \omega_{1n})^{-1} \quad (33)$$

Furthermore, the relationship, $\omega_{1n}^2 \tau_1 = \omega_{2n}^2 \tau_2$, has been introduced; consequently the time dependence can be completely cast in terms of one dimensionless time, τ_1. Proceeding, the trial functions, $\bar{T}_{0i}$, are now substituted respectively into the general equation (11). Hence, the reducing function, $f_i(\eta_i, \tau_1)$ is established for each layer under consideration, and it follows from equation (6) that the equivalent differential equation for each layer is

$$\frac{\partial \bar{T}_1}{\partial \tau_1} = \frac{\partial^2 \bar{T}_1}{\partial \eta_1^2} + \beta_1 A \times \sum_{n=1}^{\infty} \frac{\omega_{1n}^2 D_{2n} e^{-\omega_{1n}^2 \tau_1} \cos \omega_{1n}\eta_1}{\sin \omega_{1n}} - \frac{\beta_1}{2} A^2 \sum_{m,n=1}^{\infty} \omega_{1m} D_{2n} D_{2m} \times \left[\frac{(\omega_{1m} + \omega_{1n}) \cos (\omega_{1m} + \omega_{1n})\eta_1 + (\omega_{1m} - \omega_{1n}) \cos (\omega_{1m} - \omega_{1n})\eta_1}{\sin \omega_{1n} \sin \omega_{1m}} \right] \times e^{-(\omega_{1m}^2 + \omega_{1n}^2)\tau_1} \quad (34)$$

and

$$\frac{\partial \bar{T}_2}{\partial \tau_2} = \frac{\partial^2 \bar{T}_2}{\partial \eta_2^2} + \beta_2 \sum_{n=1}^{\infty} \omega_{2n}^2 D_{2n} [P_n \cos \omega_{2n}\eta_2 - \sin \omega_{2n}\eta_2] e^{-\omega_{1n}^2 \tau_1} + \frac{\beta_2}{2} \sum_{m,n=1}^{\infty} \omega_{2n} D_{2n} D_{2m} [(\omega_{2m} + \omega_{2n})(1 - P_n P_m) \cos (\omega_{2m} + \omega_{2n})\eta_2 + (\omega_{2m} - \omega_{2n})(1 + P_n P_m) \cos (\omega_{2m} - \omega_{2n})\eta_2] e^{-(\omega_{1m}^2 + \omega_{1n}^2)\tau_1} + \beta_2 \sum_{m,n=1}^{\infty} D_{2m} D_{2n} [(\omega_{2m}^2 + \omega_{2n}^2) P_n + 2\omega_{2n}\omega_{2m} P_m] \times e^{-(\omega_{1m}^2 + \omega_{1n}^2)\tau_1} \sin \omega_{2m}\eta_2 \cos \omega_{2n}\eta_2 \quad (35)$$

At the interface, $\eta_1 = 1$, $\eta_2 = 0$, the continuity of temperatures must be satisfied as well as the fluxes. This latter term introduces a nonlinearity at the interface due to the temperature dependence in the thermal conductivity. An approximation for this has been previously derived, see equation (15), thus the resultant flux condition at the interface is accordingly,

$$\left.\frac{\partial \bar{T}_1}{\partial \eta_1}\right|_{\eta_1 = 1} = \frac{\lambda_{\text{ref},2}}{\lambda_{\text{ref},1}} \left(\frac{L_2 - L_1}{L_3 - L_2}\right) \left.\frac{\partial \bar{T}_2}{\partial \eta_2}\right|_{\eta_2 = 0} + (\beta_2 - \beta_1) A \left[\sum_{n=1}^{\infty} \omega_{1n} D_{2n} e^{-\omega_{1n}^2 \tau_1} \right.$$

$$- \sum_{n,m=1}^{\infty} \omega_{1n} P_m D_{2m} D_{2n} e^{-(\omega_{1m}^2 + \omega_{1n}^2)\tau_1} \Bigg] \quad (36)$$

The approximate differential system is now linear in its entirety, and the respective temperature solutions follow from extensions of classical methods. Obviously, the heat generation terms that appear in both differential equations, plus those at the interface, contribute to an expanded temperature function. After some algebraic manipulation, the temperature for the inner or first layer, is

$$\overline{T}_1(\eta_1, \tau_1) = 1 - A \sum_{n=1}^{\infty} \frac{D_{2n} \cos \omega_{1n}\eta_1 e^{-\omega_{1n}^2 \tau_1}}{\sin \omega_{1n}} + (\beta_2 - \beta_1)A$$
$$\times \Bigg[\sum_{m,n=1}^{\infty} \frac{\omega_{1n} P_m D_{2m} D_{2n} \sin \sqrt{\omega_{2n}^2 + \omega_{2n}^2} \cos \sqrt{\omega_{1m}^2 + \omega_{1n}^2}\, \eta_1 e^{-(\omega_{1m}^2 + \omega_{1n}^2)\tau_1}}{\sqrt{\omega_{1m}^2 + \omega_{1n}^2}\, Q(m,n)}$$
$$- \sum_{m,n,p=1}^{\infty} \frac{\omega_{1n}\omega_{1p} P_m D_{2m} D_{2n} D_{2p} \sin \omega_{2p} \cos \omega_{1p}\eta_1 e^{-\omega_{1p}^2 \tau_1}}{(\omega_{1m}^2 + \omega_{1n}^2 - \omega_{1p}^2) \sin \omega_{1p}} \Bigg]$$
$$+ (\beta_2 - \beta_1)A \sum_{n=1}^{\infty} \Bigg\{ \Bigg[4\omega_{1n}^2 \tau_1 + 1 - 2\omega_{2n} \operatorname{cotan} \omega_{2n} - \left(\frac{\omega_{1n}\omega_{2n} D_{2n} \sin \omega_{2n}}{A} \right) (A^2 - 1) \Bigg]$$
$$\times [\cos \omega_{1n}\eta_1] + 2\omega_{1n}\eta_1 \sin \omega_{1n}\eta_1 \Bigg\} \left\{ \frac{D_{2n}^2 \sin \omega_{2n} e^{-\omega_{1n}^2 \tau_1}}{4 \sin \omega_{1n}} \right\}$$
$$+ (\beta_2 - \beta_1)\, A \sum_{n,p=1}^{n \neq p} \frac{\omega_{1n}\omega_{1p} D_{2n} D_{2p} \sin \omega_{2p} \cos \omega_{1p}\eta_1 e^{-\omega_{1n}^2 \tau_1}}{(\omega_{1n}^2 - \omega_{1p}^2) \sin \omega_{1p}}$$
$$+ \sum_{n=1}^{\infty} \Bigg\{ \tau_1 K(n) e^{-\omega_{1n}^2 \tau_1} + \sum_{m=1}^{\infty} \frac{S(m,n)\, [e^{-\omega_{1n}^2 \tau_1} - e^{-(\omega_{1m}^2 + \omega_{1n}^2)\tau_1}]}{\omega_{1m}^2} \Bigg\} \cos \omega_{1n}\eta_1$$
$$+ \sum_{n,p=1}^{\infty} \Bigg\{ K(n \neq p, p) \frac{[e^{-\omega_{1p}^2 \tau_1} - e^{-\omega_{1n}^2 \tau_1}]}{\omega_{1n}^2 - \omega_{1p}^2}$$
$$+ \sum_{m=1}^{\infty} S(m, n \neq p, p) \frac{[e^{-\omega_{1n}^2 \tau_1} - e^{-(\omega_{1n}^2 + \omega_{1m}^2)\tau_1}]}{\omega_{1m}^2 + \omega_{1n}^2 - \omega_{1p}^2} \Bigg\} \cos \omega_{1p}\eta_1 \quad (37)$$

and

$$\overline{T}_2(\eta_2, \tau_1) = 1 - \sum_{n=1}^{\infty} \Bigg[1 + \left(\frac{\beta_2 - \beta_1}{4} \right) \left(1 + \langle \omega_{1n}\omega_{2n} D_{2n} \sin \omega_{2n} \rangle \left(\frac{A^2 - 1}{A} \right) \right) D_{2n} \sin \omega_{2n} \Bigg]$$
$$\times [P_n \cos \omega_{2n}\eta_2 - \sin \omega_{2n}\eta_2]\, D_{2n} e^{-\omega_{1n}^2 \tau_1} + (\beta_2 - \beta_1)\, A$$
$$\times \sum_{m,n=1}^{\infty} \omega_{1n} P_m D_{2n} D_{2m} \frac{[\tan \sqrt{\omega_{2m}^2 + \omega_{2n}^2} \cos \sqrt{\omega_{2m}^2 + \omega_{2n}^2}\, \eta_2 - \sin \sqrt{\omega_{2m}^2 + \omega_{2n}^2}\, \eta_2]}{\sqrt{\omega_{1m}^2 + \omega_{1n}^2}\, Q(m,n)}$$
$$\times [\cos \sqrt{\omega_{1m}^2 + \omega_{1n}^2} \cos \sqrt{\omega_{2m}^2 + \omega_{2n}^2}\, e^{-(\omega_{1m}^2 + \omega_{1n}^2)\tau_1}]$$
$$- (\beta_2 - \beta_1) \sum_{m,n,\, p=1}^{\infty} \omega_{1n}\omega_{1p} P_m D_{2m} D_{2n} D_{2p} \left[\frac{\tan \omega_{2p} \cos \omega_{2p}\eta_2 - \sin \omega_{2p}\eta_2}{\omega_{1m}^2 + \omega_{1n}^2 - \omega_{1p}^2} \right] [\sin \omega_{2p} e^{-\omega_{1p}^2 \tau_1}]$$
$$+ \left(\frac{\beta_2 - \beta_1}{2} \right) \sum_{n=1}^{\infty} \{ [2\omega_{1n}^2 \tau_1 + 1] [\tan \omega_{2n} \cos \omega_{2n}\eta_2 - \sin \omega_{2n}\eta_2] - [\omega_{2n}(1 - \eta_2) - A\omega_{1n}] \cos \omega_{2n}\eta_2$$
$$- [\omega_{2n}(1 - \eta_2) \tan \omega_{2n} + \omega_{1n} \tan \omega_{1n}] \sin \omega_{2n}\eta_2 \}\, D_{2n}^2 \sin \omega_{2n} e^{-\omega_{1n}^2 \tau_1}$$
$$+ (\beta_2 - \beta_1) \sum_{n,p=1}^{n \neq p} \left[\frac{\omega_{1n}\omega_{1p} D_{2n} D_{2p}}{\omega_{1n}^2 - \omega_{1p}^2} \right] [\tan \omega_{2p} \cos \omega_{2p}\eta_2 - \sin \omega_{2p}\eta_2] \sin \omega_{2p} e^{-\omega_{1p}^2 \tau_1}$$
$$+ \sum_{n=1}^{\infty} \Bigg\{ \tau_1 K(n) e^{-\omega_{1n}^2 \tau_1} + \sum_{m=1}^{\infty} \frac{S(m,n)\, [e^{-\omega_{1n}^2 \tau_1} - e^{-(\omega_{1m}^2 + \omega_{1n}^2)\tau_1}]}{\omega_{1m}^2} \Bigg\}$$
$$\times \{ A^{-1} \sin \omega_{1n} [P_n \cos \omega_{2n}\eta_2 - \sin \omega_{2n}\eta_2] \}$$
$$+ \sum_{n,p=a}^{\infty} \Bigg\{ K(n \neq p, p) \frac{[e^{-\omega_{1p}^2 \tau_1} - e^{-\omega_{1n}^2 \tau_1}]}{\omega_{1n}^2 - \omega_{1p}^2}$$
$$+ \sum_{m=1}^{\infty} S(m, n \neq p, p) \frac{[e^{-\omega_{1n}^2 \tau_1} - e^{-(\omega_{1n}^2 + \omega_{1m}^2)\tau_1}]}{\omega_{1m}^2 + \omega_{1n}^2 - \omega_{1p}^2} \Bigg\} \{ A^{-1} \sin \omega_{1p} [P_p \cos \omega_{2p}\eta_2 - \sin \omega_{2p}\eta_2] \} \quad (38)$$

In equations (37) and (38) the algebraic symbol $\sum^{n \neq p}$, has been used throughout to signify that a double summation is called for over all the indices, n and p, excluding the values satisfying the relationship, $n = p$. The definitions of the other algebraic contractions are indicated in the Appendix. As in all the situations thus far presented, the Eigenvalues are those associated with the linear solution, hence the general root, $\omega_{1,n}$ is computed from the relationship, $\tan \omega_{1n} \tan \omega_{2n} = A$.

Numerical Results for Composite Wall. In the dimensionless temperature expressions for the individual layers $\overline{T}_i(\eta_i, \tau_1)$, four parameters appear. These are the terms, A, η, τ and β, the last of which occurs due to introduction of the nonlinearity. Because there are now four parameters, a generalized comparison between the approximate solution, equations (37) and (38) and any numerical solution entails a protracted effort. Instead a rather direct and simpler approach will be taken, a specific numerical illustration will be presented. Hence, a two-layered wall is considered exposed to a constant surface temperature, and for thermal symmetry, the inner or first face of the first layer is insulated. The assumed thermal physical properties of the first and second layers are respectively: $\lambda_{ref,1} = 202.45$ W/m.°C, $\delta_{ref,1} = 8.6028 \times 10^{-5}$ m^2/s, $\beta_1 = 0.25$ and $\lambda_{ref,2} = 13.84$ W/m.°C, $\delta_{ref,2} = 3.8611 \times 10^{-6}$ m^2/s, $\beta_2 = 0.50$. In addition, the outer layer of the composite wall is half the thickness of the inner segment, consequently $L_3 - L_2 = (L_2 - L_1)/2$. Comparisons between the approximate solutions, equations (37) and (38) are indicated in Fig. 6, for two values of the dimensionless time, τ_1, 2 and 7. In the main, the comparisons indicate a close correspondence between the two solutions. It should be noted that this example represents a real world problem, since the aforementioned composite wall is in reality, a stainless steel sheet, 18-8, backed with a layer of aluminum.

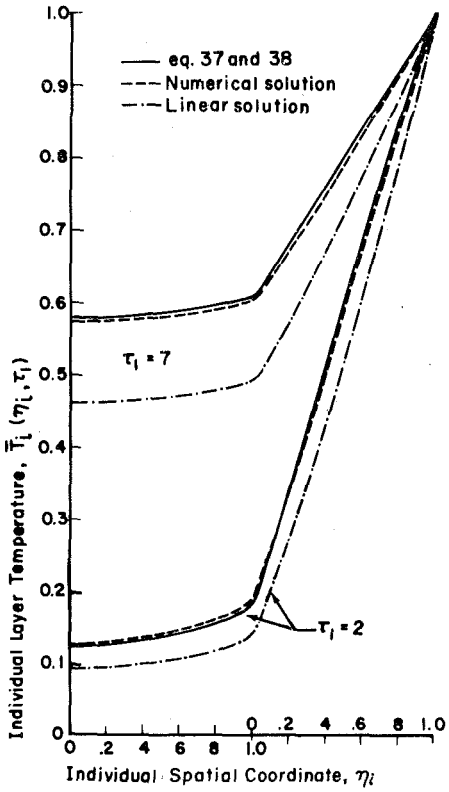

Fig. 6 Comparison of composite wall temperatures for $\tau = 2, 7$

Conclusions

From the method of equivalent linearization, approximate analytical solutions, as distinct from numerical or finite difference solutions, have been derived. The optimization procedure used entails a single and complete reduction, equation (11); consequently no further iterations are necessary. For boundary conditions of the third kind, an approximation is presented which takes into consideration the local variation in the thermal conductivity, equation (25). As an extension of the method, the layered configuration is considered, and as shown in the development a correction must be generated for the continuity of fluxes at the interface, equation (15). In all instances, optimal adjustments produce in a straightforward manner, the result that $a_i = \lambda_{\text{ref},i}$. Because of this, all solutions generated will have the linear solution as part of the complete solution, and the Eigenvalues are determined from the same root equation as for the linear solution. This feature simplifies the associated computations considerably. In the main, the computations indicate good correspondence between the developed method and the finite difference solutions.

Acknowledgments

This material is based upon work supported by the National Science Foundation under Grant No. CME 78-10703. The author wishes to express his deep appreciation to Dr. R. T. Corry for his invaluable assistance in the numerical solutions associated with the illustrative examples.

References

1 Imber, M., "Nonlinear Heat Transfer in Planar Solids: Direct and Inverse Applications," *AIAA Journal*, Vol. 17, Feb. 1979, pp. 204–212.

2 Vujanovic, B., "Application of the Optimal Linearization Method to the Heat Transfer Problem," *International Journal of Heat and Mass Transfer*, Vol. 16, 1973, pp. 1111–1117.

3 Baclic, B. S., "Optimal Reformulation of Transient Heat Conduction Problems with Temperature Dependent Properties," ASME Paper No. 80-HT-120, 1980.

4 Yang, K. T., "Calculation of Unsteady Heat Conduction in Single Layer and Composite Finite Slab With and Without Property Variations by an Improved Integral Procedure," ASME *International Developments in Heat Transfer*, 1963, pp. 18–27.

5 Chung, B. T. F., and Yeh, L. T., "Nonlinear Transient Heat Transfer in Composite Slabs," ASME Paper No. 76-HT-39, 1976.

6 Sugiyama, S., Nishimura, M., and Watanabe, H., "Transient Response of Composite Slabs," *International Journal of Heat and Mass Transfer*, Vol. 17, 1974, pp. 875–883.

APPENDIX

For contraction purposes, the following definitions have been introduced in equations (37) and (38)

$$K(n) = \frac{A(\sin\omega_{1n}^2)^{-1}\beta_1\omega_{1n}^2 D_{2n}\,[2\omega_{1n} + \sin 2\omega_{1n}]}{N(n)} + \beta_2\,\omega_{1n}^2 D_{2n}\sin\omega_{1n}\,[2\omega_{2n}\,(P_n^2+1) + (P_n^2-1)\sin 2\omega_{2n} - 4P_n\sin^2\omega_{2n}] \Big/ N(n) \quad \text{(A1)}$$

$$K(n,p) = \{2A(\sin\omega_{1n})^{-1}\beta_1\omega_{1n}^2\omega_{1p}D_{2n}\,[k_1(n,p) + k_1(n,-p)][\omega_{1n}^2 - \omega_{1p}^2]^{-1} + 2\beta_2\omega_{1n}\omega_{2n}\omega_{1p}D_{2n}\sin\omega_{1p} \times [k_2(n,p) - k_2(n,-p)][\omega_{2n}^2 - \omega_{2p}^2]^{-1}\}\{N(p)\}^{-1}, \quad \text{(A2)}$$

in which

$$k_1(n,p) = (\omega_{1n} - \omega_{1p})\sin(\omega_{1n} + \omega_{1p}) \quad \text{(A3)}$$

$$k_2(n,p) = [P_nP_p - 1][(\omega_{2n} - \omega_{2p})\sin(\omega_{2n} + \omega_{2p})] - [P_n - P_p][(\omega_{2n} + \omega_{2p})(\cos\langle\omega_{2n} - \omega_{2p}\rangle - 1)] \quad \text{(A4)}$$

$$N(n) = 2\omega_{1n} + \sin 2\omega_{1n} + A^{-1}\sin^2\omega_{1n}\,[2\omega_{2n}\,(P_n^2+1) + (P_n^2-1)\sin 2\omega_{2n} - 4P_n\sin^2\omega_{2n}] \quad \text{(A5)}$$

$$S(m,n,p) = \Big\{-\beta_1A^2\omega_{1m}\omega_{1p}D_{2n}D_{2m}(\sin\omega_{1n}\sin\omega_{1m})^{-1} \times [s_1(m,n,p) + s_1(m,-n,p)] + \beta_2\omega_{1n}\omega_{1p}D_{2n}D_{2m}\sin\omega_{1p} \times [s_2(m,n,p) + s_2(m,-n,p)] - \beta_2\frac{P_p\omega_{1n}\omega_{1p}D_{2n}D_{2m}\sin\omega_{1p}}{\omega_{2n}} \times [(\omega_{2m}^2 + \omega_{2n}^2)P_n + 2\omega_{2m}\omega_{2n}P_m]\Big[s_3(m,n,p) + s_3(m,-n,p) + \frac{s_4(m,n,p) + s_4(m,-n,p)}{P_p}\Big]\Big\}\{N(p)\}^{-1}, \quad \text{(A6)}$$

in which

$$s_1(m,n,p) = \left\{\frac{\omega_{1m} + \omega_{1n}}{(\omega_{1m} + \omega_{1n})^2 - \omega_{1p}^2}\right\}[(\omega_{1m} + \omega_{1n} - \omega_{1p})\sin(\omega_{1m} + \omega_{1n} + \omega_{1p}) + (\omega_{1m} + \omega_{1n} + \omega_{1p})\sin(\omega_{1m} + \omega_{1n} - \omega_{1p})] \quad \text{(A7)}$$

$$s_2(m,n,p) = \left\{\frac{\omega_{2m} + \omega_{2n}}{(\omega_{2m} + \omega_{2n})^2 - \omega_{2p}}\right\}\{1 - P_nP_m\}\{P_p[(\omega_{2m} + \omega_{2n} - \omega_{2p})\sin(\omega_{2m} + \omega_{2n} + \omega_{2p}) + (\omega_{2m} + \omega_{2n} + \omega_{2p}) \times \sin(\omega_{2m} + \omega_{2n} - \omega_{2p})] + (\omega_{2m} + \omega_{2n} - \omega_{2p}) \times (\cos\langle\omega_{2m} + \omega_{2n} + \omega_{2p}\rangle - 1) - (\omega_{2m} + \omega_{2n} + \omega_{2p})(\cos\langle\omega_{2m} + \omega_{2n} - \omega_{2p}\rangle - 1)]\} \quad \text{(A8)}$$

$$s_3(m,n,p) = [\omega_{2m} + \omega_{2n} - \omega_{2p}][\cos((\omega_{2m} + \omega_{2n} + \omega_{2p}) - 1] + [\omega_{2m} + \omega_{2n} + \omega_{2p}] \Big/ (\omega_{2m} + \omega_{2n})^2 - \omega_{2p}^2 \times [\cos(\omega_{2m} + \omega_{2n} - \omega_{2p}) - 1] \quad \text{(A9)}$$

$$s_4(m,n,p) = \frac{[\omega_{2m} + \omega_{2n} + \omega_{2p}][\sin(\omega_{2m} + \omega_{2n} - \omega_{2p})] - [\omega_{2m} + \omega_{2n} - \omega_{2p}]}{(\omega_{2m} + \omega_{2n})^2 - \omega_{2p}^2} \times [\sin(\omega_{2m} + \omega_{2n} + \omega_{2p})] \quad \text{(A10)}$$

The term $S(m,n)$ is obtained from equation (A6) where the indicated

operations in the terms s_1, s_2, a_3 and s_4 are first performed and in turn, the substitution, $p = n$, is then made. Lastly,

$$Q(m, n) = \sin \sqrt{\omega_{1m}^2 + \omega_{1n}^2} \sin \sqrt{\omega_{2m}^2 + \omega_{2n}^2} - A \cos \sqrt{\omega_{1m}^2 + \omega_{1n}^2} \cos \sqrt{\omega_{2m}^2 + \omega_{2n}^2} \quad \text{(A11)}$$

In all instances, negative subscripted values in the arguments are synonymous with the following operations:

$$\omega_{-p} = -\omega_p, \tan \omega_{-p} = -\tan \omega_p, P_{-p} = -P_p \quad \text{(A12)}$$

A. Goldman
Assistant Professor,
Mem. ASME

Y. C. Kao
Graduate Student,
Mem. ASME

Department of Mechanical Engineering,
Texas Tech University,
Lubbock, Tex 79409

Numerical Solution to a Two-Dimensional Conduction Problem Using Rectangular and Cylindrical Body-Fitted Coordinate Systems

The temperature distribution in a rectangular plate with a circular void at the center was calculated using a body-fitted coordinate system. Three different transformed geometries were considered: rectangular-rectangular, cut-line, and cylindrical. Problems involving insulated outer surfaces could not be solved using the rectangular-rectangular transformation but could be solved with both the cut-line and cylindrical transformations. The cylindrical transformation also appears to have the capability of being extended to three-dimensional problems.

Introduction

Analysis in the field of heat transfer has undergone radical change in methodology in recent years because of the growth in speed and power of modern digital computers. These changes fostered creation of various numerical techniques to solve the partial differential equation that governs conduction heat transfer. One technique, the finite difference method, approximates the differential equation by transforming it into a set of algebraic equations. The solution to the original problem is then the solution to the set of algebraic equations.

The heat conduction equation, or more generally the diffusion equation, is an elliptic type partial differential equation. Elliptic problems require information on all boundaries; therefore, the key to these problems is the accurate coupling of the boundaries to the interior. This is best accomplished when the boundaries coincide with coordinate lines so that node points in the finite difference grid also coincide with the boundaries of the system under study. Finite difference expressions on or near regular boundaries, i.e., where boundaries and node points coincide, can be obtained without special interpolating formulas. However, most real problems involve irregular boundaries which require interpolation between boundaries and interior grid points. Such representations are inaccurate and produce large errors in the vicinity of strong curvature and shape discontinuities, i.e., irregular boundaries.

These difficulties may be overcome through the use of a curvilinear coordinate system. Methods for generation of such systems are available in the literature [1–4]. Chu [5] transformed an irregular domain to an equilateral triangular mesh by taking the curvilinear coordinates to be the solutions of a Laplace equation in the physical plane. As presented, the technique generates a uniform space grid. However, when large gradients exist in a region, it is necessary to increase the density of node points within the region in order to increase accuracy. Amsden and Hirt [6] extended the method to allow for concentration of grid points in areas of large gradients. Thompson, et al. [7] further extended the method to include multiconnected domains, automated the procedure for concentrating node points, and applied the solution to a fluid mechanics problem. McWhorter and Sadd [8] applied the method to steady-state anisotropic heat conduction problems with specified temperature on the boundaries.

A large portion of the above work concerned the techniques of generating the body-fitted coordinate systems and only a comparatively small amount of work was devoted to the actual implementation of the method to solve engineering problems. The work presented here solves a simple, but general, unsteady, conduction problem in sufficient depth to isolated difficulties within the method and presents methods for overcoming the difficulties. The solution technique for generation of the curvilinear coordinate system is SOR and the solution to the conduction problem is by ADI. Both methods enjoy wide popularity for solving finite difference problems and any difficulties encountered in solving the test problems presented here will most certainly be encountered when the method is applied to actual engineering problems. This is important because one of the objectives for using the body-fitted technique is the generation of "black box" codes which can be used by anyone for a wide range of problems.

The problem initially chosen for study is shown in Fig. 1. Although both inner and outer surfaces appear to be regular, one of the surfaces will not coincide with coordinate lines when presented in either the rectangular cartesian or cylindrical coordinate systems. Thus, the body has one irregular boundary, yet the body is sufficiently regular to allow solution by standard finite difference methods and thus provide a solution against which the body-fitted solution may be checked.

Generation of Body-Fitted Coordinate System

The general transformation from the physical x-y plane to the transformed ξ-η plane is given by $\xi = \xi(x,y)$ and $\eta = \eta(x,y)$, where ξ and η are solutions of an eliptic equation with Dirichlet boundary conditions for the form

$$\frac{\partial^2 \xi}{\partial x^2} + \frac{\partial^2 \xi}{\partial y^2} = P(\xi, \eta), \tag{1a}$$

$$\frac{\partial^2 \eta}{\partial x^2} + \frac{\partial^2 \eta}{\partial y^2} = Q(\xi, \eta), \tag{1b}$$

where P and Q are coordinate control functions.

The physical plane is specified by the body shape and the transformed plane is any desired shape which simplifies the problem; usually a uniform rectangular region. This is shown in equation (1) which reflects the desire to work in a rectangular system. However, the rectangular system is not the only system which can be used; other transformations may be more useful under certain conditions.

Difficulties in specifying the boundary conditions in the physical plane make equation (1) difficult to solve. This can be overcome by transforming to the ξ-η plane. Although the equations are slightly more complicated in the ξ-η plane, the boundary conditions are easily specified and the transformed equation solved with standard techniques.

Equation (1) in the transformed plane is

Contributed by The Heat Transfer Division for publication in the JOURNAL OF HEAT TRANSFER. Manuscript received by The Heat Transfer Division, September 25, 1980.

$$\alpha \frac{\partial^2 x}{\partial \xi^2} + 2\beta \frac{\partial^2 x}{\partial \xi \partial \eta} + \gamma \frac{\partial^2 x}{\partial \eta^2} + P \frac{\partial x}{\partial \xi} + Q \frac{\partial x}{\partial \eta} = 0, \quad (2a)$$

$$\alpha \frac{\partial^2 y}{\partial \xi^2} + 2\beta \frac{\partial^2 y}{\partial \xi \partial \eta} + \gamma \frac{\partial^2 y}{\partial \eta^2} + P \frac{\partial y}{\partial \xi} + Q \frac{\partial y}{\partial \eta} = 0, \quad (2b)$$

where

$$\alpha = \xi_x{}^2 + \xi_y{}^2$$

$$\beta = \xi_x \eta_x + \xi_y \eta_y$$

$$\gamma = \eta_x{}^2 + \eta_y{}^2 \quad (2c)$$

$$P = \xi_{xx} + \xi_{yy}$$

$$Q = \eta_{xx} + \eta_{yy}$$

The quantity, J, is the Jacobian and is given by

$$J = \frac{\partial x}{\partial \xi}\frac{\partial y}{\partial \eta} - \frac{\partial x}{\partial \eta}\frac{\partial y}{\partial \xi}.$$

and

$$\frac{\partial \xi}{\partial x} = \frac{1}{J}\frac{\partial y}{\partial \eta}, \quad \frac{\partial \xi}{\partial y} = -\frac{1}{J}\frac{\partial x}{\partial \eta},$$

$$\frac{\partial \eta}{\partial x} = -\frac{1}{J}\frac{\partial y}{\partial \xi}, \quad \frac{\partial \eta}{\partial y} = \frac{1}{J}\frac{\partial x}{\partial \xi}. \quad (3)$$

Again, P and Q are coordinate control functions which allow node points to be concentrated in some desired region. Generation of the functions is discussed in references [3, 7], and [10] and will not be discussed here. In fact, they will be set to zero to simplify the problem. A complete set of derivatives relating the physical to the transformed plane can be found in reference [5].

The last step in the process is to transform the diffusion equation to the ξ-η plane. The unsteady diffusion equation with constant properties in rectangular coordinates is

$$\rho C \frac{\partial T}{\partial t} = k\left(\frac{\partial^2 T}{\partial x^2} + \frac{\partial^2 T}{\partial y^2}\right), \quad (4)$$

and transforms into

$$\rho C \frac{\partial T}{\partial t} = k\left(\alpha \frac{\partial^2 T}{\partial \xi^2} + 2\beta \frac{\partial^2 T}{\partial \xi \partial \eta} + \gamma \frac{\partial^2 T}{\partial \eta^2} + P \frac{\partial T}{\partial \xi} + Q \frac{\partial T}{\partial \eta}\right) \quad (5)$$

where α, β, γ, P and Q are as stated in equation (2). All of the coefficients α, β, etc., have been calculated as part of the coordinate generation process and are known quantities. The boundary condition used is

$$aT + b\frac{\partial T}{\partial n} = C \quad (6)$$

where a, b, and c can be chosen to produce specified temperature, specified heat flux, or a convection boundary condition. The quantity, n, in equation (6) represents the normal direction to the surface and must be decomposed in components in the coordinate directions. The diffusion equation, equation (5), and associated boundary conditions are finite differenced and solved using the ADI technique. The second order terms were central differenced while the first order terms were evaluated using one-sided differencing. An additional simplification was made by setting $k/\rho c$ to one. Variable property problems are easily included in the transformation process. However, the terms involving the first derivatives of temperature, which are absent in constant property problems, should be one-sided differenced. This is because the scale factors multiplying first derivative terms can change sign throughout the solution region and thus act as velocity terms in a convection problem.

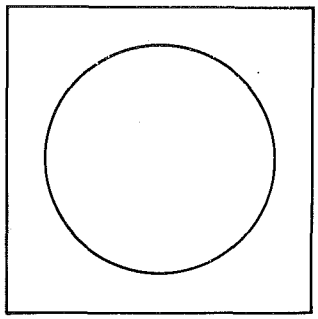

Fig. 1 Test problem-rectangular plate with circular cutout

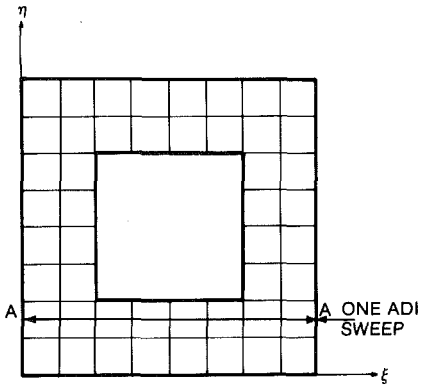

Fig. 2 Rectangular-rectangular transformation

Discussion and Results

The problem examined is shown in Fig. 1 with the general boundary given by equation (6) on both the inner and outer surfaces. The first transformation used is shown in Fig. 2. This was chosen because it produces a simple rectangular transformed geometry and because the existence of more than one hole in a region represents a straightforward extension of rectangular cut outs in the transformed plane. This presented no particular difficulties when a constant temperature was imposed on both the inner and outer surfaces. However, notice what occurs for the case of a constant temperature on the inner surface and an insulated outer surface. Line A-A shows one sweep in the ξ-direction for the ADI method. The boundary conditions for this sweep is then a gradient condition for both the right and left boundary. Roach [11] shows that ADI does not work for this case. The difficulty is avoided when a cut line is introduced to generate the transformation [7] shown in Fig. 3. Figure 4 shows the temperature distribution for constant temperature boundaries on both inner and outer surfacing using the cut line geometry. The results obtained were the same for rectangular-rectangular transformation shown in Fig. 2, and also with the results obtained using standard finite difference techniques. Again, boundary irregularities are not severe enough to prevent an accurate solution from being obtained using any of the above techniques. In fact, only when a gradient boundary exists on the outer surface is it necessary to use the cut line transformation.

Nomenclature

c = specific heat
k = thermal conductivity
t = time
x = coordinate direction, physical plane
y = coordinate direction, physical plane
P = coordinate distribution function
Q = coordinate distribution function
T = temperature
α, β, γ = scale factors
ρ = density
ξ, η = transformed coordinates

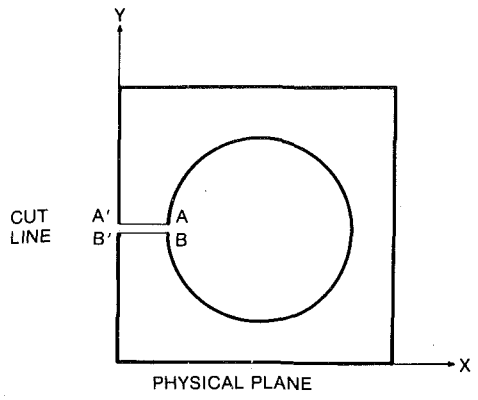

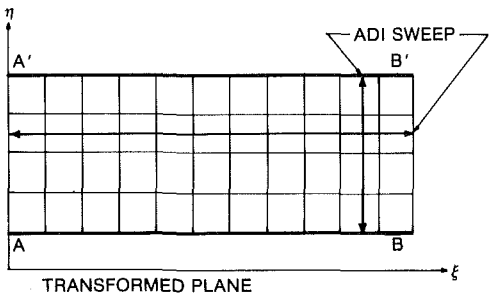

Fig. 3 Coordinate transformation

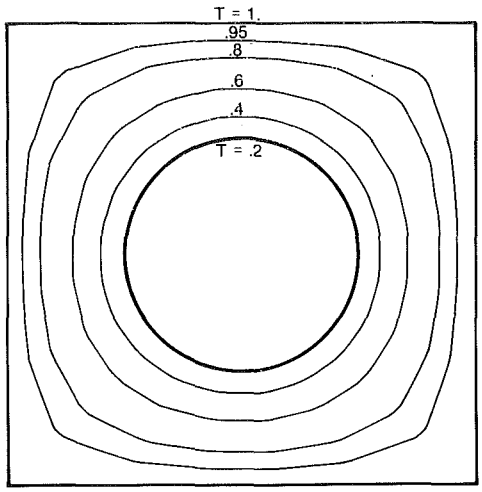

Fig. 4 Temperature distribution using cut line transformation

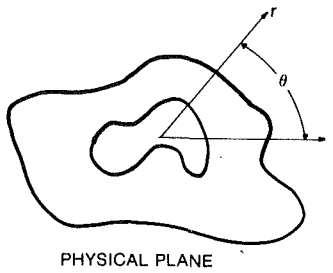

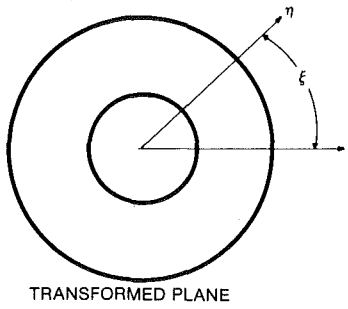

Fig. 5 Cylindrical transformation

It would thus appear that all conduction problems can be solved using the idea of a cut line. However, consider an extension to three dimensions. In this case, it is quite clear an irregularly shaped body with an interior void could easily be transformed to a cubic geometry with a cubic shaped void. Once again, problems involving specified temperatures on the inner and outer surfaces would present no special difficulty in obtaining a solution. If the outer surface is insulated, the three-dimensional problem is subject to the same difficulty as the two-dimensional problem, i.e., the ADI method creates sweep directions where both the right and left boundaries are gradient conditions. Thus, a cubic-cubic transformation for three dimensions generates the same difficulties as a rectangular-rectangular transformation for two-dimensional problems. This difficulty was overcome for the two-dimensional problem using the idea of a cut line; it is not clear how to use this idea for the three-dimensional problem.

Consider again Fig. 3 which shows the cut line transformation. Notice that one sweep direction always connects the inner and outer surfaces while the other sweep direction is always parallel to the inner and outer surfaces. This same general behavior could be obtained by transforming the irregularly shaped body so that the inner and outer surfaces form concentric cylinders. When this is done, one sweep direction always connects the inner and outer surfaces and one sweep direction is always parallel to the surfaces. This transformation is shown in Fig. 5 and may be calculated by considering the transformed coordinates to be solutions to

$$\frac{\partial^2 \xi}{\partial r^2} + \frac{1}{r}\frac{\partial \xi}{\partial r} + \frac{1}{r^2}\frac{\partial^2 \xi}{\partial \theta^2} = P(\xi, \eta), \tag{7a}$$

$$\frac{\partial^2 \eta}{\partial r^2} + \frac{1}{r}\frac{\partial \eta}{\partial r} + \frac{1}{r^2}\frac{\partial^2 \eta}{\partial \theta^2} = Q(\xi, \eta). \tag{7b}$$

The quantities r and θ are standard cylindrical coordinates in the physical plane, while ξ is the transformed coordinate in the angular direction and η is the transformed radial coordinate. As explained above, it is more advantageous to solve the equations in the transformed plane by interchanging the dependent and independent variables. The resulting equations become

$$\alpha \frac{\partial^2 \theta}{\partial \xi^2} + 2\beta \frac{\partial^2 \theta}{\partial \xi \partial \eta} + \gamma \frac{\partial^2 \theta}{\partial \eta^2} + P\frac{\partial \theta}{\partial \xi} + Q\frac{\partial \theta}{\partial \eta} = 0, \tag{8a}$$

$$\alpha \frac{\partial^2 r}{\partial \xi^2} + 2\beta \frac{\partial^2 r}{\partial \xi \partial \eta} + \gamma \frac{\partial^2 r}{\partial \eta^2} + P\frac{\partial r}{\partial \xi} + Q\frac{\partial r}{\partial \eta} = 0. \tag{8b}$$

where

$$\alpha = \left(\frac{\partial \xi}{\partial r}\right)^2 + \left(\frac{1}{r}\frac{\partial \xi}{\partial \theta}\right)^2,$$

$$\beta = \frac{1}{r^2}\frac{\partial \xi}{\partial \theta}\frac{\partial r}{\partial \theta} + \frac{\partial \xi}{\partial r}\frac{\partial r}{\partial r}, \tag{9}$$

$$\gamma = \left(\frac{\partial \eta}{\partial r}\right)^2 + \left(\frac{1}{r}\frac{\partial \eta}{\partial \theta}\right)^2,$$

$$P = \frac{\partial^2 \xi}{\partial r^2} + \frac{1}{r}\frac{\partial \xi}{\partial r} + \frac{1}{r^2}\frac{\partial^2 \xi}{\partial \theta^2},$$

$$Q = \frac{\partial^2 \eta}{\partial r^2} + \frac{1}{r}\frac{\partial \eta}{\partial r} + \frac{1}{r^2}\frac{\partial^2 \xi}{\partial \theta^2}.$$

The Jacobian is given by

$$J = \frac{\partial \theta}{\partial \xi}\frac{\partial r}{\partial \eta} - \frac{\partial \theta}{\partial \eta}\frac{\partial r}{\partial \xi},$$

with equation (3) holding true simply by inserting θ and r for x and y, respectively. Finally, the energy equation becomes

$$\rho C \frac{\partial T}{\partial t} = k\left(\alpha \frac{\partial^2 T}{\partial \xi^2} + 2\beta \frac{\partial^2 T}{\partial \xi \partial \eta} + \gamma \frac{\partial^2 T}{\partial \eta^2} + P\frac{\partial T}{\partial \xi} + Q\frac{\partial T}{\partial \eta}\right), \quad (10)$$

where the quantities α, β, etc., are defined in equation (9). Notice that equation (5) is identical to equation (10). The differences between the rectangular and cylindrical transformations are all incorporated into the scale factors, α, β, etc., which, so far as the conduction equation is concerned, are known quantities.

The cylindrical transformation was initially tested by considering heat transfer in an annular region with constant temperature boundary condition on both surfaces. This problem was solved by three different techniques and the solutions compared. The first technique was to analytically generate the steady-state solution. This is a one-dimensional steady-state problem and the solution is found in any introductory heat transfer text. The second technique is to use the rectangular transformation with a cut line, while the last technique is the cylindrical transformation. The boundary conditions were then changed to constant temperature on the inner surface and a convection boundary on the outer surface, and the problem was again solved using the same three techniques as the constant temperature problem. The results are listed in Table 1.

Both the rectangular cut line transformation and the cylindrical transformation were used on the rectangular plate with a circular cut out shown in Fig. 1. The cylindrical transformation produces essentially the same system as seen in Fig. 4. They may be different because any radial line can be used as a zero reference; however, if the zero radial line coincides with the cut line, the two transformations produce the same coordinate systems. Figure 4 shows the temperature distribution throughout the body as obtained by the cut line transformation, and Fig. 6 is the temperature distribution as obtained with the cylindrical transformation. There are minor differences between the two solutions, but both are within 1 percent of the values obtained with standard finite difference techniques.

Figure 8 shows a cut line transformation when a body contains more than one void, while Figs. 8 and 9 show two possible cylindrical transformations for bodies containing more than one void. The transformation shown in Fig. 8 avoids difficulties at $r = 0$, whereas the transformation shown in Fig. 9 will require special care at $r = 0$ [12]. However, either transformation works.

It is thus seen that the cylindrical transformation produces results equal to the rectangular transformation in terms of accuracy of solution and capability of handling multiple voids. This is important because it provides a direction to take for three-dimensional problems. Fig. 10(*a*) shows the three-dimensional analog of Fig. 1, a cubic body containing a spherical void. Mastin and Thompson [13] have used a rectangular transformation on a three-dimensional problem to generate a solid rectangular transformed region with a specified function on five sides. A logical extension to three-dimensional problems with interior voids would be a transformation with a cubic interior and exterior surface. However, this produces the same difficulty as the two-dimensional problem for an insulated interior surface; the ADI sweep will have two gradient boundary conditions. There does not seem to be any way to introduce the cut line transformation for this problem. On the other hand, the cylindrical transformation can be extended to three dimensions. The basis for this transformation was to produce one sweep direction which always connected the inner and outer surfaces and another sweep direction parallel to the surfaces. This same idea is satisfied with the spherical transformation in Fig. 10(*b*). The work on the three-dimensional problem is still in progress.

Table 1 Comparison between numerical and analytic solutions for

Type of Transformation	Max. Error Compared with Exact Solution (Percent)	No. of Time Steps to Steady-State
(1) SPECIFIED TEMPERATURE BOUNDARY CONDITIONS:		
Rectangular transformation	0.3217	589
Cylindrical transformation	0.2588	581
(2) CONVECTION BOUNDARY CONDITION ON OUTER SURFACE		
Rectangular transformation	1.0305	972
Cylindrical transformation	0.9459	908

Time step equals critical time for explicit formulation

The final aspect of the problem considered was the time step used in the ADI method. If it is desired to follow a transient problem from initial to final state, any time step which produces a stable solution is acceptable. In fact, because SOR is in reality a time-like technique [11], each iteration represents part of the transient solution and, thus, SOR could also be used for the transient solution. The steady-state solution is obtained as part of the transient solution as time becomes large. If it is desired to solve only the steady-state problem, the intermediate solutions are not important and the technique which requires the least amount of calculations should be used. Theoretically, the ADI technique is unconditionally stable for any time step, but in practice is usually kept to a value below ten times the critical time step as evaluated from an explicit method [11]. The rectangular test problem with a convection boundary at the outer surface was solved with time steps as large as 16 times the critical step. Therefore, the ADI technique retains its desirable properties in the transformed plane. This is in contrast to the SOR method, which usually requires more iterations when used for the transformed equations [5].

Conclusions

A cylindrical transformation allows solution to certain problems which cannot be solved with some of the natural appearing rectangular transformations. However, the form of the diffusion equation is the same in the transformed plane, regardless of whether a rectangular or cylindrical transformation is used. Differences between the two transformations are seen by the conduction equation as simply a difference in the magnitude of the scale factors. Therefore, a general solution program can be constructed which is independent of both the physical geometry of the problem and the specific transformation used. Both the geometry and transformation are contained within a separate code to generate the scale factors where both aspects of the problem are easy to vary.

The desired properties of the ADI technique are retained in the transformed plane. Thus, the unsteady problem with a very large time step may be used to obtain the steady-state solution. This is in contrast to the SOR technique which requires more iterations in the transformed plane than in the physical plane.

Finally, the use of the cylindrical transformation for two-dimensional problems points the way for the use of a spherical transformation in solving three-dimensional problems.

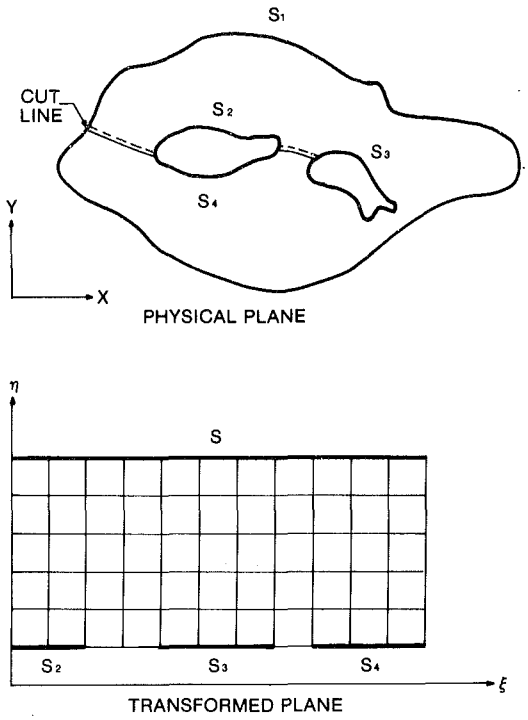

Fig. 6 Multiple void cut line transformation

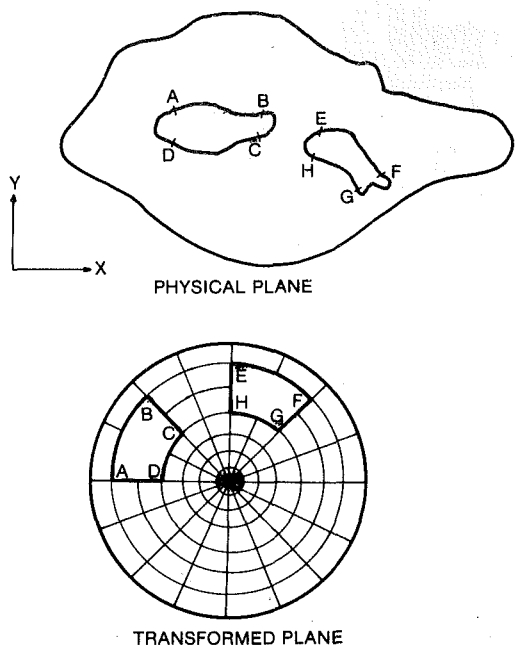

Fig. 8 Multiple void cylindrical transformation

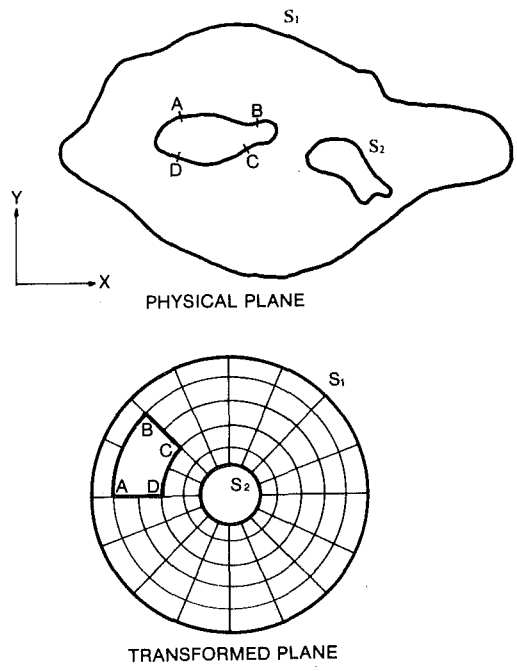

Fig. 7 Multiple void cylindrical transformation

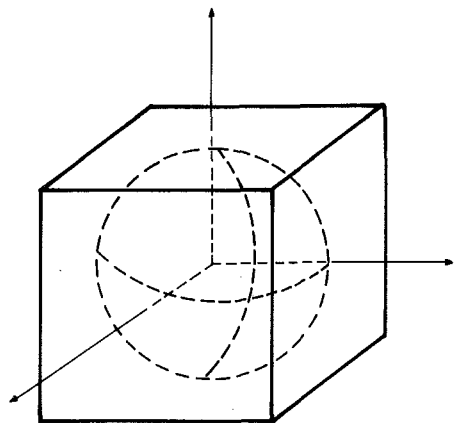

Fig. 9(*a*) Three-dimensional problem physical plane

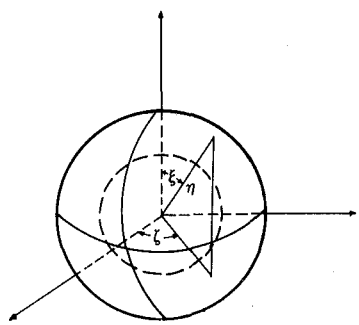

Fig. 9(*b*) Three-dimensional problem transformed plane

References

1 Winslow, A. M., "Numerical Solution of the Quasi-linear Poisson Equation in a Non-Uniform Triangular Mesh," *Journal of Comp. Physics*, Vol. 2, 1966, p. 149.

2 Barfield, W. D., "An Optimal Mesh Generator for Lagrangian Hydrodynamic Calculations in Two Space Dimensions," *Journal of Comp. Physics*, Vol. 6, 1970, p. 417.

3 Thompson, J. F., Thames, F. C., Mastin, C. W., and Shanks, S. P., "Use of Numerically Generated Body-Fitted Curvilinear Coordinate Systems for Solution of the Navier-Stokes Equations," *Proceedings of AIAA 2nd Computational Fluid Dynamics Conference*, Hartford, Conn.

4 Kao, Y. C., "Numerical Solution of Heat Conduction Problems Using the Body-Fitted Coordinate Technique," M.S. Thesis, Texas Tech University, 1980.

5 Chu, W. H., "Development of a General Finite Difference Approximation for a General Domain," *Journal of Comp. Physics*, Vol. 8, 1971, p. 392.

6 Amsden, A. A., and Hirt, C. W., "A Simple Scheme for Generating General Curvilinear Grids," *Journal of Comp. Physics*, Vol. 11, 1973, p. 348.

7 Thompson, J. F., Thames, F. C., and Mastin, C. W., "Boundary-Fitted Curvilinear Coordinate Systems for Solution of Partial Differential Equations on Fields Containing Any Number of Arbitrary Two-Dimensional Bodies," NASA CR-2729, 1976.

8 McWhorter, J. C., and Sadd, M. H., "Numerical Anisotropic Heat Conduction Solutions Using Boundary-Fitted Coordinate Systems," ASME Paper No. 79-WA/HT-41.

9 Camarero, R., and Younis, M., "Efficient Generation of Body-Fitted Coordinates for Cascades Using Multigrid," *AIAA Journal*, May 1980, p. 487.

10 Thomas, P. D., and Middlecoff, J. F., "Direct Control of the Grid Point Distribution in Meshes Generated by Elliptic Equations," *AIAA Journal*, June 1980, p. 652.

11 Roache, P. J., *Computational Fluid Dynamics*, Hermosa Publishers.

12 Arpaci, V. S., *Conduction Heat Transfer*, Addison-Wesley, New York.

13 Maslin, C. W., and Thompson, J. F., "Transformation of Three-Dimensional Regions onto Rectangular Regions by Elliptic Systems," *Numerische Mathematik*, Vol. 29, 1978, pp. 397–401.

Unsteady Surface Element Method

N. R. Keltner
Sandia National Laboratories,
Albuquerque, NM 87185
Assoc. Mem. ASME

J. V. Beck
Michigan State University,
East Lansing, Mich 48824
Mem. ASME

A method for the solution of transient heat conduction problems, called the unsteady surface element (USE) method, is developed and applied to several problems. The method is intended for thermally contacting bodies of similar or dissimilar geometries such as occur in contact conductance and intrinsic thermocouple problems. The method utilizes Duhamel's integral in several ways. Two different procedures are presented, one utilizing temperature-based kernels and the other uses heat flux-based kernels. One of the given applications is to the intrinsic thermocouple problem. Several solutions are given and the results agree very well with two finite difference solutions.

Introduction

A method for solution of transient heat conduction problems, called the unsteady surface element method (USE), is described and developed herein. The method is applicable to bodies described by the linear heat conduction equation; the bodies may be composite and of arbitrary geometry. The boundary conditions can be either linear or nonlinear; however, the present paper is limited to linear examples.

A precursor of the USE method is the quasi-coupling method of Keltner [1, 2]. Yovanovich [3] coined the name "surface element." The method is related to the boundary integral method that has been widely used in applied mechanics [4]. The boundary integral method has been developed for steady-state heat conduction cases by Schneider [5] and Khader [6]. A transient form of the boundary integral was developed by Thaler and Mueller [7].

The boundary integral methods [4–7] use as a fundamental solution (or "building block" or "kernel") either the line source or point source solutions for temperature in an *infinite* body. The line source solution is used for two-dimensional rectangular bodies and the point source is used for three-dimensional bodies. The boundary integral techniques reduce the dimensionality of the numerical solution compared to the finite difference (FD) or finite element (FE) methods in which nodes are needed in the interior of the bodies as well as at the boundaries. For two-dimensional geometries the boundary integral method reduces the problem to treating a one-dimensional surface and for three-dimensional geometries to two-dimensional surfaces. As a consequence the boundary integral method has the potential of substantial reduction of computer time over FD and FE methods.

The USE method can reduce the computer time even further for certain geometries. This is because only certain regions of the surfaces need be considered for both one, two and three-dimensional problems. This greater power is obtained at the expense of more complex building blocks, however.

Problems that are susceptible to easier treatment employing the USE method than the FD and FE methods include semi-infinite bodies that are heated only over part of the surface and bodies of similar and dissimilar basic geometries that are connected only over small surface regions on the bodies. Examples of connecting similar bodies occur in contact conductance problems such as the case of two semi-infinite cylinders connected only over a central circular region. See Fig. 1(*a*). An example involving dissimilar geometries is the thermocouple problem [1, 8–14] which involves a semi-infinite cylinder attached to a semi-infinite body (Fig. 1(*b*)) or to an infinite plate (Fig. 1(*c*)). A related case is that of a fin attached to a plate when the transient temperature distribution of the fin including the base is of interest.

For the specific problems mentioned above, FD and FE methods can be used but they are not entirely satisfactory, however, due to the necessity of providing extremely fine nodes near the interface between the basic geometries (including "corners"), many large nodes further from the interface, and potentially long computer running times. Indeed, Keltner [1, 2] developed his quasi-coupling method because of the difficulty of using the FD method for the intrinsic thermocouple problem (Fig. 1(*b*)), and Yovanovich [3] developed his method because both FD and FE methods did not seem to be adequate for contact conductance problems. Another aspect of the USE method is that only the interface nodes need be considered initially; later the temperature history at any interior or boundary location can be found. This reduces computations compared to the FD and FE methods for which the whole domain must be considered and also compared to the boundary integral technique [7] for which all surfaces or interfaces must be considered while the USE method may consider only connecting nodes.

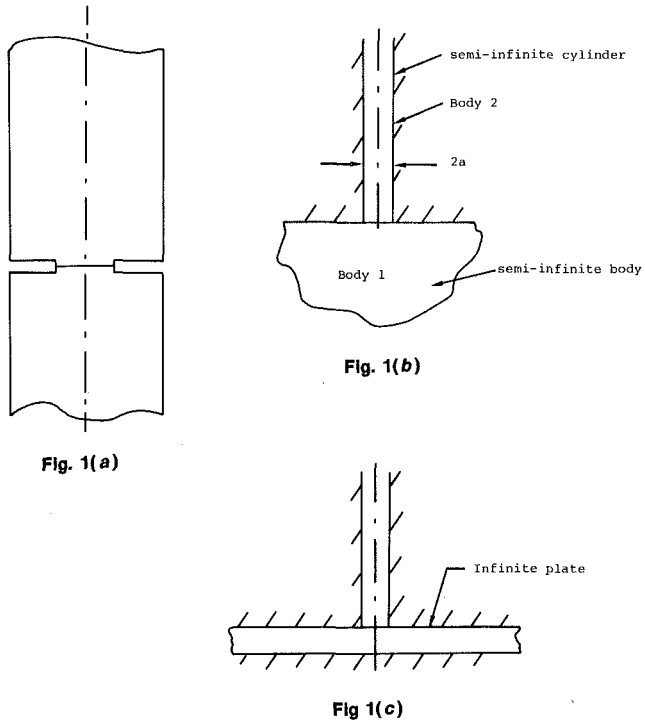

Fig. 1(*a*)

Fig. 1(*b*)

Fig 1(*c*)

Fig. 1 Some geometries that are conveniently treated using the surface element method

The solution of problems involving transient heat transfer between dissimilar geometric regions, often with differing thermophysical properties, is difficult because the separate regions are coupled by simultaneous interfacial boundary conditions which, in general, vary with time in some unspecified manner. It is sometimes possible to obtain approximate solutions by relaxing the conditions which the coupled regions must satisfy. In fact this is the approach often used when two-dimensional problems are approximated by one dimensional solutions [2, 8–11]. In developing the USE solutions, the coupling interfacial boundary conditions may be relaxed so that neither temperature nor heat flux need simultaneously match for all points along the interface and at all times. Instead, a less stringent requirement equates average heat fluxes between the coupled regions while still requiring simultaneous matching of area-average interfacial temperatures. The solution can be improved by utilizing more than one interface node. (In a future paper the case of $n > 1$ connecting

Contributed by the Heat Transfer Division for publication in the JOURNAL OF HEAT TANSFER. Manuscript received by the Heat Transfer Division January 30, 1981.

nodes is to be developed.) As in any numerical technique there is a trade-off between accuracy and simplicity; in the present paper the simplest case of a single interface node is utilized.

The objectives of this paper are to present (*i*) a form of the USE method based on temperature kernels, (*ii*) a form of USE based on heat flux kernels and (*iii*) compare the two approaches. The temperature kernel method utilizes the Duhamel's integral with a kernel for a unit step in temperature. The heat flux kernel method also utilizes a form of Duhamel's integral but the kernel is for a unit step change in heat flux. The use of these integrals puts the method on a more firm basis than the quasi-coupling procedure presented in [1, 2].

To demonstrate the USE methods based on temperature and heat flux kernels, several problems are considered using both methods. Two problems are the temperatures and/or interfacial heat flow for two semi-infinite bodies suddenly brought together with perfect contact and imperfect contact; these problems have known exact solutions. The more difficult case of the intrinsic thermocouple is also investigated and approximate results are derived and compared with those obtained by two finite difference analyses.

Temperature-Based USE Procedure

Assume that body 1, which has an arbitrary geometry, is initially at a uniform temperature T_{1i} and a portion of the surface, A, is subject to a time-varying temperature. No spatial variation of temperature over A is permitted. All other surfaces are insulated. Let the temperature rise at position $\mathbf{x}$ in body 1 due to a unit step increase in temperature at the surface A be denoted $\theta_1(\mathbf{x}, t)$. See Fig. 2. Then any temperature $T_1(\mathbf{x}, t)$ for a time varying surface temperature $T_1(0, t)$ is given by the following form of Duhamel's theorem,

$$T_1(\mathbf{x}, t) = T_{1i} + \frac{\partial}{\partial t}\int_0^t [T_1(0, \lambda) - T_{1i}]\theta_1(\mathbf{x}, t - \lambda)d\lambda \qquad (1)$$

The heat flow through the surface region is given by

$$q_1(t)A = \frac{\partial}{\partial t}\left\{A\int_0^t [T_1(0, \lambda) - T_{1i}]\theta_{q_1}(0, t - \lambda)d\lambda\right\} \qquad (2)$$

where $q_1(t)$ is the surface (or interface) heat flux and where the area average heat flux for a unit increase in surface temperature is

$$\theta_{q_1}(0, t) = \frac{1}{A}\int_A -k\left.\frac{\partial\theta_1(\mathbf{x}, t)}{\partial n}\right|_{n=0} dA \qquad (3)$$

Suppose that a second body, body 2, is initially at temperature T_{2i} and is suddenly brought into contact with body 1. The same average heat flux that enters body 1 then leaves body 2 so that

$$Aq_1(t) = -Aq_2(t) \qquad (4)$$

The statement given by (4) is always true (provided there are no interface heat sources) but the statement of uniform temperature over the surface is not true in general. Two cases for which the isothermal condition is true are now considered.

Consider now the specific classical case of two homogeneous, semi-infinite bodies initially at the different temperatures of T_{1i} and T_{2i}, see Fig. 3. These semi-infinite cases are considered to illustrate the methods rather than to present new results. For perfect and imperfect contact the kernel $\theta_i(\mathbf{x}, t)$ is [15]

$$\theta_i(\mathbf{x}, t) = \text{erfc}\frac{|x|}{2\sqrt{\alpha_i t}} \qquad (5)$$

The related heat flux is

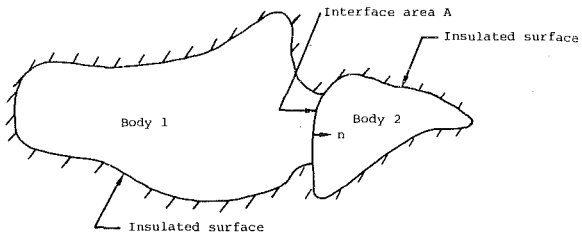

Fig. 2 Two arbitrary bodies connected over the region *A*

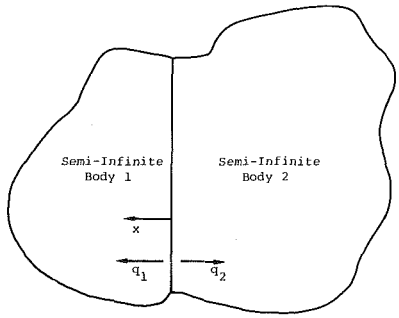

Fig. 3 Two homogeneous semi-infinite bodies initially at different initial temperatures brought into thermal contact

$$\theta_{qi}(0, t) = \pm k_i e^{-x^2/4\alpha_i t}/\sqrt{\pi\alpha_i t}\,|_{x=0}, \quad + \text{for } i = 1, \quad - \text{for } i = 2 \qquad (6)$$

For perfect contact the interface temperature (at $x = 0$) is identical for both bodies so that $T_1(0, t) = T_2(0, t) = T(0, t)$. Utilizing (2) in (4) yields

$$\frac{\partial}{\partial t}\int_0^t [T(0, \lambda) - T_{1i}]\theta_{q_1}(0, t - \lambda)d\lambda = \frac{\partial}{\partial t}\int_0^t [T(0, \lambda) - T_{2i}]\theta_{q_2}(0, t - \lambda)d\lambda \qquad (7)$$

and then employing (6) gives

$$\frac{\partial}{\partial t}\int_0^t [T(0, \lambda) - T_{1i}]\left[\frac{k_1}{\sqrt{\pi\alpha_1(t - \lambda)}}\right]d\lambda = -\frac{\partial}{\partial t}\int_0^t [T(0, \lambda) - T_{2i}]\left[\frac{k_2}{\sqrt{\pi\alpha_2(t - \lambda)}}\right]d\lambda \qquad (8)$$

which is a Volterra equation of the first kind with the unknown being the function $T(0, t)$. This equation could be solved numerically [16] but in this case a simple analytical procedure utilizing the Laplace transform is possible.

Taking the Laplace transform of (8) gives

$$sL[T(0, t) - T_{1i}]\cdot\left[\frac{k_1}{\sqrt{\alpha_1 s}}\right] = -sL[T(0, t) - T_{2i}]\cdot\left[\frac{k_2}{\sqrt{\alpha_2 s}}\right] \qquad (9)$$

where $L[T(0, t)]$ is the Laplace transform of $T(0, t)$. For convenience, let $\overline{T}[0, s] = L[T(0, t)]$. Without loss of generality let $T_{1i} = T_0$ and $T_{2i} = 0$; then

$$\left[\overline{T}(0, s) - \frac{T_0}{s}\right]\cdot\left[\frac{k_1}{\sqrt{\alpha_1 s}}\right] = -\overline{T}(0, s)\cdot\left[\frac{k_2}{\sqrt{\alpha_2 s}}\right] \qquad (10)$$

Solving for $\overline{T}(0, s)$ gives

$$\overline{T}(0, s) = \frac{T_0}{s}\frac{k_1}{(\alpha_1 s)^{1/2}}\left[\frac{k_1}{(\alpha_1 s)^{1/2}} + \frac{k_2}{(\alpha_2 s)^{1/2}}\right]^{-1} \qquad (11)$$

Nomenclature

A = contacting area
b = property group defined by (16*b*)
h = heat transfer coefficient
k = thermal conductivity
q = interface or surface heat flux
s = Laplace transform parameter
t = temperature
T_0 = initial temperature of body 1
x = coordinate
α = thermal diffusivity
β = property group defined by (12*b*)
θ_q = temperature-based kernel for Duhamel's integral
λ = dummy time variable
ϕ = heat flux-based kernel for Duhamel's integral

which has the inverse Laplace transform of

$$T(0, t) = T_0(1 + \beta)^{-1} \tag{12a}$$

where

$$\beta = [k_2\rho_2c_2/k_1\rho_1c_1]^{1/2} \tag{12b}$$

This is the desired exact solution for the surface temperature for both bodies for the case of perfect contact [15].

Next consider the more complex case of imperfect contact of two semi-infinite bodies. Let there be a contact conductance, h, between the bodies. The heat fluxes are related by

$$q_1(t) = -q_2(t) = h[T_2(0, t) - T_1(0, t)] \tag{13}$$

where now both $T_1(0, t)$ and $T_2(0, t)$ are unknown functions.

Solving (13) for $T_1(0, t)$, in terms of $q_2(t)$, substituting in (2) and again equating the heat fluxes gives

$$\frac{\partial}{\partial t}\left\{\int_0^t [T_2(0, \lambda) - T_{1i}]\theta_{q_1}(0, t - \lambda)d\lambda + \int_0^t \left[\frac{1}{h}\frac{\partial}{\partial t}\int_0^\lambda [T_2(0, \gamma) - T_{2i}]\theta_{q_2}(0, \lambda - \gamma)d\gamma\right]\theta_{q_1}(0, t - \lambda)d\lambda\right\} = -\frac{\partial}{\partial t}\int_0^t [T_2(0, \lambda) - T_{2i}]\theta_{q2}(0, t - \lambda)d\lambda \tag{14}$$

This is an integral equation of the Volterra type except now a double integration is present; the unknown function is $T_2(0, t)$.

The integral equation given by (14) would in most cases be solved numerically but again the exact solution can be found using the Laplace transform,

$$s\left\{\left[\overline{T}_2 - \frac{T_{1i}}{s}\right]\bar{\theta}_{q_1} + \frac{s}{h}\left[\overline{T}_2 - \frac{T_{2i}}{s}\right]\bar{\theta}_{q_2}\bar{\theta}_{q_1}\right\} = -s\left[\overline{T}_2 - \frac{T_{2i}}{s}\right]\bar{\theta}_{q_2} \tag{15}$$

where $\bar{\theta}_{q_i} = k_i/(\alpha_i s)^{1/2}$.

Factoring out common terms and letting $T_{1i} = T_0$ and $T_{2i} = 0$ gives

$$\overline{T}_2 = \frac{T_0}{s}\left[\frac{k_1}{\sqrt{\alpha_1 s}}\right] \Big/ \left[\frac{k_1}{\sqrt{\alpha_1 s}} + \frac{k_1k_2}{h\sqrt{\alpha_1\alpha_2}} + \frac{k_2}{\sqrt{\alpha_2 s}}\right] = \frac{T_0h}{\sqrt{k_2\rho_2c_2}} \cdot \frac{1}{s(s^{1/2} + bh)} \tag{16a}$$

$$b = [(k_1\rho_1c_1)^{-1/2} + (k_2\rho_2c_2)^{-1/2}] \tag{16b}$$

Taking the inverse Laplace transform of (16a) yields the desired exact interface temperature of

$$T_2(0, t) = \frac{T_0[1 - e^{h^2b^2t}\text{erfc}(hb\sqrt{t})]}{[1 + \beta]} \tag{17}$$

where β is defined in (12b) [15].

Interior temperatures can now be found by introducing the expression given by (17) into a Duhamel's integral similar to (1) with $\theta(x, t)$ given by (5). The heat flux across the interface can be found by using (17) in Duhamel's integral similar to (2).

Heat Flux Based USE

The heat flux based USE method is developed in a similar manner as the temperature based method. Let a portion of body 1 be subjected to a time-variable heat flux. No spatial variation of heat flux is permitted. All other surfaces are either insulated or held isothermal at the initial temperature. Let the temperature rise at position $\mathbf{x}$ in body 1 due to unit step increase in heat flux q at the surface be denoted $\phi_1(\mathbf{x}, t)$, then it can be shown at position $\mathbf{x}$ and time t that the temperature for a time-variable heat flux $q(t)$ is

$$T_1(\mathbf{x}, t) = T_{1i} + \frac{\partial}{\partial t}\int_0^t q(\lambda)\phi_1(\mathbf{x}, t - \lambda)d\lambda \tag{18}$$

where $q(t)$ is an arbitrary heat flux which is non-zero only for $t \geq 0$.

Suppose that a second body, body 2, is initially at temperature T_{2i} and is suddenly brought into either perfect or imperfect contact with body 1. The same heat flux that *enters* body 1 then *leaves* body 2 so that the temperature at any location $\mathbf{x}$ in body 2 and time t is then

$$T_2(\mathbf{x}, t) = T_{2i} - \frac{\partial}{\partial t}\int_0^t q(\lambda)\phi_2(\mathbf{x}, t - \lambda)d\lambda \tag{19}$$

where $\phi_2(\mathbf{x}, t)$ is the temperature rise in body 2 at position $\mathbf{x}$ and time t due to a unit step increase in q starting at time zero.

The assumption of a spatially uniform heat flux is not always compatible with a spatially uniform temperature. The statement in terms of an average heat flux given by (4) is always true, however.

For the special geometry of two semi-infinite bodies coming into uniform contact over the complete interface, the interface temperatures are not functions of position. The kernel $\phi_i(\mathbf{x}, t)$ is a function of a single space dimension and time [15],

$$\phi_i(x, t) = \frac{2t^{1/2}}{(k_i\rho_ic_i)^{1/2}}\text{ierfc}\left[\frac{x}{2(\alpha_i t)^{1/2}}\right] \tag{20}$$

where x is directed inward in each body and the i subscript is 1 or 2. At the surface of the body, $x = 0$ and $\text{ierfc}(0) = \pi^{-1/2}$.

Consider first the case of perfect contact for which the interface temperature must be the same for both bodies. Equating (18) and (19) with $T_{1i} = T_0$ and $T_{2i} = 0$ at $x = 0$ yields

$$T_0 + \frac{\partial}{\partial t}\int_0^t q(\lambda)\frac{2(t - \lambda)^{1/2}d\lambda}{(\pi k_1\rho_1c_1)^{1/2}} = -\frac{\partial}{\partial t}\int_0^t q(\lambda)\frac{2(t - \lambda)^{1/2}d\lambda}{(\pi k_2\rho_2c_2)^{1/2}} \tag{21}$$

which can be re-arranged to the form

$$\frac{\partial}{\partial t}\int_0^t q(\lambda)2b\pi^{-1/2}(t - \lambda)^{1/2}d\lambda = -T_0 \tag{22}$$

This is again a Volterra integral equation of the first kind and can be solved for $q(t)$ using the numerical methods in [16]. For this simple case the solution can be obtained as above by utilizing the Laplace transform to obtain

$$q(t) = -T_0b^{-1}(\pi t)^{-1/2} \tag{23}$$

Utilizing (20) (with $x = 0$) and (23) in (18) yields

$$T_1(0, t) = T_0(1 + \beta)^{-1} \tag{24}$$

which is the same as (12) which was derived using the temperature form of Duhamel's theorem.

A comparison of the above procedures for the T and q based USE methods for the perfect contact example considered shows both methods yield a Volterra integral equation of the first kind. In the temperature case the solution is for the interface temperature while in the heat flux USE case the solution is for $q(t)$.

Next for the q-based USE method consider the imperfect contact case. Equation (13) still applies but utilizing (18, 19) and (20) yields

$$-T_0 - \frac{q(t)}{h} = \frac{2b}{\sqrt{\pi}}\frac{\partial}{\partial t}\int_0^t q(\lambda)(t - \lambda)^{1/2}d\lambda \tag{25}$$

This is called a Volterra integral equation of the second kind since $q(t)$ appears both inside and outside the integral. Equation (25) is simpler than the comparable T-based equation given by (14) which has a double integral. A solution of (25) for $q(t)$ utilizing the Laplace transform is

$$q(t) = -hT_0e^{h^2b^2t}\text{erfc}(hbt^{1/2}) \tag{26}$$

where b is defined by (16b) [15]. If h goes to infinity, (26) reduces to (23). To obtain the surface temperatures, the Laplace transform of $q(t)$ obtained from (25) is used with the Laplace transform of (18) or (19).

From a comparison of the T and q based USE integral equations of (14) and (25), the q-based equation has a simpler form and poses less difficulty in numerical solution (which might be required for more

complex geometries). Furthermore the q-based equation, (25), is derived in a more straightforward manner.

Intrinsic Thermocouple Example

In the previous sections, the USE method was applied to problems for which exact solutions are available. An application for which no exact solution exists for the entire time domain is the intrinsic thermocouple problem. Some T-based and q-based solutions are given for early and late times that are relatively simple and agree surprisingly well.

The geometry for the intrinsic thermocouple problem is that of a semi-infinite cylinder attached to a semi-infinite body as shown in Fig. 1(b). At zero time the semi-infinite body is at T_0 while the initial temperature of the cylinder is zero. The interface temperature and heat flux are both functions of time and also position. In this paper, however, only the *average* spatial temperature and heat flux is considered. The two methods complement one another. In the temperature based analysis the temperature is uniform over the interface but that implies that the heat flux varies spatially. The q-based analysis has a spatially uniform q but space variable T. When there is a spatial variation the average is utilized. A more rigorous treatment of the problem would use several interface nodes with the q-based method; a paper on this subject will be written in the future.

Temperature Based Solution. The temperature based USE method starts with (7) with body 1 being the half space and body 2 being the semi-infinite cylinder. Let the equation be integrated over t to eliminate the derivatives and let the time be made dimensionless,

$$t^\star \equiv \alpha_1 t/a^2 \tag{27}$$

which is based on the thermal diffusivity of body 1.

From a third order integral solution [17], an early time approximation for $\theta_{q_1}(t)$ is

$$\theta_{q_1}(t) = k_1(a\pi)^{-1}[1.9048(t^\star)^{-1/2} + 1 - 3\sum_{n=1}^{\infty}(-1)^n(t^{\star 1/2}/0.63495)^n] \tag{28}$$

which is valid for $t^\star < 0.05$. From a solution by Norminton and Blackwell [18], a late time approximation is

$$\theta_{q_1}(t) = k_1(a\pi)^{-1}[1.4367(t^\star)^{-1/2} + 4] \tag{29}$$

Comparison with other analyses indicates that (29) is a good approximation for $t^\star > 0.1$ [18–21]. The coefficients of (28) are approximate as $t^\star \to 0$ while the coefficients of (29) are exact as $t^\star \to \infty$.

For the assumption of a spatially-uniform unit step increase in surface temperature at the end of a semi-infinite cylinder, an *exact* expression for $\theta_{q_2}(t)$ can be given and it is valid for all times; it is the same as (6) and in terms of $t^\star$ is [15]

$$\bar{\theta}_{q_2}(t) = -k_1\beta[a(\pi t^\star)^{1/2}]^{-1} \tag{30}$$

where β is defined by (12b).

Then from (7) one can get

$$[\overline{T}(0,s) - T_0 s^{-1}]\bar{\theta}_{q_1}(s) = \overline{T}(0,s)\bar{\theta}_{q_2}(s) \tag{31a}$$

or

$$\overline{T}(0,s) = \frac{T_0}{s}\frac{\bar{\theta}_{q_1}(s)}{\bar{\theta}_{q_1}(s) - \bar{\theta}_{q_2}(s)} \tag{31b}$$

using either (28) or (29) for θ_{q_1}.

This relation can be used to obtain a solution for $T(0,t)$ in terms of a power series in $(t^\star)^{1/2}$. However, if just two terms are used, then an analytical solution is possible. If the coefficients of θ_{q_1} are A_1 and A_2 then (31b) becomes

$$\overline{T}(0,s) = T_0\left[\frac{1}{s} - \frac{\beta\pi}{A_2 s^{1/2}} + \frac{\beta\pi^{3/2}(A_1 + \beta\pi^{1/2})}{A_2[(A_1 + \beta\pi^{1/2})(\pi s)^{1/2} + A_2]}\right] \tag{32}$$

Taking the inverse transform of (32) yields for the interface temperature,

$$\frac{T(0,t)}{T_0} = 1 - \frac{\beta(\pi)^{1/2}}{A_1 + \beta\pi^{1/2}} e^{C^2 t^\star}\,\mathrm{erfc}[C(t^\star)^{1/2}] \tag{33a}$$

$$C = A_2(A_1 + \beta\pi^{1/2})^{-1}\pi^{-1/2} \tag{33b}$$

It is rather remarkable that both the short and large time expressions have the same form for the temperature based USE method for the intrinsic thermocouple problem. For early and late times, however, approximations of (33) give different behavior; for early times one finds

$$\frac{T(0,t)}{T_0} \approx \frac{1.90484}{D} + \frac{2\beta(\pi t^\star)^{1/2}}{\pi D^2} \tag{34a}$$

$$D = 1.90484 + \beta\pi^{1/2} \tag{34b}$$

and for late times ($t^\star > 50$)

$$\frac{T(0,t)}{T_0} \approx 1 - \frac{\pi\beta}{4}\left(\frac{1}{\pi t^\star}\right)^{1/2} + \frac{\beta(A_1 + \beta\pi^{1/2})^2}{2}\left(\frac{\pi}{16t^\star}\right)^{3/2} \tag{34c}$$

$$A_1 = 1.43670$$

Hence for very early times ($t^\star < 0.001$) the interface temperature is the constant term of $1.90484/D$ plus a term that is proportional to $(t^\star)^{1/2}$. For late times the solution converges to 1 from below as $(t^\star)^{-1/2}$.

Heat Flux Based Solution. The heat flux based USE method starts with a generalization of (21)

$$T(0,t) = T_0 + \frac{\partial}{\partial t}\int_0^t q(\lambda)\phi_1(0, t-\lambda)d\lambda = -\frac{\partial}{\partial t}\int_0^t q(\lambda)\phi_2(0, t-\lambda)d\lambda \tag{35}$$

which can be used to obtain

$$q(t) = -L^{-1}\left\{\frac{T_0 s^{-2}}{\bar{\phi}_1(0,s) + \bar{\phi}_2(0,s)}\right\} \tag{36}$$

The interface temperature, $T(0,t)$, can then be found by introducing (36) into (35) to get

$$T(0,t) = \frac{\partial}{\partial t}\int_0^t L^{-1}\left\{\frac{T_0 s^{-2}}{\bar{\phi}_1(0,s) + \bar{\phi}_2(0,s)}\right\}\Bigg|_{t=\lambda}\phi_2(0, t-\lambda)d\lambda \tag{37}$$

Now take the Laplace transform of (37) and then the inverse transform to yield

$$\frac{T(0,t)}{T_0} = L^{-1}\left\{\frac{s^{-1}\bar{\phi}_2(0,s)}{\bar{\phi}_1(0,s) + \bar{\phi}_2(0,s)}\right\} \tag{38}$$

The early time and late time behavior for the q-based USE method can be obtained from (38) by using the early and late time expressions for $\phi_1(0,t)$ which are [22]

$$\phi_1(0,t) = \frac{a}{k_1}\left[2\left(\frac{t^\star}{\pi}\right)^{1/2} - \frac{2}{\pi}t^\star\right], \quad t^\star < 0.1 \tag{39a}$$

$$\phi_1(0,t) = \frac{a}{k_1}\left[\frac{8}{3\pi} - \frac{1}{2(\pi t^\star)^{1/2}}\right], \quad t^\star > 10 \tag{39b}$$

which are quite unlike (28) and (29) utilized in the T-based USE method. These expressions are the exact expressions obtained for the limiting cases. The ϕ_2 expression found from (20) evaluated at $x = 0$ is

$$\phi_2(0,t) = \frac{2a\beta^{-1}}{k_1}\left(\frac{t^\star}{\pi}\right)^{1/2} \tag{40}$$

Then the solution of (38) for the early times is

$$\frac{T(0,t)}{T_0} = \frac{1}{1+\beta}\left[1 + \mathrm{erf}\left\{\frac{2\beta(t^\star)^{1/2}}{\pi(1+\beta)}\right\}\right]\exp\left[\frac{4\beta^2 t^\star}{\pi^2(1+\beta)^2}\right] \tag{41a}$$

$$\approx \frac{1}{1+\beta} + \frac{4\beta}{\pi^{3/2}}\frac{(t^\star)^{1/2}}{(1+\beta)^2} + \frac{4}{\pi^2}\frac{\beta^2 t^\star}{(1+\beta)^3}, \quad t^\star < 0.1 \tag{41b}$$

To get a convenient expression for the large times the second term

of (39b) is neglected (it is also less significant); the result is

$$\frac{T(0,t)}{T_0} = 1 - \exp\left[\left(\frac{3\pi}{8\beta}\right)^2 t^\star\right] \operatorname{erfc}\left(\frac{3\pi}{8\beta}(t^\star)^{1/2}\right) \qquad (42a)$$

$$\approx 1 - \frac{8\beta}{3\pi}\frac{1}{(\pi t^\star)^{1/2}}, \quad t^\star > 100 \qquad (42b)$$

Comparison of the Intrinsic Thermocouple Results

All four solutions for the intrinsic thermocouple problem were evaluated for $\beta = 4/3$ which approximates a half-space of chromel alloy and a cylinder of alumel alloy. The results of this evaluation are given in Fig. 4 and Table 1 along with results from two finite difference solutions [1, 13]. As can be seen, there is excellent agreement between the various models in their overlapping areas of validity.

Notice that both early time solutions, (34a) and (41b), have the same form of a constant plus a $(t^\star)^{1/2}$ term. For $t^\star$ going to zero, the solution should approach that for two semi-infinite bodies given by (12a) which is $(1 + \beta)^{-1}$. The q-based solution does approach this value but the T-based solution does not. The reason for this is that the q-based solution utilizes (39a) which is the first two terms of the exact solution while the T-based solution employs (28) which comes from an approximate integral analysis [17]. Since the q-based solution approaches the exact solution for $t^\star \to 0$, it should be more accurate for the early times.

For the late times the results are again very similar; compare (34c) and (42b) with the $(\pi t^\star)^{-1/2}$ coefficients of

$$-\frac{\pi\beta}{4} = -0.7854\beta \text{ and } -\frac{8\beta}{3\pi} = -0.8488\beta$$

which differ only by 8 percent and have the same sign and linear dependence on β. For late times, the T-based solution is believed to be more accurate because the constant interface temperature assumption is expected to be better than the constant heat flux assumption for $t^\star \to \infty$.

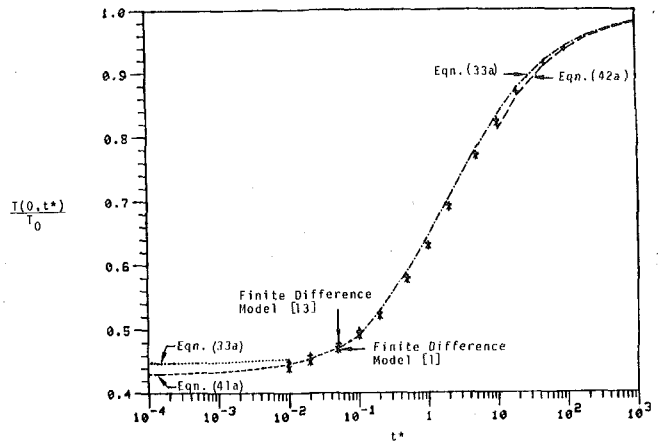

Fig. 4 Interface temperature histories, $\beta = 4/3$

Summary and Conclusions

The unsteady surface element method can be useful for problems of transient heat transfer between bodies of similar or dissimilar geometry. Starting from fundamental solutions for each region and then matching the interface boundary conditions on a global basis, a convolution equation can be developed for the time dependent interface conditions. The fundamental solutions, for a step change in either temperature of heat flux, maybe either exact or approximate; the convolution equation can be evaluated using well-developed techniques for integral equations or in some cases analytical solutions are possible.

The USE method is best suited for determining the temperature and heat flow at the interface between regions. In many applications, these are the main parameters of interest. If required, the conditions at interior points can be obtained by evaluating a convolution equation. The accuracy of the solutions is limited only by the accuracy of the fundamental solutions and the errors introduced by incomplete matching of the interface conditions.

In the present paper, the examples which use exact fundamental solutions and which match the interface conditions exactly result in solutions which are identical to classical solutions. The intrinsic thermocouple problem is used as an example in which the interface conditions are matched only on a global basis. There is a very good agreement between the temperature and heat flux USE solutions and previous numerical results.

Acknowledgments

This research was sponsored by Sandia National Laboratories which is funded by the Department of Energy and by the National Science Foundation under Grant No. CME 79-20103.

References

1 Keltner, N. R., "Heat Transfer in Intrinsic Thermocouples—Application to Transient Temperature Measurement Errors," Research Report SC-RR-72 0719, Sandia Laboratories, Albuquerque, N.M., Jan. 1973.

2 Keltner, N.R., "Quasi-Coupling—An Approximate Solution Method for Interface Conditions in Two Region Transient Heat Conduction Problems," ASME Paper No. 75-WA/HT-93.

3 Yovanovich, M.M., "Point Source Solutions" and "Surface Element

Table 1 Interface temperature histories, $\beta = 4/3$

	T-based USE Method		q-based USE Method		Finite Difference Models	
t^*	equation (33a)	equation (33a)	equation (41a)	equation (42a)	reference [1]	reference [13]
0	0.4463		0.4286			
0.00001	0.4466		0.4291			
0.0002	0.4475		0.4311			
0.001	0.4489		0.4342			
0.002	0.4500		0.4366			
0.005	0.4521		0.4413			
0.01	0.4545		0.4467		0.4402	0.4510
0.02			0.4546		0.4505	0.4599
0.05			0.4709		0.4700	0.4782
0.1		0.4907	0.4904		0.4916	0.4991
0.2		0.5280			0.5215	0.5283
0.5		0.5901			0.5770	0.5826
1.0		0.6452			0.6302	0.6338
2.0		0.7042			0.6896	0.6921
5.0		0.7810			0.7688	0.7714
10.0		0.8327		0.8091	0.8202	0.8246
20.0		0.8757		0.8614		0.8694
50.0		0.9186		0.9108		0.9139
100.0		0.9417		0.9365		0.9382
200.0		0.9585		0.9550		
500.0		0.9737		0.9715		

Method (SEM)—Outline," transparencies for a seminar at the University of Waterloo, Nov. 1976.

4 Cruse, T. A., and Rizzo, F. J., eds., *Boundary-Integral Equations Method: Computational Applications in Applied Mechanics*, ASME, New York, Applied Mechanics Division, June 1975.

5 Schneider, G. E., and LeDain, B. L., "Boundary Integral Equation Method and Corner Problem for Steady Heat Conduction," *Heat Transfer, Thermal Control and Heat Pipes*, Vol. 70, Progress in Astronautics and Aeronautics, W. B. Olstad, editor, American Institute of Aeronautics and Astronautics, 1980, pp. 63–76.

6 Khader, M. S., "Heat Conduction with Temperature Dependent Thermal Conductivity," ASME Paper No. 80-HT-4; presented at the ASME/AIChE National Heat Transfer Conference, Orlando, Fla., July 27–30, 1980.

7 Thaler, R. H., and Mueller, W. K., "A New Computational Method for Transient Heat Conduction in Arbitrarily Shapes Regions," in *Heat Transfer 1970*, Vol. 1, V. Grigull and E. Hahne, eds., Elsevier Publishing, Amsterdam, 1970, pp. Cu 1.6–1 to Cu 1.6-11.

8 Henning, C. D., and Parker, R., "Transient Response of an Intrinsic Thermocouple," ASME JOURNAL OF HEAT TRANSFER, Vol. 89, 1967, pp. 146–154.

9 Burnett, D. R., "Transient Measurement Errors in Heated Slabs for Thermocouples Located at an Insulated Surface," ASME JOURNAL OF HEAT TRANSFER, Vol. 83, 1961, pp. 505–506.

10 Larson, M. B., and Nelson, E., "Variables Affecting the Dynamic Response of Thermocouples Attached to Thin-Skinned Models," ASME JOURNAL OF HEAT TRANSFER, Vol. 91, 1969, pp. 166–168.

11 Wally, K., "The Transient Response of Beaded Thermocouples Modeled on the Surface of a Solid," Presented at the 23rd International Instrumentation Symposium, Las Vegas, Nev, May 1–5, 1977, Instrument Society of America.

12 Gat, U., Kammer, D. S., and Hahn, O. J., "The Effect of Temperature Dependent Properties Transients Measurement with Intrinsic Thermocouple," *International Journal of Heat and Mass Transfer*, Vol. 18, 1975, p. 1337.

13 Shewen, E. C., "A Transient Numerical Analysis of Conduction Between Contacting Circular Cylinders and Halfspaces Applied to a Biosensor," MS Thesis, University of Waterloo, 1976.

14 Keltner, N. R., and Bickle, L. W., "Intrinsic Thermocouple Measurement Errors," Paper No. 76-HI-65, ASME-AIChE Heat Transfer Conference, St. Louis, MO, Aug. 9–11, 1976.

15 Carslaw, H. S., and Jaeger, J. C., *Conduction of Heat in Solids*, Second ed., Oxford, 1959.

16 Beck, J. V., "Surface Heat Flux Determination Using an Integral Method," *Nuclear Engineering and Design*, Vol. 7, 1968, pp. 170–178.

17 Keltner, N. R., "Transient Heat Flow in a Half-Space Due to an Isothermal Disk on the Surface," ASME JOURNAL OF HEAT TRANSFER, Vol. 95, 1973, pp. 412–414.

18 Norminton, E. J. and Blackwell, J. H., "Transient Heat Flow from Constant Temperature Spheroids and the Thin Circular Disk," *Quarterly Journal Mechanical and Applied Mathematics*, Vol. 17, 1964, pp. 65–72.

19 Schneider, G. E., Strong, A. B., and Yovanovich, M. M., "Transient Heat Flow from a Thin Circular Disk," *Radiative Transfer and Thermal Control*, Vol. 49, Progress in Astronautics and Aeronautics, A. M. Smith, ed., Am. Inst. of Aero. & Astro., 1976, pp. 419–432.

20 Sadhal, S. S., "Transient Thermal Response of Two Solids in Contact Over a Circular Disk," *International Journal of Heat Mass Transfer*, Vol. 23, 1980, pp. 731–733.

21 Marder, B. M., and Keltner, N. R., "Heat Flow from a Disk by Separation of Variables," presented at 1981 SIAM Meeting, June 1981, Troy, NY.

22 Beck, J. V., "Average Transient Temperature Within a Semi-infinite Body Heated by a Disk Heat Source," *Heat Transfer, Thermal Control and Heat Pipes*, Vol. 70, Progress in Astronautics and Aeronautics, W. B. Olstad, ed., Am. Inst. of Aero. & Astro. 1980, pp. 3–24.

R. Siegel
Fellow ASME

A. Snyder
Lewis Research Center,
Cleveland, Ohio 44135

Heat Transfer in Cooled Porous Region with Curved Boundary

Heat transfer characteristics are analyzed for a cooled two-dimensional porous medium having a curved boundary. A general analytical procedure is given in combination with a numerical conformal mapping method used to transform the porous region into an upper half plane. To illustrate the method, results are evaluated for a cosine shaped boundary subjected to uniform external heating. The results show the effects of coolant starvation in the thick regions of the medium, and the extent that internal heat conduction causes the heated surface to have a more uniform temperature.

Introduction

Transpiration is an efficient cooling technique wherein very good thermal contact is obtained between a coolant and a metallic medium being cooled. The metal is fabricated in a porous form and coolant from a reservoir is forced through so that it exits at the boundary exposed to the heat load. For localized cooling applications and for structural strength, the porous region can be an insert in an otherwise solid wall; the heat transfer performance of such an insert will be studied here.

The present study deals with regions having a curved boundary exposed to external heating, and is a further development of the analyses in [1] and [2] combined with a generalized conformal mapping method from [3] and [4]. The flow is by forced convection and is governed by Darcy's law stating that the local fluid velocity depends on the local pressure gradient. Consequently in dimensionless form the pressure becomes the velocity potential. The inlet and outlet porous boundaries are each at constant pressure which is valid when the pressure drop through the medium is large compared with changes along the boundaries. The effect of nonuniform pressure can be estimated by use of [5]. The other two boundaries are joined to the solid wall and have no flow across them, (see Fig. 1). As a result of these conditions the porous region transforms into a rectangle in terms of velocity potential and flow direction coordinates. The streamlines are parallel straight lines in the transformed region in contrast to being complicated functions of position in the physical geometry.

The simple streamline distribution in the potential coordinate system leads to a simplified form of the energy equation transformed into this system, and a general solution is obtained by separation of variables [1]. After the solution is found, it is mapped back into the physical plane by adapting a generalized Schwarz-Christoffel method from [3] and [4]. The final results are the velocities and temperatures at the curved boundary of the porous material exposed to external heating.

Analytical Procedure

The porous cooled region is shown in Fig. 1; it can be an insert in a solid wall. The region has three straight sides, and one curved boundary that is exposed to a heat loading q_s along its length. The coolant flows out through the curved boundary. The two side boundaries are assumed insulated, and one or both of the side boundaries could be symmetry lines if the thickness variation of the porous region along the x-direction is symmetric or periodic about specific x values.

The curved surface is at pressure p_s, and the coolant reservoir is at p_∞. The flow resistance of the medium is large enough that $p_\infty - p_s$ is much greater than any pressure variations along the boundaries. The coolant velocities are low so the surface exposed to the reservoir is essentially at p_∞. The porous region has an effective thermal conductivity k_m based on the actual cross-sectional area of the porous material including both solid and pore areas. The k_m is assumed large compared with the coolant conductivity so that heat conduction in the coolant is not a consideration (if necessary a volume weighted conductivity could be defined to approximately account for coolant conductivity).

The quantity $\mathbf{v}(z)$ is the Darcy velocity of the fluid, which is the local volume flow rate divided by the local cross-sectional area including both solid and pore areas. Then the continuity equation, Darcy's law, and the energy equation are (for incompressible flow and the coolant and solid in local thermal equilibrium),

$$\nabla \cdot \mathbf{v} = 0 \tag{1}$$

$$\mathbf{v} = -\frac{\kappa}{\mu}\nabla \mathrm{p} \tag{2}$$

$$k_m \nabla^2 t - \rho c_p \mathbf{v} \cdot \nabla t = 0 \tag{3}$$

Along the curved surface there is imposed an arbitrary heat flux variation $q_s(z_s)$ giving the boundary conditions:

$$\left.\begin{aligned} p &= p_s = \text{constant} \\ k_m \mathbf{n}_s \cdot \nabla t &= q_s(z_s) = q_1 + (q_2 - q_1)F(z_s) \end{aligned}\right\} \quad \text{for } x, y \text{ on } s \tag{4}$$

As the fluid at t_∞ approaches s_0 its temperature rises within a thin region to $t_0(x_0)$ in essentially a locally one-dimensional fashion, so that along s_0:

$$\left.\begin{aligned} p &= p_0 = \text{constant} \\ k_m \mathbf{n}_0 \cdot \nabla t &= \rho c_p (t - t_\infty)\mathbf{n}_0 \cdot \mathbf{v} \end{aligned}\right\} \quad \text{for } x, y \text{ on } s_0 \tag{5}$$

In dimensionless form, equation (2) becomes,

$$\mathbf{V} = \tilde{\nabla}\phi \tag{6}$$

so that $\phi(Z)$ is a velocity potential. Using equation (6) to eliminate $\mathbf{v}$ in (1) yields

$$\tilde{\nabla}^2 \phi = 0 \tag{7}$$

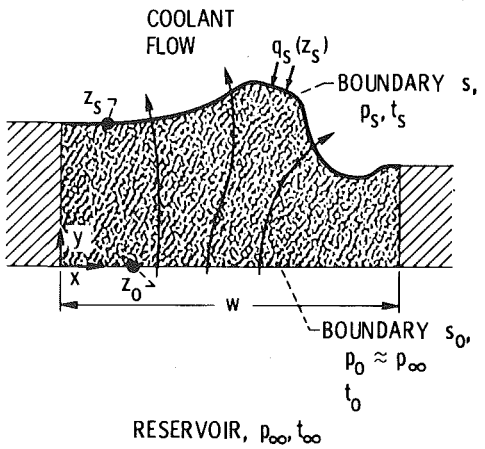

Fig. 1 Transpiration cooled two-dimensional porous region

Contributed by the Heat Transfer Division for publication in the JOURNAL OF HEAT TRANSFER. Manuscript received by the Heat Transfer Division November 17, 1980.

so that the potential can be found by solving Laplace's equation in the porous region. After eliminating **v** equation (3) becomes

$$\tilde{\nabla}^2 T - 2\Lambda \tilde{\nabla}\phi \cdot \tilde{\nabla} T = 0 \tag{8}$$

From (4) and (5), the dimensionless boundary conditions are:

$$\phi = \phi_s;\ \mathbf{n}_s \cdot \tilde{\nabla} T = 1 + \left(\frac{q_2 - q_1}{q_1}\right) F(Z_s) \quad \text{for } X, Y \text{ on } S \tag{9}$$

$$\phi = 0;\ \mathbf{n}_0 \cdot \tilde{\nabla} T = 2\Lambda T \mathbf{n}_0 \cdot \mathbf{V} \quad \text{for } X, Y \text{ on } S_0 \tag{10}$$

Since ϕ is constant on both S and S_0, the normal to these surfaces is normal to the constant ϕ lines, and the unit normal vectors are:

$$\mathbf{n}_s = \tilde{\nabla}\phi / |\tilde{\nabla}\phi| \quad \text{for } X, Y \text{ on } S \tag{11}$$

$$\mathbf{n}_0 = -\tilde{\nabla}\phi / |\tilde{\nabla}\phi| \quad \text{for } X, Y \text{ on } S_0 \tag{12}$$

Using equation (6) to eliminate **V**, and (11) and (12) to eliminate the **n**, the boundary conditions (9) and (10) become

$$\left.\begin{aligned} &\phi = \phi_s = \text{constant} \\ &\tilde{\nabla}\phi \cdot \tilde{\nabla} T = |\tilde{\nabla}\phi| \left[1 + \left(\frac{q_2 - q_1}{q_1}\right) F(Z_s)\right] \end{aligned}\right\} \quad \text{for } X, Y \text{ on } S \tag{13}$$

$$\left.\begin{aligned} &\phi = 0 \\ &\tilde{\nabla}\phi \cdot \tilde{\nabla} T = 2\Lambda T |\tilde{\nabla}\phi|^2 \end{aligned}\right\} \quad \text{for } X, Y \text{ on } S_0 \tag{14}$$

Equations (8, 13) and (14) show that T is related to ϕ, where $\phi(X, Y)$ can be found by solving equation (7).

Potential Plane Coordinates and Solution. Since ϕ satisfies Laplace's equation it can be considered as part of an analytic function $W = \psi + i\phi$ of a complex variable $Z = X + iY$. In the potential plane the porous region, Fig. 2(*a*), maps into a rectangle bounded on two sides by $\phi = 0$ and ϕ_s. The lines of constant ψ are normal to the ϕ lines, Fig. 2(*b*). Along S_0 the velocity in the Y direction is $V = \partial\phi/\partial Y$, and from the Cauchy-Riemann equations this is equal to $\partial\psi/\partial X$. The width of the rectangle in Fig. 2(*b*) is then,

$$\psi_2 - \psi_1 = \int_{X_1}^{X_2} V(X_0)\, dX_0 = \frac{\mu}{\kappa}\frac{\phi_s}{p_\infty - p_s}\int_{x_0=0}^{x_0=w} v(x_0)\, dx_0 = \frac{\mu}{\kappa}\frac{\phi_s}{p_\infty - p_s} G_f$$

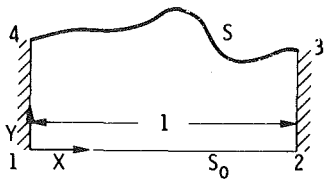

Fig. 2(*a*) Dimensionless physical plane, $Z = X + iY$

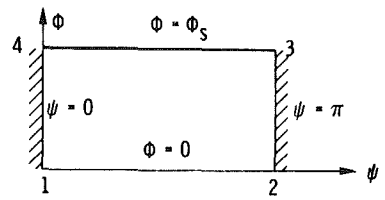

Fig. 2(*b*) Complex potential plane, $W = \psi + i\phi$

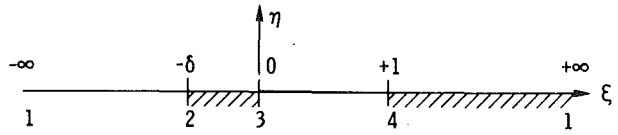

Fig. 2(*c*) Upper half-plane, $\tau = \xi + i\eta$

Fig. 2 Mapping planes for porous region

Using the relation $\phi_s = (p_\infty - p_s)\,(\kappa/\mu)\,(\pi/G_f)$ gives $\psi_2 - \psi_1 = \pi$ so that the width of the rectangle is π in Fig. 2(*b*). The value of ϕ_s is obtained during the solution thereby yielding the flow rate G_f for a given geometry.

The energy equation and boundary conditions are transformed into the coordinates of the rectangle in the W-plane so that ϕ and ψ become the independent variables. An analytical solution for the temperature distribution is obtained in terms of ϕ and ψ, and the temperature distribution in the physical plane is then found by conformally mapping into the physical plane, a valid procedure since ϕ and ψ are governed by Laplace's equation. The mapping is done by a generalized Schwarz-Christoffel transformation.

Nomenclature

A_n = Fourier coefficients defined in equation (19*b*)
C_1, C_2, C_3 = integration constants
C_{1n}, C_{2n}, C_{3n} = coefficients in polynomial, equation (24)
c_p = specific heat of coolant fluid
F = function specifying surface heat flux distribution, $F(x_s = 0) = 0$ and $F(x_s = w) = 1$; elliptic integral of the first kind
G_f = total volume flow rate of coolant
h_1, h_2 = heights of sides of porous region, $H = h/w$
K = complete elliptic integral of the first kind
k = modulus of elliptic integral, $k' = \sqrt{1 - k^2}$
k_m = effective thermal conductivity of porous material
n = integer
n = outward normal vector
p = static pressure of fluid
q = heat flux, $q_1 = q_s(x_s = 0)$, $q_2 = q_s(x_s = w)$
s_0, s = coolant inlet and exit boundaries; $S_0 = \frac{s_0}{w}$, $S = \frac{s}{w}$
T = dimensionless temperature $\frac{t - t_\infty}{q_1 w/k_m}$
t = temperature; t_∞ reservoir temperature
V, **v** = Darcy velocities of coolant, **V** is dimensionless quantity $\frac{\mu w \phi_s}{\kappa(p_\infty - p_s)}\mathbf{v} = \frac{\pi w}{G_f}\mathbf{v}$; $\mathbf{V} = U + iV$
W = complex potential, $\psi + i\phi$
w = width of porous region
Z = dimensionless physical plane $X + iY$; $X = \frac{x}{w}$, $Y = \frac{y}{w}$
z = complex variable $x + iy$; z_s is along curved boundary
α = angles at corners of porous region, Fig. 3
β = turning angles along curved boundary, Fig. 3
γ_n = the quantity $\sqrt{\Lambda^2 + n^2}$
δ = length in τ-plane corresponding to one side of porous region
θ = dependent variable defined in equation (15); angle in Fig. 3
κ = permeability of porous material
Λ = parameter, λ/ϕ_s
λ = flow/heat conduction parameter, $\frac{\rho c_p}{2k_m}\frac{\kappa(p_\infty - p_s)}{\mu}$
μ = fluid viscosity
ξ = real axis in τ-plane
ρ = fluid density
τ = intermediate mapping variable, $\xi + i\eta$
ϕ = potential function, $\phi = (p_\infty - p)\frac{\kappa}{\mu}\frac{\pi}{G_f}$ (for ϕ_s, $p = p_s$)
ψ = real part of W
$\nabla = \mathbf{i}\frac{\partial}{\partial x} + \mathbf{j}\frac{\partial}{\partial y}$; $\tilde{\nabla} = \mathbf{i}\frac{\partial}{\partial X} + \mathbf{j}\frac{\partial}{\partial Y}$

Subscripts

0 = boundary adjacent to reservoir
s = coolant exit boundary
∞ = coolant reservoir

From [1] and [2] the energy equation transforms to

$$\frac{\partial^2\theta}{\partial\psi^2}+\frac{\partial^2\theta}{\partial\phi^2}-\Lambda^2\theta=0 \quad \text{for } 0\le\phi\le\phi_s, 0\le\psi\le\pi \tag{15}$$

where

$$\theta(\phi,\psi)=e^{\Lambda(\phi_s-\phi)}\,T(\phi,\psi) \tag{15a}$$

The boundary conditions (9) and (10) become

$$\frac{\partial\theta}{\partial\phi}+\Lambda\theta=\left|\frac{dZ}{dW}\right|\left\{1+\left(\frac{q_2-q_1}{q_1}\right)F[Z_s(\psi)]\right\} \quad \text{for } \phi=\phi_s, 0\le\psi\le\pi \tag{16}$$

$$\frac{\partial\theta}{\partial\phi}-\Lambda\theta=0 \quad \text{for } \phi=0, 0\le\psi\le\pi \tag{17}$$

At the remaining two sides there is the condition of zero heat flow so that

$$\frac{\partial\theta}{\partial\psi}=0 \quad \text{for } 0\le\phi\le\phi_s, \psi=0 \text{ and } \psi=\pi \tag{18}$$

By separation of variables the solution to (15), subject to (16) to (18), is

$$\theta(\phi,\psi)=\sum_{n=-\infty}^{\infty}A_n \times\left[\frac{\Lambda\sinh\gamma_n\phi+\gamma_n\cosh\gamma_n\phi}{(\gamma_n{}^2+\Lambda^2)\sinh\gamma_n\phi_s+2\Lambda\gamma_n\cosh\gamma_n\phi_s}\right]\cos(n\psi) \tag{19a}$$

where

$$A_n=\frac{1}{\pi}\int_{\psi=0}^{\pi}\left|\frac{dZ}{d\psi}\right|_{\phi_s}\left\{1+\frac{q_2-q_1}{q_1}F[Z_s(\psi)]\right\}\cos(n\psi)\,d\psi \quad n=0,\pm1,\pm2,\ldots \tag{19b}$$

The value of ϕ_s and the relation between ϕ,ψ and X, Y are found by conformal mapping between the regions in Figs. 2(a) and (b).

The dimensionless local velocity in the porous material is given by $\mathbf{V}=\tilde{\nabla}\phi$. The exit surface is at constant ϕ and the exit velocity is normal to it. Then the magnitude of the exit velocity is given by

$$|\mathbf{V}|_{\phi_s}=|\tilde{\nabla}\phi\cdot\mathbf{n}|_{\phi_s}=\left|\frac{\tilde{\nabla}\phi\cdot\tilde{\nabla}\phi}{|\tilde{\nabla}\phi|}\right|_{\phi_s}=\left|\frac{|\tilde{\nabla}\phi|^2}{|\tilde{\nabla}\phi|}\right|_{\phi_s} =|\tilde{\nabla}\phi|_{\phi_s}=\left|\left[\left(\frac{\partial\phi}{\partial X}\right)^2+\left(\frac{\partial\phi}{\partial Y}\right)^2\right]^{1/2}\right|_{\phi_s}$$

But $dW/dZ=\partial\phi/\partial X+i\,\partial\psi/\partial X=\partial\phi/\partial X-i\,\partial\phi/\partial Y$. Hence $|\mathbf{V}|_{\phi_s}=|dW/dZ|_{\phi_s}$ which yields

$$\frac{\mu w|\mathbf{v}(\phi_s,\psi)|}{\kappa(p_\infty-p_s)}=\frac{|\mathbf{V}(\phi_s,\psi)|}{\phi_s}=\frac{1}{\phi_s}\left|\frac{dW}{dZ}\right|_{\phi_s}=\frac{1}{\phi_s}\left|\frac{d\psi}{dZ}\right|_{\phi_s} \tag{20}$$

Thus the exit velocity is determined from the same mapping relations that are in the expression for temperature, equation (19). The mapping from Fig. 2(b) to (a) is used to transform $|\mathbf{v}|$ into physical coordinates.

Conformal Mapping Relations. The required mapping is done in two parts. The rectangle in Fig. 2(b) is transformed into an upper half plane with the boundary along the ξ-axis as shown in Fig. 2(c). The physical region in the Z-plane, Fig. 2(a) is also mapped into the τ-plane; then the correspondence between the Z and W planes is known by means of the intermediate τ variable.

The mapping between W and τ can be done by a Schwarz-Christoffel transformation,

$$W=C_1\int_0^{\tau}\frac{d\tau}{\sqrt{(\tau+\delta)\tau(\tau-1)}}+C_2 \tag{21}$$

At $\tau=0$, $W=\pi+i\phi_s$ which gives $C_2=\pi+i\phi_s$. From the width of the rectangle

$$W_3-W_4=\pi=-\frac{C_1}{i}\int_0^{1}\frac{d\tau}{\sqrt{(\tau+\delta)\tau(1-\tau)}}$$

This is an elliptic integral [6], and its evaluation yields, $C_1=-i\pi/2kK(k)$ where $k=(1+\delta)^{-1/2}$.

The height of the rectangle ϕ_s maps into the length δ in the τ-plane and the relation is needed between ϕ_s and δ. The value of δ is found by mapping the geometry of the Z-plane into the τ-plane as will be discussed in the next section. Using the C_1, equation (21) yields

$$W_3-W_2=i\phi_s=-\frac{i\pi}{2kK(k)}\int_{-\delta}^{0}\frac{d\tau}{\sqrt{(\tau+\delta)\tau(\tau-1)}} =\frac{i\pi}{2kK(k)}\frac{2}{\sqrt{1+\delta}}K(k')$$

so that ϕ_s and δ are related by

$$\frac{\phi_s}{\pi}=\frac{K(k')}{K(k)} \quad \text{where } k=(1+\delta)^{-1/2} \text{ and } k'=\sqrt{1-k^2} \tag{22}$$

When the value of δ is found, the ϕ_s can be calculated, which then gives the total volume flow rate through the porous region as $G_f=(1/\phi_s)[(p_\infty-p_s)\pi\kappa/\mu]$.

Figure 2(a) can be mapped into the τ-plane by using a generalization of the Schwarz-Christoffel transformation for curved boundaries. This is treated in [3] and [4] and is further adapted here. To consider briefly the development of the method, let the curved surface be divided into increments, Fig. 3(a), with a total of N points along arc 34. Treating the geometry as a many sided polygon, the Schwarz-Christoffel transformation is

$$\frac{dZ}{d\tau}=\frac{C_3}{\sqrt{(\tau+\delta)\tau(\tau-1)}\prod_N(\tau-\xi_n)^{\Delta\theta_n/\pi}}$$

where $\Delta\theta$ is the change of angle over each short segment along the curved boundary. This can be written as

$$\frac{dZ}{d\tau}=\frac{C_3}{\sqrt{(\tau+\delta)\tau(\tau-1)}}\exp\left[\ln\prod_{n=1}^{N}(\tau-\xi_n)^{-\Delta\theta_n/\pi}\right]$$

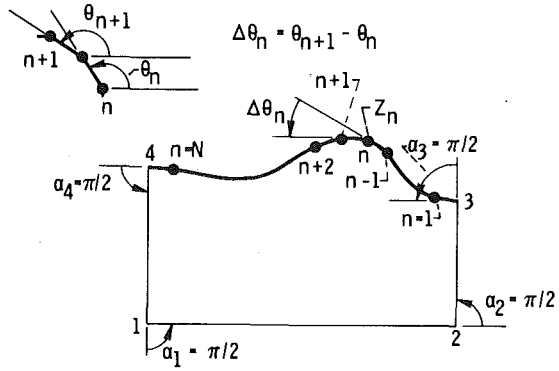

Fig. 3(a) Increments along curved boundary

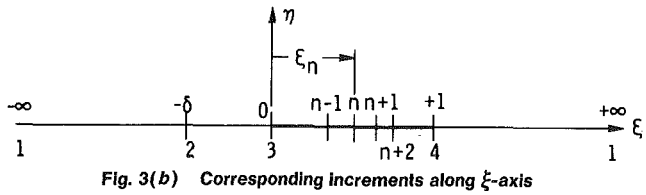

Fig. 3(b) Corresponding increments along ξ-axis

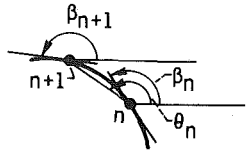

Fig. 3(c) Detail of angles β and θ

Fig. 3 Schwarz-Christoffel method for curved boundary

$$\frac{dZ}{d\tau} = \frac{C_3}{\sqrt{(\tau+\delta)\tau(\tau-1)}} \exp\left[-\frac{1}{\pi}\sum_{n=1}^{N} \Delta\theta_n \ln(\tau-\xi_n)\right]$$

The θ_n is a function of ξ_n, and for small changes in ξ_n there will be small changes in θ_n. Then using differential increments,

$$\frac{dZ}{d\tau} = \frac{C_3}{\sqrt{(\tau+\delta)\tau(\tau-1)}} \exp\left[-\frac{1}{\pi}\int_{\xi=0}^{1} \ln(\tau-\xi)\frac{d\theta}{d\xi}d\xi\right] \quad (23)$$

To define this mapping there are needed C_3, δ and θ as a function of ξ. Following [4], over a finite interval in ξ the angle β drawn to the local tangent to the boundary, Fig. 3(*c*), is approximated by a polynomial

$$\beta = C_{1n} + C_{2n}\xi + C_{3n}\xi^2 \quad (24)$$

For infinitesimal increments, $\beta \to \theta$ and the integral in (23) is then carried out to yield for the interval ξ_n to ξ_{n+1},

$$-\frac{1}{\pi}\int_{\xi_n}^{\xi_{n+1}} \ln(\tau-\xi)\frac{d\beta}{d\xi}d\xi = \ln[g_{2n}(\tau)^{-C_{2n}/\pi}\, g_{3n}(\tau)^{-C_{3n}/\pi}] \quad (25)$$

where

$$g_{2n}(\tau) = (\tau-\xi_n)^{\tau-\xi_n}\, e^{\xi_n}/(\tau-\xi_{n+1})^{\tau-\xi_{n+1}}\, e^{\xi_{n+1}}$$

$$g_{3n}(\tau) = (\tau-\xi_n)^{\tau^2-\xi_n{}^2}\, e^{(\tau+\phi q_n)^2/2}/(\tau-\xi_{n+1})^{\tau^2-\xi^2{}_{n+1}}\, e^{(\tau+\xi_{n+1})^2/2}$$

Adding all the incremental integrations from $\xi = 0$ to 1 gives a sum of logarithmic terms, or the log of a product. The exponential in (23) then yields a product of g_{2n} and g_{3n} terms, so that

$$\frac{dZ}{d\tau} = \frac{C_3}{\sqrt{(\tau+\delta)\tau(\tau-1)}} \prod_{n=1}^{N} g_{2n}{}^{-C_{2n}/\pi}\, g_{3n}{}^{-C_{3n}/\pi} \quad (26)$$

When dealing with a finite portion of the curved surface over which β varies as in equation (24), there is a β angle at each end of the increment and an average angle θ_n for a straight line connecting the end points, Fig. 3(*c*). By using equation (24) and the approximation that θ equals β at $(\xi_{n+1}+\xi_n)/2$, C_{2n} and C_{3n} are found for use in (25) as,

$$C_{3n} = 4\left(\frac{\beta_n+\beta_{n+1}}{2} - \theta_n\right)\Big/(\xi_{n+1}-\xi_n)^2 \quad (27a)$$

$$C_{2n} = \frac{\beta_{n+1}-\beta_n}{\xi_{n+1}-\xi_n} - (\xi_{n+1}+\xi_n)C_{3n} \quad (27b)$$

Note that the ξ_n and ξ_{n+1} in these expressions are unknown, and will be obtained in connection with integrating (26).

Integrating equation (26) along the real axis in the τ-plane should yield the shape of the physical geometry in the Z-plane. By using the ideas in [4], this integration can be performed to good accuracy by using,

$$Z_{n+1} - Z_n = \frac{8C_3}{(\xi_{n+1}-\xi_n)^2}\left[(\xi+\delta)^{1/2}\right]_{\xi_n}^{\xi_{n+1}}\left[\xi^{1/2}\right]_{\xi_n}^{\xi_{n+1}}\left[(\xi-1)^{1/2}\right]_{\xi_n}^{\xi_{n+1}} \prod_{n=1}^{N}\left(g_{2n}{}^{-C_{2n}/\pi}\, g_{3n}{}^{-C_{3n}/\pi}\right)_{(\xi_{n+1}+\xi_n)/2} \quad (28)$$

The C_3,δ, and ξ_n are found by iteration. Values of these quantities are guessed and (28) is used to integrate along the ξ axis to obtain Z values. These values are compared to the Z values in the physical plane and rotation and stretching are used to make the Z values be the same at the end point of the integration—this adjusts the C_3 which is a complex coefficient. Then the scaling factor required to adjust the length $Z_3 - Z_2$ from equation (28) to equal the physical arc length 23, is used to adjust δ to a new value. Similarly the $Z_{n+1} - Z_n$ is compared to the correct length of the nth increment on the curved boundary, and this is used to rescale the $\Delta\xi$. The rescaling is proportioned such that arc length 34 equals 1 along the ξ-axis. The new C_3,δ, and ξ_n are used for another iteration, and the process repeated until the integration of (28) correctly reproduces the physical geometry. The convergence was found to be very rapid.

All the quantities are now known in equation (26), and $k = (1+\delta)^{-1/2}$ is known since δ has been found. Combining (26) with the derivative of (21) yields,

$$\frac{dZ}{dW}(\xi) = \frac{dZ}{d\tau}\frac{d\tau}{dW} = \frac{iC_3}{\pi} 2kK(k) \prod_{n=1}^{N} g_{2n}{}^{-C_{2n}/\pi}\, g_{3n}{}^{-C_{3n}/\pi} \quad (29)$$

which can be used to find A_n from equation (19*b*), and $(|\mathbf{V}(\phi_s,\psi)|)/\phi_s$ from equation (20). Since these quantities are a function of ψ along ϕ_s, which corresponds to $0 \le \xi \le 1$, the relation between ψ and ξ is needed to obtain $(dZ/d\psi)|_{\phi_s}$. Quantities known in terms of $\psi(\phi_s)$ are also known in terms of Z_s since the mapping between ψ and Z_s is known from the final iteration of (28).

Along the interface, $\psi = \mathcal{R}eW$, $t = \xi$ and $0 \le \xi \le 1$. Then from equation (21)

$$\psi(\xi) = \mathcal{R}e\left[-\frac{i\pi}{2kK(k)}\int_0^{\xi}\frac{d\xi}{\sqrt{(\xi+\delta)\xi(\xi-1)}} + \pi + i\phi_s\right]$$

$$\psi(\xi) = \pi\left[1 - \frac{F(\varphi,k)}{K(k)}\right] \quad \text{where } \varphi = \sin^{-1}\sqrt{\frac{\xi(1+\delta)}{\xi+\delta}} \quad (30)$$

Solving for ξ yields

$$\xi = \frac{\delta\,\mathrm{sn}^2\left[\left(1-\frac{\psi}{\pi}\right)K(k)\right]}{\frac{1}{k^2} - \mathrm{sn}^2\left[\left(1-\frac{\psi}{\pi}\right)K(k)\right]} \quad (31)$$

To integrate equation (19*b*) for A_n, the $dZ/d\psi$ at a value of ψ is found by finding the corresponding ξ from equation (31) and then using equation (29) at that ξ.

Summary of Computational Procedure. The boundary of the porous medium is divided into increments, the angles β and θ are obtained, and C_{3n} and C_{2n} are calculated from equation (27). The g_{2n} and g_{3n} in equation (25) are evaluated for use in equation (28), which is used to iterate the values of C_3,δ, and ξ_n until the correct mapping is obtained from the ξ-axis into the specified geometry in the physical plane. These values are used in equation (29) to find $dZ/d\psi$ along ϕ_s as a function of ξ; the ξ corresponding to various ψ values are found from equation (31) for $0 \le \xi \le 1$. Cubic spline functions are employed to determine $dZ/d\psi$ at equally spaced ψ values. With δ known, the k and k' are found and ϕ_s can be obtained from equation (22). The A_n are found from equation (19*b*) by applying the fast Fourier transform [7]. The temperature variation along the curved surface is found from (19*a*) at $\phi = \phi_s$ (note from (15*a*) that $\theta = T$ at $\phi = \phi_s$), and the flow exit velocity is found from (20). This gives T and $|\mathbf{V}|$ as functions of ψ. The mapping from ψ to ξ is given by (31), and the mapping from ξ to Z by (28). Hence the T and $|\mathbf{V}|$ are known as functions of position along the curved boundary.

Performance of Porous Region with Cosine Shaped Boundary. To illustrate the technique, the behavior of a curved porous section of a wall was examined. The results illustrate the effects of flow distortion by the irregular geometry, and the effect of heat conduction on moderating temperature nonuniformities. The geometry chosen has a cosine surface of width w as shown in Fig. 4(*a*). From symmetry the results apply to a symmetric shape that is thick in the center as shown, or thin in the center if it is extended at the other side. Using w to make the lengths dimensionless, the interface shape is (Fig. 4(*b*))

$$Y_s = \frac{H_1+H_2}{2} + \frac{H_1-H_2}{2}\cos\pi X_s \quad (32)$$

Results were obtained for uniform heating q_s along the curved boundary. The surface temperature is desired so that results were evaluated at $\phi = \phi_s$. Then from equations (15*a*), and (19*a*,*b*),

$$T(\phi_s,\psi) = \frac{t_s - t_\infty}{q_s w/k_m} = \frac{A_0}{2\Lambda} + 2\sum_{n=1}^{\infty} A_n\left[\frac{\Lambda\sinh\gamma_n\phi_s + \gamma_n\cosh\gamma_n\phi_s}{(\gamma_n{}^2+\Lambda^2)\sinh\gamma_n\phi_s + 2\Lambda\gamma_n\cosh\gamma_n\phi_s}\right]\cos(n\psi) \quad 0 \le \psi \le \pi \quad (33a)$$

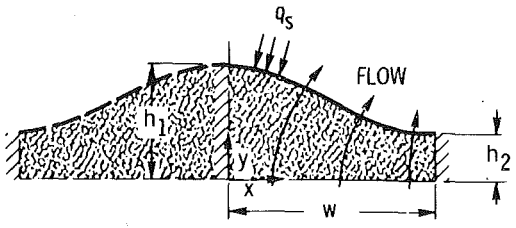

Fig. 4(*a*) Region in physical plane

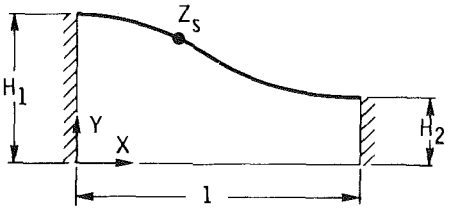

Fig. 4(*b*) One-half of symmetric region in dimensionless physical plane

Fig. 4 Porous region with cosine shaped curved boundary

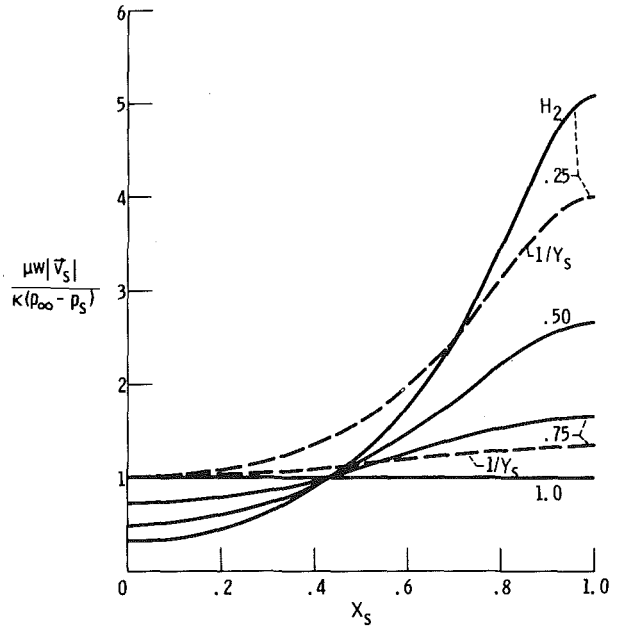

Fig. 5(*a*) Fluid exit velocity along curved boundary and comparison with local one-dimensional solution

Table 1 Mapping variables for several H_1 and H_2 combinations

H_1	H_2	δ	C_3	ϕ_s	k	$K(k)$
1.0	0.75	0.4809	0–0.3141 i	2.662	0.8217	2.040
1.0	0.50	0.1437	0–0.2558 i	2.064	0.9351	2.471
1.0	0.25	0.01136	0–0.2150 i	1.360	0.9944	3.638
0.75	0.25	0.006082	0–0.1883 i	1.253	0.9970	3.945
0.50	0.25	0.001704	0–0.1451 i	1.079	0.9991	4.576

where

$$A_n = \frac{1}{\pi}\int_{\psi=0}^{\pi}\left|\frac{dZ}{d\psi}\right|_{\phi_s}\cos(n\psi)\,d\psi \quad n = 1, 2, 3, \ldots \tag{33b}$$

$$A_0 = \frac{1}{\pi}\int_{\psi=0}^{\pi}\left|\frac{dZ}{d\psi}\right|_{\phi_s}d\psi \tag{33c}$$

Several combinations of H_1 and H_2 were used to reveal geometric effects. The corresponding C_3, δ, ϕ_s, k and $K(k)$ are in Table 1.

When $H_1 = H_2$ ($\equiv H$) the geometry is one dimensional and the transformation between the Z and W planes is $W = \pi Z$ so that $\phi_s =$

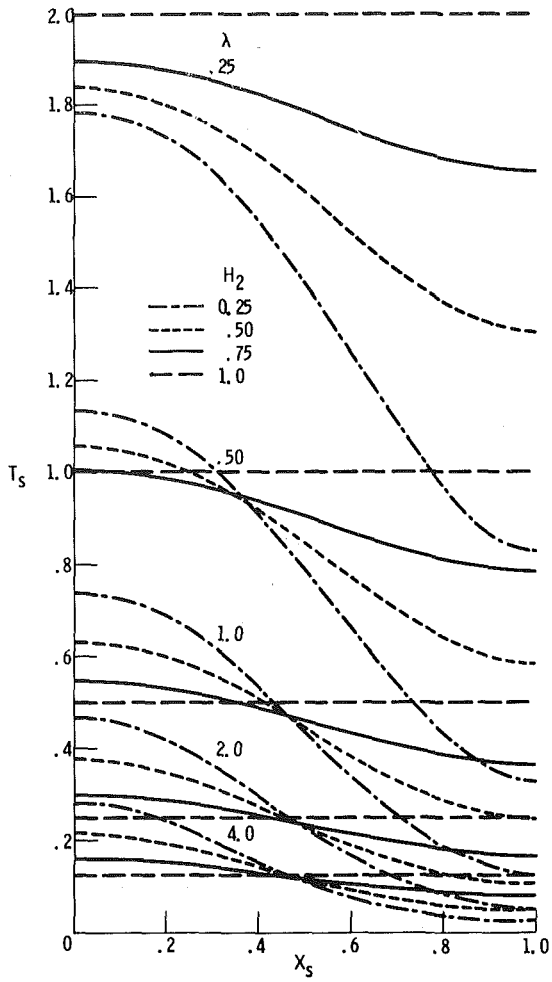

Fig. 5(*b*) Effect of flow rate on surface temperature distributions

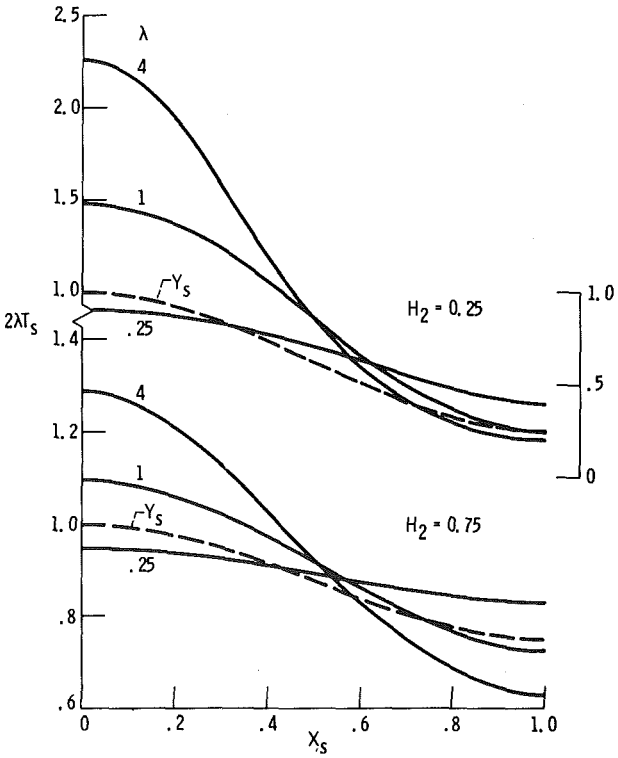

Fig. 5(*c*) Effect of heat conduction on temperature distributions and comparison with locally one-dimensional solution

Fig. 5 Behavior of porous medium with cosine shaped interface; $H_1 = 1$

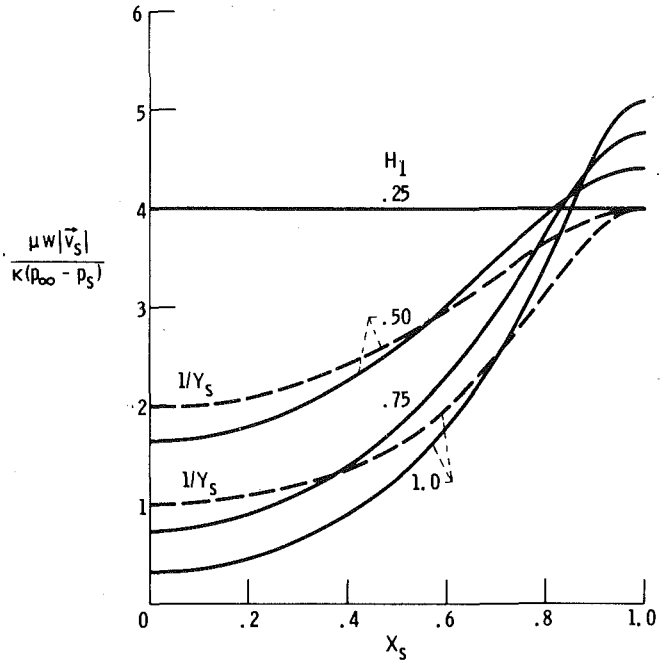

Fig. 6(*a*) Fluid exit velocity along curved boundary and comparison with local one-dimensional solution

πH. The $|d\psi/dZ|_{\phi_s} = \pi$, and equation (20) yields

$$\frac{\mu w|\mathbf{v}(\phi_s, \psi)|}{\kappa(p_\infty - p_s)} = \frac{\pi}{\phi_s} = \frac{\pi}{\pi H} = \frac{1}{H} \tag{34}$$

From equations (33*b*) and (*c*) the A_n are zero, and $A_0 = 1/\pi$. Then since $\Lambda = \lambda/\phi_s = \lambda/\pi H$, equation (33*a*) yields

$$T(\phi_s, \psi) = \frac{1}{2\pi}\frac{\pi H}{\lambda} = \frac{H}{2\lambda} \tag{35}$$

A helpful concept is a locally one-dimensional solution. This would be the result if there were no flow of fluid or heat in the X direction; the surface velocity and temperature depend only on the local thickness and from (34) and (35) become

$$\frac{\mu w|\mathbf{v}_s|}{\kappa(p_\infty - p_s)} = \frac{1}{Y_s};\ T_s = \frac{Y_s}{2\lambda} \tag{36a,b}$$

Discussion of Results

Figure 5 is for a set of geometries where $H_1 = 1$ while H_2 has various values ≤ 1. The exit velocity distributions are given in Fig. 5(*a*) where it is evident that as H_2 decreases, the velocity in the vicinity of $X_s = 1$ is increased as the coolant can be pumped more easily through the thinner region. However in the region near $X_s = 0$ the velocity decreases even though the thickness of the medium has been diminished somewhat. This is a two-dimensional effect where flow is diverted to travel along paths of less resistance toward the thinner region resulting in coolant starvation in the thick region. Figure 5(*a*) shows this quite clearly by comparison with the locally one-dimensional solution, equation (36*a*). As H_2 is decreased there is a trend of decreased flow through the thick regions and increased flow through the thin regions.

Figure 5(*b*) shows the temperature distributions as a function of the parameter λ. The λ has pressure difference in the numerator and thermal conductivity in the denominator, and is a measure of the relative effects of flow and heat conduction; as λ is increased there is a diminishing effect of heat conduction. The dimensionless temperature plotted in Fig. 5(*b*) has a k_m in it and hence it is best to consider the curves in terms of keeping k_m fixed so that the ordinate is directly a measure of surface temperature. With k_m fixed, the λ depends directly on pressure difference and hence flow rate. As λ increases, the increased coolant flow causes the exit surface temperatures to decrease. The temperatures are high in the thick regions

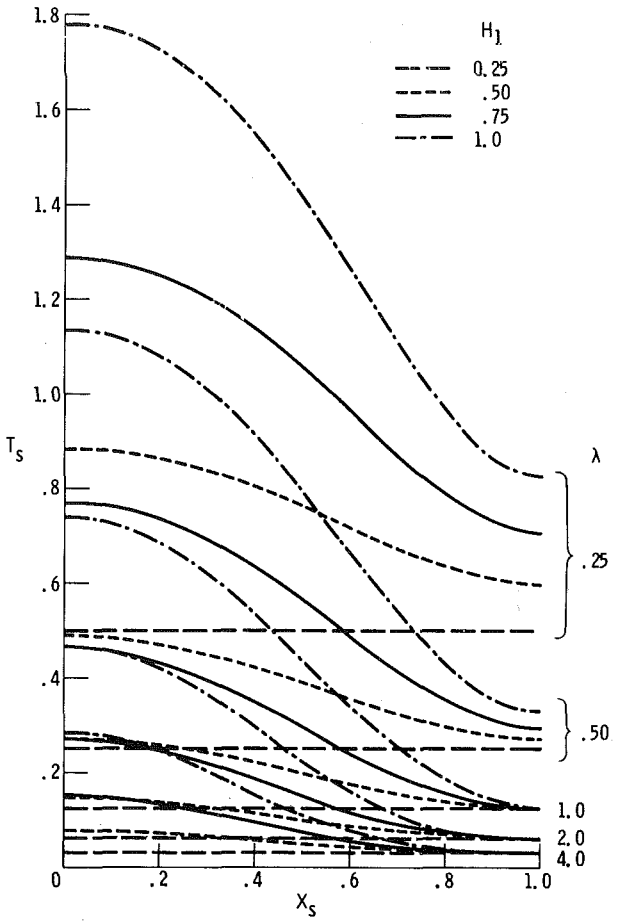

Fig. 6(*b*) Effect of flow rate on surface temperature distributions

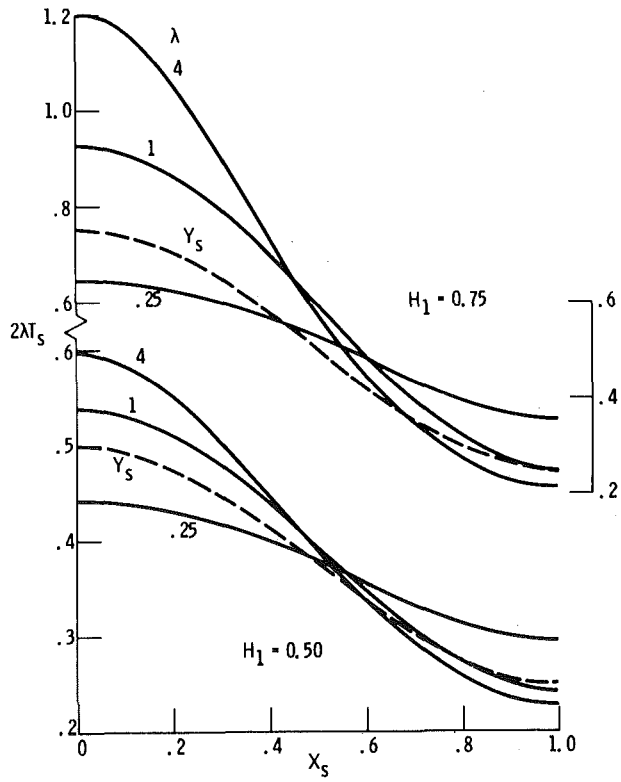

Fig. 6(*c*) Effect of heat conduction on temperature distributions and comparison with locally one-dimensional solution

Fig. 6 Behavior of porous medium with cosine shaped interface; $H_2 = 0.25$

where the velocities are especially low as a result of redirection of flow toward the thinner regions.

For small λ there is an increased effect of heat conduction from small X (thick region) toward large X (thin region). This is better shown by looking at curves of $2\lambda T_s$. For the locally one-dimensional solution this quantity equals Y_s. The quantity $2\lambda T_s$ contains the pressure difference, but not the thermal conductivity; thus for the ordinate to be proportional to temperature the pressure difference should be regarded as constant. Changes in λ are then inversely proportional to heat conduction. Figure 5(*c*) compares results for three λ values with the locally one-dimensional solution. For large λ, temperatures are high for small X because of coolant starvation in the thick region. As λ is decreased the heat conduction is able to more than compensate for the uneven coolant distribution, and for $\lambda = \frac{1}{4}$ the temperatures become more uniform than for the locally one dimensional distribution.

Figure 6 gives results for another set of geometries, in this instance $H_2 = 0.25$ while H_1 has various values. The trends are similar to those in Fig. 5.

Concluding Remarks

A combined analytical and numerical procedure was used to study the heat transfer characteristics of a cooled porous region having a curved boundary. The region would typically be a porous section of a wall having a curved exterior side exposed to a heat flux. To demonstrate the method, and show the performance of a typical curved porous medium, surface temperatures were evaluated for a medium with a cosine shaped external surface. Two effects are noted. One is coolant starvation of the thick regions as the flow tends to divert through the thinner portions. The second is the effect of heat conduction in the medium relative to convection; this decreases the temperature nonuniformity caused by the uneven flow distribution.

References

1 Siegel, R., and Goldstein, M. E., "Theory of Heat Transfer in a Two-Dimensional Porous Cooled Medium and Application to an Eccentric Annular Region," ASME JOURNAL OF HEAT TRANSFER, Vol. 94, No. 4, Nov. 1972, pp. 425–431.

2 Siegel, R., and Goldstein, M. E., "Analytical Method for Heat Transfer in Two-Dimensional Porous Media," NASA TN D-5878, 1970.

3 Woods, L. C., *The Theory of Subsonic Plane Flow*, Cambridge University Press, Cambridge, 1961.

4 Davis, R. T., "Numerical Methods for Coordinate Generation Based on Schwarz-Christoffel Transformations," *AIAA Computational Fluid Dynamics Conference, A Collection of Technical Papers*, AIAA, New York, 1979, pp. 180–194.

5 Siegel, R., and Goldstein, M. E., "Analysis of Heat Transfer in a Porous Cooled Wall with Variable Pressure and Temperature along the Coolant Exit Boundary," NASA TN D-6621, Jan. 1972.

6 Byrd, P. F., and Friedman, M. D., *Handbook of Elliptic Integrals for Engineers and Scientists*, 2nd. ed., Springer-Verlag, New York, 1971.

7 Brigham, E. Oran, *The Fast Fourier Transform*, Prentice-Hall, Englewood Cliffs, 1974.

An Integral Analysis for Heat Transfer in Turbulent Incompressible Boundary Layer Flow

L. C. Thomas[1]
M. M. Al-Sharif

Mechanical Engineering Department,
University of Petroleum and Minerals,
Dhahran, Saudia Arabia

The integral approach is utilized in this paper to analyze incompressible turbulent thermal boundary layer flow over a flat plate for nonuniform wall heating. This approach involves the use of inner variables and laws for u^+ and T^+ that apply to the important wall region as well as to the remainder of the flow field. Predictions developed for Stanton number are found to be in excellent agreement with published experimental data for uniform, step, double-step, and linear wall temperature heating of air. The results of this integral analysis compare favorably with those of the traditional numerical approach. Because of its computational efficiency, this integral approach provides a useful supplementary tool for analyzing turbulent thermal boundary layers.

Introduction

Whereas rather intensive efforts have been devoted to the development of the integral approach to momentum transfer in turbulent boundary layers over the past 10 to 15 years, relatively little attention has been given to the use of this approach in the analysis of thermal boundary layers. As a matter of fact, except for recent exploratory studies by White, et al. [1–3] and Thomas [4], the literature has been silent on this point since 1958 when Reynolds, et al. [5] developed a preliminary integral analysis of turbulent thermal boundary layer flow over a flat plate with constant free stream velocity. The analysis by Reynolds, et al. involves the use of a power law correlation for the mean temperature distribution and an artificial thermal eddy diffusivity within the sublayer which compensates for the failure of the power law in the region close to the wall (for Pr = 1). On the other hand, the integral method for analyzing convection heat transfer associated with turbulent boundary layer flow over a flat plate utilized in reference [4] involves the use of inner variables $y^+(\equiv yU^*/\nu)$, u^+ $(\equiv \overline{u}/U^*)$, and $T^+(\equiv(\overline{T}_o - \overline{T})_{\rho c_p}U^*/\overline{q_{ox}''}$, with u^+ and T^+ being specified by laws that approximately apply to the critical wall region as well as to the remainder of the flow field. (A similar approach was used by White, et al. [2] in analyzing a more complex compressible flow problem.) The underlying inner variable/integral method for momentum transfer which was introduced by White and co-workers is capable of handling a fairly wide range of pressure gradient flows and, according to Strickland and Simpson [6], is by far the simplest and most efficient of any existing boundary layer calculation method.

Because of the lack of attention given to development of the integral approach for turbulent thermal boundary layers, analyses of turbulent convection heat transfer rely almost exclusively on classical differential/numerical approaches that involve the use of the turbulent Prandtl number Pr_t. Although these field approaches have been productive, they do have certain limitations. For example, in the development of modern numerical computational schemes for analyzing turbulent convection heat transfer, relatively little attention has been given to modeling the important wall region. In this regard, Spalding [7] has suggested that the major work on modeling heat transfer through the semilaminar layer close to the wall has yet to be done. Unfortunately, little reliable experimental data are available for Pr_t for even the most simple turbulent thermal boundary layers. Further, this approach generally necessitates the use of a large digital computer.

Although recent developments in computational techniques and hardware has served as a strong stimulus to the furtherance of field methods, both integral techniques and differential/numerical methods have their place in the analysis of turbulent hydrodynamic boundary layers. And so it should be for thermal and chemical turbulent boundary layers.

The inner variable/integral analysis of reference [4] was restricted to convection heat transfer for incompressible turbulent boundary layer flow over a flat plate with step wall flux heating. As a step toward the generalization of this integral approach for turbulent thermal boundary layer flows, consideration is now given to the development of practical predictions for the local Stanton number St_x for nonuniform wall heating.

Analysis

In the present approach, the integral energy equation is written in terms of the inner variables y^+, u^+ and T^+ for both specified wall heat flux and specified wall temperature conditions. Reasonable laws for u^+ and T^+ are then set forth, after which solutions are developed for St_x for several representative thermal boundary conditions.

Integral Energy Equation. The integral energy equation for turbulent constant property flow takes the familiar form

$$\frac{d}{dx}\int_0^{\Delta}\overline{u}(\overline{T}-T_\infty)\,dy = \frac{\overline{q_{ox}''}}{\rho c_p} \tag{1}$$

where Δ is the thickness of the thermal boundary layer. Introducing the dimensionless parameters y^+, u^+, and T^+ and focusing attention on zero pressure gradient flows (i.e., U_∞ = constant), the integral energy equation takes the simple form [4]

$$\frac{d}{d\mathrm{Re}_x}\left(\overline{q_{ox}''}\sqrt{\frac{2}{f_x}}H\right) = \overline{q_{ox}''} \tag{2}$$

or

$$\frac{d}{d\mathrm{Re}_x}\left[\frac{(\overline{T}_{ox}-T_\infty)H}{T_\infty{}^+}\right] = \frac{\overline{T}_{ox}-T_\infty}{T_\infty{}^+}\sqrt{\frac{f_x}{2}} \tag{3}$$

where $\mathrm{Re}_x = U_\infty x/\nu$,

$$H = \int_0^{\Delta^+} u^+(T_\infty{}^+ - T^+)\,dy^+ \tag{4}$$

and $\Delta^+ = \Delta U^*/\nu$. The boundary condition is given by

$$H = 0 \text{ (or } \Delta^+ = 0) \text{ at } \mathrm{Re}_x = \mathrm{Re}_\xi \tag{5}$$

where ξ is the location at which heating is initiated.

With the local mean wall heat flux $\overline{q_{ox}''}$ or mean wall temperature $\overline{T}_{ox}$ specified, and with the distributions in dimensionless mean velocity u^+ and temperature T^+ approximated by reasonable inner and outer laws, equations (2–5) can be solved for Δ^+. The Stanton number can then be obtained from

[1] Present address: Mechanical and Aerospace Engineering Department, University of Tennessee, Knoxville, TN 37916.

Contributed by the Heat Transfer Division for publication in the JOURNAL OF HEAT TRANSFER. Manuscript received by the Heat Transfer Division May 16, 1980.

$$\mathrm{St}_x = \frac{\sqrt{f_x/2}}{T_\infty{}^+} \tag{6}$$

Laws for u^+ and T^+. In the integral approach to turbulent hydrodynamic and thermal boundary layers, local information within the flow field itself can be accounted for by utilizing proper inputs for u^+ and T^+. In the inner region, laws can be established for u^+ and T^+ by means of one of several modeling approaches. For example, for simple fully turbulent well developed flow over a flat plate with moderate pressure gradients, u^+ and T^+ within the inner region can be approximated by the popular van Driest approach [8, 9]; that is,

$$u^+ = \int_0^{y^+} \frac{dy^+}{1 + \epsilon_m/\nu} \tag{7}$$

$$T^+ = \int_0^{y^+} \frac{dy^+}{1/\mathrm{Pr} + \epsilon_H/\nu} \tag{8}$$

where

$$\frac{\epsilon_m}{\nu} = \frac{1}{2}\{1 + 4(\kappa y^+)^2[1 - \exp(-y^+/a^+)]^2\}^{1/2} - \frac{1}{2} \tag{9}$$

and $\epsilon_H/\nu = (\epsilon_m/\nu)/\mathrm{Pr}_t$. As in the numerical approach, Pr_t is generally set equal to a constant of the order of 0.85 to 1, as a first approximation. Equations (7) and (8) approach the logarithmic equations

$$u^+ = \frac{1}{\kappa} \ln y^+ + C \tag{10}$$

$$T^+ = \frac{1}{\kappa} \ln y^+ + A \tag{11}$$

as y^+ becomes large. The constant a^+ is related to the hydrodynamic parameters κ and C, and A is a function of Prandtl number Pr. (For $\kappa = 0.4$, $C = 5.5$, $\mathrm{Pr}_t = 1$, and a^+ is approximately equal to 27.4.) The parameter A is approximated by

$$A = 14.9\ \mathrm{Pr}^{0.623} - 9.4 \qquad 0.5 \lesssim \mathrm{Pr} \lesssim 10 \tag{12a}$$

$$A = 10\ \mathrm{Pr}^{0.741} \qquad 10 \lesssim \mathrm{Pr} \lesssim 500 \tag{12b}$$

Although the van Driest type equations strictly apply to the inner region ($y/\delta \lesssim 0.2$) for fully turbulent and well developed conditions, these equations also provide a reasonable approximation for u^+ and T^+ in the thermal developing region and in the wake region for zero pressure gradient flows. Therefore, the van Driest type inner laws will be utilized in the present analysis to approximate u^+ and T^+ in the entire flow field. (To provide more accurate information in the outer region, outer laws of the type developed for u^+ by Coles [10] and White [11] can be employed [12].)

Solution. The first step in obtaining a solution to this integral formulation is to evaluate the parameters H and $T_\infty{}^+$.

To compute H, equation (4) has been numerically integrated with u^+ and T^+ specified by equations (7–9) [12, 13]. The calculations obtained for H versus Δ^+ are shown in Fig. 1 for several values of Prandtl number. The relationship between H and Δ^+ shown in this figure is denoted by

$$H = g_H(\Delta^+) \text{ or } \Delta^+ = g_H{}^{-1}(H) \tag{13a,b}$$

For Δ^+ greater than 100, equation (13) is approximated by

$$H = 16.6\ \mathrm{Pr}^{0.105}\ \Delta^{+1.13} \tag{14}$$

The use of the van Driest type equations to approximate T^+ gives rise to

$$T_\infty{}^+ = \int_0^{\Delta^+} \frac{dy^+}{1/\mathrm{Pr} + \epsilon_m/\nu/\mathrm{Pr}_t} \tag{15}$$

where ϵ_m/ν is given by equation (9). As Δ^+ increases, this equation reduces to the form

$$T_\infty{}^+ = \frac{1}{\kappa} ln\ \Delta^+ + A \tag{16}$$

for $\mathrm{Pr}_t = 1$. Numerical values of $T_\infty{}^+$ versus Δ^+ are obtained directly from equation (8) by merely replacing T^+ and y^+ by $T_\infty{}^+$ and Δ^+, respectively. The functional relationship between $T_\infty{}^+$ and Δ^+ is represented by

$$T_\infty{}^+ = g_T(\Delta^+) \tag{17}$$

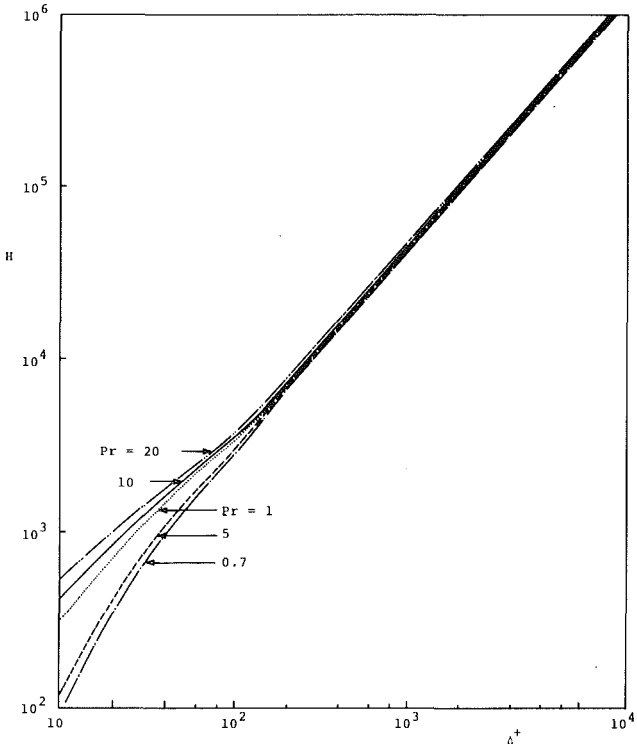

Fig. 1 Calculations for H based on van Driest type laws for u^+ and T^+ with $\kappa = 0.4$, $a^+ = 27.4$, and $\mathrm{Pr}_t = 1$

Nomenclature

a^+ = empirical constant in van Driest inner law
C = empirical constant in logarithmic inner law
c_p = specific heat at constant pressure
f_x = local skin friction coefficient
$H = \int_0^{\Delta^+} u^+(T_\infty{}^+ - T^+)\, dy^+$
k = thermal conductivity
k_t = eddy thermal conductivity
Pr = Prandtl number (ν/α)
Pr_t = turbulent Prandtl number (ϵ_m/ϵ_H)
$\overline{q_o''}$ = uniform mean wall heat flux
$\overline{q_{ox}''}$ = arbitrary mean wall heat flux
Re_x = Reynolds number (xU_∞/ν)
Re_ξ = Reynolds number based on ξ($\xi U_\infty/\nu$)
St_x = local Stanton number
$\overline{T}$ = mean temperature distribution
$\overline{T_o}$ = uniform mean wall temperature
$\overline{T_{ox}}$ = nonuniform mean wall temperature
T^+ = dimensionless mean temperature distribution $\left(\frac{\overline{T_{ox}} - \overline{T}}{\overline{q_{ox}''}} \rho c_p U^*\right)$
T_∞ = free steam temperature
U_∞ = free stream velocity
$\overline{u}$ = mean axial velocity distribution
U^* = friction velocity ($\sqrt{\overline{\tau_0}/\rho}$)
u^+ = dimensionless mean velocity distribution ($\overline{u}/U^*$)
x,y = coordinates parallel and normal to the wall
y^+ = dimensionless coordinate (yU^*/ν)
α = thermal diffusivity ($k/(\rho c_p)$)
ϵ_H = eddy thermal diffusivity ($k_t/(\rho c_p)$)
ϵ_m = eddy diffusivity
δ = hydrodynamic boundary layer thickness
Δ = thermal boundary layer thickness
Δ^+ = dimensionless thermal boundary layer thickness ($\Delta U^*/\nu$)
λ_x = dimensionless skin friction parameter ($\sqrt{2/f_x}$)
ν = fluid kinematic viscosity
ρ = fluid density
$\overline{\tau_0}$ = mean wall shear stress
κ = empirical constant in inner law

By combining equations (6), (13), and (17), the local Stanton number is expressed in terms of H by

$$\mathrm{St}_x = \frac{\sqrt{f_x/2}}{g_T[g_H^{-1}(H)]} \tag{18}$$

With H and T_∞^+ approximated by equations (14) and (16), equation (18) reduces to the analytical form

$$\mathrm{St}_x = \frac{\sqrt{f_x/2}}{\frac{1}{1.13\,\kappa}\ln\left(\frac{H}{16.6\,\mathrm{Pr}^{0.105}}\right) + A} \tag{19}$$

Attention is now turned to the development of solutions for H and St_x for arbitrarily specified wall heat flux and wall temperature boundary conditions. In the calculations that follow, the friction factor f_x is approximated by $0.059\,\mathrm{Re}_x^{-0.2}$.

Specified Wall Heat Flux. For cases in which the wall heat flux is known, the integration of equation (2) immediately gives an expression for H of the form

$$H = \frac{\sqrt{f_x/2}}{q_{ox}''}\int_{\mathrm{Re}_\xi}^{\mathrm{Re}_x} q_{ox}''\, d\mathrm{Re}_x \tag{20}$$

The substitution of this result into equation (18) gives

$$\mathrm{St}_x = \frac{\sqrt{f_x/2}}{g_T\left[g_H^{-1}\left(\frac{\sqrt{f_x/2}}{q_{ox}''}\int_{\mathrm{Re}_\xi}^{\mathrm{Re}_x} q_{ox}''\, d\mathrm{Re}_x\right)\right]} \tag{21}$$

This equation has been used to compute St_x for uniform heat flux, step heat flux, double-step heat flux, and linear heat flux conditions [12, 13]. Computations developed for St_x for these four conditions are shown in Fig. 2.

To obtain a more convenient expression for St_x, equation (20) is substituted into equation (19), with the result

$$\mathrm{St}_x = \frac{\sqrt{f_x/2}}{\frac{1}{1.13\kappa}\ln\left(\frac{\sqrt{f_x/2}}{16.6\,\mathrm{Pr}^{0.105}q_{ox}''}\int_{\mathrm{Re}_\xi}^{\mathrm{Re}_x} q_{ox}''\, d\mathrm{Re}_x\right) + A} \tag{22}$$

This equation gives rise to predictions for St_x that are in excellent agreement with the numerical calculations shown in Fig. 2.

Specified Wall Temperature. For situations in which $\overline{T}_{ox}$ is specified, the appropriate form of the integral energy equation is given by equation (3). This equation is integrated to obtain

$$(\overline{T}_{ox} - T_\infty)H - \int_0^{T_\infty^+}\frac{(\overline{T}_{ox} - T_\infty)H}{T_\infty^+}\,dT_\infty^+ = \int_{\mathrm{Re}_\xi}^{\mathrm{Re}_x}\sqrt{\frac{f_x}{2}}\,(\overline{T}_{ox} - T_\infty)\,d\mathrm{Re}_x \tag{23}$$

where H and T_∞^+ are expressed in terms of Δ^+ by equations (13) and (17).

Step Wall Temperature. For the case of step wall temperature heating, equation (23) reduces to the form

$$G(\Delta^+) \equiv H - \int_0^{T_\infty^+}\frac{H}{T_\infty^+}\,dT_\infty^+ = \int_{\mathrm{Re}_\xi}^{\mathrm{Re}_x}\sqrt{\frac{f_x}{2}}\,d\mathrm{Re}_x \tag{24}$$

With H and T_∞^+ expressed in terms of Δ^+ by equations (13) and (17), $G(\Delta^+)$ has been computed numerically. The calculations for $G(\Delta^+)$ are shown as a function of both Δ^+ and H in Fig. 3.

With Δ^+ represented by

$$\Delta^+ = G^{-1}\left(\int_{\mathrm{Re}_\xi}^{\mathrm{Re}_x}\sqrt{\frac{f_x}{2}}\,d\mathrm{Re}_x\right) \tag{25}$$

the expression for Stanton number given by equation (18) becomes

$$\mathrm{St}_x = \frac{\sqrt{f_x/2}}{g_T\left[G^{-1}\left(\int_{\mathrm{Re}_\xi}^{\mathrm{Re}_x}\sqrt{\frac{f_x}{2}}\,d\mathrm{Re}_x\right)\right]} \tag{26}$$

Numerical calculations for St_x obtained by the use of this equation are shown in Fig. 4.

To simplify the analysis, the numerical calculations for $G(\Delta^+)$ can be approximated by

$$G(\Delta^+) = cH^m\,\mathrm{Pr}^n \tag{27}$$

where $c = 0.806$, $m = 1.01$, and $n = 0.029$ for $0.5 < \mathrm{Pr} < 10$, and $c = 0.9$, $m = 1.0$, and $n = 0.0223$ for $10 < \mathrm{Pr} < 100$. Substitution of equation (27) into equation (24) gives

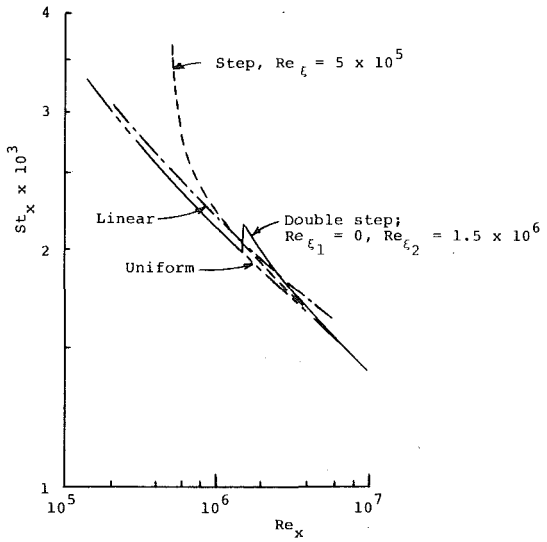

Fig. 2 Calculations for Stanton number for several specified wall flux heating conditions

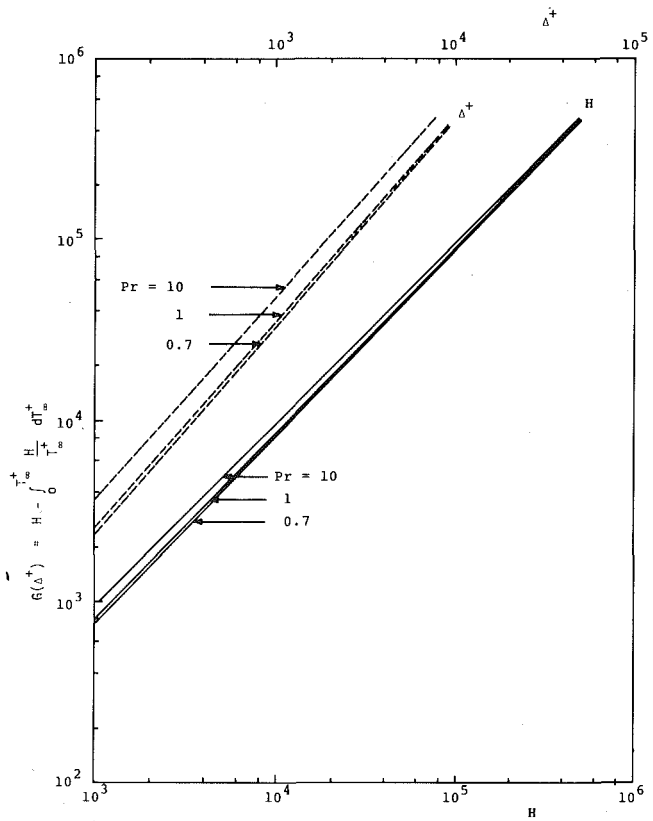

Fig. 3 Calculations for $G(\Delta^+)$ in terms of Δ^+ and H

$$H = \left(\frac{1}{c\,\mathrm{Pr}^n}\int_{\mathrm{Re}_\xi}^{\mathrm{Re}_x}\sqrt{\frac{f_x}{2}}\,d\mathrm{Re}_x\right)^{1/m} \tag{28}$$

The coupling of this equation and equation (19) gives

$$\mathrm{St}_x = \frac{\sqrt{f_x/2}}{\frac{1}{1.13\,\kappa m}\,ln\left(\frac{1}{c\,\mathrm{Pr}^n\,16.6^m\,\mathrm{Pr}^{0.105m}}\int_{\mathrm{Re}_\xi}^{\mathrm{Re}_x}\sqrt{\frac{f_x}{2}}\,d\mathrm{Re}_x\right)+A} \tag{29}$$

This equation is shown in Fig. 4.

Arbitrary Wall Temperature. Predictions can be developed for St_x for arbitrary wall temperature heating by the numerical integration of equation (23) or by use of the principle of superposition.

A numerical integration scheme for solving equation (23) is developed in references [12] and [13]. Computations for St_x obtained by this somewhat involved approach are shown in Figs. 5 and 6 for double-step wall temperature and linear wall temperature heating.

With the local Stanton number for step wall temperature heating (now represented by $\mathrm{St}_{x,\xi}$) approximated by equation (29), the superposition approach is more efficient than the above referenced numerical integration of equation (23). Based on the method of superposition, the local heat flux for arbitrary wall temperature variation is given by [14]

$$\overline{q_{\mathrm{ox}}''} = \int_0^x h(\xi,x)\frac{d\overline{T}_{\mathrm{ox}}}{dx}\,d\xi + \sum_{i=1}^{n} h(\xi_i,x)\Delta\overline{T_{\mathrm{ox},i}} \tag{30}$$

where $h(\xi,x)$ (and $h(\xi_i,x)$) is the local coefficient of heat transfer from the single-step wall temperature solution and $\Delta T_{\mathrm{ox},i}$ represents all discontinuous changes in wall temperature.

For the case of a double-step wall temperature, the use of equations (29) and (30) gives rise to an analytical expression for St_x of the form

$$\mathrm{St}_x = \mathrm{St}_{x,\xi_1} \quad \mathrm{Re}_{\xi_1} \leqslant \mathrm{Re}_x < \mathrm{Re}_{\xi_2} \tag{31a}$$

$$= \frac{\overline{T}_{01} - T_\infty}{\overline{T}_{02} - T_\infty}\mathrm{St}_{x,\xi_1} + \mathrm{St}_{x,\xi_2} \quad \mathrm{Re}_{\xi_2} < \mathrm{Re}_x \tag{31b}$$

Equation (31) is compared with the numerical solution and with experimental data in Fig. 5.

For situations in which $\overline{T}_{\mathrm{ox}}$ is nonuniform but continuous, the use of equations (29) and (30) necessitates a simple numerical integration. Calculations for St_x obtained by this approach for linear wall temperature are shown in Fig. 6.

Discussion

The inner variable/integral analysis developed in this paper provides an alternative method for analyzing turbulent boundary layer flow with nonuniform wall conditions. This approach is particularly efficient for cases in which the wall heat flux is specified since the parameter H can be obtained explicitly from equation (20). Both equation (21) and the practical analytical relationship given by equation (22) apply for any $\overline{q_{\mathrm{ox}}''}$ input. Equation (22) is in good agreement with equation (21) for uniform, step, double-step, and linear wall flux heating. This agreement holds up, except in the immediate vicinity of the point at which heating is initiated ($x = \xi$). For example, for step wall flux heating, equation (22) is within 3.1 percent of calculations based on equation (21) for $x/\xi \gtrsim 1.0$ and $0.5 \lesssim \mathrm{Pr} \lesssim 1$, and within 2.25 percent for $x/\xi \gtrsim 1.0$ and $1 \lesssim \mathrm{Pr} \lesssim 100$.

Referring to Fig. 4, equation (26) and the practical expression given by equation (29) are seen to be in excellent agreement with the experimtal data for uniform and step wall temperature heating of air. As in the case of step wall flux heating, the reliability of equation (29) deteriorates for very small values of $x - \xi$.

With f_x approximated by $0.059\,\mathrm{Re}_x^{-0.2}$, equation (29) reduces to

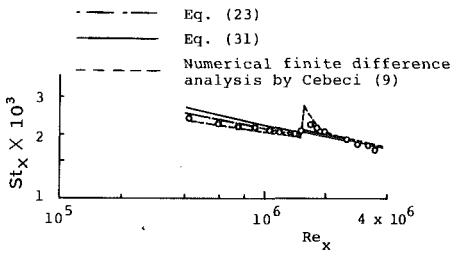

Fig. 5 Stanton number for double-step wall temperature heating. Experimental data for air (Pr = 0.72) by Reynolds, et al. (5); $\mathrm{Re}_\xi = 1.5 \times 10^6$

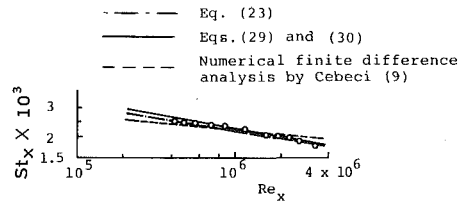

Fig. 6 Stanton number for linear wall temperature heating. Experimental data for air (Pr = 0.72) by Reynolds, et al. [5]

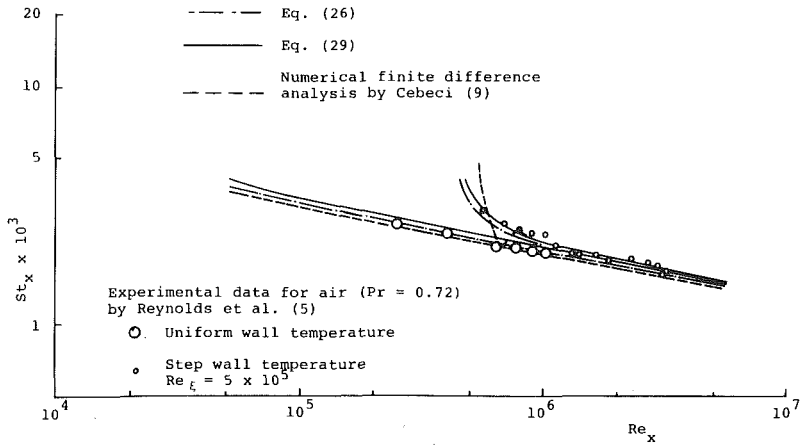

Fig. 4 Stanton number for uniform and step wall temperature heating

$$\mathrm{St}_x = \frac{\sqrt{f_x/2}}{2.19\, ln \left\{\sqrt{\frac{f_x}{2}}\,\mathrm{Re}_x \left[1 - \left(\frac{\xi}{x}\right)^{0.9}\right]\right\} - 0.296\, ln\ \mathrm{Pr} + 14.9\,(\mathrm{Pr}^{0.623} - 1)} \tag{32a}$$

for $0.5 \lesssim \mathrm{Pr} \lesssim 10$, and

$$\mathrm{St}_x = \frac{\sqrt{f_x/2}}{2.21\, ln \left\{\sqrt{\frac{f_x}{2}}\,\mathrm{Re}_x \left[1 - \left(\frac{\xi}{x}\right)^{0.9}\right]\right\} - 0.281\, ln\ \mathrm{Pr} + 10\,\mathrm{Pr}^{0.741} - 5.74} \tag{32b}$$

for $10 \lesssim \mathrm{Pr} \lesssim 500$. Equations (32*a*) and (32*b*) are shown in Fig. 7 for several values of Pr. For purpose of companion, the equation developed by Petukhov and Kirillov [15] and White [11][2] for uniform wall temperature heating is also shown.

$$\mathrm{St}_x = \frac{\sqrt{f_x/2}}{1.07\sqrt{\frac{2}{f_x}} + 12.7\,(\mathrm{Pr}^{2/3} - 1)} \tag{33}$$

This equation has been reported to be in good agreement with experimental data for moderate to high values of Prandtl number ($0.5 \lesssim \mathrm{Pr} \lesssim 2000$). In addition, the equation obtained in the early integral analysis by Reynolds, et al. (5) is shown with the correction factor $\mathrm{Pr}^{0.4}$; this equation takes the form

$$\mathrm{St}_x = \frac{f_x/2}{\left[1 - \left(\frac{\xi}{x}\right)^{0.9}\right]^{1/9} \mathrm{Pr}^{0.4}} \tag{34}$$

For small values of ξ/x, the present integral analysis is in reasonably good agreement with equation (33) over a broad range of Pr. Equation (34) is in basic agreement with the present analysis for air. However, equation (34) lies well above equation (32*b*) for larger values of Pr and is incompatible with equation (33) for Pr = 100.

The numerical solution approach of references [12] and [13] and the superposition approach presented in this paper both give rise to predictions for St_x that are in good agreement with the experimental data shown in Figs. 5 and 6 for double-step and linear wall temperature heating of air.

Calculations obtained by the differential numerical approach [9] are also shown in Figs. 4–6. The results of the present integral analysis are seen to compare quite favorably with those of the traditional numerical approach. In this connection, the computations called for in the present approach are simpler and involve much less computer time than the numerical finite difference calculations that are required in the classical approach to solving the full partial differential equations.

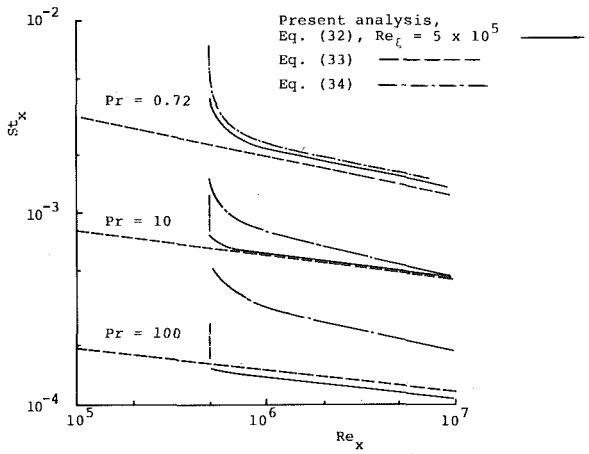

Fig. 7 Dependence of predictions for St_x on Pr

Incidently, the predictions for St_x obtained on the basis of equation (22) for specified heat flux are in basic agreement with the experimental data for the several specified wall temperature conditions considered in this study. For example, for step wall flux heating, equation (22) reduces to

$$\mathrm{St}_x = \frac{\sqrt{f_x/2}}{2.21\, ln \left[\sqrt{\frac{f_x}{2}}\,\mathrm{Re}_x \left(1 - \frac{\xi}{x}\right)\right] - 0.232\, ln\ \mathrm{Pr} + 14.9\,\mathrm{Pr}^{0.623} - 15.6} \tag{35a}$$

for $0.5 \lesssim \mathrm{Pr} \lesssim 10$, and

$$\mathrm{St}_x = \frac{\sqrt{f_x/2}}{2.21\, ln \left[\sqrt{\frac{f_x}{2}}\,\mathrm{Re}_x \left(1 - \frac{\xi}{x}\right)\right] - 0.232\, ln\ \mathrm{Pr} + 10\,\mathrm{Pr}^{0.741} - 6.21} \tag{35b}$$

for $10 \lesssim \mathrm{Pr} \lesssim 500$. These equations give rise to predictions for St_x that are in very close agreement with equations (32*a*) and (32*b*) for step wall temperature heating. Because of the relative insensitivity of St_x to the exact form of the thermal boundary condition for fully turbulent flow, the practical equation for specified heat flux, equation (22), can be used as a very efficient first estimate for situations involving arbitrary wall temperature heating.

It should be noted that integral solutions have also been developed for step wall heat flux conditions by the use of other inner laws for u^+ and T^+ [4, 16]. For example, the use of 1/7th power laws in the moderate Pr range gives rise to (16)

$$\mathrm{St}_x = \frac{0.982\sqrt{f_x/2}}{\left[\frac{(9.78 + A)}{1.75}\right]^{8/9} \left[\sqrt{\frac{f_x}{2}}\,\mathrm{Re}_x \left(1 - \frac{\xi}{x}\right)\right]^{1/9}} \tag{36}$$

Where A is given by equation (12). Predictions developed on the basis of the present integral analysis are nearly congruent with equation (36) for air.

Conclusion

The integral approach has been used to analyze convection heat transfer for incompressible turbulent boundary layer flow over a flat plate with arbitrary thermal boundary conditions. The key to this approach is the use of inner variables and appropriate laws for u^+ and T^+ for the critical wall region. The approach is simple and efficient, and is formulated on a sound theoretical basis. Because of its practicality, this inner variable/integral approach is felt to provide a useful supplementary tool for the analysis of thermal boundary layers.

Although the present analysis was developed for basic incompressible flow with constant free stream velocity, the approach can be extended to more general situations. For example, an integral analysis is developed in reference [13] for mild adverse and favorable pressure gradient flows with nonuniform wall flux heating.

References

1 White, F. M., and Christoph, G. H., "A Simple Theory for the Two-Dimensional Compressible Turbulent Boundary Layer," ASME *Journal of Basic Engineering*, 94, 636–642, 1972.

2 White, F. M., Christoph, G. H., and Lessmann, R. C., "Calculation of Turbulent Heat Transfer and Skin Friction," *AIAA Journal*, Vol. 11, 1973, pp. 1046–1052.

[2] The coefficients in the White equation are slightly different.

3 White, F. M., "A New Integral Method for Analyzing the Turbulent Boundary Layer with Arbitrary Pressure Gradient," ASME *Journal of Basic Engineering*, 91, 1969, 371–378.

4 Thomas, L. C., "A Simple Integral Approach to Turbulent Boundary Layer Flow," ASME JOURNAL OF HEAT TRANSFER, Vol. 100, 1978, pp. 744–747.

5 Reynolds, W. C., Kays, W. M., and Kline, S. J., "Heat Transfer in the Turbulent Incompressible Boundary Layer—I: Constant Wall Temperature, II: Step Wall Temperature Distribution, III: Arbitrary Wall Temperature and Heat Flux," NASA Mem., 12-1-58W, 12-2-58W, and 12-3-58W, Washington D.C., 1958.

6 Strickland, J. H., and Simpson, R. L., "The Separating Turbulent Boundary Layer: An Experimental Study of an Airfoil Type Flow," Tech. Rept. WT-2, Thermal and Fluid Sciences Center, Southern Methodist University, 1973.

7 Spalding, D. B., "Turbulence Models for Heat Transfer," *Proceedings Sixth International Heat Transfer Conference*, Vol. 6, 1978, pp. 33–39.

8 van Driest, E. R., "On Turbulent Flow Near a Wall," *Journal Aero Science*, Vol. 23, 1956, pp. 1007–1011.

9 Cebeci, T., and Smith, A. M. O., and Mosinkis, G., "Solution of the Incompressible Turbulent Boundary Layer Equations With Heat Transfer," ASME JOURNAL OF HEAT TRANSFER, Vol. 92, 1970, pp. 133–138.

10 Coles, D. E., "The Law of the Wake in the Turbulent Boundary Layer," *Journal Fluid Mechanics*, Vol. 1, 1956, pp. 191–226.

11 White, F. M., *Viscous Fluid Flow*, McGraw-Hill, New York, 1974.

12 Thomas, L. C., and Al-Sharif, M. M., "An Integral Analysis for Incompressible Turbulent Thermal Boundary Layer Flow: Nonuniform Wall Heating," 80-WA/HT-57, ASME Winter Annual Annual Meeting, Chicago, 1980.

13 Al-Sharif, M., "A Modern Integral Approach to Turbulent Thermal Boundary Layer Flow," M.S. Thesis, University of Petroleum and Minerals, Dhahran, Saudi Arabia, 1979.

14 Kays, W. M., *Convective Heat and Mass Transfer*, McGraw-Hill, New York, 1966.

15 Petukhov, V. S., and Kirillov, V. V., *Advances in Heat Transfer*, Academic, Vol. 6, 1970, pp. 503–504.

16 Thomas, L. C., *Fundamentals of Heat Transfer*, Prentice-Hall, Englewood Cliff, 1980.

E. M. Sparrow
Fellow ASME

F. Samie
Department of Mechanical Engineering,
University of Minnesota,
Minneapolis, Minn. 55455

Measured Heat Transfer Coefficients at and Adjacent to the Tip of a Wall-Attached Cylinder in Crossflow—Application to Fins

Wind tunnel studies encompassing both heat transfer measurements and flow visualization were performed for a cylinder in crossflow, with one end of the cylinder attached perpendicular to a wall and with the other end free. The focus of the work was to obtain heat transfer coefficients for the tip of the cylinder, for the tip-adjacent portion of the cylindrical surface, and for a portion of the cylindrical surface where there are no end effects. The flow visualization studies were performed to assist in the explanation and rationalization of the heat transfer results. They revealed the presence of spanwise flows adjacent to both ends of the cylinder, with accompanying modifications of the size of the separated region that washes the rear of the cylinder. The flow passing over the tip separates on the fore portion of the tip, but reattaches on the aft portion. The tip heat transfer coefficients are higher than those for the end-effect-free portion of the cylindrical surface, with deviations which grow with increasing Reynolds number (about a factor of two at Re = 25,000). For the tip-adjacent portion of the cylindrical surface, the coefficients are about fifty percent higher than those uninfluenced by end effects. The ramifications of these findings on the heat transfer analysis of fins are discussed.

Introduction

The heat transfer characteristics of the cylinder in crossflow have been subjected to more intense experimental study than has been accorded any other external flow, as witnessed, for example, by the recent compilation of Morgan [1]. For the most part, the measurements were focused on the determination of average heat transfer coefficients, which are reported in Nusselt-Reynolds correlations, with the cylinder diameter serving as the characteristic dimension. As can be seen in Table IV of [1], the available literature encompasses an enormous range of cylinder length-diameter ratios (the cylinder length is transverse to the flow). Notwithstanding this, the reported data are lumped together as representing the heat transfer characteristics of cylinders that are, effectively, of infinite length. Indeed, the length of the cylinder nowhere appears in the available correlating equations.

The foregoing discussion is intended to underscore the complete disregard, in the past, of the heat transfer and fluid flow processes which occur at the ends of the cylinder. There are two end conditions that are likely to occur in practice. One is that the end of the cylinder is attached to a wall in such a way that the cylinder is perpendicular to the wall. The other is that the end is free. As will be demonstrated later, the patterns of fluid flow adjacent to either the wall-attached end or the free end are much more complex than the already complicated flow patterns (separation and wake-region recirculation) which exist adjacent to the cylindrical surface, far from the ends.

The present experiments are concerned with the heat transfer characteristics and the patterns of fluid flow about a cylinder situated in a crossflow of air, with one end of the cylinder attached perpendicular to a wall and with the other end free. Although the pattern of fluid flow about the cylinder as a whole will be examined via flow visualization, the main focus of the research is the free end (hereafter called the tip) and the tip-adjacent portion of the cylindrical surface. The heat transfer and fluid flow characteristics of these regions will be studied in their own right, rather than as end effects with respect to the average heat transfer characteristics of the cylinder as a whole.

Contributed by the Heat Transfer Division for publication in the JOURNAL OF HEAT TRANSFER. Manuscript received by the Heat Transfer Division February 23, 1981.

The issue as to what really happens at and adjacent to the tip of a wall-attached cylinder in crossflow is raised, often implicitly, in the first course in heat transfer and thereafter continues to be a puzzlement to heat transfer practitioners. For a fin, of which the wall-attached cylinder is an example, the treatment of the tip is frequently shrouded in a degree of mystery and is, at best, uncertain. Three approaches are current. In the simplest approach, the tip is imagined to be insulated, thereby dismissing altogether the matter of the tip heat transfer coefficient. The second approach "patches up" the first approach. It is imagined that the tip surface area, which was deactivated by the adiabatic-tip assumption, is somehow relocated adjacent to the tip in such a manner as to extend the principal surface of the fin. The relocated area is assumed to actively transfer heat, with a heat transfer coefficient which is equal to that of the principal surface of the fin. Therefore, in this model, it is implicitly assumed that the tip heat transfer coefficient is equal to that which prevails on the portion of the principal surface adjacent to the tip.

The third approach is often termed the exact approach. The tip is regarded as an active heat transfer surface with a heat transfer coefficient that is specific to the tip (i.e., different from the principal surface). The difficulty with this approach is that tip heat transfer coefficients have never been measured heretofore. Whether in recognition of this or for less incisive reasons, no distinction is often made between the tip coefficient and that for the principal surface.

The present research was undertaken to provide basic information about the heat transfer characteristics which prevail at the tip and on the tip-adjacent portion of the principal surface (i.e., the cylindrical surface). To this end, heat transfer coefficients were measured at three distinct zones of the cylinder, and flow visualization studies were carried out both to guide and to illuminate the heat transfer results. One of the measurement zones is the tip itself. The second zone is a length L^* of the cylindrical surface that is situated immediately adjacent to the tip, where $L^* = \frac{1}{4}D$ (D = cylinder diameter). With this axial length, the surface area of the second zone, $\pi DL^* = \pi D^2/4$, is equal to that of the tip, thereby enabling a comparison of heat transfer coefficients that is relevant to one of the fin-tip models that was discussed earlier.

The last of the measurement zones to be considered is actually the one that was used at the very beginning of the research program. In

order to verify the experimental techniques, it was deemed mandatory to make measurements in a zone where end effects would not influence the results, thereby facilitating comparison with the literature. As will be detailed shortly, the heat transfer measurements were made for a short thermally active portion of the cylindrical surface, either centrally located between the ends of the cylinder or slightly displaced toward the attached end of the cylinder (as suggested by the flow visualization studies). For these verification experiments, the ratio of the length of the cylinder to the diameter was also varied by a factor of about two and a half.

Air was the working fluid for all the experiments, which were performed in a low-turbulence wind tunnel. The Reynolds number range of the experiments extended from about 2500 to 25,000.

The two experimental tools used in the research are the naphthalene sublimation technique, which yielded heat transfer results via the analogy between heat and mass transfer, and the oil-lampblack technique for the flow visualizations. In view of the objectives of the work, i.e., the determination of transfer coefficients for distinct zones such as the tip and the tip-adjacent cylindrical region, the use of direct heat transfer measurements is well-nigh impossible. Even for the napthalene technique, which is ideal for the zone-type results desired here, the problem is a challenging one involving remachining of the test elements for virtually every data run. The technique used to fabricate the test elements will be described shortly.

The oil-lampback technique makes visible the pattern of fluid flow adjacent to a surface, and its main features will also be described in a later part of the paper. This technique was employed to visualize the flow pattern along the entire length of the cylinder and also at the tip.

The presentation of results will encompass photographs of the flow field and Nusselt numbers for the tip, for the tip-adjacent portion of the cylindrical surface, and for the cylindrical surface without end effects. Special emphasis will be placed on comparisons of the Nusselt numbers for the three zones and on the ramifications of these comparisons. In addition, the present cylindrical-surface Nusselt numbers, uninfluenced by end effects, will be compared with literature information.

The Experiments

Test Cylinders. The experiments were performed in the rectangular test section of a low-turbulence wind tunnel (turbulence intensity ~0.2–0.3 percent) having cross sectional dimensions 61 × 30.5 cm (horizontal × vertical). The test cylinder was positioned vertically in the tunnel, with the lower end of the cylinder being attached to the floor of the tunnel and the upper end being free. A number of cylinders were employed (one at a time) during the course of the research, and these are pictured diagrammatically (to scale) in Fig. 1.

As seen there, all of the test cylinders had the same length L, equal to 17.8 cm. The cylinders were made of aluminum, but a portion of the surface of each consisted of a layer of naphthalene, the fabrication of which will be discussed shortly. For the first three cylinders (left to right in Fig. 1), the naphthalene surface is a 2.54-cm long band situated either midway between the ends of the cylinder or slightly displaced toward the bottom (third from left), this displacement being suggested by the flow visualization photographs. These three cylinders were employed to measure cylinder-in-crossflow heat transfer coefficients uninfluenced by end effects, with a view to making comparisons with the literature. To help confirm the absence of end effects, the length-to-diameter ratio for these cylinders was varied from about 7 to 19. It should also be noted that the diameter of each cylinder is represented by a range rather than by a single number. This is because the diameter actually changed from run to run in response to machining operations, as will be explained shortly.

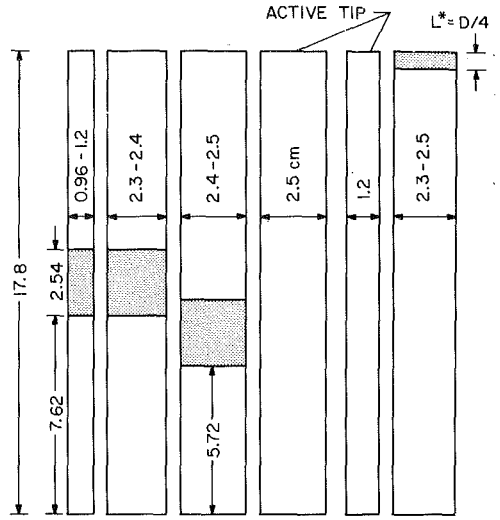

Fig. 1 Crossflow cylinders used during the research

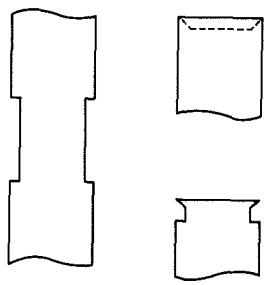

Fig. 2 Diagrams pertaining to the fabrication of the naphthalene surfaces

The third and fourth cylinders pictured in Fig. 1 were employed to determine the heat transfer coefficients at the tip of the cylinder. Since, in this case, the naphthalene surface is confined entirely to the tip, it is not visible in the side view that is shown in Fig. 1. Two cylinders of different diameters were employed to demonstrate the diameter-independence of the dimensionless representation of the results and to obtain the desired range of Reynolds numbers. There was no run-to-run machining of the diameters of these cylinders, so that they are each shown with a unique diameter. The tips were machined between runs, but to such a slight extent as not to warrant specifications of the range of the length dimension.

The last of the cylinders was used for the determination of the tip-adjacent heat transfer coefficients on the cylindrical surface. As shown in the figure, the active length L^* was maintained equal to $D/4$, even as the diameter D varied due to machining.

Mass Transfer Surfaces. The fabrication of the naphthalene surfaces will now be described and, for this purpose, it is convenient to refer to Fig. 2. The diagram at the left of Fig. 2 is intended to typify a portion of any one of the three cylinders used for the measurement of cylinder-in-crossflow heat transfer coefficients without end effects (i.e., the leftmost three cylinders of Fig. 1). As seen in this diagram, which is to scale, a square-shouldered recess was machined into the

Nomenclature

D = cylinder diameter
$\mathcal{D}$ = naphthalene-air diffusion coefficient
h = heat transfer coefficient
K = mass transfer coefficient
k = thermal conductivity
L = length of cylinder
L^* = length of tip-adjacent mass transfer zone
Nu = Nusselt number, hD/k
Pr = Prandtl number
Re = Reynolds number, $U_\infty D/\nu$
Sc = Schmidt number
Sh = Sherwood number, $KD/\mathcal{D}$
U_∞ = freestream velocity
ν = kinematic viscosity

Subscript

cyl,∞ = cylinder uninfluenced by end effects

circumference of the aluminum surface. Molten naphthalene was then poured into the recess and allowed to solidify, and the pouring was continued until the solid naphthalene protruded beyond the diameter of the cylinder. Then, using a lathe, the entire length of the cylinder was carefully machined so as to produce a uniform diameter (i.e., no discontinuity at the naphthalene-aluminum interface). The naphthalene surface resulting from the machining was at least as smooth as that of the aluminum surface.

During a data run, sublimation of mass occurred from the naphthalene surface. The extent of the sublimation was controlled by limiting the duration of the run, so that the average recession of the naphthalene did not exceed 0.0025 cm (0.001 in.). Prior to the initiation of each new data run, the surface was refinished to eliminate the recession which resulted from the prior run. This involved remachining of the entire length of the cylinder so as to obtain a completely uniform diameter, without discontinuity at the naphthalene-aluminum interface. It is this machining which was responsible for the range of cylinder diameters indicated in Fig. 1.

The upper diagram at the right of Fig. 2 is intended to illustrate the operations involved in the preparation of the naphthalene surface for the measurement of the tip heat transfer coefficient. As seen there, a bowl-like depression was machined into the tip of the cylinder, and molten naphthalene was poured into the cavity so as to form a solidified layer that protruded beyond the confines of the cavity. Prior to the pouring, the tip-adjacent portion of the cylindrical surface was tightly wrapped with a layer of aluminum foil to avoid solidification of naphthalene on that surface. Subsequent to the pouring and solidification, the cylinder was placed in a lathe and the excess naphthalene was removed. The final passes were made with great care to avoid cutting into the metal rim that surrounded the naphthalene. The machining was deemed satisfactory if the exposed metal rim had a thickness of approximately 0.0025 cm (0.001 in.). Renewal of the tip surface for each data run was accomplished as described in the foregoing—pouring of additional naphthalene and subsequent machining.

The preparation of the naphthalene test surface for the tip-adjacent portion of the cylindrical face was an especially painstaking task. First, a recess in the cylindrical surface was machined as shown in the lower right-hand diagram of Fig. 2. Molten naphthalene was poured to fill and then to overfill the recess. In this process, a film of solid naphthalene was inevitably deposited on the tip of the cylinder. Then, the cylindrical surface was machined to achieve a uniform diameter without discontinuities at the naphthalene-aluminum interface. Typically, this operation removed about 0.008–0.010 cm (0.003–0.004 in.) of aluminum (on the diameter) and thereby created a flat on the rim of the beveled surface that bounded the naphthalene. Next, the tip of the cylinder was painstakingly machined, both to remove the unwanted naphthalene coating and to eliminate the aforementioned flat. The machining was regarded as satisfactory if the exposed metal rim of the beveled surface was on the order of 0.0025 cm (0.001 in.). The aforementioned pouring and machining operations were performed for each data run.

From the foregoing paragraphs, it is evident that the preparation of the naphthalene test surfaces played a significant role in the overall effort required to carry out the research.

Other Features of the Apparatus. To facilitate attachment of the cylinders to the wind tunnel floor, a 2.5-cm length of each was axially drilled and tapped from its lower end, and a threaded rod was inserted into the tapped hole. A section of rod which protruded from the end of the cylinder was passed through a tight-fitting aperture in the tunnel floor, and a washer and nut were fitted onto the rod from below, thereby holding the cylinder firmly in place.

For convenience in handling, each cylinder was made of two parts which were held together by a threaded rod which resided in axially drilled and tapped holes in the respective parts. The two parts were machined together to ensure continuity and precise alignment. The lower of the two parts was anchored to the floor of the wind tunnel at the beginning of the preparatory stage of a data run, while the upper part, which contained the mass transfer section, was removed for weighing both at the beginning and end of the run.

With regard to instrumentation, the quantities to be measured for each data run included the air velocity, the temperature of the cylinder, the mass of the cylinder (both before and after the run), and the static pressure in the wind tunnel. The velocity was sensed by an impact tube in conjunction with a wall static tap. The impact-static pressure difference was detected by a Baratron solid-state capacitance-type pressure meter capable of discriminating 10^{-3} mm Hg. For the static pressure, the wall tap reading was supplemented by the measurement of the room barometric pressure.

The cylinder temperature was measured with a calibrated copper-constantan thermocouple in conjunction with a 0.1°F ASTM-certified thermometer, as will be described shortly. The mass of the cylinder was determined both before and after each data run with a vernier-equipped Mettler analytical balance with a smallest scale division of 10^{-4} g (0.1 mg).

Experimental Procedure and Flow Visualization. Various aspects of the experimental procedure have already been mentioned in connection with the description of the apparatus. Additional information relevant to the conduct of the experiments will now be conveyed.

Each data run was initiated with a newly prepared naphthalene surface situated in the selected test cylinder. Prior to its installation in the wind tunnel, the upper portion of the cylinder was weighed with the analytical balance. Immediately following the weighing, the naphthalene surface was sealed with an impermeable covering—either a Teflon cap for the tip or a plastic wrap for the other locations. Then, the cylinder was placed in the tunnel and the thermocouple clamped tightly between the upper and lower parts of the cylinder, with tape used to seal the small gap between the two parts that was created by the presence of the thermocouple.[1]

The airflow was then initiated and adjusted to the desired Reynolds number. After about an hour, periodic readings were made of the thermocouple and of the precision thermometer, which was situated downstream and to the side of the test cylinder. Once these readings became uniform, the equilibration period was judged to be completed. The thermocouple was extracted from the cylinder, and the two parts of the cylinder were brought into intimate contact (the thermocouple was removed because of concern that its presence might affect the flow pattern during the data run). Then, the impermeable covering was withdrawn from the naphthalene surface and, at that moment, the timing of the run began.

During the run, the duration of which extended from 15 to 45 minutes depending on the operating conditions, periodic readings were made of the temperature (via the thermometer) and of the velocity and static pressures. The duration of the run was chosen so that the mean recession of the naphthalene surface was about 0.0025 cm (0.001 in.). At the termination of the run, the naphthalene surface was covered, and the upper part of the cylinder was withdrawn from the wind tunnel and immediately weighed (with the cover removed).

The flow visualization experiments were carried out in a set of data runs separate from the mass transfer runs. As noted earlier, the oil-lampblack technique was employed as the visualization tool. For the visualization runs, the cylindrical surface and the tip were covered with a white, plastic-coated self-adhering contact paper which provided a contrasting background for the oil-lampblack mixtures which were brushed on it.

Lampblack is a very fine black powder now primarily available as an ingredient of paint. It mixes readily with oil, and the mixture, when brushed on a surface, produces a smooth, glossy-black coating. The fluidity of the mixture can be regulated by the selection of the viscosity of the oil and by the proportions of the oil and the lampblack powder. The general procedure for using the technique is to brush the oil-lampblack mixture on a surface and then to expose the surface to the airflow whose characteristics are to be studied. Under the action of

[1] It was verified that any residual adhesive that might have remained on the cylinder when the tape was removed had a negligible effect on the mass measurement ($\leq$0.1 mg).

the shear stresses exerted by the flow, the mixture will move along the surface, following the paths of the fluid particles that pass adjacent to the surface. In regions of low velocity (e.g., stagnation regions), the shear stresses are small and the mixture will remain stationary, so that such regions show themselves as black streak-free zones on the surface.

The ideal fluidity is such that the mixture will move slowly over the surface under the action of the shear forces. For such an ideal mixture, any excess will be blown off, leaving an array of streaks which indicate the direction of the fluid flow adjacent to the surface. A mixture that is too fluid will be completely blown off the surface, so that no indication of the flow pattern remains. In addition, a too-fluid mixture tends to sag under the action of gravity. On the other hand, a too-stiff mixture will not move at all, again providing no information about the flow. The attainment of the proper mixture fluidity is a trial and error process. Furthermore, a fluidity that is appropriate at a particular Reynolds number may not be effective at another Reynolds number, owing to differences in the shear stresses that are exerted.

The oil-lampblack technique can provide flow pattern information via three types of observations. First, observation of the movement of the freshly applied mixture immediately after initiation of the airflow reveals the direction of fluid motion. Next, after the excess mixture is blown off the surface, a fixed pattern of streaks is established which gives further confirmation of the flow direction. Finally, in separate experiments, the mixture can be applied locally at selected positions on the surface to identify the details of the motion at those positions.

In the present experiments, the flows adjacent to the cylindrical surface and adjacent to the tip were visualized, and the corresponding oil-lampblack patterns were photographed.

Results and Discussion

The presentation of results will begin with the information obtained from the flow visualization studies, with the mass (heat) transfer results to follow.

Flow Visualization Results. Attention is first turned to the pattern of fluid flow adjacent to the cylindrical surface. Inasmuch as the cylinder was positioned vertically in the wind tunnel, a fairly stiff oil-lampblack mixture was used to avoid sagging, and the tunnel was run at the highest Reynolds number (~25,000) to ensure a sharp streak-line pattern.

A photograph of the visualized flow pattern is presented in Fig. 3, where the bottom edge of the photo corresponds to the wall-attached end of the cylinder and the top edge corresponds to the free end. The photograph is a head-on view, looking at the cylinder from the direction of the oncoming flow.

The vertical black line at the center of the photograph marks the stagnation of the oncoming flow on the cylinder. This line extends over most of the length of the cylinder, but fades away near the top and bottom ends. Emanating outward from the stagnation line is a network of very fine lines which, except near the ends of the cylinder, are more or less horizontal. In actuality, these fine horizontal lines (such lines are also pictured in Fig. 6 of [4]) represent the flow that passes circumferentially around the cylinder. The vertical black bands at the left- and right-hand borders of the photograph correspond to a portion of the separated region.

Closer inspection of the photograph indicates a downflow adjacent to the lower end of the cylinder and an upflow adjacent to the upper end. These are strong flows, as witnessed by the fact that they have eaten away the stagnation line adjacent to the ends of the cylinder. The presence of these flows is readily rationalized.

To facilitate the discussion, it should be noted that the stagnation of the flow against the cylinder causes a pressure rise, the extent of which depends on the velocity of the oncoming flow. The fluid approaching the bottom of the cylinder is a relatively slow moving flow because it is contained within the boundary layer of the wall to which the cylinder is attached. Therefore, there is only a modest pressure rise due to stagnation near the bottom of the cylinder. However, at higher elevations, above the wall boundary layer, the full velocity

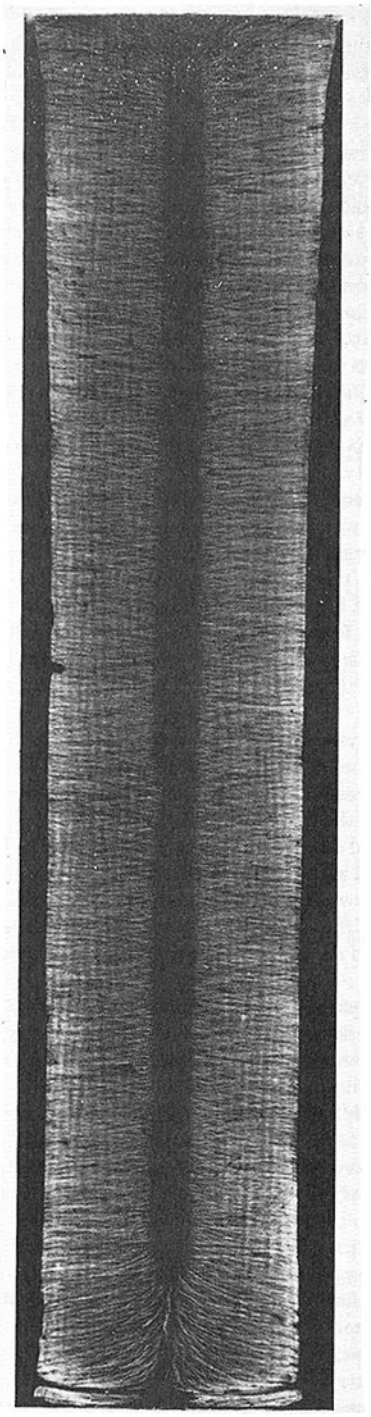

Fig. 3 Flow field visualization as seen in a head-on view, looking at the cylinder from the direction of the oncoming flow

prevails and there is an appreciably larger pressure rise due to stagnation. As a consequence, the pressure at the lower reaches of the stagnation line decreases in the downward direction, and this pressure gradient is responsible for the downflow adjacent to the bottom edge of the cylinder. As shown in [5], frontispiece and Fig. XII.32, the downflow gives rise to an eddy which stands just upstream of the cylinder, adjacent to the wall to which the cylinder is attached.

A related argument applies to the upflow near the top of the cylinder. In the free space above the cylinder, there is neither stagnation nor pressure rise. Therefore, near the upper reaches of the cylinder, the pressure at the stagnation line decreases in the upward direction, thereby inducing the upflow. This upflow should have a marked effect on the heat transfer coefficients at the tip-adjacent portion of the cylindrical surface, and this matter will be revisited when the mass

(heat) transfer results are presented.

The angular position marking the onset of flow separation on the cylindrical surface is proportional to the distance between the central stagnation line and the black bands at the side of the photograph. It is seen from the photo that the three-dimensional flow near the top of the cylinder significantly delays the onset of separation; near the bottom of the cylinder, separation is only slightly delayed by the three-dimensional effects. Over most of the length of the cylinder, the inner boundary lines of the separated region, respectively to the left and right of the stagnation line, are nearly parallel. Strict parallelism occurs just below mid-height, and mass transfer measurements were performed in this region as well as at mid-height.

The flow pattern adjacent to the tip of the cylinder will now be considered, and to facilitate the discussion attention will be focused on Fig. 4. This figure is a photograph taken looking directly downward at the tip of the cylinder from above. The photograph reveals a flow pattern which is remarkable both for its sheer complexity and for its aesthetic beauty.

For purposes of orientation with respect to Fig. 4, it should be noted that the flow approaching the cylinder lies in planes parallel to the plane of the figure. The flow approaches the cylinder in the direction from the top of the photograph to the bottom.

Inspection of Fig. 4 reveals six distinct zones. In discussing these zones, the term forward flow will be used to denote fluid motion that is in the same direction as the oncoming flow, while the term backflow will denote fluid motion whose direction is opposite to that of the oncoming flow.

From the physical point of view, the freestream flow approaching the upper reaches of the cylinder can be envisioned as rising to avoid the blockage created by the cylinder. The rising fluid tends to brush lightly against the forward portion of the tip, thereby creating the broad, sideward-curving streaks that are seen in the topmost zone of Fig. 4. This is a zone of weak forward flow.

The rising flow separates from the tip of the cylinder, and it is the recirculation of the separated flow and the reattachment downstream of the separated region that shapes most of the other zones seen in the figure.

The dark crescent-shaped region situated in the lower part of the photograph marks the reattachment of the separated flow, so that the separated region and its recirculating flow are located fore of the crescent. The sharply etched lines that populate the separated region are lines of backflow (i.e., opposite to the freestream direction). These backflow lines terminate in a broad black band (in reality, the backflow lifts off the surface at the border of the black band). The black band is a zone of very low velocity. It is, in a sense, a neutral zone that stands between the forward and backflows that exist at its upstream and downstream edges. Careful local probing within the black band, utilizing local application of the oil-lampblack mixture, revealed regions of weak forward flow, especially near the flanks of the band. Photographic records of the local probing are available, but they are not included here because of journal space limitations.

Aft of the crescent, the flow is reattached and is forward in direction (i.e., in the same direction as the freestream). At the downstream extremity of the tip, at the rim, there is a small black region. Extensive visual observation indicated this to be a stagnation zone, from which flow could not pass downstream (i.e., over the rim) because of a blocking current which moved upward along the cylindrical surface.

The extreme complexity of the just-discussed flow pattern adjacent to the tip of the cylinder makes even intuitive predictions about the tip heat transfer uncertain. However, some comments appear appropriate. First of all, considering the major differences in the flow patterns on the tip and on the cylindrical surface, there is ample reason to expect that the heat transfer coefficients for the two surfaces will display different Reynolds number dependences. Furthermore, the more complex flow at the tip may well give rise to greater mixing and, by this mechanism, higher heat transfer coefficients.

Heat Transfer Results. In the presentation which follows, attention will first be focused on the cylindrical surface heat transfer

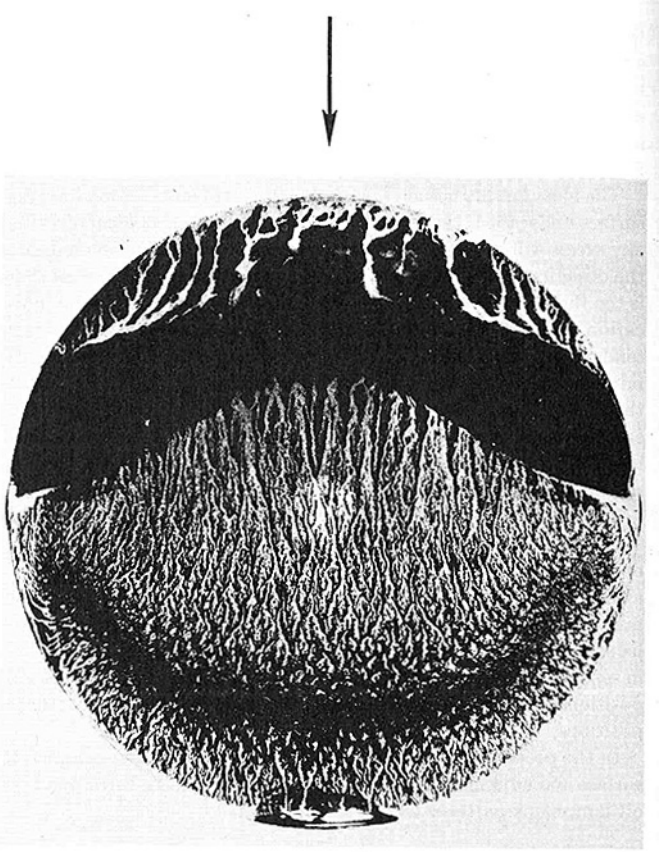

Fig. 4 Flow field visualization as seen looking directly downward at the tip of the cylinder from above

coefficients that are uninfluenced by end effects. These will be followed by the coefficients for the tip-adjacent cylindrical surface and for the tip, with comparisons being made throughout the presentation, when appropriate.

Before presenting the numerical results, the data reduction procedure will be briefly described. From the mass measurements made before and after each data run, the rate of mass transfer $\dot{m}$ per unit naphthalene surface area was evaluated.[2] The mass transfer coefficient K is the ratio of $\dot{m}$ to the difference in the naphthalene vapor densities at the surface and in the approach flow. The latter density is zero, while the former was determined by employing the Sogin vapor pressure—temperature relation [2] in conjunction with the perfect gas law.

For a dimensionless representation, the Sherwood number Sh, which is the mass transfer counterpart of the Nusselt number, is used. It is defined as

$$\mathrm{Sh} = KD/\mathcal{D} \tag{1}$$

in which D is the cylinder diameter and $\mathcal{D}$ is the naphthalene-air diffusion coefficient [3]. The mass transfer counterpart of the Prandtl number is the Schmidt number $\mathrm{Sc} = \nu/\mathcal{D}$, whose value for the present experiments is 2.55. In view of the minute concentrations of naphthalene vapor, ν was evaluated as the kinematic viscosity of pure air. The final dimensionless parameter is the Reynolds number

$$\mathrm{Re} = U_\infty D/\nu \tag{2}$$

where U_∞ is the freestream velocity of the approach flow. Owing to the well-established analogy between heat and mass transfer, the words heat and mass will be used interchangeably throughout the presentation.

The results for the cylindrical surface Sherwood (Nusselt) number, uninfluenced by end effects, are presented in Fig. 5, where they are

[2] In evaluating $\dot{m}$ a small correction was made for mass sublimed during the equilibration period.

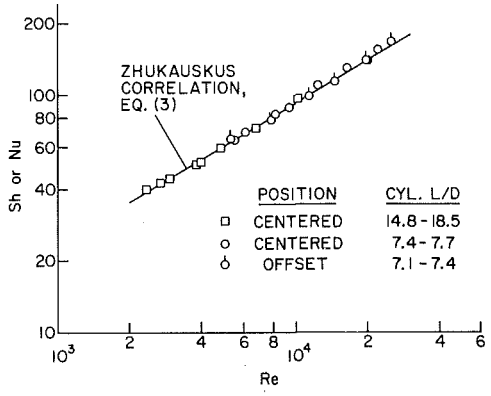

Fig. 5 Sherwood (Nusselt) number results for the end-effect-free portion of the cylindrical surface

plotted as a function of the Reynolds number. Different data symbols are employed to identify the cylinder length-diameter ratio L/D and the position of the mass transfer element, and these designations can, in turn, be identified by referring to the three leftmost cylinders pictured in Fig. 2. In addition to the data, Fig. 5 also contains a straight line whose significance will be discussed shortly.

The data in Fig. 5 indicate no effect of the cylinder L/D on the Sherwood (Nusselt) number in the range investigated, i.e., L/D between 7.1 and 18.5. Furthermore, the measured Sherwood numbers are the same for the mass transfer element at mid-height and that which is offset below mid-height. These characteristics affirm that the data are uninfluenced by end effects, as was asserted at the outset. In considering the significance of this finding, it should be reiterated that it has been demonstrated to be applicable to an element of transfer surface situated well away from the ends. There is no basis for inferring that the average Sherwood or Nusselt number for the entire cylinder would be independent of L/D in the range investigated.

Attention will now be turned to a comparison of the data of Fig. 5 with literature correlations for the cylinder in crossflow. In general, the available correlations do not include the cylinder L/D as a parameter [1], thereby implying that they are independent of end effects. It should also be noted that the overwhelming majority of the literature data are for Pr (or Sc) = 0.7, whereas the present data are for Sc = 2.55. It is believed that the most reliable correlation for Pr (or Sc) > 0.7 is that of Zhukauskus [6], and that correlation will, therefore, be used for comparison with the present data.

The Zhukauskus correlation contains provisions for variable property effects, but these are omitted here because property variations are entirely negligible for naphthalene sublimation in air. With these simplifcations, the correlation becomes

$$\mathrm{Nu} = 0.26\mathrm{Re}^{0.6}\mathrm{Pr}^{0.37} \tag{3}$$

where the exponent 0.6 of the Reynolds number and the constant 0.26 are specific to the range Re = 10^3 to 2×10^5. The solid line in Fig. 5 is a representation of equation (3) for Pr = Sc = 2.55.

Examination of Fig. 5 reveals a remarkably good level of agreement between the present data and the Zhukauskus correlation. This impressive level of agreement not only affirms the present experimental technique, but also lends strong support to the general validity of the naphthalene sublimation technique. With Fig. 5 as background, the results for the tip and for the tip-adjacent part of the cylindrical surface can be presented with confidence.

The Sherwood (Nusselt) number data for the tip-adjacent portion of the cylindrical surface are presented as a function of the Reynolds number in Fig. 6, where a curve has been faired through the data points to provide continuity. As was noted earlier, the length L^* of the tip-adjacent cylindrical surface to which these results correspond is defined by $L^*/D = 1/4$. The area of this length of cylindrical surface is identical to that of the tip.

In Fig. 6, the tip-adjacent results are compared with those for the cylindrical surface without end effects. The latter results, already

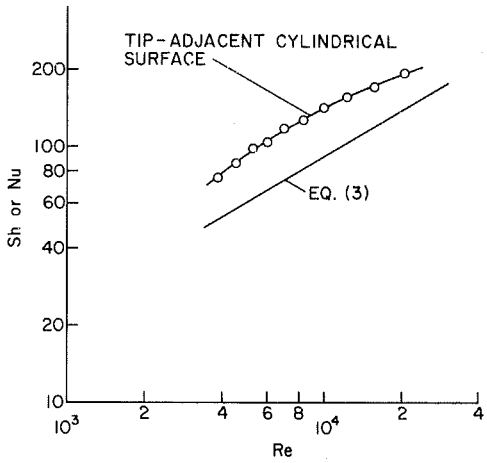

Fig. 6 Sherwood (Nusselt) number results for the tip-adjacent portion of the cylindrical surface

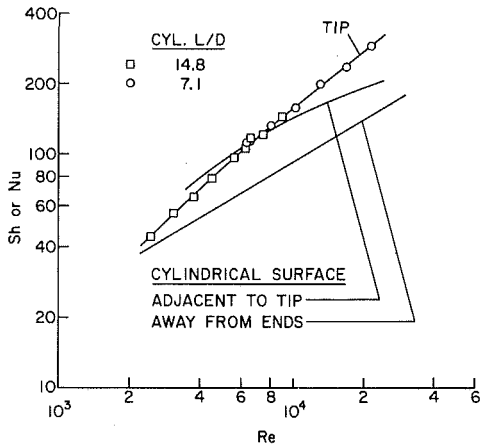

Fig. 7 Sherwood (Nusselt) number results for the tip of the cylinder

presented in Fig. 5, are so well represented by equation (3) that the equation, rather than the actual data, is shown in Fig. 6.

Figure 6 indicates that in the range of Reynolds numbers investigated, the end effects associated with the free end of the cylinder enhance the heat transfer coefficients on the cylindrical surface. The enhancement, which is somewhat dependent on Reynolds number, is on the order of 50 percent.

There are two factors, both related to the fluid flow patterns of Fig. 3, that are primarily responsible for the differences between the cylindrical-surface transfer coefficients adjacent to the tip and away from the tip. One of these is the tip-adjacent turning, acceleration, and redirection of the flow toward the free end of the cylinder, a process which can be expected to enhance heat transfer. The second factor is the decrease in the angular extent of the separated region which occurs as the free end is approached. At lower Reynolds numbers, the separated region is a zone of degraded heat transfer, whereas at higher Reynolds numbers it is a zone of enhanced heat transfer. Therefore, at the higher Reynolds numbers, the smaller separation zone in the tip-adjacent region tends to be less enhancing than the larger separated region that prevails away from the tip. This behavior is believed responsible for the closing of the gap between the tip-adjacent results and those away from the tip, as is in evidence in Fig. 6 at the higher Reynolds numbers.

The measured Sherwood (Nusselt) numbers for the tip are presented in Fig. 7 which also includes, for comparison purposes, the already presented results for the cylindrical surface. To maintain clarity, the latter are portrayed as curves rather than as data points. The data points for the tip are interconnected by a faired curve to provide continuity.

The figure shows that in the Reynolds number range investigated, $2500 \leq \mathrm{Re} \leq 25{,}000$, the tip heat transfer coefficients exceed those

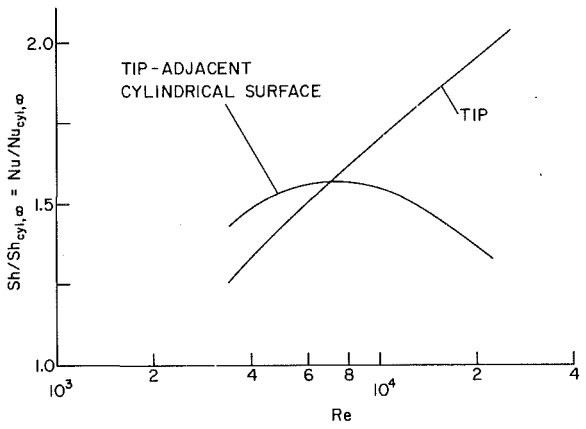

Fig. 8 Comparison of Sherwood (Nusselt) numbers for the tip and the tip-adjacent region with those for the end-effect-free portion of the cylindrical surface

for the end-effect-free cylindrical surface, with deviations that increase with Reynolds number. At the upper end of the range, the tip Sherwood (Nusselt) numbers are twice as large as those for the cylindrical surface. To rationalize this finding, reference may be made to the flow patterns portrayed in Fig. 4. There, it can be seen that most of the tip area is washed by flows that are highly responsive to Reynolds number—namely, in the separated region and the reattachment zone. On the other hand, for the cylindrical surface, away from the ends, about half of the circumference—the forward half—is washed by a less responsive flow. It is, therefore, quite reasonable that the variation of Sh or Nu with Re at the tip has a steeper slope than that for the end-effect-free cylindrical surface.

From the foregoing, it is evident that in the Reynolds number range investigated, the tip heat transfer would be underestimated if it were to be evaluated using the conventional cylinder-in-crossflow Nusselt number correlation.

Attention is now turned to the comparison between the tip heat transfer coefficients and those for a tip-adjacent length of cylindrical surface $L^* = D/4$. As noted in the Introduction, such a length of cylindrical surface has the same area as the tip. Figure 7 shows that over part of the investigated range of Reynolds numbers, between 4500 and 10,000, the coefficients for the two zones are within ten percent of each other. At larger Reynolds numbers, the tip-adjacent coefficients increase relatively slowly, with the result that at Re = 25,000 the tip coefficients exceed those for the near-tip region by about 60 percent. The deviations at the larger Reynolds numbers can be rationalized by arguments similar to those employed earlier in this section. Below Re = 4500, insufficient data are available to quantify the extent of the deviations between the two sets of results.

The ramifications of the foregoing comparisons with respect to fin theory will be discussed in the Concluding Remarks.

In the final figure, Fig. 8, a compact comparison of the Sherwood (Nusselt) numbers for the three zones of measurement is presented. For this comparison, the results for the end-effect-free cylindrical surface, designated here as $Sh_{cyl,\infty}$ or $Nu_{cyl,\infty}$, are used as a baseline. The Sherwood (Nusselt) numbers for the other zones were ratioed with $Sh_{cyl,\infty}$ ($Nu_{cyl,\infty}$), and the ratios are plotted in Fig. 8. The figure affirms that in the range investigated, both the tip heat transfer coefficient and the tip-adjacent heat transfer coefficient exceed $h_{cyl,\infty}$. In particular, $Sh/Sh_{cyl,\infty}$ for the tip ranges from 1.25 to 2.03, monotonically increasing with Reynolds number. For the tip-adjacent region, $1.34 \leq Sh/Sh_{cyl,\infty} \leq 1.57$ and is not monotonic.

Concluding Remarks

As was noted in the Introduction, there are various approaches used in fin theory to deal with the tip of the fin. Because of the heretofore universal unavailability of fin-tip heat transfer coefficients, all of the approaches are, to various degrees, approximations. It is standard practice in fin theory to ignore possible variations of the heat transfer coefficient along the principal surface(s) of the fin; rather, a single constant value is used. For a wall-attached cylindrical fin, the fin heat transfer coefficient would be obtained from literature correlations for the cylinder-in-crossflow (without end effects). This same coefficient would also be used at the fin tip and at fictive extensions of the cylindrical surface (when the tip heat transfer is conceptually suppressed).

The experimental data obtained here show that the tip heat transfer coefficients are higher than those for the cylindrical surface of an end-effect-free cylinder in crossflow. Therefore, all of the prior approaches tend to underestimate the heat transfer from the tip and, therefore, the heat transfer from the fin. With regard to the replacement of a conceptually insulated tip with a fictive extension of the cylindrical surface, such an approach would be more accurate if tip-adjacent heat transfer coefficients were to be used rather than those for the end-effect-free cylindrical surface. This is because the former are in closer agreement with the tip coefficients than are the latter.

It is also shown that there is not a simple relationship between the tip coefficients and those for the end-effect-free cylindrical surface, and the absence of such a relationship is a deterrent to the proper treatment of the fin tip in design calculations. The different Reynolds number dependences of the two sets of coefficients are due to profound differences in the respective patterns of fluid flow.

Acknowledgment

This research was performed under the auspices of the National Science Foundation.

References

1 Morgan, V. T., "The Overall Convective Heat Transfer from Smooth Circular Cylinders," in *Advances in Heat Transfer*, Vol. 11, Academic Press, New York, 1975, pp. 199–264.

2 Sogin, H. H., "Sublimation from Disks to Air Streams Flowing Normal to their Surfaces," *Trans. ASME*, Vol. 80, 1958, pp. 61–69.

3 Skelland, A. H. P., *Diffusional Mass Transfer*, Wiley, New York, 1974, p. 51.

4 Kestin, J., and Wood, R. T., "On the Stability of Two-Dimensional Stagnation Flow," *Journal of Fluid Mechanics*, Vol. 44, 1970, pp. 461–480.

5 Thwaites, B., ed., *Incompressible Aerodynamics*, Clarendon Press, Oxford, 1960.

6 Zhukauskus, A. A., "Heat Transfer from Tubes in Crossflow," in *Advances in Heat Transfer*, Vol. 8, Academic Press, New York, 1972, pp. 93–160.

Steady Laminar Flow through Twisted Pipes

Fluid Flow in Square Tubes

J. H. Masliyah
K. Nandakumar

Department of Chemical Engineering,
University of Alberta,
Edmonton, Alberta,
Canada T6G 2G6

The Navier-Stokes equation in a rotating frame of reference is solved numerically to obtain the flow field for a steady, fully developed laminar flow of a Newtonian fluid in a twisted tube having a square cross-section. The macroscopic force and energy balance equations and the viscous dissipation term are presented in terms of variables in a rotating reference frame. The computed values of friction factor are presented for dimensionless twist ratios, (i.e., length of tube over a rotation of π radians normalized with respect to half the width of tube) of 20, 10, 5 and 2.5 and for Reynolds numbers up to 2000. The qualitative nature of the axial velocity profile was observed to be unaffected by the swirling motion. The secondary motion was found to be most important near the wall.

Introduction

It has been well established that secondary flow can significantly enhance transfer processes such as heat and mass transfer. Secondary flows are normally generated in the presence of curved walls. Literature abounds with papers on flow through curved tubes of various cross sections [1–6]. In a series of papers, Marris [7, 8] provided a fundamental insight on the generation of secondary flow. His objective was to provide qualitative results applicable to a wide variety of flow situations, rather than precise quantitative data of engineering importance. Todd [9] studied a more specific problem of flow through twisted tubes. His analysis was restricted to pipes in which the orientation of the cross-section changes slowly with distance along the axis of the pipe. With this restriction he was able to simplify the Navier-Stokes equation in a rotating frame of reference to a classical equation in elasticity theory, viz. a fourth order partial differential equation governing the transverse displacement of a clamped elastic plate. His analysis up to that point is valid for a pipe of any cross section. Todd also presented approximate solution to the simplified equations for a specific geometry of elliptic tubes. His analysis was restricted to tubes with small twist rates. The twist rate is defined as π/H' where H' is the distance along the axis of the pipe over a rotation of π radians. Todd pointed out the necessity to use a numerical method to solve the complete Navier-Stokes equation. Date [10] presented a numerical solution for flow through a circular tube with a twisted tape insert. He solved the Navier-Stokes equation in a rotating cylindrical coordinate. The twist rate of the tape insert was varied from 4.50 to 31.44.

In a series of papers we will present both qualitative analysis of the flow field and precise quantitative data on pressure drop and heat transfer rates in twisted tubes. It should be pointed out that twisted tubes of various cross sections are available commercially. In this paper we present a detailed numerical solution for fully developed viscous flow in twisted tubes with a square cross section. The Navier-Stokes equation in the stream function-vorticity form will be solved in a rotating rectangular coordinate system. The rotating coordinate system is preferred because the flow field is two-dimensional in such a system.

Governing Differential Equations

The dimensional form of the Navier-Stokes equation (NSE) for steady laminar flow is,

$$\rho\bar{\mathbf{v}}' \cdot \nabla' \bar{\mathbf{v}}' = -\nabla' \bar{p}' + \mu\nabla'^2 \bar{\mathbf{v}}' \tag{1}$$

and the continuity equation for an incompressible fluid is,

$$\nabla' \cdot \bar{\mathbf{v}}' = 0 \tag{2}$$

A suitable length scale for making the equations dimensionless is a, where $(2a)$ is the width of a rectangular tube (see Fig. 1). Define the following dimensionless quantities

$$\nabla = a\nabla' \qquad \nabla^2 = a^2\nabla'^2$$

$$\bar{\mathbf{v}} = \bar{\mathbf{v}}'/(\nu/a) \qquad \overline{\mathbf{Q}} = (\nabla'\bar{p}')a^3/\nu\mu$$

where the vector $\overline{\mathbf{Q}}$ has three components $\{\overline{Q}_{\bar{x}}, \overline{Q}_{\bar{y}}, \overline{Q}_{\bar{z}}\}$. Equations (1) and (2) can then be written in dimensionless form as

$$\bar{\mathbf{v}} \cdot \nabla \bar{\mathbf{v}} = -\overline{\mathbf{Q}} + \nabla^2 \bar{\mathbf{v}} \tag{3}$$

$$\nabla \cdot \bar{\mathbf{v}} = 0 \tag{4}$$

All the quantities with an overbar are defined in a fixed co-ordinate system $(\bar{x}, \bar{y}, \bar{z})$ whereas quantities without an overbar are defined in a rotating coordinate system (x, y, z). The presentation is restricted to square pipes of constant twist rates. Let the cross section of the tube undergo a complete rotation (2π radians) over a length of $2H'$. The rotating coordinate system (x, y, z) will also undergo an identical rotation. The spatial coordinates of a point are transformed into the rotating coordinate as,

$$\begin{bmatrix} x \\ y \\ z \end{bmatrix} = \begin{bmatrix} \cos\theta_z & \sin\theta_z & 0 \\ -\sin\theta_z & \cos\theta_z & 0 \\ 0 & 0 & 1 \end{bmatrix} \begin{bmatrix} \bar{x} \\ \bar{y} \\ \bar{z} \end{bmatrix} \tag{5}$$

where θ_z is the angle of rotation, and it is a function of z. For a constant twist rate, we have $\theta_z(z) = \pi z'/H' = \pi z/H$; both z' and H' are normalized with the length scale a. As pointed out by Todd [9] it is not convenient to decompose the velocity vector into contravariant

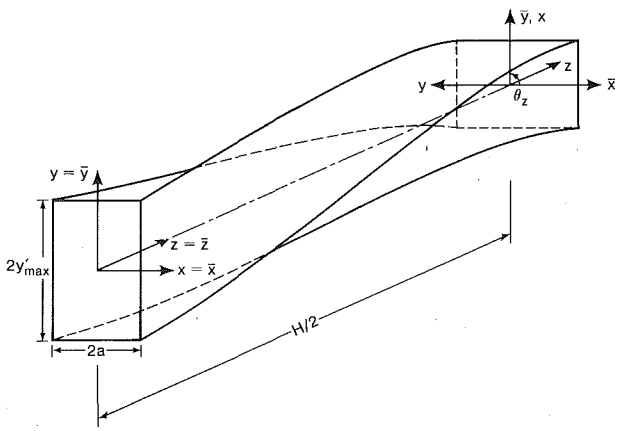

Fig. 1 Tube geometry and the rotating coordinate system

Contributed by The Heat Transfer Division for publication in The JOURNAL OF HEAT TRANSFER. Manuscript received by the Heat Transfer Division January 2, 1981.

components. Hence the velocity vector $\mathbf{v}$ is decomposed in the rotating coordinate system as,

$$\mathbf{v} = \mathbf{i}_x v_x + \mathbf{i}_y v_y + \mathbf{i}_z v_z \tag{6}$$

where $\mathbf{i}_x$, $\mathbf{i}_y$ and $\mathbf{i}_z$ are the unit vectors in the ox, oy and oz directions Note that $\mathbf{i}_z = \bar{\mathbf{i}}_z$; i.e., the z-direction is the same in both coordinate systems. The velocity $\bar{\mathbf{v}}$ in equations (3) and (4) are transformed into the rotating coordinate as follows:

$$\mathbf{v} = \begin{bmatrix} \text{coz}\,\theta_z & -\sin\theta_z & 0 \\ \sin\theta_z & \cos\theta_z & 0 \\ 0 & 0 & 1 \end{bmatrix} \tag{7}$$

The derivatives of a scalar function f in the stationary coordinate system are transformed into the rotating coordinate system using,

$$\begin{bmatrix} \frac{\partial f}{\partial \bar{x}} \\ \frac{\partial f}{\partial \bar{y}} \\ \frac{\partial f}{\partial \bar{z}} \end{bmatrix} = \begin{bmatrix} \cos\theta_z & -\sin\theta_z & 0 \\ \sin\theta_z & \cos\theta_z & 0 \\ \theta_z' y & -\theta_z' x & 1 \end{bmatrix} \begin{bmatrix} \frac{\partial f}{\partial x} \\ \frac{\partial f}{\partial y} \\ \frac{\partial f}{\partial z} \end{bmatrix} \tag{8}$$

where $\theta_z' = \pi/H$ is the twist rate, obtained by differentiating $\theta_z(z) = \pi z/H$ with respect to z. Using the transformations given in equations (7) and (8), the components of equations (3) and (4) can be transformed into the rotating coordinate. In the case of fully developed steady flow, all the gradients in the z direction (except for pressure) are zero in the transformed coordinates. The resulting two-dimensional equations are:

Continuity equation in rotating coordinates

$$\frac{\partial v_x}{\partial x} + \frac{\partial v_y}{\partial y} + \frac{\pi}{H}\left\{y\frac{\partial v_z}{\partial x} - x\frac{\partial v_z}{\partial y}\right\} = 0 \tag{9}$$

***x*-component of equation (1) in rotating coordinates**

$$\begin{aligned} v_x\frac{\partial v_x}{\partial x} + v_y\frac{\partial v_x}{\partial y} + \frac{\pi}{H}v_z\left\{y\frac{\partial v_x}{\partial x} - x\frac{\partial v_x}{\partial y} - v_y\right\} \\ = -Q_x + \frac{\partial^2 v_x}{\partial x^2} + \frac{\partial^2 v_x}{\partial y^2} + \left(\frac{\pi}{H}\right)^2\left\{x^2\frac{\partial^2 v_x}{\partial y^2} + y^2\frac{\partial^2 v_x}{\partial x^2}\right. \\ \left. - 2xy\frac{\partial^2 v_x}{\partial x\,\partial y} - y\frac{\partial v_x}{\partial y} - x\frac{\partial v_x}{\partial x} - v_x + 2x\frac{\partial v_y}{\partial y} - 2y\frac{\partial v_y}{\partial x}\right\} \end{aligned} \tag{10}$$

***y*-component of equation (1) in rotating coordinates**

$$\begin{aligned} v_x\frac{\partial v_y}{\partial x} + v_y\frac{\partial v_y}{\partial y} + \frac{\pi}{H}v_z\left\{y\frac{\partial v_y}{\partial x} - x\frac{\partial v_y}{\partial y} + v_x\right\} \\ = -Q_y + \frac{\partial^2 v_y}{\partial x^2} + \frac{\partial^2 v_y}{\partial y^2} + \left(\frac{\pi}{H}\right)^2\left\{y^2\frac{\partial^2 v_y}{\partial x^2} + x^2\frac{\partial^2 v_y}{\partial y^2}\right. \\ \left. -2xy\frac{\partial^2 v_y}{\partial x\,\partial y} - y\frac{\partial v_y}{\partial y} - x\frac{\partial v_y}{\partial x} - v_y + 2y\frac{\partial v_x}{\partial x} - 2x\frac{\partial v_x}{\partial y}\right\} \end{aligned} \tag{11}$$

***z*-component of equation (1) in rotating coordinates**

$$\begin{aligned} v_x\frac{\partial v_z}{\partial x} + v_y\frac{\partial v_z}{\partial y} + \frac{\pi}{H}v_z\left\{y\frac{\partial v_z}{\partial x} - x\frac{\partial v_z}{\partial y}\right\} \\ = -Q_z - \frac{\pi}{H}\{yQ_x - xQ_y\} + \frac{\partial^2 v_z}{\partial x^2} + \frac{\partial^2 v_z}{\partial y^2} \\ + \left(\frac{\pi}{H}\right)^2\left\{y^2\frac{\partial^2 v_z}{\partial x^2} + x^2\frac{\partial^2 v_z}{\partial y^2} - x\frac{\partial v_z}{\partial x} - y\frac{\partial v_z}{\partial y} - 2xy\frac{\partial^2 v_z}{\partial x\,\partial y}\right\} \end{aligned} \tag{12}$$

The equations of motion in the rotating coordinates have additional terms of order π/H and $(\pi/H)^2$ which are responsible for the secondary flow. A stream function which satisfies the continuity equation (9), can be defined in the transformed coordinate system as,

$$v_x = \frac{\partial \psi}{\partial y} - \frac{\pi}{H}yv_z \tag{13a}$$

$$v_y = -\frac{\partial \psi}{\partial x} + \frac{\pi}{H}xv_z \tag{13b}$$

where the stream function has been normalized as $\psi = \psi'/\nu$. Vorticity is defined in the stationary coordinate system as, $\bar{\omega} = \nabla\times\bar{\mathbf{v}}$, the $\bar{z}$-component of which is,

$$\bar{\omega}_z = \frac{\partial \bar{v}_{\bar{y}}}{\partial \bar{x}} - \frac{\partial \bar{v}_{\bar{x}}}{\partial \bar{y}} \tag{14}$$

In the rotating coordinate system this transforms to:

$$\omega_z = \frac{\partial v_y}{\partial x} - \frac{\partial v_x}{\partial y} \tag{15}$$

The stream-function equation is obtained from equations (13) and (15) as,

Stream function-vorticity equation

$$\omega_z = -\frac{\partial^2 \psi}{\partial x^2} - \frac{\partial^2 \psi}{\partial y^2} + \frac{\pi}{H}\left[2v_z + x\frac{\partial v_z}{\partial x} + y\frac{\partial v_z}{\partial y}\right] \tag{16}$$

The vorticity transport equation is obtained from equations (10) and (11) by eliminating the pressure gradients in the usual manner.

Vorticity transport equation

$$\begin{aligned} \frac{\partial \psi}{\partial y}\frac{\partial \omega_z}{\partial x} - \frac{\partial \psi}{\partial x}\frac{\partial \omega_z}{\partial y} + \omega_z\frac{\pi}{H}\left(x\frac{\partial v_z}{\partial y} - y\frac{\partial v_z}{\partial x}\right) \\ + \frac{\pi}{H}\left[y\frac{\partial v_y}{\partial x} - x\frac{\partial v_y}{\partial y} + v_x\right]\frac{\partial v_z}{\partial x} - \frac{\pi}{H}\left[y\frac{\partial v_x}{\partial x} - x\frac{\partial v_x}{\partial y} - v_y\right]\frac{\partial v_z}{\partial y} \\ = \frac{\partial^2 \omega_z}{\partial x^2} + \frac{\partial^2 \omega_z}{\partial y^2} + \left(\frac{\pi}{H}\right)^2\left[x^2\frac{\partial^2 \omega_z}{\partial y^2} + y^2\frac{\partial^2 \omega_z}{\partial x^2}\right. \\ \left. - x\frac{\partial \omega_z}{\partial x} - y\frac{\partial \omega_z}{\partial y} - 2xy\frac{\partial^2 \omega_z}{\partial x\,\partial y}\right] \end{aligned} \tag{17}$$

Equations (12, 16) and (17) together with the appropriate boundary conditions to be presented later define the flow field of a Newtonian fluid in a twisted tube.

Nomenclature

a = dimensional half width of tube
e_v = energy loss factor, dimensionless
f^* = friction factor, dimensionless
H = length of tube over a rotation of π radians, dimensionless ($H = H'/a$)
$\mathbf{i}_j$ = unit vectors in $j = x, y, z$ directions
p' = pressure, dimensional
$\mathbf{Q}$ = a vector of pressure gradient in rotating coordinate $\{Q_x, Q_y, Q_z\}$, dimensionless
$\bar{\mathbf{Q}}$ = a vector of pressure gradient in stationary coordinate $\{\bar{Q}_{\bar{x}}, \bar{Q}_{\bar{y}}, \bar{Q}_{\bar{z}}\}$, dimensionless
Re = Reynolds number, $2a\langle v_z'\rangle/\nu$
r = radial coordinate, dimensionless
$\mathbf{v}$ = velocity vector $\{v_x, v_y, v_z\}$, dimensionless
x = coordinate
y = coordinate
y_{max} = height of tube in y direction, dimensionless ($y_{max} = y_{max}'/a$)
z = coordinate
Δx = grid size in x-direction, dimensionless
Δy = grid size in y-direction, dimensionless
θ = angular coordinate
θ_z = angle of rotation of the coordinate
v1m = fluid viscosity
ν = kinematic viscosity
ρ = fluid density
ψ = stream function, dimensionless
ω_z = axial vorticity, dimensionless
Φ_v = energy dissipation term, dimensionless
$\langle\cdot\rangle$ = average quantity (e.g., $\langle v_z\rangle$)

Subscripts

x = x-component of a vector (e.g., v_x)
y = *y-component of a vector* (e.g., v_y)
z = *z-component of a vector* (e.g., v_z)

Superscripts

$\bar{\ }$ = a variable in stationary coordinate
$'$ = a dimensional variable

The Reynolds number, defined as $\mathrm{Re} = 2a\langle v'_z\rangle\rho/\mu$, can be expressed in terms of dimensionless mean axial velocity as,

$$\mathrm{Re} = 2\langle v_z\rangle \tag{18}$$

The friction factor, f^*, is defined as

$$f^* = \frac{\langle \tau'_w{}^*\rangle}{\frac{1}{2}\rho\langle v_z'\rangle^2} \tag{19}$$

where $\langle \tau'_w{}^*\rangle$ is an average equivalent shear stress which acts on an area $A'_w{}^* = 8\,a\,H'$ and counter balances the pressure force. This definition for f^* was chosen in order to avoid the evaluation of the true twisted tube surface area. The product $f^*\mathrm{Re}$ is given by

$$f^*\,\mathrm{Re} = \frac{2(-Q_z)}{\langle v_z\rangle} \tag{20}$$

It should be pointed out that the pressure gradient, Q_z, used in equation (20) is defined along a constant (x, y) path in the moving coordinate system, which is a helical path. In contrast, the pressure gradient measured by a manometer will be $\overline{Q}_{\bar{z}}$. This linear pressure gradient depends on the location of the manometer probe in the (x, y) plane. However, along the center line, both pressure gradients are identical.

Boundary Conditions. The equations of motion in the stream-function vorticity form, viz. equations (12, 16) and (17), have rotational symmetry about the z-axis. As these equations must be solved numerically, we must take full advantage of any symmetry in the flow field.

Because of the rotational symmetry at every 90 deg, only one quadrant of the tube needs to be considered. It is convenient to choose the region of interest as $-1 \leqslant x \leqslant 0, -1 \leqslant y \leqslant 0$. The boundary conditions for stream function and axial velocity are specified as zero along the solid walls.

$$v_z(x = -1, y) = v_z(x, y = -1) = 0 \tag{21}$$

$$\psi(x = -1, y) = \psi(x, y = -1) = 0 \tag{22}$$

For vorticity, the boundary condition along the wall is specified in terms of stream function as shown below.

$$\omega_z(x = -1, y) = -\frac{\partial^2\psi}{\partial x^2} + \frac{\pi}{H}x\frac{\partial v_z}{\partial x} \tag{23}$$

$$\omega_z(x, y = -1) = -\frac{\partial^2\psi}{\partial y^2} + \frac{\pi}{H}y\frac{\partial v_z}{\partial y} \tag{24}$$

It is clear that along the center lines, the rotational symmetry implies the following,

$$v_z(x, y = 0) = v_z(x = 0, y) \tag{25}$$

$$\psi(x, y = 0) = \psi(x = 0, y) \tag{26}$$

$$\omega_z(x, y = 0) = \omega_z(x = 0, y) \tag{27}$$

Equations (21–27) provide the basic set of boundary conditions required to solve for the flow field. Additional conditions on v_x, v_y, Q_x, and Q_y can be derived using symmetry arguments.

Method and Validity of Numerical Solution. Due to the complexity of the basic equations (12, 16) and (17), a finite difference method is used to solve the above equations for axial velocity, stream function and vorticity, respectively. All the derivatives are approximated by second order central difference approximations over a uniform grid in the region $-1 \leqslant x \leqslant 0, -1 \leqslant y \leqslant 0$. Note that the basic equations (12, 16) and (17) depend on the secondary variables v_x, v_y, Q_x and Q_y. The secondary velocities v_x, v_y are calculated from the discretized form of the defining equations (13a) and (13b), while Q_x and Q_y are calculated from the discretized form of equations (10) and (11). A relaxation type of iterative procedure is used to solve the flow equations.

Accuracy of the numerical results were estimated through a number of procedures. First, the limiting case of a straight tube was simulated by setting $H = 1000$. The $f^*\mathrm{Re}$ was computed to be 14.25 for this case. From an analytical solution [12] for flow through straight square tube, the $f^*\mathrm{Re}$ is calculated to be 14.23. The numerical value of $f^*\mathrm{Re}$ for $H = 1000$ is within 0.2 percent of the limiting value for $H \to \infty$.

Another means of checking the accuracy of the numerical solution is to compute $f^*\mathrm{Re}$ by integrating the shear stress along the wall and compare it with that of equation (20). In an orthogonal coordinate system this is tantamount to making a force balance. However, for a nonorthogonal system the force balance must be done with care and the correct equation to use is

$$\begin{aligned}-4y_{\max}[-Q_z] = &-\int_{-1}^{+1}\int_{-y_{\max}}^{y_{\max}}\frac{\pi}{H}(yQ_x - xQ_y)\,dx\,dy \\ &+\int_{-y_{\max}}^{y_{\max}}\tau_{xz}(x = 1, y) + \tau_{xz}(x = -1, y)]\,dy \\ &+\int_{-1}^{1}[\tau_{yz}(x, y = -y_{\max}) + \tau_{yz}(x, y = y_{\max})]\,dx\end{aligned} \tag{28}$$

where

$$\tau_{xz}(x = \pm 1, y) = \frac{\partial v_z}{\partial x}\left[1 + \frac{\pi^2 y^2}{H^2}\right]$$

$$\tau_{yz}(x, y = \pm y_{\max}) = \frac{\partial v_z}{\partial y}\left[1 + \frac{\pi^2 x^2}{H^2}\right]$$

and τ is the dimensionless shear stress.

In addition the mechanical energy balance is also used to check the accuracy. For an incompressible Newtonian fluid under fully developed steady flow it is given by (see Bird, et al. [11])

$$\begin{aligned}-\int_{-1}^{1}\int_{-y_{\max}}^{y_{\max}}\left\{v_zQ_z + \left[v_xQ_x + v_yQ_y + v_z\frac{\pi}{H}(yQ_x - xQ_y)\right]\right\}dy\,dx \\ = \int_{-1}^{1}\int_{-y_{\max}}^{y_{\max}}\Phi_v dy\,dx = \tfrac{1}{2}\langle v_z\rangle^2 e_v\end{aligned} \tag{29}$$

where

$$\begin{aligned}\Phi_v = 2\left[\left(\frac{\partial v_x}{\partial x}\right)^2 + \left(\frac{\partial v_y}{\partial y}\right)^2\right] + \left[\frac{\partial v_x}{\partial y} + \frac{\partial v_y}{\partial x}\right]^2 \\ + \left[\frac{\partial v_x}{\partial z} + \frac{\partial v_z}{\partial x} + \frac{\pi}{H}\delta v_x\right]^2 \\ + \left[\frac{\partial v_y}{\partial z} + \frac{\partial v_z}{\partial y} + \frac{\pi}{H}\delta v_y\right]^2 + 2\left[\frac{\partial v_z}{\partial z} + \frac{\pi}{H}\delta v_z\right]^2\end{aligned} \tag{30}$$

where,

$$\delta = \left[y\frac{\partial}{\partial x} - x\frac{\partial}{\partial y}\right]$$

and e_v is the friction loss factor.

Making use of equations (28) and (29), the following example illustrates the closure errors. The pair of numbers given in the parenthesis gives the percent of the closure error in energy and momentum balances, respectively. For $H = 20$ and $Q_z = -4000$, ($\mathrm{Re} = 1094$), the error for a 15×15 grid was (0.41, 0.13). It came down to (0.13, 0.1) for a grid size of 21×21. However, as H becomes smaller the decrease in the closure error becomes more pronounced. For example for $H = 2.5$ and $Q_z = -3000$, ($\mathrm{Re} = 709$) the error for a 15×15 grid was (6.10, 10.71). It came down to (2.52, 4.28) for a grid size of 21×21.

To further verify the numerical results, flow solutions were obtained for a grid of 31×31 for selected flow situations. Comparing $f^*\mathrm{Re}$ values for a grid of 21×21, the change in $f^*\mathrm{Re}$ with the finer grid was not more than 1 percent and in general it was below 0.5 percent for $H \geqslant 5$. For the case of $H = 2.5$ and high Reynolds numbers, the difference was about 3–4 percent. This indicates that the requirements of very fine grids become important for the case of $H = 2.5$ at a Reynolds number higher than, say 400. It appears then that the central difference scheme adopted in this study begins to fail to give accurate solutions for $H = 2.5$ at the higher Reynolds number ($\mathrm{Re} = 709$). In the light of the type of secondary flows predicted in this study, other schemes such as those proposed by Spalding [13], Raithby and Torrance [14] and Raithby [15] should be employed to extend the range of H and Re of this study.

Results and Discussions

Qualitative aspects of the flow field are best illustrated with perspective drawing and contours of such quantities as axial velocity and secondary velocity. The perspective drawing of axial velocity profile is shown in Fig. 2 for the case of $H = 20$, $Q_z = -2000$ (Re = 553) and $H = 2.5$, $Q_z = -2000$ (Re = 479), respectively. The profile for $H = 20$ is similar to the flow profile in a straight square duct. However, for $H = 2.5$ the profile is similar to Poiseuille flow in a circular tube (i.e., axial velocity near the corner is close to zero). If the twisted tube is projected along the axis on to the (x, y) plane, one will see an inner circular core of radius a and an annular ring corresponding to the solid portions of the pipe. As H becomes small the resistance to flow in the annular portion of the pipe becomes large. Hence the bulk of the fluid flows through the inner core and the axial velocity near the corners is small as is evident in Fig. 2(b). Another observation, from Fig. 2 is that the swirling secondary motion does not alter the axial velocity profile significantly. This is in contrast to flow in curved tubes where the axial velocity profile is significantly different from the parabolic profile for small curvature ratios and large Reynolds numbers (See Masliyah and Nandakumar [6]).

The normalized axial velocity along the center line $(x, y = 0)$ and along the diagonal $(x, y = x)$ are shown in Fig. 3 for the case of $H = 20$ and 2.5 for an axial pressure drop of $Q_z = -2000$. The velocity profile for a straight tube ($H = \infty$) and a reference parabolic profile are included for comparison. The latter two profiles are very close to the centre line velocity profile indicating that the velocity profile along the centre line is little affected by the tube twist. The velocity profiles along the diagonal are shown in Fig. 3 in a compressed scale, where the diagonal is projected onto the x-axis. For comparison, the velocity profile along the diagonal for a straight tube and a reference parabolic profile are also shown. For $H = 20$, the computed points are close to the curve for a straight square duct, while for $H = 2.5$, the profile approaches the parabolic profile for a circular tube of unit radius.

It is not surprising to find that the swirling motion in laminar flow does not alter the axial velocity profile. It can be shown through a simple example (White [12], problem 3–11) that the parabolic profile for a Poiseuille flow in circular tubes is unaltered by superimposing a pure swirling motion, i.e., $v_r = 0$, $v_\theta = v_\theta(r)$. For a pure swirling motion the axial component of the NSE is uncoupled from the radial and the angular components. Hence, for a constant pressure gradient in the axial direction, one obtains the well known parabolic profile. However, for a non-circular geometry one can expect only a qualitative similarity with this example.

Although the definition of stream function as given in equations (13) is helpful in solving the momentum equations, a contour of the stream function does not reflect the strength of the secondary flow. This is because the axial velocity appears in the definition of stream function (equation (13)) and it is the dominant component of the velocity vector. Hence a contour of the stream function resembles very much the contour of the axial velocity. The strength of the swirling flow is perhaps best illustrated by showing the secondary velocity vector at each grid point in the (x, y) plane. This is done in Fig. 4. Figure 4(a) is for $H = 2.5$ and $Q_z = -2000$ and is typical for all $H \geq 2.5$ studied here. Note that the swirling motion is strongest in the annular region and almost nonexistent in the inner core. Figure 4(b) shows the swirling motion for an extreme case of $H = 1.0$, $Q_z = -10$. A converged solution for this case was obtained with some difficulty. For this case both the axial and the secondary flows were insignificant in the annular region. In contrast to the cases for $H \geq 2.5$, the swirling motion is fairly strong in the inner core, as seen in Fig. 4(b).

In order to appreciate the relative importance of cross flow with respect to the axial flow, a perspective contouring of the quantity, $S = (v_x^2 + v_y^2)^{1/2}/v_z$ is shown in Fig. 5 for the cases, $H = 20$, $Q_z = -2000$ and $H = 2.5$, $Q_z = -2000$. It is clear from Fig. 5(a) that the axial velocity v_z dominates the inner core, while the secondary flow is important in the annular region. Figure 5(b) shows essentially the same characteristic feature. The only difference is that in Fig. 5(a) the ratio of secondary to axial velocity reaches maximum very close to the corner, while in Fig. 5(b) this maximum is reached further inside in the annular region. The important point to note is that the strong secondary flow in the annular region will help enhance the convective heat and mass transfer processes near the wall. The maximum values of S for $H = 2.5$ and 20 are 2.24 and 0.21, respectively.

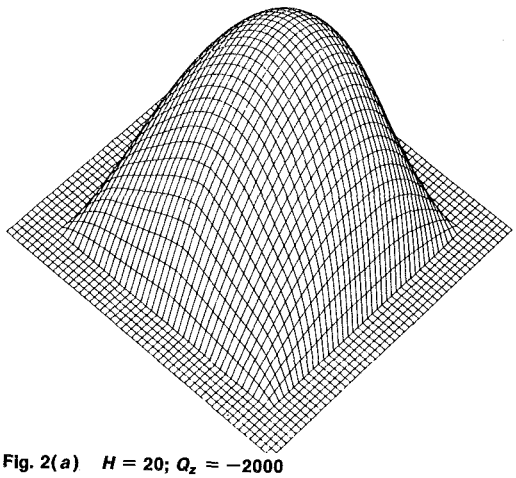

Fig. 2(a) $H = 20$; $Q_z = -2000$

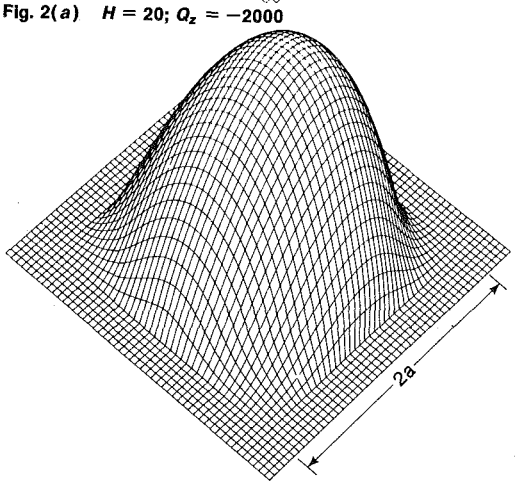

Fig. 2(b) $H = 2.5$; $Q_z = -2000$

Fig. 2 Axial velocity profile

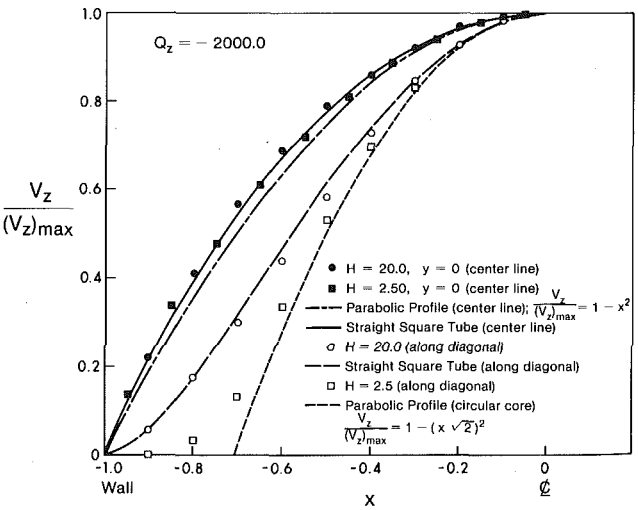

Fig. 3 Normalized axial velocity profile along center line and diagonal

The quantity $f^*\mathrm{Re}$ is shown as a function of Reynolds number for each H in Fig. 6. Also shown is the reference line for a straight square tube. In contrast to straight tube, the product $f^*\mathrm{Re}$ for a twisted tube is not independent of Reynolds number. The secondary flow inertial effects in a twisted tube become important at a Reynolds number of

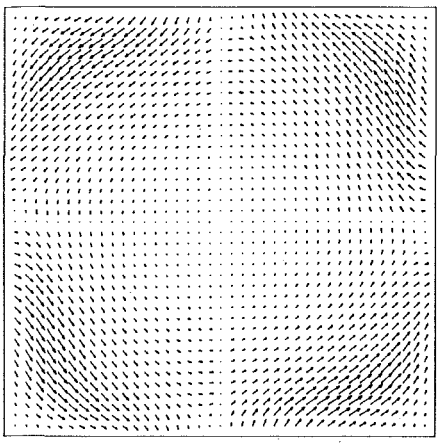

Fig. 4(*a*) $H = 2.5$; $Q_z = -2000$

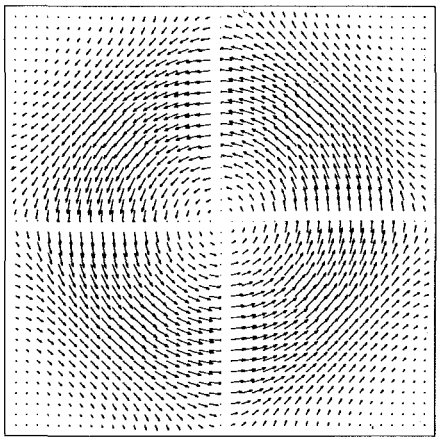

Fig. 4(*b*) $H = 1$; $Q_z = -10$

Fig. 4 Secondary velocity portrait

about 100. Figure 6 can be used in conjunction with the expressions for Re and f^*Re (equations (18) and (20), respectively), to evaluate the corresponding values of the axial pressure gradient, Q_z. Using the definition of f^*Re in equation (20) and the energy equation (29), it can be seen that f^*Re and the friction loss factor, e_v, become identical at the limiting case of a straight tube with $H = \infty$. The difference between f^*Re and e_v is due to the additional terms involving H, Q_x and Q_y of the square brackets on the left-hand side of equation (29). The relative difference between the two quantities was found to become more important at lower H; but the difference was never higher than 4 percent for all cases with $H \geq 2.5$. In other words, if the power requirement is calculated from $[-Q_z \langle v_z \rangle (4y_{max})]$, then it matches the viscous dissipation term $[\frac{1}{2}\langle v_z \rangle^2 \phi_v]$ within 4 percent. Hence from an engineering point of view, the power requirement can be calculated from the center line pressure gradient, Q_z, alone which is embodied in the f^*Re data.

Conclusion

The Navier-Stokes equation, the macroscopic force and energy balance equations, and the viscous dissipation term are all presented in a rotating frame of reference. Using of a rotating coordinate system simplified the equations of motion for a fully developed, laminar flow of a Newtonian fluid in a twisted tube to a two-dimensional problem. The resulting set of coupled elliptic partial differential equations are solved numerically using a relaxation type of procedure.

The axial velocity profile was observed to be unaffected by the swirling motion. As the twist rate is increased the axial velocity profile changes from that of a straight square tube to that of a straight circular tube. The secondary velocity is most important in the annular region near the wall and is almost nonexistant in the inner core for $H \geq 2.5$.

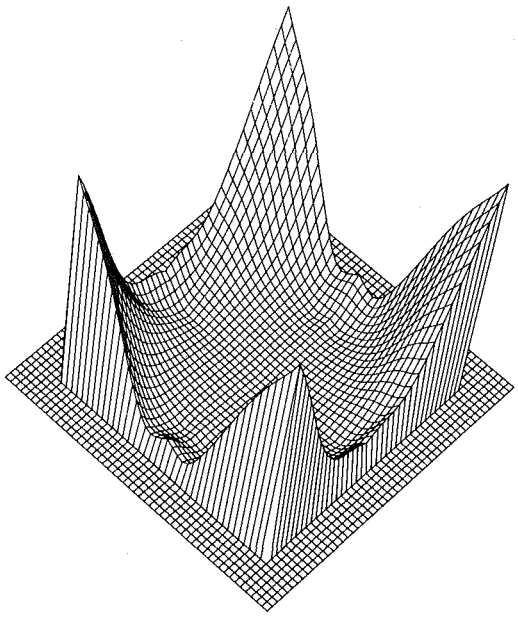

Fig. 5(*a*) $H = 20$; $Q_z = -2000$

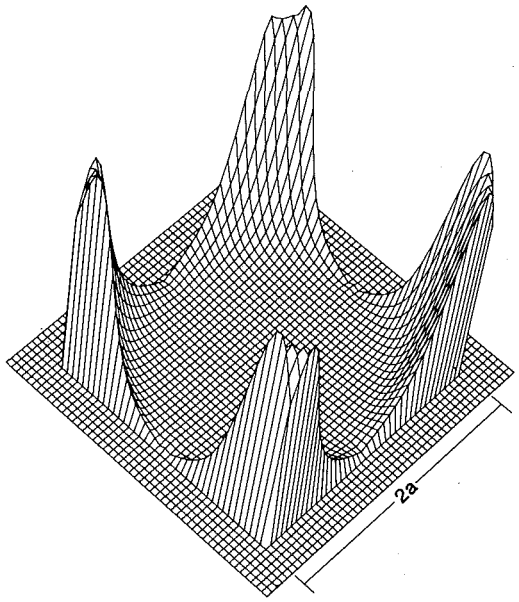

Fig. 5(*b*) $H = 2.5$; $Q_z = -2000$

Fig. 5 Relative importance of secondary velocity with respect to axial velocity

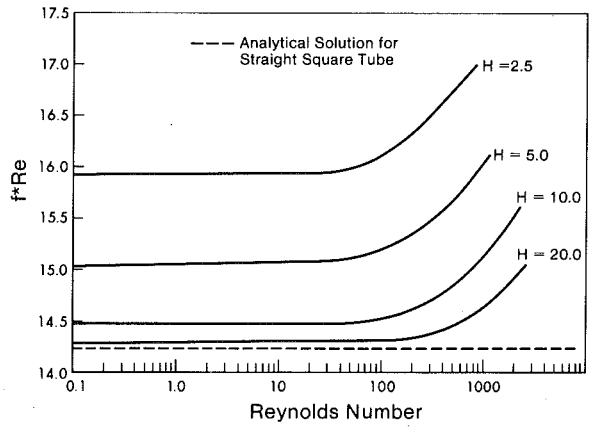

Fig. 6 Variation of f^*Re with Reynolds number

References

1 Austin, L.R., and Seader, J. D., "Fully Developed Viscous Flow in Coiled Circular Pipes," *AIChE Journal*, Vol. 19, 1973, pp. 85–94.

2 Kalb, C. E., and Seader, J. D., "Heat and Mass Transfer Phenomena for Viscous Flow in Curved Circular Tubes," *International Journal Heat Mass Transfer*, Vol. 15, 1972, pp. 801–816.

3 Cheng, K. C., and Akiyama, M., "Laminar Forced Convection Heat Transfer in Curved Rectangular Channels," *International Journal Heat Mass Transfer*, Vol. 13, 1970, pp. 471–490.

4 Cuming, H. G., "The Secondary Flow in Curved Pipes," *Aeronautical Research Council Reports and Memoranda*, No. 2880, 1952.

5 Joseph, B., Smith, E. P., and Alder, R. J., "Numerical Treatment of Laminar Flow in Helically Coiled Tubes of Square Cross-Section," *AIChE Journal*, Vol. 21, 1975, pp. 965–974.

6 Masliyah, J. H., and Nandakumar, K., "Fully Developed Viscous Flow and Heat Transfer in Curved Semicircular Sectors," *AIChE Journal*, Vol. 25, 1979, pp. 478–487.

7 Marris, A. W., "The Generation of Secondary Vorticity in an Incompressible Fluid," ASME *Journal of Applied Mechanics*, Vol. 85, 1963, pp. 525–531.

8 Marris, A. W., "Secondary Flows in an Incompressible Fluid of Varying Density in a Rotating Reference Frame," ASME *Journal of Basic Engineering*, Vol. 88, 1966, pp. 533–538.

9 Todd, L., "Some Comments on Steady, Laminar Flow Through Twisted Pipes," *Journal of Engineering Mathematics*, Vol. 11, 1977, pp. 29–48.

10 Date, A. W., "Prediction of Fully-Developed Flow in a Tube Containing a Twisted Tape," *International Journal Heat Mass Transfer*, Vol. 17, 1974, pp. 845–859.

11 Bird, B. R., et al., *Transport Phenomena*, John Wiley & Sons, New York, 1960.

12 White, F. M., *Viscous Fluid Flow*, McGraw Hill, New York, 1974.

13 Spalding, D. B., "A Novel Finite Difference Formulation for Differential Expressions Involving Both First and Second Derivatives," *International Journal of Numerical Methods in Engineering*, Vol. 4, 1972, pp. 551–559.

14 Raithby, G. D., and Torrance, K. E., "Upstream-Weighted Differencing Schemes and Their Application to Elliptic Problems Involving Fluid Flow," *Computers and Fluids*, Vol. 2, 1974, pp. 191–206.

15 Raithby, G. D., "Skew-Upstream Differencing Schemes for Problems Involving Fluid Flow," *Computer Methods in Applied Mechanics and Engineering*, Vol. 9, 1976, pp. 153–164.

J. H. Masliyah
K. Nandakumar

Department of Chemical Engineering,
University of Alberta,
Edmonton, Alberta,
Canada T6G 2G6

Steady Laminar Flow through Twisted Pipes

Heat Transfer in Square Tubes

The potential of a twisted square pipe for heat transfer applications is examined. A numerical solution of the energy equation in a rotating frame of reference is used for the analysis. The case of axially uniform wall temperature is considered. The rectilinear nature of the axial velocity profile makes the overall Nusselt number insensitive to changes in Reynolds and Prandtl numbers. However, the swirling motion provides significant enhancement in heat transfer across individual walls. Hence the use of twisted square pipes in a multichannel configuration is proposed.

Introduction

Laminar forced convective heat transfer through straight ducts of various cross-sections have been studied quite extensively in the past. The most exhaustive compilation of all the available results can be found in London and Shah [1]. It is well known that heat and mass transfer rates are enhanced by inducing a secondary flow and/or providing increased surface area, often at the expense of increased friction. Secondary flow can be generated in the presence of curved walls. A coiled tube is one such example which has the advantage of providing a compact size as well as increased heat transfer rate because of the secondary flow. Hence, curved tubes (toroidal geometry) of various cross sections have been studied quite extensively [2–5]. Internally finned tubes is one example of enhancing the heat transfer rate by providing increased surface area. See for example Hu and Chang [6] and Masliyah and Nandakumar [7].

A unique geometry which provides increased surface area without fins and also induces secondary flow is a twisted tube of constant cross section. This geometry has not received much attention in the literature. Todd [8] studied fluid flow in twisted tubes with elliptical cross-section. His intent was to understand and model flow behavior in flexible pipes. Date [9] and Lopina and Bergles [10] have studied fluid flow and forced convective heat transfer in circular tubes with a twisted tape insert. In the companion paper [11] we analyzed the fluid flow behavior in twisted square tubes. It was observed that the axial velocity profile did not depart significantly from a parabolic profile. However, the swirling motion was observed to be important at small twist rates, π/H, where H' is the length over which the cross-section of the pipe rotates through π radians.

In this work we develop and solve the differential energy balance equation in a rotating coordinate system. The study is restricted to fully developed velocity and temperature profiles. Axial conduction in the moving coordinate system is neglected to preserve the two-dimensional nature of the problem. Consequently the solutions are restricted to low thermal conductivity (high Prandtl number) fluids. The objective is to investiate the heat transfer characteristics for the case of uniform axial temperature. The effect of swirling motion on heat transfer across individual walls is studied for potential application in multichannel heat exchanger design. Temperature along the periphery is assumed to be constant for each wall; but it may be different for the four walls. Various boundary conditions to be studied in this work are identified in Fig. 1.

Governing Equations

The differential form of the energy balance equation for a constant property, incompressible fluid with negligible viscous dissipation is,

$$\bar{\mathbf{v}}' \cdot \bar{\nabla}' T' = \alpha \, \bar{\nabla}'^2 T' \tag{1}$$

Contributed by the Heat Transfer Division for publication in the JOURNAL OF HEAT TRANSFER. Manuscript received by the Heat Transfer Division January 2, 1981.

Case No.	Wall Temperature				Domain of Interest		
	T_{w_1}	T_{w_2}	T_{w_3}	T_{w_4}	x	y	
1	0	0	0	0	(−1, 0)	(−1, 0)	Quadrant
2	1	1	0	0	(−1, 1)	(−1, 1)	Full
3	0	1	0	1	(−1, 1)	(−1, 0)	Half
4	0	0	0	1	(−1, 1)	(−1, 1)	Full

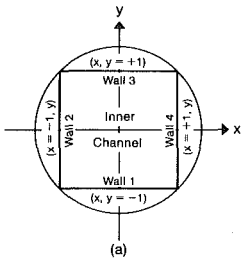

Fig. 1 Twisted square tube configuration

where $\alpha = k/\rho C_p$ and all the primed variables are dimensional quantities. All quantities with an overbar are defined in a stationary coordinate system $(\bar{x},\bar{y},\bar{z})$ while quantities without an overbar are defined in a rotating coordinate system (x,y,z). The velocity vector $\bar{\mathbf{v}}$, the gradient $\bar{\nabla}'$ and the Laplacian $\bar{\nabla}'^2$ are transformed into the rotating coordinate system using the transformations given in [11]. The resulting energy balance equation in terms of the variables in a rotating coordinate system is,

$$v_{x'}\frac{\partial T'}{\partial x'} + v_{y'}\frac{\partial T'}{\partial y'} + v_{z'}\frac{\partial T'}{\partial z'} + \frac{\pi}{H'} v_{z'}\left\{y'\frac{\partial T'}{\partial x'} - x'\frac{\partial T'}{\partial y'}\right\} = \alpha\left[\nabla'^2_{x',y'} T' + \frac{\pi^2}{H^2}\left\{y'^2\frac{\partial^2 T'}{\partial x'^2} + x'^2\frac{\partial^2 T'}{\partial y'^2} - 2x'y'\frac{\partial^2 T'}{\partial x'\partial y'} - y'\frac{\partial T'}{\partial y'} - x'\frac{\partial T'}{\partial x'}\right\}\right] \tag{2}$$

A suitable length scale for making the equation dimensionless is a, where $(2a)$ is the width of the tube. In addition, define the following dimensionless quantities.

$$\mathbf{v} = \mathbf{v}'/(\nu/a) \qquad \nabla = a\nabla'$$

$$\nabla^2 = a^2 \nabla'^2 \qquad \mathrm{Pr} = \frac{C_p \mu}{k}$$

$$\mathrm{Re} = 2a\,\langle v_z' \rangle/\nu$$

In this study, two main heat transfer situations are considered. The first situation is for the four walls having the same temperature; this will be referred to as the uniform peripheral wall temperature case. The second situation is for at least two walls having different temperatures; this will be referred to as the nonuniform peripheral wall temperature case. The fully-developed temperature profile for the

uniform peripheral wall temperature case is a standard eigenvalue problem with the bulk temperature as an unknown, whereas for the nonuniform peripheral wall temperature case, a fully-developed temperature profile implies that the fluid temperature, T', is invariant with the axial position. As a consequence it is more convenient to dimensionalize the energy equations differently for the two heat transfer situations:

For the uniform peripheral wall temperature case

$$T = \frac{(T_w' - T')}{a \,\mathrm{Re}\,\mathrm{Pr}\,(dT_b'/dz')} \tag{3}$$

where the bulk mean temperature is defined as

$$T_b' = \frac{\iint v_z' \, T' \, dx' \, dy'}{\iint v_z' \, dx' \, dy'} \tag{4}$$

For the nonuniform peripheral wall temperature case,

$$T = \frac{T_{w_i}' - T'}{T_{w_i}' - T_{w_j}'} \tag{5}$$

where T_{w_i}' and T_{w_j}' are two different wall temperatures.

Thermally developed flow for the nonuniform peripheral wall temperature case is a trivial case in the sense that fluid inside the tube gains no net energy (i.e., the heat gained through the hot walls equals the heat lost through the cold walls). However this is still an interesting case for a twisted tube because the secondary flow provides a convection mechanism, acting as a carrier of heat from a hot wall to a cold wall. Such a setup would be ideal in a multichannel configuration where different process fluids must be heated or cooled to different extent. The heat transfer across individual walls in a twisted tube will be shown to be significantly greater than a corresponding straight tube.

The energy equation can be written in dimensionless form as

$$\mathrm{Pr}\left[v_x \frac{\partial T}{\partial x} + v_y \frac{\partial T}{\partial y} + \frac{\pi}{H} v_z \left\{y \frac{\partial T}{\partial x} - x \frac{\partial T}{\partial y}\right\}\right] - A = \left[\frac{\partial^2 T}{\partial x^2} + \frac{\partial^2 T}{\partial y^2} + \frac{\pi^2}{H^2}\left\{y^2 \frac{\partial^2 T}{\partial x^2} + x^2 \frac{\partial^2 T}{\partial y^2} - 2xy \frac{\partial^2 T}{\partial x \partial y} - y \frac{\partial T}{\partial y} - x \frac{\partial T}{\partial x}\right\}\right] \tag{6}$$

where A is given by

$$A = T v_z/(\mathrm{Re}\, T_b) \tag{7a}$$

for uniform peripheral wall temperature, and by

$$A = 0 \tag{7b}$$

for nonuniform peripheral wall temperature.

The velocity vector $\mathbf{v} = \{v_x, v_y, v_z\}$ was obtained as outlined in [11]. Note that the energy equation has three parameters, viz. {Re, Pr, H}. In addition, imposing different temperature boundary conditions along the periphery gives rise to numerous possible cases to be studied.

Boundary Conditions

The domain of interest in the x and y directions are $x \in [-1, 1]$ and $y \in [-1, 1]$, respectively. If we take advantage of rotational symmetry conditions, then for certain temperature boundary conditions it is sufficient to consider a smaller domain. Four different cases of boundary conditions are identified in Fig. 1 together with the domain over which the energy equation must be solved for each case. The rotational symmetry conditions for cases (1) and (3) are imposed as follows:

Case (1)

$$T(x, y = 0) = T(x = 0, y) \tag{8}$$

Case (3)

$$T(0 \geqslant x \geqslant -1, y = 0) = T(0 \leqslant x \leqslant 1, y = 0) \tag{9}$$

Macroscopic Results

The local Nusselt numbers are based on the temperature difference between the local wall temperature and the fluid bulk temperature, viz;

$$\mathrm{Nu}_\ell(\xi) = \frac{2}{[T_w(\xi) - T_b]}\left(1 + \frac{\pi^2}{H^2}\xi^2\right)^{1/2} \frac{\partial T}{\partial n} \tag{10}$$

where $\xi = x$ or y and $n = y$ or x respectively, depending on the wall. The characteristic length used in defining Nusselt number is 2. In addition, an average Nusselt number for each wall is obtained by integrating equation (10) as follows:

$$\overline{\mathrm{Nu}_i} = \frac{\int \mathrm{Nu}_\ell(\xi)\left(1 + \frac{\pi^2}{H^2}\xi^2\right)^{1/2} d\xi}{\int \left(1 + \frac{\pi^2}{H^2}\xi^2\right)^{1/2} d\xi} \tag{11}$$

where the limits of integration depend on the domain over which the energy equation is solved. Equations (10) and (11) are applicable to both heat transfer situations discussed earlier.

For the uniform wall temperature case, it is possible to define an overall Nusselt number, $\overline{\mathrm{Nu}_0}$, based on the wall and bulk temperature difference and a characteristic length of $2a$:

$$\overline{\mathrm{Nu}_0} = A_x H/A_w T_b \tag{12}$$

Nomenclature

A_x = dimensionless cross-sectional or flow area, (A_x'/a^2)
A_w = dimensionless total heat transfer area, (A_w'/a^2)
A_{w_i} = dimensionless wall area over which $\overline{\mathrm{Nu}_i}$ is evaluated, A_{w_i}'/a^2
a = half width of tube
C_p = specific heat
f^* = friction factor based on straight tube area (see [11]).
H = dimensionless length of tube over which the cross-section rotates through π radians (H'/a)
k = thermal conductivity
$\overline{\mathrm{Nu}_0}$ = overall Nusselt number
$(\overline{\mathrm{Nu}_0})_{\mathrm{abs}}$ = overall Nusselt number based on absolute wall Nusselt numbers (equation (14))
Nu_ℓ = local Nusselt number
$\overline{\mathrm{Nu}_i}$ = i = 1, 2, 3, 4 wall average Nusselt number defined by equation (18). (averaged over only that portion of the wall for which the energy equation is solved)
Pr = Prandtl number, $\frac{C_p \mu}{k}$
$\dot{Q}$ = heat transfer rate
Re = Reynolds number, $2a\langle v_z'\rangle/\nu$
T = dimensionless temperature
$T_w(\xi)$ = dimensionless wall temperature at ξ, ($\xi = x, y$) constant for a given wall
$\mathbf{v}$ = dimensionless velocity vector $\{v_x, v_y, v_z\}$, $\mathbf{v}'/(\nu/a)$
x = coordinate
y = coordinate
z = coordinate
α = thermal diffusivity
μ = viscosity
ν = kinematic viscosity
ρ = fluid density
Δx = grid size in x direction
Δy = grid size in y direction

Subscripts

b = bulk mean value (e.g., T_b)
ℓ = local value (e.g., h_ℓ)
1 = quantity on wall 1 $(x, -1)$ (e.g., T_1)
2 = quantity on wall 2 $(-1, y)$ (e.g., T_2)
3 = quantity on wall 3 $(x, +1)$ (e.g., T_3)
4 = quantity on wall 4 $(+1, y)$ (e.g., T_4)
$(.)_s$ = a quantity for a straight tube (e.g., $(\mathrm{Re})_s$)
$(.)_t$ = a quantity for a twisted tube (e.g., $(\mathrm{Re})_t$)

Superscripts

$\bar{}$ = a quantity in a fixed coordinate, (e.g., $\bar{\mathbf{v}}$)
$'$ = dimensional quantity (e.g., T')

Table 1 Nusselt numbers for straight square tubes, ($H = 1000$, $Q_z = -10$, Pr = 0.7)

Case No.	Temperature B.C. T_1	T_2	T_3	T_4	$\overline{Nu_0}$	$\overline{Nu_1}$	$\overline{Nu_2}$	$\overline{Nu_3}$	$\overline{Nu_4}$	$(\overline{Nu_0})_{abs}$
1	0	0	0	0	2.974	2.966	2.966	—	—	2.966
2	1	1	0	0	—	5.286	5.285	−5.285	−5.284	5.285
3	0	1	0	1	—	−9.683	9.690	—	9.688	9.686
4	0	0	0	1	—	−9.687	−0.884	−9.684	6.752	6.752

where A_x is the flow area and A_w is the total heat transfer area, defined by

$$A_w = 8\pi[0.5\left(1+\frac{H^2}{\pi^2}\right)^{1/2} + \frac{H^2}{2\pi^2}\ell n\left\{\frac{\pi}{H}+\left(1+\frac{\pi^2}{H^2}\right)^{1/2}\right\}] \quad (13)$$

For the case of nonuniform peripheral wall temperature, $\overline{Nu_0}$ is not meaningful. However, a new overall Nusselt number can defined as

$$(\overline{Nu_0})_{abs} = \frac{\sum|Nu_i|A_{w_i}}{\sum A_{w_i}} \quad (14)$$

where $(\overline{Nu_0})_{abs}$ is the absolute overall Nusselt number. It can be used to quantify the effectiveness of a twisted tube in receiving and transmitting heat to the neighbouring channels for the case of nonuniform peripheral wall temperature. A_{w_i} is the wall area over which Nu_i is evaluated.

For the uniform wall temperature case, the overall Nusselt number can also be obtained from the wall average Nusselt numbers using

$$\overline{Nu_0} = \frac{\sum_{i=1}^{2} A_{w_i} Nu_i}{\sum_{i=1}^{2} A_{w_i}} \quad (15)$$

Accuracy of the numerical solution can be assessed by comparing the overall Nusselt numbers from equation (12) and (15).

For the nonuniform wall temperature case, the condition that the net flux is zero results in

$$T_b = \frac{\oint Nu_\ell(\xi)\, T_w(\xi)\left(1+\frac{\pi^2}{H^2}\xi^2\right)^{1/2} d\xi}{\oint Nu_\ell(\xi)\left(1+\frac{\pi^2}{H^2}\xi^2\right)^{1/2} d\xi} \quad (16)$$

where the integration is around the periphery. The bulk temperature can also be calculated from

$$T_b = \frac{\iint v_z T\, dx\, dy}{\langle v_z \rangle} \quad (17)$$

Equations (16) and (17) provide a means of assessing the accuracy of the solution for the nonuniform wall temperature case.

Method and Validity of Numerical Solution

The energy equation (6) is discretized using second-order central difference approximations over a uniform grid size. For a particular set of parameters $\{H, Q_z\}$ the grid size is chosen to be the same as that used in solving the momentum equations. Since the grid size is kept the same as in the fluid flow solution, the total number of grid points in one or both directions must be doubled for those cases where the energy equation must be solved over a half or full domain. A relaxation type of iterative procedure is used to solve the discretized energy equation. A converged solution for lower Reynolds and Prandtl numbers is normally used as the initial guess for higher values for the parameters. The bulk mean temperature is evaluated using Simpson's rule. The temperature gradients at the wall are required to evaluate the local and average wall Nusselt numbers. The gradients are evaluated using second-order forward and backward differences as well as through a spline fit.

The limiting case of a straight square tube with uniform wall temperature was simulated by setting $H = 1000$. For this case the overall Nusselt number was 2.974 which compares well with the literature [1] value of 2.976. For this case a grid size of $\Delta x = \Delta y = 1/14$ was found to be adequate. But for all cases with $H = 2.5$ a grid size of $\Delta x = \Delta y = 1/20$ was required.

Table 2 Nusselt number variation with parameters for uniform temperature boundary condition (case 1)

H	$-Q_z$	Pr	Re	$\overline{Nu_0}$	$\overline{Nu_1}$	$\overline{Nu_2}$
1000	10	0.7	2.81	2.974	2.97	2.97
20	10	0.7	2.80	2.958	2.95	2.95
10	10	0.7	2.77	2.91	2.91	2.90
5	10	0.7	2.66	2.75	2.75	2.75
2.5	10	0.7	2.51	2.35	2.36	2.35
2.5	10	5.0	2.51	2.35	2.37	2.35
2.5	10	30.0	2.51	2.35	2.37	2.34
2.5	200	0.7	50.0	2.34	2.31	2.37
2.5	1000	0.7	243	2.32	2.15	2.47
2.5	2000	0.7	479	2.31	2.05	2.56
2.5	3000	0.7	709	2.31	1.98	2.65

The difference in the overall Nusselt numbers from equations (12) and (15) was less than 2 percent for all the cases presented here with the uniform wall boundary condition (i.e., case 1). For the nonuniform wall temperature cases the difference in the bulk temperatures from equations (16) and (17) was always less than 1 percent.

Discussion of Results

In order to understand the effect of twist on heat transfer characteristics we need reference cases for each of the four boundary conditions when there is no twist (i.e., straight square tubes). The case of uniform wall temperature in straight square tubes has been studied by earlier workers [1]. For the three nonuniform wall temperatures cases a straight tube solution was simulated by setting $H = 1000$, $Q_z = -10$ and Pr = 0.7. The various Nusselt numbers are presented in Table 1. These Nusselt numbers represent purely conductive heat transfer from a hot wall to a cold wall as there is no secondary flow at this limit. The average Nusselt number for each wall serves as reference against which the convective effects of secondary flow can be compared.

Effect of Parameters H, Re and Pr on Nusselt Number.

Uniform Wall Temperature Case. For the case of uniform wall temperature the effect of twist rate (π/H) on Nusselt numbers can be seen in Table 2. As H is decreased from 1000 to 2.5, the overall Nusselt number drops by about 20 percent from 2.974 to 2.35. This, however, does not reflect a 20 percent reduction in heat transfer rate for the twisted tube. A discussion on the enhancement aspects is deferred till the end. The immediate task is to understand the effect of parameters H, Re and Pr on the overall and wall average Nusselt numbers. The effect of Reynolds number and Prandtl number is shown in Table 2 for a constant $H = 2.5$. The overall Nusselt number does not change by more than 2 percent as the Reynolds number is increased from 2.51 to 709. This is not hard to understand once we realize that the overall Nusselt number reflects the energy convected in the axial direction. The Nusselt number depends on the temperature profile which in turn depends most significantly on the axial velocity profile. The axial velocity profile for $H = 2.5$ was shown in [11] to be essentially parabolic in the inner core. Hence, as in rectilinear flow, we should expect very little dependence on $\overline{Nu_0}$ on Reynolds number or Prandtl number. The overall Nusselt number can be seen in Table 2 to be independent of Prandtl number as well. We should make no mistake about the importance of swirling motion at higher Reynolds numbers. The individual wall Nusselt numbers, which reflect the heat transfer across a particular surface, show a slightly stronger dependence on Reynolds number. It is the weak coupling between the axial flow and the swirling motion that is responsible for the insensitivity of $\overline{Nu_0}$ to the parameters Re and Pr. However, as the swirling motion itself is sensitive to Re, the wall Nusselt numbers $\overline{Nu_1}$ and $\overline{Nu_2}$ are sensitive to Reynolds number and Prandtl number. This characteristic is brought out more dramatically for non-uniform wall temperatures.

Table 3 Nusselt numbers for twisted square tubes ($H = 2.5$, $Q_z = -10$, Pr = 0.7)

Case No.	Temperature B.C. T_1	T_2	T_3	T_4	$\overline{Nu_0}$	$\overline{Nu_1}$	$\overline{Nu_2}$	$\overline{Nu_3}$	$\overline{Nu_4}$	$(\overline{Nu_0})_{abs}$
1	0	0	0	0	2.353	2.358	2.355	—	—	2.357
2	1	1	0	0	—	11.42	11.06	−11.41	−11.05	11.24
3	0	1	0	1	—	−21.53	21.68	—	21.39	21.53
4	0	0	0	1	—	−21.85	−0.943	−21.13	14.68	14.65

Table 4 Nusselt number variation with parameters for case (3) boundary condition (0, 1, 0, 1), $H = 2.5$

$-Q_z$	Pr	Re	$\overline{Nu_1}$	$\overline{Nu_2}$	$\overline{Nu_4}$	$(\overline{Nu_0})_{abs}$
10	0.7	2.51	−21.53	21.68	21.39	21.53
10	5.0	2.51	−21.84	22.67	20.96	21.83
10	30.0	2.51	−23.45	25.65	21.28	23.45
200	0.7	50.0	−22.55	24.06	20.97	22.53
1000	0.7	243	−24.72	27.60	22.06	24.77
2000	0.7	479	−26.28	29.73	23.08	26.34
3000	0.7	709	−27.49	31.33	23.92	27.56

Nonuniform Wall Temperature Cases. The Nusselt numbers for a twisted tube with $H = 2.5$ for the four different boundary conditions are presented in Table 3 for the case of Pr = 0.7 and $Q_z = -10$. The corresponding Reynolds number is 2.51 and these cases can be taken to represent the creeping flow limit. The most interesting comparison between Tables 1 and 3 is the twofold increase in the average wall Nusselt numbers $\overline{Nu_1}$ to $\overline{Nu_4}$ for the cases (2–4). This clearly must be attributed to the swirling motion which is very effective in receiving heat from a hot wall and transmitting it to a cold wall. Of the three nonuniform wall temperature cases presented in Table 3, case 3 is the most effective for multichannel heat exchanger applications. This case corresponds to alternate walls having the same temperature. The overall absolute Nusselt number, $(\overline{Nu_0})_{abs}$ shows an increase of 122 percent over a straight tube for the same boundary conditions.

A perspective drawing of the two-dimensional temperature profile is presented in Figs. (2*a*) to (2*d*) for the four cases considered in Table 3. These provide an overall qualitative picture of the temperature field for the four types of boundary conditions. A common feature of Figs. 2(*a*), 2(*b*), and 2(*d*), is the small temperature gradient near those corners which do not experience a discontinuity in the boundary condition. Figure 2(*c*), which shows a discontinuity at every corner, exhibits the sharpest gradients along the wall and this case shows the highest heat transfer rate. It is interesting to note that, even though the temperature profiles in Figs. 2(*b*) and 2(*c*) are very dissimilar, the bulk mean temperature of the fluid for both cases is identical, (T_b = 0.5). But case (3) is much more effective in exchanging heat with the neighbouring channels.

The Nusselt number variation with Reynolds and Prandtl numbers for case (3) boundary condition is presented in Table 4. The individual wall Nusselt numbers show a significant dependence on both Re and Pr. The temperature profile is also drastically altered as shown in Fig. 3 for Re = 709 and Pr = 5. The temperature profile is flat in the inner core, but sharp gradients exist in the annular region.

The local variation in Nusselt number along walls 1 and 2 is shown in Fig. 4 for case (3) boundary condition for three sets of parameters. The distribution is altered significantly as Reynolds number is increased from 2.51 ($Q_z = -10$) to 243 ($Q_z = -1000$) and even more drastically when Prandtl number is increased to 5. The apparent asymmetric distribution is best rationalized by following a fluid element along its swirling path. For a counter clockwise swirling motion then, starting at the point (−1, 1) and tracing the profile along wall 2 and then along wall 1, we see that the maxima and minima occur at the same location along each wall.

Heat Transfer Enhancement. For the case of uniform peripheral heat temperature, (case (1)), it was earlier pointed out that the effect of decreasing H (from $H = \infty$ to $H = 2.5$) is to decrease the overall Nusselt number by about 20 percent. This does not reflect a 20 percent reduction in heat transfer rate. The increase in surface area due to twist must be accounted for. The two factors that affect the total heat transfer rate act in opposite sense as H is decreased. The net effect is perhaps best measured by comparing the heat transfer rates for a straight and twisted tube for the same driving force (i.e., temperature difference) and pumping power. The ratio of the two heat transfer rates is,

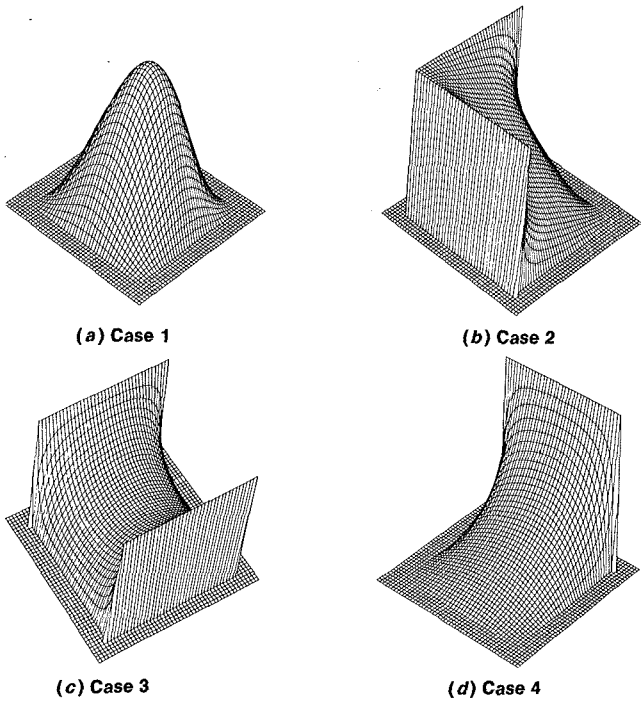

Fig. 2 Temperature profile for four boundary conditions ($H = 2.5$, $Q_z = -10$, Pr = 0.7)

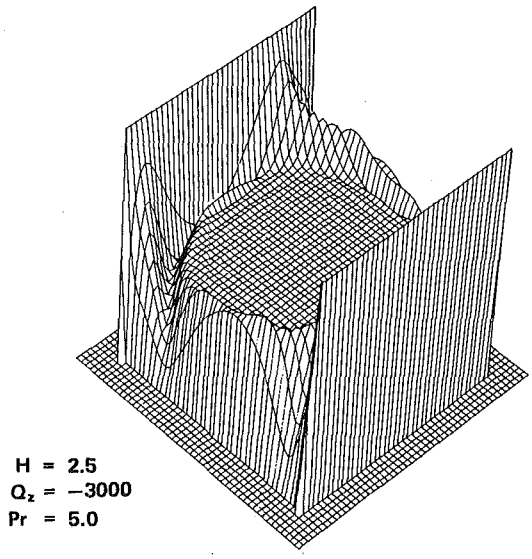

Fig. 3 Temperature profile for case 3 boundary condition ($H = 2.5$, $Q_z = -3000$, Pr = 5.0)

$$\frac{\dot{Q}_t}{\dot{Q}_s} = \frac{(A_w)_t\ (\overline{\mathrm{Nu}_0})_t}{(A_w)_s\ (\overline{\mathrm{Nu}_0})_s} \tag{18}$$

This ratio turns out to be 0.966 for the case of $H = 2.5$, Pr = 0.7 and $Q_z = -10$. Hence there is no enhancement in heat transfer to a fluid flowing inside a twisted tube. In fact there is a 4 percent reduction which can be attributed to lower throughput in a twisted tube. Although the swirling motion is important in a twisted tube, it does not contribute to a *net* increase in the thermal energy of the fluid flowing inside a twisted tube. Consequently, for uniform peripheral wall temperature, no heat enhancement can be obtained by using twisted tubes. However, the swirling motion is very effective in receiving and transmitting heat through individual walls, provided they are maintained at different temperatures. Such a configuration will be most useful when several fluids at different temperatures have to be heated or cooled to different extent. This enhancement is achieved without adding to the pumping cost as will be shown next.

The enhancement in heat transfer is often measured at constant pumping power. The Reynolds numbers in a straight square tube (reference case) and a twisted square tube are related, at constant pumping power by [10],

$$(A_x f^* \mathrm{Re}^3)_t = (A_x f\ \mathrm{Re}^3)_s \tag{19}$$

Using $(f\ \mathrm{Re})_s = 14.23$ and $(A_x)_t = (A_x)_s$ equation (19) can be written as,

$$(\mathrm{Re})_s = \left[\left\{\frac{(f^*\ \mathrm{Re})_t}{14.23}\right\}^{1/2}\right](\mathrm{Re})_t \tag{20}$$

Since the factor in square brackets is always greater than unity (see [11]), the Reynolds number in a straight square tube is always greater than that in a twisted tube, at constant pumping power. However, as the Nusselt number for a straight tube is independent of $(\mathrm{Re})_s$, the heat transfer enhancement given by equation (18) turns out to be that based on constant pumping power. Instead of overall Nusselt numbers $\overline{\mathrm{Nu}_0}$, the wall average Nusselt numbers $\overline{\mathrm{Nu}_i}$ could be used in equation (18) to assess the enhancement across each wall. Equation (18) then takes the form,

$$\frac{\dot{Q}_t}{\dot{Q}_s} = \frac{(A_{w_i})_t\ (\overline{\mathrm{Nu}_i})_t}{(A_{w_i})_s (\overline{\mathrm{Nu}_i})_s}; \quad i = 1, \ldots 4$$

A similar expression can be used for the overall absolute value, $(\overline{\mathrm{Nu}_0})_{\mathrm{abs}}$. The enhancement factors for a few typical values of Re and Pr are presented in Table 5 for case 3 boundary condition. Significant enhancement up to a factor of 7.09 occurs across the individual walls. Hence twisted square tubes will be most useful in a multichannel configuration.

Finally the overall and wall average Nusselt number variation with Reynolds number is shown in Fig. 5 for case 3 boundary condition. Also shown are the limiting Nusselt numbers for a straight tube. The Nusselt numbers for walls 2 and 4 are averaged over only half of the wall length; hence the difference in their value. This difference becomes more pronounced at higher Re and Pr.

Concluding Remarks

The objective has been to understand the effect of different parameters (H, Re, Pr and different boundary conditions) on the Nusselt number, albeit no attempt is made to provide a vast compilation of data. The potential of a twisted square tube in multichannel heat exchange system has been demonstrated. The overall absolute Nusselt numbers can serve as a measure of effectiveness of twisted tubes for multichannel application, however, individual wall average Nusselt numbers are needed for design purposes.

Table 5 Enhancement in Nusselt number for case (3) boundary condition (0, 1, 0, 1) at constant pumping power ($H = 2.5$)

		← Enhancement (from equation (18)) →				
Pr	Re	Wall 1	Wall 2	Wall 3	Wall 4	abs
0.7	2.51	2.72	2.73	2.72	2.70	2.72
30	2.51	2.96	3.23	2.96	2.68	2.96
0.7	709	3.47	3.95	3.47	3.02	3.48
5.0	709	5.89	7.09	5.89	4.76	5.90

References

1 London, A. L., and Shah, R. K., *Advances in Heat Transfer*, "Supplement I, Laminar Forced Convection in Ducts," Academic Press, New York, 1978.

2 Kalb, C. E., and Seader, J. D., "Heat and Mass Transfer Phenomena for Viscous Flow in Curved Circular Tubes," *International Journal Heat Mass Transfer*, Vol. 15, 1972, pp. 801–816.

3 Cheng, K. C., and Akiyama, M., "Laminar Forced Convection Heat Transfer in Curved Rectangular Channels," *International Journal Heat Mass Transfer*, Vol. 13, 1970, pp. 471–490.

4 Mori, Y., and Uchida, Y., "Study on Forced Convective Heat Transfer in Curved Square Channel," *Transaction Japan Society of Mechanical Engineers*, Vol. 33, 1967, pp. 1836–1846.

5 Masliyah, J. H., and Nandakumar, K., "Fully Developed Viscous Flow and Heat Transfer in Curved Semicircular Sectors," *AIChE Journal*, Vol. 25, 1979, pp. 478–487.

6 Hu, M. H., and Chang, Y. P., "Optimization of Finned Tubes for Heat Transfer in Laminar Flow," ASME JOURNAL OF HEAT TRANSFER, Vol. 95, 1973, pp. 332–338.

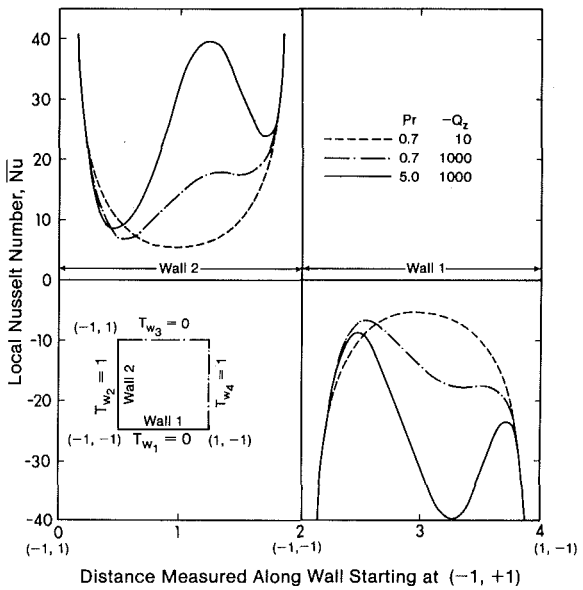

Fig. 4 Local variation of Nusselt number along the wall for case 3 boundary condition ($H = 2.5$)

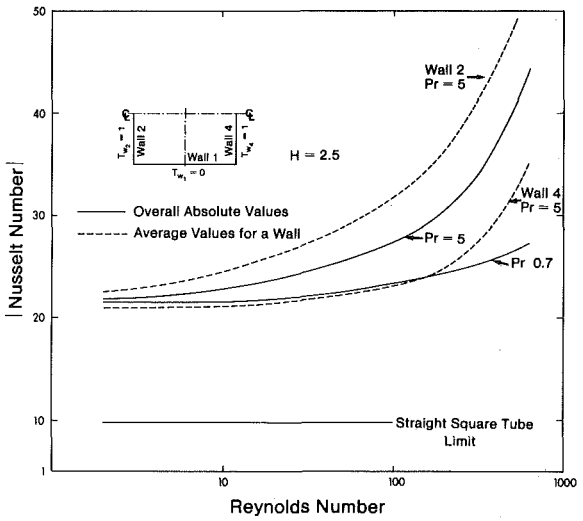

Fig. 5 Average Nusselt number variation with Reynolds number for case 3 boundary condition ($H = 2.5$)

7 Masliyah, J. H., and Nandakumar, K., "Fluid Flow and Heat Transfer in Internally Finned Helical Coils," *The Canadian Journal of Chemical Engineering*, Vol. 55, 1977, pp. 27–36.

8 Todd, L., "Some Comments on Steady Laminar Flow Through Twisted Pipes," *Journal of Engineering Mathematics*, Vol. 11, 1977, pp. 29–48.

9 Date, A. W., "Prediction of Fully-Developed Flow in a Tube Containing a Twisted Tape," *International Journal Heat Mass Transfer*, Vol. 17, 1974, pp. 845–859.

10 Lopina, R. F., and Bergles, A. E., "Heat Transfer and Pressure Drop in Tape Generated Swirl Flow in Single-Phase Water," ASME JOURNAL OF HEAT TRANSFER, Vol. 91, 1969, pp. 434–442.

11 Masliyah, J. H., and Nandakumar, K., "Steady Laminar Flow Through Twisted Pipes: Fluid Flow in Square Tubes," ASME JOURNAL OF HEAT TRANSFER, Vol. 103, Nov. 1981, pp. 785–790.

C. E. Hickox
Mem. ASME

D. K. Gartling
Assoc. Mem. ASME

Fluid and Thermal Sciences Department,[2]
Sandia National Laboratories,
Albuquerque, N.M. 87185

A Numerical Study of Natural Convection in a Horizontal Porous Layer Subjected to an End-to-End Temperature Difference[1]

A numerical study of steady, natural convection in a fluid-saturated, horizontal, porous layer subjected to an end-to-end temperature difference is reported. The analysis is performed using a finite element computer program based on the Galerkin form of the finite element method. Heat transfer rates are predicted for aspect ratios ranging from 0.1 to 0.5 and Rayleigh numbers in the range 25 to 200. Representative plots of temperature and velocity fields are presented. Comparisons are made with an approximate analytical solution and regions of validity are identified for the analytical solution.

Introduction

In a previous paper, Burns, et al. [1] presented results of a numerical study of natural convection in a vertical slot filled with a porous insulation. Their study was concerned with aspect ratios (height/width) in the range 0.5 to 50 and Rayleigh numbers of 50 and 100, based on slot width. The calculated overall heat transfer rates were compared with those obtained numerically by Bankvall [2]. Both of these prior studies utilized finite difference schemes for the numerical solution of the differential equations of natural convective flow in a porous medium.

More recently, Bejan and Tien [3] developed an approximate analytical method for the study of natural convection in a porous layer of small aspect ratio subjected to an end-to-end temperature difference. No appropriate numerical or experimental results are available with which to compare the results of this analysis. A comparison was made with the numerical results mentioned previously for an aspect ratio of 0.5. However, this value is somewhat larger than is appropriate for a comparison with the analytical method, and it was suggested by Bejan and Tien that the accuracy of the numerical results was questionable due to the coarse grid employed for low aspect ratios.

In the present study, numerical solutions are presented for the problem originally considered by Bejan and Tien for aspect ratios in the range 0.1 to 0.5 and Rayleigh numbers, based on layer height, ranging from 25 to 200, a range for which numerical or experimental results are not currently available. The differential equations which describe the natural convection process are formulated in a standard manner assuming the validity of Darcy's law and the Boussinesq approximation. The numerical solution technique differs, however, from those identified previously in that the Galerkin form of the finite element method is used to obtain solutions to the basic equations. Numerical results are compared with the heat transfer rates calculated previously by Burns, et al. and Bankvall as well as with the approximate analytical results of Bejan and Tien.

The Planar, Horizontal, Porous Layer

The basic two-dimensional, planar configuration which is to be studied is illustrated in Fig. 1. The height of the layer is denoted by H and the width by L. For future reference, we note here that the aspect ratio (height/width) is denoted by H/L. All boundaries of the rectangular region are impermeable. Both horizontal boundaries are adiabatic and the vertical boundaries are held at constant temperatures T_0 and T_1. For definiteness, we assume that $T_0 > T_1$. The rectangular region is filled with a rigid, fluid-saturated, porous medium. Gravity acts in the negative x_2-direction. We wish to determine the steady-state natural convective flow pattern and temperature distribution which are established in the porous layer. In addition, we shall also calculate the net rate of thermal energy transport across the layer.

Mathematical Formulation

In this section, we identify a mathematical model which is appropriate for the description of steady, two-dimensional, free convection in a fluid-saturation porous medium and which forms the basis for the numerical study to be described subsequently. The porous matrix is assumed to be rigid and the fluid incompressible, with density changes occurring only as a result of changes in the temperature according to

$$\rho = \rho_0[1 - \beta(T - T_0)], \tag{1}$$

where ρ is the fluid density, T is the temperature, β is the coefficient of thermal expansion, and the subscripts refer to reference conditions. In accordance with the Boussinesq approximation, the effects of fluid density changes are accounted for in the buoyancy term of the equations of motion and are neglected elsewhere. All other fluid and solid properties are assumed constant. It is also assumed that the fluid and matrix are in thermal equilibrium and that the fluid motion can be adequately described by Darcy's law. The equations of continuity, motion, and thermal transport can then be expressed, respectively, as

$$\frac{\partial v_i}{\partial x_i} = 0, \tag{2}$$

$$v_i = -\frac{k}{\mu}\left[\frac{\partial P'}{\partial x_i} - \rho_0 g\beta(T - T_0)\frac{\partial z}{\partial x_i}\right], \tag{3}$$

$$\rho_0 c v_i \frac{\partial T}{\partial x_i} = \kappa_e \frac{\partial}{\partial x_i}\left(\frac{\partial T}{\partial x_i}\right), \tag{4}$$

where the indices i and j take on the values (1,2) and summation is implied by repeated indices. The pressure term P' represents the quantity $(P + \rho_0 gz)$ where P is the pore volume averaged pressure. The bulk volume average Darcy velocity component associated with the x_i coordinate direction is denoted by v_i. The symbols k, κ_e, c, μ, and g are, respectively, permeability, effective thermal conductivity, specific heat, viscosity, and acceleration of gravity. The elevation z is measured vertically upward. The effective thermal conductivity can be related to the fluid and solid matrix properties by the assumed relation

[1] This work was supported by the U.S. Department of Energy under contract DE-AC04-76DP00789.

[2] A U.S. Department of Energy facility.

Contributed by the Heat Transfer Division for publication in the JOURNAL OF HEAT TRANSFER. Manuscript received by the Heat Transfer Division June 16, 1980

$$\kappa_e = \phi\kappa + (1 - \phi)\kappa_s, \tag{5}$$

where ϕ is the porosity and the subscript s refers to solid matrix properties.

Rather than solving equations (2–4) directly, the numerical method to be considered subsequently utilizes the scalar equation for pressure

$$\frac{\partial}{\partial x_i}\left(\frac{\partial P'}{\partial x_i}\right) = \rho_0 g\beta \frac{\partial T}{\partial x_i}\frac{\partial z}{\partial x_i}, \tag{6}$$

obtained by combining equations (2) and (3). Elimination of the velocity v_i from equation (4) through use of equation (3) provides an equation which can be solved simultaneously with equation (6) for the pressure P' and temperature T. Darcy's law, equation (3), can then be used to obtain the velocity field.

In order to complete the mathematical description, appropriate boundary conditions must be specified for the specific problem under consideration. Since all boundaries of the porous layer are impermeable, the velocity component normal to a boundary must vanish on the boundary. This condition is expressed by

$$v_i n_i = 0 \text{ on } \Gamma_V \text{ and } \Gamma_H, \tag{7}$$

where n_i is the unit outward normal to the boundary, the velocity v_i is given by equation (3), and Γ_V, Γ_H denote the vertical and horizontal boundaries, respectively. The horizontal boundaries are insulated; hence, the condition of zero heat flux normal to the boundary is imposed,

$$\frac{\partial T}{\partial x_i} n_i = 0 \text{ on } \Gamma_H. \tag{8}$$

The temperatures on the vertical boundaries are given by

$$\begin{aligned} T(0, X_2) &= T_0, \\ T(L, X_2) &= T_1, \end{aligned} \tag{9}$$

as indicated in Fig. 1.

Approximate Analytical Solution

Bejan and Tien [3] obtained an approximate analytical solution to the problem under consideration by assuming the natural convection pattern to consist of a core region situated in the middle of the porous layer plus two end regions in which the flow adjusts to the imposed boundary conditions. Under the further assumption that $H/L \ll 1$, the streamlines are essentially parallel to the horizontal boundaries in the core region. Thus, by setting $v_2 = 0$ and allowing all thermophysical properties to be constant in equations (2) through (4), the resulting steady-state velocity and temperature distributions in the core region are

$$\frac{v_1 H}{\alpha} = \mathrm{Ra} K_1 \left(\frac{x_2}{H} - \frac{1}{2}\right), \tag{10}$$

$$\frac{T - T_1}{T_0 - T_1} = K_1\left(\frac{L - x_1}{H}\right) + K_2 + \mathrm{Ra}K_1^2\left[\frac{1}{4}\left(\frac{x_2}{H}\right)^2 - \frac{1}{6}\left(\frac{x_2}{H}\right)^3\right] \tag{11}$$

where K_1 and K_2 must be determined from conditions in the end regions. The parameter α is the effective thermal diffusivity ($\kappa_e/\rho_0 c$) and Ra is the Rayleigh number

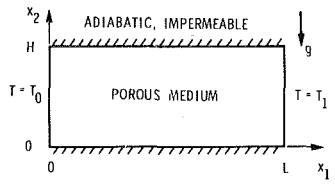

Fig. 1 The planar, horizontal, porous layer

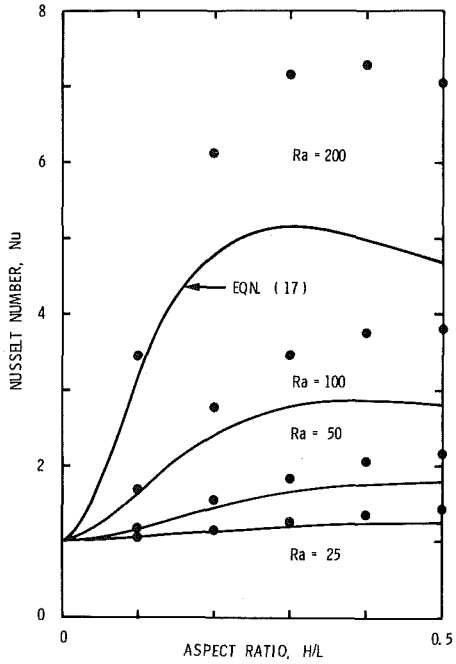

Fig. 2 Comparison of numerically predicted values of the Nusselt number with approximate analytical results of Bejan and Tien [3]. Symbols are numerical results.

$$\mathrm{Ra} = \frac{\rho_0 g\beta H k\,(T_0 - T_1)}{\alpha\mu}. \tag{12}$$

By using assumed forms for the temperature and velocity distributions, Bejan and Tien developed integral solutions for the end regions and upon matching these solutions to the core region, deduced the following expressions from which K_1 and K_2 can be determined:

$$60\left(\frac{1}{K_1} - \frac{L}{H}\right)\left[1 + \frac{1}{30}(\mathrm{Ra}K_1)^2\right]^{1/2} = (\mathrm{Ra}K_1)^2, \tag{13}$$

$$K_2 = \frac{1}{2}K_1\left(\frac{1}{K_1} - \frac{L}{H} - \frac{1}{12}\mathrm{Ra}K_1\right) \tag{14}$$

Nomenclature

c = specific heat
g = acceleration of gravity
H = layer height
h = mesh parameter
K_1, K_2 = functions in analytic solution
k = permeability
L = layer width
Nu = Nusselt number
n_i = outward normal to boundary
P = pore volume average pressure
P' = effective pressure ($P + \rho_0 gz$)
Q = heat transfer rate per unit thickness
Ra = Rayleigh number
T = temperature
v_i = bulk volume average velocity components
x_i = spatial coordinates
z = elevation
α = effective thermal diffusivity ($\kappa_e/\rho_0 c$)
β = thermal expansion coefficient
Γ = boundary coordinate
κ_e = effective thermal conductivity
μ = viscosity
ρ = density
ϕ = porosity
ψ = stream function

Subscripts

e = effective
i = coordinate direction
s = solid
V, H = vertical, horizontal
0 = reference condition or hot boundary
1 = cool boundary

The Nusselt number for the layer is thus given approximately by

$$\mathrm{Nu} = \frac{Q}{\kappa_e H(T_0 - T_1)/L} = \frac{LK_1}{H}\left[1 + \frac{1}{120}(\mathrm{Ra}K_1)^2\right], \qquad (15)$$

where Q is the heat transfer rate per unit thickness for the layer. The analytical results outlined in this section will be used later for comparison with the numerical results.

Computational Approach

Numerical solutions to equations (3, 4), and (6) were obtained through use of the finite element computer program, MARIAH [4, 5] which is based on the Galerkin form of the finite element method. The program structure parallels those of previous finite element computer programs developed by Gartling [6, 7] and thus shares many of the conventions and capabilities of these programs. The application of the Galerkin form of the finite element method has received comprehensive treatment in previous publications [8, 9] and will not be considered in detail here. Complete details concerning the construction and capabilities of the program are available in references [4] and [5].

The computer program MARIAH is, in general, capable of treating a rather broad class of transient or steady-state problems in arbitrarily shaped, two-dimensional, porous regions. In the present study, we have considered only steady, natural convective flow in a rectangular porous region. Hence, our discussion will be limited to a brief description of the specific numerical approach utilized for the solution of the problem at hand.

Implementation of the finite element method is accomplished by first dividing the region of interest into a number of simply shaped sub-regions called finite elements. Then, within each element, a set of nodal points is established at which the dependent variables v_i, P′, T are evaluated. The dependent variables are represented within an element by suitably chosen approximating (basis) functions. In the particular method utilized in the present study, the pressure and temperature were approximated using quadratic basis functions and the velocity components were taken to be linear within each element. Application of this procedure to equations (3, 4), and (6) ultimately results in a system of coupled, nonlinear, algebraic equations for the nodal point unknowns v_i, P', T. A numerical procedure based on Picard iteration was used to obtain converged solutions for the steady-state problem considered in the present work. The actual solution of the system of algebraic equations was accomplished by a frontal elimination procedure which is a special variant of Gaussian elimination.

For purposes of analysis, the planar, horizontal, porous layer described in a previous section was discretized using a 20 × 20 mesh of quadrilateral elements. A uniform mesh spacing was used in the vertical direction. The spacing was graded in the horizontal direction in order to provide increased resolution near the vertical boundaries (see Fig. 8). The same number of elements and horizontal spacing was used for all aspect ratios considered. The number of elements used in the analysis was significantly larger than that required for acceptable accuracy. Justification of this assertion is presented in the following section.

The natural convective flow in the porous layer under consideration is uniquely characterized by the specification of the Rayleigh number Ra and the aspect ratio (H/L). For the numerical studies described in the following section, we have considered aspect ratios in the range 0.1 to 0.5 and Rayleigh numbers from 25 to 200. The upper limit for the aspect ratio corresponds to the lowest value considered by Burns, et al. Hence, our studies extend those of previous workers. The Rayleigh numbers considered cover the range of values regarded as typical of insulation systems. As will be shown subsequently, analytical results are available which provide adequate descriptions of the thermal and flow fields for aspect ratios and Rayleigh numbers less than the smallest values considered in our studies. We have thus attempted to study situations which lie between those adequately described by analytical means and those which have previously been treated numerically.

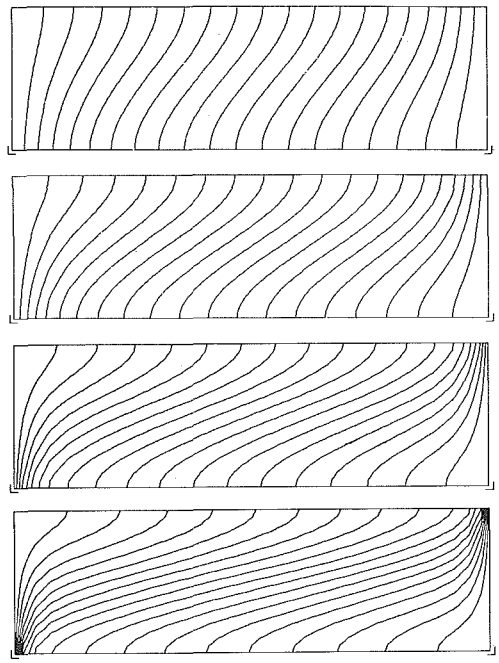

Fig. 3 Isotherms for an aspect ration of 0.3. (Isotherms are equally spaced between nondimensional values of 1 on the left boundary and 0 on the right boundary. From top to bottom, the corresponding Rayleigh numbers are 25, 50, 100, and 200.)

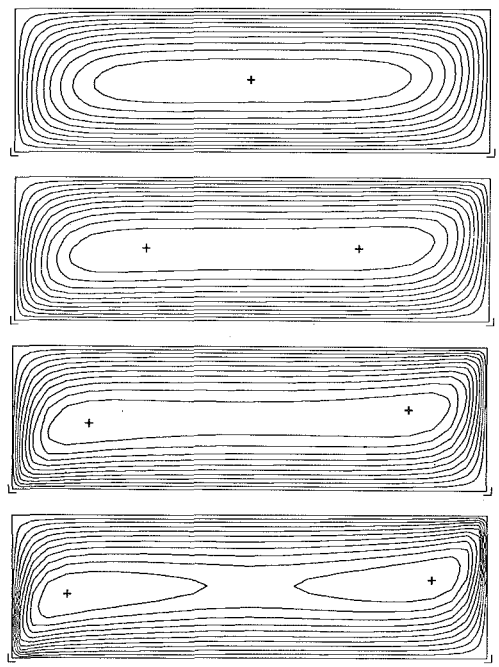

Fig. 4 Streamlines for an aspect ratio of 0.3. (Streamlines are equally spaced between nondimensional values for the streamfunction, ψ/α, of 0 on the boundary and maximum values of 0.857, 1.560, 4.969 and 5.010 as read from top to bottom. The small crosses are locations of the maximum values. From top to bottom, the corresponding Rayleigh numbers are 25, 50, 100, and 200.)

Table I Comparison of calculated Nusselt number with numerical results of Burns, Chow, and Tien [1] (B,C,T) and Bankvall [2] (B) and approximate analytical results of Bejan and Tien [3] (B,T) for an aspect ratio of 0.5

Rayleigh Number Ra	Nusselt Number Nu	$(Nu)_{B,C,T}$	$(Nu)_B$	$(Nu)_{B,T}$
25	1.410	1.54	1.43	1.253
50	2.155	2.81	2.30	1.765

Table 2 Calculated values for the Nusselt number, Nu

Rayleigh Number Ra	Aspect Ratio, H/L 0.1	0.2	0.3	0.4	0.5
25	1.046	1.151	1.264	1.353	1.410
50	1.182	1.543	1.835	2.057	2.155
100	1.690	2.770	3.454	3.750	3.810
200	3.439	6.117	7.167	7.290	7.046

Numerical Results

Comparison with Previous Work. We are not aware of any experimental results for the configuration of Fig. 1. Numerical results for the Nusselt number have been obtained by Burns, et al. [1] and by Bankvall [2]. However, these authors were primarily interested in large aspect ratios and considered only aspect ratios in the range 0.5 to 50 for Rayleigh numbers of 25 and 50. The largest aspect ratio which we have considered is 0.5. In Table 1, our results for the Nusselt number are compared with those of the previously mentioned authors as well as with the approximate analytical results of Bejan and Tien [3] as given by equation (15).

From Table 1, it is apparent that our results compare favorably with those of Bankvall. There is less agreement with the results reported by Burns, Chow, and Tien. However, it was conjectured by Bejan and Tien that the accuracy of these latter results was questionable because of the coarse grid employed for small aspect ratios.

The approximate analytical results of Bejan and Tien are included in Table 1 in order to correct a comparison which they reported in their previous study. Bejan and Tien reported Nusselt numbers of 1.77 and 2.80 for Rayleigh numbers of 50 and 100, respectively. These results were then compared directly with the values reported by Burns, et al. and Bankvall. However, both the Nusselt and Rayleigh numbers defined by Bejan and Tien should have been multiplied by the factor (L/H) in order to correspond to the definitions used by the previous authors. In Table 1, we have compared all results on a common basis. The comparison presented by Bejan and Tien led them to conclude that the analytical solution corresponded more closely to the numerical solutions as the Rayleigh number increased. We have observed the opposite trend.

Heat Transfer Rate. Numerical results obtained for the heat transfer rate between the ends of the horizontal layer are tabulated in Table 2 in terms of the Nusselt number (defined by equation (15)) for Rayleigh numbers in the range 25 to 200 and aspect ratios ranging from 0.1 to 0.5. These same results, along with the analytical solution given by equation (15), are plotted in Fig. 2 in order to allow a comparison of the two solutions.

From a consideration of Fig. 2, it is apparent that the agreement between the numerical and analytical results improves as the Rayleigh number and aspect ratio are reduced. This behavior is not surprising since the analytical results were derived under the assumption of small aspect ratio, $H/L \ll 1$. Also, as the Rayleigh number is decreased, heat transfer by conduction becomes relatively more important than that due to convection, and the Nusselt number approaches unity. Hence,

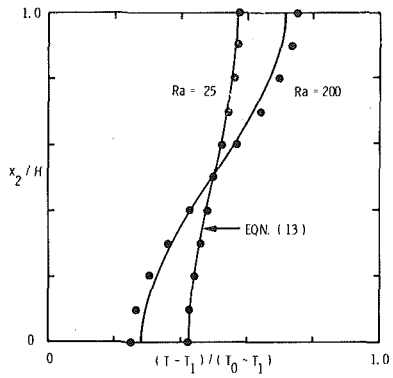

Fig. 5 Comparison of numerical and analytical predictions for temperature distribution on the vertical mid-plane. (Aspect ratio is 0.3. Symbols are numerical results.)

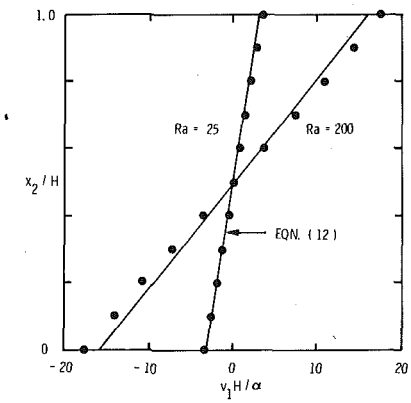

Fig. 6 Comparison of numerical and analytical predictions for horizontal velocity distribution on the vertical mid-plane. (Aspect ratio is 0.3. Symbols are numerical results.)

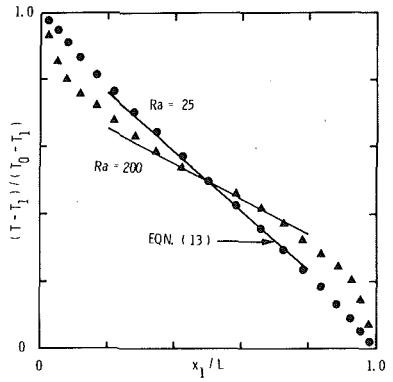

Fig. 7 Comparison of numerical and analytical predictions for temperature distribution on horizontal mid-plane. (Aspect ratio is 0.3. Symbols are numerical results.)

we expect agreement between the analytical and numerical results for small Rayleigh number or small aspect ratio. Figure 2 can be used to identify those situations for which the analytical result is appropriate, depending on the accuracy required. It is also apparent from Fig. 2 that, for a Rayleigh number of 200, the heat transfer rate attains a maximum value for an aspect ratio less than 0.5. The other cases considered apparently attain maxima for larger aspect ratios. This latter observation is consistent with the results of Burns, et al. for Rayleigh numbers of 25 and 50.

Temperature and Velocity Distributions. Representative isotherms and streamlines, as calculated for an aspect ratio of 0.3, are presented in Figs. 3 and 4 for all four Rayleigh numbers considered in the study. The isotherms plotted in Fig. 3 are equally spaced between nondimensional values at the ends of the layer of 0 and 1, where the nondimensional temperature is given by $(T - T_1)/(T_0 - T_1)$. In Fig. 4, the streamlines are equally spaced between a value of zero for the nondimensional stream function on the boundary of the layer and the maximum value quoted on the figure, where the stream function is rendered nondimensional by division by the effective thermal diffusivity α.

The small crosses in Fig. 4 indicate the location of the maximum value of the stream function. For Rayleigh numbers of 50, 100, and 200, the central portion of the flow field is observed to contain two recirculating regions. Since the streamlines are equally spaced in the figure, closed streamlines are plotted only for a Rayleigh number of 200. The formation of recirculating regions was also observed for the other aspect ratios treated in the study.

In Figs. 5–7, calculated and analytically predicted temperature and velocity distributions are compared for an aspect ratio of 0.3 and Rayleigh numbers of 25 and 200. In Fig. 5, we compare the calculated temperature distribution on a vertical plane midway between the ends of the layer with the distribution predicted by the analytical solution given by equation (11). Similarly, velocity distributions calculated for the vertical mid-plane are compared with the analytical result, given by equation (10), in Fig. 6. The temperature distribution calculated for the horizontal mid-plane is plotted in Fig. 7 and the analytical result is included for comparison in the central portion of the layer. It was observed, from the numerical results, that the horizontal thermal gradient midway between the ends of the layer remains relatively constant over the vertical mid-plane.

From Figs. 5–7, it is apparent that the calculated results are predicted reasonably well by the analytical solutions. It is interesting to note, however, that the relatively small differences which exist between the calculated and analytically predicted temperature and velocity distributions can result in rather large differences in the overall heat transfer rates. This result becomes more apparent when one considers that it is the integral of the product of the velocity and temperature distributions which comprise the convective thermal transport for the layer. We have verified the result by performing an approximate integration using the computed distributions.

Porous Layer with an Open End. When one end of a horizontal, porous, layer opens into a constant temperature reservoir, a question arises as to the correct form for the inflow or outflow condition which must be applied. In their analytical solution to the open end case, Bejan and Tien assumed that the flow was parallel and symmetric about the horizontal mid-plane at the open end of the layer. Numerically, this is a difficult situation to attain, since a specific pressure distribution at the open end is required in order to produce a specified velocity distribution.

The condition of parallel flow at an open end can be attained by requiring the pressure distribution to be hydrostatic. This specification is arbitrary to within a constant. If a symmetrical hydrostatic pressure distribution is imposed, the resulting flow at an open end will not necessarily be symmetric; a result which we have verified numerically. In fact, in some situations, fluid from the reservoir will not penetrate the full length of the horizontal layer. Hence, a rather special choice for the pressure distribution is required if the flow is to be symmetric at an open end. Since, in reality, the pressure distribution at an open end is controlled by conditions in the reservoir, it is arbitrary to specify a particular velocity distribution for an open end. As a result of the above considerations, we have included no numerical results for porous layers with open ends.

Comments on the Numerical Approach and Results. We have taken all normal precautions to insure that the accuracies associated with the numerical method utilized and results obtained are within the range of values typically associated with numerical studies of natural convective flow in porous media. For example, finite element approximations of typical elliptic equations of second order with biquadratic interpolation functions are known to exhibit convergence rates of $O(h^3)$ where h is a mesh parameter. Detailed discussions of error estimates are contained in the book by Strang and Fix [10]. An advantage of the finite element method is that, unlike difference methods, special considerations are not required to maintain the local accuracy at nodes where boundary conditions are imposed.

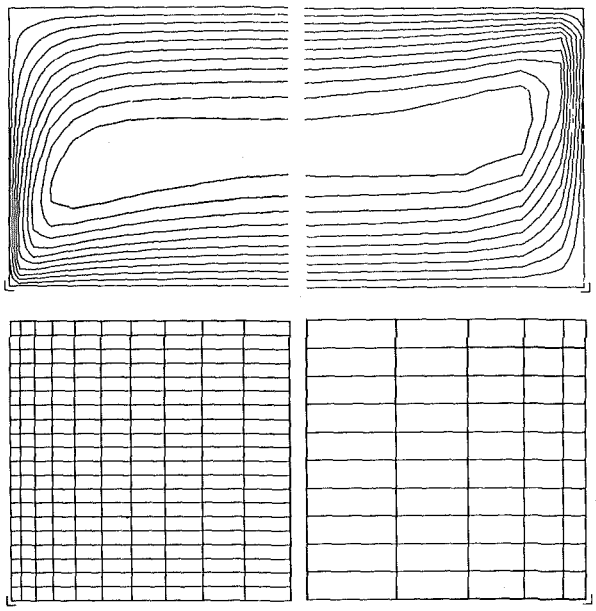

Fig. 8 Computed streamlines for 20 × 20 and 10 × 10 meshes. (One-half the flow field is displayed above the mesh used in the analysis. Identical values for the stream function are plotted for each mesh.)

As stated previously, a method based on Picard iteration was used to obtain converged solutions to the steady-state problems treated in this paper. The solution was assumed to have been adequately converged when the maximum difference between successive iterates of the temperature was less than a prescribed tolerance for all nodal points. The number of iterations required varied with the problem parameters, but was typically in the range from 10 to 20. For the results quoted, tolerances attained varied from 10^{-2} for a Rayleigh number of 200 with an aspect ratio of 0.5 to 10^{-12} for a Rayleigh number of 25 with an aspect ratio of 0.1. In addition, the computed results were studied carefully in order to ascertain that overall conservation of energy requirements were met. Finally, we note that the numerical predictions of Nusselt number compare favorably with an analytical solution for small Rayleigh numbers and aspect ratios and with previous numerical results for Rayleigh numbers of 25 and 50 with an aspect ratio of 0.5.

The number of elements used in the simulations was considerably larger than that required for acceptable accuracy. As mentioned previously, all calculations were performed using a 20 × 20 element mesh that was graded in the horizontal direction to provide increased resolution near the vertical boundaries. In order to assess the effects of mesh spacing on the solutions, a numerical simulation for a Rayleigh number of 200 and aspect ratio of 0.5 was performed on a relatively coarse 10 × 10 element mesh. The relative horizontal grading of the mesh was the same as that used with the 20 × 20 mesh. That is, elements on the vertical boundary were one-fifth as wide as elements at the center of the layer. The Rayleigh number (200) and aspect ratio (0.5) selected for the comparison were chosen because this combination of parameters produced a strong convective flow and exhibited the slowest convergence to steady-state. The overall Nusselt number predicted using the 10 × 10 mesh spacing was 0.3 percent lower than the value predicted with the 20 × 20 mesh spacing. In Fig. 8 we have compared plots of the streamlines predicted with each mesh.

Identical numerical values for the stream function are plotted on each mesh. Except for some apparent inaccuracy in plotting associated with the coarse grid, the flow fields are virtually identical. No distinguishable differences were evident in plots of the isotherms, hence these plots are not included for comparison. This latter result is expected since the overall Nusselt number is essentially unaffected by the mesh refinement.

Typical computing times on a CDC7600 computer ranged from 320 s for a Rayleigh number of 25 with an aspect ratio of 0.1 to 750 s for a Rayleigh number of 200 with an aspect ratio of 0.5.

Concluding Remarks

We have used a computer program based on the Galerkin form of the finite element method to perform a numerical study of steady, natural convective, flow in a horizontal porous layer subjected to an end-to-end temperature difference. Numerical predictions of the heat transfer rate were obtained for aspect ratios and Rayleigh numbers not previously considered by numerical or experimental methods. Representative temperature and velocity distributions were presented for an aspect ratio of 0.3.

We have compared our results to previously published numerical results for an aspect ratio of 0.5 and Rayleigh numbers of 25 and 50. Our results were also compared to a previously published approximate analytical solution and regions of validity for the analytical results were delineated.

The results presented in this paper provide information useful for the analysis of insulating layers. It is also possible that these results may prove useful in geothermal applications.

References

1 Burns, P. J., Chow, L. C., and Tien, C. L., "Convection in a Vertical Slot Filled with Porous Insulation," *International Journal Heat and Mass Transfer*, Vol. 20, 1977, pp. 919–926.

2 Bankvall, C. G., "Natural Convection in Vertical Permeable Space," *Warme-und Stoffubertragung*, Vol. 7, 1974, pp. 22–30.

3. Bejan, A., and Tien, C. L., "Natural Convection in a Horizontal Porous Medium Subjected to an End-to-End Temperature Difference," ASME JOURNAL OF HEAT TRANSFER, Vol. 100, May 1978, pp. 191–198.

4 Gartling, D. K., and Hickox, C. E., "MARIAH—A Finite Element Computer Program for Incompressible Porous Flow Problems, Part I—Theoretical Background," SAND79-1622, Sandia Laboratories, Albuquerque, N.M., in preparation.

5 Gartling, D. K., and Hickox, C. E., "MARIAH—A Finite Element Computer Program for Incompressible Porous Flow Problems," SAND79-1623, Sandia Laboratories, Albuquerque, N.M., Aug. 1980.

6 Gartling, D. K., "NACHOS—A Finite Element Computer Program for Incompressible Flow Problems, Part I—Theoretical Background," SAND77-1333, Sandia Laboratories, Albuquerque, N.M., Apr. 1978.

7 Gartling, D. K., "COYOTE—A Finite Element Computer Program for Nonlinear Heat Conduction Problems," SAND77-1332, Sandia Laboratories, Albuquerque, N.M., June 1978.

8 Gartling, D. K., "Convective Heat Transfer Analysis by the Finite Element Method," *Computer Methods in Applied Mechanics and Engineering*, Vol. 12, No. 3, 1977, pp. 365–382.

9 Zienkiewicz, O. C., *The Finite Element Method in Engineering Science*, McGraw-Hill, London, 1971.

10 Strang, G., and Fix, G. J., *An Analysis of the Finite Element Method*, Prentice-Hall, Englewood Cliffs, 1973.

R. H. Nilson

Fluid and Thermal Sciences Department,
Sandia National Laboratories,
Albuquerque, NM 87185
Assoc. Mem. ASME

Natural Convective Boundary-Layer on Two-Dimensional and Axisymmetric Surfaces in High-Pr Fluids or in Fluid-Saturated Porous Media[1]

In natural convective boundary layers on inclined surfaces, the surface-normal component of the buoyancy force induces a pressure gradient across the boundary layer. For the class of flows in which inertial effects are unimportant (including flows at high Prandtl number as well as flow through fluid-saturated porous media), a local nonsimilarity analysis indicates that the effects of the surface-normal pressure gradient on the temperature profile can be characterized by a single local configuration-parameter which depends on the local geometry and on the Rayleigh Number. Under Mangler's transformation the reported computational results become applicable to axisymmetric as well as two-dimensional geometries of arbitrary contour. In contrast to the single-parameter dependence of the temperature profiles, the velocity profiles depend upon two local geometric parameters, as illustrated for the example of an inclined flat plate.

Introduction

The natural-convective boundary layer on an isothermal surface has been studied extensively in a great variety of applications, including internal as well as external flows at high Rayleigh number. Most analyses address the prototypic case of a vertical plate, with the tacit understanding that an inclined plate is essentially the same (provided that the effective buoyancy force includes only that component which lies parallel to the surface) and that a curved surface is also essentially the same (in a local sense, at least). Unfortunately, the effects of surface inclination and of surface curvature are much more complex than this, as demonstrated in some previous analytical and numerical studies.

1 Surface inclination results in a pressure gradient across the boundary layer (induced by the surface-normal component of the buoyancy force) as investigated by Hasan and Eichhorn [1] for the particular case of an inclined plate.

2 Surface curvature requires that the boundary layer must continually adjust to the changing strength of the surface-parallel component of the buoyancy force, as investigated for general surfaces by Saville and Churchill [2] and by Lin and Chao [3].

There are no previous studies which address the combined effects of both inclination and curvature; nor are there any studies which address either inclination or curvature for natural convective boundary layers in fluid-saturated porous media [4].

The combined effects of surface inclination and surface curvature are investigated for natural convective boundary layers in which inertial effects are unimportant, as is true in both of the following general classes: fluid flow at high Prandtl number, where the inner shear-and-buoyancy region becomes uncoupled from the outer shear-and-inertia region [5] (generally, asymptotic results for $\mathrm{Pr} \to \infty$ give reasonably good heat flux estimates for Pr as low as 7); fluid flow in porous media [4], where the Reynolds number is nearly always sufficiently small to justify the use of Darcy's Law.

In the absence of inertia, the boundary layer adjusts instantaneously to the changing local conditions, and the effects of curvature can be accounted for by a coordinate transformation, originally stated by Acrivos [6] for high-Pr flows and here adapted to porous flows. Moreover, it is found that, under these same transformations, the effect of surface inclination (i.e., normal pressure gradient) on the temperature profile is characterized by a single configuration-parameter which depends on the Rayleigh Number and on local geometric conditions. Under Mangler's transformation, these results are further generalized to include thin boundary layers on bodies of revolution.

Flow at High Prandtl Number

The transport equations for a steady natural convective boundary layer on an arbitrary two-dimensional surface of moderate curvature are as follows [1]

$$\frac{\partial u}{\partial x} + \frac{\partial v}{\partial y} = 0 \tag{1}$$

$$\nu \frac{\partial^3 u}{\partial y^3} + g\beta \cos\gamma \frac{\partial T}{\partial y} - Rg\beta \sin\gamma \frac{\partial T}{\partial x} = u \frac{\partial^2 u}{\partial x \partial y} + v \frac{\partial^2 u}{\partial y^2} \tag{2}$$

$$u \frac{\partial T}{\partial x} + v \frac{\partial T}{\partial y} = \alpha \frac{\partial^2 T}{\partial y^2}, \tag{3}$$

where all properties are presumed to be constant except for the Boussinesq treatment of the density variations due to thermal expansion. The x-coordinate is everywhere tangent to the surface and points in the direction of flow; γ is the local inclination angle between the primary flow direction (x-direction) and the gravitational vector; y is everywhere normal to the surface and points from the surface into the fluid. The normal component of the buoyancy force ($g \sin\gamma$) causes a pressure variation across the boundary layer, and this has been incorporated into the momentum equation (2) by cross differentiation of the x-momentum and y-momentum equations followed by an elimination of the mixed derivative of the pressure as explained in [1]. There are two distinct cases to be considered: R is +1 when the y-component of buoyancy tends to carry the fluid away from the surface (as on the top side of a hot surface); and R is −1 when the y-buoyancy is directed toward the surface (as on the down side of a hot surface).

The quasi-similarity form of the partial differential equations is derived by the introduction of a normalized stream function f ($u = \psi_y$ and $v = -\psi_x$) and a dimensionless temperature θ which are each functions of the independent variables $\xi(x)$ and $\eta(x, y)$

$$f = \frac{1}{4\nu C_2} \frac{\psi}{a(x)}; \quad \theta = \frac{T - T_w}{T_\infty - T_w}; \quad \eta = C_1 \frac{y}{b(x)} \tag{4}$$

The arbitrary constants are chosen as in [2] to be

[1] This work was supported by the U. S. Department of Energy under contract DE-AC04-76-DP00789.

Contributed by the Heat Transfer Division for publication in the JOURNAL OF HEAT TRANSFER. Manuscript received by the Heat Transfer Division February 3, 1981.

$$C_1 = \left(\frac{g\beta\Delta T \cos\gamma_0}{4\nu^2}\right)^{1/4} \mathrm{Pr}^{1/4}; \quad C_2 = \frac{C_1}{\mathrm{Pr}} \tag{5}$$

except that the dependence on Prandtl Number has been introduced in the manner suggested by Kuiken [5] and as also given in equations (23) of [1]. The scaling functions $a(x)$, $b(x)$, and $\xi(x)$ which appear in the transformation must then satisfy the following system or ordinary differential equations, sometimes called similarity equations [7], (in which $(\ )_x = d(\ )/dx$)

$$\frac{4}{3} ba_x = 1; \quad a/b^3 = \frac{\cos\gamma}{\cos\gamma_0}; \quad \xi_x = -\frac{\xi}{a} a_x \tag{6}$$

in order that the partial differential equations can take the following, rather simple, form in which $(\ )' = \partial(\ )/\partial\eta$ and $(\ )_\xi = \partial(\ )/\partial\xi$,

$$f''' + \theta' + \Lambda\left\{\eta\theta' - \frac{b}{b_x}\xi_x\theta_\xi\right\} = \frac{1}{\mathrm{Pr}}\{\text{inertial terms}\} \to 0 \tag{7}$$

$$\theta'' + 3(f - \xi f_\xi)\theta' = -3\xi f'\theta_\xi \tag{8}$$

subject to the boundary conditions

$$f = f' = 0 \quad \text{and} \quad \theta = 1 \text{ at } \eta = 0 \tag{9}$$

$$f'' = f''' = 0 \quad \text{and} \quad \theta = 0 \text{ as } \eta \to \infty \tag{10}$$

The local configuration parameter Λ, which appears in (7), is a function of ξ (or, alternatively, of x) alone.

$$\Lambda \equiv R\frac{\tan\gamma}{C_1} b_x \tag{11}$$

This system comprises the zeroth-order inner problem [5] in the limit as $\mathrm{Pr} \to \infty$, and accordingly the inertial terms are dropped from the momentum equation. Physically, when Pr becomes large, the thermal boundary layer (or inner region) becomes much narrower than the viscous boundary layer (or outer region), and the velocity reaches its maximum value at the inner edge of the inner region. The boundary conditions (10) are formally justified by the zeroth-order matching principle (equation (41) of [5]) which enforces agreement between the outer expansion of the inner solution and the inner expansion of the outer solution.

The local nonsimilarity method, as explained in [1, 8], accounts for the departure from local similarity through a sequence of successive approximations. The transformed equations (7, 8) are retained exactly as stated, even including the nonsimilar terms, f_ξ *and* θ_ξ. An additional pair of auxiliary equations, for f_ξ and θ_ξ, are then generated by differentiating the system (7, 8) with respect to ξ, and so on to higher order derivatives. The experience of others [1, 8, 9] has shown that it is generally sufficient to retain only f_ξ and θ_ξ and, hence, neglect the higher order corrections, $f_{\xi\xi}$ and $\theta_{\xi\xi}$, which would appear in the auxiliary equations. Thus, by a single differentiation and the exclusion of second order ξ-derivatives, there results the following auxiliary equations for $g = f_\xi$ and $\Phi = \theta_\xi$

$$g''' + \Lambda_\xi\eta\theta' = \{\Phi \quad \text{and} \quad \Phi_\xi \text{ terms}\} = 0 \tag{12}$$

$$\Phi'' + 3(f\Phi' + f'\Phi) + 3\xi(g'\Phi - g\Phi') = 0, \tag{13}$$

subject to the boundary conditions

$$g = g' = 0 \quad \text{and} \quad \Phi = 0 \text{ at } \eta = 0 \tag{14}$$

$$g'' = g''' = 0 \quad \text{and} \quad \Phi = 0 \text{ as } \eta \to \infty \tag{15}$$

Φ satisfies a homogeneous equation with homogeneous boundary conditions and must, therefore, vanish identically.

The temperature profile and the local heat flux can now be determined from the following reduced system of ordinary differential equations which evolve directly from (7, 8, 12) under the introduction of an effective stream function F which satisfies the same boundary conditions as f (compare with (17, 18) in [1]). Here $(\ )' = d(\ )/d\hat{\eta}$.

$$F = (f - \xi g)/(1 + |\lambda|)^{1/5}; \quad \hat{\eta} = \eta(1 + |\lambda|)^{1/5} \tag{16}$$

$$F''' + \theta'[(1 + |\lambda|)^{-4/5} + \hat{\eta}\lambda/(1 + |\lambda|)] = 0 \tag{17}$$

$$\theta'' + 3F\theta' = 0 \tag{18}$$

Thus, the only parameter which appears in the thermal problem (17, 18) is a local geometric configuration parameter, λ.

$$\lambda \equiv \Lambda - \xi\Lambda_\xi = \Lambda + \frac{a}{a_x}\Lambda_x. \tag{19}$$

The scaling of F and $\hat{\eta}$, as stated in (16) above, insures that the solution becomes independent of λ both as $\lambda \to 0$ and as $\lambda \to \pm\infty$ because in those limits (17) becomes $F''' + \theta' = 0$ and $F''' \pm \hat{\eta}\theta' = 0$, respectively. Once $\theta(\hat{\eta}; \lambda)$ has been numerically calculated from (17, 18), the corresponding local velocity distributions $f'(\eta; \lambda, \Lambda)$ can be calculated from (7).

Flow through Porous Media

In a fluid-saturated porous medium, the natural convective boundary layer is still governed by the continuity and energy equations (1, 3), but the force-balance is now, according to Darcy's Law [4]

$$\frac{\nu}{\kappa}\frac{\partial u}{\partial y} - g\beta\cos\gamma\frac{\partial T}{\partial y} + Rg\beta\sin\gamma\frac{\partial T}{\partial x} = 0 \tag{20}$$

in which κ is the permeability, and in essence, u_{yy} in (2) is simply replaced by u/κ in (20). The definitions of f, θ, and η are precisely the same as in (4); the scaling constants are now defined the same as in [7]

$$C_1 = \left(\frac{\kappa g\beta\Delta T\cos\gamma_0}{\alpha\nu}\right)^{1/2}, \quad C_2 = \frac{C_1}{4\mathrm{Pr}}; \tag{21}$$

and the scaling functions $a(x)$, $b(x)$, $\xi(x)$ must now satisfy

$$2ba_x = 1, \quad \frac{a}{b} = \frac{\cos\gamma}{\cos\gamma_0}, \quad \xi_x = -\frac{\xi}{a}a_x \tag{22}$$

in order that the partial differential equations (1, 3, 20) can take the following form (in which $\Lambda = Rb_x \tan\gamma/C_1$, as before, and $(\ )' = d(\ )/d\eta$)

Nomenclature

C_1, C_2 = constants in similarity transformation (5, 21)
Nu = Nusselt number in (42, 46)
Pr = Prandtl number
Ra = Rayleigh number defined below (39, 41, 43, 46)
$R = \pm 1$, denotes orientation of surface-normal buoyancy
Λ, λ = configuration parameters defined in (11, 19, 36, 38)
ν, β = viscosity, thermal expansion coefficient
g = gravitational acceleration
κ = permeability of porous medium
x, y = two-dimensional boundary-layer coordinates
γ = inclination angle of surface
γ_0 = arbitrary reference angle
X, Y = axisymmetric boundary-layer coordinates
r = distance from axis of symmetry
ξ, η = similarity coordinates defined in (4, 6c, 22c)
$\hat{\eta}$ = similarity coordinate defined in (16, 28)
a, b = scale functions in similarity transformation (6, 22, 36)
u, v = two-dimensional velocity components
U, V = axisymmetric velocity components
T = temperature, $\Delta T = |T_w - T_\infty|$
θ = dimensionless temperature $= (T - T_\infty)/(T_w - T_\infty)$
ψ = stream function
f = dimensionless stream function (4)
F = effective stream function defined in (16, 28)
$\Phi, g = \partial\theta/\partial\xi, = \partial f/\partial\xi$

$$f'' - \theta' - \Lambda\left\{\eta\theta' - \frac{b}{b_x}\xi_x\theta_\xi\right\} = 0 \tag{23}$$

$$\theta'' + \frac{1}{2}(f - \xi f_\xi)\theta' = -\frac{1}{2}\xi f'\theta_\xi \tag{24}$$

subject to the boundary conditions

$$f = 0 \quad \text{and} \quad \theta = 1 \text{ at } \eta = 0 \tag{25}$$

$$f' \to 0 \quad \text{and} \quad \theta \to 0 \text{ as } \eta \to \infty, \tag{26}$$

which now permit the fluid to slip at the wall, but still prohibit any flow through the wall, and require a vanishing velocity at infinity.

The local nonsimilarity procedure is nearly the same as before, both in methodology and in outcome. Taking the ξ-derivative of (23, 24) and then suppressing $f_{\xi\xi}$ and $\theta_{\xi\xi}$, it is again found that $\Phi = \theta_\xi = 0$, and that $g = f_\xi$ then satisfies $g'' - \Lambda_\xi\eta\theta' = 0$. The thermal information can be extracted by solving the following ordinary differential equations for the temperature $\theta(\hat{\eta})$ and the effective stream function $F(\hat{\eta})$

$$F = (f - \xi g)/(1 + |\lambda|)^{1/3}; \tag{27}$$

$$\hat{\eta} = \eta(1 + |\lambda|)^{1/3} \tag{28}$$

$$F'' - \theta'[(1 + |\lambda|)^{-2/3} + \hat{\eta}\lambda/(1 + |\lambda|)] = 0 \tag{29}$$

$$\theta'' + \frac{1}{2}F\theta' = 0, \tag{30}$$

in which the only parameter is again λ as defined previously in (19).

Axisymmetric Geometries

The boundary layer equations for an axisymmetric flow are as follows [10], for a thin boundary-layer ($\delta(x) \ll r(x)$) on a smooth surface

$$\frac{\partial}{\partial X}(rU) + \frac{\partial}{\partial Y}(rV) = 0 \tag{31}$$

$$\nu\frac{\partial^3 U}{\partial Y^3} + g\beta\cos\gamma\frac{\partial T}{\partial Y} - Rg\beta\sin\gamma\frac{\partial T}{\partial X} = U\frac{\partial^2 U}{\partial X\partial Y} + V\frac{\partial^2 U}{\partial Y^2} \tag{32}$$

$$U\frac{\partial T}{\partial X} + V\frac{\partial T}{\partial Y} = \alpha\frac{\partial^2 T}{\partial Y^2}, \tag{33}$$

in which U, V, X, and Y are the velocity components and coordinates of the axisymmetric flow, and $r(X)$ is the distance from the axis to the surface, measured normal to the axis. Under Mangler's transformation (in which L is a characteristic length and $r' = dr/dX = r_x(r/L)^2$) [10],

$$x = \int_0^X \left(\frac{r}{L}\right)^2 dX, \quad y = \left(\frac{r}{L}\right)Y, \quad u = U, \quad v = \frac{L}{r}\left(V + \frac{r'}{r}YU\right) \tag{34}$$

the axisymmetric problem (31–33) becomes identical to the two-dimensional problem (1–3) except that the momentum equation is now, in place of (2),

$$\nu\frac{\partial^3 u}{\partial y^3} + g\beta\cos\gamma\left(\frac{L}{r}\right)^2\frac{\partial T}{\partial y} - Rg\beta\sin\gamma\left\{\frac{\partial T}{\partial x}\left(\frac{L}{r}\right) + y\frac{\partial T}{\partial y}\frac{r'}{r}\left(\frac{L}{r}\right)^3\right\} = u\frac{\partial^2 u}{\partial x\partial y} + v\frac{\partial^2 u}{\partial y^2}. \tag{35}$$

The similarity transformation (4, 5, 6a, 6c) is the same as in the two-dimensional case, except that (6b) and (11) must be redefined as follows

$$\frac{a}{b^3} = \frac{\cos\gamma}{\cos\gamma_0}\left(\frac{L}{r}\right)^2; \quad \Lambda = R\frac{\tan\gamma}{C_1}\left(\frac{L}{r}\right)b_x\left(1 - \frac{br_x}{rb_x}\right) \tag{36}$$

in order that the transformed energy and momentum equations can take identically the same form as before (7, 8).

Similarly in flow through porous media, a thin boundary layer on an axisymmetric surface obeys (31, 33) as well as the previously-stated force-balance equation (20) which should now be rewritten in terms of the upper case variables U, X, Y. Under Mangler's transformation (34) the axisymmetric problem for a porous flow becomes the same as the two-dimensional porous problem (1, 3, 20) except that the force-balance equation is now, instead of (20),

$$\frac{\nu}{\kappa}\frac{\partial u}{\partial y} - g\beta\cos\gamma\frac{\partial T}{\partial y} + Rg\beta\sin\gamma\left(\frac{r}{L}\right)\left\{\frac{\partial T}{\partial x} + y\frac{\partial T}{\partial y}\frac{r'}{r}\left(\frac{L}{r}\right)^2\right\} = 0. \tag{37}$$

The similarity variables are still the same as in the two-dimensional porous flow (4), with the same constants (21), and the same similarity conditions (22). Only the geometric function Λ need be redefined as follows

$$\Lambda = R\frac{\tan\gamma}{C_1}\left(\frac{r}{L}\right)b_x\left(1 - \frac{br_x}{rb_x}\right) \tag{38}$$

in order that the transformed force-balance and energy equations can take identically the same form as before (23, 24).

Results for High-Pr Flow

The temperature profiles of Fig. 1 for a high-Pr flow, either two-dimensional or axisymmetric, are calculated by solving the ordinary differential equations (17, 18) subject to the boundary conditions from (9, 10, 14, 15). The chosen numerical procedure is a standard shooting method which utilizes library routines for the two major tasks: fourth order Runge Kutta integration, and iterative adjustment of the shooting parameters ($\theta'(0)$, $F''(0)$, $F'''(0)$) by a nonlinear equation solver which seeks zeros for $F''(\infty)$, $F'''(\infty)$, and $\theta(\infty)$. For $\lambda = 0$, the surface-normal buoyancy is absent, and the numerical result is the same as Kuiken's [5] with a surface heat flux of $\theta'(0) = \partial\theta/\partial\hat{\eta} = -0.711$. For positive λ, there is a thinning of the thermal boundary layer and a corresponding increase in the heat flux, as apparent both in the temperature profiles of Fig. 1 and in the heat-flux plot of Fig. 2. As $\lambda \to \infty$ the heat flux approaches the limit $\theta'(0) = -0.758$. Conversely for negative λ, there is a thickening of the boundary layer and a corresponding decrease in heat flux. There is a minimum value of $\lambda(\lambda_{\min}$

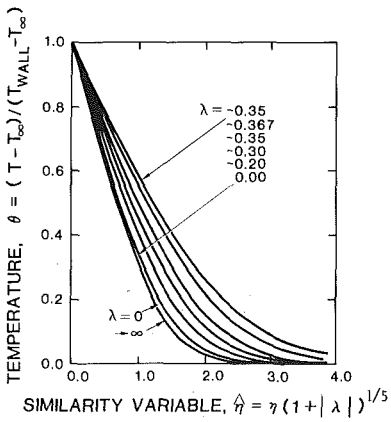

Fig. 1 Temperature profiles for high-Pr natural convection

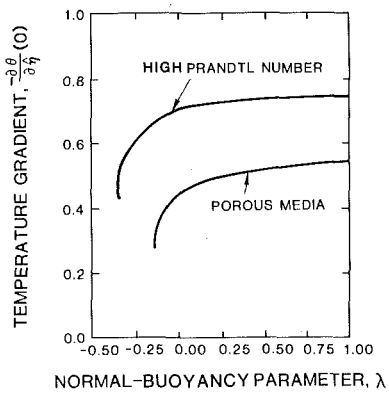

Fig. 2 Heat flux at the wall for high-Pr natural convection and for natural convection in porous media

$\simeq -0.367$) for which solutions exist, and in that neighborhood there are multiple solutions for some λ. To numerically combat this nonuniqueness, $F''(0)$ (which happens to be a single-valued parameter for the solution family) is treated as a prescribed-parameter and λ is treated as a shooting-parameter, rather than the reverse. Soon after turning the corner onto the lower branch, the solution curve must terminate at $\lambda_{last} \simeq -0.32$, because beyond that point $F'(\infty)$ becomes negative with the implication that $F(\infty) < 0$ (since $F \to$ const $+ F'(\infty)\hat{\eta}$ as $\hat{\eta} \to \infty$) in which case θ cannot have an acceptable decaying-exponential asymptotic behavior, as apparent from the energy equation (18). The lower-branch solutions are probably not physical (due to stability considerations not investigated here), but the existence of λ_{min} does place a mathematical limitation on the method of solution.

The velocity profile depends upon two local geometric parameters: Λ which appears explicitly in equation (7), and λ which exerts an indirect influence through $\theta(\eta)$. As an illustrative example, consider the case of an inclined flat plate, which inclination angle γ, for which the similarity equations (6) can be readily integrated to find that

$$a = x^{3/4}, \quad b = x^{1/4}, \quad \lambda = 0, \quad \Lambda = \pm\tan\gamma/2\sqrt{2}\mathrm{Ra}_x{}^{1/4} \tag{39}$$

in which $\mathrm{Ra}_x = 4C_1{}^4x^3$ is a Rayleigh number based upon the local length of run, x, and on the surface-parallel component of buoyancy, $g\cos\gamma$. Since λ is everywhere zero, the temperature profile is entirely unaffected by the surface-normal buoyancy and is therefore self-similar, as noted previously in [1]. There is, however, an influence on the velocity profile as illustrated in Fig. 3 which presents numerical solutions to (7, 9, 10) for $\lambda = 0$ and for all Λ. The scaling of f' on the ordinate is motivated by the substitution $f^* = f/(1 + |\Lambda|)$ which reduces the differential equation (7) to the Λ-independent forms $f^{*'''} \pm \eta\theta' = 0$ in the limits as $\Lambda \to \pm\infty$, without disrupting the behavior as $\Lambda \to 0$; also note that $f^*(\eta; \Lambda \to -\infty) = -f^*(\eta; \lambda \to +\infty)$. Near the origin of the flow, where $\mathrm{Ra}_x \to 0$, the velocity is strongly distorted by the normal buoyancy force, but with increasing length of run, Ra_x increases until ultimately, the velocity profile approaches the self-similar form (i.e., $\Lambda \to 0$ as $\mathrm{Ra}_x \to \infty$) which signifies an insensitivity to normal buoyance. On a plate of finite length, L, the nonsimilarity will therefore be localized near the nose of the plate whenever $|\tan\gamma/\mathrm{Ra}_L{}^{1/4}|$ is sufficiently small.

On any surface of contour the inclination angle, γ, depends upon the position, x, but the similarity equations (e.g., (6)) can still be integrated to find λ and Λ as functions of position, as for example in the two-dimensional case where

$$\Lambda = \pm\frac{\sqrt{2}\tan\gamma}{\mathrm{Ra}_L{}^{1/4}}\frac{d}{d\sigma}\left[\left(\frac{\cos\gamma}{\cos\gamma_0}\right)^{-1/3}\left(\int_0^\sigma\left(\frac{\cos\gamma}{\cos\gamma_0}\right)^{1/3}d\sigma\right)^{1/4}\right] \tag{40}$$

$$\lambda = \Lambda + \frac{4}{3}\frac{d\Lambda}{d\sigma}\left(\frac{\cos\gamma}{\cos\gamma_0}\right)^{-1/3}\int_0^\sigma\left(\frac{\cos\gamma}{\cos\gamma_0}\right)^{1/3}d\sigma \tag{41}$$

in which $\mathrm{Ra}_L = 4C_1{}^4L^3$ is a Rayleigh number based on a characteristic length L (e.g., radius of cylinder) and $\sigma = x/L$ is the normalized position coordinate (e.g., $\sigma = x/L$ = azimuth angle on a cylinder). For given Ra_L; λ and Λ and all of the physical quantities become known functions of the position σ as, for example, the local Nusselt number for a two-dimensional flow

$$\mathrm{Nu} = \frac{hL}{k} = \frac{-\partial\theta}{\partial\hat{\eta}}(1 + |\lambda|)^{1/5}\mathrm{Ra}_L{}^{1/4}\frac{1}{\sqrt{2}}\left(\frac{\cos\gamma}{\cos\gamma_0}\right)^{1/3}\left[\int_0^\sigma\left(\frac{\cos\gamma}{\cos\gamma_0}\right)^{1/3}d\sigma\right]^{-1/4} \tag{42}$$

in which $\partial\theta/\partial\hat{\eta}$ is a known function of λ as given in Fig. 2. At high Rayleigh number ($\mathrm{Ra}_L \to \infty$) λ and $\Lambda \to 0$, and the surface-normal buoyancy becomes unimportant except in the regions where $\tan\gamma \to \infty$ (e.g., near the poles of a sphere or cylinder).

Results for Flow in Porous Media

The temperature profiles of Fig. 4 for flow through porous media, either two-dimensional or axisymmetric, are calculated by solving equations (29, 30) subject to the boundary conditions from (25, 26).

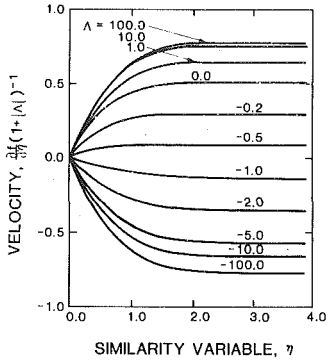

Fig. 3 Velocity profiles for high-Pr natural convection on an incined plate (for which $\lambda = 0$) illustrating flow reversal for sufficiently negative Λ

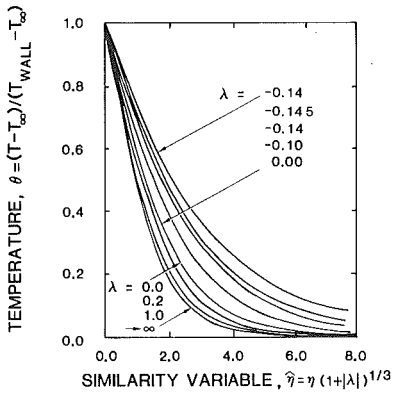

Fig. 4 Temperature profiles for natural convection in porous media

In the numerical solution procedure the shooting parameters, $\theta'(0)$ and $F'(0)$, are adjusted until $F'(\infty) = 0$ and $\theta(\infty) = 0$. The solutions are qualitatively similar to the previous high-Pr results. For $\lambda = 0$, normal buoyancy is absent and the temperature profile is the same as Cheng and Minkowycz's [7] with a wall flux $\theta'(0) = -0.444$. As $\lambda \to \infty$, the boundary layer becomes progressively thinner and the heat flux approaches the limit $\theta'(0) = -0.568$. For negative λ, the boundary layer thickens. There is a minimum value of λ for which solutions exist ($\lambda_{min} \simeq -0.145$ in Figs. 2 and 4), and there are multiple solutions in that neighborhood.

The velocity profiles depend upon λ and Λ. For the exemplary case of an inclined flat plate, the similarity equations (22) are integrated to find that

$$a = x^{1/2}, \quad b = x^{1/2}, \quad \lambda = 0, \quad \Lambda = \pm\tan\gamma/2\mathrm{Ra}_x{}^{1/2} \tag{43}$$

in which $\mathrm{Ra}_x = C_1{}^2x$. The corresponding velocity profiles are presented in Fig. 5 for different values of Λ. The influence of normal buoyancy is strongest near the origin of the boundary layer where $\mathrm{Ra}_x \to 0$ and, hence, $\Lambda \to \pm\infty$.

On a general two-dimensional surface, the similarity equations (22) are integrated to find that

$$\Lambda = \frac{\pm\tan\gamma}{\mathrm{Ra}_L{}^{1/2}}\frac{d}{d\sigma}\left[\left(\frac{\cos\gamma}{\cos\gamma_0}\right)^{-1}\left(\int_0^\sigma\left(\frac{\cos\gamma}{\cos\gamma_0}\right)d\sigma\right)^{1/2}\right] \tag{44}$$

$$\lambda = \Lambda + 2\frac{d\Lambda}{d\sigma}\left(\frac{\cos\gamma}{\cos\gamma_0}\right)^{-1}\int_0^\sigma\left(\frac{\cos\gamma}{\cos\gamma_0}\right)d\sigma \tag{45}$$

$$\mathrm{Nu} = \frac{-\partial\theta}{\partial\hat{\eta}}(1 + |\lambda|)^{1/3}\,\mathrm{Ra}_L{}^{1/2}\left(\frac{\cos\gamma}{\cos\gamma_0}\right)\left[\int_0^\sigma\left(\frac{\cos\gamma}{\cos\gamma_0}\right)d\sigma\right]^{-1/2} \tag{46}$$

in which $\mathrm{Ra}_L = C_1{}^2L$ and $\sigma = x/L$, in analogy to the high-Pr results.

Variations in local heat flux due to surface curvature and surface-inclination are now illustrated for some additional examples of external flow in porous media. On a cone (with vertex half-angle γ_0, and side of length L) the local Nusselt number varies according to the following expressions, respectively, for the cases in which the primary flow direction is away from or toward the vertex

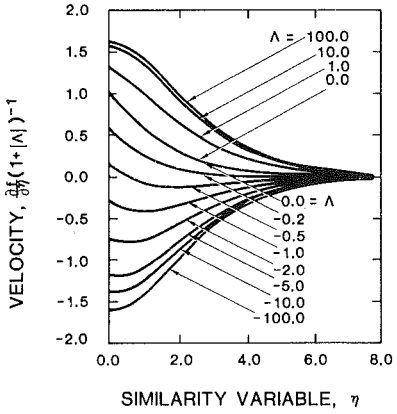

Fig. 5 Velocity profiles for natural convection on an inclined plate imbedded in a porous medium (for which λ = 0) illustrating flow reversal for sufficiently negative Λ

$$\frac{\mathrm{Nu}_L}{\mathrm{Ra}_L{}^{1/2}} = -\sqrt{3}\frac{\partial\theta}{\partial\hat{\eta}}(1+|\lambda|)^{1/3}(X/L)^{1/2} \tag{47}$$

$$\frac{\mathrm{Nu}_L}{\mathrm{Ra}_L{}^{1/2}} = -\sqrt{3}\frac{\partial\theta}{\partial\hat{\eta}}(1+|\lambda|)^{1/3}(X/L)/(1-(X/L)^3)^{1/2} \tag{48}$$

in both of which X is measured away from the vertex. On a cylinder and a sphere, respectively,

$$\frac{\mathrm{Nu}_L}{\mathrm{Ra}_L{}^{1/2}} = -\frac{\partial\theta}{\partial\hat{\eta}}(1+|\lambda|)^{1/3}\sin\theta/(1\text{-}\cos\theta)^{1/2} \tag{49}$$

$$\frac{\mathrm{Nu}_L}{\mathrm{Ra}_L{}^{1/2}} = -3\frac{\partial\theta}{\partial\hat{\eta}}(1+|\lambda|)^{1/3}\sin^2\theta/[2\text{-}\cos\theta(\sin^2\theta+2)] \tag{50}$$

in which L is the radius and $\cos\gamma_0 = 1$ in the definition of Ra_L, and θ is increasing in the primary flow direction. In all four of these expressions the affect of surface-normal buoyancy is embodied by the dependence on λ, both explicitly and through $\partial\theta/\partial\hat{\eta}$ as illustrated in Fig. 2. The variation in λ along each body shape is determined by integration of the similarity equations (22) and substitution into the definition of Λ and λ (11) or (19, 38). The results in Fig. 6 (where λ is negative on dotted lines) show that $|\lambda|$ is largest near stagnation points and that, for example, $|\lambda| > 1$ throughout the polar quadrants ($0 < \theta < \pi/4$ and $3\pi/4 < \theta < \pi$) of a sphere whenever $\mathrm{Ra}_L \leq 10^2$. At higher Ra_L, the normal-buoyancy effects become confined to smaller regions near the stagnation points.

Summary

The combined effects of surface-normal buoyancy and of surface curvature have been examined for viscous-dominated natural convection as occurs in high-Pr fluids and in fluid-saturated porous media. For isothermal surfaces, either two dimensional or axisymmetric, the local nonsimilarity method [1, 8] is used to obtain temperature profiles (Figs. 1 and 4) which depend upon only one local configuration parameter, λ, and to obtain velocity profiles which depend upon two such parameters, λ and Λ.

$$\Lambda = \pm\frac{\tan\gamma}{\mathrm{Ra}_L{}^n}F\,(\text{geometry}) \quad \text{and} \quad \lambda = \Lambda - \xi\Lambda_\xi$$

in which Ra_L is the Rayleigh number based on a characteristic length of run, L, and the premultiplier, $\pm\tan\gamma/\mathrm{Ra}_L{}^n$, represents the nominal ratio between the normal and parallel components of buoyancy (normal/parallel $\sim T_x \sin\gamma/T_y \cos\gamma \sim \tan\gamma$. δ/L, in which $\delta \sim L/\mathrm{Ra}_L{}^n$ is the nominal boundary-layer thickness). Many special cases of interest are contained within the present generalized results.

1 At high Rayleigh Number ($\mathrm{Ra}_L \to \infty$), λ and Λ become small, except where $\tan\gamma \to \infty$, and: the high-Pr solution approaches Acrivos' [6] self-similar result; while the porous-flow solution approaches an analogous self-similar form. In these flows the normal buoyancy is absent, and the surface curvature is accounted for by the similarity transformation.

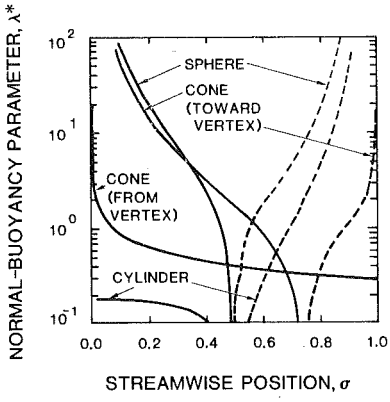

Fig. 6 Local influence of surface-normal buoyancy is indicated by streamwise variation of λ for porous flow over several different body-shapes: sphere and cylinder ($\lambda^* = \lambda\mathrm{Ra}_L{}^{1/2}$, $\sigma = \theta/\pi$, L = radius and $\cos\gamma_0 = 1$ in Ra_L, θ increases in flow direction); cone with flow toward vertex or away from vertex ($\lambda^* = \lambda\mathrm{Ra}_L{}^{1/2}/\tan\gamma_0$, $\sigma = X/L$, γ_0 = half-angle of vertex, L = length of side, X measured from vertex). Lines are dotted when λ is negative.

2 For an inclined plate ($\tan\gamma$ = constant): the high-Pr flow has self-similar temperature profiles (since λ = 0, as noted previously by Hasan and Eichhorn [1]) but nonsimilar velocity profiles (Fig. 3); and in flow through porous media the qualitative behavior is the same (Figs. 4 and 5). In these flows the surface curvature is absent, and the normal buoyancy is accounted for through the nonsimilarity approach.

3 For a vertical plate ($\tan\gamma = 0$, λ = 0 and Λ = 0) the high-Pr result becomes identical to Kuiken's similarity solution [5], and the porous flow solution becomes identical to Cheng and Minkowycz's similarity solution [7]. In these flows there is neither normal buoyancy nor surface curvature.

In general boundary-layer applications, the high-Ra results (i.e., λ and Λ → 0) provide a zeroth order estimate which includes the effects of surface curvature. The finite-Ra corrections, as calculated from the nonsimilarity procedure, are indicative of the first perturbations due to surface-normal buoyancy (as explained in Hasan and Eichhorn's [1] comparison of the nonsimilar boundary-layer analysis with the formal matched-asymptotic-expansion analysis of the finite-Ra perturbations for an inclined flat plate). The nonuniformity of the high-Ra approximation is apparent in the first-order nonsimilar solutions which may even fail to exist in those regions where the surface-normal buoyancy lifts away from the surface and where $\tan\gamma$ is sufficiently large (i.e., sufficiently negative λ in Figs. 2 and 6).

References

1 Hasan, M. M., and Eichhorn, R., "Local Nonsimilarity Solution for Free Convection Flow and Heat Transfer from an Inclined Isothermal Plate," ASME JOURNAL OF HEAT TRANSFER, Vol. 101, 1979, pp. 642–647.

2 Saville, D. A., and Churchill, S. W., "Laminar Free Convection in Boundary Layers Near Hotizontal Cylinders and Vertical Axisymmetric Bodies," *Journal of Fluid Mechanics*, Vol. 29, No. 2, 1967, pp. 391–399.

3 Lin, F. N., and Chao, B. T., "Laminar Free Convection Over Two-Dimensional and Axisymmetric Bodies of Arbitrary Contour," ASME JOURNAL OF HEAT TRANSFER, Vol. 96, 1974, pp. 435–442.

4 Cheng, P., "Heat Transfer in Geothermal Systems," *Advances in Heat Transfer*, Vol. 14, 1978, pp. 1–105.

5 Kuiken, H. K., "An Asymptotic Solution for Large Prandtl Number Free Convection," Journal of Engineering Mathematics, Vol. II, No. (4) 1968, pp. 355–371.

6 Acrivos, A., "A Theoretical Analysis of Laminar Natural Convection Heat Transfer to Non-Newtonian Fluids," *AIChE Journal*, Vol. 6, No. (4), 1960, pp. 584–590.

7 Cheng, P., and Minkowycz, W. J., "Free Convection About a Vertical Flat Plate Embedded in a Porous Medium with Application to Heat Transfer From a Dike," *Journal Geophysical Research*, Vol. 82, No. 14, 1977, pp. 2040–2044.

8 Sparrow, E. M., and Yu, H. S., "Local Nonsimilarity Thermal Boundary-Layer Solutions," ASME JOURNAL OF HEAT TRANSFER, Vol. 93, 1971, pp. 328–334.

9 Minkowycz, W. J., and Cheng, P., "Free Convection About a Vertical Cylinder Embedded in a Porous Medium," *International Journal of Heat Mass Transfer*, Vol. 19, 1976, pp. 805–813.

10 White, F. M., *Viscous Fluid Flow*, McGraw Hill, New York, 1974.

W. W. Yuen
Department of Mechanical and Environmental Engineering, University of California, Santa Barbara, Calif. 93106

A Simplified Approach to the Evaluation of the Geometric-Mean Transmittance and Absorptance for Gas Enclosures

Utilizing a simple mathematical relation and Stoke's theorem, the geometric-mean transmittance and total absorptance between an infinitesimal area and a finite planar element is reduced to a line integral around the planar element and an area integral. A concept of fundamental solutions is introduced. These are solutions in which the finite areas are horizontal right triangle with three specific orientations. Based on superposition, solutions for arbitrary finite areas are shown to be readily generated algebraically from these fundamental solutions. The geometric-mean transmittance and total absorptance between two finite areas are reduced to single numerical integrations, thus reducing much of the mathematical complexity.

Fundamental solutions for mean beam lengths of the geometric-mean total absorptance in the weak-band, strong-band and very-strong-band limits are generated analytically in closed form. Based on the existing one-dimensional wide band correlation, these limiting expressions are shown to be sufficient for the calculation of the geometric-mean total absorptance at all optical thicknesses. A sample calculation is presented.

Introduction

In many heat transfer calculations for practical engineering systems with high temperature such as fires and combustion furnaces, the evaluation of the surface-surface and surface-medium radiative exchange in an enclosure with an intervening absorbing-emitting medium is a problem of considerable importance. Mathematically, this task involves the evaluation of the so-called geometric-mean transmittance and absorptance for the considered enclosure.

Formally, definitions of the geometric-mean transmittance and absorptance are quite simple and straight-forward and their importance was realized more than 30 years ago [1]. A great deal of effort has been made since then to tabulate these quantities for various systems. The success of these efforts, however, is quite limited largely because of the mathematical complexity of the problem. Today, exact evaluations for these quantities are restricted only to a few cases with special geometric symmetry or optical thickness limits [2–6]. For most other cases, the current state-of-the-art technique is to utilize an empirical "mean beam length" and the corresponding one-dimensional results [1, 2]. While this method appears to be reasonably accurate for some selected enclosures, its applicability to general enclosures still remains unproven and has uncertain accuracy.

The major difficulty in the calculation of the geometric-mean transmittance and absorptance for a given enclosure is that they require the evaluation of a complicated integral The integral involves not only the geometry of the two considered surfaces, but also their relative orientation. Because of the presence of angular variables, many traditional numerical techniques for integral evaluation cannot be applied. The integral can also become singular for some selected cases. The objective of this work is to show that by using a simple mathematical relation and Stoke's theorem, the geometric-mean transmittance and absorptance between an infinitesimal area element and a finite area can be expressed as sums of a simple line integral around the boundary of the finite surface and an area integral. These integrals can be evaluated analytically for some selected cases. For all cases, they can be tabulated numerically by standard technique.

Contributed by the Heat Transfer Division for publication in the JOURNAL OF HEAT TRANSFER. Manuscript received by the Heat Transfer Division December 8, 1980.

For general application, the present work proposes a concept of fundamental solutions. These solutions are geometric-mean transmittance and absorptance between an infinitesimal area of arbitrary orientation and horizontal right triangles of three specific orientations. Utilizing the principle of superposition, the geometric-mean transmittance and absorptance between an infinitesimal area and any finite area can be written as sums and differences of these fundamental solutions. Based on the present approach, these fundamental solutions are readily generated in closed-form. If the intervening medium is a non-gray gas, the important physical quantity is the geometric-mean total absorptance (which is the integral over wavelengths of the geometric-mean absorptance). Fundamental solutions for this quantity in the weak-band, strong-band and very-strong-band limits are also readily generated. Using the existing wide-band correlations, these limiting expressions are demonstrated to be sufficient for the evaluation of the geometric-mean total absorptance at all optical thickness. It is interesting to note that until now, only tabulations of the weak-bank limit of the geometric-mean total absorptance for some selected simple systems are available in the literature [1, 2, 4] largely because of the mathematical complexity.

To illustrate the accuracy and the simplicity of the present approach, the weak-band, strong-band and very-strong-band limit of the total geometric-mean absorptance between two rectangles of different orientations is generated. For the weak-band cases which were considered by Dunkle [4] with a different approach, the agreement is excellent. The present approach, however, is readily seen to be more general and simple to use.

Mathematical Formulation

Utilizing the geometry and coordinate system as shown in Fig. 1, the geometric-mean transmittance between areas dA_1 and A_2, $\tau_{\lambda,d1-2}$, can be written

$$\tau_{\lambda,d1-2} = \frac{1}{F_{d1-2}} \int_{A_2} \frac{(\mathbf{n}_1 \cdot \mathbf{r}_1)(\mathbf{n}_2 \cdot \mathbf{r}_2) e^{-a_\lambda r}}{\pi r^2} dA_2 \qquad (1)$$

where F_{d1-2} is the shape factor [1] between dA_1 and A_2, $\mathbf{n}_1$ and $\mathbf{n}_2$ are the unit normal vectors to areas dA_1 and dA_2 respectively, $\mathbf{r}_1$ is a unit vector pointing away from dA_1 to dA_2, r is the distance between the two areas, and a_λ is the absorption coefficient. Physically, $\tau_{\lambda,d1-2}$ is the fraction of energy leaving surface dA_1 which is transmitted

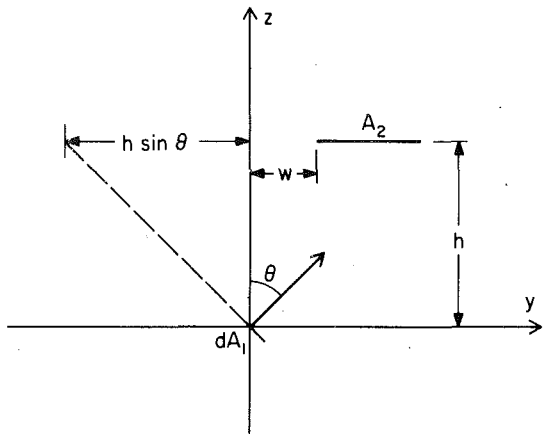

Fig. 1 Coordinate system used in equation (1)

through the medium and arrives at A_2. To calculate the fraction of energy leaving surface dA_1 which is absorbed by the intervening medium, the concept of geometric-mean absorptance is important. It is

$$\alpha_{\lambda,d1-2} = \frac{1}{F_{d1-2}} \int_{A_2} \frac{(\mathbf{n}_1 \cdot \mathbf{r}_1)(\mathbf{n}_2 \cdot \mathbf{r}_1)(1 - e^{-a_\lambda r})}{\pi r^2} dA_2. \quad (2)$$

If the medium is a non-gray gas with absorption bands, equation (2) can be integrated over one band to yield the total geometric mean absorptance as

$$\alpha_{i,d1-2} = \int_{\Delta i} \alpha_{\lambda,d1-2} d\lambda = \frac{1}{F_{d1-2}} \int_{A_2} \frac{(\mathbf{n}_1 \cdot \mathbf{r}_1)(\mathbf{n}_2 \cdot \mathbf{r}_1)\overline{A}_i(r)}{\pi r^2} dA_2 \quad (3)$$

where $\int_{\Delta i} d\lambda$ represents integration over the ith absorption band and $\overline{A}_i$ is the corresponding effective bandwidth for a one-dimensional system of thickness r. Effective bandwidths for various important bands for different gases have been demonstrated to be adequately approximated by the so-called wide-band correlation [2]. The correlation proposed by Edwards, et al. [2, 7] is presented in Table 1.

Substituting results presented in Table 1 into equation (3), it can be readily seen that the evaluation of $\alpha_{i,d1-2}$ requires only the following integrals:

$$R_{d1-2} = \frac{1}{F_{d1-2}} \int_{A_2} \frac{(\mathbf{n}_1 \cdot \mathbf{r}_1)(\mathbf{n}_2 \cdot \mathbf{r}_2)}{\pi r} dA_2 \quad (4)$$

$$(S_{d1-2})^{1/2} = \frac{1}{F_{d1-2}} \int_{A_2} \frac{(\mathbf{n}_1 \cdot \mathbf{r}_1)(\mathbf{n}_2 \cdot \mathbf{r}_1)}{\pi r^{3/2}} dA_2 \quad (5)$$

$$\ln W_{d1-2} = \frac{1}{F_{d1-2}} \int_{A_2} \frac{(\mathbf{n}_1 \cdot \mathbf{r}_1)(\mathbf{n}_2 \cdot \mathbf{r}_1)}{\pi r^2} \ln r dA_2 \quad (6)$$

It is interesting to note that R_{d1-2} is the weak-bank geometric mean beam length originally introduced by Dunkle [4]. Since $\overline{A}_i(r)$ is proportional to $r^{1/2}$ and $\ln r$ in the strong band and very-strong band limit, respectively. S_{d1-2} and W_{d1-2} can be interpreted as the corresponding geometric mean beam length in those limits. For two finite areas A_1 and A_2, equations (4, 5) and (6) are generalized to

$$R_{1-2} = \frac{1}{A_1 F_{12}} \int_{A_1} F_{d1-2} R_{d1-2} dA_1, \quad (4a)$$

$$S_{1-2}{}^{1/2} = \frac{1}{A_1 F_{12}} \int_{A_1} F_{d1-2} S_{d1-2}{}^{1/2} dA_1, \quad (5a)$$

$$\ln W_{1-2} = \frac{1}{A_1 F_{12}} \int_{A_1} F_{d1-2} \ln W_{d1-2} dA_1. \quad (6a)$$

In terms of R_{1-2}, S_{1-2} and W_{1-2}, a correlation analogous to Table 1 for the total geometric-mean absorptance between two finite areas A_1 and A_2 can be generated. It is presented in Table 2.

Since equations (1, 4, 5), and (6) are all of the same general form as the left hand side of equation (A3) in Appendix I, they can be simplified. Equation (1), for example, can be written as

$$\pi F_{d1-2} \tau_{\lambda,d1-2} = \int_{S_2} g_1(r)(\mathbf{r}_1 \times \mathbf{n}_1) \cdot \mathbf{dS}_2 + \int_{A_2} (\mathbf{n}_1 \cdot \mathbf{n}_2) \left[g'_1(r) + \frac{g_1(r)}{r} \right] dA_2 \quad (7)$$

where $g_1(r)$ satisfies the equation

$$g'_1(r) - \frac{g_1(r)}{r} = \frac{e^{-a_\lambda r}}{r^2} \quad (8)$$

Equations (4, 5), and (6) can be written as

$$\pi F_{d1-2} R_{d1-2} = \int_{S_2} g_2(r)(\mathbf{r}_1 \times \mathbf{n}_1) \cdot \mathbf{dS}_2 + \int_{A_2} (\mathbf{n}_1 \cdot \mathbf{n}_2) \left[g'_2(r) + \frac{g_2(r)}{r} \right] dA_2 \quad (9)$$

$$\pi F_{d1-2} S_{d1-2}{}^{1/2} = \int_{S_2} g_3(r)(\mathbf{r}_1 \times \mathbf{n}_1) \cdot \mathbf{dS}_2 + \int_{A_2} (\mathbf{n}_1 \cdot \mathbf{n}_2) \left[g'_3(r) + \frac{g_3(r)}{r} \right] dA_2 \quad (10)$$

$$\pi F_{d1-2} \ln W_{d1-2} = \int_{S_2} g_4(r)(\mathbf{r}_1 \times \mathbf{n}_1) \cdot \mathbf{dS}_2 + \int_{A_2} (\mathbf{n}_1 \cdot \mathbf{n}_2) \left[g'_4(r) + \frac{g_4(r)}{r} \right] dA_2 \quad (11)$$

with $g_2(r)$, $g_3(r)$, and $g_4(r)$ satisfying

Nomenclature

a_λ = absorption coefficient
A_1, A_2 = area elements
$\overline{A}_i$ = effective bandwidth of the ith band
d = parameter defined in Fig. 2(b)
E_3 = exponential function
$F\left(\Gamma, \frac{1}{2^{1/2}}\right)$ = elliptic function of the first kind
f_{i-j} = shape factor between area A_i and A_j
$g_i (i = 1, 2, 3, 4)$ = functions defined by equations (15) thru (18)
G = functions defined by equations (22, 26) and (30)
h = parameter defined in Fig. 2(a)
H = functions defined by equations (23, 28) and (31)
$\mathbf{n}_1, \mathbf{n}_2$ = unit vectors defined in Fig. 1
$\mathbf{r}_1, \mathbf{r}_2$ = unit vectors defined by equations (1) and (2)
r = distance between areas dA_1 and dA_2
R_{l-j} = weak-band geometric mean beam length, equation (4)
S_{i-j} = strong-band geometric mean beam length, equation (4)
u = parameter defined in Fig. 2(b)
v = parameter defined in Fig. 2(b)
w = parameter defined in Fig. 2(b)
W_{1-2} = very-strong-band geometric mean beam length, equation (6)
$Z_{\mathrm{I}}, Z_{\mathrm{II}}, Z_{\mathrm{III}}$ = fundamental solutions defined by equations (21, 32) and (33)
Z_{i-j} = generalized mean beam length defined by equation (21)
$\alpha_{\lambda,1-2}$ = geometric-mean absorptance defined by equation (2)
$\alpha_{i,1-2}$ = total geometric-mean absorptance of the ith band
$\gamma(y)$ = function defined by equation (29)
θ = parameter defined in Fig. 2(a)
λ = wavelength
$\rho(x)$ = function defined by equation (27)
$\tau_{\lambda,1-2}$ = geometric-mean transmittance defined by equation (1)

Table 1 Effective bandwidth correlation equations for isothermal gas

Pressure-broadening Parameter $\beta = \frac{C_2^2 P_e}{4C_1C_3}$	Lower limit of $\overline{A}$ η, cm^{-1}	Upper limit of $\overline{A}$ η, cm^{-1}	Effective bandwidth $\overline{A}$ η, cm^{-1}
$\beta \leq 1$	0	βC_3	$\overline{A} = C_1 X$
	βC_3	$C_3(2-\beta)$	$\overline{A} = C_2(XP_e)^{1/2} - \beta C_3$
	$C_3(2-\beta)$	∞	$\overline{A} = C_3\left(\ln \frac{C_2^2 X P_e}{4C_3^2} + 2 - \beta\right)$
$\beta > 1$	0	C_3	$\overline{A} = C_1 X$
	C_3	∞	$\overline{A} = C_3\left(\ln \frac{C_1 X}{C_3} + 1\right)$

C_1, C_2, C_3, b, and n given in reference [7]. X is mass path length, ρS, g/m^2. $P_e = [(P + P_{N_2})/P_0]^n$ where $P_{N_2} = 1$ atm, P is partial pressure of absorbing gas, and P_{N_2} is partial pressure of N_2 broadening gas in atmospheres.

Table 2 Effective bandwidth correlation equations for multidimensional isothermal gas

Pressure-broadening Parameter $\beta = \frac{C_2^2 P_e}{4C_1C_3}$	Lower limit of $\overline{A}$ η, cm^{-1}	Upper limit of $\overline{A}$ η, cm^{-1}	Effective bandwidth $\overline{A}$ η, cm^{-1}
$\beta \leq 1$	0	βC_3	$\overline{A} = C_1 \rho R_{1-2}$
	βC_3	$C_3(2-\beta)$	$\overline{A} = C_2(\rho S_{1-2} P_e)^{1/2} - \beta C_3$
	$C_3(2-\beta)$	∞	$\overline{A} = C_3\left(\ln \frac{C_2^2 \rho W_{1-2} P_e}{4C_3^2} + 2 - \beta\right)$
$\beta > 1$	0	C_3	$\overline{A} = C_1 \rho R_{1-2}$
	C_3	∞	$\overline{A} = C_3\left(\ln \frac{C_1 \rho W_{1-2}}{C_3} + 1\right)$

C_1, C_2, C_3, b, and n given in reference [7]. ρ is mass density g/m^3, and S is pathlength m, $P_e = [(P + P_{N_2})/P_0]^n$ where $P_{N_2} = 1$ atm, P is partial pressure of absorbing gas, and P_{N_2} is partial pressure of N_2 broadening gas in atmospheres.

$$g'_2(r) - \frac{g_2(r)}{r} = \frac{1}{r} \tag{12}$$

$$g'_3(r) - \frac{g_3(r)}{r} = \frac{1}{r^{3/2}} \tag{13}$$

$$g'_4(r) - \frac{g_4(r)}{r} = \frac{\ln r}{r^2}. \tag{14}$$

Equations (8, 12, 13), and (14) can be readily solved to yield

$$g_1(r) = -\frac{E_3(a_\lambda r)}{r} \tag{15}$$

$$g_2(r) = -1 \tag{16}$$

$$g_3(r) = -\frac{2}{3r^{1/2}} \tag{17}$$

$$g_4(r) = -\frac{\ln r}{2r} - \frac{1}{4r} \tag{18}$$

with $E_3(a_\lambda r)$ in equation (15) being the familiar exponential integral function defined by

$$E_n(x) = \int_1^\infty \frac{e^{-xt}}{t^n}\, dt. \qquad n \geq 1 \tag{19}$$

Utilizing equations (15–18), equations (7, 9, 10), and (11) become

$$\pi F_{d1-2} \tau_{\lambda,d1-2} = -\int_{S_2} \frac{E_3(a_\lambda r)}{r} (\mathbf{r}_1 \times \mathbf{n}_1) \cdot \mathbf{dS}_2 + \int_{A_2} (\mathbf{n}_1 \cdot \mathbf{n}_2) \frac{a_\lambda}{r} E_2(a_\lambda r) dA_2 \tag{20}$$

$$\pi F_{d1-2} R_{d1-2} = -\int_{S_2} (\mathbf{r}_1 \times \mathbf{n}_1) \cdot \mathbf{dS}_2 - \int_{A_2} (\mathbf{n}_1 \cdot \mathbf{n}_2) \frac{dA_2}{r} \tag{21}$$

$$\pi F_{d1-2} S_{d1-2}{}^{1/2} = -\frac{2}{3} \int_{S_2} \frac{(\mathbf{r}_1 \times \mathbf{n}_1) \cdot \mathbf{dS}_2}{r^{1/2}} - \frac{1}{3} \int_{A_2} \frac{(\mathbf{n}_1 \cdot \mathbf{n}_2) dA_2}{r^{3/2}} \tag{22}$$

$$\pi F_{d1-2} \ln W_{d1-2} = -\frac{1}{2} \int_{S_2} \left(\frac{\ln r}{r} + \frac{1}{2r}\right) (\mathbf{r}_1 \times \mathbf{n}_1) \cdot \mathbf{dS}_2 - \frac{1}{2} \int_{A_2} (\mathbf{n}_1 \cdot \mathbf{n}_2) \frac{dA_2}{r^2} \tag{23}$$

In terms of actual evaluation, equations (20–23) represent a great reduction in complexity in contrast to equations (1, 4, 5), and (6).

Fundamental Solutions

Equations (20–23) can be readily evaluated in closed-form for some systems with simple geometry. But for general application, the most important results are fundamental solutions for these expressions in which dA_1 is an infinitesimal area at the origin with arbitrary orientation and A_2 is a right triangle at a horizontal plane above the origin. It can be shown that it is sufficient to consider only four particular orientations of A_2. The geometry and the associated coordinate systems for the four fundamental solutions are illustrated in Figs. 2(*a*) and 2(*b*). The superposition procedure can be generated from these fundamental solutions as outlined in Appendix II.

For the right triangle I as shown in Fig. 2(*b*), equations (20–22) and (23) can be readily simplified into the following form

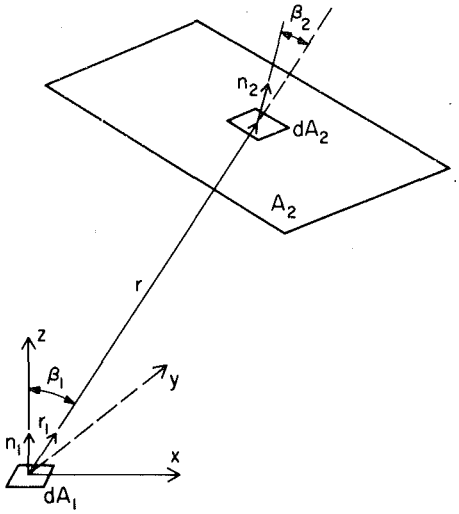

Fig. 2(a) Side-view of the relative position and orientation of dA_1 and A_2 for the fundamental solutions

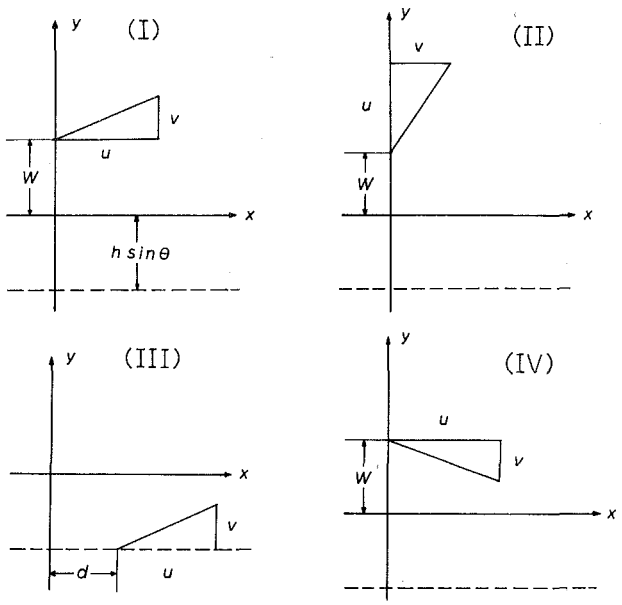

Fig. 2(b) Top view of orientations of A_2 for the four fundamental solutions

$$Z_{\mathrm{I}}(u, v, w, h\,\theta) = (h\sin\theta - w\cos\theta)G(0, u, 1, 0, w^2+h^2) + u\cos\theta G(w, w+v, 1, 0, u^2+h^2) + (w\cos\theta - h\sin\theta)G\left(0, u, \frac{u^2+v^2}{u^2}, \frac{2wv}{u}, w^2+h^2\right) - \cos\theta H(u, v, w, 0, 0). \quad (24)$$

For the geometric-mean transmittance, Z_{I} stands for $(F_{d1\text{-}2}\tau_{\lambda,d1\text{-}2})^I$, and $G(m, n, A, B, C)$ and $H(u, v, w, d, \phi)$ are given by

$$G(m, n, A, B, C) = \frac{1}{\pi}\int_m^n \frac{E_3[a_\lambda(At^2+Bt+C)^{1/2}]}{(At^2+Bt+C)}dt \quad (25)$$

$$H(u, v, w, d, \phi) = -\frac{a_\lambda}{\pi}\int_{x_1}^{x_2}\int_{y_1}^{y_2}\frac{E_2[a_\lambda(x^2+y^2+h^2)^{1/2}]}{(x^2+y^2+h^2)^{1/2}}dydx \quad (26)$$

where $y_1 = w\cos\phi$, $y_2 = w\cos\phi + v/u(x - d - w\sin\phi)$, $x_1 = w\sin\phi + d$ and $x_2 = w\sin\phi + d + u$. For the weak-band limit of the geometric-mean total absorptance, Z_{I} stands for $(F_{d1\text{-}2}R_{d1\text{-}2})^I$ with

$$G(m, n, A, B, C) = \frac{1}{\pi A^{1/2}}\ln\left[\frac{2(An^2+Bn+C)^{1/2}+2A^{1/2}n+A^{1/2}B}{2(Am^2+Bm+C)^{1/2}+2A^{1/2}m+A^{1/2}B}\right] \quad (27)$$

$$H(u, v, w, d, \phi) = \frac{1}{\pi}\int_{x_1}^{x_2}\ln\left[\frac{(y_2^2+x^2+h^2)^{1/2}+y_2}{(y_1^2+x^2+h^2)^{1/2}+y_1}\right]dx. \quad (28)$$

Equation (28) can be integrated in closed-form with a standard integration table [8]. For the strong-band limit of the geometric-mean total absorptance, Z_{I} stands for $(F_{d1\text{-}2}S_{d1\text{-}2}{}^{1/2})^I$ with

$$G(m, n, A, B, C) = \frac{4}{3\pi[A(4AC-B^2)]^{1/4}}\left[\frac{n+B/2A}{|n+B/2A|}F\left(\rho(n), \frac{1}{2^{1/2}}\right) - \frac{m+B/2A}{|m+B/2A|}F\left(\rho(m), \frac{1}{2^{1/2}}\right)\right] \quad (29)$$

where

$$\rho(x) = \cos^{-1}\left[\frac{1}{\dfrac{(2Ax+B)^2}{4AC-B^2}+1}\right]^{1/4}. \quad (30)$$

The function $F(\Gamma, 1/2^{1/2})$ in equation (29) is the elliptic integral of the first kind. The function $H(u, v, w, d)$ is given by

$$H(u, v, w, d, \phi) = \frac{2^{1/2}}{3}\int_{x_1}^{x_2}\frac{1}{(x^2+h^2)^{1/4}}\left[F\left(\gamma(y_2), \frac{1}{2^{1/2}}\right) - F\left(\gamma(y_1), \frac{1}{2^{1/2}}\right)\right]dx \quad (31)$$

where

$$\gamma(y) = \cos^{-1}\left[\frac{x^2+h^2}{y^2+x^2+h^2}\right]^{1/4}. \quad (32)$$

At the very-strong-band limit, Z_{I} stands for $(F_{d1\text{-}2}\ ln\ w_{d1\text{-}2})^I$ where

$$G(m, n, A, B, C) = \frac{1}{4\pi}\int_m^n \frac{ln\,[At^2+Bt+C]}{[At^2+Bt+C]}dt + \frac{1}{2\pi(4AC-B^2)^{1/2}}\left[\tan^{-1}\frac{B+2An}{(4AC-B^2)^{1/2}} - \tan^{-1}\frac{B+2Am}{(4AC-B^2)^{1/2}}\right] \quad (33)$$

and

$$H(u, v, w, d, \phi) = \frac{1}{2\pi}\int_{x_1}^{x_2}\frac{1}{(x^2+h^2)^{1/2}}\left[\tan^{-1}\frac{y_2}{(x^2+h^2)^{1/2}} - \tan^{-1}\frac{y_1}{(x^2+h^2)^{1/2}}\right]dx \quad (34)$$

Similarly, the fundamental solutions for right triangles II, III, and IV as shown in Fig. 2(*b*) are given by

$$Z_{\mathrm{II}}(u, v, w, h, \theta) = -[(u+w)\cos\theta - h\sin\theta]G\left(0, v, 1, 0, h^2 + (u+w)^2\right) + \frac{v}{u}(w\cos\theta - h\sin\theta)G\left(w, w+u, \frac{u^2+v^2}{u^2}, -\frac{2v^2}{u^2}w, \frac{w^2v^2}{u^2}+h^2\right) - \cos\theta H(u, v, w, 0, \pi/2) \quad (35)$$

$$Z_{\mathrm{III}(u, v, d, h, \theta)} = -h\sin\theta(\cos\theta+1)G(d, d+u, 1, 0, h^2(1+\sin^2\theta)) - (u+d)\cos\theta G(-h\sin\theta, -h\sin\theta+v, 1, 0, h^2+(u+d)^2) + \left[h\sin\theta(1+\cos\theta) + \frac{v}{u}d\cos\theta\right]G\left(d, d+u, \frac{u^2+v^2}{u^2}, 2\frac{v}{u}\left(-h\sin\theta - \frac{v}{u}d\right), h^2 + \left(h\sin\theta + \frac{v}{u}d\right)^2\right) - \cos\theta H(u, v, -h\sin\theta, d, 0) \quad (36)$$

$$Z_{IV}(u, v, d, h, \theta) = (w \cos\theta - h \sin\theta)\, G(0, u, 1, 0, w^2 + h^2) - u \cos\theta G(w, w - v, 1, 0, u^2 + h^2) + (h \sin\theta - w \cos\theta) G(0, u, 1, + u^2/u^2, - 2wv/u, w^2 + h^2) + \cos\theta H(u, - v, w, 0, 0) \quad (36a)$$

The functions G and H in equations (35) and (36) are defined indentically as in equations (25–35).

To demonstrate the utility and simplicity of the present mathematical approach in application for finite area, the weak-band, strong-band, and very-strong-band limits of the geometric-mean beam length between two rectangular plates with orientation as shown in Fig. 3 is now calculated. This example is selected because some results in the weak-bank limit with $\beta = 0$ and $\beta = \pi/2$ have already been tabulated by Dunkle [4] with a different approach. A direct comparison is thus possible. The strong-band and very-strong-band limits, on the other hand, have never been reported in the literature.

Consider a differential area dA_I at $(x, y, 0)$; A_{II} can be readily broken up relative to dA_I into four fundamental right triangles. Using superposition, the three limits of the geometric mean beam can be written in the following generalized form

$$Z_{dA_I - A_{II}} = \sum_{i=1}^{4} Z_{dA_I - A_i} \quad (37)$$

where

$$Z_{dA_I - A_1} = Z_I\left(\frac{a}{2} - y, b, - x \cos\beta, h + x \sin\beta, \beta\right) \quad (38)$$

$$Z_{dA_I - A_2} = Z_{II}\left(b, \frac{a}{2} - y, - x \cos\beta, h + x \sin\beta, \beta\right) \quad (39)$$

$$Z_{dA_I - A_3} = Z_{II}\left(b, y + \frac{a}{2}, - x \cos\beta, h + x \sin\beta, \beta\right) \quad (40)$$

$$Z_{dA_I - A_4} = Z_I\left(y + \frac{a}{2}, b, - x \cos\beta, h + x \sin\beta, \beta\right) \quad (41)$$

Equation (37) can be integrated over A_I to yield

$$Z_{A_I - A_{II}} = \frac{2}{ab} \int_0^a \int_0^b Z_{dA_I - A_{II}} dx dy \quad (42)$$

In the above expression, $Z_{A_I - A_{II}}$ stands for $F_{A_I - A_{II}} R_{A_I - A_{II}}$, $F_{A_I - A_{II}} S_{A_I - A_{II}}{}^{1/2}$ and $F_{A_I - A_{II}} \ln W_{A_I - A_{II}}$ in the weak-band, strong-band and very-strong-band limit, respectively.

Equation (42) can be readily evaluated numerically in all three limits. For all cases, the integral converges quickly with no difficulty. Results for the three limits for various values of a, b, and β with $h = 1.0$ are presented in Tables 3, 4 and 5. For the weak-band cases with $\beta = 0$ and $\beta = \pi/2$, the agreement with Dunkle's result [4] is exact. It is interesting to note that for the considered cases, the difference between the geometric-mean beam lengths at the three limits is quite insignificant.

Acknowledgment

This work is based partially upon work supported by the National Science Foundation Grant No. ENG78-05587.

APPENDIX I

For an arbitrary function $f(r)$ and utilizing the coordinate system as shown in Fig. 1, it can be shown by direct differentiations that the following identity holds.

$$\nabla \times [f(r)\mathbf{r}_1 \times \mathbf{n}_1] = (\mathbf{n}_1 \cdot \mathbf{r}_1)\mathbf{r}_1 \left[f'(r) - \frac{f(r)}{r}\right] - \mathbf{n}_1 \left[f'(r) + \frac{f(r)}{r}\right]. \quad (A1)$$

In the above expression, ∇ is the gradient operator, $\mathbf{n}_1$ and $\mathbf{r}_1$ are vectors as defined in Fig. 1 and $f'(r) = df/dr$. If equation (A1) is integrated over the area A_2, one obtains

Table 3 $F_{A_I - A_{II}} R_{A_I - A_{II}}$ between two rectangular plates with different values of a, b, and β with $h = 1.0$. (Values in parentheses are $R_{A_I - A_{II}}$).

β	a \ b	0.4	1.0	4.0
		(1.20)	(1.47)	(2.84)
	0.4	0.006	0.022	0.054
		(1.25)	(1.55)	(3.02)
$\pi/2$	1.0	0.015	0.051	0.133
		(1.43)	(1.76)	(3.40)
	4.0	0.030	0.120	0.415
		(1.14)	(1.35)	(2.28)
	0.4	0.032	0.066	0.123
		(1.19)	(1.39)	(2.34)
$\pi/4$	1.0	0.070	0.150	0.295
		(1.33)	(1.56)	(2.65)
	4.0	0.141	0.329	0.838
		(1.02)	(1.06)	(1.20)
	0.4	0.047	0.102	0.194
		(1.06)	(1.11)	(1.25)
0	1.0	0.102	0.222	0.431
		(1.20)	(1.25)	(1.42)
	4.0	0.194	0.431	0.897

Table 4 $F_{A_I - A_{II}} S_{A_I - A_{II}}{}^{1/2}$ between two rectangular plates with different values of a, b, and β with $h = 1.0$ (values in parentheses are $S_{A_I - A_{II}}$).

β	a \ b	0.4	1.0	4.0
		(1.00)	(1.44)	(2.66)
	0.4	0.005	0.018	0.031
		(1.17)	(1.54)	(2.91)
$\pi/2$	1.0	0.013	0.041	0.075
		(1.41)	(1.75)	(3.25)
	4.0	0.025	0.090	0.220
		(1.00)	(1.35)	(2.19)
	0.4	0.028	0.057	0.080
		(1.18)	(1.38)	(2.25)
$\pi/4$	1.0	0.064	0.127	0.189
		(1.30)	(1.53)	(2.57)
	4.0	0.121	0.261	0.507
		(1.04)	(1.06)	(1.19)
	0.4	0.047	0.099	0.177
		(1.09)	(1.11)	(1.26)
0	1.0	0.099	0.211	0.384
		(1.18)	(1.23)	(1.45)
	4.0	0.176	0.384	0.746

Table 5 $F_{A_I - A_{II}} \ln W_{A_I - A_{II}}$ between two rectangular plates with different values of a, b, and β with $h = 1.0$ (values in parentheses are $W_{A_I - A_{II}}$).

β	a \ b	0.4	1.0	4.0
		(1.22)	(1.49)	(2.71)
	0.4	0.001	0.006	0.019
		(1.28)	(1.53)	(2.78)
$\pi/2$	1.0	0.003	0.014	0.045
		(1.40)	(1.72)	(3.17)
	4.0	0.007	0.037	0.141
		(1.15)	(1.36)	(2.14)
	0.4	0.004	0.015	0.041
		(1.18)	(1.38)	(2.21)
$\pi/4$	1.0	0.010	0.035	0.100
		(1.30)	(1.53)	(2.52)
	4.0	0.028	0.090	0.292
		(1.02)	(1.06)	(1.17)
	0.4	0.001	0.006	0.025
		(1.06)	(1.11)	(1.21)
0	1.0	0.006	0.020	0.067
		(1.17)	(1.21)	(1.36)
	4.0	0.025	0.067	0.194

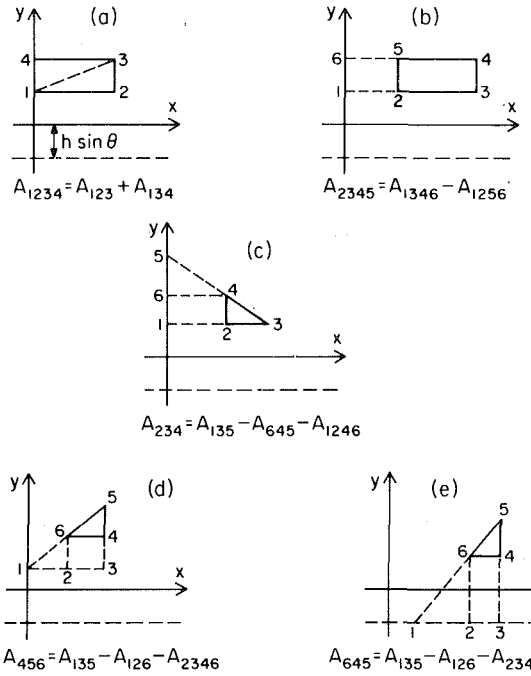

Fig. 3 Illustration on how an arbitrary right triangle can be constructed from fundamental right triangles

$$\int_{A_2} \nabla \times [f(r)\mathbf{r}_1 \times \mathbf{n}_1] \cdot \mathbf{n}_2 dA_2 = \int_{A_2} (\mathbf{n}_1 \cdot \mathbf{r}_1)(\mathbf{n}_2 \cdot \mathbf{r}_1) \left[f(r) - \frac{f(r)}{r}\right] dA_2 - \int_{A_2} (\mathbf{n}_1 \cdot \mathbf{n}_2) \left[f'(r) + \frac{f(r)}{r}\right] dA_2 \quad \text{(A2)}$$

The first term of the above equation can be simplified by Stoke's theorem. Equation (A2) thus becomes

$$\int_{A_2} (\mathbf{n}_1 \cdot \mathbf{r}_1)(\mathbf{n}_2 \cdot \mathbf{r}_1) \left[f'(r) - \frac{f(r)}{r}\right] dA_2 = \int_{S_2} [f(r)\mathbf{r}_1 \times \mathbf{n}_1] \cdot \mathbf{dS}_2 + \int_{A_2} (\mathbf{n}_1 \cdot \mathbf{n}_2) \left[f'(r) + \frac{f(r)}{r}\right] dA_2 \quad \text{(A3)}$$

where $\mathbf{dS}_2$ indicates a line integral around the boundary of A_2. To yield the correct result, the line integral must be performed in a clockwise direction around A_2 when it is viewed from the origin. Because of the mathematical restriction on Stoke's theorem, it is important to note that equation (A3) is applied only when A_2 is a simply connected area (i.e., it has no "hole"). It is interesting to note that in the limit of

$$f(r) - \frac{f(r)}{r} = \frac{1}{r^2} \quad \text{(A4)}$$

equation (A3) is reduced to

$$\int_{A_2} \frac{(\mathbf{n}_1 \cdot \mathbf{r}_1)(\mathbf{n}_1 \cdot \mathbf{r}_1)}{r^2} dA_2 = -\frac{1}{2} \int_{A_2} \frac{(\mathbf{r}_1 \times \mathbf{n}_1)}{r} \mathbf{dS}_2 \quad \text{(A5)}$$

Equation (A4) is exactly the "contour-integral" expression for shape factor proposed originally by Moon [9] and Sparrow [10].

APPENDIX II

Since dA_1 cannot "see" any area with $y < -h \sin\theta$ or the plane $z = h$, it suffices to show that any area A_2 with $y \geq -h \sin\theta$ can be constructed from fundamental right triangles with orientations as shown in Fig. 2(*b*).

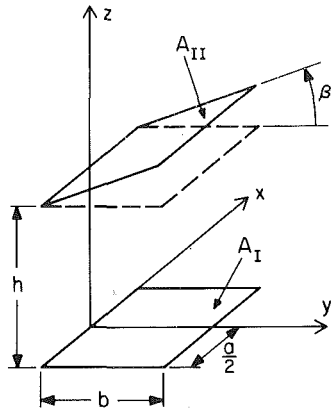

Fig. 4 Coordinate system used in the sample calculation

Figure 3(*a*) shows how an arbitrary rectangle with one edge lying on the y axis can be constructed as a sum of two fundamental right triangles. A rectangle situated away from the y axis can be generated as difference of these rectangles as shown in Fig. 3(*b*). Figure 3(*c*) shows how a "right oriented" right triangle can be constructed as a combination of rectangles and fundamental right triangles. Note that right triangles such as Δ_{135} can be constructed as a combination of a rectangle and the fourth fundamental right triangle. There are two possibilities for "left oriented" right triangles. They are demonstrated by Figs. 3(*d*) and 3(*e*).

Geometrically, it can be readily observed that any triangle on the plane $z = h$ with $y > -h \sin\theta$ can be constructed from right triangles oriented as shown in Figs. 3(*c*), 3(*d*) and 3(*e*). Since any polygon can by principle be expressed as a combination of a finite number of triangles, the fundamental solutions can thus serve as "building blocks" for solutions with A_2 being an arbitrary polygon. If A_2 has curve boundary, it can be approximately to any degree of accuracy by a finite number of a rectangle. The corresponding solution for the geometric transmittance and absorptance can therefore be approximated accurately as sum and difference of a finite number of fundamental solutions.

References

1 Hottel, H. C., and Sarofim, A. F., *Radiation Transfer*, McGraw-Hill, New York, 1967.

2 Siegel, R., and Howell, J. R., *Thermal Radiation Heat Transfer*, McGraw-Hill, New York, 1972.

3 Oppenheim, A. K., and Bevans, J. T., "Geometric Factors for Radiative Heat Transfer Through an Absorbing Medium in Cartesian Co-ordinates," ASME JOURNAL OF HEAT TRANSFER, Nov. 1960, pp. 360–368.

4 Dunkle, R. V., "Geometric Mean Beam Lengths for Radiant Heat-transfer Calculations," ASME JOURNAL OF HEAT TRANSFER, Vol. 86, No. 1, 1964, pp. 75–80.

5 Tien C. L., and Wang, L. S., "On the Calculation of Mean Beam Length to a Radiating Gas," *Journal of Quantitative Spectroscopy and Radiative Transfer*, Vol. 5, 1965, p. 465.

6. Tien, C. L., and Ling, G. R., "On a Simple Correlation of Total Band Absorptance of Radiating Gases," *International Journal of Heat and Mass Transfer*, Vol. 12, 1969, pp. 1179–1181.

7 Edwards, D. K., et al., "Radiation Heat Transfer in Nonisothermal Nongray Gases," ASME JOURNAL OF HEAT TRANSFER, Vol. 89, No. 3, 1967, pp. 219–229.

8 Gradshteyn, I. S., and Ryzhik, I. M., *Table of Integrals, Series, and Products*, 4th ed., Academic Press, New York, 1965.

9 Moon, P., *The Scientific Basis of Illuminating Engineering*, rev. ed., Dover Publication, New York, 1961.

10 Sparrow, E. M., "A New and Simpler Formulation for Radiative Angle Factor," ASME JOURNAL OF HEAT TRANSFER, Vol. 85, No. 2, 1963, pp. 81–88.

Journal of Heat Transfer

Technical Notes

Optimum Cylindrical Pin Fin

A. Sonn and A. Bar-Cohen[1]

Introduction

Cylindrical pin fins, shown in Fig. 1, are a common geometry for extended surfaces in applications ranging from evaporator coils in room air-conditioners to heat sinks for airborne electronic equipment. As with other fin geometries, weight and material-cost constraints often dictate that fin dimensions be optimized in such a manner that the least amount of material be used to dissipate a specified heat flow, or alternately that the highest dissipation rate be obtained from a given volume of fin material. It is the intent of this technical note to derive an expression for the diameter of the least-material cylindrical pin fin and to briefly explore the consequences of this optimization.

Analysis

Following [1], the fin heat dissipation, or equivalently heat flow through the fin base, q_b, can be expressed as

$$q_b = k\frac{\pi}{4}D^2\left.\frac{d\theta}{dx}\right|_{x=b} = \frac{\pi}{4}D^2 km\theta_b \tanh mb \tag{1}$$

where the geometric variables are identified in Fig. 1, θ equals the temperature difference between the fin surface and the ambient, k the fin thermal conductivity, h the convective heat transfer coefficient and $m \equiv (4h/kD)^{1/2}$.

To determine the optimum fin dimensions, it is convenient to define a fin volume parameter, V_p, equal to D^2b, and express equation (1) in terms of D and V_p as

$$q_b = \frac{\pi}{2}\theta_b(khD^3)^{1/2}\tanh\{2V_p(h/kD^5)^{1/2}\} \tag{2}$$

For a fixed fin volume or mass, V_p is constant and, in the absence of variations in θ_b, k and h, the heat flow through the fin base is dependent only on the diameter, D.

Differentiating equation (2) with respect to D and evaluating at the point where the derivative vanishes, i.e.,

$$\frac{dq_b}{dD} = \frac{\pi}{2}\theta_b(kh)^{1/2}\left[\frac{3}{2}D^{1/2}\tanh\{2V_p(h/kD^5)^{1/2}\} - 5V_p(h/kD^4)^{1/2}\operatorname{sech}^2\{2V_p(h/kD^5)^{1/2}\}\right] = 0 \tag{3}$$

and inserting $\beta_s \equiv 2V_p(h/kD^5)^{1/2}$, yields

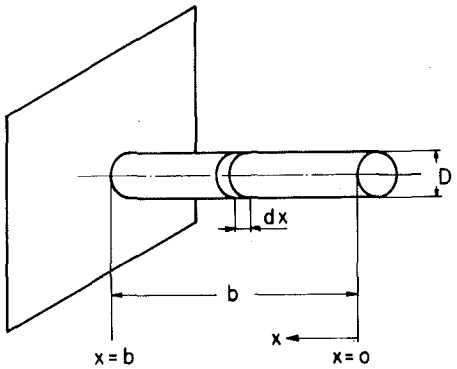

Fig. 1 Cylindrical pin fin

$$\tanh\beta_s = \frac{5}{3}\beta_s\operatorname{sech}^2\beta_s \tag{4}$$

Or, following the appropriate trigonometric substitution

$$\sinh 2\beta_s = \frac{5}{3}(2\beta_s) \tag{5}$$

Equation (5) is a transcendental equation in β_s and can be solved by trial and error to yield the root $\beta_s = 0.919296$ and the optimum fin diameter as

$$D_{\text{opt}} = 1.366\,(hV_p^2/k)^{1/5} = 4.73\,hb^2/k \tag{6}$$

Using this relation, the heat dissipation of the optimum pin fin is found as

$$q_{\text{opt}} = 11.736\,\theta_b\,h^2b^3/k \tag{7}$$

Discussion

Due to the identity in the form of the governing differential equations for the cylindrical pin fin and the longitudinal fin of rectangular profile (e.g., [1]), it is interesting to compare the optimum performance and dimensional relations of these two fins. In performing such a comparison, it must be recalled that while the fin parameter m^2 is nearly the same for both fins ($4h/kD$ for the pin fin and $4h/k$ (2δ) for the longitudinal rectangular fin), the pin fin volume, of importance in the optimizing relation, is dependent on the square of the diameter while the longitudinal, rectangular fin volume is linearly dependent on δ. As a consequence, the optimization procedure yields different optimum values of the mb product and fin efficiency for each of these two cases.

The Optimum *mb* Product. A closer examination of the three fin parameters: m, V_p, and β_s reveals that β_s is equal to mb—a common parameter in fin analysis. The optimum mb product for the

[1] Department of Mechanical Engineering, Ben-Gurion University of the Negev, Beer Sheva, Israel.

Contributed by the Heat Transfer Division for publication in the JOURNAL OF HEAT TRANSFER. Manuscript received at ASME Headquarters February 10, 1981.

cylindrical pin was found to be 0.9193 which is, thus, substantially lower than the $(mb)_{opt}$ value of 1.4192 for the longitudinal rectangular fin [1].

Due to the similarity in the governing equation, it is not uncommon to find the optimum pin fin diameter evaluated on the basis of the optimum mb for the longitudinal fin. Such an erroneous calculation yields a D_{opt} value only 42 percent of the correct optimum pin fin diameter.

Fin Efficiency. The pin efficiency, η, defined as the ratio of the heat *actually* transferred by the fin to the heat transferred by an ideal isothermal (at the base temperature) fin, can be expressed as

$$\eta = \frac{\tanh \beta_s}{B_s} .$$

The η_{opt} for the cylindrical pin fin is thus found to equal 0.7893, considerably higher than the 0.627 η_{opt} for the longitudinal rectangular profile fin.

Reference

1 Kern, D. Q., and Kraus, A. D., *Extended Surface Heat Transfer*, McGraw Hill, New York, 1972.

Heat Transfer from a Cone Spinning in a Corotating Fluid

N. R. Vira[1] and Dah-Nien Fan[2]

Nomenclature

C_p = specific heat at constant pressure
$E = \omega\nu \sin\alpha / C_p(T_0 - T_\infty)$ for cone ($\alpha = \pi/2$ for disk)
F, G, H = velocity-similarity variables defined by equation (1)
h_r = local heat transfer coefficient for disk
h_x = local heat transfer coefficient for cone
n = exponent in equation (3)
Nu_r = local Nusselt number for rotating disk, rh_r/k
Nu_x = local Nusselt number for spinning cone, xh_x/k
Pr = Prandtl number, $\mu C_p/k$
Q_n = dimensionless temperature
r = radial co-ordinate for disk
Re_r = local Reynolds number for disk, $\omega r^2/\nu$
Re_x = local Reynolds number for cone, $\omega \sin\alpha x^2/\nu$
s = ratio of angular speeds, χ/ω
T = temperature
T_n = constant temperature (see equation (3))
T_∞ = ambient temperature, a constant
u, v, w = velocity components in x, y and z directions, respectively
x = coordinate along cone generator
z = coordinate normal to cone surface
α = semi-vertex angle of cone
δ_v = thickness of viscous boundary-layer
k = thermal conductivity
ν = kinematic viscosity
ρ = density
χ = angular velocity of fluid at infinity
ω = angular velocity of cone or disk

[1] Graduate Research Assistant, Department of Mechanical Engineering, Howard University, Washington, D.C. 20059.
[2] Professor, Department of Mechanical Engineering, Howard University, Washington, D.C. 20059.
Contributed by the Heat Transfer Division for publication in the JOURNAL OF HEAT TRANSFER. Manuscript received by the Heat Transfer Division December 1, 1980.

Introduction

The present note reports an application of the heat transfer solution of the generalized von Karman rotating disk flow [1] to that of a cone spinning in a corotating fluid.

The similarity between the laminar flow velocity fields of the von Karman rotating disk flow and the boundary layer flow near a spinning core was pointed out by Wu [2]. This similarity is extended to include an ambient coaxial rotations of the fluid. A corresponding extension of the similarity in associated convective heat tranfer problems due to Tien [3] is derived in detail. Solutions for both isothermal and prescribed (power function) surface temperature variations are obtained with viscous heating in the boundary layer. Limitations to the heat-transfer solution of the spinning cone problem under the boundary layer approximation are delineated by a critical examination of the exact solution of the rotating-disk ($\alpha = \pi/2$) problem.

Analysis

Velocity Field. The mathematical formulation for the present problem is parallel to that of [3] except that the pressure-gradient term, $-\chi^2 x \sin^2\alpha$, should be added to the right-hand side of the x-momentum equation and the boundary condition $v(x, \infty)$ should be equal to $\chi x \sin\alpha$.

The velocity-similarity variables are defined by

$$u = (\omega\, x \sin\alpha)\, F(z^*),$$
$$v = (\omega\, x \sin\alpha)\, G(z^*), \qquad (1)$$
$$w = (\omega\, \nu \sin\alpha)^{1/2}\, H(z^*)$$

where,

$$x^* = (\omega/\nu)^{1/2}\, x \sin\alpha$$
$$z^* = (\omega \sin\alpha/\nu)^{1/2}\, z$$

The functions F, G and H satisfy a set of ordinary-differential equations identical to those governing the generalized von Karman rotating-disk flows with corotating ambient fluid. The same holds for the transformed boundary condutions. Thus, the velocity field in the boundary layer of a cone spinning in a corotating fluid is obtainable from that of the generalized rotating-disk flow first obtained by Rogers and Lance [4].

Temperature Field. Under boundary-layer approximation the energy equation after substituting the similarity functions for the velocity components is

$$\omega x \sin\alpha\, F \frac{\partial T}{\partial x} + \sqrt{\omega\nu \sin\alpha}\, H \frac{\partial T}{\partial z} - \frac{k}{\rho C_p} \frac{\partial^2 T}{\partial z^2}$$
$$= \frac{\omega^3 \sin^3\alpha}{C_p} x^2 (G'^2 + F'^2) \qquad (2)$$

The inhomogeneous term in equation (2) represents heating by viscous dissipation. The prime denotes differentiation with respect to z^*.

The boundary condition at the cone surface is taken to be

$$T(x, 0) = \sum_{n=0}^{N} (\omega \sin\alpha/\nu)^{n/2}\, x^n T_n \qquad (3)$$

As z^* approaches infinity the temperature approaches a constant

$$T(x, \infty) = T_\infty \qquad (4)$$

Note that T_n, $n = 0, 1, 2, \ldots N$, can be positive or negative.

Following the method suggested in [1], it can be easily shown that the temperature and the local Nusselt number are, respectively, given by

$$\frac{T - T_\infty}{T_0 - T_\infty} = Q_0(z^*) + \mathrm{Re}_x\, E\overline{Q}_2(z^*)$$
$$+ \sum_{n=1}^{N} \mathrm{Re}_x{}^{n/2} \left(\frac{T_n}{T_0 - T_\infty}\right) Q_n(z^*) \qquad (5)$$

cylindrical pin was found to be 0.9193 which is, thus, substantially lower than the $(mb)_{opt}$ value of 1.4192 for the longitudinal rectangular fin [1].

Due to the similarity in the governing equation, it is not uncommon to find the optimum pin fin diameter evaluated on the basis of the optimum mb for the longitudinal fin. Such an erroneous calculation yields a D_{opt} value only 42 percent of the correct optimum pin fin diameter.

Fin Efficiency. The pin efficiency, η, defined as the ratio of the heat *actually* transferred by the fin to the heat transferred by an ideal isothermal (at the base temperature) fin, can be expressed as

$$\eta = \frac{\tanh \beta_s}{B_s} .$$

The η_{opt} for the cylindrical pin fin is thus found to equal 0.7893, considerably higher than the 0.627 η_{opt} for the longitudinal rectangular profile fin.

Reference

1 Kern, D. Q., and Kraus, A. D., *Extended Surface Heat Transfer*, McGraw Hill, New York, 1972.

Heat Transfer from a Cone Spinning in a Corotating Fluid

N. R. Vira[1] and Dah-Nien Fan[2]

Nomenclature

C_p = specific heat at constant pressure
$E = \omega\nu \sin\alpha / C_p(T_0 - T_\infty)$ for cone ($\alpha = \pi/2$ for disk)
F, G, H = velocity-similarity variables defined by equation (1)
h_r = local heat transfer coefficient for disk
h_x = local heat transfer coefficient for cone
n = exponent in equation (3)
Nu_r = local Nusselt number for rotating disk, rh_r/k
Nu_x = local Nusselt number for spinning cone, xh_x/k
Pr = Prandtl number, $\mu C_p/k$
Q_n = dimensionless temperature
r = radial co-ordinate for disk
Re_r = local Reynolds number for disk, $\omega r^2/\nu$
Re_x = local Reynolds number for cone, $\omega \sin\alpha x^2/\nu$
s = ratio of angular speeds, χ/ω
T = temperature
T_n = constant temperature (see equation (3))
T_∞ = ambient temperature, a constant
u, v, w = velocity components in x, y and z directions, respectively
x = coordinate along cone generator
z = coordinate normal to cone surface
α = semi-vertex angle of cone
δ_v = thickness of viscous boundary-layer
k = thermal conductivity
ν = kinematic viscosity
ρ = density
χ = angular velocity of fluid at infinity
ω = angular velocity of cone or disk

[1] Graduate Research Assistant, Department of Mechanical Engineering, Howard University, Washington, D.C. 20059.
[2] Professor, Department of Mechanical Engineering, Howard University, Washington, D.C. 20059.
Contributed by the Heat Transfer Division for publication in the JOURNAL OF HEAT TRANSFER. Manuscript received by the Heat Transfer Division December 1, 1980.

Introduction

The present note reports an application of the heat transfer solution of the generalized von Karman rotating disk flow [1] to that of a cone spinning in a corotating fluid.

The similarity between the laminar flow velocity fields of the von Karman rotating disk flow and the boundary layer flow near a spinning core was pointed out by Wu [2]. This similarity is extended to include an ambient coaxial rotations of the fluid. A corresponding extension of the similarity in associated convective heat tranfer problems due to Tien [3] is derived in detail. Solutions for both isothermal and prescribed (power function) surface temperature variations are obtained with viscous heating in the boundary layer. Limitations to the heat-transfer solution of the spinning cone problem under the boundary layer approximation are delineated by a critical examination of the exact solution of the rotating-disk ($\alpha = \pi/2$) problem.

Analysis

Velocity Field. The mathematical formulation for the present problem is parallel to that of [3] except that the pressure-gradient term, $-\chi^2 x \sin^2\alpha$, should be added to the right-hand side of the x-momentum equation and the boundary condition $v(x, \infty)$ should be equal to $\chi x \sin\alpha$.

The velocity-similarity variables are defined by

$$u = (\omega\, x \sin\alpha)\, F(z^*),$$
$$v = (\omega\, x \sin\alpha)\, G(z^*), \qquad (1)$$
$$w = (\omega\, \nu \sin\alpha)^{1/2}\, H(z^*)$$

where,

$$x^* = (\omega/\nu)^{1/2}\, x \sin\alpha$$
$$z^* = (\omega \sin\alpha/\nu)^{1/2}\, z$$

The functions F, G and H satisfy a set of ordinary-differential equations identical to those governing the generalized von Karman rotating-disk flows with corotating ambient fluid. The same holds for the transformed boundary condutions. Thus, the velocity field in the boundary layer of a cone spinning in a corotating fluid is obtainable from that of the generalized rotating-disk flow first obtained by Rogers and Lance [4].

Temperature Field. Under boundary-layer approximation the energy equation after substituting the similarity functions for the velocity components is

$$\omega x \sin\alpha\, F \frac{\partial T}{\partial x} + \sqrt{\omega\nu \sin\alpha}\, H \frac{\partial T}{\partial z} - \frac{k}{\rho C_p} \frac{\partial^2 T}{\partial z^2}$$
$$= \frac{\omega^3 \sin^3\alpha}{C_p} x^2 (G'^2 + F'^2) \qquad (2)$$

The inhomogeneous term in equation (2) represents heating by viscous dissipation. The prime denotes differentiation with respect to z^*.

The boundary condition at the cone surface is taken to be

$$T(x, 0) = \sum_{n=0}^{N} (\omega \sin\alpha/\nu)^{n/2}\, x^n T_n \qquad (3)$$

As z^* approaches infinity the temperature approaches a constant

$$T(x, \infty) = T_\infty \qquad (4)$$

Note that T_n, $n = 0, 1, 2, \ldots N$, can be positive or negative.

Following the method suggested in [1], it can be easily shown that the temperature and the local Nusselt number are, respectively, given by

$$\frac{T - T_\infty}{T_0 - T_\infty} = Q_0(z^*) + \mathrm{Re}_x\, E\overline{Q}_2(z^*)$$
$$+ \sum_{n=1}^{N} \mathrm{Re}_x{}^{n/2} \left(\frac{T_n}{T_0 - T_\infty}\right) Q_n(z^*) \qquad (5)$$

$$\mathrm{Nu}_x = -\mathrm{Re}_x^{1/2}\left\{Q_0'(0) + \mathrm{Re}_x E\overline{Q}_2'(0) + \sum_{n=1}^{N} \mathrm{Re}_x^{n/2}\left(\frac{T_n}{T_0 - T_\infty}\right) Q_n'(0)\right\} \Big/ \left\{1 + \sum_{n=1}^{N} \mathrm{Re}_x^{n/2}\left(\frac{T_n}{T_0 - T_\infty}\right)\right\} \quad (6)$$

where Q_n and $\overline{Q}_2$ satisfy the following differential equations

$$nFQ_n + HQ_n' - (1/\mathrm{Pr})\, Q_n'' = 0$$

$$2F\overline{Q}_2 + H\overline{Q}_2' - (1/\mathrm{Pr})\, \overline{Q}_2'' = G'^2 + F'^2 \quad (7)$$

with boundary conditions

$$Q_n(0) = 1 \quad \text{and} \quad \overline{Q}_2(0) = 0$$

$$Q_n(\infty) = \overline{Q}_2(\infty) = 0 \quad (8)$$

The initial slopes of $\overline{Q}_2$ and Q_n functions in equation (6) for $N \leq 3$ were tabulated in [1] as $\overline{Q}_{22v}'(0)$ and $Q_{nnb}'(0)$, respectively. Ranges of parameter values investigated in [1] were $10^{-2} \leq \mathrm{Pr} \leq 10^3$ and $0 \leq s \leq 1$. It was concluded there that the function $Q_n(z^*)$ cannot be found when $s > 1$. Equations (5) and (6), clearly, delineate the dependence of T and Nu_x on the dimensionless parameters Re_x, E, Pr and s. The former two appear explicitly, while the latter two appear implicitly in the Q_n's. Parameters arising from the boundary conditions appear as scale factors in the corresponding Q_n's.

Isothermal Case. Nu_x in isothermal case can be obtained from equation (6) by letting $T_n = 0, n = 1, 2, \ldots, N$ as

$$\mathrm{Nu}_x = -\mathrm{Re}_x^{1/2}[Q_0'(0) + \mathrm{Re}_x E\overline{Q}_2'(0)] \quad (9)$$

Note that E can be positive or negative depending upon the sign of $T_0 - T_\infty$. It can be seen from equation (9) that the product $\mathrm{Re}_x E$ indicates the relative importance of internal viscous heating to an externally imposed temperature difference. In the neighborhood of the cone tip, viscous heating has a negligible effect in comparison to that of the imposed temperature differences; while far away downstream the viscous-heating contribution overshadows that from the temperature difference. This is clearly shown in Fig. 1 and the following observations can be made:

(*a*) $E = 0$ (*No viscous heating or infinite imposed temperature difference*). In the absence of viscous heating the Nusselt number increases monotonically with Re_x for a given s. For a given Re_x, the Nusselt number decreases with increasing s reflecting a lessening in fluid convection. The curve $s = 0$ (no ambient fluid rotation) corresponds to Tien [3] and Hartnett and Deland [5].

(*b*) $E > 0$. Nu_x increases with Re_x initially, reaches a maximum value and then decreases with increasing Re_x for a given s. The value of Re_x where Nu_x attains its maximum is given by

$$\mathrm{Re}_x^* = -\frac{Q_0'(0)}{3E\overline{Q}_2'(0)} \quad (10)$$

Note that $Q_0'(0)$ has a negative value whereas $\overline{Q}_2'(0)$ is always positive. When $\mathrm{Re}_x < \mathrm{Re}_x^*$, the heat transfer due to the imposed boundary condition ($Q_0'(0)$) dominates over that due to viscous heating ($\overline{Q}_2'(0)$), and heat is transferred from the cone to the fluid. When $\mathrm{Re}_x > \mathrm{Re}_x^*$, $\overline{Q}_2'(0)$ becomes more important than $Q_0'(0)$. Eventually for sufficiently large Re_x heat due to viscous dissipation is transferred from the fluid to the cone and Nu_x becomes negative even though the cone surface temperature remains higher than the temperature of fluid at infinity.

It should be remarked that for a given E the transition of Nu_x from positive to negative occurs at increasing Re_x with increasing s. It means the curves with higher values of s will cross those with lower values of s as Re_x increases. This behavior is clearly exhibited in Fig. 1 for the case $E = 10^{-4}$. For $E = 10^{-3}$ the cross-over occurs at $\mathrm{Re}_x < 10^3$.

(*c*) $E < 0$. The condition $E < 0$ implies that $T_0 - T_\infty$ is negative. Thus the sum in the right-hand side of equation (9) is always negative and results in a positive Nu_x which increases monotonically with Re_x. Physically the imposed boundary condition and the viscous heating cooperatively cause heat to be transferred from the fluid to the cone. This is shown in Fig. 1 for the case $\mathrm{E} = 10^{-3}$. The Nusselt number

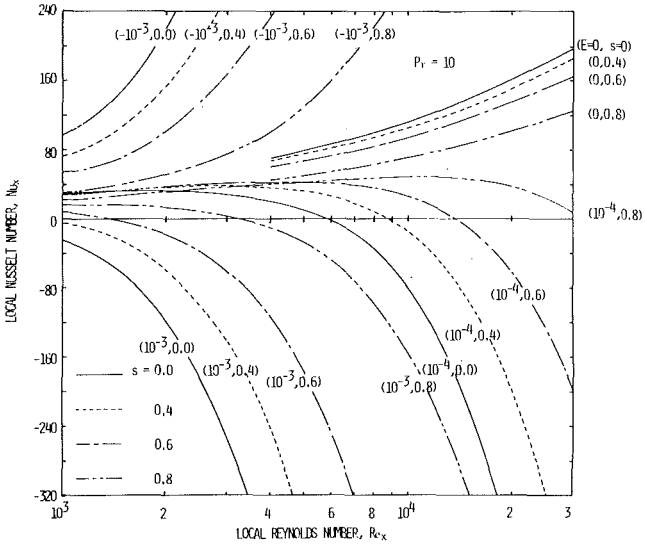

Fig. 1 Variation of Nu_x with Re_x for an isothermal cone at Pr = 10 ($-10^{-3} \leq E \leq 10^{-3}$ and $0 \leq s \leq 0.8$)

decreases with increasing s for a fixed Re_x. The reduction results from the decrease of viscous dissipation at a given x with increasing s.

Limitations to the Solution of Boundary Layer Equations. The heat transfer results presented above are valid under the boundary-layer approximation. To examine critically the range of validity, the comparison with the exact solution of a spinning cone is necessary. Even though the exact solution corresponding to a spinning cone is not available, the limitations of the boundary-layer solution can be illustrated by a critical comparison of the exact and the boundary-layer solutions for the rotating-disk flows [1]. Thus we conclude that the present results of a spinning cone are applicable only when the local Reynolds number is sufficiently large. The boundary-layer approximation breaks down completely in the neighborhood of the cone tip. Furthermore, the solution to the boundary-layer equations deteriorates when N is large or Pr is small. This can easily be seen by an order-of-magnitude analysis of the radial heat conduction term to that of normal heat conduction. Thermal boundary-layer approximation is valid provided $x \gg N\delta_v/\sqrt{Pr}$, $N \geq 2$.

The effect of boundary-layer approximation on viscous heating will now be illustrated by examining the exact solution of an isothermal spinning disk. The exact local Nusselt number for the isothermal disk is obtained from [1] as

$$\mathrm{Nu}_r = \frac{rh_r}{k} = -\mathrm{Re}_r^{1/2}\{Q_{00b}'(0) + E[\overline{Q}_{02v}'(0) + \overline{Q}_{00v}'(0) + \mathrm{Re}_r\overline{Q}_{22v}'(0)]\} \quad (11)$$

The initial slopes $Q_{00b}'(0)$ and $\overline{Q}_{22v}'(0)$ in [1] should be identified, respectively, here as $Q_0'(0)$ and $\overline{Q}_2'(0)$. $\overline{Q}_{02v}(0)$ and $\overline{Q}_{00v}'(0)$ are the contributions from the higher-order viscous heating to Nu_r. It is clear from equation (11) that for sufficiently small Re_r the higher-order viscous heating can be more important than the boundary-layer viscous heating. The effect of this higher-order viscous heating becomes noticeable, however, only when E is not too small. Thus the higher-order viscous heating neglected in the boundary-layer approximation can again invalidate the boundary-layer solution in the vicinity of the cone tip. The numerical values of $Q_{00b}'(0)$, $\overline{Q}_{02v}'(0)$, $\overline{Q}_{00v}'(0)$ and $\overline{Q}_{22v}'(0)$ are comparable. This can be seen from the case Pr = 2.4 and $s = 0$. They are, respectively, -0.6161776, 0.683929, 0.8057361 and 0.6314723. The case of Pr = 2.4 and $s = 0$ is of interest because there are some experimental data available from mass-diffusion experiments [7].

In Fig. 2, the solid curve with $E = 0$ corresponds to Sparrow and

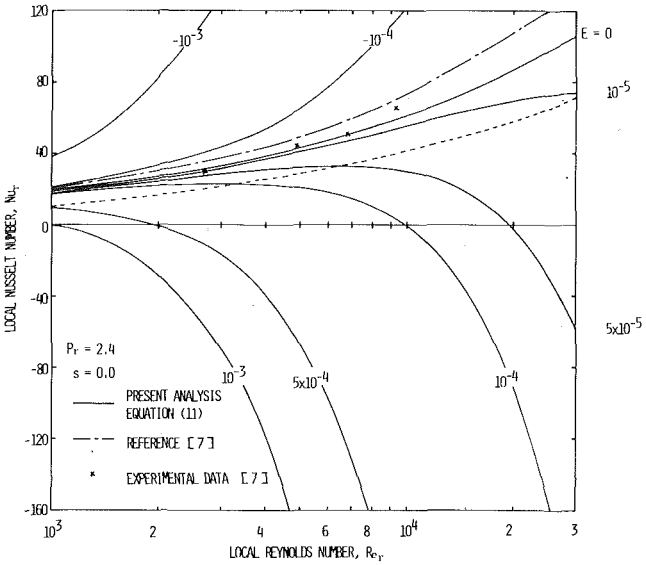

Fig. 2 Variation of Nu_r with Re_r for an isothermal disk at Pr = 2.4 and s = 0 ($-10^{-3} \leq E \leq 10^{-3}$)

Gregg [6]. It is not surprising that the experimental data fall closely to the $E = 0$ curve since the mass diffusion experiments presumably had no mass-source (thus no viscous heating) in the boundary layer. The correlation of the experimental data points by Koong and Blackshear [7] is shown to lie considerably above the exact result for $E = 0$.

The dotted curve in Fig. 2 is the locus of maximum Nu_r that occurs at the Reynolds number

$$Re_r^* = \frac{Q_{00b}'(0) + E(\overline{Q}_{02v}'(0) + \overline{Q}_{00v}'(0))}{-3E\overline{Q}_{22v}'(0)} \tag{12}$$

It is interesting to note that when

$$E \geq -\frac{Q_{00b}'(0)}{\overline{Q}_{02v}'(0) + \overline{Q}_{00v}'(0)} \tag{13}$$

the Nu_r always remains negative (see equation (11)). This means that the heat is transferred from the fluid to the entire disk even when the disk surface temperature is higher than the temperature of fluid at infinity because of viscous heating.

References

1 Vira, N. R., and Fan, D. N., "Temperature Distribution in Generalized von Karman Rotating-Disk Flows," *Numerical Heat Transfer, An International Journal of Computation and Methodology*, Vol. 3, No. 4, 1980, pp. 483–497.

2 Wu, C. W., "The Three Dimensional Incompressible Boundary Layer on a Spinning Cone," *Applied Scientific Research*, Sec. A, Vol. 8, 1959, pp. 140–146.

3 Tien, C. L., "Heat Transfer by Laminar Flow from a Rotating Cone," ASME JOURNAL OF HEAT TRANSFER, Vol. 82, 1960, pp. 252–253.

4 Rogers, M. H., and Lance, G. N., "The Rotating Symmetric Flow of a Viscous Fluid in the Presence of an Infinite Rotating Disk," *Journal of Fluid Mechanics*, Vol. 7, 1960, pp. 617–631.

5 Hartnett, J. P., and Deland, E. C., "The Influence of Prandtl Number on the Heat Transfer From Rotating Nonisothermal Disks and Cones," ASME JOURNAL OF HEAT TRANSFER, Vol. 83, 1961, pp. 95–96.

6 Sparrow, E. M., and Gregg, J. L., "Heat Transfer from a Rotating Disk to Fluids of Any Prandtl Number," ASME JOURNAL OF HEAT TRANSFER, Vol. 81, 1959, pp. 249–251.

7 Koong, S. S., and Blackshear, P. L., "Experimental Measurements of Mass Transfer from a Rotating Disk in a Uniform Stream," ASME JOURNAL OF HEAT TRANSFER, Vol. 87, 1965, pp. 422–423.

Experimental Free Convection from an Inclined Cylinder

W. E. Stewart, Jr.[1]

Introduction

This study was concerned with the experimental determination of free convective heat transfer from circular cylinders as the cylinders were varied from horizontal to vertical at angles α from the horizontal. Cylinders in axially horizontal and vertical positions have bouyancy forces only normal and parallel to their axes, respectively. In these two limiting cases, the flow past the cylinders and hence the heat transfer will be two-dimensional. Cylinders inclined from the horizontal will have flow patterns that are then three-diemsional.

Many analytical and experimental studies have been done on cylinders both in the horizontal and vertical positions, see for example, references [1–5]. Typically cylinders in the horizontal positions are assumed to be infinitely long in the axial direction and hence the characteristic dimension is based upon the diameter. Cylinders in the vertical position with small angles of curvature are treated essentially as flat plates and the characteristic dimension is usually the length of the cylinder. Though the need for data correlations for inclined cylinders for applications, such as in the design of inclined solar absorber tubing, would seem apparent, the topic has received less attention.

Bosworth [6] performed several experiments on the convective loss from fine wires in water and glycerine inclined at various angles. Morgan [4] and Koch [7] performed similar fine wire experiments in air. Oosthiuzen [8] performed experiments on aluminum cylinders in air with relatively small ratios of L/D (8.0 to 16.0).

Experimental Procedure

Two methods were used to determine the free convective heat loss from 6061-T6 aluminum cylinders, as described below. Common to both methods of experiment were the cylinders of the dimensions as shown in Table 1. The arrangement of the cylinders is shown schematically in Fig. 1, where the cylinders were held by two Nylon 6,6 insulating end pieces, 15.24 cm long and of the same diameter as the aluminum cylinders.

Method 1. The first series of experiments were performed on solid 6061-T6 aluminum cylinders in a manner similar to the experiments of Oosthiuzen [8]. Four holes of approximately 3.2 mm dia were drilled longitudinally at 90 deg intervals near the cylinder surface and a single hole drilled along the centerline. Three thermocouples were inserted into each of the holes, two placed at the cylinder ends and the other at the cylinder center to determine the average temperature of the cylinder.

Table 1 Dimensions of cylinders

Cylinder Number	Diameter, D cm	Length, L cm	Aspect Ratio L/D
1	2.54	15.24	6.00
2	2.54	22.86	9.00
3	2.54	30.48	12.00

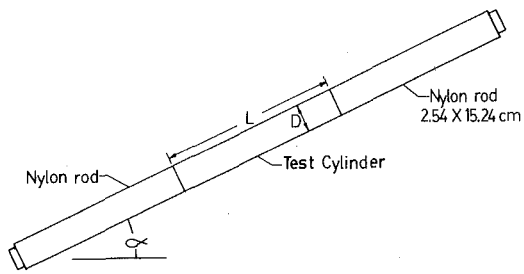

Fig. 1 Experiment schematic

[1] Assistant Professor, Department of Mechanical Engineering, University of Missouri-Kansas City, Kansas City, MO. Mem. ASME.

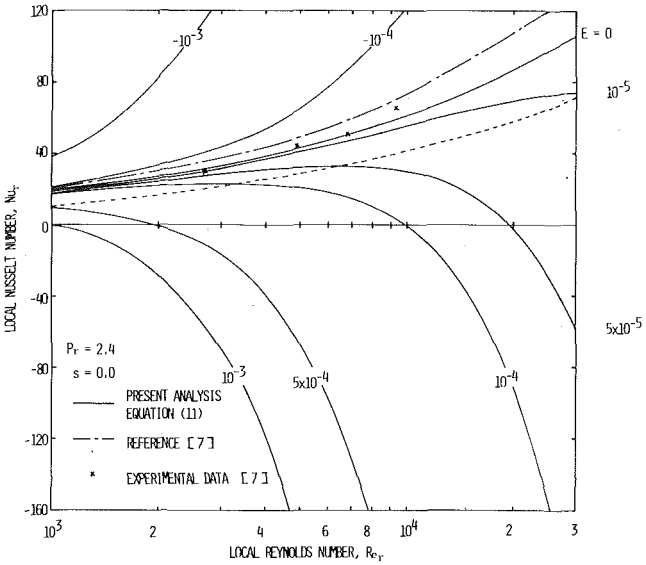

Fig. 2 Variation of Nu_r with Re_r for an isothermal disk at Pr = 2.4 and s = 0 ($-10^{-3} \leq E \leq 10^{-3}$)

Gregg [6]. It is not surprising that the experimental data fall closely to the $E = 0$ curve since the mass diffusion experiments presumably had no mass-source (thus no viscous heating) in the boundary layer. The correlation of the experimental data points by Koong and Blackshear [7] is shown to lie considerably above the exact result for $E = 0$.

The dotted curve in Fig. 2 is the locus of maximum Nu_r that occurs at the Reynolds number

$$Re_r^* = \frac{Q_{00b}'(0) + E(\overline{Q}_{02v}'(0) + \overline{Q}_{00v}'(0))}{-3E\overline{Q}_{22v}'(0)} \tag{12}$$

It is interesting to note that when

$$E \geq -\frac{Q_{00b}'(0)}{\overline{Q}_{02v}'(0) + \overline{Q}_{00v}'(0)} \tag{13}$$

the Nu_r always remains negative (see equation (11)). This means that the heat is transferred from the fluid to the entire disk even when the disk surface temperature is higher than the temperature of fluid at infinity because of viscous heating.

References

1 Vira, N. R., and Fan, D. N., "Temperature Distribution in Generalized von Karman Rotating-Disk Flows," *Numerical Heat Transfer, An International Journal of Computation and Methodology*, Vol. 3, No. 4, 1980, pp. 483–497.

2 Wu, C. W., "The Three Dimensional Incompressible Boundary Layer on a Spinning Cone," *Applied Scientific Research*, Sec. A, Vol. 8, 1959, pp. 140–146.

3 Tien, C. L., "Heat Transfer by Laminar Flow from a Rotating Cone," ASME JOURNAL OF HEAT TRANSFER, Vol. 82, 1960, pp. 252–253.

4 Rogers, M. H., and Lance, G. N., "The Rotating Symmetric Flow of a Viscous Fluid in the Presence of an Infinite Rotating Disk," *Journal of Fluid Mechanics*, Vol. 7, 1960, pp. 617–631.

5 Hartnett, J. P., and Deland, E. C., "The Influence of Prandtl Number on the Heat Transfer From Rotating Nonisothermal Disks and Cones," ASME JOURNAL OF HEAT TRANSFER, Vol. 83, 1961, pp. 95–96.

6 Sparrow, E. M., and Gregg, J. L., "Heat Transfer from a Rotating Disk to Fluids of Any Prandtl Number," ASME JOURNAL OF HEAT TRANSFER, Vol. 81, 1959, pp. 249–251.

7 Koong, S. S., and Blackshear, P. L., "Experimental Measurements of Mass Transfer from a Rotating Disk in a Uniform Stream," ASME JOURNAL OF HEAT TRANSFER, Vol. 87, 1965, pp. 422–423.

Experimental Free Convection from an Inclined Cylinder

W. E. Stewart, Jr.[1]

Introduction

This study was concerned with the experimental determination of free convective heat transfer from circular cylinders as the cylinders were varied from horizontal to vertical at angles α from the horizontal. Cylinders in axially horizontal and vertical positions have bouyancy forces only normal and parallel to their axes, respectively. In these two limiting cases, the flow past the cylinders and hence the heat transfer will be two-dimensional. Cylinders inclined from the horizontal will have flow patterns that are then three-diemsional.

Many analytical and experimental studies have been done on cylinders both in the horizontal and vertical positions, see for example, references [1–5]. Typically cylinders in the horizontal positions are assumed to be infinitely long in the axial direction and hence the characteristic dimension is based upon the diameter. Cylinders in the vertical position with small angles of curvature are treated essentially as flat plates and the characteristic dimension is usually the length of the cylinder. Though the need for data correlations for inclined cylinders for applications, such as in the design of inclined solar absorber tubing, would seem apparent, the topic has received less attention.

Bosworth [6] performed several experiments on the convective loss from fine wires in water and glycerine inclined at various angles. Morgan [4] and Koch [7] performed similar fine wire experiments in air. Oosthiuzen [8] performed experiments on aluminum cylinders in air with relatively small ratios of L/D (8.0 to 16.0).

Experimental Procedure

Two methods were used to determine the free convective heat loss from 6061-T6 aluminum cylinders, as described below. Common to both methods of experiment were the cylinders of the dimensions as shown in Table 1. The arrangement of the cylinders is shown schematically in Fig. 1, where the cylinders were held by two Nylon 6,6 insulating end pieces, 15.24 cm long and of the same diameter as the aluminum cylinders.

Method 1. The first series of experiments were performed on solid 6061-T6 aluminum cylinders in a manner similar to the experiments of Oosthiuzen [8]. Four holes of approximately 3.2 mm dia were drilled longitudinally at 90 deg intervals near the cylinder surface and a single hole drilled along the centerline. Three thermocouples were inserted into each of the holes, two placed at the cylinder ends and the other at the cylinder center to determine the average temperature of the cylinder.

Table 1 Dimensions of cylinders

Cylinder Number	Diameter, D cm	Length, L cm	Aspect Ratio L/D
1	2.54	15.24	6.00
2	2.54	22.86	9.00
3	2.54	30.48	12.00

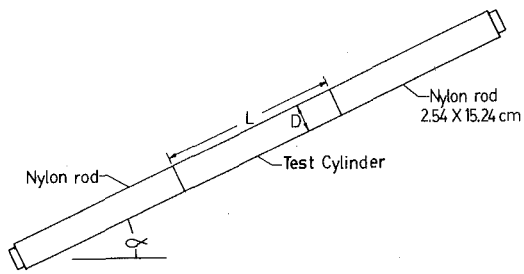

Fig. 1 Experiment schematic

[1] Assistant Professor, Department of Mechanical Engineering, University of Missouri-Kansas City, Kansas City, MO. Mem. ASME.

The cylinders were then heated by an electric hot air blower to an average temperature of approximately 80°C. The cylinders were then allowed to cool and the transient change in temperature was measured with a strip chart recorder. The length of time, Δt, required for the cylinders to cool between average temperatures of 70 and 60°C was, depending upon the angle of inclination, typically on the order of 360 s. The rate of heat loss was then approximated as:

$$h = mC_p \frac{(\Delta T_c)}{(\Delta t)} / A(\Delta T_\infty)$$

where m = cylinder mass; ΔT_c = change in average cylinder temperature in time step Δt; ΔT_∞ = difference between time averaged cylinder and ambient temperatures; C_p = specific heat of cylinder; and A = surface area of cylinder. (1)

Surface temperatures in the calculation of ΔT_∞ in equation (1) were assumed to be the average of the temperatures measured near the surface in the longitudinal holes, approximately 2.5 mm from the outside surface. Differences in average surface temperature and centerline temperature were only on the order of 1°C. This small difference is to be expected since the ratio of heat transfer coefficient to conductivity was small. The Biot number, $hD/4k_c$, typically on the order of .0001, was small and hence the difference between the measured and actual surface temperature should be small. Additionally, temperatures measured throughout the cylinders only varied by a few degrees.

Method 2. Hollow 6061-T6 aluminum tubes with 1.59 mm wall thickness were used in this series of experiments of the same dimensions as for Method 1 and as listed in Table 1. These tests differed from Method 1 in that the cylinders were subjected to a constant heat flux, but similar experimental results should be expected.

Thermocouples were attached only to the inside surface of the cylindrical tubes, spaced along the length of each tube as in Method 1. A nichrome wire heating element was encapulated in a glass tube and placed along the center line of each aluminum tube. The gap between the glass and aluminum tube was filled with a heat transfer cement. As in Method 1 the cylinders were held with nylon end pieces mounted in a moveable frame for data collection at various angles of inclination.

A direct current (d-c) power supply was used to provide current to the nichrome wire and heat the cylinder. The d-c voltage and current were measured to determine the heat input, Q, of the cylinder, assumed to be uniform along the cylinder length.

With a given heat input, surface temperatures were allowed to come to equilibrium. The average of measured surface temperatures was then used as the average surface temperature, nominally near 70°C. The heat transfer coefficient was then calculated by:

$$h = \frac{Q}{A(\Delta T_\infty)} \quad (2)$$

where A is the cylinder surface area.

Heat losses other than by free convection for both methods would be due to radiation from the cylinder and end losses through the nylon end pieces. Estimates of radiation losses from the cylinders to the chamber walls based upon average surface temperature varied between 4.5 and 5 percent. The necessary corrections were made to equations (1) and (2) to account for the radiation losses.

For both methods solid nylon cylinders were used to support the aluminum cylinders. Temperature distributions within the nylon rods were not measured and hence the heat loss through the ends of the aluminum cylinders is difficult to estimate. The ratio of thermal conductivities of aluminum 6061-T6 and extruded nylon is over 700. Once the aluminum cylinders reached a steady-state condition in both methods, the nylon rods were assumed to have reached steady-state also. Considering the large difference in conductivities, it has been assumed that the heat loss through the nylon rods was negligible.

Discussion and Results

The results of the experimental work are presented in terms of Nusselt number, Rayleigh number, angle of inclination and aspect ratio. Fluid properties were based upon the average of the measured cylinder surface temperature and the ambient temperature.

The ratio of Nusselt number based upon cylinder diameter at an angle of inclination to that determined at the horizontal position is shown in Fig. 2. Figure 2 shows the difference between results for very large and small aspect ratio cylinders. The data of [4] and [7] are for thin heated wires of large aspect ratio and that of [8] are for short cylinders of small aspect ratio. The variation of the ratio of Nusselt numbers with α decreases dramatically, for thin wires, [1], but will have some relatively large value at $\alpha = 90$ deg for short cylinders as indicated by [8] and the results of this experiment.

Morgan [1] correlated the results of many investigations for both horizontal and vertical cylinders. The suggested correlation for horizontal cylinders is the same as that originally developed by McAdams [11] as:

$$\mathrm{Nu}_D = 0.53\ (\mathrm{Ra}_D)^{0.25},\ 10^4 \le \mathrm{Ra}_D \le 10^8 \quad (3)$$

More recent correlations such as that of Faud, *et al.* [12], have shown that equation (3) relates Nu_D to Ra_D as well as any of the more recent correlations developed, for the range of Ra_D concerned. A similar correlation [13] for vertical cylinders for small aspect ratios has been given as:

$$\mathrm{Nu}_L = 0.555\ (\mathrm{Ra}_L)^{0.25},\ 10^4 \le \mathrm{Ra}_L \le 10^8 \quad (4)$$

Equation (4) can be modified by substitution of the aspect ratio to yield Nu_D for vertical cylinders,

$$\mathrm{Nu}_D(\alpha = 90\ \mathrm{deg}) = 0.555\ (\mathrm{Ra}_D\ D/L)^{0.25} \quad (5)$$

As noted in Fig. 2, the initial variation of Nu_D follows that of a horizontal cylinder

$$\mathrm{Nu}_D\ (\alpha\ \mathrm{small}) \simeq 0.53\ (\mathrm{Ra}_D \cos\alpha)^{0.25} \quad (6)$$

while for large values of α, the Nu_D should approach values given by equation (5). Considering the limiting cases of equations (3) and (5), the following equation was developed to approximate the variation in Nu_D with inclination and aspect ratio.

$$\mathrm{Nu}_D(\alpha, D/L) = 0.53\ (\mathrm{Ra}_D \cos\alpha)^{0.25} + 0.555(\mathrm{Ra}_D\ D/L)^{0.25}\ (1 - (\cos\alpha)^{0.25}) \quad (7)$$

Equation (7) satisfies equation (3) for $\alpha = 0$ deg and equation (5) for $\alpha = 90$ deg and provides for a linear correlation of Nu_D between the horizontal and vertical position.

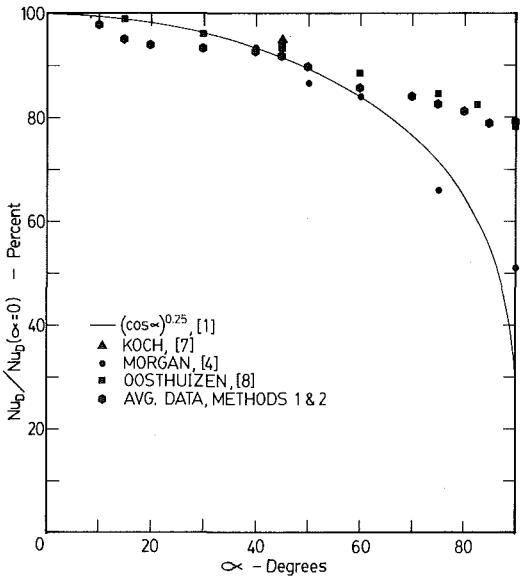

Fig. 2 Variation of Nusselt Number with angle of inclination

Equation (7) can be arranged to:

$$Nu_D/(Ra_D \cos\alpha)^{0.25} = 0.53 + 0.555[D/(L\cos\alpha))^{0.25} - (D/L)^{0.25}] \quad (8)$$

Data obtained from the experiments are correlated to equation (8) in Fig. 3. The data fits the correlation fairly well, within 10 percent.

Conclusions

For inclined cylinders of small aspect ratios, the Nusselt number for free convective heat transfer can be approximated by equation (8). The experimental results indicate reasonable agreement to the predicted results. The correlation of equation (7) also yields results for horizontal and vertical cylinders as predicted in previous publications.

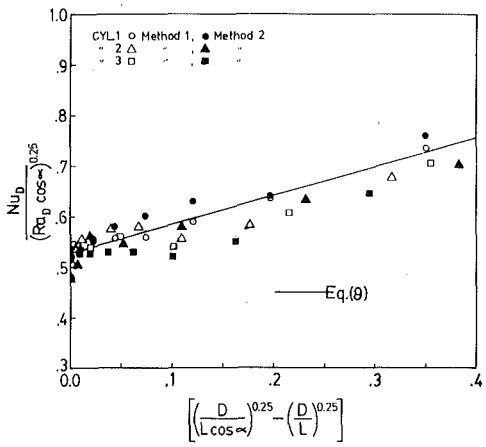

Fig. 3 Correlated results of experimental data

References

1 Morgan, V. T., "The Overall Convective Heat Transfer from Smooth Circular Cylinders," *Advances in Heat Transfer*, Vol. II, Academic Press, New York, 1975, pp. 199–264.

2 Sparrow, E. M., and Gregg, J. L., "Laminar-Free Convection Heat Transfer from the Outer Surface of a Vertical Circular Cylinder," *Trans. ASME*, Vol. 78, 1956, pp. 1823–1829.

3 Gebhart, B., *Heat Transfer*, McGraw-Hill, New York, 1971, pp. 370–374.

4 Morgan, V. T., "The Heat Transfer from Bare Standard Conductors by Natural and Forced Convection in Air," *Internal Journal Heat Mass Transfer*, Vol. 16, 1973, pp. 2023–2034.

5 Bosworth, R. C. L., *Heat Transfer Phenomena*, Associated General Publishers, Sydney, 1952, p. 101.

6 Bosworth, R. C. L., "A New Method for the Comparison of the Thermal Conductivities of Fluids," Part 1, *Journal of the Proceedings of the Royal Society N.S.W. 81*, 1947, pp. 156–166.

7 Koch, W., "Über die Wärmeabgabe geheizter Rohre verschiedener Neigung der Rohrachse," *Gesundheits Ingenieur, Beihefte*, Ser. 1, No. 22, 1927, pp. 1–29.

8 Oosthuizen, P. H., "Experimental Study of Free Convective Heat Transfer from Inclined Cylinders, ASME JOURNAL OF HEAT TRANSFER, Nov., 1976, pp. 672–674.

9 Kreith, F., *Principles of Heat Transfer*, Third ed., Intext, New York, 1973, pp. 392–398.

10 Karlekar, B. V., and Desmond, R. M., *Engineering Heat Transfer*, West Publishing, St. Paul, MN, 1977, pp. 443–446.

11 McAdams, W. H., *Heat Transmission*, Third ed., McGraw-Hill, New York, 1954.

12 Faud, R. M., Morris, E. W. and Lum, M., "Natural Convective Heat Transfer from Horizontal to Air, Water, and Silicone Oils for Rayleigh Numbers between 3×10^2 and 2×10^7," *Internal Journal Heat Mass Transfer*, Vol. 20, 1977, pp. 1173–1184.

13 Jakob, M., and Linke, W., "Der Wärmeübergang beim Verdampfen von Flüssigkeiten an senkrechten und waagerechten Fläschen," *Physics Abstracts 36*, 1935, pp. 267–380.

Laminar Free Convection Boundary Layer Heat Transfer over Non-Isothermal Surface

F. N. Lin[1]

S. Y. Chern[2]

1. Introduction

In a recent paper by Lin and Chao [1], the predictive capabilities of various series solution methods for laminar free convection boundary layer heat transfer over isothermal circular and elliptical cylinders were assessed. It was found that the solution method reported in [2] can predict accurate heat transfer results for not only circular cylinder, but also elliptical cylinder, in either slender or blunt configuration.

In this paper we shall extend the solution method reported in [2] to the treatment of nonisothermal objects. The additional universal fractions associated with the method will be tabulated for Pr = 0.72 and 100. The method will be applied to a non-isothermnal, horizontal, circular cylinder with the dimensionless wall temperature function $S = 1 - 0.25\,(\bar{x}/R)^2 + 0.125\,(\bar{x}/R)^4$.

2. Analysis and Results

Consider the steady, laminar, free convection boundary layer flow over two-dimensional or rotationally symmetrical bodies of non-uniform surface temperature $Tw(\bar{x})$ situated in an infinite ambient fluid of undisturbed temperature T_∞, as illustrated in Fig. 1 [2]. The governing conservation equations are well known and were given by equations (1–3) in [2]. They can also be recast into equations (10–12) in [2] by the same stretched coordinates, except that Θ in equations (11) and (12) in [2] is now replaced by $S\Theta$, and the temperature difference in Gr is now taken as $|T_{wo} - T_\infty|$. The dimensionless wall temperature function S is such that

$$T_w\,(\bar{x}) - T_\infty = (T_{w0} - T_\infty)\,S\,(\bar{x}) \quad (1)$$

where T_{w0} is the local wall temperature at the stagnation point, $\bar{x} = 0$. Clearly, $S = 1$ for isothermal objects. The boundary conditions (13a, b, c) and (14a, b) in [2] remain unchanged. As was stated in [2], one needs only to set $r = 1$ for two-dimensional bodies.

Replacing ϕ in equation (15c) in [2] by ϕS and using the coordinate transformation indicated by equations (16a,b), (17a, b) and (18) in [2], it can be shown that the momentum equation can be transformed to equation (21) in [2]. However, the configuration function Λ is now redefined as

$$\Lambda = 2\frac{S\phi\xi}{r^2U^3} \quad (2)$$

Further, it can be demonstrated that the energy equation now takes the form

$$P_r^{-1}\Theta'' + f\theta' - \omega f'\Theta = 2\xi\frac{\partial(\Theta,f)}{\partial(\xi,\eta)} \quad (3)$$

wherein

$$\omega = \frac{2\,\xi}{r^2U}\frac{\frac{dS}{dx}}{S} \quad (4)$$

Clearly, $\omega = 0$ for isothermal bodies. The associated boundary conditions expressed by equation (23a, b, c) and (24a, b) in [2] remain unaltered.

To minimize the number of parameters affecting the universal function, we expand the ω function into the following series

$$\omega\,(\xi) = \xi\frac{d\Lambda}{d\xi}\omega_1 + \xi^2\frac{d^2\,\Lambda}{d\,\xi^2}\omega_2 + \text{----} \quad (5)$$

[1] NASA Kennedy Space Center, Fla. 32899.

[2] Martin Marietta Aerospace, Denver, Colo. 80201.

Contributed by the Heat Transfer Division for publication in the JOURNAL OF HEAT TRANSFER. Manuscript received by the Heat Transfer Division 31 July 1981.

Equation (7) can be arranged to:

$$Nu_D/(Ra_D \cos\alpha)^{0.25} = 0.53 + 0.555[D/(L\cos\alpha))^{0.25} - (D/L)^{0.25}] \quad (8)$$

Data obtained from the experiments are correlated to equation (8) in Fig. 3. The data fits the correlation fairly well, within 10 percent.

Conclusions

For inclined cylinders of small aspect ratios, the Nusselt number for free convective heat transfer can be approximated by equation (8). The experimental results indicate reasonable agreement to the predicted results. The correlation of equation (7) also yields results for horizontal and vertical cylinders as predicted in previous publications.

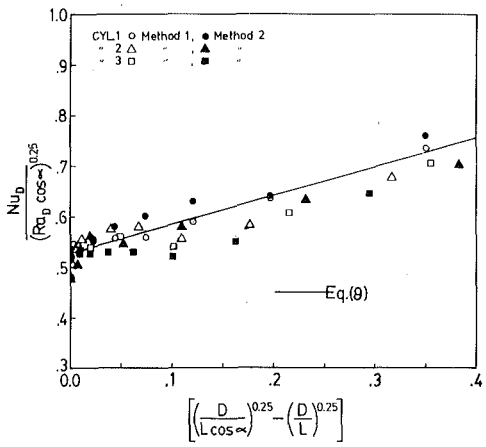

Fig. 3 Correlated results of experimental data

References

1 Morgan, V. T., "The Overall Convective Heat Transfer from Smooth Circular Cylinders," *Advances in Heat Transfer*, Vol. II, Academic Press, New York, 1975, pp. 199–264.

2 Sparrow, E. M., and Gregg, J. L., "Laminar-Free Convection Heat Transfer from the Outer Surface of a Vertical Circular Cylinder," *Trans. ASME*, Vol. 78, 1956, pp. 1823–1829.

3 Gebhart, B., *Heat Transfer*, McGraw-Hill, New York, 1971, pp. 370–374.

4 Morgan, V. T., "The Heat Transfer from Bare Standard Conductors by Natural and Forced Convection in Air," *Internal Journal Heat Mass Transfer*, Vol. 16, 1973, pp. 2023–2034.

5 Bosworth, R. C. L., *Heat Transfer Phenomena*, Associated General Publishers, Sydney, 1952, p. 101.

6 Bosworth, R. C. L., "A New Method for the Comparison of the Thermal Conductivities of Fluids," Part 1, *Journal of the Proceedings of the Royal Society N.S.W. 81*, 1947, pp. 156–166.

7 Koch, W., "Über die Wärmeabgabe geheizter Rohre verschiedener Neigung der Rohrachse," *Gesundheits Ingenieur, Beihefte*, Ser. 1, No. 22, 1927, pp. 1–29.

8 Oosthuizen, P. H., "Experimental Study of Free Convective Heat Transfer from Inclined Cylinders, ASME JOURNAL OF HEAT TRANSFER, Nov., 1976, pp. 672–674.

9 Kreith, F., *Principles of Heat Transfer*, Third ed., Intext, New York, 1973, pp. 392–398.

10 Karlekar, B. V., and Desmond, R. M., *Engineering Heat Transfer*, West Publishing, St. Paul, MN, 1977, pp. 443–446.

11 McAdams, W. H., *Heat Transmission*, Third ed., McGraw-Hill, New York, 1954.

12 Faud, R. M., Morris, E. W. and Lum, M., "Natural Convective Heat Transfer from Horizontal to Air, Water, and Silicone Oils for Rayleigh Numbers between 3×10^2 and 2×10^7," *Internal Journal Heat Mass Transfer*, Vol. 20, 1977, pp. 1173–1184.

13 Jakob, M., and Linke, W., "Der Wärmeübergang beim Verdampfen von Flüssigkeiten an senkrechten und waagerechten Fläschen," *Physics Abstracts 36*, 1935, pp. 267–380.

Laminar Free Convection Boundary Layer Heat Transfer over Non-Isothermal Surface

F. N. Lin[1]

S. Y. Chern[2]

1. Introduction

In a recent paper by Lin and Chao [1], the predictive capabilities of various series solution methods for laminar free convection boundary layer heat transfer over isothermal circular and elliptical cylinders were assessed. It was found that the solution method reported in [2] can predict accurate heat transfer results for not only circular cylinder, but also elliptical cylinder, in either slender or blunt configuration.

In this paper we shall extend the solution method reported in [2] to the treatment of nonisothermal objects. The additional universal fractions associated with the method will be tabulated for Pr = 0.72 and 100. The method will be applied to a non-isothermnal, horizontal, circular cylinder with the dimensionless wall temperature function $S = 1 - 0.25\,(\bar{x}/R)^2 + 0.125\,(\bar{x}/R)^4$.

2. Analysis and Results

Consider the steady, laminar, free convection boundary layer flow over two-dimensional or rotationally symmetrical bodies of non-uniform surface temperature $Tw(\bar{x})$ situated in an infinite ambient fluid of undisturbed temperature T_∞, as illustrated in Fig. 1 [2]. The governing conservation equations are well known and were given by equations (1–3) in [2]. They can also be recast into equations (10–12) in [2] by the same stretched coordinates, except that Θ in equations (11) and (12) in [2] is now replaced by $S\Theta$, and the temperature difference in Gr is now taken as $|T_{wo} - T_\infty|$. The dimensionless wall temperature function S is such that

$$T_w\,(\bar{x}) - T_\infty = (T_{w0} - T_\infty)\,S\,(\bar{x}) \quad (1)$$

where T_{w0} is the local wall temperature at the stagnation point, $\bar{x} = 0$. Clearly, $S = 1$ for isothermal objects. The boundary conditions (13a, b, c) and (14a, b) in [2] remain unchanged. As was stated in [2], one needs only to set $r = 1$ for two-dimensional bodies.

Replacing ϕ in equation (15c) in [2] by ϕS and using the coordinate transformation indicated by equations (16a,b), (17a, b) and (18) in [2], it can be shown that the momentum equation can be transformed to equation (21) in [2]. However, the configuration function Λ is now redefined as

$$\Lambda = 2\,\frac{S\phi\xi}{r^2U^3} \quad (2)$$

Further, it can be demonstrated that the energy equation now takes the form

$$P_r^{-1}\Theta'' + f\theta' - \omega f'\Theta = 2\xi\,\frac{\partial(\Theta,f)}{\partial(\xi,\eta)} \quad (3)$$

wherein

$$\omega = \frac{2\,\xi}{r^2U}\,\frac{\frac{dS}{dx}}{S} \quad (4)$$

Clearly, $\omega = 0$ for isothermal bodies. The associated boundary conditions expressed by equation (23a, b, c) and (24a, b) in [2] remain unaltered.

To minimize the number of parameters affecting the universal function, we expand the ω function into the following series

$$\omega\,(\xi) = \xi\,\frac{d\Lambda}{d\xi}\,\omega_1 + \xi^2\,\frac{d^2\,\Lambda}{d\,\xi^2}\,\omega_2 + \text{----} \quad (5)$$

[1] NASA Kennedy Space Center, Fla. 32899.

[2] Martin Marietta Aerospace, Denver, Colo. 80201.

Contributed by the Heat Transfer Division for publication in the JOURNAL OF HEAT TRANSFER. Manuscript received by the Heat Transfer Division 31 July 1981.

Thus, the appropriate series solutions are:

$$f(\xi, \eta) = f_0(\Lambda, \eta) + \xi \frac{d\Lambda}{d\xi}[f_1(\Lambda, \eta) + \omega_1 F_{12}(\Lambda, \eta)] + \xi^2 \frac{d^2\Lambda}{d\xi^2}[f_2(\Lambda, \eta) + \omega_1 F_{22}(\Lambda, \eta) + \omega_2 F_{23}(\Lambda, \eta)] + \text{----} \quad (6)$$

$$\theta(\xi, \eta) = \Theta_0(\Lambda, \eta) + \xi \frac{d\Lambda}{d\xi}[\Theta_1(\Lambda, \eta) + \omega_1 H_{12}(\Lambda, \eta)] + \xi^2 \frac{d^2\Lambda}{d\xi^2}[\Theta_2(\Lambda, \eta) + \omega_1 H_{22}(\Lambda, \eta) + \omega_2 H_{23}(\Lambda, \eta)] + \text{----} \quad (7)$$

It can be readily established that the functions (f_0, Θ_0), (f_1, Θ_1) and (f_2, Θ_2) are governed by equations (28) to (37 a,b) in [2]. They are universal and have been tabulated in [2] for a wide range of Λ values.

The functions (F_{12}, H_{12}), (F_{22}, H_{22}) and (F_{23}, H_{23}) are, respectively, governed by the following equation sets:

$$F_{12}''' + f_0 F_{12}'' + 3f_0'' F_{12} - 2(\Lambda + 1) f_0' F_{12}' + \Lambda H_{12} = 0 \quad (8a)$$

$$P_r^{-1} H_{12}'' + f_0 H_{12}' - 2f_0' H_{12} - 3\Theta_0' F_{12} = f_0' \Theta_0 \quad (8b)$$

$$F_{12}(\Lambda, 0) = F_{12}'(\Lambda, 0) = H_{12}(\Lambda, 0) = F_{12}'(\Lambda, \infty) = H_{12}(\Lambda, \infty) = 0 \quad (8c)$$

$$F_{22}''' + f_0 F_{22}'' + 5f_0'' F_{22} - 2(\Lambda + 2) f_0' F_{22}' + \Lambda H_{22} = 2(f_0' F_{12}' - f_0'' F_{12}) \quad (9a)$$

$$P_r^{-1} H_{22}'' + f_0 H_{22}' - 4f_0' H_{22} + 5\Theta_0' F_{22} = 2(f_0' H_{12} - \Theta_0' F_{12}) \quad (9b)$$

$$F_{22}(\Lambda, 0) = F_{22}'(\Lambda, 0) = H_{22}(\Lambda, 0) = F_{22}'(\Lambda, \infty) = H_{22}(\Lambda, \infty) = 0 \quad (9c)$$

and,

$$F_{23}''' + f_0 F_{23}'' + 5f_0'' F_{23} - 2(\Lambda + 2) f_0' F_{23}' + \Lambda H_{23} = 0 \quad (10a)$$

$$P_r^{-1} H_{23}'' + f_0 H_{23}' - 4f_0' H_{23} + 5\Theta_0' F_{23} = f_0' \theta_0 \quad (10b)$$

$$F_{23}(\Lambda, 0) = F_{23}'(\Lambda, 0) = H_{23}(\Lambda, 0) = F_{23}'(\Lambda, \infty) = H_{23}(\Lambda, \infty) = 0 \quad (10c)$$

Like other functions, they depend on P_r and Λ only and can be tabulated once for all. In addition, they are all linear and do not depend upon (f_1, θ_1) or (f_2, Θ_2).

The foregoing three sets of coupled differential equations have been numerically integrated for $P_r = 0.72$ and 100 and for 26 values of Λ ranging from 1.4 to 2/7. A tabulation of the appropriate wall derivatives is given in Tables 1 and 2.

In technological applications, it is often the surface heat flux q_w that is of the greatest interest. In terms of the local Nusselt number, it is given by

$$\frac{\mathrm{Nu}}{\mathrm{Gr}^{1/4}} = \frac{q_w L}{\mathrm{Gr}^{1/4} k (T_{w0} - T_\infty)} = rUS\,(2\xi)^{-1/2}\left[-\frac{\partial\Theta}{\partial\eta}(\xi, 0)\right] \quad (11a)$$

where

$$\frac{\partial\Theta}{\partial_y}(\xi, 0) = \Theta_0'(\Lambda, 0) + \xi \frac{d\Lambda}{d\xi}[\Theta_1'(\Lambda, 0) + \omega_1 H_{12}'(\Lambda, 0)] + \xi^2 \frac{d^2\Lambda}{d\xi^2}[\Theta_2'(\Lambda, 0) + \omega_1 H_{22}'(\Lambda, 0) + \omega_2 H_{23}'(\Lambda, 0)] + \text{----} \quad (11b)$$

Equations (11a) and (11b) and Tables 1 and 2 together with the tables given in the Appendix in [2] constitute a simple and rapid procedure for calculating the local heat transfer rate over a non-isothermal surface.

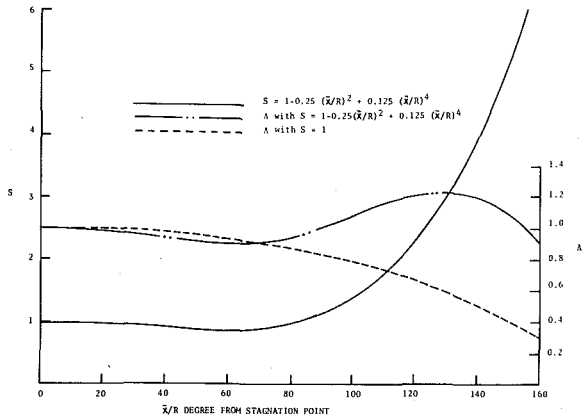

Fig. 1 Variation of S and Λ over circular cylinder

Table 1. Wall derivatives of universal functions for Pr = 0.72

Λ	$F_{12}''(\Lambda, 0)$	$H_{12}'(\Lambda, 0)$	$F_{22}''(\Lambda, 0)$	$H_{22}'(\Lambda, 0)$	$F_{23}''(\Lambda, 0)$	$H_{23}'(\Lambda, 0)$
1.40	−0.05568	−0.15582	0.01967	0.03004	−0.03602	−0.12577
1.20	−0.05114	−0.15138	0.01835	0.02921	−0.03279	−0.12217
1.00	−0.04605	−0.14615	0.01680	0.02823	−0.02925	−0.11793
0.99	−0.04578	−0.14586	0.01671	0.02817	−0.02907	−0.11769
0.98	−0.04550	−0.14557	0.01663	0.02812	−0.02888	−0.11746
0.97	−0.04523	−0.14528	0.01654	0.02806	−0.02869	−0.11722
0.95	−0.04468	−0.14469	0.01636	0.02795	−0.02831	−0.11674
0.93	−0.04411	−0.14408	0.01619	0.02783	−0.02793	−0.11625
0.90	−0.04326	−0.14315	0.01591	0.02766	−0.02734	−0.11549
0.85	−0.04179	−0.14152	0.01544	0.02735	−0.02635	−0.11417
0.80	−0.04028	−0.13980	0.01495	0.02703	−0.02533	−0.11278
0.75	−0.03870	−0.13798	0.01443	0.02668	−0.02427	−0.11130
0.70	−0.03707	−0.13604	0.01389	0.02631	−0.02319	−0.10973
2/3	−0.03595	−0.13467	0.01351	0.02606	−0.02244	−0.10862
0.65	−0.03538	−0.13397	0.01331	0.02592	−0.02207	−0.10805
0.60	−0.03362	−0.13174	0.01271	0.02550	−0.02091	−0.10624
0.57	−0.03252	−0.13032	0.01233	0.02523	−0.02019	−0.10509
0.55	−0.03178	−0.12933	0.01207	0.02504	−0.01970	−0.10429
0.54	−0.03140	−0.12883	0.01194	0.02494	−0.01946	−0.10388
0.53	−0.03102	−0.12831	0.01181	0.02485	−0.01921	−0.10347
0.52	−0.03064	−0.12779	0.01167	0.02475	−0.01896	−0.10304
0.51	−0.03025	−0.12726	0.01154	0.02465	−0.01871	−0.10261
0.50	−0.02986	−0.12672	0.01140	0.02454	−0.01846	−0.10218
0.40	−0.02573	−0.12070	0.00992	0.02339	−0.01581	−0.09730
0.30	−0.02114	−0.11317	0.00824	0.02195	−0.01290	−0.09121
2/7	−0.02043	−0.11192	0.00797	0.02171	−0.01246	−0.09020

Table 2. Wall derivatives of universal functions for Pr = 100

Λ	$F_{12}''(\Lambda, 0)$	$H_{12}''(\Lambda, 0)$	$F_{22}''(\Lambda, 0)$	$H_{22}''(\Lambda, 0)$	$F_{23}''(\Lambda, 0)$	$H_{22}'(\Lambda, 0)$
1.40	−0.03732	−0.54961	0.01215	0.10807	−0.02517	−0.44155
1.20	−0.03337	−0.52917	0.01088	0.10401	−0.02249	−0.42516
1.00	−0.02921	−0.50593	0.00954	0.09940	−0.01967	−0.40652
0.99	−0.02900	−0.50468	0.00947	0.09915	−0.01953	−0.40552
0.98	−0.02878	−0.50341	0.00940	0.09891	−0.01938	−0.40451
0.97	−0.02857	−0.50214	0.00933	0.09865	−0.01924	−0.40349
0.95	−0.02814	−0.49957	0.00919	0.09814	−0.01895	−0.40142
0.93	−0.02770	−0.49695	0.00905	0.09763	−0.01865	−0.39933
0.90	−0.02705	−0.49295	0.00884	0.09683	−0.01821	−0.39612
0.85	−0.02594	−0.48605	0.00848	0.09547	−0.01746	−0.39058
0.80	−0.02481	−0.47882	0.00811	0.09404	−0.01669	−0.38478
0.75	−0.02366	−0.47125	0.00774	0.09255	−0.01592	−0.37870
0.70	−0.02249	−0.46328	0.00736	0.09097	−0.01513	−0.37231
2/3	−0.02170	−0.45773	0.00711	0.08988	−0.01459	−0.36785
0.65	−0.02130	−0.45487	0.00697	0.08931	−0.01432	−0.36556
0.60	−0.02008	−0.44595	0.00658	0.08755	−0.01350	−0.35840
0.57	−0.01933	−0.44032	0.00634	0.08644	−0.01299	−0.35388
0.55	−0.01883	−0.43644	0.00617	0.08568	−0.01266	−0.35077
0.54	−0.01857	−0.43447	0.00609	0.08529	−0.01248	−0.34918
0.53	−0.01832	−0.43246	0.00601	0.08489	−0.01231	−0.34757
0.52	−0.01806	−0.43042	0.00592	0.08449	−0.01214	−0.34593
0.51	−0.01781	−0.42836	0.00584	0.08408	−0.01197	−0.34427
0.50	−0.01755	−0.42626	0.00576	0.08367	−0.01179	−0.34259
0.40	−0.01488	−0.40331	0.00488	0.07915	−0.00999	−0.32416
0.30	−0.01202	−0.37550	0.00395	0.07368	−0.00807	−0.30182
2/7	−0.01159	−0.37098	0.00381	0.07279	−0.00778	−0.29819

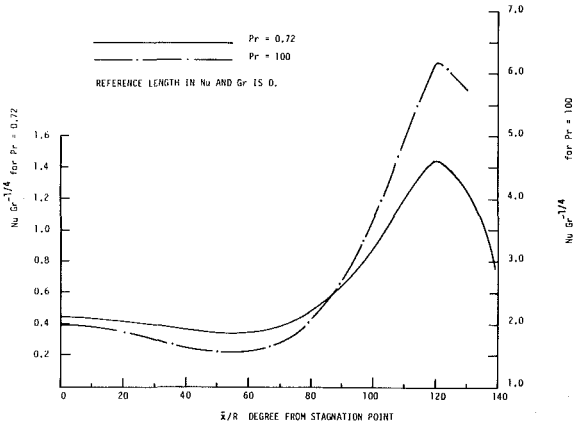

Fig. 2 Heat transfer over non-isothermal circular cylinder

To present some heat transfer results, we consider a horizontal circular cylinder with

$$S(\bar{x}) = 1 - 0.25\,(\bar{x}/R)^2 + 0.125\,(\bar{x}/R)^4 \tag{12}$$

Upon selecting its radius R as the reference length L, one has

$$\phi = \sin x \tag{13}$$

With (12) and (13), one can calculate U, ξ, Λ, $\xi\, d\Lambda/d\xi$, $\xi^2\, d^2\Lambda/d\xi^2$, ω_1 and ω_2. The Λ and S functions are shown in Fig. 1. Also shown in Fig. 1 is the Λ function for an isothermal cylinder.

The heat transfer results calculated from (11) for $P_r = 0.72$ and 100, after converting to reference length of cylinder diameter, are shown in Fig. 2. Our computer printouts indicate that the series behaves well up to $\bar{x}/R = 130$ degrees. Beyond this point the present constant property analysis, in view of the S curve in Fig. 1, may not be good even if the flow is still laminar.

Acknowledgement

Special thanks is given to Ms Evelyn Hoppes of Martin Marietta, Propulsion and Mechanical Division, for her skillful preparation of the manuscript.

References

1 Lin, F. N. and Chao, B. T., "Predictive Capabilities of Series Solutions for Laminar Free Convection Boundary Layer Heat Transfer," ASME JOURNAL OF HEAT TRANSFER, Vol. 100, 1978, pp. 160–163.

2 Lin, F. N. and Chao, B. T., "Laminar Free Convection Over Two-Dimensional and Axisymmetric Bodies of Arbitrary Contour," ASME JOURNAL OF HEAT TRANSFER, Vol. 96, 1974, pp. 435–442.

Conduction Shape Factors for Certain Multi-Hole Prismatic Bars[1]

A. K. Naghdi[2]

Introduction

On the basis of the two recent investigations [1, 2], the shape factors per unit length for the cases of steady-state heat flow in infinitely long cylinders are calculated. Comprehensive and accurate results are presented for the following two cases: (*a*) a circular cylinder with a row of equally spaced circular cavities, (*b*) a rectangular cross-section prismatic bar with two symmetrical holes (see Figs. 1(a, b)). In both cases it is assumed that the inner and outer temperatures are uniform and that the thermal conductivity is a constant.

Analysis

In recent years a few authors have investigated the problem of steady-state heat conduction in a circular cylinder with one or several circular cavities. Among these authors are El-Saden [3] and Rowley and Payne [4]. El-Saden, using bipolar coordinates, derived a solution for the problem of heat conduction in an eccentrically hollow cylinder with or without internal heat generation. Rowley and Payne, using a class of functions defined by Howland [5], solved the problem of heat conduction in a cylinder cooled by a ring of holes. However, they gave

[1] The author wishes to thank the Department of Computing Services of IUPUI for providing CDC 6600 computer time for this investigation.

[2] Professor of Aeronautical-Astronautical Engineering and Mathematical Sciences, Purdue University, Indianapolis, Indiana 46205

Contributed by the Heat Transfer Division for publication in THE JOURNAL OF HEAT TRANSFER. Manuscript received by the Heat Transfer Division, December 16, 1980.

Table 2. Wall derivatives of universal functions for Pr = 100

Λ	$F_{12}''(\Lambda, 0)$	$H_{12}''(\Lambda, 0)$	$F_{22}''(\Lambda, 0)$	$H_{22}''(\Lambda, 0)$	$F_{23}''(\Lambda, 0)$	$H_{22}'(\Lambda, 0)$
1.40	−0.03732	−0.54961	0.01215	0.10807	−0.02517	−0.44155
1.20	−0.03337	−0.52917	0.01088	0.10401	−0.02249	−0.42516
1.00	−0.02921	−0.50593	0.00954	0.09940	−0.01967	−0.40652
0.99	−0.02900	−0.50468	0.00947	0.09915	−0.01953	−0.40552
0.98	−0.02878	−0.50341	0.00940	0.09891	−0.01938	−0.40451
0.97	−0.02857	−0.50214	0.00933	0.09865	−0.01924	−0.40349
0.95	−0.02814	−0.49957	0.00919	0.09814	−0.01895	−0.40142
0.93	−0.02770	−0.49695	0.00905	0.09763	−0.01865	−0.39933
0.90	−0.02705	−0.49295	0.00884	0.09683	−0.01821	−0.39612
0.85	−0.02594	−0.48605	0.00848	0.09547	−0.01746	−0.39058
0.80	−0.02481	−0.47882	0.00811	0.09404	−0.01669	−0.38478
0.75	−0.02366	−0.47125	0.00774	0.09255	−0.01592	−0.37870
0.70	−0.02249	−0.46328	0.00736	0.09097	−0.01513	−0.37231
2/3	−0.02170	−0.45773	0.00711	0.08988	−0.01459	−0.36785
0.65	−0.02130	−0.45487	0.00697	0.08931	−0.01432	−0.36556
0.60	−0.02008	−0.44595	0.00658	0.08755	−0.01350	−0.35840
0.57	−0.01933	−0.44032	0.00634	0.08644	−0.01299	−0.35388
0.55	−0.01883	−0.43644	0.00617	0.08568	−0.01266	−0.35077
0.54	−0.01857	−0.43447	0.00609	0.08529	−0.01248	−0.34918
0.53	−0.01832	−0.43246	0.00601	0.08489	−0.01231	−0.34757
0.52	−0.01806	−0.43042	0.00592	0.08449	−0.01214	−0.34593
0.51	−0.01781	−0.42836	0.00584	0.08408	−0.01197	−0.34427
0.50	−0.01755	−0.42626	0.00576	0.08367	−0.01179	−0.34259
0.40	−0.01488	−0.40331	0.00488	0.07915	−0.00999	−0.32416
0.30	−0.01202	−0.37550	0.00395	0.07368	−0.00807	−0.30182
2/7	−0.01159	−0.37098	0.00381	0.07279	−0.00778	−0.29819

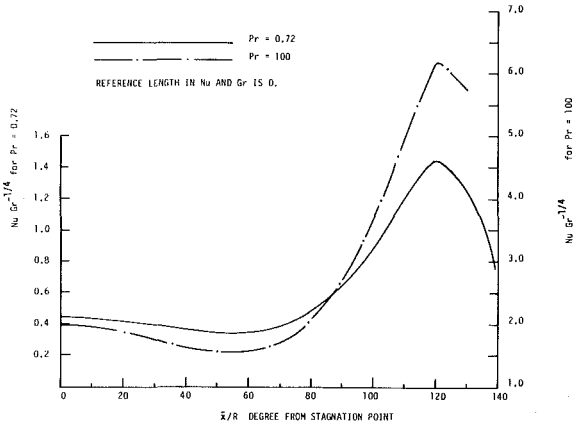

Fig. 2 Heat transfer over non-isothermal circular cylinder

To present some heat transfer results, we consider a horizontal circular cylinder with

$$S(\bar{x}) = 1 - 0.25\,(\bar{x}/R)^2 + 0.125\,(\bar{x}/R)^4 \tag{12}$$

Upon selecting its radius R as the reference length L, one has

$$\phi = \sin x \tag{13}$$

With (12) and (13), one can calculate U, ξ, Λ, $\xi\, d\Lambda/d\xi$, $\xi^2\, d^2\Lambda/d\xi^2$, ω_1 and ω_2. The Λ and S functions are shown in Fig. 1. Also shown in Fig. 1 is the Λ function for an isothermal cylinder.

The heat transfer results calculated from (11) for $P_r = 0.72$ and 100, after converting to reference length of cylinder diameter, are shown in Fig. 2. Our computer printouts indicate that the series behaves well up to $\bar{x}/R = 130$ degrees. Beyond this point the present constant property analysis, in view of the S curve in Fig. 1, may not be good even if the flow is still laminar.

Acknowledgement

Special thanks is given to Ms Evelyn Hoppes of Martin Marietta, Propulsion and Mechanical Division, for her skillful preparation of the manuscript.

References

1 Lin, F. N. and Chao, B. T., "Predictive Capabilities of Series Solutions for Laminar Free Convection Boundary Layer Heat Transfer," ASME JOURNAL OF HEAT TRANSFER, Vol. 100, 1978, pp. 160–163.

2 Lin, F. N. and Chao, B. T., "Laminar Free Convection Over Two-Dimensional and Axisymmetric Bodies of Arbitrary Contour," ASME JOURNAL OF HEAT TRANSFER, Vol. 96, 1974, pp. 435–442.

Conduction Shape Factors for Certain Multi-Hole Prismatic Bars[1]

A. K. Naghdi[2]

Introduction

On the basis of the two recent investigations [1, 2], the shape factors per unit length for the cases of steady-state heat flow in infinitely long cylinders are calculated. Comprehensive and accurate results are presented for the following two cases: (*a*) a circular cylinder with a row of equally spaced circular cavities, (*b*) a rectangular cross-section prismatic bar with two symmetrical holes (see Figs. 1(a, b)). In both cases it is assumed that the inner and outer temperatures are uniform and that the thermal conductivity is a constant.

Analysis

In recent years a few authors have investigated the problem of steady-state heat conduction in a circular cylinder with one or several circular cavities. Among these authors are El-Saden [3] and Rowley and Payne [4]. El-Saden, using bipolar coordinates, derived a solution for the problem of heat conduction in an eccentrically hollow cylinder with or without internal heat generation. Rowley and Payne, using a class of functions defined by Howland [5], solved the problem of heat conduction in a cylinder cooled by a ring of holes. However, they gave

[1] The author wishes to thank the Department of Computing Services of IUPUI for providing CDC 6600 computer time for this investigation.

[2] Professor of Aeronautical-Astronautical Engineering and Mathematical Sciences, Purdue University, Indianapolis, Indiana 46205

Contributed by the Heat Transfer Division for publication in THE JOURNAL OF HEAT TRANSFER. Manuscript received by the Heat Transfer Division, December 16, 1980.

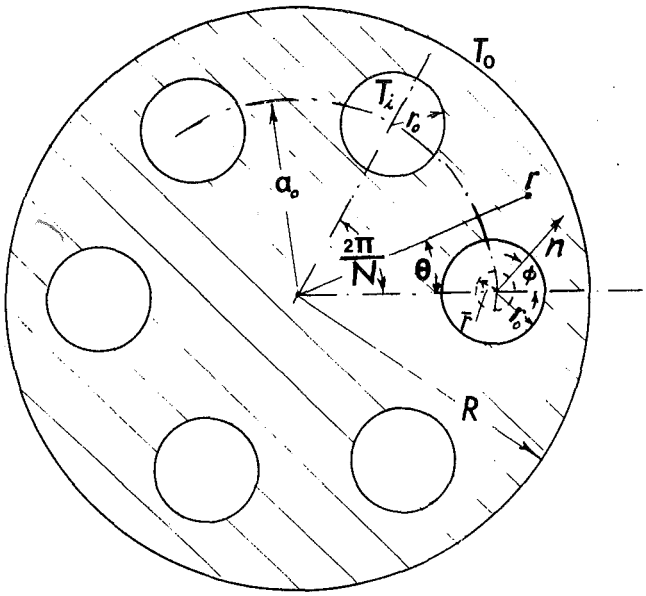

Fig. 1a Circular region with equally spaced circular cavities

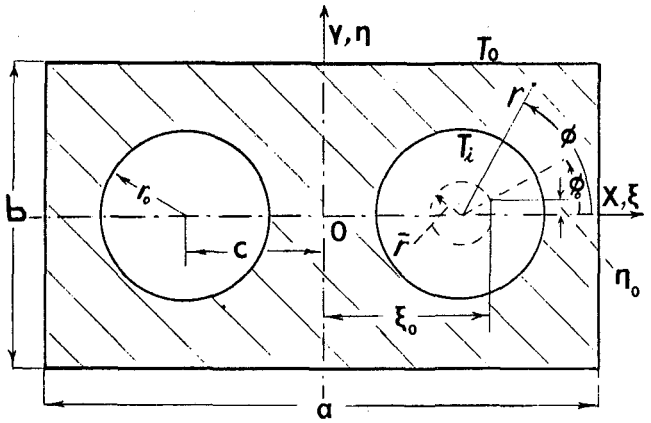

Fig. 1b Rectangular region with two inner circular cavities

numerical results for the shape factors only in the case of a cylinder with two holes.

The technique of calculation of the temperature field and the shape factors in either a circular or a rectangular cross-section bar is based upon the derivations of the Green's functions $\bar{\psi}_c(\rho, \theta, \rho_0, \theta_0)$, and $\tilde{\psi}_c(\xi, \eta, \xi_0, \eta_0)$ in which ρ, θ, and ξ, η are the positions of any given points, and ρ_0, θ_0 and ξ_0, η_0 are the locations of the concentrated sources in the two different regions. These Green's functions, which automatically satisfy a homogeneous outer boundary condition, are then multiplied by appropriate functions $\cos j\phi_0$, and are integrated over a small circular path with radius $\bar{r}$ (see Figs. 1(a, b)). This procedure gives the following linearly independent eigenfunctions in the form of integrals:

$$\bar{\psi}_j = \oint \bar{\psi}_c(\rho, \theta, \rho_0, \theta_0) \cos j\,\phi_0 \frac{\bar{r}}{R} d\,\phi_0,$$
$$\bar{\psi}_j{}^* = \oint \tilde{\psi}_c(\xi, \eta, \xi_0, \eta_0) \cos j\,\phi_0 \frac{\bar{r}}{R} d\,\phi_0. \tag{1}$$

The linear combination of these eigenfunctions, involving certain unknown constants, is utilized to form the desired solutions for the problems under consideration. The unknown constants are then determined through the point-by-point satisfaction of the inner boundary condition and the use of the technique of least square error [6]. For further details of the analysis the reader is referred to references [1, 2].

Numerical results. For simplicity, a dimensionless temperature $\bar{T}$ is defined such that

$$\bar{T} = \frac{T - T_0}{T_i - T_0}, \tag{2}$$

in which T_0 and T_i are the uniform outer and inner surface temperatures, respectively. In Table 1, the values of $\bar{T}$ are compared with those calculated from the solution given by El-Saden [3] for the case of a circular cylinder with one circular cavity. The shape factor per unit length S is defined as

$$S = \frac{q}{K(T_i - T_0)}, \tag{3}$$

in which q is the rate of heat flow per unit length of the cylinder from the inner surfaces to the outer surface, and K is thermal conductivity. The value of q is found from

$$q = -NKr_0 \int_0^{2\pi} \frac{\partial T}{\partial n} d\phi, \tag{4}$$

where N is the number of holes, and n, ϕ are the polar coordinates measured from the center of each circular cavity [in the rectangular case n is the same as r (see Fig. 1b)]. Employing the nondimensional length $\bar{n} = n/R$ (or n/a), and making use of relation (3), the shape factor per unit length is written as:

$$S = -Nr^* \int_0^{2\pi} \frac{\partial \bar{T}}{\partial \bar{n}} \mathrm{d}\phi,$$
$$r^* = \begin{cases} \dfrac{r_0}{R} \text{ (circular cylinder case)} \\ \dfrac{r_0}{a} \text{ (rectangular bar case)} \end{cases} \tag{5}$$

Table 1 Comparison of dimensionless temperature $\bar{T}$ along radial direction $\theta = 0$ obtained in this investigation with those from El-Saden's work for the case $\bar{T} = 1$, $\bar{T} = 0$ respectively at the inner and outer circles, $r^* = 0.14$, $\bar{a}_0 = 0.5$, $N = 1$

$\frac{r}{R}$	Present investigation	El-Saden
0.64	0.99999347	1.
0.73	0.63528812	0.63529751
0.82	0.38101403	0.38100978
0.91	0.17692150	0.17692122
1.0	0	0

The integral in relation (5) has been evaluated numerically for the cases presented in this investigation. In Table 2, the obtained values of S for circular cylinders having one cavity are compared with those calculated from the exact solution [3, 7]. In Tables 3–6, the shape factors for circular cylinders with 2, 3, 4, and 6 circular cavities are given. In each case various r^*, and $\bar{a}_0 = a_0/R$ are considered. In Tables 7, 8, 9 the shape factors for rectangular cross-section bars having two holes are presented for various r^*, $\bar{c} = c/a$, and $\bar{b} = b/a$. The numerical results for the shape factors for the case of a circular cylinder with two holes match closely with those given by Rowley and Payne in the form of a graph (see [4], page 535).

Table 2 Comparison of the obtained values of S for circular cylinders having one cavity with those calculated from the exact solution

r^*	0.1	0.125	0.1
$\bar{a}_0$	0.5	0.5	0.65
Present investigation	3.1253916	3.5208004	3.6102274
Calculated from either reference [3, 7]	3.1253914	3.5208015	3.6102235

Table 3 The values of S for circular cylinders with $N = 2$

r^* / $\bar{a}_0$	0.100	0.125	0.150
0.50	5.656	6.316	6.996
0.65	6.895	7.918	9.046
0.80	10.10	12.83	17.07

Table 4 The values of S for circular cylinders with $N = 3$

r^* / $\bar{a}_0$	0.100	0.125	0.150
0.50	7.446	8.250	9.086
0.65	9.665	11.05	12.58
0.80	14.80	18.79	25.03

Table 5 The values of S for circular cylinders with $N = 4$

r^* / $\bar{a}_0$	0.100	0.125	0.150
0.50	8.654	9.538	10.47
0.65	11.89	13.53	15.38
0.80	19.13	24.29	32.44

Table 6 The values of S for circular cylinders with $N = 6$

r^* / $\bar{a}_0$	0.100	0.125	0.150
0.50	10.05	11.02	12.08
0.65	14.98	16.99	19.30
0.80	26.58	33.81	45.52

Table 7 The values of S for rectangular section bars with $N = 2$, $\bar{b} = 0.5$

r^* / $\bar{c}$	0.100	0.125	0.150
0.200	10.10	12.53	15.75
0.225	10.57	13.19	16.69
0.250	11.06	13.92	17.81
0.275	11.63	14.84	19.35

Table 8 The values of S for rectangular section bars with $N = 2$, $\bar{b} = 0.6$

r^* / $\bar{c}$	0.100	0.125	0.150
0.200	8.693	10.46	12.65
0.225	9.178	11.13	13.58
0.250	9.711	11.91	14.73
0.275	10.30	12.90	16.35

Table 9 The values of S for rectangular section bars with $N = 2$, $\bar{b} = 0.7$

r^* / $\bar{c}$	0.100	0.125	0.150
0.200	7.847	9.293	11.04
0.225	8.340	9.966	11.96
0.250	8.897	10.77	13.14
0.275	9.567	11.80	14.80

References

1 Naghdi, A. K., "Closed Form Eigenfunctions of Laplace's Equation in Multiply Connected Regions and Applications," *Proceedings of the 16th Midwestern Mechanics Conference: Developments in Mechanics*, Vol. 10, Sept. 1979, pp. 131–135.

2 Naghdi, A. K., "Solution of Poisson's Equation in a Rectangular Region with Multiple Holes," *Proceedings of the 10th South Eastern Conference on Theoretical and Applied Mechanics: Developments in Theoretical and Applied Mechanics*, Vol. 10, pp. 151–161.

3 El-Saden, M. R., "Heat Conduction in an Eccentrically Hollow, Infinitely Long Cylinder with Internal Heat Generation," *Trans. ASME* Vol. 83, Nov. 1961, pp. 510–512.

4 Rowley, J. C., and Payne, J. B., "Steady State Temperature Solution for a Heat Generating Circular Cylinder Cooled by a Ring of Holes," ASME JOURNAL OF HEAT TRANSFER, Vol. 86, 1964, pp. 531–536.

5 Howland, R. C. J., "Potential Functions with Periodicity in One Coordinate," *Proceedings of the Cambridge Philosophical Society*, London, England, Vol. 30, 1935, pp. 315–326.

6 Hildebrand, F. B., *Introduction to Numerical Analysis*, McGraw-Hill, 1956.

7 Giedt, W. H., *Principles of Engineering Heat Transfer*, Van Nostrand Co., Inc., 1957.

Journal of Heat Transfer

Discussion

Force Convection Heat Transfer at an Inclined and Yawed Square Plate—Application to Solar Collectors[1]

Local Heat Transfer and Fluid Flow Characteristics for Airflow Oblique or Normal to Square Plate[2]

Effect of Finite Width on Heat Transfer and Fluid Flow about an Inclined Rectangular Plate[3]

B. Nimmo[4] and S. Zubair.[5] Sparrow, et al. have presented a series of papers covering studies on wind-related film heat transfer coefficients with application to solar collectors. In their work, mass transfer rates were measured for both square and rectangular plates oriented at different angles to an oncoming air stream. Using the analogy between heat and mass transfer, it was then possible to arrive at correlating equations for the heat transfer coefficient for different plate aspect ratios and different angles of attack. It was concluded that a single equation would correlate the results within ±10 percent for angles of attack between 90 and 25 deg and over an aspect ratio range of 0.4 to 2.5. The single correlation, as presented in reference [3] is

$$j = 0.86\ \mathrm{Re}_L^{-1/2} \tag{1}$$

here, j represents the Colburn j-factor, defined for heat transfer as

$$j = \mathrm{StPr}^{2/3},\ \mathrm{St} = h/\rho C_p V,\ \mathrm{Pr} = C_p\mu/k$$

The Reynolds number is based on a characteristic length of $4A/C$ where A is the plate surface area and C represents the plate perimeter.

We would like to make two comments relating to the work of Sparrow, et al. First, the range of Reynolds numbers covered in the test was 20,000 to 100,000. For a practical solar collector with characteristic length of one meter, the upper Reynolds number value results in a wind velocity of only about 2 m/s. In order to include a wider range of practical wind speeds, as would be required in practice, one must assume the correlating equation (1) holds beyond the range of the experimental points.

The second and perhaps more subtle point relates to the presence of natural convection as a heat transfer mechanism for practically sized solar collectors. Kreith [4] has shown by dimensional analysis of the applicable governing differential equations that natural convection will influence the forced convection velocity field (and therefore the temperature distribution) if

$$\mathrm{Gr}/\mathrm{Re}^2 \simeq 1 \tag{2}$$

where Gr is the Grashof number. Reference [5] shows that the effect of buoyancy on the average heat transfer coefficient for pure forced convection over a vertical flat plate will be less than 5 percent if $\mathrm{Gr} \leq 0.255\ \mathrm{Re}^2$. If we take some liberty in applying this criteria to a typical (perhaps tilted) collector some feeling for the relative importance of natural convection can be achieved. For the case where ambient temperature is 20°C, cover plate temperature is 30°C and the characteristic length is one meter, the Grashof number has a value of about 11×10^8. For Reynolds numbers of 20,000 and 100,000, the extreme values of the experimental work in [1, 2, 3], the corresonding values of the parameter $0.255\ \mathrm{Re}^2$ are aproximately 1×10^8 and 25×10^8. It seems clear that had the tests been performed over the stated Reynolds number range with a full size collector, natural convection would have played an important role in the thermal losses from the collector at lower velocities. In the experimental work of references [1, 2, 3], the characteristic length of the test plate (collector) was on the order of 0.1m: i.e., relatively small. Since this length appears to the third power in the Grashof number, the criteria that $\mathrm{Gr} \ll \mathrm{Re}^2$ was satisfied for the experiments. It would be difficult to envision an analogous natural convection pheomenon with the mass transfer experiments using napthalene since it has a relatively high molecular weight compared to that of air (about 5 to 1). Examination of equation (1) shows that the film heat transfer coefficient has a zero value for a zero value of wind velocity, but, as stated, a solar collector will lose heat from its top cover by natural convection under such conditions. Inclusion of a natural convection component in the equation would increase the h_w values particularly at the lower Reynolds numbers.

Additional References

1 Sparrow, E. M., and Tien, K. K., see footnote 1.
2 Tien, K. K., and Sparrow, E. M., see footnote 2.
3 Sparrow, E. M., Ramsey, J. W., and Mass, E. A., see footnote 3.
4 Kreith, F., *Principles of Heat Transfer*, 3rd ed., Intet Press, New York, 1973, pp. 405–407.
5 Sparrow, E. M. and Gregg, J. L., "Laminar Free Convection from a Vertical Plate with Uniform Heat Flux," *Trans ASME*, Vol. 78, 1956, pp. 435–440.

[1] By E. M. Sparrow and K. K. Tien, published in the July 1977 issue of the JOURNAL OF HEAT TRANSFER, pp. 507–512.
[2] By K. K. Tien and E. M. Sparrow, published in Vol. 22, 1979 issue of the *Internation Journal of Heat and Mass Transfer*, pp. 349–359.
[3] By E. M. Sparrow, J. W. Ramsey, and E. A. Mass, published in the April 1979 issue of the JOURNAL OF HEAT TRANSFER, pp. 199–204.
[4] Solar Program Manager, Research Institute, University of Petroleum and Minerals, Dhahran, Saudia Arabia, Mem. ASME.
[5] Research Assistant, Research Institute, University of Petroleum and Minerals, Dhahran, Saudia Arabia.

Authors' Closure

We believe that our correlating equation can be employed for Reynolds numbers substantially higher than the range for which it was originally determined, since the boundary layer should remain laminar for Re $\geq$ 100,000. For flow parallel to a flat plate, it is common to assume that laminar flow persists up to a Reynolds number of 500,000. The inclined plates that formed the basis of our correlation were characterized by favorable pressure gradients, so that laminar flow should persist to Reynolds numbers higher than those for the parallel flow case. Thus, for example, we believe that our correlation should accommodate wind velocities of at least 10 m/s.

With regard to natural convection effects, they were not a factor in our experiments, not only because of the small characteristic dimension of the test apparatus but also because of the small density differences that characterize naphthalene sublimation. In the case of combined-mode heat transfer, it is well known that the contributions of the two modes are not additive.[1] For example, for aiding forced convection and natural convection flow along a vertical plate

$$\mathrm{Nu} \simeq (\mathrm{Nu}_{fc}{}^{3.25} + Nu_{nc}{}^{3.25})^{1/3.25}$$

where fc denotes forced convection and nc denotes natural convection. Thus, even when $\mathrm{Nu}_{nc} = 0.5\ \mathrm{Nu}_{fc}$, it follows that $\mathrm{Nu}/\mathrm{Nu}_{fc} \simeq 1.03$.

[1] Churchill, S. W., *The Interpretation and Use of Experimental Data*, McGraw-Hill, New York, 1974.

The Transition from Natural-Convection-Controlled Freezing to Conduction-Controlled Freezing[1]

G. D. Ashton.[2] The research reported was undertaken to provide fundamental information about the roles of solid-phase conduction and liquid-phase natural convection in determining the rates of freezing. In analyzing their results obtained for a particular geometry, the authors have introduced two new terms to add to our already excessive heat transfer jargon, namely "conduction-controlled freezing" and "convection-controlled freezing." The concepts the authors are describing by these terms can be better conveyed by writing the energy balance equation at the interface in the form

$$q_s - q_L = \rho_s \lambda \frac{ds}{dt} \tag{1}$$

and then examining the relative magnitude of the three terms. In equation (1), q_L is the heat flux to the interface from the liquid and represents the influence of convection. q_s is the conductive flux away from the interface and represents the influence of conduction. ρ_s is the density of the material; λ is the heat of fusion; and ds/dt is the interfacial velocity with a positive value indicating freezing and a negative value indicating melting. The authors use the term "natural-convection-controlled freezing" for the case when $ds/dt = 0$ and the convective flux balances the conductive flux, i.e., $q_s = q_L$. They use the term "conduction-controlled freezing" for the case when $q_L = 0$ and "transitional freezing" for the case when $q_s > q_L$ but $q_L > 0$.

There are several objections to this proposed terminology. First, on a local basis, q_s and q_L are largely uncoupled since both are determined largely by temperature differences relative to the freezing (melting) point of the interface and by the geometry of the respective domains of conduction or convection. The authors' terminology thus refers to the residual of two independent processes. By not relating their observations to the simple energy balance condition of equation (1), the authors have proposed rather generalized terms for phenomena they observed in a highly specific geometry of apparatus that are not capable of being easily extrapolated to more general conditions, and, in fact, could lead to wrong conclusions when applied to other geometries.

Apparently, the temperature of the liquid was measured. If so, it would be useful to have reported the variation of temperature with time particularly for the purpose of quantitatively interpreting the temperature at which dendritic surface growth begins. Dendritic growth is often associated with supercooling of the liquidus. If supercooling did exist, it is even possible to have $q_L < 0$. The logical extension of the authors' terminology would lead to the rather absurd term "convection-augmented freezing."

[1] By E. M. Sparrow, J. W. Ramsey, and J. S. Harris, published in February 1981 issue of the JOURNAL OF HEAT TRANSFER, Vol. 103, No. 1, pp. 7–12.

[2] Chief, Snow and Ice Branch, U.S. Army Cold Regions Research and Engineering Laboratory, Hanover, N.H. 03755.

Authors' Closure

We are sorry that Dr. Ashton did not sense our meaning with regard to the terms natural-convection-controlled freezing and conduction-controlled freezing. By the former, we meant that natural convection plays a significant role in slowing the rate of freezing; i.e., in terms of equation (1) of the Discussion, we meant that q_L is at least as large as q_s. The term conduction-controlled freezing was intended to describe cases where $q_L \ll q_s$, but not necessarily zero.

Authors' Closure

We believe that our correlating equation can be employed for Reynolds numbers substantially higher than the range for which it was originally determined, since the boundary layer should remain laminar for Re $\geq$ 100,000. For flow parallel to a flat plate, it is common to assume that laminar flow persists up to a Reynolds number of 500,000. The inclined plates that formed the basis of our correlation were characterized by favorable pressure gradients, so that laminar flow should persist to Reynolds numbers higher than those for the parallel flow case. Thus, for example, we believe that our correlation should accommodate wind velocities of at least 10 m/s.

With regard to natural convection effects, they were not a factor in our experiments, not only because of the small characteristic dimension of the test apparatus but also because of the small density differences that characterize naphthalene sublimation. In the case of combined-mode heat transfer, it is well known that the contributions of the two modes are not additive.[1] For example, for aiding forced convection and natural convection flow along a vertical plate

$$\mathrm{Nu} \simeq (\mathrm{Nu}_{fc}{}^{3.25} + Nu_{nc}{}^{3.25})^{1/3.25}$$

where fc denotes forced convection and nc denotes natural convection. Thus, even when $\mathrm{Nu}_{nc} = 0.5\ \mathrm{Nu}_{fc}$, it follows that $\mathrm{Nu}/\mathrm{Nu}_{fc} \simeq 1.03$.

[1] Churchill, S. W., *The Interpretation and Use of Experimental Data*, McGraw-Hill, New York, 1974.

The Transition from Natural-Convection-Controlled Freezing to Conduction-Controlled Freezing[1]

G. D. Ashton.[2] The research reported was undertaken to provide fundamental information about the roles of solid-phase conduction and liquid-phase natural convection in determining the rates of freezing. In analyzing their results obtained for a particular geometry, the authors have introduced two new terms to add to our already excessive heat transfer jargon, namely "conduction-controlled freezing" and "convection-controlled freezing." The concepts the authors are describing by these terms can be better conveyed by writing the energy balance equation at the interface in the form

$$q_s - q_L = \rho_s \lambda \frac{ds}{dt} \tag{1}$$

and then examining the relative magnitude of the three terms. In equation (1), q_L is the heat flux to the interface from the liquid and represents the influence of convection. q_s is the conductive flux away from the interface and represents the influence of conduction. ρ_s is the density of the material; λ is the heat of fusion; and ds/dt is the interfacial velocity with a positive value indicating freezing and a negative value indicating melting. The authors use the term "natural-convection-controlled freezing" for the case when $ds/dt = 0$ and the convective flux balances the conductive flux, i.e., $q_s = q_L$. They use the term "conduction-controlled freezing" for the case when $q_L = 0$ and "transitional freezing" for the case when $q_s > q_L$ but $q_L > 0$.

There are several objections to this proposed terminology. First, on a local basis, q_s and q_L are largely uncoupled since both are determined largely by temperature differences relative to the freezing (melting) point of the interface and by the geometry of the respective domains of conduction or convection. The authors' terminology thus refers to the residual of two independent processes. By not relating their observations to the simple energy balance condition of equation (1), the authors have proposed rather generalized terms for phenomena they observed in a highly specific geometry of apparatus that are not capable of being easily extrapolated to more general conditions, and, in fact, could lead to wrong conclusions when applied to other geometries.

Apparently, the temperature of the liquid was measured. If so, it would be useful to have reported the variation of temperature with time particularly for the purpose of quantitatively interpreting the temperature at which dendritic surface growth begins. Dendritic growth is often associated with supercooling of the liquidus. If supercooling did exist, it is even possible to have $q_L < 0$. The logical extension of the authors' terminology would lead to the rather absurd term "convection-augmented freezing."

[1] By E. M. Sparrow, J. W. Ramsey, and J. S. Harris, published in February 1981 issue of the JOURNAL OF HEAT TRANSFER, Vol. 103, No. 1, pp. 7–12.

[2] Chief, Snow and Ice Branch, U.S. Army Cold Regions Research and Engineering Laboratory, Hanover, N.H. 03755.

Authors' Closure

We are sorry that Dr. Ashton did not sense our meaning with regard to the terms natural-convection-controlled freezing and conduction-controlled freezing. By the former, we meant that natural convection plays a significant role in slowing the rate of freezing; i.e., in terms of equation (1) of the Discussion, we meant that q_L is at least as large as q_s. The term conduction-controlled freezing was intended to describe cases where $q_L \ll q_s$, but not necessarily zero.